INTER

International Network on Timber Engineering Research

MEETING FIFTY-FIVE

BAD AIBLING, GERMANY

AUGUST 2022

INTER PROCEEDINGS MEETING FIFTY-FIVE 2022

INTER - International Network on Timber Engineering Research

2014 the International Network on Timber Engineering Research (INTER) was founded.

Scope
Presentation, discussion and documentation of research results in timber engineering and development of application rules for timber design codes or standards related to timber engineering.
Approach
Annual meetings in different countries/places hosted by meeting participants
Presentation and discussion of papers
Peer review of the abstracts before the meeting and of the papers during the meeting
Decision of the acceptance of the abstracts before the meeting by a well-defined review process
Decision of the acceptance of the papers for the proceedings during the meeting
Publication of the papers and the discussion in proceedings
Rules
All decisions including the appointment of the chairperson or the location of annual meetings are made by the participants attending a meeting.
Membership
Persons contributing to or being interested in research related to timber engineering.

INTER

International Network on Timber Engineering Research

Proceedings

Meeting 55

22 - 25 August 2022

Bad Aibling, Germany

Edited by Rainer Görlacher

Timber Scientific Publishing
KIT Holzbau und Baukonstruktionen
Karlsruhe, Germany
2022

Publisher:
Timber Scientific Publishing
KIT Holzbau und Baukonstruktionen
Reinhard-Baumeister-Platz 1
76131 Karlsruhe
Germany
2022

ISSN 2199-9740

Table of Contents

1 List of participants

AUSTRIA	
R Brandner	Graz University of Technology
T Demschner	Stora Enso Wood Products GmbH, Brand
A Eckert	Graz University of Technology
D Glasner	Graz University of Technology
T Hillberger	University of Innsbruck
G Hochreiner	Vienna University of Technology
J Lapere	Stora Enso Wood Products GmbH, Brand
R Maderebner	University of Innsbruck
U Mahlknecht	Graz University of Technology
A Ringhofer	Graz University of Technology
R Sieder	Graz University of Technology
T Stieb	University of Innsbruck
C Vida	Vienna University of Technology
CANADA	
G Doudak	University of Ottawa, Gatineau
F Lam	University of British Columbia, Vancouver
T Tannert	UNBC. Prince George
ESTONIA	
A Just	Tallinn University of Technology
K N Mäger	Tallinn University of Technology
J L Nurk	Tallinn University of Technology
GERMANY	
S Aicher	MPA University Stuttgart
H J Blaß	Karlsruhe Institute of Technology (KIT)
L Buchholz	University fo Stuttgart
G D'Arenzo	University of Kassel
P Dietsch	Karlsruhe Institute of Technology (KIT
R Görlacher	Karlsruhe Institute of Technology (KIT)
H Kreuzinger	Technical University of Munich
U Kuhlmann	University fo Stuttgart
S Mönch	University of Stuttgart
A Münzer	MPA University Stuttgart
M Rauch	Technical University of Munich
C Sandhaas	Karlsruhe Institute of Technology (KIT)
M Schenk	Technical University of Munich

H Schwab	Fraunhofer Institut für Holzforschung
S Schwendner	University of Kassel
W Seim	University of Kassel
K Simon	MPA University Stuttgart
S Siby	MPA University Stuttgart
M Steilner	Karlsruhe Institute of Technology (KIT)
L Stimpfle	MPA University Stuttgart
C Tapia Camu	MPA University Stuttgart
J Töpler	University of Stuttgart
T Uibel	FH Aachen
M Westermayr	Technical University of Munich
K Winter	Technical University of Munich
S Winter	Technical University of Munich
ITALY	
D Casagrande	Istituto per la Bioeconomi, San Michele
Y De Santis	Università degli Studi dell'Aquila
M Fragiacomo	Università degli Studi de l'Aquila
R Scotta	University of Padova
A Polastri	CNR - IBE, Dambel
JAPAN	
A G Aljuhmani	Tohoku University
A Minegishi	Tohoku University
SLOVENIA	
B Azinovic	Slovenian National Building Institute, Ljubljana
SPAIN	
J M Cabrero	Universidad de Navarra, Pamplona
SWEDEN	
T Bader	Linnaeus University, Vaxjö
D Caprio	Chalmers Technical University
H Danielsson	Lund University
R Jockwer	Chalmers Technical University
V Öberg	Chalmers Technical University
M Schweigler	Linnaeus University, Vaxjö
E Serrano	Lund University

SWITZERLAND	
A Frangi	ETH Zurich
S Franke	University of applied sciences BFH, Biel
P Grönquist	ETH Zürich
C Karannagodage	ETH Zürich
M Kleinhenz	ETH Zürich
N Manser	EMPA, Duebendorf
P Palma	EMPA, Duebendorf
S Schilling	ETH Zürich
UNITED KINGDOM	
E Toumpanaki	University of Bristol
L Vojnovic	University of Bristol
USA	
B Yeh	APA - The Engineered Wood Association, Tacoma

2 Minutes of the Meeting

by F Lam, Canada

CHAIRMAN'S INTRODUCTION

P Dietsch welcomed the delegates to the 9th meeting of the International Network of Timber Engineering Research (INTER). In total 74 participants from 12 countries registered of this INTER meeting. He also thanked Simon Aicher, Cristobal Tapia and the team from MPA and Stefan Winter for hosting of this meeting.

This was the 55th meeting of the group including the series of former CIB-W18 meetings. This meeting also constitutes the 4th meeting in Germany, after three meetings in Karlsruhe and one meeting in 1989 in Berlin. INTER continues its tradition of yearly meetings to discuss research results related to timber structures with the aim of transferring them into practical applications.

The chair asked for a minute of silence to remember the loss of two influential timber engineering colleagues last year, Julius Natterer (EPFL) and Heinz Brüninghoff (University of Wuppertal).

Twenty-seven papers were accepted for this meeting including 1 accepted but withdrawn, hence 26 accepted papers were presented. The papers were selected from 38 submitted abstracts based on a review process with 4 acceptance criteria (state of the art, originality, assumed content, and relation to standards or codes). 17 members acted as reviewers and each abstract was reviewed by at least 8 reviewers. Full papers were requested to be submitted one month before the meeting to facilitate distribution to the participants prior to the meeting.

Papers brought directly to the meeting were not accepted for presentation, discussions, or publication. The same rule applied to papers where none of the authors was present or papers which were not defended by one of the authors. The presentations were limited to 20 minutes each, allowing time for meaningful discussions after each presentation. The Chair asked the presenters to conclude the presentation with a general proposal or statement concerning the impact of research results on existing or future potential applications and development in codes and standards.

The topics covered in this meeting were: Structural Design Codes (1), Loading Codes (1), Test Methods (1), Fracture Mechanics (1), Fire (4), Structural Stability (4), Timber Rafters (10), Laminated Members (3), Timber Beams (1), Timber Joints and Fasteners (8), and Timber Columns (1). Numbers in parentheses are the number of papers presented in each topic based on initial allocation.

Next year Inter Meeting will be held in Biel and hosted by S Franke. The Chair suggested that the delegates think about the timing of the meeting as to whether we want to join with WCTE 2023 (June) or stay with our usual time slot near the end of August.

There is an invitation from Shanghai to host the 2024 INTER meeting. The chair asked the delegates to provide feedback on whether this seems feasible.

Information from other organizations.

The revision of Eurocode 5 is in full effect with producing the drafts for official formal enquiry in approximately one year. The first paper to be presented this year covered this work.

CEN/TC 124 activities are still slowed down due to the unclear situation that the European Commission has stopped publishing new or updated product standards in the Official Journal of the European Union until further notice. Currently the European Commission has drafted a revised Construction Products Regulation, the period for feedback by practice has ended mid-July this year.

A new COST Action named HELEN, Holistic design of taller timber buildings, has started this year. It is led by Iztok Šušteršič from Innorenew in Slovenia. https://www.cost.eu/actions/CA20139/

A larger European research initiative, Forest Value, will end its first generation of projects in fall this year. Results will be given at the website forestvalue.org.

U Kuhlmann and J Töpler have started working on a guideline “Finite Element based design of timber structures”.

TIMBER COLUMNS

55 - 2 - 1 In-Plane Buckling of Beech LVL Columns -J Töpler, U Kuhlmann

Presented by J Töpler

H Blass asked if an upper limit of compression strain was applied for the stress strain curve. J Töpler replied no. H Blass asked if the maximum compression strain was observed in the model. J Töpler said the numerical approach information was not available at hand.

G Hochreiner shared his experience on material modelling. The current approach limits plasticity of the compression side. He suggested that consideration of plasticity can lead to good results. J Töpler replied this is similar to the approach with consideration of large imperfections.

B Azinovic asked for an explanation of the boundary conditions and how to eliminate the boundary conditions effect. J Töpler replied that roller bearing was used in the tests and a friction coefficient from the manufacturer was used in the model.

Furthermore, elongation of the column was also needed to account for the column space. J Töpler further confirmed the boundary condition is a hinge.

P Dietsch asked it if is possible to benchmark strain measurements from visual data of the column tests to get MOE. T Töpler replied that the resolution may be too low to get accurate strain results as the camera distance was too far.

A Frangi agreed in general with the test results. He asked about the impact of different inputs to FEM for comparisons with accepted approach with other materials. J Töpler replied in some cases the matching was not perfect. A Frangi asked why the power of 2 on the left side of the equation was used for second order theory. J Töpler said the proposed equation seemed to be consistent with β_c.

TIMBER JOINTS AND FASTENERS

55 - 7 - 1 Head Pull-Through Properties of Self-Tapping Screws - C Sandhaas, H J Blass

Presented by C Sandhaas

S Winter and C Sandhaas discussed the difference in deformation of machine versus transducer measurements. C Sandhaas said the slip in the machine measurements due to screws can be clarified by the definition in the test method. S Winter said f_{head} values can be misleading for different diameters as diameters are mixed. C Sandhaas said steel failures are excluded.

R Brandner commented that using Leijten (2009) equation to obtain compression perpendicular strengths may be inaccurate. He said density influence is there and asked if mean density was considered. C Sandhaas replied that density influence is there but density influence based on individual data points are not clear.

S Aicher commented about EN1383 specimen edge distance requirements and said that requirements for radial and tangential directions are different. He said one may need to glue specimens. C Sandhaas agreed EN1383 needs to be revised. Definition for f_{head} has already changed with the correction factor. They discussed that changes of the f_{head} equation need to be clearly communicated and this could cause confusion. Also one may need to consider this as an intrinsic property.

S Schwendner received confirmation of the large variability observed.

R Jockwer received confirmation that LVDT and machine deformations were not both available for all tests. He asked which deformation should be used. C Sandhaas said the deformation should be based on the acceptable failure of crushing or compression perpendicular to grain.

T Tannert commented that spline joints with head pull through failure mode can have safety factor of 5 here and safety factor of 2 for friction. This can lead to large overstrength. H Blass said this point was commented in paper 55-15-4.

55 - 7 - 2 Performance, Design and Execution of Screwed Steel-Timber End-Grain Connections - M Westermayr, R Brandner, A Ringhofer, U Mahlknecht, J W G van de Kuilen

Presented by M Westermayr

H Blass commented on the factor $k_{mc,k}$=0.82 and asked if one should use a lower factor of say 0.8. M Westermayr agreed. H Blass commented on the embedment length and said partially threaded screws may be more practical for embedment length considerations. M Westermayr agreed.

A Frangi and M Westermayr discussed long term tests with drying and wetting. The specimens after a while did not look good as fungi was found growing even though the tests were prepared carefully. A Frangi suggested some specimens with small eccentricity should be considered. M Westermayr said this was considered in the paper but was not provided in the presentation.

P Dietsch commented that in design for short term EC5 has a k_{mod} factor of 0.9 but the tests show a k_{mod} of rather 0.75. He asked, if 0.9 should still be used. M Westermayr replied maybe one should think about the whole system design approach to bring this in. R Brandner discussed the lower and upper limits of the Wood’s curve and EC5.

S Aicher commented that the TUM’s slope is higher for DOL compared to the TUG’s slope. M Westermayr agreed and will examine this further. S Aicher suggested weighted values using regression.

A Frangi commented that k_{mod} for a connection is important and should consider k_{mod} of timber properties.

55 - 7 - 3 Block Shear Model for Axially-Loaded Groups of Screws - U Mahlknecht, R Brandner, A Ringhofer

Presented by U Mahlknecht

T Tannert and U Mahlknecht discussed that shear perpendicular to grain failure did not happen, but the mechanical model considered load sharing and stress redistribution offered by the material in shear perpendicular to grain with their stiffness values coming from CLT documents.

JM Cabrero asked how the stress concentration factor was developed. U Mahlknecht responded that they were obtained from FEM analysis with parametric studies (0.8 to 1.).

S Winter and U Mahlknecht discussed the failure did not occur as a real block failure but with two main failure planes. S Aicher added that contribution of failure can be observed with saw cutting of the specimen.

R Jockwer questioned whether distribution of screws over the surface can help avoid this failure. U Mahlknecht replied that different arrangements of screw groups could help but one needs to be careful to avoid tension perpendicular to grain failures.

A Frangi and U Mahlknecht discussed what might be the volume of the block shear mode if inclined screws were used.

55 - 7 - 4 Brittle Failures of Connections with Self-Tapping Screws on CLT Plates - J M Cabrero, J Niederwestberg, B Azinović, H Danielsson, Y H Chui, T Pazlar, C Ni

Presented by J M Cabrero

P Dietsch commented that the input properties in the model for different countries are very different. There is a need to harmonize how to measure these properties. JM Cabrero agreed as the brittle failure model relies on input parameters and stiffness information is also important.

T Tannert asked about the eccentricity in the test set up. JM Cabrero said lateral support was provided to counter this.

H Blass asked if slender fasteners also only have failure planes at the fastener tips. JM Cabrero replied mostly in the tip. H Blass commented that in EC5 the thickness of block for shear is different for shear and tension. JM Cabrero said this is a model assumption and seems to work.

S Aicher commented that looking at different scenarios with the variety of layups, engineers would not have control of the laminate thickness, width, etc. JM Cabrero agreed in general; however, this information is needed in advance in terms of where the lamination is with respect to the screws.

A Frangi received confirmation that the connections were originally designed to fail in brittle mode.

G Doudak asked if the observed failure modes agreed with the predicted ones. JM Cabrero said it was difficult to distinguish through observation the exact brittle failure mode.

M Fragiacomo asked if it would be appropriate to use the solid wood approach in EC5 with a statement that this would be a conservative approach. JM Cabrero said this would be too conservative by a factor of 2.

T Demscher and JM Cabrero discussed the contribution of the lateral shear plane.

55 - 7 - 5 Low Cycle Ductility of Self-Tapping Screws - M Steilner, H Kunkel, C Sandhaas

Presented by M Steilner

F Lam commented that this issue is also important in steel-wood-steel connections.

M Fragiacomo commented that it is nice to confirm cyclic tests versus static tests. Tests according to EN 12512 should be revised. One should consider preparing a proposal revision for EN 12512. M Steilner agreed.

55 - 7 - 6 Fatigue Behaviour of Notched Connections for Timber-Concrete-Composite Bridges – Failure Modes and Fatigue Verification - S Mönch, U Kuhlmann

Presented by S Mönch

A Frangi and S Mönch discussed that the safety margins are not consistent. The TCC bridge is only a small part of a larger project. Furthermore, the length of the notch relative to the geometry of concrete can control the failure. A Frangi said material properties of concrete are optimistic (compression and tension strength of 65 MPa and 6 MPa, respectively). S Mönch said test results show even higher values.

M Fragiacomo asked if k_{fat} for notch can be adjusted and whether there is any clear proposal for change. S Mönch said adjustment of k_{fat} for the notch can be considered as a possibility. The fatigue work is aimed at verification only.

H Blass asked about the screw producer. He commented that the inclined compression strut will result in tension force. This is already an issue for the static case as the screw head is embedded in the concrete but is worst for the fatigue case. He said that the failure mode of screws should be considered. U Kuhlmann said partners tested fatigue of screws.

H Kreuzinger discussed the availability of only a small test database including fatigue. He asked, if k_{mod} and k_{fat} should be used in combination.

A Frangi commented that in Switzerland there are TCC applications in commercial building showing good results even without the screw.

55 - 7 - 7 Design of Moment Loaded Steel Contact Connections at the Narrow Face and Side Face of CLT Panels - M Schweigler, T K Bader, S Sabaa

Presented by M Schweigler

S Winter was critical about the robustness of CLT in balconies and said reasonable protection to ensure durability is needed. M Schweigler agreed but replied the method is general and can be applied to other applications. S Winter commented that distribution of stresses perpendicular to grain will change. M Schweigler said this will be researched in future.

E Serrano asked about the stiffness of the steel plate and said that different products will have different stiffness of the lever arm. M Schweigler replied that the steel plate was considered stiff.

G Doudak questioned if the model fits when the plate is not centred and thicker CLT plates are used. M Schweigler replied additional tests showed no influence.

A Frangi commented that this work should not be considered as part of a standard. He asked about moment/shear interaction. M Schweigler replied other work is studying this aspect and no influence can be observed because shear forces are carried by the connectors.

S Franke questioned why the arrangement of connectors between narrow and wide face was changed. M Schweigler replied this was recommended by the commercial partner.

S Franke and M Schweigler discussed evaluation of influence of stiffness by use of nonlinear spring models.

T Demschner discussed possibilities of other applications and the shear force when the steel plate was installed on the edge of the panel and the possibility of development of tensile stress perpendicular to grain. He also commented that engineers would not know the CLT layup a priori. M Schweigler did not think CLT layup is an issue and only small shear force needs to be considered.

P Dietsch commented that the load dispersion concept into CLT using $k_{c,90}$ was not intended for this use.

D Glasner commented that one needs to be careful to account for prestressing effects.

55 - 7 - 8 Reinforced Rigid Glulam Joints with Glued-in Rods Subjected to Axial and Lateral Force Action - K Simon, S Aicher

Presented by K Simon

F Lam received confirmation that the glue was phenolic based.

P Dietsch asked why the edge distances were reduced compared to the ETA. K Simon replied that he wanted to use this according to EC proposal.

P Dietsch asked about the long-term performance of unreinforced end grain case. K Simon replied few EN 408 tests were prepared and seems to be okay, but more tests are needed.

T Tannert received confirmation that the intended failure mode was observed in the unreinforced cases.

S Franke suggested that more tests should be conducted with deeper beams.

S Winter asked why high CV was observed for the reinforced beam. K Simon said it could be density of the wood and failure mode of the wood. S Winter asked what would happen if you do a pure bending case, would the stiffness of the glued in rod also participate in splitting. K Simon replied that in pure bending the rod will pull out.

E Serrano received clarification on the test set up with contact in compression at the end grain. Also the use of 3D load cell provided information on shear force.

R Jockwer commented that with different potential failure modes, embedment strength information from EC5 should fit well. K Simon stated that embedment strength values in EC5 seem to be much conservative. R Jockwer commented that relative edge distance information is useful and asked which interaction proposal should be made for the unreinforced case. K Simon replied that linear interaction.

T Demschner, K Simon and S Aicher discussed load transfer mechanisms in the test set up which may result in increase in measured axial capacity of the bond strength.

F Lam received confirmation that there was no splitting.

A Frangi commented on shear transfer mechanisms of the end grain reinforcement such that even if the bonding is durable the shear transfer is not.

E Serrano commented that it is important to add information on the failure mode of different tests.

TIMBER BEAMS

55 - 10 - 1 Proposed Design Approach for Lateral Stability of Timber Beams - G Doudak, M Mohareb, Yang Du

Presented by G Doudak

H Blass stated that the original bucking equation is based on constant or uniform moment. He asked about the effect of different length factor (US 1.84, Canada 1.92 and EU 1.0). G Doudak replied that load applied on top of the beam is the reason. H Blass said that load cannot be applied on top of the beam if there is a uniform moment. Further E in the wide direction could be different from E in the narrow face and mentioned that the product E · G is taken as mean value in EC 5..

A Frangi stated that the proposal is complicated and asked about imperfections. G Doudak said the equation in the current standard is not usable for many load and support conditions. He said geometric nonlinearity is important but is not considered here.

H Kreuzinger received clarification that it is necessary to run a model to go from unbraced length to obtain effective length.

M Schenk asked if is this needed in the code as there are many cases in the code where solutions are not available. He queried whether this should be part of education for background rather than a code provision. M Schenk and G Doudak discussed the need of information for stiffness and imperfection. There were further comments on how much mechanics is needed in design standards with calculation methods existing outside the code.

U Kuhlmann and G Doudak discussed the differences between European and Canadian approaches with proposal focusing on the buckling range.

G Hochreiner asked about the combined loading case. G Doudak said the Canadian code considers this aspect.

P Dietsch mentioned that a large part of the given systems are already covered in e.g. the German National Annex to EC5 and suggested to study also European literature on this item.

LAMINATED MEMBERS

55 - 12 - 1 Shear Stiffness and Strength of European Ash Glued Laminated Timber - P Palma, R Steiger, T Strahm, E Gehri

Presented by P Palma

P Dietsch asked why k is different for Spruce and Ash. P Palma replied that he is also surprised by the findings of the Spruce results; with decrease in CV one expects decrease in size effect. P Dietsch commented that with the aspect ratio of the specimens, they look more like a diaphragm rather than a beam; however, the beam formula was used. P Palma agreed.

R Jockwer asked if the proposal for EC with k factor of 0.2 only applies to Glulam and if it can be applied to other products such as LVL. Palma said this is for Glulam only. P Dietsch commented that the range of application should be limited.

S Aicher commented that the exponent for Beech Glulam is similar.

F Lam commented that size effect for shear design of glulam in Canadian code is volume dependent with a reference volume of 2 m^3 and k of 0.18. F Lam asked whether the width b being a parameter of study. P Palma agreed but will not examine this now.

C Sandhaas asked if there is any issue of getting Ash. P Palmar said 20% of forest resource in Switzerland is Ash.

55 - 12 - 2 Size Effect of Glulam Made of Oak Wood under Consideration of the Finite Weakest Link Theory - C Tapia, S Aicher

Presented by C Tapia

E Serrano received clarification about the numerical model. In the FEM mesh, a 100 mm cell has 5 FEs lengthwise and one in the depth direction. Gauss integration for each element was performed with an average value taken. Influence of element size was not considered but should be mesh independent. When one element fails, the 100 mm section was removed.

R Brandner and C Tapia discussed the representativeness of the length of 100 mm. In past work on MOE versus strength, a 80 mm volume was found in the literature. R Brandner questioned that the distance between the knots is larger than 100 mm. C Tapia said smaller knots exists and that a representative length 2 or 3 times the size of the large knots would be appropriate. R Brandner asked if other distributions were tried. C Tapia said other distributions have not been tried as the chosen distribution needs to have a theoretical base.

H Blass and C Tapia discussed about RVE versus the size with tests at different lengths.

S Franke received clarification about model correlations.

R Jockwer asked about the tension tests of laminate in relation to the relatively small beam height. He suggested that bending laminate tests are needed for calibration. C Tapia disagreed as the difference is the number of finger joints in small beams.

F Lam commented that the AR approach that assumes statistical dependency with a certain lag, but the Weibull approach is based on statistical independency between elements. This contradiction should be noted. F Lam received clarification about poor tension fit being presented and suggested that clear explanations are needed in the text.

H Danielson and C Tapia discussed that fracture energy in the paper was assumed to be 500 N mm/mm^2 based on fitting.

P Dietsch commented that a load deformation curve based on load control is closer to reality. C Tapia agreed.

55 - 12 - 3 Size Effect of Large Glued Laminated Timber Beams – Contribution to the Ongoing Discussion - C Vida, M Lukacevic, G Hochreiner, J Füssl

Presented by C. Vida

H Blass stated that the cited GLT bending tests were conducted by other institutes such as in Scandinavia. He asked if detailed information on the bending tests and failure modes were considered. C Vida stated that the data was informative.
H Blass commented that in bending tests of GLT, finger joint failures would typically also influence the failure of beams. C Vida said that the model did not consider finger joints as the boards in the model were 5.4 m long. Also the model assumed that finger joints were stronger than boards because knots were cut out before finger jointing. H Blass said that this is a rough assumption and stated that also clear wood stiffness is lower than finger joint stiffness, hence finger joints would attract higher loads.

F Lam agreed with H Blass comments on importance of considering finger joints in models. The UBC database on GLT beams (including 1.2 m deep 21 m long beams) showed that finger joints often govern beam capacity. The CV of these large beams is consistent with the smaller beams. F Lam stated that it would be better to show cumulative probability distributions with data points rather than probability density functions when verifying models. He questioned the assumption of the factor m being size dependent as this contradicts Weibull weakest link theory which is the basis of the size effect model. C Vida said that at the end the size effect provision is based on power law fitting not Weibull.

S Aicher stated that finger joint strengths have large variations and can have an influence on beam bending strength. He asked how MOE's were considered and if there was any correlation between MOE and strength. C Vida replied that KAR was used to determine tensile strengths and was correlated via regression from a different distribution.

C Tapia stated that the size effect curves presented cannot be easily assessed and suggested log-log plots would show clearer trends. Also showing cumulative distributions would be clearer. C Vida replied that rough evaluation with long beam sections were considered, and the model fitted well with characteristic bending strength based on log-normal distribution. Other distributions might have different results. Also 400 simulations with large size beams were conducted.

A Frangi stated that the benchmarking would have a bias if not compared with other data. He stated that he was surprised by such a large difference between the different failure criteria. C Vida replied that the model could have a bias and that he was also surprised by the difference offered by the failure criterions. He stated that with smaller dimension beams, beam theory was used and failure was only depended on bending moments.

P Palma received clarification that in fitting of distributions C Vida did not fit to different ranges.

R Brandner received confirmation that the simulation data base had 140 boards and the simulated 3 m high beams used all these boards. Also most of the boards did not contribute to failure. He stated that a bigger database is needed to be representative, also for width effect considerations.

P Dietsch stated that the model results seemed to show unrealistic lag between occurrence of first crack until final failure. He stated there are large data sets on glulam bending tests in Europe and they should be mirrored in the results of the model. He also questioned whether the minimum CV of 6% for 3 m beams is appropriate. C Vida said that the 1st crack may not correspond to tensile failure of the outer lamina. P Dietsch stated that in this case the model does not represent Frese's failure criterion as stated in the paper. They also discussed the influence of dynamic impact in failure. Both agreed that industry should invest in testing larger GLT beams to clarify the issue.

E Serrano questioned benchmarking a model that does not consider finger joints to models that do consider the influence of finger joints. E Serrano also received confirmation that the model can consider finger joints if data was available.

A Frangi received confirmation that Fink's failure criterion based on stiffness reduction was not used here.

S Aicher stated that the GLT model must consider finger joint failure and its variability. He also mentioned that finger joint failure can have larger variability than knots, as shown in reports of factory production control. MPA Stuttgart has also datasets on large beams. S Aicher stated that one should also examine the N. American data base on GLT beam tests and check N. American m-values.

S Winter stated that size effect in GLT is needed to be considered and asked, if this was common understanding in the group.

TRUSSED RAFTERS

55 - 14 -1 Design of Timber Trusses with Dowelled Steel-to-Timber Connections - S Schilling, N Manser, P Palma, R Steiger, A Frangi

Presented by S Schilling

R Jockwer asked are you designing for nonlinearity. S Schilling replied non-linear information is for research only.

M Fragiacomo asked about the difference in stiffness between SIA and EC5 models as it should be a constant. S Schilling said the EC5 model is currently the one and the new version of EC5 will not change. P Dietsch commented that the EC5 model is intended for a single fastener. There may be a need to consider alternatives for connections.

S Aicher asked about the difference between K_{ser} in parallel and perpendicular directions. S Schilling said tests are only for perpendicular to grain direction and a $k_{parallel}$ to $k_{perpendicular}$ factor of 3 was found. SIA has a factor of 2.

G Hochreiner commented that in the level of normal design maybe a more sophisticated approach is needed.

P Dietsch commented that S Egner at KIT is working on combination of loads in connections.

STRUCTURAL STABILITY

55 - 15 - 1 Multilinear Load-Displacement Relationship of LFT Shear Walls Based on Code Regulations - S Schwendner, W Seim, G D'Arenzo

Presented by S Schwendner

M Fragiacomo asked about the prediction of stiffness from experimental results. EC results were based on predictions. α factor was not used for prediction of strength where K_m factors were used. S Schwendner said $\tau\eta\varepsilon$ α factor can be easily applied, and ductility is the important aspect for consideration.

D Casagrande asked about the stiffness of the hold-down and angle bracket. How would α change if connection stiffness are considered in future codes. S Schwendner responded that the α approach can be established for connections but database for connections are needed. D Casagrande commented that nail properties can be improved. S Schwendner said nail properties cannot be used directly for stiffness of assembly.

A Frangi questioned α factors for staples. S Schwendner agreed that more refinements can be made.

G Doudak expressed concerns that explanations were not given why values were adjusted. Adjustment of code to match test results without explanations may be a concern. S Schwendner agreed as the finding were simply based on 50 or so test results from literature.

55 - 15 - 2 A Proposal for Evaluating the Lateral Displacements of Multi-Storey CLT Lateral Load Resisting Systems - D Casagrande, G D'Arenzo, I Gavric, G Doudak

Presented by G D'Arenzo

P Dietsch and G D'Arenzo discussed the analytical and cantilever approach giving largest contributions from sliding and rocking. Panel deformation may be considered relatively small especially for common hold-downs and angle brackets.

T Tannert commented about cumulative overturning that assumed floor and diaphragm can rock individually. G D'Arenzo is aware of this aspect and the model has a limitation. Further work is needed.

T Tannert stated in most tests angle brackets tested may have different boundary conditions for the single storey case versus a multi-storey case as multi-storey wall systems have more degrees of freedom. G D'Arenzo said the paper has information that the model can address this aspect.

S Winter stated that timber concrete floors tend to be more rigid. He received clarification of the deformation mechanism of multiple walls.

S Winter asked what is the recommendation for practice. G D'Arenzo said more dissipative elements may be desirable. D Casagrande added elastic behaviour is considered here whereas seismic cases need to consider yielding, energy dissipation and ductility.

H Blass commented that buckling of CLT elements may be important with large vertical loads. G D'Arenzo responded that boundary conditions are an adjustment factor that can be used and agreed that vertical loads in tall building can lead to CLT deformations.

T Demscher has concerns about having to model this in FEM. G D'Arenzo responded that the plan is to generalize the analytical approach to buildings.

55 - 15 - 3 Rocking Capacity Model of CLT Walls with Openings and Timber Plasticization - Y De Santis, A Aloisio, M Sciomenta, M Fragiacomo

Presented by Y De Santis

G Hochreiner and Y De Santis discussed limitations of the model which considers central openings only.

G Doudak received clarification that the existing EC model does not account for openings and the model under discussion considers in-plane deformability of the panel and stress block. G Doudak said the two rocking behaviours are dependent on λ and asked what about the hold-down connection stiffness versus the lintel stiffness. De Santis agreed that this is a parameter that has an influence.

D Casagrande and D Santis discussed how to find the lever arm and how to account for other failure modes based on capacity-based design concept.

A Frangi commented that one tries to avoid compression perpendicular to grain stresses in tall buildings with continuous walls and how to account for this as well as for connected walls. J De Santis said that wall on concrete foundation cases would work for continuous walls. In connected walls, the stiffness of the connection is considered more.

W Seim received confirmation that the panel and lintel were assumed strong enough and did not check for their failures.

T Demschner asked about testing for validation. De Santis said testing with openings was not done. T Demschner commented cutting of the openings would be an issue in practice.

A Polastri commented that stiffness of the hold-down is an important parameter.

P Dietsch questioned the stress block assumptions. De Santis said that his FEM model confirmed them.

S Schwendner and De Santis discussed the impact of the vertical load.

55 - 15 - 4 Capacity-Based Design of CLT Shear Walls with Hyperelastic Hold Downs - T Tannert, A A Oyawoye, M Popovski

Presented by T Tannert

F Lam asked about the strength degradation characteristics under repeated loading in relation to low damage claims. T Tannert said the strength degradation occurred primarily in the spline connection and yielding of the steel which could be improved by capacity-based design of these components.

P Dietsch said optimization of the spline connection is needed with more clear determination of their resistance. T Tannert agreed and said the use of plywood spline is easy for installation.

U Kuhlmann said the system is based on a sequence of failure and steel yielding is an over stress. T Tannert said yielding in the spline defines the capacity of the shear wall. Yielding of the steel rod would not be catastrophic. U Kuhlmann asked if aging tests of the rubber were done. T Tannert said the choice was bridge bearing rubber which should be quite safe.

H Blass asked where designers would get information on the spline capacity. T Tannert said the Canadian code requires information on mean and 95 percentile values of yielding of the connection. This however is not readily available to the designers and would need to be tested in house.

M Fragiacomo was surprised that Canadian structural design of LCT shear walls requires elastic performance of the hold-downs. T Tannert said leading companies come up with innovative solutions. The standardization committee based their decision on concrete wall design philosophy.

G Doudak asked how the spline joints contribute to energy dissipation when hold-downs do not dissipate energy.

T Tannert discussed the analogy that angle brackets can contribute in energy dissipation only in uplift and not in sliding, so shear keys with oval shaped slot are typically used now.

G Doudak said the original work on CLT shearwalls requires energy dissipation of the angle brackets and asked whether this system can meet the Rd Ro target. T Tannert said he does not know and will work on this.

W Seim asked if there was any time history analysis with strain rate consideration and asked about overall building performance. T Tannert said no strain rate consideration was done and the whole building performance is under consideration.

A Polastri questioned whether one can have this large uplift with this hold-down. T Tannert said inter-story drift of 5% was intended as limitation of the hold-down system. He acknowledged the floor will be lifted.

FIRE

55 - 16 - 1 Influence of Temperature Resistance of Bond Lines on Charring of Glulam Beams - A Just, S Aicher, J L Nurk, M Henning

Presented by A Just

S Winter disagreed with the conclusions. 1) EC5 acceptance of the results in full range would need information on the type of glue tested, beam cross section, layup details, and density. 2) He commented about 3 side charring with rate of 0.7mm/min. He commented about the uncertainties in fire tests and discussed the differences in performance of different adhesives. 3) He commented about different charring depths with different methods for the side and edge. He could not see a real need to consider different charring rate for different directions. 4) As lamination thickness is not known a priori for design, he questioned whether one needs to recalculate after lamination thickness is known. S Aicher said that detailed information will be available in a workshop for adhesive suppliers and will be open to public soon. S Aicher said that there is extreme difference in adhesive behaviour for temperature about 250 °C. Classification of adhesives based on fire behaviour will be available. He commented that extreme care was needed in selection of laminae to eliminate laminae effects and make the results more repeatable.

S Winter asked if there was any observation of falling down of laminae in glulam fire tests. A Just said are we sure of the suitability of adhesive of CLT for use in GLT. Falling down of laminae in GLT fire tests was not observed.

P Palma and A Just discussed if fire testing of twin beams in a chamber might have influenced the results.

BJ Yeh asked if any charred layer fell off in poor performing adhesives. A Just said it must have fallen off but was not clearly observable.

BJ Yeh and A Just discussed difference between charring directions and whether bondline integrity was maintained or not.

H Blass commented that the data showed difference in performance between different adhesives which could not be ignored; hence, the only solution is to take the worst case. S Aicher said that poor performing adhesive manufacturers are aware of the results and are working to improve their product performance. K Mäger said that the intent of the project was to compare different test methods and confirm the charring rate.

A Frangi was not happy with the results but was prepared to accept them. He commented that in EC5 adhesive class will be proposed to distinguish the differences in performance. A Just agreed that the information will be opened and will need to discuss with manufacturers. S Aicher commented as we have different strength classes for timber, we are proposing similar philosophy for adhesives in fire. S Winter stated that it would be important to find a solution with which you don’t point on producers.

55 - 16 -2 The Effective Width of Cross-Laminated Timber Rib Panels in Fire - M Kleinhenz, A Frangi, A Just,

Presented by M Kleinhenz

H Blass commented about shear deformation. Rigid connection for the GLT and rolling shear deformation in the CLT.

M Kleinhenz replied that the gamma method or advanced gamma method was considered. In long members shear was not a problem. Consideration of the cross layer showed real stress distribution for comparison with the simplified stress distribution.

M Fragiacomo commented that the width of the rib reduced a lot which would affect the glueline between the CLT and GLT. M Kleinhenz responded that the model would overestimate the temperature of the glueline as the falling off of charred material was assumed to occur instantaneously which is conservative.

55 - 16 - 3 Fire Design Methods for Timber Frame Assemblies – an Improved Model for the Separating Function Method - M Rauch, N Werther, A Just, S Winter

Presented by M Rauch

K Mäger received confirmation that a calibration method can be found in PhD thesis. They also agreed that the current method is more conservative when the number of protection layer increases. M Rauch said for long fires, the problem was the quasi-mechanical behaviour. M Rauch added that different input values were used and the stone wool would stay in place.

A Frangi and M Rauch discussed the long fire performance and the choice of temperature criterion. The criterion of 270 °C was used for wood-based boards. For other materials different values should be considered. A Frangi referred to the chosen power equation and questioned whether there is a need for such precision given the variability. M Rauch agreed but this was based on test results.

55 - 16 - 4 The Fire Protection of Timber Members using Gypsum Boards - A Just, M Rauch, J Walker, N Werther

Presented by A Just

P Dietsch and A Just confirmed the findings that TFA with void has a later failure time and TFA filled with mineral wool is the worst. A Just said in cases of CLT with gypsum, wood can absorb the heat while mineral wool does not. P Dietsch and A Just discussed how this might affect failure time of CLT.

S Winter said in terms of failure times spacing of members and fasteners has an influence on the failure of gypsum boards. M Rauch said fastener spacing was not considered. A Just added that the worst case was considered and agreed that this aspect could be examined further.

A Frangi and A Just discussed the observed increases were based on the 20th percentile. The choice of 20th percentile was based on the intent to have the 1st barrier as safe as possible. One can consider the mean value and this issue warrants further investigation and discussions.

S Winter stated that for insulated void cavity, there should be no airgaps between insulation and wood assembly.

FRACTURE MECHANICS

55 - 19 - 1 Beams with Notches or Slits – Extensions of the Gustafsson approach - E Serrano, R Jockwer, H Danielsson

Presented by E Serrano

P Dietsch asked if the authors were aware of test data that can be used to benchmark their numerical results. E Serrano said original database was available but do not have data on small β.

H Blass questioned the choice of 20 mm crack length defined as failure for critical load. Would the conclusion be different if different crack length was used. E Serrano explained that the influence is not that important as 10 to 30 mm would be a reasonable choice based on fracture mechanics. FEM versus analytical solutions would yield slight difference.

G Hochreiner and E Serrano discussed the issue of lone versus multiple internal forces and assumption of stress distribution based on the original work of Gustafsson.

S Aicher asked why not consider the more realistic situation of the notch having a curvature which would change the energy release. E Serrano said this was a choice and said that the micro angle length should be practically considered. P. Dietsch commented the hole and notch conditions need to be differentiated in terms of potential to add curvature in practice.

R Brander asked why used f_v=3.5 rather than 2.5 in the analysis. E Serrano said that the curve would be shifted slightly.

TEST METHODS

55 - 21 - 1 Contribution to the Testing, Evaluation and Design of Cross Laminated Timber (CLT) in Respect to Rolling Shear - D Glasner, A Ringhofer, R Brandner, G Schickhofer

Presented by D Glasner

H Blass commented that the overlap/overhang at the support will have an influence and questioned about its consideration in the data. D Glasner agreed in general.

H Blass asked about the meaning of FE modeling as rolling shear strength depends on annual ring orientation. D Glasner said that the approach considered system properties where influence of annual ring orientation would be masked. H Blass said thah smeared shear stress can be considered here.

H Blass did not understand the need for the criterion of f_r. He asked why not just use max load. In cases where bending failures occurred rolling strength estimated based on max load would still be conservative. D Glasner responded that rolling shear cracks would typically occur before bending failure hence rolling shear mode governed. H Blass disagreed as max load should be considered. D Glasner said final failure would always be single bending failure but rolling shear failure occurred first. H Blass stated max load is needed for design. A Ringhofer commented that experimental conditions were different from real conditions. H Blass said one should test under realistic conditions as the recommended approach is too conservative.

T Tannert said as the proposed empirical equation only depended on lamination thickness would a_1 be important. D Glasner said a_1 should be dependent on CLT and this has always been considered. Also volume dependency is noted.

T Tannert asked would there be dependency on species and edge gluing conditions. D Glasner said both non edge glued and edge glued material were considered. Past research indicated that with larger board aspect ratio edge gluing influence can be neglected. Only softwood species was considered.

S Aicher said that one has to treat rolling shear strength as an intrinsic property for design. He preferred 4 point bending tests with realistic conditions. One should examine this problem with a more scientific approach including anisotropic behaviour. Gaps between boards also have a large influence. D Glasner responded that gaps could be included as reduction factor.

H Danielsson received confirmation that rolling shear stiffness was not considered.

P Dietsch disagreed with the notion of replacing observations in experiments by interpretation of load-deformation curves.

S Aicher added that a method for intrinsic properties should show failure relative to the target test properties. A Ringhofer disagreed because ETA for CLT would always lead to bending failures.

LOADING CODES

55 -101 -1 Proposed Design Methodologies for Timber Assemblies Subjected to Blast Loading - G Doudak, C Viau, D Lacroix

Presented by G Doudak

F Lam received clarification that that trial-and-error loading procedures did not cause damage accumulations in the specimens and readings from dynamic load cells were able to estimate the strength of the specimen adequately.

T Tannert asked if the DIF factors were established with matched specimens. G Doudak said that matched specimens were considered at the start of the program. T Tannert said only far field conditions were considered and asked about the near field consideration. G Doudak said far field represented explosion occurring 20 to 100 m away. Near field consideration would be too complicated.

R Jockwer asked if this information can be applicable to other loadings. G Doudak said earthquake conditions may be applicable although cyclic loading should be considered. Also collapse from fire loading may be applicable. R Jockwer asked if conclusions on ductility would be applicable to these cases. G Doudak ductility consideration in this study would be out of plane only whereas seismic conditions could be both out of plane and in plane. F Lam disagreed that this information can be applicable to seismic cases. Along with the points already stated, damping considerations are important in seismic situation and this would not be considered appropriately here.

H Blass asked about the DIF for connections. G Doudak said that only one DIF for the system should be used although he disagreed with the approach as failure mode is important. H Blass said that the research is based on stud wall tests and asked how to consider system behaviour of different components. G Doudak said that different components were also tested but stud failures dictated the DIF.

U Kuhlmann received confirmation that the design was based on average strength and not the 5th percentile.

P Palma asked about the importance of considering the load reversal. G Doudak said that in design you only need to consider positive pressure but have to detail for negative pressure.

STRUCTURAL DESIGN CODES

55 -102-1 EN 1995-1-1 for CEN Formal Enquiry –The Evolution of the Design of Timber Structures - M Schenk, S Winter

Presented by M Schenk

R Jockwer asked what will happen to new knowledge and content as the draft is already being finalized. M Schenk said other CEN documents or amendment documents may be suitable. National Annex and European Technical Approvals are also available; National level for design is also available. S Winter stated that there will not be any amendments within a 2 year period and totally new knowledge is beyond the "state of the art".

G Doudak asked about the logic behind putting some information in the Annex. M Schenk said that normative alternatives are to be avoided and the information in the Annex should be supplemental with provisions of expanded or extended methods.

T Tannert asked what would happen if a single country vote NO to the approval process in 2025. M Schenk said the vote is based on majority and it is also a weighted vote.

U Kuhlmann stated that if the approved version has some mistakes, then possibility of early amendments should be available.

G Hochreiner and M Schenk discussed the target user group of the Eurocode as well-trained engineers with 3 years of experience.

P Dietsch commented about the number of added pages being very large and stated that the suitability of items in the Annex which are only relevant for few countries should be reviewed. A National Annex might be more appropriate. M Schenk agreed in principle. However, he stated the number of pages may not be important as we have electronic version. He agreed that it is more important to consider what do we need in the code.

S Aicher questioned why an informative annex is needed for expanded tube fasteners as a national annex may sufficeS Winter stated that this issue was considered in the past as some countries may need this type of information and some may not. S Aicher also stated that it is questionable to place a proprietary system in a code even more if the used products have no harmonized standards or ETAs.

M Fragiacomo stated that Annex M is important for seismic design. EC 8 specifically asked for this information.

NOTES

One note was presented by R Jockwer.

ANY OTHER BUSINESS

U Kuhlmann presented information on an initiative on the development of guidelines of FE based design of timber members.

M Schweigler provided information on ICEM 20 Wood Mechanics and Timber Engineering 2 to 7 July 2023 Porto Portugal.

Finalized papers should arrive at Rainer Görlacher latest at the end of September.

VENUE AND PROGRAMME FOR NEXT MEETING

S Franke invited the participants to the 2023 INTER meeting in Biel Switzerland.

Date: August 20 to 24, 2023

Possible Venue for future meetings:

2024 Padua, Italy (based on feedback from participants, the venue for Shanghai China was postponed).

2025 Turkey

2026 Chile (as an option)

CLOSE

The Chair thanked S Aicher and S Winter for hosting this meeting. Thanks especially to C Tapia and S Aicher and the team for the organization around this meeting.

The Chair thanked R Görlacher for his work for INTER throughout the year and congratulated him on 40 years membership in CIB W-18 and INTER.

The Chair thanked F Lam for his support and advice during the meeting. The INTER meeting minutes are key to perpetuate the important discussions which form the foundation of this group.

3 INTER Papers, Bad Aibling 2022

55 - 2 - 1	In-Plane Buckling of Beech LVL Columns -J Töpler, U Kuhlmann
55 - 7 - 1	Head Pull-Through Properties of Self-Tapping Screws - C Sandhaas, H J Blass
55 - 7 - 2	Performance, Design and Execution of Screwed Steel-Timber End-Grain Connections - M Westermayr, R Brandner, A Ringhofer, U Mahlknecht, J W G van de Kuilen
55 - 7 - 3	Block Shear Model for Axially-Loaded Groups of Screws - U Mahlknecht, R Brandner, A Ringhofer
55 - 7 - 4	Brittle Failures of Connections with Self-Tapping Screws on CLT Plates - J M Cabrero, J Niederwestberg, B Azinović, H Danielsson, Y H Chui, T Pazlar, C Ni
55 - 7 - 5	Low Cycle Ductility of Self-Tapping Screws - M Steilner, H Kunkel, C Sandhaas
55 - 7 - 6	Fatigue Behaviour of Notched Connections for Timber-Concrete-Composite Bridges – Failure Modes and Fatigue Verification -S Mönch, U Kuhlmann
55 - 7 - 7	Design of Moment Loaded Steel Contact Connections at the Narrow Face and Side Face of CLT Panels - M Schweigler, T K Bader, S Sabaa
55 - 7 - 8	Reinforced Rigid Glulam Joints with Glued-in Rods Subjected to Axial and Lateral Force Action - K Simon, S Aicher
55 - 10 - 1	Proposed Design Approach for Lateral Stability of Timber Beams - G Doudak, M Mohareb, Yang Du
55 - 12 - 1	Shear Stiffness and Strength of European Ash Glued Laminated Timber - P Palma, R Steiger, T Strahm, E Gehri
55 - 12 - 2	Size Effect of Glulam Made of Oak Wood under Consideration of the Finite Weakest Link Theory - C Tapia, S Aicher
55 - 12 - 3	Size Effect of Large Glued Laminated Timber Beams – Contribution to the Ongoing Discussion - C Vida, M Lukacevic, G Hochreiner, J Füssl
55 - 14 - 1	Design of Timber Trusses with Dowelled Steel-to-Timber Connections - S Schilling, N Manser, P Palma, R Steiger, A Frangi
55 - 15 - 1	Multilinear Load-Displacement Relationship of LFT Shear Walls Based on Code Regulations - S Schwendner, W Seim, G D'Arenzo

55 - 15 - 2 A Proposal for Evaluating the Lateral Displacements of Multi-Storey CLT Lateral Load Resisting Systems - D Casagrande, G D'Arenzo, I Gavric, G Doudak

55 - 15 - 3 Rocking Capacity Model of CLT Walls with Openings and Timber Plasticization - Y De Santis, A Aloisio, M Sciomenta, M Fragiacomo

55 - 15 - 4 Capacity-Based Design of CLT Shear Walls with Hyperelastic Hold Downs - T Tannert, A A Oyawoye, M Popovski

55 - 16 - 1 Influence of Temperature Resistance of Bond Lines on Charring of Glulam Beams - A Just, S Aicher, J L Nurk, M Henning

55 - 16 - 2 The Effective Width of Cross-Laminated Timber Rib Panels in Fire - M Kleinhenz, A Frangi, A Just,

55 - 16 - 3 Fire Design Methods for Timber Frame Assemblies – an Improved Model for the Separating Function Method - M Rauch, N Werther, A Just, S Winter

55 - 16 - 4 The Fire Protection of Timber Members using Gypsum Boards - A Just, M Rauch, J Walker, N Werther

55 - 19 - 1 Beams with Notches or Slits – Extensions of the Gustafsson approach - E Serrano, R Jockwer, H Danielsson

55 - 21 - 1 Contribution to the Testing, Evaluation and Design of Cross Laminated Timber (CLT) in Respect to Rolling Shear - D Glasner, A Ringhofer, R Brandner, G Schickhofer

55 -101 -1 Proposed Design Methodologies for Timber Assemblies Subjected to Blast Loading - G Doudak, C Viau, D Lacroix

55 -102-1 EN 1995-1-1 for CEN Formal Enquiry –The Evolution of the Design of Timber Structures - M Schenk, S Winter

In-plane buckling of beech LVL columns

Janusch Töpler, Institute of Structural Design, University of Stuttgart, Germany

Ulrike Kuhlmann, Institute of Structural Design, University of Stuttgart, Germany

Keywords: Stability, in-plane buckling, beech LVL, imperfections, experimental results, numerical modelling, Finite Element based design, effective length method

1 Introduction

Glulam made of beech laminated veneer lumber (beech LVL) is increasingly used in timber construction, due to improved availability and high strengths and stiffnesses, especially for columns in multi-storey buildings and high-rise buildings.

Beech LVL columns in building practice are usually at risk of in-plane buckling and can currently be designed according to EN 1995-1-1 (2004) with the equivalent length method (ELM; EC5, section 6.3.2) or interaction equations with calculation of internal forces according to second order theory (T2O; EC5, section 6.2.4). These design methods were developed for softwood columns (EHLBECK & BLAß (1987)). A validation of these design methods for beech LVL by means of experimental investigations has not yet been carried out. Differences between design of softwood and hardwood column are to be expected, since on the one hand the stress-strain relationships of the materials parallel to the grain differ significantly (EHRHART ET AL. (2021 b)), and on the other hand the production-related imperfections (bow) may be different.

Figure 1.1. Buckling test of a beech LVL column with length x width x height = 2500 x 200 x 200 mm.

Within the Cluster of Excellence *Integrative Computational Design in Architecture and Construction* (IntCDC) (KUHLMANN ET AL. (2022)) 27 buckling tests on beech LVL columns were carried out by the Institute of Structural Design at the MPA Stuttgart in spring 2022 (Figure 1.1), in order to determine the buckling behaviour of beech LVL columns.

This paper presents the experimental results of 27 buckling tests (Figure 1.1) and preceding tests for determination of the modulus of elasticity of each test specimen and the stress-strain curve of beech LVL under compression parallel to the grain. Subsequently, a numerical model was developed and validated using the experimental results. Based on numerical calculations with nominal values for geometry, material and bow imperfections the maximum load-bearing capacities for in-plane buckling of beech LVL columns were determined and a provisional safe-sided design proposal was developed. This derivation follows the design method *Numerical design with direct resistance check* as it is defined in TÖPLER ET AL. (2022) or prEN 1993-1-14 (2022). The findings are compared with literature and current design rules.

Incorporated in the investigations are results of the DIBt research project P 52-5-13.194-2048/19 (KUHLMANN & TÖPLER (2022 b)), where, among others, bow imperfections of beech LVL columns and beams were measured in newly erected buildings.

This paper is intended to form a basis for the derivation of the in-plane buckling verification of beech LVL columns.

2 State of the art

EN 1995-1-1 (2004) gives two design approaches for slender timber columns, the effective length method (ELM) and design verification based on calculation of internal forces according to second order theory (T2O).

In ELM the compression strength is reduced by the factor k_c, accounting for second order effects (geometrically nonlinear behaviour) and to a certain extend also for materially nonlinear behaviour. The formulas for determination of k_c in EN 1995-1-1 (2004) can be derived directly from the verification according to T2O assuming a linear interaction of axial force and bending moment as demonstrated by SCHÄNZLIN (2022). It is necessary to consider that the compressive strength parallel to the grain $f_{c,0,k}$ was determined on test specimen with a relative slenderness ratio λ_{rel} = 0.3. Therefore, a reduction of the relative slenderness (λ_{rel} – 0.3) is applied. k_c depends on the β_c factor which covers the effects of bow imperfections and the ratio of $E_{0,05} : f_{c,0,k} : f_{m,k}$. β_c may also be used accounting for plasticizing in compression parallel to the grain. $\lambda_{rel,0}$ and β_c were defined based on the numerical investigations by EHLBECK & BLAß (1987) on softwood columns made of glulam (grade I and II, DIN 4074 (1958)) and solid timber (grade II) including stochastic material modelling and measured geometrical imperfections. For softwood columns made of glulam β_c = 0.1 (≙ bow imperfection of $e_y \approx$ L/1100) and for solid timber β_c = 0.2 (≙ bow imperfection of $e_y \approx$ L/470) were determined.
Effects of load eccentricities and sway imperfections (e.g. for design of cantilever columns, see SCHÄNZLIN (2022)) should be considered separately.

When internal forces are determined using T2O, the interaction formula for verification according EN 1995-1-1 (2004) includes a squaring of the axial force component, which was derived empirically based on the investigations of BUCHANAN ET AL. (1985). The equivalent bow imperfections given in EN 1995-1-1 (2004) for T2O (e_y = L/400) are not the same as assumed within ELM, but on the safe side.

For columns made of spruce glulam GL 24h and GL 32h FRANGI ET AL. (2015) and for beech glulam GL 40h, GL 48h and GL 55h EHRHART ET AL. (2019) experimentally and numerically determined lower load-bearing capacities (up to 18 %) than those obtained by ELM with β_c = 0.1 according to EN 1995-1-1(2004). This is partly due to the larger assumed imperfections (e_y = L/380 to L/570) and partly because of a different ratio of $E_{0,05} : f_{c,0,k} : f_{m,k}$ for beech glulam.

In the current revision process of Eurocode 5 (prEN 1995-1-1 (2021)) the mentioned parts and formulas of ELM and T2O for in-plane buckling are kept largely unchanged, but issues of the application limits of ELM and the named inconsistencies of imperfection assumptions are discussed.

3 Experiments

3.1 General

Buckling tests on 27 beech LVL columns made of GL75 according to ETA-14/0354 (2018) were conducted in order to experimentally determine the buckling behaviour and serve as validation for a FE model, which is subsequently used to assess the characteristic buckling resistance. Additional relevant input values for the FE model are the modulus of elasticity and the stress-strain curve for compression parallel to the grain, which were determined in preceding tests. The test specimens were wrapped in vapour-proof foil during the test period to prevent changes in the wood moisture content. The test specimens are given in Table 3.1.

Table 3.1. Beech LVL GL75 test specimens for buckling and preceding elastic 4-point bending tests

Series number	Number of specimens	Length [mm]	Width x Height [mm²]	λ_{rel} [1]	Orientation of lamellae	Load eccentricity
S01 - S03	3	3000	120 x 120	1.88	flatwise	Width / 10
S04 - S06	3	3000	160 x 160	1.41	flatwise	Width / 10
S07 - S09	3	3000	200 x 200	1.13	flatwise	Width / 10
S10 - S12	3	2500	200 x 200	0.94	flatwise	Width / 6.7
S13 - S15	3	2500	200 x 200	0.94	edgewise	Width / 10
S16 - S18	3	2500	200 x 200	0.94	flatwise	Width / 10
S19 - S21	3	2500	200 x 200	0.94	flatwise	Width / 20
S22 - S24	3	2000	200 x 200	0.75	flatwise	Width / 10
S25 - S27	3	2000	200 x 200	0.75	edgewise	Width / 10

[1] Calculated with $E_{0,05}$ = 16469 N/mm² and $f_{c,0}$ = 76.9 N/mm²

3.2 Preceding elastic 4-point bending tests

For each column test specimen one elastic 4-point bending test according to EN 408 (2010) was conducted to determine the bending modulus of elasticity $E_{L,m}$ (Figure 3.1). The orientation of the lamellae was chosen along the column tests (Table 3.1).

The results are summarized in Table 3.2. $E_{L,m}$ is in good agreement with previous test results (KUHLMANN & TÖPLER (2022 a)) and literature (e.g. EHRHART ET AL. (2021 a)), indicating a low wood moisture content (approximately 6 to 7 %).

Table 3.2. Results of elastic 4-point bending tests on beech LVL GL75

	Mean	COV
Modulus of elasticity $E_{L,m}$ [N/mm²]	16469	0.048
Density ρ [kg/m³]	803	0.011

3.3 Preceding compression tests parallel to the grain

Five compression tests parallel to the grain according to EN 408 (2010) were conducted to determine the compression strength $f_{c,0}$ and the stress-strain curve of beech LVL GL75 (Figure 3.2). The dimensions were chosen to length x height x width = 300 x 120 x 50 mm³ to correspond with compression tests for determination of the compressive strength $f_{c,0,k}$ of GL75 carried out by DILL-LANGER (2014). The ratio height / width = 6 also defines $\lambda_{rel,0}$. The orientation of the lamellae was parallel to the short side (width).

The vertical deformations were measured with two displacement transducers at both sides of the test specimens over a length of 230 mm (Figure 3.2).

Exemplary, Figure 3.3 shows the axial force-deformation curve of test specimen 2_1. On the horizontal axis the mean of both displacement transducers is displayed. The vertical axis exhibits the machine force. The curve is linear elastic up to approx. 65 %

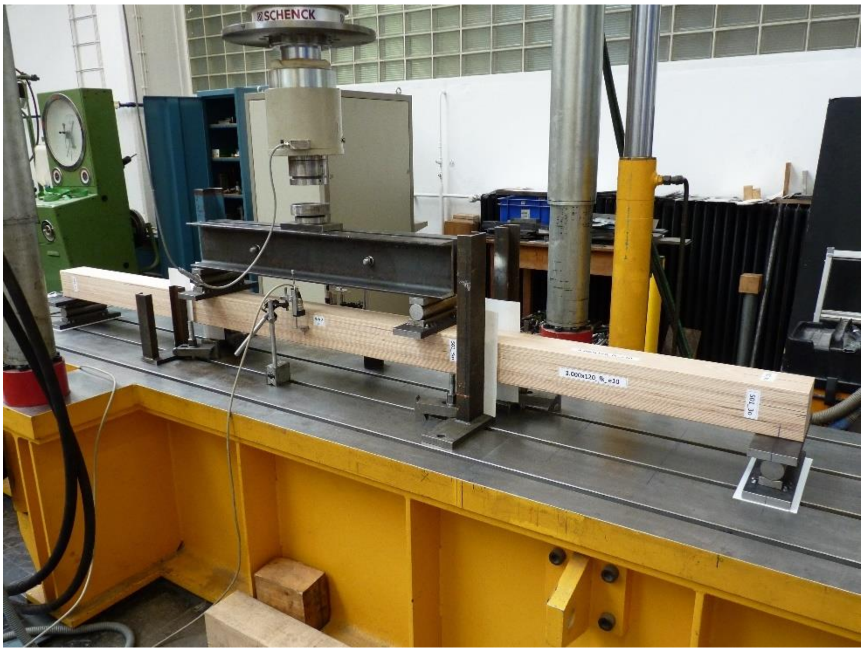

Figure 3.1. Elastic 4-point bending test with length x width x height = 2500 x 200 x 200 mm³.

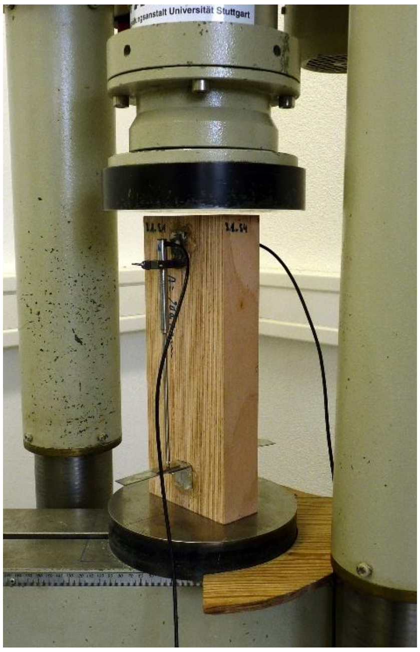

Figure 3.2. Compression test parallel to the grain.

of F_{max}. Subsequently, a considerable plasticising occurs until the compressive strength $f_{c,0,2}$ is reached, followed by a drop in load. During plasticising, a visible buckling of the fibres occurred at the corners of the test specimen and, after reaching the compressive strength, the fibre buckling (partly in the form of a kink band with an inclination of approx. 45 °) spread over the entire cross-section. In the evaluation, the beginning of plasticising / proportionality limit $f_{c,0,1}$ (Figure 3.3, point 1) is defined as the point, at which the total strains ε_{el+pl} exceed the linear elastic strains $\varepsilon_{el} = \sigma / E_{c,0}$ by 5 %. The mean results of the tests are summarized in Table 3.3.

Table 3.3. Results of 5 compression tests parallel to the grain on beech LVL GL75

	Mean	COV
Compression strength $f_{c,0,2}$ [N/mm²]	76.9	0.038
Proportionality limit $f_{c,0,1}$ [N/mm²]	48.1	0.189
Plastic strain $\varepsilon_{pl,0,2}$ when reaching $f_{c,0,2}$ [-]	1.26 x $\varepsilon_{el,0,2}$	0.188
Modulus of elasticity $E_{c,0}$ [N/mm²]	16216	0.030
Density ρ [kg/m³]	798	0.004

The scatter of $f_{c,0,2}$ and the $E_{c,0}$ is very low, which is due to the fact that all test specimens were fabricated from the same residual piece of a column test specimen and that the material was very homogeneous.

The large plastic strains of beech LVL are remarkable (Table 3.3). For softwood, $\varepsilon_{pl,0,2} = 0.25 \times \varepsilon_{el,0,2}$ according to GLOS (1978) is usually assumed. For beech LVL the experimentally determined plastic strains $\varepsilon_{pl,0,2}$ are 4 to 6.5 times higher.

Fortunately, the experimental data of EHRHART ET AL. (2021 b) could be evaluated to validate the own results. These values are presented in Table 3.4. This evaluation of the strains was based on the cylinder displacement and is therefore subject to some uncertainty. The plastic strain was determined to $\varepsilon_{pl,0,2} \approx 1.5 \times \varepsilon_{el,0,2}$ and the proportionality limit to $f_{c,0,1} \approx 0.75 \times f_{c,0,2}$. For high moisture contents (u = 16.9 %, service class (SC) 2) smaller plastic strains $\varepsilon_{pl,0,2} \approx 1.15 \times \varepsilon_{el,0,2}$ were observed.

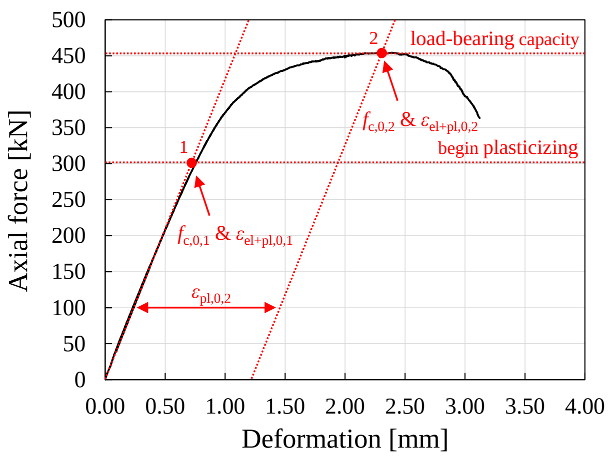

Figure 3.3. Axial force-deformation curve of compression test 2_1, including important points for derivation of stress-strain curve.

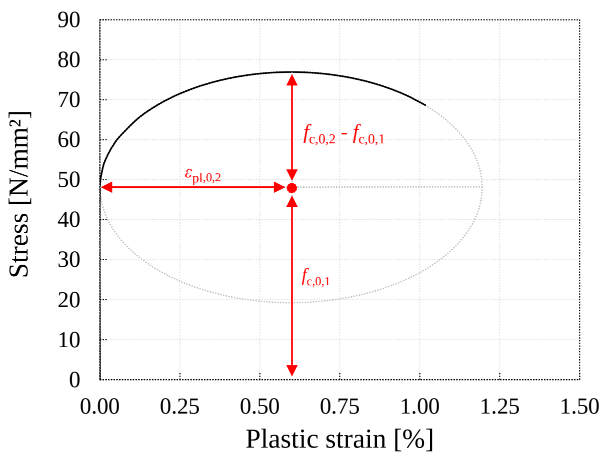

Figure 3.4. Mean stress-plastic strain curve mapped by an ellipse with radii $\varepsilon_{pl,0,2}$ and ($f_{c,0,2}$ - $f_{c,0,1}$), values derived from the compression tests.

Table 3.4. Evaluation of the stress-strain curves of compression tests parallel to the grain on beech LVL by EHRHART ET AL. (2021 b), mean values with (COV), 6 tests per moisture content

Moisture content [%]	$E_{c,0}$ [N/mm²]	$f_{c,0,2}$ [N/mm²]	$f_{c,0,1}$ [N/mm²]	$\varepsilon_{pl,0,2}$ [-]	*Ellipse for plasticising* $\varepsilon_{pl,0,2}$ [x $\varepsilon_{el,0,2}$]	$f_{c,0,2}$ - $f_{c,0,1}$ [x $f_{c,0,2}$]
6.1	16156 (0.026)	80.4 (0.011)	59.3 (0.030)	0.0076 (0.116)	1.52 (0.103)	0.26 (0.058)
7.0	16052 (0.025)	73.1 (0.031)	56.1 (0.027)	0.0076 (0.133)	1.66 (0.118)	0.23 (0.062)
8.9	15828 (0.01)	64.0 (0.014)	49.8 (0.020)	0.0061 (0.068)	1.50 (0.054)	0.22 (0.082)
16.9	14815 (0.039)	39.1 (0.034)	29.4 (0.150)	0.0030 (0.064)	1.14 (0.061)	0.25 (0.379)

The plastic strains can be mapped by means of an ellipse (Figure 3.4) as proposed by GROSSE (2005), where ($f_{c,0,2}$ - $f_{c,0,1}$) and $\varepsilon_{pl,0,2}$ represent the ellipse radii. Numerical comparative calculations modelling plasticising with such an approach show good agreement with the experimental results.

Based on the results in Table 3.3 $\varepsilon_{pl,0,2} = 1.25 \times \varepsilon_{el,0,2}$ and $f_{c,0,1} = 0.65 \times f_{c,0,2}$ are chosen for further calculations.

3.4 Column tests

3.4.1 General

Buckling tests on 27 beech LVL columns made of beech LVL GL75 were conducted in a 15 MN testing facility at MPA Stuttgart in order to experimentally investigate the buckling behaviour and serve as validation for a FE model. The column dimensions (slenderness), load eccentricity and lamellae orientation were varied.

3.4.2 Test programme, setup and execution

The test specimens, dimensions, orientations of lamellae and load eccentricities are given in Table 3.1. The dimensions were chosen to represent typical values of medium slender columns in building practice. As the flatwise bending strength is expected to be lower, this orientation was chosen as default. To force an in-plane buckling in a defined direction, the axial load was applied eccentrically.

Tilting bearings were arranged at the column top and base in order to allow for an unrestricted rotation around one axis (Figure 1.1). The structural system thus corresponds to Euler buckling mode 2 with a minimal rotational spring at the supports. The rotation points of the tilting bearings had a distance of 153 mm and 154 mm to the column surface. The load eccentricity was realised via a similar offset of the columns at both tilting bearings. As protection when the columns fail, horizontal timber beams were arranged to prevent the test specimen from falling out of the test facility (Figure 1.1). Loading was applied displacement-controlled from the bottom at a speed of 2 mm/min. The first load cycle was conducted up to 80 kN and the second load cycle until failure of the column. The measurements were conducted with the optical measuring system ARAMIS Adjustable 12M, which very precisely determined the position of defined points in space in time steps (here every 10 s) by means of digital image correlation. For this purpose, a stochastic pattern was applied onto two sides of the test specimens at midspan (Figure 1.1). This was supplemented by measurement points attached to the supports. The measuring system was set up at a 45 ° angle to the sides of the columns in order to measure two sides in parallel (according to direction of view in Figure 1.1). Beforehand, the member dimensions and the weight were documented.

3.4.3 Results and evaluation

The horizontal and vertical deformations at midspan and at the supports and the rotations at the supports were analysed. The results of column S01 are not shown because there the bottom support was realised differently so that high friction occurred and the bearing acted as a restraint.

The horizontal deformations at midspan U_y and the corresponding axial forces F are exemplary displayed in Figure 3.5 for column S08. The curve is non-linear from the beginning. After the load-bearing capacity F_{max} was reached, the horizontal deformations U_y increased significantly with a moderate load drop until the brittle failure of the test specimen occurred. This behaviour was the same for all columns, with different maximum load-bearing capacities F_{max} (192 to 1634 kN) and maximum horizontal deformations U_y (60 to 190 mm).

The experimentally determined normalised load-bearing capacities k_c of all columns are plotted in Figure 3.6 over the relative slenderness ratio λ_{rel}. The data show a very low scatter and follow well the expected shape of a buckling curve. k_c and λ_{rel} are computed using the measured modulus of elasticity of each column and $f_{c,0}$ = 76.9 N/mm². N_{crit} is calculated with $E_{L,m}$ = 16469 N/mm² (Figure 3.2).

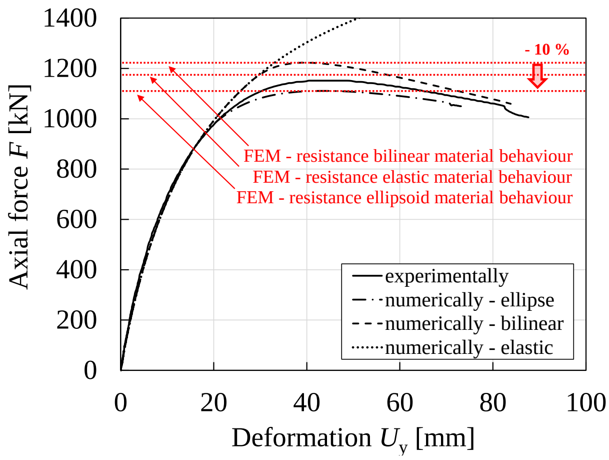

Figure 3.5. Axial force F and horizontal deformation U_y at midspan of column S08 with length x width x height = 2500 x 200 x 200 mm³, experimental and numerical results considering different material models.

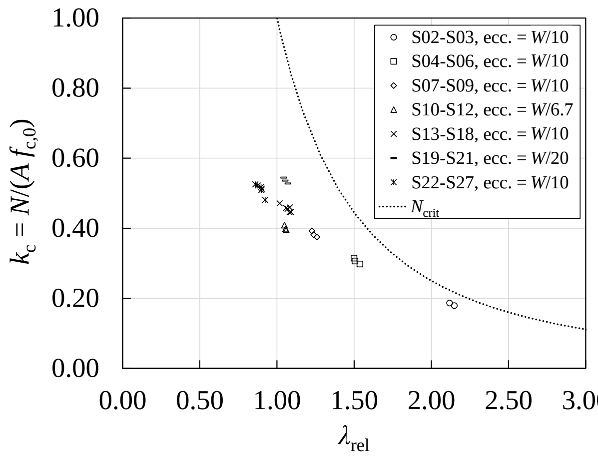

Figure 3.6. Experimentally determined, normalised load-bearing capacities k_c of columns S02 to S27 plotted over the slenderness ratio λ_{rel} with variing eccentricity depending on the width W.

Figure 3.7. Column S22 after failure; test specimen "jumped" out of the tilting bearings when failure occurred.

Figure 3.8. Combined tensile and transverse tension/shear failure at midspan of column S20.

Figure 3.9. Fibre buckling over the entire width of the compression zone of column S23.

A crackling sound indicated coming failure in most cases. Rarely (2 of 27), a localized tensile failure occurred at the tension side of the cross-section, before failure of the whole cross-section. The failure of the cross-section took place suddenly, with a loud bang and consisted of a tensile failure at the tension side of the section and a combined transverse tension/shear failure, which expanded to different extent towards the supports (Figure 3.8). When failing, the column sometimes "jumped" out of the supports due to the released energy (Figure 3.7). The tensile fracture was usually strongly defibrated over a length of up to 80 cm (Figure 3.8). The combined transverse tension/shear failure occurred in several planes (Figure 3.8) and, in the case of stocky columns, sometimes led to a splitting of the cross-section over the entire width and length. In the case of flatwise bending, the failure arose over a longer area; in the case of edgewise bending, the failure was rather punctual and led to a pronounced kink at midspan. For stockier columns, minor fibre buckling occurred at the cross-section corners in the compression zone, along 0.25 to 0.75 of the column length. In some cases, kink bands extended across the entire cross-section width at midspan (Figure 3.9).

4 Numerical simulations

4.1 General

The numerical calculations were executed with a FE model in Abaqus/CAE 2020. The aim was to create a model for analysing in-plane buckling of beech LVL columns and to verify and validate it according to TÖPLER ET AL. (2022) or prEN 1993-1-14 (2022).

4.2 Numerical modelling, model verification and validation

The columns were modelled with measured geometry and material values for validation and nominal geometry and material values in all other cases. At this stage, no imperfections were considered. 20-node quadratic brick elements with a mesh fineness of 50 elements in length, 10 elements in height and 4 elements in width were chosen. For considering a minimum friction coefficient of 0.02 in the tilting bearings according to manufacturer's specifications, a rotational spring was implemented, which generated a comparable moment. An orthotropic material model with linear elastic material properties according to Table 4.1 and a bending / tensile strength of f_m = 100 N/mm² was used.

Table 4.1. Material properties for modelling of beech LVL columns (see KUHLMANN & TÖPLER (2022 a))

E_L [N/mm²]	E_R [N/mm²]	E_T [N/mm²]	G_{LR} [N/mm²]	G_{LT} [N/mm²]	G_{RT} [N/mm²]	ν_{LR} [-]	ν_{LT} [-]	ν_{RT} [-]
16469	840	966	909	1006	50	0.3127	0.5167	0.1978

L = longitudinal, R = radial, T = tangential; 1st index = force direction, 2nd index = deformation direct.

Plasticising in compression was implemented via the von Mises yield criterion, as only longitudinal stresses and strains are of relevant magnitude. An elliptical stress-plastic strain curve according to Figure 3.4 with $f_{c,0,2}$ = 76.9 N/mm², $f_{c,0,1}$ = 0.65 x $f_{c,0,2}$ and $\varepsilon_{pl,0,2}$ = 1.25 x $\varepsilon_{el,0,2}$ was assumed.

Within the verification a sensitivity check and a discretization check according to TÖPLER ET AL. (2022) or prEN 1993-1-14 (2022) were conducted. A detailed report is given by BRÜGEL (2022).

For model validation, a numerical analysis was conducted for each column test considering the measured geometries and moduli of elasticity. The experimental and numerical results were compared. For column S08 the experimentally and numerically determined load-deformation curves are displayed in Figure 3.5. The values agree well, although the numerically determined load-bearing capacities are usually slightly lower (mean 1.6 %, for S08: 3.7 %). This systematic deviation may be due to a too low assumed spring stiffness at the supports in the model.

In the design method *Numerical design with direct resistance check* according to TÖPLER ET AL. (2022) or prEN 1993-1-14 (2022), the reliability of the numerical model (model uncertainty) should be evaluated using the model factor γ_{FE} according to Eq. (1). The experimentally and numerically determined load-bearing capacities R_{test} and R_{check} deviate from each other by a maximum of 5.6 %. The mean value is m_x (R_{test} / R_{check}) = 1.016, the coefficient of variation is V_x (R_{test} / R_{check}) = 0.023 and k_n = 1.76 (EN 1990 (2010)). The model factor can be determined to a very low value of γ_{FE} = 1.026. Characteristic load-bearing capacities R_k can be obtained using numerically computed load-bearing capacities R_{check} with Eq. (2).

$$\gamma_{\mathrm{FE}} = \frac{1}{m_{\mathrm{x}}(1 - k_{\mathrm{n}} V_{\mathrm{x}})} \tag{1}$$

with m_x mean value of the ratio $R_{\mathrm{test}}/R_{\mathrm{check}}$

R_{test} measured load-bearing capacity / resistance

R_{check} computed load-bearing capacity / resistance

k_n characteristic fractile factor according to EN 1990 (2010), Annex D, Table D.1 (V_X unknown)

V_x coefficient of variation of the ratio $R_{\mathrm{test}}/R_{\mathrm{check}}$

$$R_{\mathrm{k}} = \frac{R_{\mathrm{check}}}{\gamma_{\mathrm{FE}}} \tag{2}$$

The numerical model could thus be verified and validated and the calculated load-bearing capacities agree very well with experimental results. For the verification based on the design approach *Numerical design with direct resistance check* the partial factor for the material failure is assumed to be kept according to the standards.

4.3 Parameter study, results and evaluation

4.3.1 Input

The parameter study was carried out to investigate the buckling behaviour of beech LVL using the verified and validated numerical model. No load eccentricity was considered, but a sinusoidal bow imperfection e_y. In terms of cross-sectional dimensions, only λ_{rel} significantly affects the buckling behaviour (Brügel (2022)). Therefore, the length is varied between 6 x width and 50 x width, for a fixed width x height = 200 x 200 mm².

In deviation from section 4.2, the following nominal (characteristic) material values according to ETA-14/0354 (2018) were assumed for **beech LVL GL75**: E_L = 15300 N/mm², $E_R = E_T$ = 400 N/mm² and $G_{LR} = G_{LT}$ = 760 N/mm². Only the results for service class SC1 with $f_{m,k}$ = 75 N/mm² and $f_{c,0,k}$ = 59.4 N/mm² are shown, as the adjustments of the strengths depending on the size effect and service class according to ETA-14/0354 (2018) have no significant influence on the buckling behaviour (Brügel (2022)). To achieve k_c ($\lambda_{\mathrm{rel,0}}$ = 0.412) = 1.0, the compressive strength $f_{c,0,k}$ was increased iteratively in the numerical model to the corresponding value $f_{c,0,\mathrm{mod}}$ (see discussion of Figure 4.1). This procedure implies that the test specimens, on which the compressive strength $f_{c,0,k}$ was determined, were also imperfect (with e_y = L/1500). Such an assumption is important in terms of mechanical consistency (also for T2O). For determination of $\lambda_{\mathrm{rel,0}}$ an Euler buckling mode 2 was assumed.

In the research project DIBt P 52-5- 13.194-2048/19 (Kuhlmann & Töpler (2022 b)), imperfection measurements were carried out on 4 buildings with 95 columns and beams made of beech LVL. The mean value of the determined bow imperfections of the columns was $m_x(e_y)$ = L / 3040, the standard deviation $s_x(e_y)$ = L / 5160 and the 95 % quantile value $e_{y,95}$ = L / 1660. Therefore, a bow imperfection of e_y = L / 1500 has been assumed in the parameter study.

Finite element analyses (FEA) with 4 different material models were conducted for GL75: (a) elliptical plastic strains and $f_{c,0,k}$, (b) elliptical plastic strains and $f_{c,0,mod}$, (c) bilinear elasto-plastic material behaviour and $f_{c,0,mod}$, (d) linear elastic material behaviour and $f_{c,0,mod}$.

For comparison with design methods in EN 1995-1-1 (2004) and literature, FE calculations were also performed on **glulam GL 24h** with nominal (characteristic) material values according to EN 14080 (2013): E_L = 9600 N/mm², E_R = E_T = 250 N/mm², G_{LR} = G_{LT} = 540 N/mm², G_{RT} = 54 N/mm², $f_{m,k}$ = 24 N/mm² and $f_{c,0,k}$ = 24 N/mm². To achieve k_c ($\lambda_{rel,0}$ = 0.331) = 1.0, $f_{c,0,k}$ was increased iteratively in the numerical model to the corresponding value $f_{c,0,mod}$. A bow imperfection of e_y = L/1100 was applied.

FEA with 3 different material models were conducted for GL 24h: (a) elliptical plastic strains ($\varepsilon_{pl,0,2} = 0.25 \times \varepsilon_{el,0,2}$ and $f_{c,0,1} = 0.75 \times f_{c,0,2}$) and $f_{c,0,mod}$, (b) bilinear elasto-plastic material behaviour and $f_{c,0,mod}$, (c) linear elastic material behaviour and $f_{c,0,mod}$.

Structural imperfections were neglected, since for the independent input variables material parameters and geometric imperfections characteristic and 95 % quantile values were used. It is assumed that these safe-side assumptions cover negative influences of structural imperfections.

4.3.2 Results and discussion

The computed normalised load-bearing capacities k_c of beech LVL GL75 are plotted in Figure 4.1 over the relative slenderness ratio λ_{rel}. The diagram is supplemented with calculation results of ELM with β_c = 0.1, T2O with e_y = L/1500 and the critical buckling load N_{crit}. The shaded area highlights the difference between ELM and FEA with elliptical plasticising. It can be shown that the adjustment $f_{c,0,mod}$ is necessary to obtain accurate results for slenderness $\lambda_{rel,0}$. Nevertheless, the numerically determined load-bearing capacities using a realistic plasticising approach are up to 15 % below the results of calculations with ELM and T2O (see shaded area). The curves of ELM and T2O agree well with numerical results with bilinear or linear elastic material behaviour under compression. The influence of the plastic material behaviour is also illustrated in Figure 3.5 for column S08 where, assuming bilinear material behaviour, 10 % higher load-bearing capacities can be achieved than with the realistic assumption of plasticising according to Figure 3.4. It has to be concluded that the reduction of the stiffness *EI* due to plasticising significantly reduces the load-bearing capacity of medium slender columns (λ_{rel} = 0.4 to 1.3). For GL 24h a slightly less pronounced reduction of the load-bearing capacities from FE analyses can also be observed in comparison with ELM (Figure 4.2).

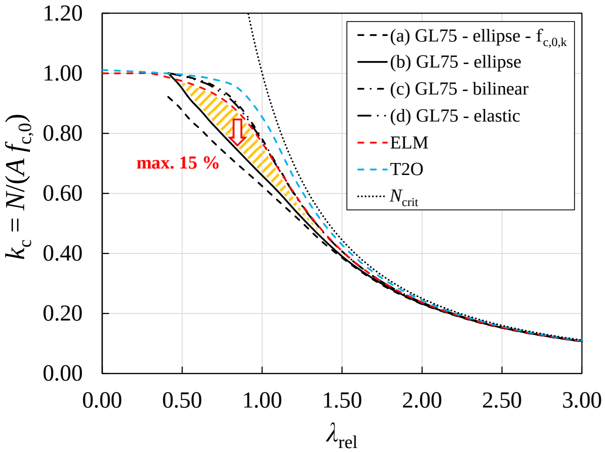

Figure 4.1. Numerically determined buckling curves of ***beech LVL GL75*** *in comparison with T2O and ELM, the shaded area is the difference between ELM and FEA with elliptical plasticising.*

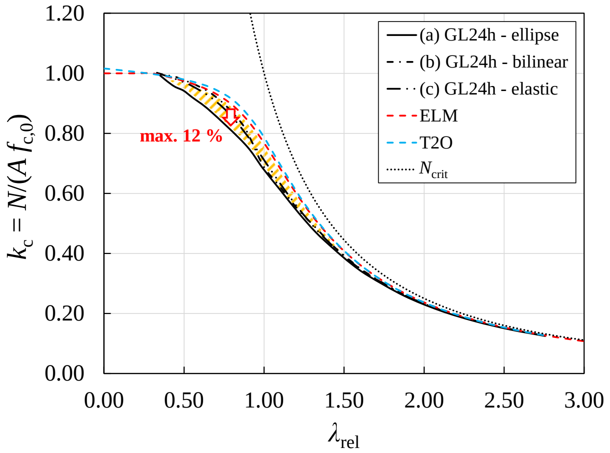

Figure 4.2. Numerically determined buckling curves of ***glulam GL 24h*** *in comparison with T2O and ELM, the shaded area is the difference between ELM and FEA with elliptical plasticising.*

Possible reasons for the deviations between ELM and FEA are discussed below:

- FE model itself: Since it showed very good agreement with the experimental investigations this reason can be ruled out.
- Input parameters of FEM: β_c in ELM method was derived based on extensive numerical investigations by EHLBECK & BLAß (1987) with scattering input parameters for material (*Karlsruher Rechenmodell*) and bow imperfections using the Monte Carlo method. The characteristic buckling curve was determined from 5 % fractile of the load-bearing capacities. As a simplification, in the FE model presented in this paper characteristic and 95 % quantile values were used for material parameters and geometric imperfections. It is expected, that these two different approaches (full probabilistic with Monte Carlo method vs characteristic input values) may lead to differences. However, differences of up to 12 % can probably not be explained by this.
- Geometrical imperfections: As these are chosen according to EHLBECK & BLAß (1987) for GL 24h, this cannot be the reason.
- Structural imperfections: Their neglect should have a positive impact on the load-bearing capacities from FEA, if any.
- Size effect on tensile / bending strength: As the load-bearing capacity of the presented numerical model was always governed by the peak of the load-deformation curve (Figure 3.5), where tensile stresses were still lower than $f_{m,k}$, this can be ruled out.
- Plasticising – values of assumed stress-strain curve: For the presented comparative calculations of GL 24h the proportionality limit $f_{c,0,1}$ and the plastic strain $\varepsilon_{pl,0,2}$ were chosen according to GLOS (1978) and EHLBECK & BLAß (1987).
- Plasticising – reduction of bending stiffness *EI*: The reduction of the bending stiffness *EI* due to plasticising and the modelling of this behaviour (ellipsoid stress-strain or bilinear stress-strain) plays a decisive role for the column behaviour, see Figure 4.1 and Figure 4.2.

- Models from literature – model uncertainty: In the past, usually strain-based models were used for the investigations of the load-deformation behaviour of timber columns (EHLBECK & BLAß (1987), THEILER (2014), FRANGI ET AL. (2015), EHRHART ET AL. (2019)).
  Results of the strain-based model of THEILER (2014) (see Figure 4.9 in THEILER (2014)) were recalculated with the FE model presented here. Differences of load-bearing capacities were below 2 %. As the strain-based model of THEILER (2014) was, except for negligible simplifications, identical to the one of EHLBECK & BLAß (1987), the different modelling techniques (strain-based and FEA) should not have a significant influence.

From this discussion it is concluded that the deviations of load-bearing capacities between ELM and own numerical calculations for GL 24h (Figure 4.2) are mainly caused by different input parameters (full probabilistic vs characteristic values). For beech LVL GL75 the deviations of ELM and own numerical calculations (Figure 4.1) are additionally increased by the high plastic strains of beech LVL.

5 Design proposal

Based on the safe-side approach considering nominal values for strengths, stiffnesses and bow imperfections and without redefining the partial safety factor in a full probabilistic approach, for the design verification of slender beech LVL columns made of GL75 (ETA-14/0354 (2018)) following adaptions (red) of the effective length method (ELM) in EN 1995-1-1 (2004) may be applied:

$$\frac{\sigma_{c,0,d}}{k_c\, f_{c,0,d}} \leq 1 \tag{3}$$

$$k_c = \frac{1}{k + \sqrt{k^2 - \lambda_{rel}^2}} \tag{4}$$

$$k = 0.5\left(1 + \beta_c\left(\lambda_{rel} - \lambda_{rel,0}\right) + \lambda_{rel}^2\right) \tag{5}$$

$$\beta_c = k_{pl} \cdot \frac{e_y}{L} \cdot \pi \sqrt{\frac{3 \cdot E_{0,05}}{f_{c,0,k}}} \cdot \frac{f_{c,0,k}}{f_{m,k}} \tag{6}$$

with	$\lambda_{rel,0} = 0.4$	critical relative slenderness ratio of beech LVL GL75
	$k_{pl} = 6$	factor accounting for the bending stiffness reduction due to plasticising of beech LVL GL75 (empirically derived from FEA)
	$e_y / L = 1 / 1500$	bow imperfection of beech LVL GL75

Alternatively, β_c = 0.3 may be assumed.

The mechanically correct decomposition of β_c based on SCHÄNZLIN (2022) allows to adjust β_c depending on material parameters and bow imperfections. The additional introduction of the factor k_{pl} accounts for the bending stiffness reduction due to plasticising. Thereby, the different effects are clearly separated. Alternatively, similar results are achieved by assuming a value of β_c = 0.3.

For design verification based on calculations of second order theory (T2O) it is proposed to account for the effects of plasticising on the bending stiffness *EI* by adapting the equivalent bow imperfections $e_{y,equ}$ analogous to Eq. (6):

$$e_{y,equ} = k_{pl} \cdot e_y \tag{7}$$

Results of the adapted design methods ELM with β_c = 0.3 and T2O in Figure 5.1 show good agreement with the numerically determined characteristic load-bearing capacities of beech LVL columns. It remains to be discussed whether T2O should generally be adapted to account for k_c ($\lambda_{rel,0}$) = 1.0 (see modification of $f_{c,0,k}$ in Figure 4.1). The experimental results are also well represented by the proposed design equations (Figure 5.2). The slight overestimation (5 %) of the load-bearing capacities with the modified ELM occurs in both numerical (Figure 5.1) and experimental results (Figure 5.2) for 0.5 ≤ λ_{rel} ≤ 1.0 due to the shape of the k_c curve.

Creep, load eccentricities and sway imperfections should be considered separately. Application limits of ELM for large external bending moments should be considered.

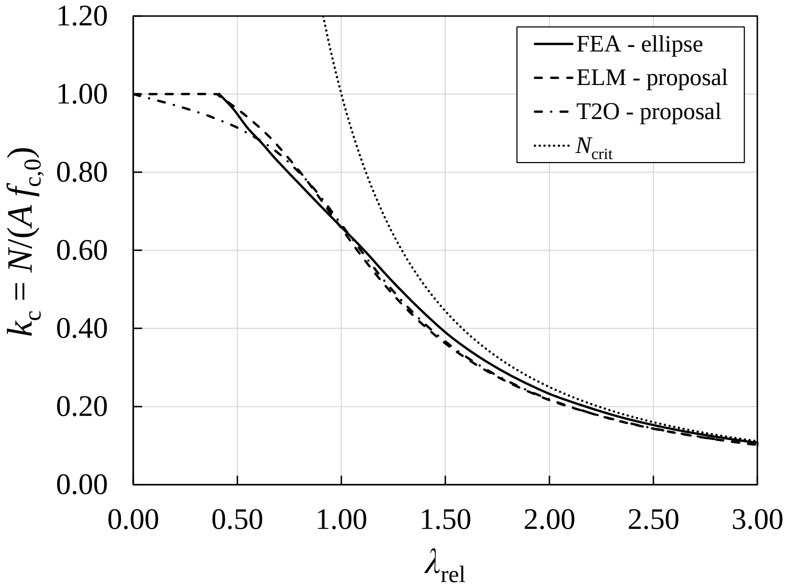

Figure 5.1. Numerically determined buckling curves of beech LVL GL75 in comparison with proposed adapted T2O and ELM.

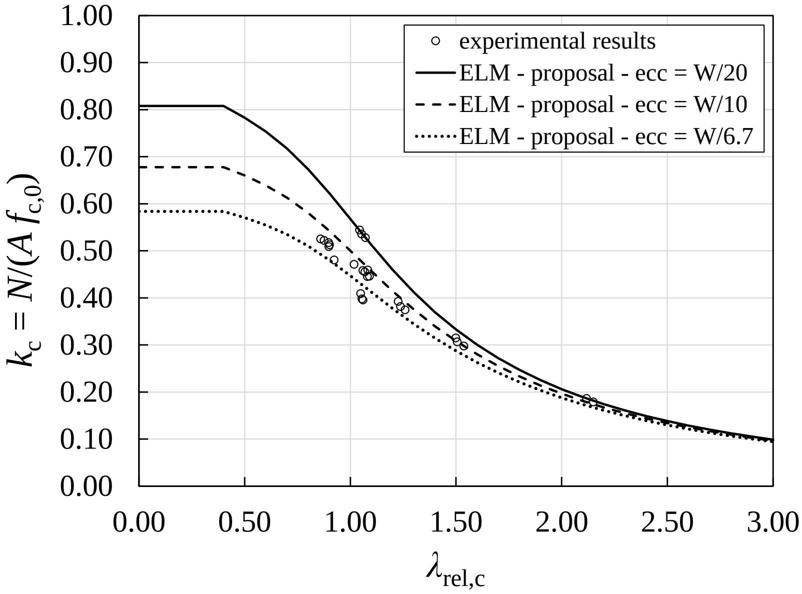

Figure 5.2. Experimentally determined, normalised load-bearing capacities k_c in comparison with proposed adapted ELM.

6 Summary and outlook

This paper aims to study the in-plane buckling behaviour of columns made of beech LVL GL75 (ETA-14/0354 (2018)) with extensive experimental and numerical investigations.

Results of 27 buckling tests on full size timber columns and preceding tests to determine the bending modulus of elasticity and the stress-strain behaviour under compression parallel to the grain are described. The experimentally determined normalised load-bearing capacities k_c of the columns show only minor scattering and follow well the expected shape of a buckling curve (Figure 3.6 and Figure 5.2). All columns experience large horizontal deformations (> 60 mm) before failure. The maximum load-bearing capacity was not determined by the first point of partial failure, but by the peak of the load-deformation curve (Figure 3.5). From the preceding compression tests, it is concluded, that plasticising before reaching the compressive strength $f_{c,0,2}$ has a significant influence and should be considered for beech LVL GL75. The mean value of the proportionality limit (beginning of plasticising) for compression parallel to the grain was observed at 65 % of the compression strength ($f_{c,0,1} \approx 0.65 \times f_{c,0,2}$) and plastic strains of 4 to 6.5 times the elastic strains ($\varepsilon_{pl,0,2} \approx 1.25 \times \varepsilon_{el,0,2}$) occurred when the compression strength $f_{c,0,2}$ was reached.

A numerical model for analysing the in-plane buckling behaviour of beech LVL columns was developed, verified and validated by the experimental results according to TÖPLER ET AL. (2022) or prEN 1993-1-14 (2022). The mean and maximum deviations of experimental and numerical load-bearing capacities were 1.6 % and 5.6 %.

Based on measurements on columns and beams made of beech LVL, a bow imperfection of e_y = L / 1500 was included in the numerical calculations.

The numerical calculations revealed that the load-bearing capacity of medium slender beech LVL columns is up to 15 % smaller compared to the current verifications according to ELM, which is to a large extend due to plasticising reducing the bending stiffness *EI*.

Based on the experimental and numerical investigations, an adjustment of β_c = 0.3 and $\lambda_{rel,0}$ = 0.4 is recommended for the design of columns made of beech LVL GL75 using the effective length method (ELM). For calculations according to second order theory (T2O) an adaption of the equivalent bow imperfection $e_{y,equ} = k_{pl} \times e_y$ is proposed (with e_y = L / 1500 and k_{pl} = 6 for beech LVL to account for a reduced bending stiffness *EI* due to plasticising).

Future investigations on the effects of statistical scattering in form of a reliability analysis may allow for further modifications.

7 Acknowledgements

The research was supported by the Deutsche Forschungsgemeinschaft (DFG, German Research Foundation) under Germany´s Excellence Strategy – EXC 2120/1 – 390831618. The research project (P 52-5- 13.194-2048/19) was supervised by Deutsches Institut für Bautechnik (DIBt) and carried out with financial support from the Federal States. These supports are gratefully acknowledged.

We thank the Material Testing Institute (MPA) of the University of Stuttgart, Department Building Construction and Component Testing and the Department Timber Constructions for their support.

We thank Pollmeier Massivholz GmbH & Co. KG for the provision of the test specimens.

Many thanks to Andrea Frangi, Thomas Ehrhart and Stephan Schilling from ETH Zürich for sharing their tests results and experiences from the research project WHFF-CH 2020.11.

We thank Heni Architekten, Implenia Schweiz AG and Pollmeier Massivholz GmbH & Co. KG (in alphabetical order) for allowing measurements of the assembly tolerances on selected timber buildings.

Many thanks to the Institute for Photogrammetry (ifp) of the University of Stuttgart and especially to Lena Joachim and Edward Necşulescu for carrying out the laser scanning and advising on the measurements' evaluation.

8 References

Buchanan, A. H.; Johns, K. C.; Madsen, B. (1985): Column Design Methods for Timber Engineering. CIB-W18, 18-2-1, Beit Oren, Israel.

Brügel, F. (2022): Experimentelle und numerische Untersuchung des Tragverhaltens von Buchen LVL (in German). Master thesis, Institute for Structural Design, University of Stuttgart, Germany.

Dill-Langer, G. (2014): Tragfähigkeit und Baupotenziale von Buchen-Furnierschichtholz (in German). In: Internationales Holzbau Forum (IHF), Garmisch, Germany.

DIN 4074 (1958): Blatt 1 – Bauholz für Holzbauteile – Gütebedingungen für Bauschnittholz (Nadelholz) (in German). German Institute of Standardization (DIN), Berlin.

Ehlbeck, J.; Blaß, H. J. (1987): Zuverlässigkeit von Holzdruckstäben (in German). Research report, University Fridericiana Karlsruhe, Germany.

Ehrhart, T.; Steiger, R.; Frangi, A. (2021 a): Influence of the moisture content on the compressive strength and modulus of elasticity parallel to the grain of engineered hardwood products (EHP). In: Proceedings of the 8th meeting of International Network on Timber Engineering Research (INTER), 54-12-2, online, 2021.

Ehrhart, T.; Steiger, R.; Frangi, A.; Strahm, T.; Bernasconi, A. (2021 b): Laubholzstützen - Druckfestigkeit und E-Modul parallel zur Faserrichtung und Einfluss der Holzfeuchte (in German). Research report, WHFF-CH 2020.11, ETH Zürich, Switzerland.

Ehrhart, T.; Steiger, R.; Palma, P.; Gehri, E.; Frangi, A. (2019): Compressive strength and buckling resistance of GLT columns made of European beech (Fagus sylvatica L.). In: Proceedings of the 6th meeting of International Network on Timber Engineering Research (INTER), 52-12-1, Tacoma, USA.

EN 408 (2010): Structural Timber and Glued Laminated Timber – Determination of Some Physical and Mechanical Properties. European Committee for Standardization (CEN), Brussels, Belgium, with corrections and amendments + A1:2012.

EN 1990 (2010): Eurocode 0: Basis of structural design. European Committee for Standardization (CEN), Brussels, Belgium, with corrections and amendments + A1:2005 and AC:2010.

EN 1995-1-1 (2004): Eurocode 5: Design of timber structures – Part 1-1: General – Common rules and rules for buildings. European Committee for Standardization (CEN), Brussels, with corrections and amendments + AC:2006 and A1:2008.

EN 14080 (2013): Timber structures - Glued laminated timber and glued solid timber - Requirements. European Committee for Standardization (CEN), Brussels.

ETA-14/0354 (2018): Beam BauBuche GL75. Austria Institute of Construction Engineering (OIB), Vienna, Austria.

Frangi, A.; Steiger, R.; Theiler, M. (2015): Design of timber members subjected to axial compression or combined axial compression and bending based on 2nd order theory. In: Proceedings of the 2nd meeting of International Network on Timber Engineering Research (INTER), 48-2-2, Šibenik, Croatia.

Glos, P. (1978): Zur Bestimmung des Festigkeitsverhaltens von Brettschichtholz bei Druckbeanspruchung aus Werkstoff- und Einwirkungskenngrößen (in German). Dissertation, Technical University of Munich, Germany.

Grosse, M. (2005): Zur numerischen Simulation des physikalisch nichtlinearen Kurzzeittragverhaltens von Nadelholz am Beispiel von Holz-Beton-Verbundkonstruktionen (in German). Dissertation. Bauhaus-Universität Weimar, Germany.

Kuhlmann, U.; Töpler, J.; Gauß, J.; Buchholz, L. (2022): Integrated approach of testing and numerical verifications (IATN). Research project RP 7, DFG Cluster of Excellence "Integrative Computational Design and Construction for Architecture", EXC 2120/1 – 390831618, Institute of Structural Design, University of Stuttgart, Germany.

Kuhlmann, U.; Töpler, J. (2022 a): Experimentelle und numerische Untersuchungen von Brettschichtholz aus Buchen-Furnierschichtholz (BauBuche) (in German). In: Doktorandenkolloquium Holzbau Forschung und Praxis. online.

Kuhlmann, U.; Töpler, J. (2022 b): Imperfektionsmessungen an stabilitätsgefährdeten Holzbauteilen - Schlussbericht (in German). Research report, DIBt P 52-5- 13.194-2048/19, Institute of Structural Design, University of Stuttgart, Germany.

prEN 1993-1-14 (15 February 2022): Eurocode 3: Design of steel structures – Part 1-14: Design assisted by finite element analysis (draft version). CEN/TC 250/SC 3/WG 22 N 55.

prEN 1995-1-1 (28 October 2021): Eurocode 5: Design of timber structures – Common rules and rules for buildings – Part 1-1: General (Consolidated draft for informal inquiry). CEN/TC 250/SC 5 N 1488.

Schänzlin, J. (10 February 2022): kc-method – consideration of creep deformations. CEN/TC 250/SC 5/WG 3 N 354.

Theiler, M. (2014): Stabilität von axial auf Druck beanspruchten Bauteilen aus Vollholz und Brettschichtholz (in German). Dissertation. ETH Zürich, Switzerland.

Töpler, J.; Buchholz, L.; Machanek, S.; Kuhlmann, U. (2022): Guidelines for a Finite Element Based Design of Timber Structures (unpublished). Institute for Structural Design, University of Stuttgart, Germany.

DISCUSSION

The paper was presented by J Töpler

H Blass asked if an upper limit of compression strain was applied for the stress strain curve. J Töpler replied no. H Blass asked if the maximum compression strain was observed in the model. J Töpler said the numerical approach information was not available at hand.

G Hochreiner shared his experience on material modelling. The current approach limits plasticity of the compression side. He suggested that consideration of plasticity can lead to good results. J Töpler replied this is similar to the approach with consideration of large imperfections.

B Azinovic asked for an explanation of the boundary conditions and how to eliminate the boundary conditions effect. J Töpler replied that roller bearing was used in the tests and a friction coefficient from the manufacturer was used in the model. Furthermore, elongation of the column was also needed to account for the column space. J Töpler further confirmed the boundary condition is a hinge.

P Dietsch asked it if is possible to benchmark strain measurements from visual data of the column tests to get MOE. T Töpler replied that the resolution may be too low to get accurate strain results as the camera distance was too far.

A Frangi agreed in general with the test results. He asked about the impact of different inputs to FEM for comparisons with accepted approach with other materials. J Töpler replied in some cases the matching was not perfect. A Frangi asked why the power of 2 on the left side of the equation was used for second order theory. J Töpler said the proposed equation seemed to be consistent with β_c.

Head pull-through properties of self-tapping screws

Carmen Sandhaas, Karlsruhe Institute of Technology

Hans Joachim Blass, Karlsruhe Institute of Technology

Keywords: self-tapping screw, head pull-through, timber, wood

1 Introduction

The head pull-through capacity F_{head} is, together with the withdrawal capacity F_w, especially important for joints with screws as screws can transmit high axial forces. However, whereas F_w is always relevant for design, this is not the case for F_{head}. If the head side member is made of e.g. steel, then – depending on the steel plate thickness – the screw head cannot be pulled through and either steel or withdrawal failure occurs. Differently to withdrawal, few publications covering head pull-through were found; these include publications dealing with the head pull-through resistance of nails and screws in plywood and OSB (Chui and Craft, 2002; Munch-Andersen and Sorensen, 2011) and investigations discussing screw-press gluing (Bratulic et al., 2019; Fürst, 2019).

Currently, characteristic head pull-through parameters $f_{head,k}$ must be taken from technical documentation of screws, hence are proprietary information given as so-called declared values by the individual screw producers. Indeed, the current Eurocode 5 (2010) states that characteristic head pull-through parameters must be determined in accordance with EN 14592 (2012). Concerning head pull-through tests, both EN 14592 and the EAD (EAD 130118-01-0603, 2019) refer to the test standard EN 1383 (2016). Whereas EN 14592 requires ten head pull-through tests to be carried out in order to establish a declared value for $f_{head,k}$, the EAD allows for the declaration of a conservative $f_{head,k}$-value of 10 MPa for timber with a characteristic density of 380 kg/m^3 without testing. A difficulty with EN 1383 is that not enough specifications are given concerning precise test setup and execution. It seems that historically, EN 1383 was drafted for staples, which are pulled-through (thin) wood-based panels, as the protocol for staples is rather extensively explained while imprecise specifications concern issues not relevant for staples. Particularly the prescription concerning the timber thickness t, through which fasteners with a diameter d are pulled, covers a wide range by stating that "$t \leq 7 \cdot d$". Additionally, EN 1383 only refers to "the maximum pull-through load F_{max}”, which is then used to calculate the head pull-through parameter f_{head}. However, the value of F_{max} will very much depend on the thickness through which the fastener is pulled resp. the deformation at which F_{max} is read.

The aim of this contribution is to analyse a database containing head-pull through test results with self-tapping screws. The analyses help to understand if valid design equations can be derived that cover a whole range of screws and timber products. This could help to reduce the effort of designers that currently need to consult a large number of proprietary documents. Furthermore, additional tests were carried out in order to identify influencing factors on test results and important parameters that should be specified in a future version of EN 1383.

2 Database

A database containing 2854 test results stemming from certification test reports was assembled, grouped in 245 series. The results contained in the database are the maximum values in kN reached until a displacement of the test machine’s crosshead of 15 mm. The thickness of the timber product, through which the screws are pulled, is usually 8 times the nominal diameter d_{nom}, and the screws were inserted at an angle of 90° between screw axis and grain direction. The used timber products were mainly spruce (76% of all tests, not predrilled), followed by beech LVL (11%, all predrilled) oak (8%), beech (4%) and ash (1%). The predrilling diameters ranged between $0.67 \cdot d_{nom}$ and $0.8 \cdot d_{nom}$. The used timber was stored at a normal climate with 20°C and a relative humidity of 65% and the moisture content was not measured. This is important to note, as the moisture content of beech LVL usually is only around 6% to 8%, whereas that of spruce lies between 10% and 12%. The recorded density was measured as global value of one test specimen. Half of the tests per series with beech LVL were inserted in the face grain and the other half in the edge grain. All screws in oak, beech and ash solid wood specimens were oriented in radial and tangential direction with respect to the annual rings. This information is not given for all tests with spruce, where 1660 tests contain no information concerning the annual ring orientation.

Figure 1 shows a classification of the screws. These were mostly partially threaded screws (87%), 11% had two threaded parts and fully threaded screws constituted only 2% of all tests. A fundamental difference exists between screws with a partial thread and screws with a full thread or two threaded parts. The last two screw types have a thread directly underneath the head that contributes to the head pull-through resistance, whereas partially threaded screws have a smooth shank directly underneath the head. This means that a head pull-through resistance can only be determined for partially threaded screws, whereas for the other screws, it is rather the withdrawal resistance that is determined. If the smooth shank part of partially threaded screws was not long enough to protrude from the timber, i.e. that part of the thread was embedded in the timber contributing to the head pull-through resistance, the timber piece was predrilled such that the threaded part was loose inside the timber. These screws were inserted until the threaded part protruded from the timber specimen, then the specimen including screw was inserted in the testing rig and it was pulled until the screw head was flush with the timber surface. Afterwards, the specimen was unloaded. Screws with a thread directly underneath the head instead were tested subdividing the series in half of the tests pulling through only the threaded part (i.e. the screw head was protruding from the timber) and the other half was tested including screw head and thread. These screws were inserted until the screw head was flush with the timber surface (tests with head and thread), and then the specimens were inserted in the testing rig.

Concerning head types, 250 screws had a cylinder head, 810 screws had a washer head, 1624 a countersunk head and 180 screws had a “steel-timber” head used to fasten steel plates to timber. The ratio of nominal diameter divided by the head diameter was 0.37 to 0.68 for screws with countersunk heads, 0.32 to 0.52 for screws with washer heads and 0.72 to 0.83 for screws with cylinder heads. No information about the angle of the countersunk heads is given, except for one series with 60° countersunk heads. Looking randomly at some photos of screws contained in the test reports, it seems that most screws had 90° countersunk heads (i.e. the “inclination” of the countersunk with respect to the screw axis was 45°). Also concerning the finishing of the side underneath the head, no information was given, e.g. concerning the presence of milling pockets or milling ribs. Furthermore, countersunk heads may need some pre-milling in order to allow for a screw insertion until the head is flush with the surface, especially for beech LVL with its high density. This information, however, is not given in the reports nor can it be retrieved retrospectively. As a rule, it can be said that in a first step, screws were inserted without pre-milling and if it was possible to fully insert these screws without any splitting, no pre-milling was carried out. This procedure is valid for all species and timber products.

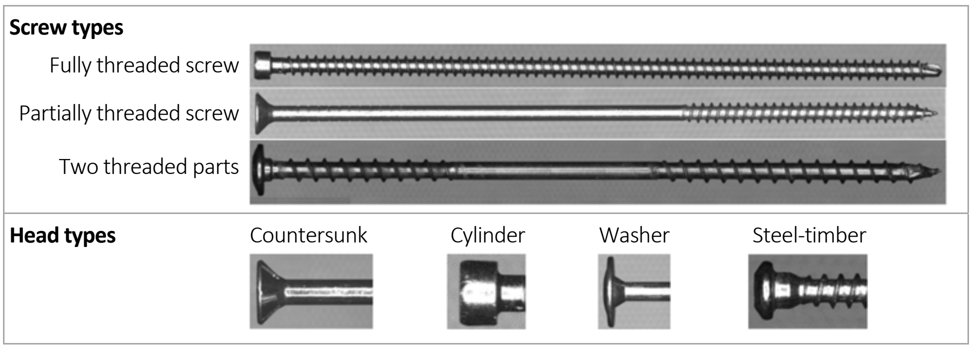

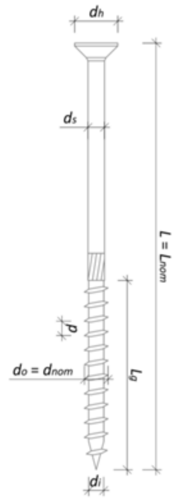

Figure 1. Left: Classification of screws. Right: Geometrical properties with d_h = head diameter, d_s = diameter of smooth shank, d_o = outer thread diameter = nominal diameter d_{nom}, d_i = inner thread diameter, p = pitch, L = length = nominal length L_{nom}, L_g = length of threaded part.

3 Analysis and discussion

3.1 General

Observed coefficients of variation are shown in Figure 2 on the left. For beech LVL, coefficients of variation for density are low. The coefficients of variation for F_{head} are high, and this high scatter is confirmed when looking at Figure 2 on the right, where the influence of the head types on the head pull-through capacity is shown. It can be seen that, obviously, for heads with large diameters, i.e. washer heads, higher F_{head}-values on average are reached. Particularly for beech LVL, however, results scatter considerably and screws with countersunk heads reach the highest values. As in Figure 2 on the right, the vertical axis simply shows the measured F_{head}-values in kN, these values must be normalised prior to any further analysis. In general, however, it can already be stated that the scatter observed for all species is surprising, as the head pull-through behaviour is thought to be similar to the behaviour of wood under a compressive load perpendicular to the grain, where the (ductile) compressive strength perpendicular to the grain together with a load distribution area governs and hence, shows rather little variation.

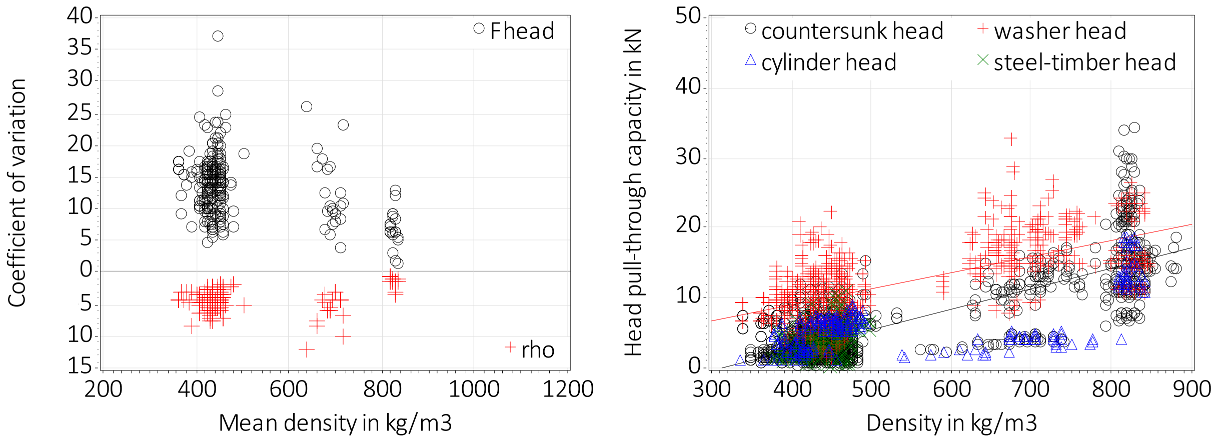

Figure 2. Left: Observed coefficients of variation in %. Right: Head pull-through capacity F_{head} in kN versus density ρ in kg/m^3 differentiated by head types. Linear trendline is shown for screws with washer heads (red line) and countersunk heads (black line).

The normalisation is done by dividing the head pull-through capacity F_{head} through the square of the head diameter d_h, obtaining the head pull-through parameter f_{head}:

$$f_{head} = \frac{F_{head}}{d_h^2} \tag{1}$$

The "head pull-through parameter" for fully threaded screws and screws with two threaded parts, i.e. screws with a thread directly underneath the head, is instead calculated differently and in analogy to the withdrawal parameter:

$$f_{head} = \frac{F_{head}}{d_{nom} \cdot t} \tag{2}$$

where d_{dom} = nominal diameter and t = thickness of the timber piece.

Figure 3 on the left shows all head pull-through parameters versus the density. The minimum value of 10 MPa of $f_{head,k}$, that can be declared without testing in accordance with the EAD, is shown. For spruce, this value of 10 MPa is obviously a good (albeit conservative) choice, whereas a stepwise or linear increase could be introduced for timber products with a density > 500 kg/m^3. In general, the scatter is significant, with individual f_{head}-

values for spruce ranging between 9 MPa and 53 MPa and for beech LVL between 29 MPa and 129 MPa. This scatter is not reduced when showing mean values per series instead of individual testing values. Concerning screw types, it seems that partially threaded screws can reach higher f_{head}-values, which holds when considering that rather a withdrawal parameter is established when pulling through screws with a thread underneath the head. If additionally considering the head type, this seems to hold for partially threaded screws with any head type, whereas for higher densities, particularly for beech LVL, it seems to hold for partially threaded screws with countersunk heads (i.e. head types acting as wedge). Seeing the scarcity of data for species with densities > 500 kg/m^3, it is difficult to judge if this observed relationship is true or fictitious. However, remembering the previous statement on the need of pre-milling or not in order to fully insert screws with countersunk heads, it may well be that an insertion of screws with countersunk heads without pre-milling leads to a higher local densification underneath the head resulting in a higher head pull-through resistance. However, as no comparative testing series are available, it is difficult to draw reliable conclusions. Comparative testing series instead were carried out with solid hardwoods, where the same screws were used in different species. The results showed that oak with its lower density has lower f_{head}-values than beech or ash. This confirms the trend of increasing f_{head}-values with increasing density that can be seen for solid hardwoods in Figure 3 on the left, and which is not discernible for spruce and beech LVL.

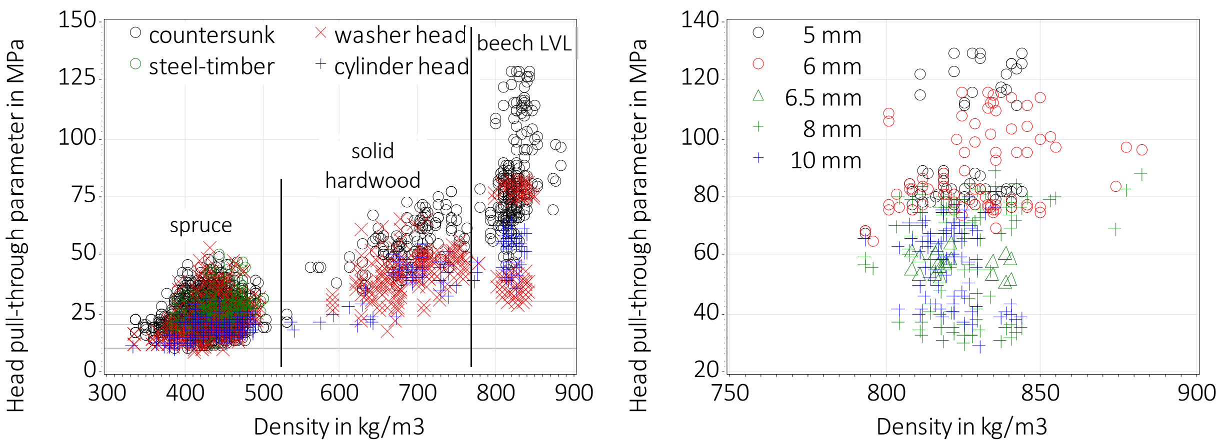

Figure 3. *Left: Head pull-though parameter f_{head} versus density ρ, differentiated by screw types and with horizontal lines at 10, 20 and 30 MPa. Lowest f_{head}-value was 9.3 MPa, all other values > 10 MPa. Right: Head pull-though parameter f_{head} versus density ρ for beech LVL (all predrilled) and differentiated by nominal diameter.*

If giving a further look into the tests with beech LVL, further subsets can be identified. The screws in beech LVL were inserted in either the face or the edge grain, where this info is only given for partially threaded screws. However, no difference at all was observed concerning the direction of insertion (also when considering the overall database). If instead differentiating by nominal diameter as shown in Figure 3 on the right, a trend of higher f_{head}-values for screws with smaller nominal diameters and countersunk heads can be observed. Again recalling the statement on the need of pre-milling of countersunk heads inserted in high-density timber, a possible hypothesis arises. As the screws must be inserted until the screw head is flush with the timber surface, it may be that the countersunk heads of small diameter screws did not need pre-milling in order to ensure proper insertion. This, in turn, may have led to densification underneath the screw head with subsequent higher f_{head}-values.

Re-considering the analogy between head pull-though tests and compressive tests perpendicular to the grain, another approach to calculate the head pull-through capacity arises. The most simple approach is to apply a modified version of Eq. (5) given in Leijten (2009):

$$F_c = 3 \cdot f_{c,90} \cdot A_{head} = 3 \cdot f_{c,90} \cdot \pi \cdot \frac{(d_h)^2}{4} \tag{3}$$

where F_c = compressive capacity in N, $f_{c,90}$ = compressive strength perpendicular to the grain in MPa, A_{head} = gross area underneath the screw head in mm^2.

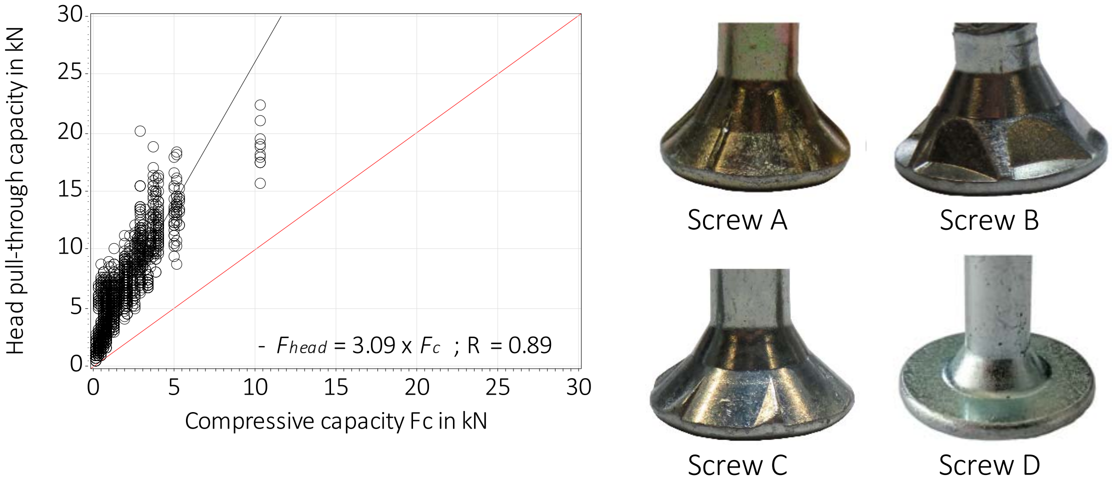

Figure 4. *Left: Head pull-through capacity versus "compressive capacity F_c" in accordance with Eq. (3) with $f_{c,90}$ = 2.6 MPa. Only data for spruce is considered. Bisect line is shown in red; linear regression is shown in black and regression equation is given. The values at F_c > 10 kN are for screws with d_h = 41 mm (12 mm screw with countersunk head and washer).*
Right: Shapes underneath screw heads.

Concerning a value for $f_{c,90}$, the findings of Franke (2008) can be taken into account, who determined compressive strength values for spruce on small cubic specimens (40 x 40 x 40 mm^3) with different annual ring orientation. Franke evaluated a mean compressive strength perpendicular to the grain at a strain of 1% of 3.7 MPa for tangential compression, 2.6 MPa for radial compression and 1.5 MPa for specimens with annual rings oriented at 45°. Figure 4 on the left shows the head pull-through capacities contained in the database versus the results of Eq. (3) with $f_{c,90}$ = ⅓ · (3.7 + 2.6 + 1.5). Eq. (3) underestimates head pull-through capacities by a factor of three. Therefore, a simple approach as specified in Eq. (3) can only be used after further statistical calculations that establish a relationship between head pull-through capacity and compressive strength.

Differently to compressive tests, splitting underneath a screw head during insertion will influence results. The scatter observed for screws with washer heads, however, cannot be explained with this, at least not fully, because washer heads may not be even on their underside (see Figure 4 on the right) and hence still penetrate the timber and it cannot be controlled when exactly the insertion process is stopped. It must hence be questioned how valid the head pull-through capacities are, which are read at a crosshead displacement of the testing rig of 15 mm. The following questions arise:

- By how much is a screw head pulled in at 15 mm machine displacement?
  During testing, transducers should be used to measure deformations.
- How is the general load-displacement behaviour?
  Load-displacement curves are needed to assess the nonlinear shape of the curve.
- Does the thickness of the timber piece or support conditions influence test results?
  Here, the question is for instance if additional bending of the timber member influences head pull-through values in cases where a screw is pulled through a rather thin timber member that is supported only at a large distance from the screw.
- Are there any elastic effects?
  Elastic effects will certainly occur, in particular for the tests in beech LVL, seeing that a screw with a Young's Modulus of 21000 GPa is pulled through a high-density product with a certain thickness. This question is in direct relation to the question before.
- Is there a difference in load-displacement behaviour between screws with countersunk heads and those with washer heads?
  As long as no curves are registered, this question cannot be answered.
- Does predrilling influence head pull-through values?
  When no predrilling is carried out, more wood material must be pushed aside when inserting a screw, which may influence the behaviour.
- Does pre-milling influence head pull-through results?
  This question is especially important for screws with countersunk heads inserted in high-density timber.
- Is there an influence of the insertion process?
  This question addresses the observation that results for screws with washer heads scatter significantly. For these screws, it is difficult to define a clear end to the insertion process. But also results for screws with other heads may be depending on how the screws are inserted and what "flush with the timber surface" means.
- Are there geometrical features of countersunk heads that influence results?
  This question addresses the observation that results for screws with countersunk heads scatter significantly. As no geometrical data is given for countersunk heads, e.g. the angles of the heads or if milling pockets are present, this observed scatter cannot be assessed.

To answer these questions, additional testing series must be carried out; with specified boundary conditions and well documented manufacturing and testing procedures. As a consequence, small systematic testing series presented in the next section were carried out to address some of the above-mentioned questions. Such bespoke test series will however impact on the representativeness of the data, as such series will be carried out only on very few different screws.

3.2 Additional testing series

Table 1 gives an overview over the additional testing series and the results. In all tests, the screw head displacement was measured using transducers, together with the machine load and displacement. Two different test rigs were used (tests with screw A on rig 1, and tests with screws B to F on rig 2), with probably individual influences on the machine displacement. The machine displacement (and not any transducer displacement) is currently considered to determine F_{head}-values. Consequently, it was also used to determine the test results given in Table 1, in analogy to all other data contained in the database. Figure 4 on the right shows photos of the underside head shapes of the used screws. The mean moisture content of beech LVL was 6.3% and that of spruce 11.6%. In the following, different aspects of the test results are discussed.

Machine versus transducer displacement

Figure 5 shows four load-displacement curves, where machine displacement and transducer displacement is differentiated. Two systematic differences can be pointed out. Firstly, load-displacement curves for screws with washer heads, upper right figure, show a steady increase until tests are stopped. This is not the case for screws with countersunk heads, which show a more pronounced nonlinear behaviour with a maximum load reached before tests are stopped. And secondly, whereas the difference in measurement method is small for tests with countersunk heads in spruce, this is not the case for screws with washer heads and in beech LVL, i.e. for tests with more rigid behaviour. It must be underlined that the four chosen curves are by no means representative for all other tests of the same series, and the qualitative load-displacement behaviour may look different from test to test, see also Figure 7 on the right. Figure 6 on the left shows opened test specimens, where the fundamental difference to compressive tests perpendicular to the grain can be seen. In the latter tests, wood fibres are not separated and can act as ropes transferring tensile loads. In head pull-through tests instead, fibres are separated and can be better compared to cantilever beams. However, these simple static models underestimate the influence of shear very considerably as was shown by Bocquet (1997, there Figure 1.22). The exemplary curves given in Figure 5 show very clearly that the current determination of F_{head} at a machine displacement of 15 mm takes place when the load-displacement curves are already far in the ductile range. The permanent deformations visible in Figure 6 on the left confirm this; current values of F_{head} go hand in hand with large deformations, and in the case of washer heads, F_{max} is not reached at a machine displacement of 15 mm.

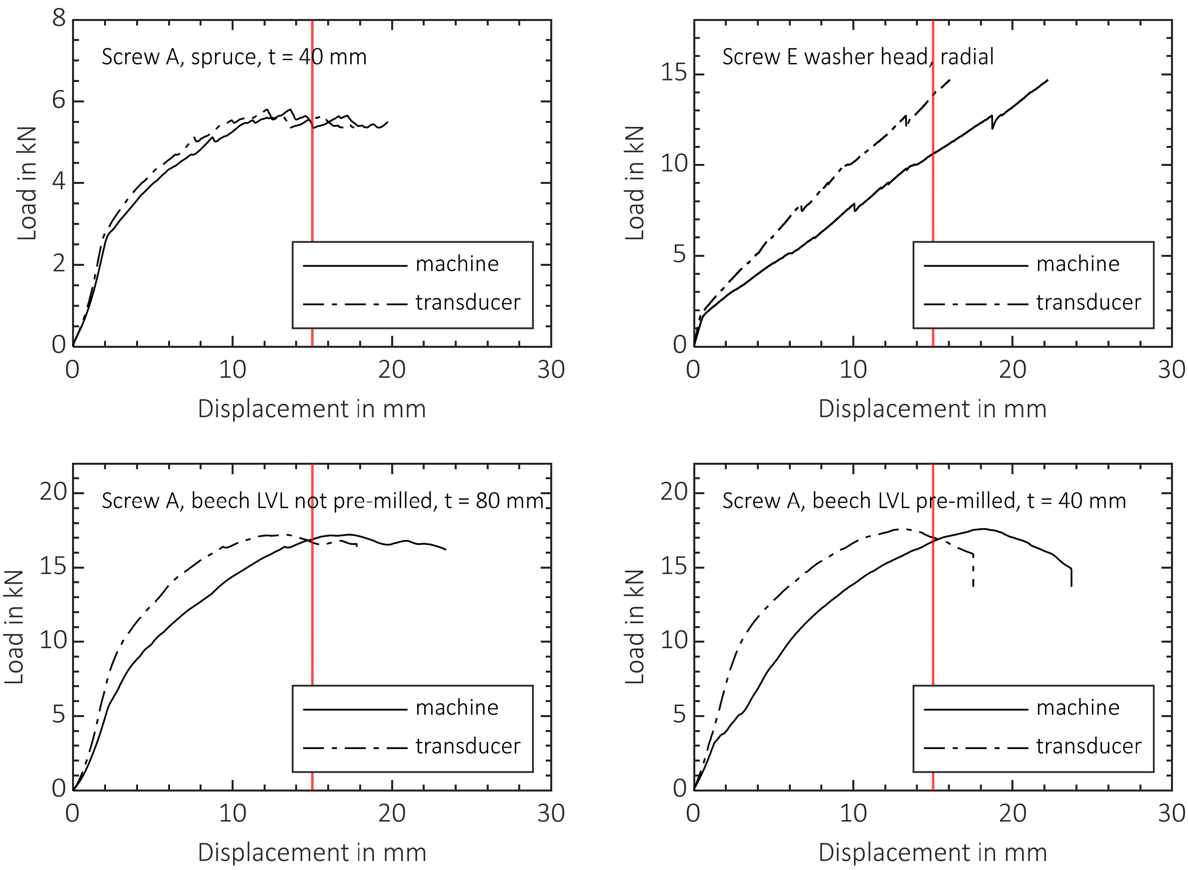

Figure 5. Four exemplary load-displacement curves. Red vertical line indicates 15 mm displacement.

This is a very unsatisfying situation, considering the vague prescriptions in EN 1383 (2016) and the effect this may have on results from different testing institutions. Clear prescriptions are needed at which deformation limit head pull-through capacities should be read. These deformation limits may vary depending on the application, similar to the proposal for compression perpendicular to the grain by Windeck and Blass (2017). Further prescriptions are required as to how deformations shall be measured, in particular for rigid systems, i.e. with high-density timbers and large washer heads, where larger differences between machine and transducer displacement can be observed. Quantitative differences between machine and transducer displacement are given in Table 1, where differences of up to 5 mm at a machine displacement of 15 mm were observed. This means, screw heads are pulled in by a maximum of 10 mm at a crosshead displacement of 15 mm. These 10 mm consist of an elastic and a plastic part, as can be seen in Figure 6 on the left, where the permanent deformation is less than the maximum (machine) displacement of ca. 20 to 25 mm during the test.

Timber thickness

The test specimens were supported such that no bending deformation could occur, i.e. with a steel plate with an opening of 80 x 80 mm^2 to support the tip side timber surface (as prescribed in EN 1383) and a clear distance of 15 to 20 cm between two anchorings fastening the test specimen and steel plate to the test rig. When looking at the results with screw A in Table 1, no difference can be observed for the tests with spruce with a thickness of 40 and 80 mm. The same holds for the tests with beech LVL, where, however, the series with 40 mm thick beech LVL and screws inserted in the face grain had higher densities than all other series, obfuscating results.

Table 1. Test results in terms of mean values with coefficients of variation, thickness t in mm, N = number of tests, displacement u of transducer when machine displacement is 15 mm. All partially threaded screws, and underside head shapes are shown in Figure 4 on the right.

	t	N	Variation	ρ in kg/m^3	u in mm	f_{head} in MPa	
Screw A, countersunk, d_h = 14.8 mm, d_{nom} = 8 mm, $d_{predrill}$ = 6 mm in beech LVL, not predrilled in spruce							
Beech LVL,	40	5	Face grain	835 | 0.5%	10.1 | 9.2%	90.7 | 4.8%	
pre-milled		5	Edge grain	806 | 1.1%	9.9 | 5,7%	79.2 | 5.9%	
(14 mm)	80	5	Face grain	807 | 0.9%	10.3 | 14.5%	71.2 | 9.3%	
		5	Edge grain	802 | 0.3%	10.4 | 4.5%	82.9 | 2.9%	81.0 | 10.5%
Beech LVL,	40	5	Face grain	835 | 0.5%	12.2 | 2.4%	94.1 | 3.2%	
not pre-		5	Edge grain	806 | 1.1%	10.8 | 11.1%	85.5 | 4.0%	
milled	80	5	Face grain	806 | 1.0%	11.7 | 3.7%	81.9 | 6.9%	
		5	Edge grain	804 | 0.4%	11.4 | 4.1%	82.8 | 6.3%	86.1 | 7.7%
Spruce	40	10		460 | 3.6%	12.9 | 5.8%	24.0 | 9.4%	
	80	10		460 | 3.8%	13.1 | 3.9%	24.4 | 5.8%	24.2 | 7.9%
Screw B, countersunk with milling pockets, d_h = 11.7 mm, d_{nom} = 6 mm, not predrilled							
Spruce	60	10	Radial	466 | 3.7%	13.0 | 4.2%	31.6 | 13.3%	
		10	Tangential	466 | 3.7%	13.0 | 4.5%	28.7 | 11.7%	30.1 | 13.5%
Screw C, countersunk, d_h = 11.4 mm, d_{nom} = 6 mm, not predrilled							
Spruce	60	10	Radial	472 | 3.3%	12.8 | 3.5%	36.2 | 17.8%	
		10	Tangential	472 | 3.3%	13.6 | 3.3%	30.2 | 21.9%	33.2 | 21.6%
Screw D, washer head, d_h = 13.6 mm, d_{nom} = 6 mm, not predrilled							
Spruce	60	10	Radial	469 | 3.0%	11.6 | 4.9%	36.4 | 17.2%	
		10	Tangential	469 | 3.0%	12.4 | 2.2%	29.4 | 10.1%	32.9 | 18.3%
Screw E, washer head, d_h = 21.4 mm, d_{nom} = 8 mm, not predrilled							
Spruce	80	10	Radial	457 | 3.5%	11.1 | 7.4%	23.5 | 7.4%	
		10	Tangential	457 | 3.5%	11.4 | 6.7%	20.8 | 11.2%	22.2 | 11.2%
Screw F, washer head, d_h = 22.4 mm, d_{nom} = 10 mm, not predrilled							
Spruce	100	10	Radial	388 | 3.1%	12.0 | 3.5%	19.6 | 13.3%	
		10	Tangential	388 | 3.1%	12.0 | 2.0%	17.3 | 11.1%	18.4 | 13.9%

Pre-milling versus not pre-milling in beech LVL

As expected, no pre-milling to facilitate the insertion of countersunk heads leads to higher f_{head}-values, see Table 1 (and Figure 7 on the left). However, this trend is only weak and cannot explain the large scatter observed in the database. The weak trend is confirmed when looking at the load-displacement curves of all tests with beech LVL given in Figure 6 on the right.

Density

Figure 7 on the left shows f_{head}-values versus density of the tests with screw A in beech LVL, including the trendlines. The trend based on the in total 40 tests is clear; f_{head}-values are increasing with increasing density. Such a clear trend, however, cannot be observed when looking at the database, see Figure 3 on the right. The general issue of discernible trends within bespoke series that vanish when looking at more representative data can be underlined.

Insertion direction

Concerning insertion in edge or face grain of beech LVL (screw A), the picture is blurry when looking at Table 1, The test results for 40 mm thick beech LVL cannot be interpreted due to the difference in density. The test results for 80 mm thick beech LVL instead show a larger difference between edge and face grain for the pre-milled specimens, and no difference for the not pre-milled specimens. Concerning the tests with spruce, tests with screws inserted in radial direction lead to higher f_{head}-values, which can be explained with homogenisation effects when inserting screws in radial direction. It is, however, contradictory to the already cited findings from Franke (2008), who evaluated higher compressive strength values in tangential direction in comparison to the radial direction.

Influence of shapes underneath screw heads

Figure 7 on the right shows the load-displacement curves for the tests with screws B and C, which had different shapes underneath their countersunk heads, see Figure 4 on the right. The scatter is significant, also when looking at the coefficients of variation given in Table 1, and this scatter cannot be explained when giving a closer look to the test specimen, production and execution. No conclusive statement can be made based on these few tests. For screws with washer heads, f_{head}-values seem to decrease with larger screw diameters (with consequentially larger head diameters); a trend that can be confirmed considering the whole database.

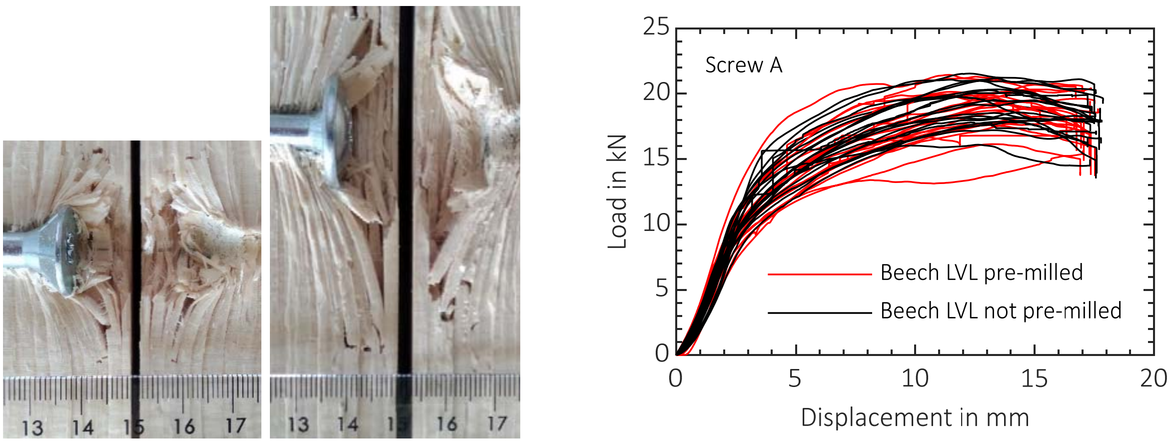

Figure 6. Left: Opened test specimens (not predrilled). Right: Load-displacement curves of head pull-through tests showing transducer displacement. Results screw A in beech LVL.

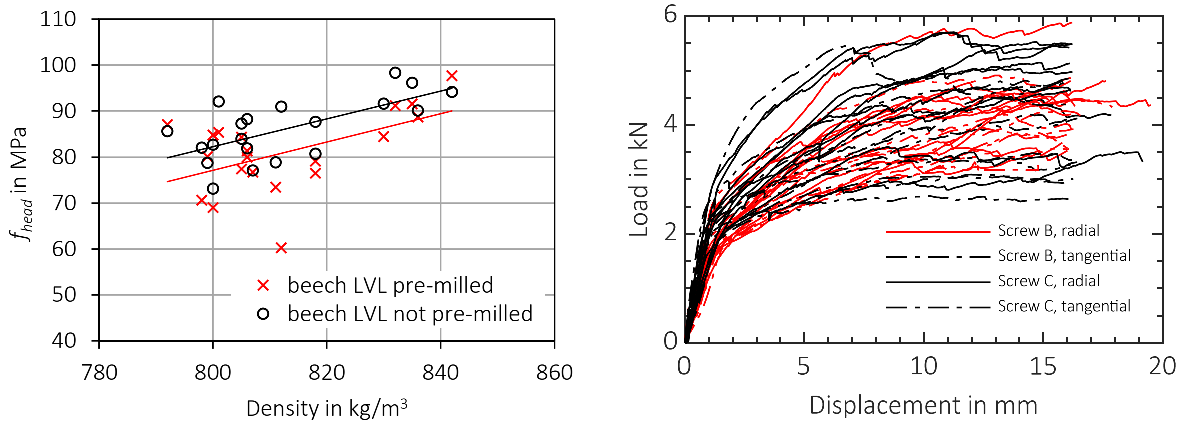

Figure 7. Left: f_{head}-values versus density. Results for screws A in beech LVL with trendlines for pre-milled and not pre-milled specimens. Right: Load-displacement curves of head pull-through tests showing transducer displacement. Results for screws B and C.

3.3 Characteristic values

Irrespective of the observed scatter and the resulting challenges in finding meaningful relationships, characteristic values are needed for design. Therefore, conventional characteristic values are calculated applying EN 14358 (2016) and prEN 14592 (2017). In a first step, a nonlinear regression using 2854 individual test results was carried out in order to determine a correction factor, the exponent in Eq. (4) (R^2 = 0.7):

$$f_{head} = 9.5 \cdot 10^{-4} \cdot \rho^{1.67} \tag{4}$$

where f_{head} = head pull-through parameter, ρ = density.

This nonlinear regression did not comprise a thorough residual analysis with corresponding deletion of outliers with studentised residuals larger than |3|. Moreover, no differentiation, e.g. with respect to different wood species, was made. Further nonlinear regressions revealed an exponent of 1.00 for all tests with spruce, 1.61 for the tests with solid hardwoods, and no convergence was possible for the tests with beech LVL. The exponent of 1.67 is used to correct the head pull-through parameters of each test series, hence also of the series with spruce, using reference densities ρ_{ref} that correspond to the mean densities of all series per wood type.

$$f_{head,corr} = f_{head} \cdot \left(\frac{\rho_{ref}}{\rho_{mean}} \right)^{1.67} \tag{5}$$

where $f_{head,corr}$ = corrected head pull-through parameter, ρ_{ref} = mean density of all series per wood type: spruce $\rho_{ref,spruce}$ = 433 kg/m^3, solid hardwood $\rho_{ref,solidHW}$ = 690 kg/m^3, beech LVL $\rho_{ref,beechLVL}$ = 826 kg/m^3, ρ_{mean} = mean density of each test series.

The corrected head pull-through parameters $f_{head,corr}$ are assumed to have a lognormal distribution and the logarithm is taken. A normal distribution is assumed for the density. Figure 8 shows the histograms of both values for all tests with spruce, confirming the distribution assumptions taken. Using the approach given in Annex D of prEN 14592 (2017), the standard deviations of the corrected head pull-through parameter can now be adjusted so that they reflect the timber population:

$$std_{fhead,corr} = \sqrt{std_{fhead}^{2} + 1.67^{2} \cdot \left(0.10^{2} - COV_{\rho}^{2}\right)} \tag{6}$$

where $std_{fhead,corr}$ = corrected standard deviation of head pull-through parameter, std_{fhead} = observed standard deviation of head pull-through parameter, 1.67 = correction factor, see Eq.(5), 0.10 = target COV of density of timber population, COV_{ρ} = observed COV of density, per test series, see Figure 2 on the left.

Finally, in accordance with EN 14358 (2016), 5th percentiles for $f_{head,corr}$ were estimated using the corrected standard deviations $std_{fhead,corr}$. The limited amount of test results per test series was considered applying the k_s-factor given in EN 14358.

The calculated characteristic $f_{head,k}$-values are shown in Figure 9, where in total 14 $f_{head,k}$-values were smaller than 10 MPa, although only one original f_{head}-value was smaller than 10 MPa (the lower bound value defined in the EAD), see Figure 3 on the left. This, however, is a consequence of the corrections in accordance with Eqs. (5) and (6). Scatter is, again, persistent. Higher $f_{head,k}$-values can be reached for smaller diameters (Figure 9 on the left), which may be an effect of data scarcity for larger diameters. However, a similar trend was observed for nails (Sandhaas and Görlacher, 2018). This, together with the similarity to head pull-through behaviour of nails, leads to the obvious step of combining databases as is done in Figure 10. In general, data clouds for nails and screws look similar, although nails can reach higher values, where the underside shape of nail heads in general is even (nails with trumpet heads were not pulled through). The data discussed here confirms the lower bound constant of $f_{head,k}$ = 10 MPa for screws pulled through spruce given in the EAD (2019), whereas for nails, a lower bound constant of $f_{head,k}$ = 15 MPa was found by Sandhaas and Görlacher. However, data for other species than spruce are missing for nails. If it is now postulated that nails pulled through higher density timber behave similar to screws, then a lower bound equation encompassing a correction of density for both fastener types is possible. As exponential approaches are very sensitive at their boundaries, the exponent of 1.67 found in Eq. (4) should not be considered. This exponent is furthermore deemed to be too high due to the large scatter of data for beech LVL. Instead, the exponent of 1.25 found for nails could be applied, leading to the following equation shown also in Figure 10:

$$f_{head,k} = 10 \cdot \left(\frac{\rho_k}{350}\right)^{1.25} \tag{7}$$

where 10 = constant value of f_{head} of 10 MPa, adjustment of $f_{head,k}$ for density with reference density of 350 kg/m^3 = ρ_k of C24, EN 338 (2016), and the exponent of 1.25 for nails taken from Sandhaas and Görlacher (2018).

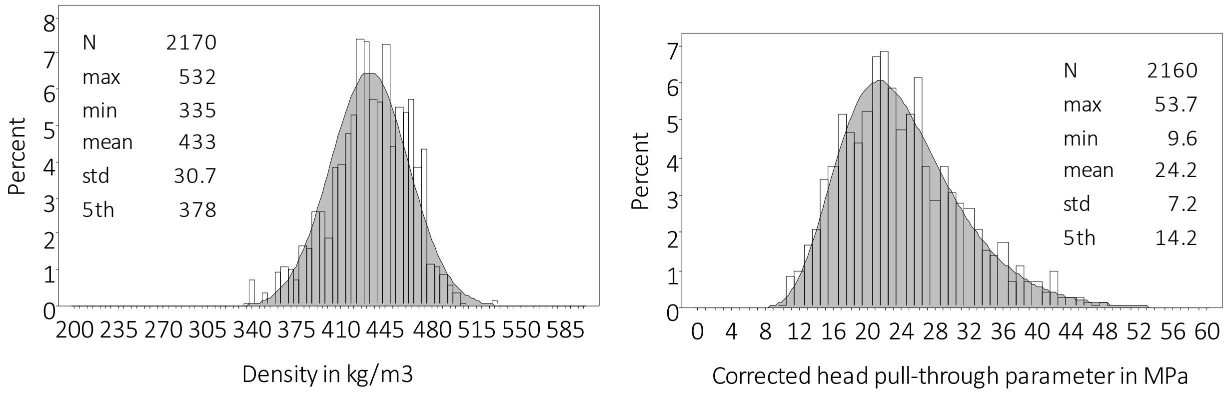

Figure 8. *Head pull-through tests with spruce. Left: Histogram of density with fitted normal distribution. Right: Histogram of $f_{head,corr}$-values with fitted lognormal distribution (for one series of 10 tests, d_h was not recorded and hence, f_{head} could not be calculated).*

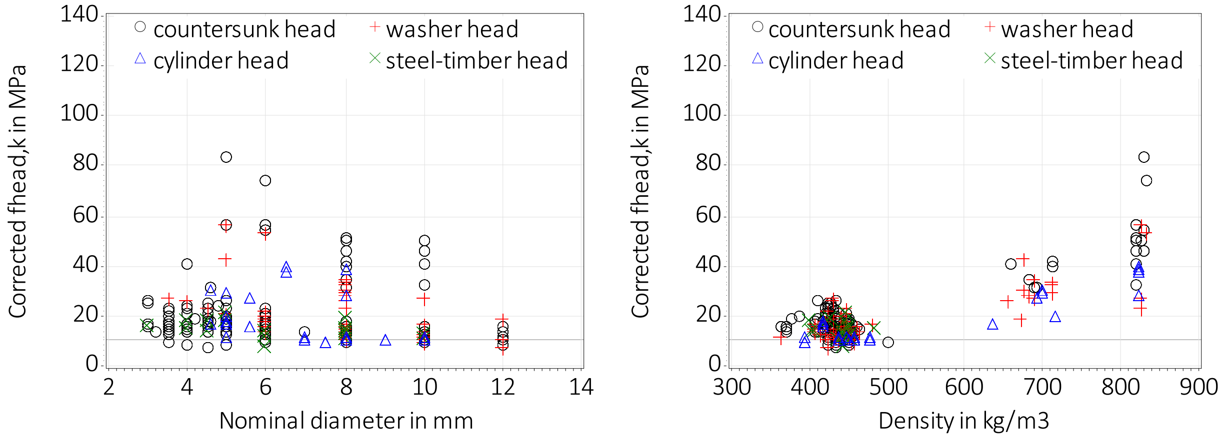

Figure 9. *Characteristic values of the head pull-through parameter $f_{head,k}$ based on corrected standard deviations. 14 of 245 $f_{head,k}$-values < 10 MPa (only spruce).*

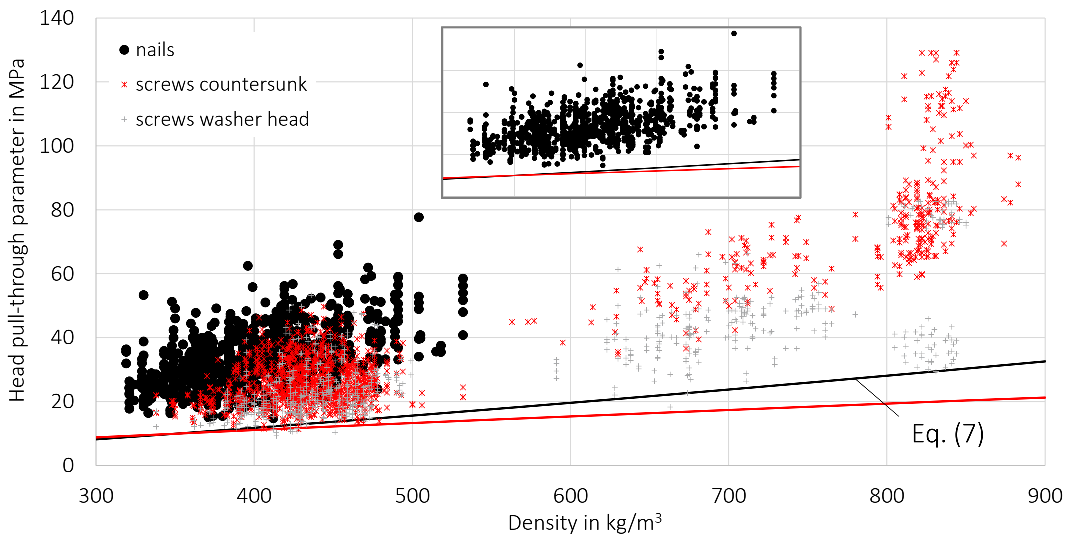

Figure 10. *Individual f_{head}-values versus density for nails, screws with countersunk heads and screws with washer heads. The box inset shows only data for nails together with Eq. (7) for better identification of data cloud position with respect to Eq. (7). The red line corresponds to Eq. (7), but with an exponent of 0.8 as in the current Eurocode 5 (2010).*

Eq. (7) obviously delivers conservative values for the head pull-through parameter, and it is not derived by applying accepted statistical procedures. However, the persistent large scatter, in particular for beech LVL, does not allow for any meaningful, more sophisticated regressions. Moreover, considering the load-displacement behaviour shown e.g. in Figure 5, remaining conservative may be a good choice as f_{head}-values are currently determined at rather large displacements, and hence represent upper bound values (except for screws with washer heads). Finally, a lack of understanding of the source of the observed scatter, even after having analysed the additional tests discussed in section 3.2, makes further analyses rather pointless. Within a wood type, i.e. spruce, solid hardwood and beech LVL, no or only a weak trend of higher f_{head}-values at higher densities can be observed. An alternative scenario to Eq. (7) could be to keep the lower bound value of 10 MPa for screws pulled through softwood. Similar, for timber with 500 kg/m^3 < ρ < 900 kg/m^3, a constant minimum value could be used, without considering any differences in density. Such minimum values for $f_{head,k}$ could be 20 MPa for solid hardwoods, and 30 MPa for beech LVL, see Figure 3 on the left.

4 Conclusions

In general, the observed scatter of the assembled representative database is large, and neither analyses of potential influence factors nor additional tests clarified the source of this scatter. However, the tests indicated that features not reported up to now may impact on results and should be recorded in future. Such features are e.g. more exact geometrical definitions of the screws and of the timber specimens. Above all, the lack of definition at which deformation level head pull-through capacities should be determined, is a major omission. Furthermore, also the insertion process should be more precisely prescribed, including information on predrilling and pre-milling. All this should be part of a future version of EN 1383. Concerning the source of the large observed scatter, further possible hypotheses are the impact of other wood characteristics than the density (or insertion direction) alone, e.g. local properties of the wood directly underneath resp. closely around the screw, together with certain features of the individual screws, e.g. underside head shapes. In particular for beech LVL, a highly homogenised product, the scatter is significant and does not allow for meaningful regressions. Currently, in accordance with the EAD, a minimum characteristic value of the head pull-through parameter $f_{head,k}$ of 10 MPa for softwood can be declared. This value could be confirmed. Analogously, lower bound constants could be defined also for higher-density timber products. Nevertheless, all these approaches remain conservative.

To sum up, different scenarios are possible how $f_{head,k}$-values needed for design could be defined as long as no further investigations are available that help understanding the source of the observed scatter with subsequent tailor-made solutions for design. These scenarios encompass e.g. (i) maintenance of the state-of-the-art, i.e. $f_{head,k}$-values can be declared as proprietary properties by the individual screw producers, (ii) the definition of lower bound values or equations that will not allow for higher $f_{head,k}$-values and that potentially lead to wrong predictions of the failure modes, or (iii) technical classes are defined to keep simple constant values or equations whilst allowing for higher $f_{head,k}$-values.

5 Acknowledgements

This work has been carried out within the project hardwood_joint, which is supported under the umbrella of ERA-NET Cofund ForestValue by BMLFUW (AT), ADEME (FR), FNR (DE) and Vinnova, Swedish Energy Agency and Formas (SE). ForestValue has received funding from the European Union's Horizon 2020 research and innovation programme under grant agreement N° 773324.

6 References

Bocquet JF (1997) *Modélisation des deformations locales du bois dans les assemblages brochés et boulonnés*. Dissertation, University Blaise Pascal Clermont-Ferrand.

Bratulic K, Augustin M, Schickhofer G (2019) Investigations concerning screw-press gluing of assemblies with CLT. Paper 52-18-1. *INTER Meeting 52*, Tacoma, USA.

Chui YH, Craft S (2002) Fastener head pull-through resistance of plywood and oriented strand board. *Canadian Journal of Civil Engineering* **29**(3):384-388. doi:10.1139/l02-019.

EN 1995 1-1 (2010) *Eurocode 5. Design of timber structures – Part 1-1: General – Common rules and rules for buildings.* Comité Européen de Normalisation (CEN), Brussels, Belgium.

Franke S (2008) *Zur Beschreibung des Tragverhaltens von Holz unter Verwendung eines photogrammetrischen Messsystems*. Dissertation, Bauhaus-Universität Weimar.

Fürst H (2019) *Überprüfung und Optimierung der Regelungen für streifen- und plattenförmige Schraubpressverklebungen in ÖNORM B-1995-1-1*. Master thesis, Technische Universität Graz.

Leijten AJM (2009) Withdrawal capacity of washers in bolted timber connections. *Wood Material Science and Engineering* **4**(3-4):131-139. doi:10.1080/17480270903411066.

Munch-Andersen J, Sorensen JD (2011) Pull-through capacity in plywood and OSB. Paper 44-7-1. *INTER Meeting 44*, Alghero, Italy.

Sandhaas C, Görlacher R (2018) Analysis of nail properties for joint design. *Engineering Structures* **173**:231-240. doi:10.1016/j.engstruct.2018.06.071.

EAD 130118-01-0603 (2019) *Screws and threaded rods for use in timber constructions.* European Assessment document, EOTA, Brussels, Belgium.

EN 338 (2016) *Structural timber – Strength classes.* Comité Européen de Normalisation (CEN), Brussels, Belgium.

EN 14358 (2016) *Timber structures – Calculation and verification of characteristic values.* Comité Européen de Normalisation (CEN), Brussels, Belgium.

EN 14592 (2012) *Timber structures – Dowel-type fasteners – Requirements.* Comité Européen de Normalisation (CEN), Brussels, Belgium.

prEN 14592 (2017) *Timber structures – Dowel-type fasteners – Requirements.* Comité Européen de Normalisation (CEN), Brussels, Belgium.

EN 1383 (2016) *Timber structures – Test methods – Pull through resistance of timber fasteners.* Comité Européen de Normalisation (CEN), Brussels, Belgium.

Windeck L, Blass HJ (2017) Querdruckverhalten von Brettschichtholz aus Nadelholz. *Bautechnik* **94**(11):767-775. doi:10.1002/bate.201700048.

DISCUSSION

The paper was presented by C Sandhaas

S Winter and C Sandhaas discussed the difference in deformation of machine versus transducer measurements. C Sandhaas said the slip in the machine measurements due to screws can be clarified by the definition in the test method. S Winter said f_{head} values can be misleading for different diameters as diameters are mixed. C Sandhaas said steel failures are excluded.

R Brandner commented that using Leijten (2009) equation to obtain compression perpendicular strengths may be inaccurate. He said density influence is there and asked if mean density was considered. C Sandhaas replied that density influence is there but density influence based on individual data points are not clear.

S Aicher commented about EN1383 specimen edge distance requirements and said that requirements for radial and tangential directions are different. He said one may need to glue specimens. C Sandhaas agreed EN1383 needs to be revised. Definition for f_{head} has already changed with the correction factor. They discussed that changes of the f_{head} equation need to be clearly communicated and this could cause confusion. Also one may need to consider this as an intrinsic property.

S Schwendner received confirmation of the large variability observed.

R Jockwer received confirmation that LVDT and machine deformations were not both available for all tests. He asked which deformation should be used. C Sandhaas said the deformation should be based on the acceptable failure of crushing or compression perpendicular to grain.

T Tannert commented that spline joints with head pull through failure mode can have safety factor of 5 here and safety factor of 2 for friction. This can lead to large overstrength. H Blass said this point was commented in paper 55-15-4.

Performance, design and execution of screwed steel-timber end-grain connections.

Maximilian Westermayr[1)], Reinhard Brandner[2)], Andreas Ringhofer[2)], Ursula Mahlknecht[2)], Jan-Willem G. van de Kuilen[1,3)]

[1)]Technical University of Munich, Professorship of Wood Technology, Germany

[2)]Graz University of Technology, Institute of Timber Engineering and Wood Technology, Austria

[3)]Delft University of Technology, Biobased Structures and Materials, The Netherlands

Keywords: axially-loaded screws, withdrawal failure, screw failure, end-grain connection, parallel to grain, screw group, design model, minimum spacing, embedment

1 Introduction and aim

In timber construction, screws are frequently used in a passive manner as reinforcement or in an active way as fasteners to join structural components. In joints, they are preferably loaded axially and are applied in timber-to-timber connections like floor-to-wall systems made of CLT (see abbreviations at the end of the paper) or in joints of diverse timber products in combination with outer steel plates. Such steel-to-timber connections for the transfer of tensile loads may be realized either by inclined screws, as examined for example by Krenn (2018) or screws applied parallel to grain in the end-grain of timber components in combination with thick steel plates. Recent studies on the properties of end-grain connections performing short-term tests with axially loaded screw groups inserted parallel to the grain given in Grabner and Ringhofer (2014), Brandner (2019), Westermayr and Van de Kuilen (2019), Meyer (2020) and Mahlknecht et al. (2021) indicate promising load carrying capacity and high stiffness. However, no standardized design procedure is available for such connections. Possible reasons are discussed in brief: With regard to the withdrawal strength of single screws, there is a characteristic approach published by Brandner et al. (2019a), which bases on comprehensive investigations on screws inserted in different timber products made of softwood species ("CONF", c. f. Ringhofer et al., 2015 and Ringhofer, 2017) and which was extended for the application in usual hardwood products ("RP" and "DP") as well:

$$f_{\mathrm{ax,k}} = f_{\mathrm{ax,ref,k}} \cdot k_{\mathrm{ax,k}} \cdot k_{\mathrm{sys,k}} \cdot \left(\frac{\rho_{\mathrm{k}}}{\rho_{\mathrm{ref,k}}}\right)^{k_\rho}, \text{ with} \tag{1}$$

$$f_{\mathrm{ax,ref,k}} = k_{\mathrm{diam}} \cdot \begin{cases} 0.0130 \cdot \rho_{\mathrm{ref,k}}^{1.10} & \text{for CONF} \\ 0.0029 \cdot \rho_{\mathrm{ref,k}}^{1.40} & \text{for RP} \\ 0.0004 \cdot \rho_{\mathrm{ref,k}}^{1.70} & \text{for DP} \end{cases}, \; k_{\mathrm{diam}} = d^{-0.33}, \tag{2}$$

$$k_{\mathrm{ax,k}} = \begin{cases} 0.70\, k_{\mathrm{gap,k}} + \alpha \frac{1-0.70\, k_{\mathrm{gap,k}}}{30} & \text{for } 0° \leq \alpha \leq 30° \\ 1.00 & \text{for } 30° \leq \alpha \leq 90° \end{cases}, \text{ with} \tag{3}$$

$$k_{\mathrm{gap,k}} = \begin{cases} 0.90 & \text{for CLT narrow face} \\ 1.00 & \text{else} \end{cases}, \tag{4}$$

$$k_{\mathrm{sys,k}} = \begin{cases} 1.00 & \text{for SO, } n = 1 \\ 1.10 & \text{for CLT side face}, n \geq 3 \\ 1.13 & \text{for GLT}, n \geq 5 \end{cases}, \tag{5}$$

$$k_\rho = \begin{cases} 1.10 & \text{for CONF \& } 15° \leq \alpha \leq 90° \\ 1.25 - 0.05d & \text{for CONF \& } 0° \leq \alpha < 15° \\ 1.40 & \text{for RP \& } 0° \leq \alpha \leq 90° \\ 1.70 & \text{for DP \& } 0° \leq \alpha \leq 90° \end{cases}, \text{ and} \tag{6}$$

ρ_k and $\rho_{ref,k}$ as characteristic density of the basis material of the timber product in which the screw is inserted and the one of the reference material, *d* as (nominal) outer thread diameter of the screw, α as axis-to-grain angle and *n* as number of layers penetrated by the screw. In fact, this model covers a wide range of densities and various kinds of timber products. However, it lacks of two important aspects, which are necessary to reasonably apply it for end-grain joints with axially loaded self-tapping screws:

First, the model was developed for single screws only, while group effects resulting for such joints remain partly unclear. This concerns on the one hand the effective number of screws (n_{ef}) and on the other hand the minimum spacing between screws (a_2) and to the timber members' edges ($a_{2,CG}$) in order to achieve the same failure of the screw group as it is given for the single fastener. And second, it does not take the long-term performance of self-tapping screws into account, which are inserted in grain direction. The results of some related studies made in the past (e.g. Pirnbacher and Schickhofer, 2012 or Uibel and Blaß, 2013) indicate increased long-term failure rates of parallel to grain inserted screws. This also led to the fact, that axially loaded screws and screw groups applied in grain direction cannot be designed according to EN 1995-1-1:2010 (EC5) and suffer inefficient design and execution rules given in EAD 130118-00-0603:2016.

On basis of extensive experimental campaigns during the past years at TU Graz (TUG) and TU Munich (TUM), including numerous test series regarding the short- and long-term loading of single screws and screw groups, the study at hand aims to develop a safe but also efficient design procedure for steel-timber end-grain connections with axially loaded screw groups applied in grain direction. For this, important findings in publications of the past years were verified by or combined with yet unpublished data. Due to the limited extent of this paper and the big amount of contents, only the most important information is given in this study as further details can be found in the cited references. The content of this study can be structured into three main groups: Group 1 deals with the withdrawal behaviour of single screws, where it is aimed to verify given approaches for describing the effects of selected parameters on the withdrawal strength (Eq. (2) to Eq. (6)) and to simplify and extend the empirical design model given in Eq. (1), especially by including the long-term loading. In Group 2, geometrical and practical requirements like minimum spacing and predrilling were derived to allow the geometric design and practical execution of end-grain connections with multiple screws. Group 3 finally summarizes the outcomes of destructive tests on steel-timber end-grain connections with axially loaded screw groups aiming the validation, adjustment and extension of the aforementioned design model.

2 Materials, test plan and experimental setup

2.1 Materials

This paper aims to provide design models and execution advice for widely used as well as potentially interesting wood species for timber construction. A broad range of softwood and hardwood species was thus considered to represent different density levels and wood anatomical features: the softwood (SW) species spruce (NS, *Picea abies*) and pine (PI, *Pinus sylvestris*), the ringporous (RP) hardwood species sweet chestnut (SC, *Castanea sativa*), ash (AS, *Fraxinus excelsior*), oak (OA, *Quercus robur/petrea*) and robinia (RO, *Robinia pseudoacacia*) and the diffuse porous (DP) hardwood species black poplar (BP, *Populus nigra*), birch (BI, *Betula pendula*) and beech (BE, *Fagus sylvatica*). Predrilling and minimum spacing advice were derived involving BE and NS solid timber (SO), BE and NS glued laminated timber (GLT) and laminated veneer lumber (LVL) made of BE (BB). The tests on screw groups were performed in GLT made of NS, BE and BI as well as BB. The timber material originated from Northern and Central Europe. Mainly three self-drilling and hardened screw types (ST) for application in structural timber construction of two different manufacturers (manufacturer 1 = ST1; manufacturer 2 = ST2 + ST3) were applied in the present investigations. The withdrawal experiments at TUM were mainly conducted using ST1 with an outer thread diameter d_o = 11 mm, some additional experiments were performed with other d_o of ST1 or with ST2/ST3. At TUG, the majority of tests presented in this contribution involved ST2 and ST3. The geometrical properties of the applied screws and the allocation to the test plan are given in Table 1 and Table 2.

Table 1: Geometrical properties of the screw types considered in this study.

	d [mm]	d_i [mm]	p [mm]	v [°]
ST1[1,4]	7.0; 9.0; 11.0; 13.0	4.6; 5.9; 6.6; 8.0	5.3; 5.5; 5.8; 6.0	40
ST2[1,3]	8.0; 12.0	5.2; 7.0	3.7; 6.2	40
ST3[2,3]	8.0	6.1	4.0	40

1) partial tip; 2) full tip; 3) compressor; 4) notched cut tip

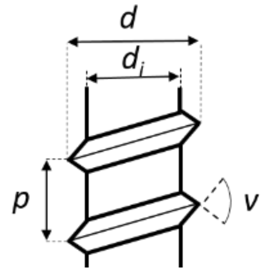

2.2 Test plan

The test plan with the parameters examined in this study is summarized in Table 2 and was divided into three groups, which are explained in the following.

Table 2: Withdrawal test plan with main parameters of the investigation.

Parameter	Instit.	d_o [mm]	l_{ef} / d [–]	l_{emb} / d [–]	α [°]	species	ST
diameter d_o; density ρ	TUM[1]	7; 9; 11; 13	6; 10	0	0	AS; BE; NS; PI	1
eff. insertion length l_{ef}	TUM[1]	11; 12(NS)	≈2 – 25	0	0	AS; BE; NS; PI	1; 2
embedment length l_{emb}	TUM[1]	11	≈6	0; 1; 2; 4	0	BE	1
	TUG	8	6.5	0; 2; 4	0	BE; BB; NS	2; 3
screw axis-to-grain angle α	TUM	11	≈4.5	0	0 – 90	AS[1]; BE; NS; PI[1]	1
Moisture content u	TUM	11	≈5.5	0	0	BE; PI[1]	1
duration of load	TUM[1]	9	5	0	0	BE	1
	TUG	8	7.5	0; 2; 4	0	BE; BB; NS	2; 3
predrilling	TUG	8	6.25	0	0	BE; BB	3
minimum spacing $a_{2(,CG)}$	TUM	11	≈6	0	0	BE; NS	various
	TUG	8	12.5	0; 2	0	BE; BB	3
screw group	TUM	8; 11	≈4.5 – 37.5	0; ≈4.5; ≈6.25	0	BE; NS	1; 3
	TUG	8; 10	various	2; 6.3; 8.4; 10	0	BE; BI; BB	various

1) not yet published (nyp) data

<u>Group 1</u> of the investigation focused on the effects of varying screw and timber parameters on the withdrawal strength of single screws. The examined parameters to verify and extend Eq. (1) were mainly conducted at TUM and comprised the outer thread diameter d, the timber density ρ, the effective screw insertion length l_{ef} and the embedment length l_{emb}, the screw axis-to-grain angle α, the timber moisture content u and the duration of load effect. All single screw withdrawal specimens at TUM were predrilled (PD) with d_i, whereas no predrilling was applied in the single screw withdrawal tests at TUG apart from the investigation dealing with the effect of predrilling. With regard to the effective insertion length, the program at TUM consisted of l_{ef} = {20; 30; …; 80} mm in BE and AS and l_{ef} = {50; 75; 90; 100; 110; 120; 135; 150} mm and l_{ef} = {50; 100; 150; 200; 250; 300} mm in PI and NS respectively (nyp). Also at TUM, the screw axis-to-grain angle α was varied between 0 – 30° in 5° steps with additional tests at 90° in NS/BE (Westermayr and Van de Kuilen, 2020) and in

PI/AS (nyp). The approach to verify moisture content adjustment coefficients k_{mc} as summarised in Ringhofer (2017) for NS involved BE (Westermayr and Van de Kuilen, 2020) and PI (nyp). The specimens were therefore stored in four different relative humidity (rh) levels of 40; 65; 75 and 85 % and 20 °C until constant mass was reached, which resulted in moisture contents of u_{mean} = {9.0; 11.8; 14.1; 18.2} % for BE and u_{mean} = {8.4; 12.3; 14.7; 18.7} % for PI. The DOL effect was examined measuring the time-to-failure (T_f) at TUG (see Brandner et al., 2019b; Gstettner et al., 2022) and TUM (nyp) at load levels (LL) of 60, 70 and 80 % of the mean short-term capacity under constantly humid conditions (TUG; 85 % rh) as well as varying humidity (TUM; ≈30 ≤ rh ≤ 85 %). The short-term capacity for calibration of the load levels was determined at TUG and TUM on specimens conditioned at 85 % rh. The first climatic period at TUM was following the procedure for glued-in rods given in EN 17334:2021 with a humidification of the specimens at 85 % rh after conditioning at 65 % rh. After six months, the humidity in the climate chamber was changed sharply from 85 % rh to ≈30 % rh. The dry period continued until three control specimens reached constant mass, which took 40 days. After the dry period, a weekly change between 85 and 30 % rh was set for six weeks, followed again by a constantly humid climate with 85 % rh for six months. This climate protocol with a weekly change in humidity for six weeks and a subsequent humid period for six months was then repeated in a loop.

<u>Group 2</u> included test programs to obtain minimum spacing and edge distance and to provide predrilling advice. Screw insertion and screw withdrawal tests were performed at TUG (Brandner, 2019) and TUM (Westermayr, 2022) to determine required minimum values of {a_2, $a_{2,CG}$} for BE, BB and NS. The screw insertion tests at TUM (PD) considered five different screw types of four manufacturers in BE and NS with edge distances of $a_{2,CG}$ = {1; 1.25;1.5} d. The screw insertion tests at TUG (PD and not PD) included edge distances of 1.5 $d \leq a_{2,CG} \leq$ 3.75 d for single screws in BB/BE and additional group insertion tests (n_{screws} = 9) with a_2 = 2 d and $a_{2,CG}$ = {1.5; 2} d in BB. The screw withdrawal tests were performed with $a_{2,CG}$ = {1; 1.25; 1.5} d and a_2 = {2; 3} d at TUM (PD; push-pull; n_{screws} = 2) and with multiple combinations of $a_{2,CG}$ and a_2 at TUG (PD; pull-pull; n_{screws} = 3). The effect of predrilling on the withdrawal properties was examined in single screw pull-out tests by TUG for PD diameters of d_{PD} = {5.5; 6; 6.5; 7} mm in BE and BB.

<u>Group 3</u> finally covers axial load tests of screwed end-grain connections consisting of screw groups in combination with thick steel plates. The aims were the optimization of capacity reaching withdrawal or screw tension failure and the reduction of brittle failure risk of the connection with and without additional and unplanned lateral loads and moments as well as to validate, adjust and extend the single screw withdrawal design model for screw groups. Consequently, based on the findings in Group 2, all screws were inserted predrilled. Screw groups in GLT with quadratic cross section (78 × 78 mm²) were tested with groups of nine ST1 screws (d = 11 mm, BE and NS, target failure withdrawal) and with groups of nine ST3 screws (d = 8 mm;

l_{ef} = 300 mm; BE; target failure steel failure) at TUM (partly published in Westermayr and Van de Kuilen, 2019). Experiments at TUG dealt with tests in BE and BI GLT and BB with hexagonal cross sections and groups of 19 ST3 screws (d = 8 mm) per end-grain (Brandner, 2019, Mahlknecht et al., 2021) and with tests in BI and BE GLT with quadratic cross sections and twelve screws (d = 10 mm) in each end-grain (Mahlknecht et al., 2021). As a supplement to these pure axial loading tests, a series (BI GLT; n_{screws} = 12; d = 10 mm; l_{emb} = 10 d; l_{ef} = 23 d) was carried out at TUG (nyp) with additional lateral loading, leading to shear forces and bending moments in the joint.

2.3 Data assessment and experimental setup

All withdrawal tests were conducted with constant feed speed and withdrawal strength f_{ax} was calculated according to Eq. (7) with $F_{ax,max}$ as maximum withdrawal force and n as number of screws in the screw group withdrawal tests.

$$f_{\mathrm{ax}} = \frac{F_{\mathrm{ax,max}}}{d \cdot \pi \cdot l_{\mathrm{ef}} \cdot n} \tag{7}$$

Apart from the DOL tests, which followed a pull-pull test setup, all other single screw tests were performed with push-pull setups following EN 1382:1999/2016 (TUG/TUM). For testing of the end-grain connections, the screws of the screw groups were inserted crosswise in the predrilled ($d_{PD} \approx d_i$; $l_{PD} = l_{ef}$) specimens until the screw heads had flush contact with the thick steel plate and a predefined torque was reached. As additional moments were possibly leading to lower capacity due to the one-sided pull-pull test setup of Westermayr and Van de Kuilen (2019), additional tests were performed at TUM (nyp) using a two-sided pull-pull configuration following the approach of TUG (see e.g. Mahlknecht et al., 2021). The statistical evaluation of all single screw and screw group withdrawal strength values gained with pull-pull test configurations involved right-censored and equi-correlated data analysis. After testing, the moisture content of each specimen was obtained according to EN 13183-1:2002 and density according to ISO 3131:1996 (TUG) or buoyancy method (TUM).

3 Results and discussion

3.1 Single screw withdrawal (Group 1)

At first, the latest outcomes regarding single screw withdrawal properties are discussed, in particular the influence of the main parameters as screw diameter, density, screw axis-to-grain angle and thread embedment. Starting with the effects of d and ρ_{12} on $f_{ax,12}$, these are commonly expressed by power functions:

$$f_{\mathrm{ax,12}} = a \cdot d^{k_{\mathrm{diam}}} \cdot \varepsilon_{\mathrm{d}} \tag{8}$$

$$f_{\mathrm{ax,12}} = a \cdot \rho_{12}^{k_{\rho}} \cdot \varepsilon_{\rho} \tag{9}$$

with a and k_{diam}/k_ρ as regression parameters and ε_d and ε_ρ as error terms of the models. Table 3 compares values of k_{diam} and k_ρ recently determined at TUM with the ones gained in previous series at TUG, which served to determine Eq. (2) and Eq. (6).

Table 3: Values of k_{diam} and k_ρ for different screw axis-to-grain angles and species.

Study	α [°]	Species	$k_{diam,mean}$	$k_{diam,k}$	k_ρ
Hübner (2013)	0 – 90	AS; BE; RO	–0.33	–0.34	1.60
	0	AS	–0.38	–0.47	–
Ringhofer (2017)	0; 90	NS	–0.69; –0.36	–	0.70; 1.10
Brandner (2019)	0	NS; RP¹⁾; DP²⁾	–0.33*	–0.33*	0.85; 1.40; 1.65
	90	NS; RP¹⁾; DP²⁾	–0.33*	–0.33*	1.20; 1.40; 1.75
TUM (nyp)	0	NS+PI; AS; BE	–0.32	–0.40	0.75; 1.10; 1.85

1) {SC; AS; OA}; 2) {BP; BI; BE}; * value adopted from Ringhofer et al. (2015)

Regarding the mentioned studies in Table 3, an exponent of –0.33 can be confirmed once again by the results obtained at TUM to describe the effect of d on f_{ax} as proposed in the design models by Hübner (2013), Ringhofer (2017), Brandner (2019) and Brandner et al. (2019a) for 0 – 90° application in hardwood and softwood species. In terms of k_ρ, more pronounced differences appear in the exponent depending on screw axis-to-grain angle and species group as higher values of k_ρ are determined for perpendicular to grain inserted screws and in hardwoods. This specific behaviour, described by Eq. (6), is confirmed by the novel results from TUM. To simplify the slightly differing values of k_ρ for different species groups and to combine the impacts of d and the characteristic density ρ_k for calculation of the characteristic reference withdrawal strength $f_{ax,ref,k}$ for screws inserted perpendicular to the grain in solid soft- or hardwoods, the separate proposals for soft- and hardwood in Brandner et al. (2019a) can be simplified to:

$$f_{\mathrm{ax,ref,k}} = 8.17 \cdot d^{-0.33} \cdot \left(\frac{\rho_{\mathrm{k}}}{\rho_{\mathrm{ref,k}}}\right)^{k_{\mathrm{p}}} \tag{10}$$

with $\rho_{ref,k}$ = 350 kg/m³ as the characteristic reference density for SW and HW and the density coefficient k_ρ with $k_\rho = \begin{cases} 1.10 & \text{for SW \& } 15° \leq \alpha \leq 90° \\ 1.25 - 0.05\,d & \text{for SW \& } 0° \leq \alpha \leq 15° \\ 1.6 & \text{for HW \& } 0° \leq \alpha \leq 90° \end{cases}$.

As the latest study of TUM found constant withdrawal strength of screws applied in grain direction over a large bandwidth of l_{ef} in hardwood species as well, l_{ef} must still not be considered when determining $f_{ax,ref,k}$. However, a noteworthy negative impact of thread irregularities on f_{ax}, which appear partly as a result of the screw production process especially concerning long screws (and thus increasing l_{ef}), was found in the investigation at TUM for 0° application, which underlines the absolute need of proper quality control of screws. A neglecting effect of l_{emb} on the short-term withdrawal capacity of single screws applied parallel to the grain in BE was found in the study at TUM as no significant differences in mean withdrawal strength were found between the reference (l_{emb} = 0 d) and the three embedded groups (l_{emb} = {1; 2; 4} d) on basis of ANOVA (p-value = 0.90).

This can be explained by the local shear failure around d concerning 0° screw application with a very limited lateral stress distribution in contrast to 90° inserted screws, see also Hübner (2013) and Ringhofer (2017). Short-term reference tests for the DOL investigations in Brandner et al. (2019b) report a positive embedment effect, i.e. 1.05 to 1.25 times higher average withdrawal capacities for l_{emb} = {2; 4} d than for l_{emb} = 0 d. Due to a potential contact between timber and screw thread in the embedded zone in these investigations and in view of the above stated argumentation it is further suggested not to consider an embedment effect on $f_{ax,k}$ in case of axially-loaded screws inserted parallel to the grain.

The influence of the screw axis-to-grain angle on the withdrawal strength can be expressed by the factor k_{ax}, which was in Eq. (3) chosen to represent a bilinear model with a linear reduction of f_{ax} for screw axis-to-grain angles below 30° and constant f_{ax} for angles between 30 and 90° (Brandner et al. 2019a). Similar results were obtained at TUM for the softwood species NS (see Westermayr and Van de Kuilen, 2020) and PI (nyp) as characteristic strength reductions of 0.7 and 0.4 % were found per ° angle decrease between 30 and 0°. In contrast, the two hardwood species AS and BE investigated at TUM showed surprisingly almost constant f_{ax} independent of the screw axis-to-grain angle, which may be a result of the tested material (e.g. low density AS, narrow growth rings) and the low inserted thread length of 50 mm. The approach given in Eq. (3), however, seems to be on the safe side to respect the withdrawal strength reduction for angles below 30°. Shear strength reacts with a severe strength reduction under increasing moisture content and especially end-grain connections experience a rather high moisture variability under changing humidity. For each % increase in moisture content, Hübner (2013) suggests a strength reduction of 2.5 % for each % moisture increase for AS (11 % ≤ u ≤ 31 %). Ringhofer (2017) summarises a withdrawal strength reduction of 3.4 % for NS and 12 % ≤ u ≤ 20 % and no moisture adjustment between 8 % and 12 %, while the studies at TUM found respective values of 2.5 % for BE (Westermayr and Van de Kuilen, 2020) and 3.0 % for PI (nyp) for a moisture range of 9 % ≤ u ≤ 18 %. The analysed softwood species obviously lead to a slightly higher decrease in f_{ax} with increasing moisture content compared to the two hardwoods. Due to an almost equal treatment of the k_{mod} factors for service class 1 and 2 in the current EC5, it is suggested to take this strength reducing effect into account via an additional factor k_{mc}, which considers a general strength loss of 3 % per % increase of u and u = 12 % in service class 1 and u = 18 % in case of service class 2:

$$k_{\mathrm{mc,k}} = \begin{cases} 1.00 & \text{for service class 1} \\ 0.82 & \text{for service class 2} \end{cases} \tag{11}$$

With regard to the long-term behaviour, uncertainties related to the withdrawal strength of parallel to the grain inserted axially-loaded screws forbid this application in EC5 and led to a rather conservative regulation in current European Technical Assessments (ETAs). Following the guidelines in EAD 130118-00-0603:2016, i.e. only 30 % of $f_{ax,ref,k}$ can be considered although short-term tests indicate 70 %; see Eq. (3).

Some intermediate long-term test results are thus presented in this study after testing periods of ≈4.7 years at TUG (Gstettner et. al, 2022) and ≈1.7 years at TUM (nyp), from which linear regression functions were derived on logarithmic time scale in Figure 1 (BE; 0°) using equal-rank assumption (Madsen, 1992). The relationship between *LL* and time-to-failure (T_f) is therefore commonly described by the model approach given for example in Wood (1947) and Pearson (1972) as shown in Eq. (12).

$$LL = c - d\log_{10}(T_{\mathrm{f}}) \tag{12}$$

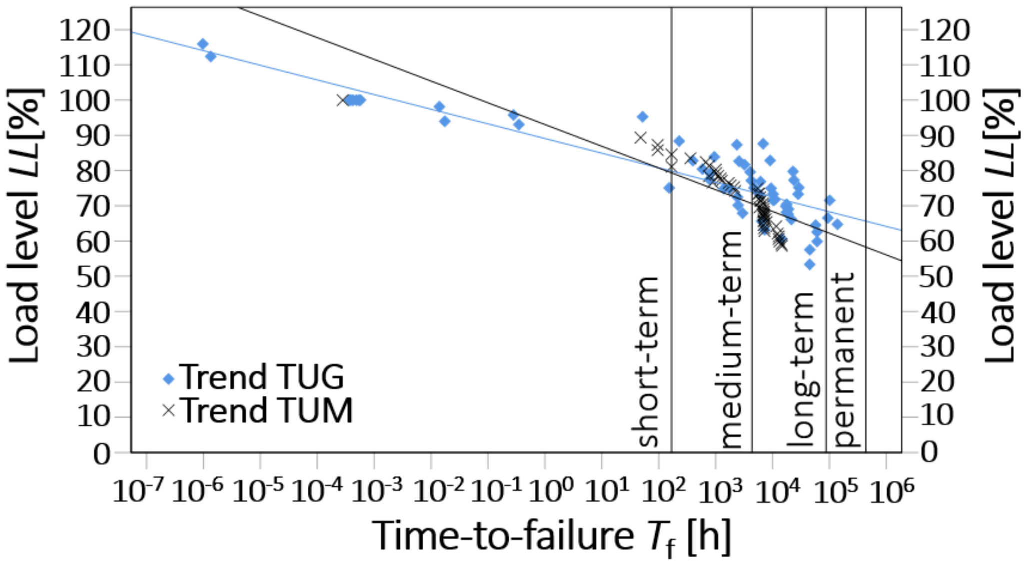

Figure 1: TUG and TUM DOL test data and regression functions for BE and 0° application.

In the studies at TUG and TUM, almost all specimens of *LL* = 70 and 80 % already failed, while some specimens of *LL* = 60 % are still under testing. At this point, it is mentioned, that the regression analysis react very sensitive (i) on the type of the fitted function (e.g. linear, multi-linear, non-linear) and (ii) on the time-to-failure data involved for the analysis, especially concerning specimens with instantaneous failures during loading (see Van de Kuilen, 1999). As an example, the exclusion of the instantaneously failed specimen in the study at TUM would lead to a more pronounced DOL-effect with a resulting k_{mod} factor of ≈0.5. Table 4 summarizes values of k_{mod} calculated for the lower boundary of each DOL group from the linear regressions involving all data points derived at TUG/TUM (ST2 & 3 of TUG combined) using the model of Eq. (12) and compiles them with models of Wood (1951), Pearson (1972) and EC5.

Table 4: Estimated k_{mod} factors from TUG/TUM and calculated k_{mod} factors from references.

DOL	NS_{TUG}*	BB_{TUG}*	BE_{TUG}*	BE_{TUM}*	Pearson (1972)*	Wood (1951)*	EC5
permanent (10 – 50 y[1)])	0.60	0.57	0.66	0.58	0.52	0.59	0.60
long-term (26 w – 10 y)	0.63	0.60	0.69	0.63	0.57	0.62	0.70
medium-term (1 – 26 w)	0.68	0.66	0.74	0.71	0.66	0.69	0.80
short-term (0.1 s[1)] – 1 w)	0.75	0.73	0.80	0.79	0.76	0.77	0.90
instantaneous (0.1 s[1)])	1.04	1.07	1.07	1.07	1.16	1.27	1.10

[1)] assumed load duration as value is not specified in EC5; * k_{mod} factors were calculated using the lower boundary of DOL, e.g. 50 years for DOL = permanent

The current results show, that the k_{mod} factors determined at TUG and TUM for axially loaded screws applied in grain direction are in a similar range like the k_{mod} factors given in the current EC5 and the models of Wood (1951) and Pearson (1972). It is further remarkable, that the varying climate in the tests of TUM did not lead to a stronger decrease of the k_{mod} factors so far compared to the tests at TUG performed under constantly humid conditions. The study at TUG further concludes that l_{emb} has no significant effect on T_f and ST2 & 3 showed comparable DOL behaviour; similar outcomes are also reported for DOL tests at $\alpha = \{15; 30; 45\}$ ° (Gstettner et al., 2022). Given that, there is strong evidence that the generic model presented in section 1 can be safely applied also for long-term loadings.

Considering these latest findings from TUG and TUM regarding the selected parameter verifications and the impact of DoL, the characteristic withdrawal capacity $R_{ax,k}$ of single screws in various timber products (SO, GLT, CLT, LVL) made of soft- or hardwood can be determined by:

$$R_{\mathrm{ax,k}} = d\, l_{\mathrm{ef}}\, \pi\, f_{\mathrm{ax,ref,k}}\, k_{\mathrm{ax,k}}\, k_{\mathrm{sys,k}}\, k_{\mathrm{mc,k}} \tag{13}$$

with the modified $f_{ax,ref,k}$ according to Eq. (10), the additional $k_{mc,k}$ according to Eq. (11) and the remaining parameters according to section 1.

3.2 Geometrical and practical requirements (Group 2)

For the design of end-grain connections with multiple screws, geometrical and practical requirements were derived in several test programs. Minimum spacing a_2 and edge distance $a_{2,CG}$ were investigated with screw insertion tests as well as withdrawal tests. As predrilling is supposed to be crucial for the efficient design of compact screw groups in the end-grain, the minimum spacing and edge distances given in Table 5 are limited to predrilled specimens.

Table 5: Minimum spacing and edge distances determined in insertion and withdrawal tests.

			Insertion tests		Withdrawal tests	
Species/product	Instit.	l_{emb} / d [–]	a_2 / d [–]	$a_{2,CG}$ / d [–]	a_2 / d [–]	$a_{2,CG}$ / d [–]
BE	TUM	0	–	1.5	2	1.5
	TUG	0/2	–	1.25	3/2	>1.5/>1.5
NS	TUM	0	–	1.5	3	1.5
BB (rad.)	TUG	0/2	2	2	5/4	3/3
BB (tan.)	TUG	0	2	2	3	3

Summarizing the results of TUM and TUG for different species, a minimum edge distance of $a_{2,CG} = 3\,d$ and a minimum spacing between screws of $a_2 = 2.5\,d$ is proposed for SP, GLT and CLT. For LVL $a_{2,rad} = 4\,d$ and $a_{2,tan} = 3\,d$ are proposed because of the given lathe checks in veneers and the more brittle behaviour. The recommendations above apply to end-grain joints with screw groups inserted predrilled and sufficiently embedded in the timber; see Sections 3.1 and 3.3. It is worth mentioning, that the screw and especially tip type had a big impact on splitting during screw insertion, as two screw types led to 30 % splitting failure and no splitting was observed at all for another screw type (see Westermayr, 2022). It is further stated, that such narrow spacing requires high precision and adequate technical equipment in the overall production process. Especially for screws with high slenderness, special drilling equipment might become necessary to prevent too much deviation of the drilling axis from the target axis and to avoid potential contact between screws or a lateral exit of the screw from the cross section of the timber component, see Oboril (2021) and Westermayr (2022). Concerning predrilling, Brandner (2019) found a loss in withdrawal strength if the minimum lateral penetration depth of the screw thread in the timber volume was lower than 0.75 – 0.8 mm. For practical application, predrilling with PD = d_i is recommended to allow a controlled position of the screw in the timber component and minimized spacing a_2 and edge-distance $a_{2,CG}$ as well as to reduce the insertion moment and the risk of splitting during screw application.

For a balanced distribution of loads on the screws in the screw group, thick outer steel plates applied on clean-cut and flat end-grain surfaces are required to prevent significant bending deformations. Mahlknecht et al. (2021) recommend to keep the maximum deformation difference between two farthermost screws in the group below 0.1 mm. In respect to the screw insertion, crosswise application, i.e. the insertion of screws in a chronological order, in combination with a predefined torque is crucial to assure balanced loading and tight fit of screw heads in the steel plate. In this regard screws with countersunk heads are suggested. The torque has to be sufficient for the tight fit but shall not be too high preventing overturning of the thread in the timber, thus an adjustment with the wood species/product in dependency of the parameters ρ, d and l_{ef} is essential. Experience from testing of such joints shows that for BI, BE and BB, respectively, 15 to 40 Nm may be applied in cases of d = {8; 10} mm and l_{ef} = {10 – 23} d (Mahlknecht et al., 2021; Oboril, 2021; Schweiger, 2021) and needs to be individually chosen according to the specific joint configuration. The joint further gets pre-stressed by applying torque with the advantage of much higher stiffness in the initial phase of the load-displacement characteristic (Schweiger, 2021).

3.3 End-grain connection with screw groups and steel plates (Group 3)

From an engineering perspective, it is aimed to avoid brittle failure modes, like splitting or block shear, which result mainly from multiple fasteners interacting in a group and leading to adverse stress states in the timber volume. With this background, the failure modes withdrawal and steel failure were targeted in the investigations at TUM and TUG. Decisive factors to achieve withdrawal failure or steel failure and to avoid splitting are sufficient minimum spacing, edge distance and embedment of the screws, as outlined in previous Section 3.2.

On basis of the screw insertion and withdrawal tests described in Section 3.2, all tests at TUM were conducted using an edge distance of $a_{2,CG} \approx 1.5\ d$ and a spacing of a_2 = 2 d. A first test series on screw groups in the end-grain caused splitting failure as no embedment of the screws was applied. After an embedment of $l_{emb} \approx 4.5\ d$ in the second test series, the failure mode changed from splitting to withdrawal (see Westermayr and Van de Kuilen, 2019). In consequence, all further tests at TUM with target failure withdrawal were performed with an embedment of $l_{emb} \approx 4.5\ d$ and with a slightly deeper embedment of $l_{emb} \approx 6.25\ d$ to prevent splitting as a result of the higher loads in case of steel failure. This widely confirms earlier tests at TUG (BI; $a_2 = 2.1\ d$; $a_{2,CG} = 2.8\ d$; $l_{emb} \geq 5\ d$). In these examinations $l_{emb} = 5\ d$ was sufficient to achieve withdrawal failure whereas some samples in a series with intended steel failure featured brittle group failure modes; see Grabner and Ringhofer (2014). Schweiger (2021) reports successful withdrawal tests on large end-grain joints in hexagonal cross sections ($n_{screw} = 19$; $a_2 = 3\ d$; $a_{2,CG} = 3\ d$; $l_{emb} = 10\ d$) in BI, whereas at the same setting but $l_{emb} = 5\ d$ splitting occurred in some samples. The same was observed for BB even at $l_{emb} = 11\ d$. Oboril (2021) tested end-grain joints in squared cross sections of BI and BE ($n_{screw} = 12$) and observed steel failure mode even at $l_{emb} = 10\ d$ in BI and $5\ d$ in BE, given $a_2 = 2.1\ d$, $a_{2,CG} = 2\ d$ (BI) and $2.6\ d$ (BE). Beside loading and spacing conditions, the kind of timber product and wood species have an impact on the splitting tendency, as brittle failure modes appear more frequent in LVL than SO and may be more likely in species with distinct wood features influencing the tensile strength perpendicular to the grain, like shrinking cracks along the frequent radial wood rays in BE. In conclusion, large embedment lengths appear advantageous by (i) increasing the resistance against brittle group failure modes as splitting and block tear-out, (ii) to provide a moisture buffer zone at the end-grain of structural timber components, which reacts sensitive to moisture changes and may lead to shrinking cracks as well as (iii) by increasing the elastic deformation within the screw group; see Section 3.1. Given that, $l_{emb} \geq 10\ d$ is recommended for end-grain connections, see Brandner (2019) and Mahlknecht et al. (2021).

In a further test series at TUM, the effective number of screws n_{ef} acting together in the screw group was examined. Concentrating on the failure mode withdrawal, groups with $n = \{1; 2; 5; 9\}$ screws were tested using the same base material and $l_{ef} = 70$ mm in BE and $l_{ef} = 100$ mm in NS. The $f_{ax,12}$ data were moisture and density corrected and involved right-censored and equi-correlated analysis. For both species, the characteristic withdrawal strength values for the groups with $n = \{1; 2; 5; 9\}$ screws were calibrated with power functions resulting in the factors $n_{ef,k} = n^{0.95}$ for BE and $n_{ef,k} = n^{0.91}$ for NS or can alternatively be described by $\approx 0.8\ n \leq n_{ef,k} \leq \approx 0.9\ n$. Concerning steel failure, the capacities of ten single screws and four end-grain specimens with nine screws per specimen were determined, resulting in the ratios $\frac{R_{\mathbf{tens,k,n=9}}/9}{R_{\mathbf{tens,k,n=1}}} = 1.01$ and $\frac{R_{\mathbf{tens,mean,n=9}}/9}{R_{\mathbf{tens,mean,n=1}}} = 1.00$ and thus to $n_{ef,mean} = n_{ef,k} = n$ for steel failure. Mahlknecht et al. (2021), summarizing TUG investigations on end-grain joints in hardwood, report $n_{ef,mean} \geq 0.83\ n$ for series failing in withdrawal and concludes that the current regulation in EC5 with $n_{ef,k} = n^{0.9}$ is on the safe side, although not intended for such joints. For end-grain joints targeting steel failure they confirm $n_{ef,k} = n$. By considering common uncertainties in execution and minor unplanned restrained forces in the joint, $n_{ef,k} = n^{0.9}$ is recommended for end-grain connections independent of the failure mode, although $n_{ef,k} = 0.9\ n$ may be applied, if steel failure can be guaranteed.

Although no influence of l_{ef} on f_{ax} was found in the single screw withdrawal tests in Section 3.1 using defect free material, the probability to penetrate knots in timber components in practical applications increases with deeper screw insertion. The effect of penetrating knots with increasing l_{ef} was thus checked in a further test series with screw groups inserted in defect free material (reference) with l_{ef} = {50 (BE); 100 (NS)} mm as well as timber components including knots in the area of screw insertion with l_{ef} = {90; 110; 150} mm (BE) and {150; 200; 250} mm (NS), as shown in Figure 2.

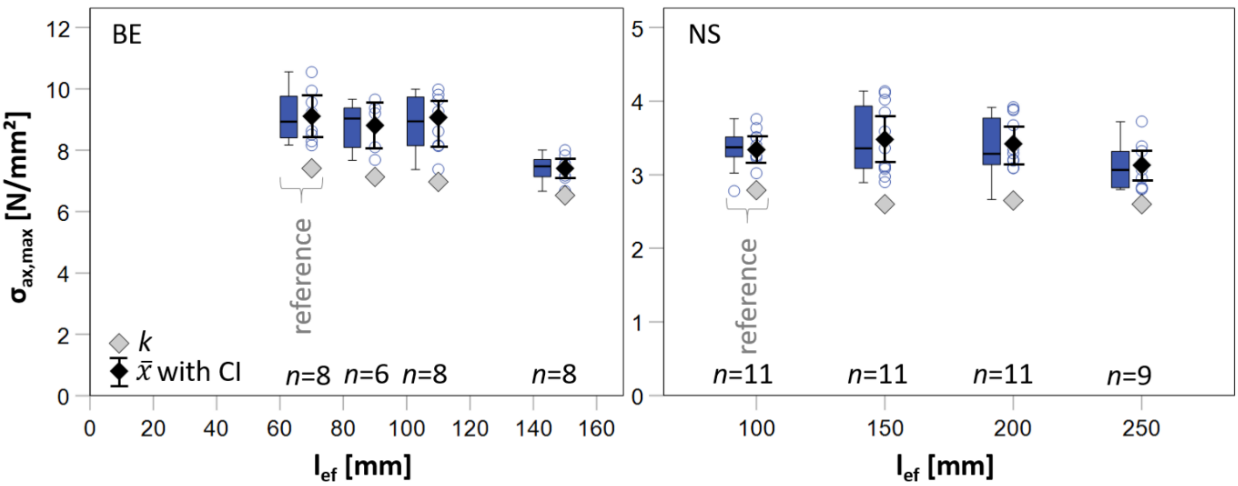

Figure 2: $\sigma_{ax,max}$ depending on l_{ef} for BE (left) and NS (right) including 95 % confidence intervals (CI).

As the majority of BE specimens with l_{ef} = 150 mm failed already due to steel failure of the screws, no f_{ax} but a maximum shear stress $\sigma_{ax,max}$ could be calculated for this test group explaining the lower value. Considering all other l_{ef} test groups of BE and all l_{ef} test groups of NS, ANOVA did not indicate any significant differences in $\sigma_{ax,max}$ for BE (p-value = 0.79) and NS (p-value = 0.22). It can be summarized, that knots in the area of screw insertion do not seem to have a negative impact on the capacity of screwed end grain connections.

End grain joints are commonly able and designed to resist high axial loads in tension. In practical applications, possible inaccuracies in production, material and execution might cause additional transverse (shear) loads and moments. Such additional transverse loads and moments in combination with a tight group design in end-grain joints optimised for axial loading may have the potential to significantly reduce the joint capacity in tension. Since reliable data for the quantitative estimation of the effect of additional transverse loads and moments on the tensile capacity of such joints was missing, corresponding initial tests were carried out at TUG, see Figure 3.

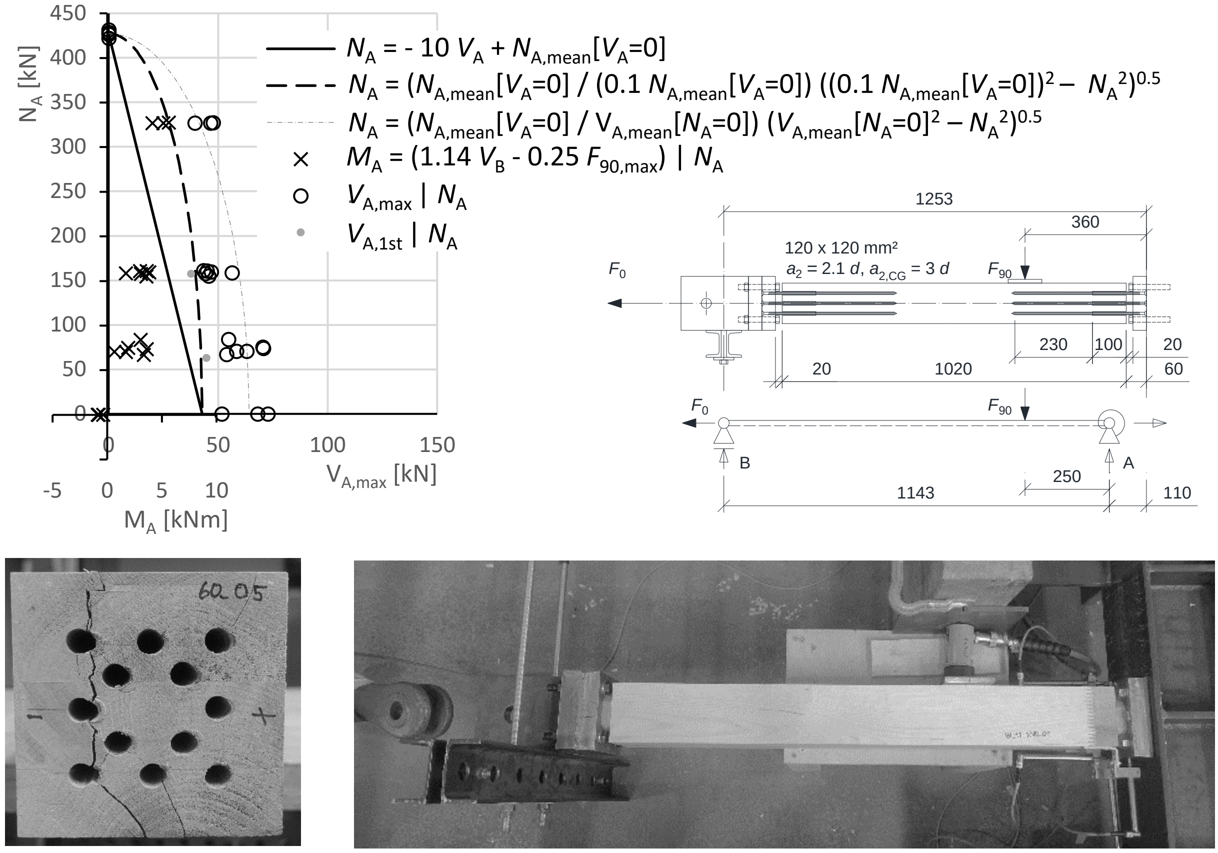

Figure 3: (left above) maximum transverse load and corresponding moments vs. axial load (first applied) and linear and elliptic relationship between the axial and the transversal load for VA[NA=0] = 0.1 NA and elliptic for mean test values; (right above) principle test setup, dimensions and static system; (left below) typical splitting failure in the joint at support A; (right below) image of realised test setup.

In addition to pure axial loading in tension (Oboril 2021), in these new tests the joint was fixed at support A, the specimens loaded axially until a predefined load level and afterwards loaded transversely until the joint at support A failed by splitting. Knowing F_{90} and the corresponding reaction load at support B (determined from parallel calibrated measurements with strange gauges fixed on steel rods), the transverse load V_A and the moment M_A of the semi-rigid support A at half of the embedment length can be determined. Note, that the bending resistance of such a slender beam is limited (approximately $M_{y,net,k}$ = 7.5 kNm). The outcomes of these calculations are summarised in Figure 3 (above left). The data points represent maximum transverse load and the corresponding axial load ($V_{A,max} \mid N_A[V_{A,max}]$) at support A and moment ($M_A \mid N_A[V_{A,max}]$). For two specimens the formation of inner cracks was acoustically clearly perceptible and in combination with a load drop, these data points are marked as first failures ($V_{A,1st} \mid N_A[V_{A,1st}]$). In a first data evaluation, it can be shown that due to the approximately elliptic relationships between N_A and V_A and the relationship between N_A and corresponding M_A, the influence of a few percentages of additional, unplanned shear force and moment is not that significant concerning the axial capacity. In analogy to glued-in rods in end grain joints, the linear relation between N and V = 0.1 N prospect a design on the safe side and the elliptic relationship allows a closer description of the observed N-V interaction.

4 Summary, conclusions and outlook

The study at hand summarizes the outcomes of extensive experimental campaigns performed at TUG and TUM regarding the withdrawal behaviour of axially loaded single screws and screw groups applied in grain direction in different timber products and wood species featuring withdrawal or screw failure. A simplified and extended form of the model approach by Brandner et al. (2019a) is presented to calculate the withdrawal capacity of single screws on a wood species independent level, which is also reflected in terms of long-term loading and moisture changes indicating the applicability of the current k_{mod} regulations given in EC5. For the design of end-grain connections with multiple screws, minimum spacings of $a_{2,\mathrm{CG}}$ = 3 d and of a_2 = 2.5 d are proposed for SP, GLT and CLT with slightly higher spacing suggestions for LVL. Predrilling with d_{i} and l_{ef} with adequate technical equipment especially for screws with high slenderness and an embedment of the screw thread ($l_{\mathrm{emb}} \geq 10\ d$) are seen to be crucial as well as a chronological and torque-controlled insertion of the screws to ensure safe and efficient end-grain connections with reduced risk of brittle failure modes. Group effects can be taken into account by the factor $n_{\mathrm{ef}} = n^{0.9}$ (n_{ef} = 0.9 n if steel failure can be guaranteed), which appears to be on the safe side for axially loaded screw groups as knots do not seem to influence the load-carrying capacity of screwed end-grain connections in a negative way. With regard to the impact of additional lateral loads, the linear relation between N and V = 0.1 N prospects a design on the safe side. It is finally proposed that screwed end-grain connections should be preferably designed with a overstrength concept concerning the screw-timber interaction to target steel failure of the screw group instead of screw withdrawal. The pre-assembled steel-timber joints with screwed on anchoring components at the end-grain surfaces can subsequently be mounted time-efficiently at the construction site with steel-steel field joints, which act as weakest link of the overall system and may provide plastic deformation ability in case of extreme loading. Possible concepts regarding steel-timber anchoring components to be screwed onto the end-grain surfaces as well as for the overall joint are given in Figure 4.

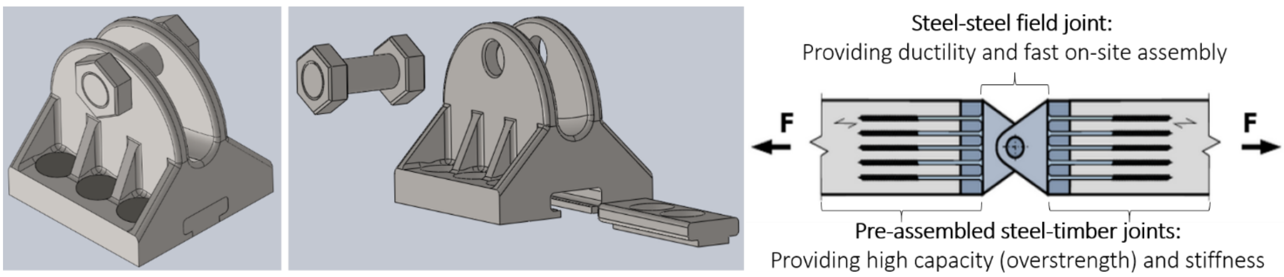

Figure 4: Concepts for end-grain anchoring components (left; middle) and overall joint (right).

In follow-up actions, the focus should be on stiffness, ductility and overstrength design of such connections and be reflected in further design approaches as the limited content of this paper did not allow an inclusion of the mentioned aspects. Future work will deal with extensive DOL investigations involving multi-linear and non-linear regression analysis.

5 Acknowledgements

The investigations at TUG are part of the research project FFG BRIDGE 1 "harwood_SCREWS" (No. 850748), and the FFG BRIDGE 1 "SCREW_STIFFNESS" (No. 861554). Both received public funding by The Austrian Research Promotion Agency (FFG). Their support and the support by the commercial partners, Schmid Schrauben Hainfeld GmbH, Pollmeier Furnierwerkstoffe GmbH, the Landeskammer für Land und Forstwirtschaft Steiermark, ARGE Holzwerbebeitrag, and the WIEHAG GmbH are thankfully acknowledged. In addition, the investigations are part of the European Research Area Networking (ERA-NET) project FOREST VALUE hardwood_joint project with funding by European Union. Thank goes to the scientific project partners of Karlsruhe Institute of Technology (KIT) in Germany, Linneaus University in Sweden, Universite de Lorraine in France and commercial partners Schmid Schrauben Hainfeld GmbH, Adolf Würth GmbH & Co. KG, Pollmeier Furnierwerkstoffe GmbH and Hasslacher Group for their valuable input and support. TUM wants to thank the Bavarian Institute of Forestry (LWF) as well as the industrial partners Rothoblaas SRL, Schmid Schrauben Hainfeld GmbH, Microtec GmbH SRL, Pollmeier Furnierwerkstoffe GmbH and Schaffitzel Holzindustrie GmbH + Co. KG.

6 References

Literature

Brandner, R (2019) Properties of axially loaded self-tapping screws with focus on application in hardwood. Wood Material Science & Engineering, DOI 10.1080/17480272.2019.1635204

Brandner, R; Ringhofer, A; Reichinger, T (2019a): Performance of axially-loaded self-tapping screws in hardwood: Properties and design. Engineering Structures 188, p.677-699.

Brandner, R; Ringhofer, A; Sieder, R (2019b): Duration of load effect on axially-loaded self-tapping screws inserted parallel to grain in soft- and hardwood. 6th International Network on Timber Engineering Research INTER, Tacoma, USA.

Grabner, M; Ringhofer, A (2014): Investigations Concerning the Loadbearing Behaviour of End-Grain Joints in Hardwood (in German). Internationales Holzbau-Forum, Prolog IV, Garmisch-Partenkirchen, Germany.

Gstettner, M; Brandner, R; Ringhofer, A; Sieder, R (2022): Axial-beanspruchte, selbstbohrende Holzbauschrauben unter Dauerlast: Untersuchungen in Nadel- und Hartlaubhölzern (in German). Doktorandenkolloquium Holzbau Forschung + Praxis, Universität Stuttgart, Stuttgart, Germany.

Hübner, U (2013): Mechanische Kenngrößen von Buchen-, Eschen- und Robinienholz für lastabtragende Bauteile (in German). Dissertation. Monographic series TU Graz, Timber Engineering & Technology, Volume 3, ISBN: 978-3-85125-314-6

Krenn, H (2018): Die Stahlblech-Holz-Laschenverbindung mit schrägen Schrauben (in German). Monographic series TU Graz, Timber Engineering & Technology, Volume 7, DOI 10.3217/978-3-85125-622-2.

Mahlknecht, U; Brandner, R; Ringhofer, A (2021): Minimum geometric and execution requirements for axially loaded groups of screws in hardwood. 8th International Network on Timber Engineering Research INTER, Online-Meeting.

Madsen, B (1992): Structural behaviour of timber. Timber Engineering Ltd., Vancouver, Canada, ISBN 0-9696162-0-1.

Meyer, N (2020): Tragfähigkeit mechanischer und geklebter Verbindungsmittel in Buchenfurnierschichtholz (in German). Dissertation. Karlsruher Berichte zum Ingenieurholzbau, Band 36. KIT Scientific Publishing, DOI 10.5445/KSP/1000122863.

Oboril, M (2021) Aspekte der Bemessung, Herstellung und Prüfung von Hirnholzanschlüssen in den Laubholzarten Buche und Birke (in German). Master Project, Graz University of Technology.

Pearson, R G (1972): The effect of duration of load on bending strength of wood. Holzforschung 26, p.153–158.

Pirnbacher, G; Schickhofer, G (2012): Zeitabhängige Entwicklung der Traglast und des Kriechverhaltens von axial beanspruchten, selbstbohrenden Holzschrauben (in German). Re-search Report, Competence Centre Holz.Bau Forschungs GmbH, Graz University of Technology, Graz, Austria.

Ringhofer, A (2017): Axially loaded self-tapping screws in solid timber and laminated timber products. Dissertation. Monographic series TU Graz, Timber Engineering & Technology, Volume 5, DOI 10.3217/978-3-85125-555-3.

Ringhofer, A; Brandner, R; Schickhofer, G (2015): Withdrawal resistance of self-tapping screws in unidirectional and orthogonal layered timber products. Mater Struct 48, p.1435-1447.

Schweiger, K (2021) Verhalten von axial beanspruchten Schraubengruppen in Laubholz-Hirnholzanschluss und Zuglaschenstoß (in German). Master Thesis, Graz University of Technology.

Uibel, T; Blaß, H J (2013): Joints with Dowel Type Fasteners in CLT Structures. Focus Solid Timber Solutions: European Conference on Cross Laminated Timber (CLT): The State-of-the-Art in CLT Research. COST Action FP1004, Graz, Austria.

Van de Kuilen, J W (1999): Duration of load effects in timber joints. Dissertation TU Delft, ISBN 90-407-1980-2.

Westermayr, M (2022): Capacity and stiffness of end-grain connections with axially loaded screw groups: required minimum spacing (in German). Doktorandenkolloquium Holzbau Forschung + Praxis, Universität Stuttgart, Stuttgart, Germany.

Westermayr, M; Van de Kuilen, J W (2019): Withdrawal strength of screws and screw groups in European beech (Fagus s.) parallel to the grain. 6th International Network on Timber Engineering Research INTER, Tacoma, USA.

Westermayr, M; Van de Kuilen, J W (2020): A conceptual model to predict the withdrawal capacity of screws inserted parallel to grain in beech, ash and spruce. 7th International Network on Timber Engineering Research INTER, Online-Meeting.

Wood, L W (1947): Behavior of wood under continued loading. Engineering News-Record 139, p.108-111.

Wood, L W (1951): Relation of strength of wood to duration of load. United States Department of Agriculture, Forest Service, Forest Products Laboratory, Madison, WI, Report No. 1916.

Standards and technical documents

EAD 130118-00-0603:2016: Screws for use in timber constructions. EOTA.

EN 1382:1999/2016: Timber structures – Test methods – Withdrawal capacity of timber fasteners. CEN.

EN 1995-1-1:2010: Eurocode 5: Design of timber structures – Part 1-1: General - Common rules and rules for buildings. CEN.

EN 13183-1:2002: Moisture content of a piece of sawn timber - Part 1: Determination by oven dry method. CEN.

EN 17334:2021: Glued-in rods in glued structural timber products – Testing, requirements and bond shear strength classification. CEN.

ISO 3131:1996: Wood – Determination of Density for Physical and Mechanical Tests.

7 Abbreviations

AS – ash	ETA – Europ. Technical Assessment	rh – relative humidity
BB – beech LVL/BauBuche	GLT – glued laminated timber	RO – robinia
BI – birch	HW – hardwood	RP – ringporous
BE – beech	LL – load level	SC – sweet chestnut
BP – black poplar	LVL – laminated veneer lumber	SO – solid timber
CLT – cross laminated timber	NS – spruce	ST – screw type
DOL – duration of load	nyp – not yet published	SW – softwood
DP – diffuse porous	OA – oak	T_f – time-to-failure
EAD – Europ. Assessment Document	PD – predrilled	TUG – TU Graz
EC5 – Eurocode 5 (EN 1995-1-1:2010)	PI – pine	TUM – TU Munich

DISCUSSION

The paper was presented by M Westermayr

H Blass commented on the factor $k_{mc,k}$*=0.82 and asked if one should use a lower factor of say 0.8. M Westermayr agreed. H Blass commented on the embedment length and said partially threaded screws may be more practical for embedment length considerations. M Westermayr agreed.*

A Frangi and M Westermayr discussed long term tests with drying and wetting. The specimens after a while did not look good as fungi was found growing even though the tests were prepared carefully. A Frangi suggested some specimens with small eccentricity should be considered. M Westermayr said this was considered in the paper but was not provided in the presentation.

P Dietsch commented that in design for short term EC5 has a k_{mod} *factor of 0.9 but the tests show a* k_{mod} *of rather 0.75. He asked, if 0.9 should still be used. M Westermayr replied maybe one should think about the whole system design approach to bring this in. R Brandner discussed the lower and upper limits of the Wood's curve and EC5.*

S Aicher commented that the TUM's slope is higher for DOL compared to the TUG's slope. M Westermayr agreed and will examine this further. S Aicher suggested weighted values using regression.

A Frangi commented that k_{mod} *for a connection is important and should consider* k_{mod} *of timber properties.*

Block Shear Model for Axially-Loaded Groups of Screws

Ursula Mahlknecht[1)*)], Reinhard Brandner[1)], Andreas Ringhofer[1)]

[1)] Institute of Timber Engineering and Wood Technology, Graz University of Technology, Graz, Austria, [*)] u.mahlknecht@tugraz.at

Keywords: axially-loaded groups of screws; hanger loaded perpendicular-to-grain; block shear failure mechanism; load sharing;

1 Introduction

Primary axially-loaded screw groups inserted perpendicular- or under an angle-to-the-grain of structural timber elements, see Figure 1.1 (left), cause locally shear, rolling shear and tensile perpendicular-to-the-grain stresses. Under certain conditions, these stresses lead to brittle joint failure mechanisms in timber, such as tension perpendicular-to-the-grain (splitting), row or block shear. The row shear failure mechanism is characterised by tearing out of narrow timber slices in-between the rows of screws parallel-to-the-grain; see Figure 1.3 (right). Carradine (2009), Plieschounig (2010), Mayer and Blaß (2018), Blaß et al. (2019), Blaß and Flaig (2019) and Mahlknecht et al. (2021) observed row shear in their tests in Norway spruce at $a_1 < 5\ d$ as well as in some hardwoods at $a_1 \leq 5\ d$. The block shear failure mechanism constitutes a combined rolling shear / shear and tensile perpendicular-to-the-grain failure of the timber volume comprising the entire screw group; see Figure 1.1 (middle and right). Compared with failure mechanisms analogue to that of single screws, e.g. withdrawal or steel tension failure, these brittle timber failure mechanisms are less predictable and have the potential to significantly reduce the resistance and reliability of such joints. This is because of their high complexity due to the large number of parameters describing the material, geometry and stress distribution, as outlined in the following, and the still missing engineering models, which allow verification of these potential failure mechanisms for all the possible joint configurations.
The focus of this contribution is on the block shear failure mechanism for common rectangular designs of screw groups. The block shear volume is principally limited in depth by the penetration length l_p, as sum of the effective threaded length l_{ef} (threaded length without tip length l_{tip}) and embedment length l_{emb}, and in plane by the circumference of the screw group; typically characterizing cracks are shown in

Figure 1.1 (middle and right). This failure mechanism has to be differentiated from the block shear failure mechanisms associated with groups of laterally-loaded dowel-type fasteners, which are frequently addressed in literature. The block shear failure mechanism of axially-loaded screw groups could be observed for $\alpha = 90°$ and even for screw groups inserted in timber members at an angle between the screw axis and the grain of 45° and loaded axially in tension. This although the minimum geometric conditions were met acc. to EN 1995-1-1 (2014; EC 5) and SIA 265 (2021), with $(a_1 \mid a_2 \mid a_{2,CG}) / d = (7 \mid 5 \mid 4)$, as well as acc. to various ETAs of well-known screw producers, with $(a_1 \mid a_2 \mid a_{2,c}) / d \geq (5 \mid 2.5 \mid 3)$ and $a_1\, a_2 \geq (21)\ 25\ d^2$; see e.g. Mahlknecht and Brandner (2013), Mahlknecht et al. (2014), Ringhofer and Schickhofer (2015), Mahlknecht et al. (2016), Mahlknecht and Brandner (2019) and Blaß and Flaig (2019). The referenced test series comprise Norway spruce (*Picea abies*), various timber products (solid timber; glulam (GLT); cross laminated timber (CLT)), self-tapping screws, various geometrical parameter settings and test configurations (near; in-between; distant supports); see Figure 1.2. Recently, Mahlknecht et al. (2021) reported a similar behaviour also for screw groups in solid timber, glulam and laminated veneer lumber (LVL) made of hardwood.

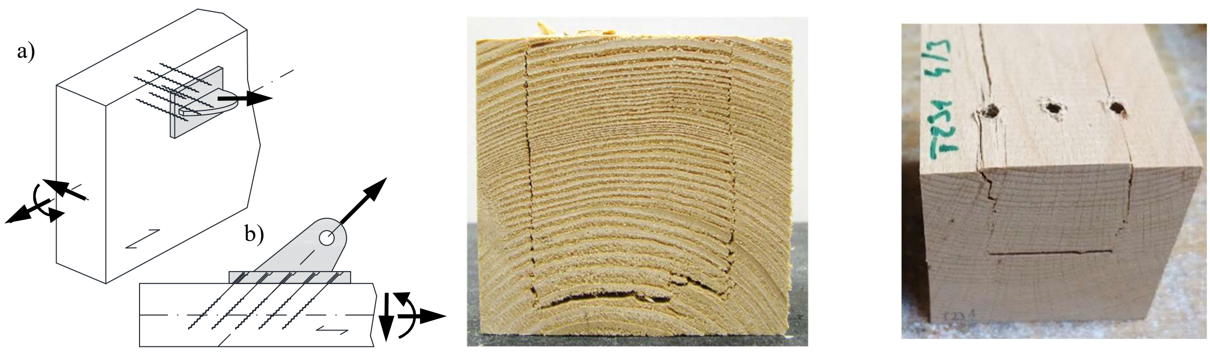

Figure 1.1 (left) examples for unilateral joints of primary axially-loaded screw groups with a risk for block shear failure mechanism: a) wind bracing joint on side-face and b) hangered beam; (middle); typical block shear failure pattern on a cross section cut in the middle of a screw joint, exemplarily for a group of 5 x 5 screws in Norway spruce and (right) for a group of 3 x 5 screws in birch.

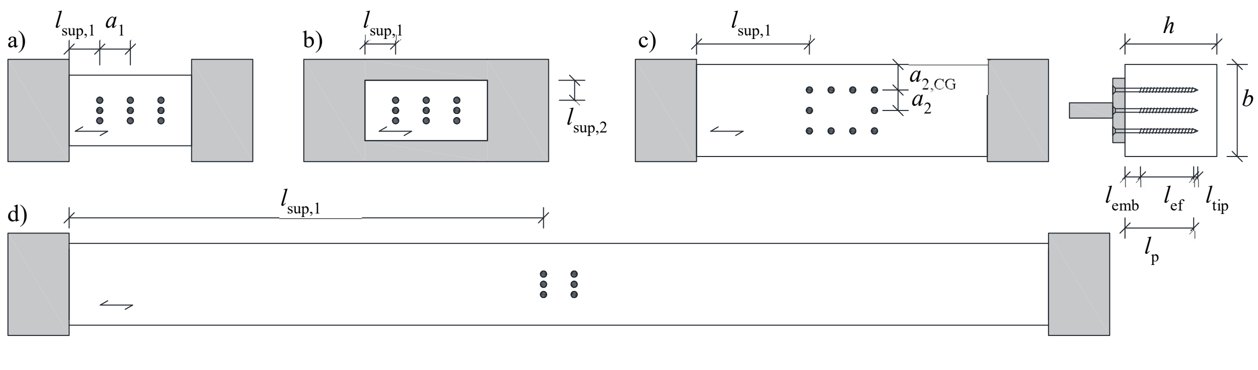

Figure 1.2 Schematic view on the dimensions of tested screw groups at $\alpha = 90°$ with a) near end and b) near circumferential, with $l_{sup,1} \approx a_1$ and $l_{sup,2} \approx a_2$, respectively, c) in-between, with $l_{sup,1} \approx h$, and d) distant supports, with $l_{sup,1} \approx 3\ h$.

Block shear failures were commonly observed in joints (i) with outer steel plates taking off when loaded (see Figure 1.1, left) together with (ii) tight group designs, i.e.

screw groups featuring small spacings parallel- (a_1) and especially perpendicular-to-the-grain ($a_2 < 5\ d$). Thereby, failure patterns with clear block shear cracks (see Figure 1.3 a)) and in addition that alike of Figure 1.3 b) and c) were observed and due to their overall characteristic brittle load-deformation curves assigned to block shear.

EC 5 (2014) and SIA 265 (2021) demand the verification of block shear also for axially-loaded screw groups; but related design rules are not provided. In the same context, the current draft of prEC 5 (2021) does not address this failure mechanism at all explicitly. Anyway, EC 5 (2014), based on Leijten and Jorissen (2001), provides design provisions against splitting for joints of laterally-loaded dowel-type fasteners loading hangers perpendicular-to-the-grain. The national annexes of Austria (ÖNORM B 1995-1-1, 2019) and Germany (DIN EN 1995-1-1/NA, 2013) provide for laterally loaded fasteners and also for joints with axially-loaded glued in rods a design provisions based on Ehlbeck et al. (1989) and note, that the risk of splitting can be neglected as long as the distance from loaded timber end to the farthest fastener h_e is $\geq 0.7\ h$, with h as the depth of the beam. The same provisions apply for axially-loaded glued-in rods or screws in SIA 265 (2021) and prEC 5 (2021), correspondingly equating $h_e = l_p$; see also Dietsch and Brandner (2015). However, there is experimental evidence that block shear failure may occur even in joints fulfilling $l_p \geq 0.7\ h$; see Mahlknecht and Brandner (2013) and (2019).

In case of block shear failures so far there have been no fractures/cracks visible in the transversal shear planes. Considering this, Blaß et al. (2019) proposed to reduce the verification of block shear to (i) tension-perpendicular-to-the-grain (splitting) of the timber member at plane of the screw tips following the approach in EC 5 (2014) for hangers, and (ii) rolling shear at the planes of both outer screw rows parallel-to-the-grain; see Figure 1.3 (d); e)). Their approach appears to be especially suitable for screw groups with >> l_p and edge distances close to $a_{2,CG}$. The validation of their suggested parameters, as the effective widths and lengths of the potential failure planes, remains open for a broader range of screw groups, especially for joints in deep beams and/or joints with embedded screw threads ($l_{emb} > 0$; see Figure 1.2).

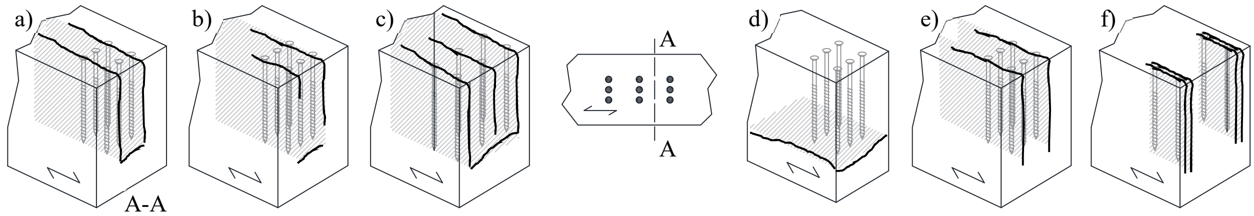

Figure 1.3 Schematic illustration of potential brittle timber fracture patterns in case of in tension axially-loaded screw groups: block shear failure mechanisms as defined by Mahlknecht and Brandner (2019) featuring a) clear, b) partial and c) clear and additional crack pattern; d) tension perpendicular-to-the-grain, and e) rolling shear failure mechanism as described in Blaß et al. (2019); (f) row shear failure mechanism.

2 Block shear model of Mahlknecht et al. (2014) and extensions

2.1 Basic principles

The block shear model of Mahlknecht et al. (2014) and subsequent extensions represent in a way an analogy to the block shear model for parallel-to-the-grain loaded joints of laterally-loaded rivets from Zarnani and Quenneville (2012). Mahlknecht et al. (2014) basically describe the resistance of a timber member at the joint against block shear by means of a parallel system of in total five planes: two planes each acting against transversal shear ($A_{s,s}$) and rolling shear ($A_{s,r}$) at the circumference of the screw group and one plane at the tips resisting tensile-stresses perpendicular-to-the-grain ($A_{t,90}$); see Eq. (1) and Figure 2.1. These equations contain a_1 and a_2, s and r are the numbers of screws in a row perpendicular- and parallel-to-the-grain, respectively, and h_b is the depth of the block shear volume, which may differ from the penetration length l_p (see Section 2.2). To account for the proportional contribution of these planes in load sharing and redistribution, corresponding stiffnesses, i.e. parallel acting springs, are defined by assuming a uniform deformation Δ as well as a linear-elastic and quasi-brittle material behaviour; see Eqs. (2) to (4). In doing so, the elastic material properties (Young's modulus perpendicular-to-the-grain $E_{t,90}$ and shear moduli G_0 and G_r) as well as stress distribution parameters are defined: $C_{t,90}$, to describe the ratio of a non-uniform to a uniform tensile stress distribution over h_b, C_t, C_s and C_r, to account for the non-uniform stress distribution along the corresponding planes, and X_s and X_r as lengths of the lateral volume parallel and perpendicular-to-the-grain, respectively, which are activated by the shear deformations; see Figure 2.1.

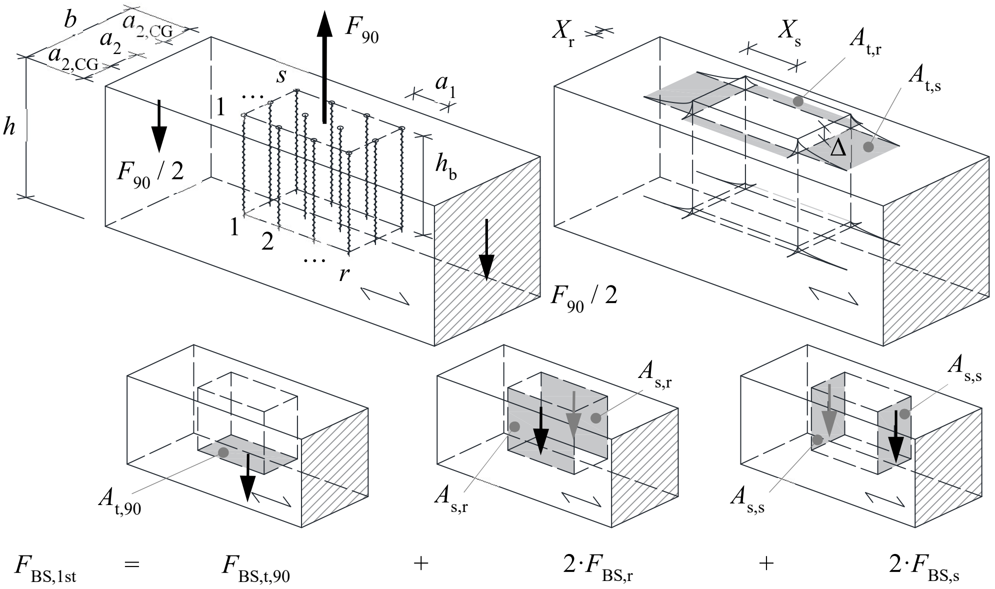

Figure 2.1 Contributing planes and geometric parameters of the block shear model for a group of axially-loaded screws together with some schematic assumptions.

$A_{t,90} = (r - 1)\, a_1\, (s - 1)\, a_2$; $A_{s,s} = (s - 1)\, a_2\, h_b$; $A_{s,r} = (r - 1)\, a_1\, h_b$ (1)

$K_{t,90} = E_{t,90}\, A_{t,90} / (C_{t,90}\, h_b)$ (2)

$K_s = G_0\, A_{s,s} / X_s + E_{t,90}\, A_{t,s} / (10\, h_b)$, with $A_{t,s} = (s - 1)\, a_2\, X_s$ (3)

$K_r = G_r\, A_{s,r} / X_r + E_{t,90}\, A_{t,r} / (10\, h_b)$, with $A_{t,r} = (r - 1)\, a_1\, X_r$ (4)

Due to the assumed parallel system action together with linear-elastic and (quasi) brittle material behaviour, the maximum load at 1st failure, $F_{BS,1st} = K_{1st}\, e_{f,(1)}$, corresponds to the resistance of the system at the deformation at 1st fracture $e_{f,(1)} = \min(e_{f,(i)})$, with $e_{f,(i)} = C_i\, f_i\, A_i / K_i$ and $K_{1st} = K_{t,90} + 2\, K_s + 2\, K_r$. This coincides with the corresponding strength f_i ($f_{t,90}$ tension perpendicular-to-the-grain, f_v shear or f_r rolling shear strength) at the corresponding (theoretically potential) failure plane(s) A_i ($A_{t,90}$, $2\, A_{s,r}$ or $2\, A_{s,s}$); see Figure 2.2. Subsequent maximum loads of remaining planes, which are still active in load sharing, can be calculated analogously; see Mahlknecht and Brandner (2019) and Figure 2.2. The overall maximum load the block can resist, is consequently given as the maximum of these intermediate maxima. The first failure criterion was directly derived from test observations. Also there, first (partial) failures associated with load drop and stiffness loss, followed by further load increase, were observed. This phenomenon, however, was not observed in all tests; some of them failed without these apparent first failures. Because of the uncertainty related to the residual long-term capacity of already partially failed timber volumes at such joints, for the design models presented and discussed further only $F_{BS,1st}$ is considered. More details are provided in Mahlknecht and Brandner (2019) and Mahlknecht (pr 2023).

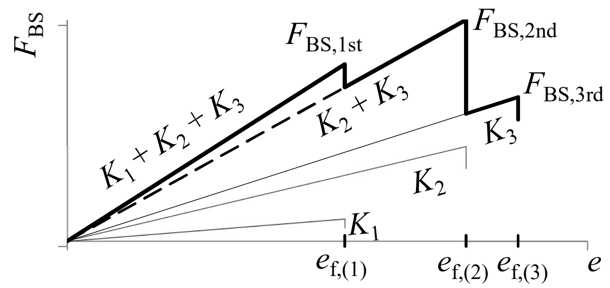

Figure 2.2 Schematic load-deformation-curves in case of block shear failure with suczessive, linear-elastic and (quasi) brittle material behaviour acc. to Mahlknecht and Brandner (2019).

2.2 Model parameters

A comprehensive discussion on the model parameters based on Mahlknecht et al. (2014) and (2016) is given in Mahlknecht and Brandner (2019). The basic parameter settings are listed in Table 2.1 and Table 2.2. Because of well-known size effects, values for $f_{t,90}$ and f_v are related to the dimensions of $A_{t,90}$ and $A_{s,s}$. As the position of the failure plane, it's depth, in clearly defined, $f_{t,90}$ relates to solid timber without pith. The stress distribution parameters were determined on the basis of a mechanical approach analogue to compression perpendicular-to-the-grain together with FE-and test data analysis. Latter is done in particular as decision aid for the dimension of X_s and X_r by a classification between block shear and single fastener failure in dependency of the spacing. Namely, this provides the information up to which spacing (a_1 and a_2) an overlapping of inserted loads per screw is given and a conclusion alike an effective thickness or width per screw can be done.

Table 2.1 Average material properties as well as geometric and stress distribution parameter settings for the block shear model of Mahlknecht and Brandner (2019).

[N/mm²]	$f_{t,90,mean}$	$E_{t,90,mean}$	$f_{v,mean}$	$G_{0,mean}$	$f_{r,mean}$	$G_{r,mean}$
GLT	$2.04\ (3{,}150\ /\ A_{t,90})^{0.2}$ [a]	300 [b]	$40.2\ A_{s,s}^{-0.2}$ [d]	650 [b]	1.9 [f]	100 [f]
ST	$2.04\ (3{,}150\ /\ A_{t,90})^{0.2}$ [a]	350 [c]	$55.2\ A_{s,s}^{-0.22}$ [d]	690 [e]	1.9 [f]	100 [f]

[a] reference data from Blaß et al. (1998); [b] GL 24h acc. to EN 14080 (2013); [c] close to C24 acc. to EN 338 (2016); [d] acc. to Brandner et al. (2012); [e] C24 acc. to EN 338 (2016); [f] acc. to Ehrhart and Brandner (2018)

support distance	$C_{t,90}$	C_t	$C_s = C_r$	X_s	X_r
close	0.5	1.0	0.9	5 d	min(2.5 d; $l_{sup,2}$)
in-between; $l_{sup,1} \approx h$	0.5	1.0	1.0	50 mm	5 d

Mahlknecht and Brandner (2019) focused on near support conditions. Aiming on a more general application of the block shear model and supported with new data sets Mahlknecht (pr 2023) provides a complement, more specified set of parameters:

- given the predefined failure plane at the screw tips, for $f_{t,90}$ in solid timber and glulam (series h21_E) the influence of pith is neglected and $f_{t,90,mean}$ kept as in Table 2.1; for all other glulam series and by means of data from Blaß et al. (1998) $f_{t,90,mean} = 1.85\ (3{,}150\ /\ A_{t,90})^{0.2}$ is set;
- acc. to EN 338 (2016) $E_{t,90,mean}$ for C24 is set to 370 N/mm²;
- FE-analyses in Mahlknecht (pr 2023) outline the necessity to consider $l_{emb} > 0$ in the theoretical height h_b of the block shear volume, with $h_b = l_{emb} + l_{ef}$ for near and $h_b = 0.5\ l_{emb} + l_{ef}$ for in-between and distant support conditions;
- FE-analyses showed that for in-between ($l_{sup,1} \approx h$) and distant supports ($l_{sup,1} > h$) the same values for C_s and C_r can be applied;
- X_r is corrected to 2.5 d, independent of the support distance;
- in close agreement with Mahlknecht and Brandner (2019), for distant supports and in consideration of the insertion depth $X_s = (10 - 5\ l_p\ /\ h)\ d$ is set.

Table 2.2 Coefficients of variation and correlations between material properties, Mahlknecht (pr2023).

CoV [%]	$E_{t,90}$	G_0	G_r	$f_{t,90}$	f_v	f_r
ST [a]	15	12	20	25	15	20
GLT [b]	15	12	15	25	15	20

[a] C24 acc. to EN 338 (2016); [b] GL 24h and GL 28h acc. to EN 14080 (2013)

$\rho_{Xi,Xj}$ [–]	$E_{t,90}$	G_0	G_r	$f_{t,90}$	f_v	f_r
$E_{t,90}$	1	0.6 [c]	0.6 [e)f]	0.4 [c]	0.6 [c]	0.6 [e)f]
G_0		1	0.2	0.4 [c]	0.6 [c]	0.2
G_r			1	0.4 [e]	0.2	0.8 [d]
$f_{t,90}$				1	0.6 [c]	0.4 [e]
f_v	symm.				1	0.2 [e]

[c] acc. to JCSS (2006); [d] analogue to $\rho(f_{t,0}; E_0)$ acc. to JCSS (2006) and similar to Ehrhart and Brandner (2018); [e] correlation measures assumed due to lack of information; [f] dependencies of $E_{t,90}$ with G_r and $E_{t,90}$ with f_r argued with the common dependency on the annual ring orientation.

In addition to the mechanical formulation of the block shear model by means of average properties and parameter settings it has been extended to a stochastic-mechanical model. This allows now to consider the corresponding uncertainties and correlations, as summarised in Table 2.2, and to formulate the block shear model also on the characteristic (5 %-quantile) level.

The material properties, expressed via the random variable vector $Y = [E_{t,90}; G_0; G_r; f_{t,90}; f_v; f_r]$, are assumed to be lognormal distributed; see JCSS (2006), except $f_{t,90}$. For the stochastic analyses of the block shear model, each series is represented by 1,000 pseudo random samples. For each sample block shear resistance $F_{BS,1st,i}$ and the corresponding theoretical failure plane are determined. Figure 2.3 left exemplarily for series s12_S illustrates the PP-plot of $\ln(F_{BS,1st})$ assuming again a normal distribution by classifying the 1,000 repetitions acc. to the three failure planes. This graph also contains the average material properties of the simulated sample and the relative shares of the three failure plane classes.

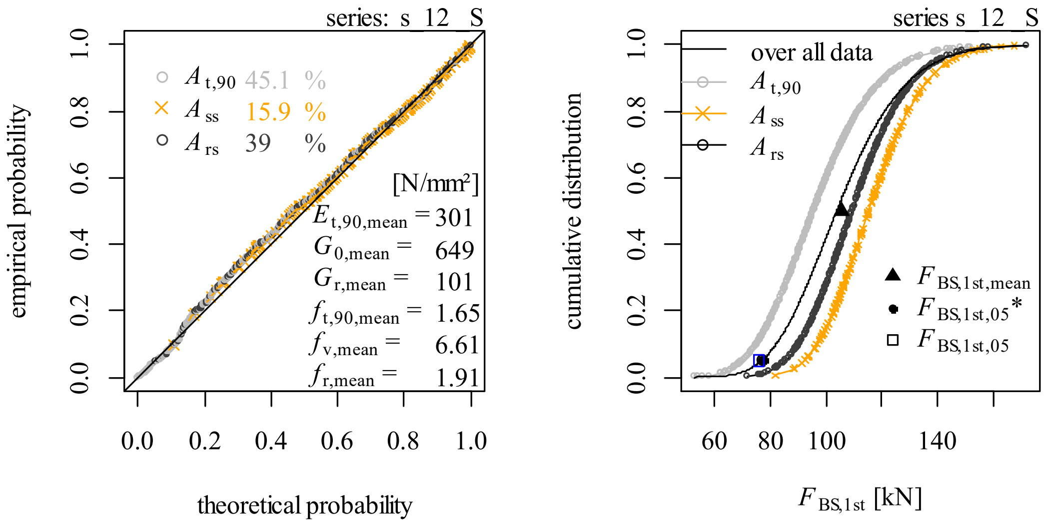

Figure 2.3 outcomes of the stochastic-mechanical model expemplarily for series s12_S (GLT; r = 3; s = 4; d = 6 mm; $a_1 = a_2 = 5$ d; $l_{ef} = 15.3$ d): (left) PP-plot of $\ln(F_{BS,1st})$ separate for each 1st failure plane together with corresponding relative shares and the average values from the random sample; (right) cumulative distributions for the overall sample outcome and individually for each 1st failure plane class together with mean and 5 %-quantile values

From these data sets empirical mean ($F_{BS,1st,mean}$) and empirical 5 %-quantile ($F_{BS,1st,05}$) values based on rank statistics are estimated as well as the 5 %-quantiles assuming a lognormal distribution ($F_{BS,1st,05}$*). Figure 2.3 right gives the distribution function of the whole date set, the individual distributions for each class of 1st failure planes as well as the mean and both 5 %-quantile values.

The presented simulated data mirroring test series s12_S visualizes well the separation in the three classes of corresponding theoretical failure planes. In fact, in series s12_S by testing 3 / 5 joints failed in withdrawal and 2 / 5 block in block shear. Series, which ended total in block shear, show a clear responsible failure plane with a high relative frequency. The $\ln(F_{BS,1st})$ in Figure 2.3 left agrees widely with an assumed normal distribution, consequently, $F_{BS,1st}$ follows a lognormal distribution.

2.3 Differentiation from other failure mechanisms

The probability of occurrence for the block shear failure mechanism is, as usual, limited by all other potential failure mechanisms, e.g. withdrawal, steel failure and net cross-section failure. It is common practice in design to declare the minimum of all associated design resistances as design value for the corresponding joint. In view of the single screw failure mechanisms this corresponds to $R_{joint,d}$ = min {$F_{ax,sgl,d}\ n_{ef}$; $F_{tens,sgl,d}\ n_{ef}$}.

In the following, the average single screw withdrawal capacity, $F_{ax,sgl}$, is determined acc. to the model of Ringhofer et al. (2015), by taking the average density of each series into account, as well as the system coefficient k_{sys}, to consider the number of penetrated layers N. Due to the partially low number of tests per series (≥ 4 #), the corresponding 5 %-quantile values are determined by assuming a lognormal distribution and CoV[ρ] = 0.08 for solid timber and CoV[ρ] = 0.08 / $N^{0.5}$ for glulam as suggested in Ringhofer et al. (2015). The average screw tensile capacity, $F_{tens,sgl,mean}$, is available from reference tests. In calculating the 5 %-quantiles, a CoV[F_{tens}] = 0.05 and a lognormal distribution are assumed. For model validation based on tests conducted under laboratory conditions $n_{ef} = n$ is applied; see Mahlknecht and Brandner (2019). In respect to practical applications of such joints, also the regulations of EC 5 (2014) ($n_{ef} = n^{0.9}$) is applied, as well as for completeness the proposal, which apply for lap joints acc. to Krenn (2017) and regulations of various ETAs, with $n_{ef} = 0.9\ n$.

For the calculation of the resistance of screw groups against tensile stresses perpendicular-to-the-grain, Blaß et al. (2019) made the following proposal:

$$F_{t,90,Blaß} = (k_s\ h) / (h - l_p)\ (6.5 + 18\ l_p^2 / h^2)\ (t_{ef}\ h)^{0.8}\ f_{t,90} \quad (5)$$

$$\text{with } k_s = \max\{1.0; 0.7 + 1.4\ (r - 1)\ a_1 / h\} \text{ and } t_{ef} = \min\{b; (s - 1)\ a_2 + 6\ d; 6\ s\ d\} \quad (6)$$

For comparison with screw groups featuring $l_{emb} > 0$, in Eq. (5) l_{ef} is substituted by l_p.

Acc. to SIA 265 (2021) the characteristic value (design value times 1.7) for the same property can be calculated acc. to Eq. (7), by considering the effective width b_{ef} and the factor k_{ar}, with the joint length $a_r = (r - 1)\ a_1$, acc. to Eq. (8), and the factor k_{hm} interpreted of the authors acc. to Eq. (9) with the effective threaded length.

$$F_{t,90,SIA,k} = 1.7\ F_{t,90,SIA,d} = 1.7\ (8.4\ b_{ef}\ (l_p / (1 - (l_p / h)^3))^{0.5}\ k_{ar}\ k_{hm}) \quad (7)$$

$$\text{with } b_{ef} = \min\{2\ l_{ef} \tan 15°; b\};\ k_{ar} = \min\{1 + 0.75\ (a_r / h); 2.0\} \quad (8)$$

$$\text{and } k_{hm} = 1 + 0.75\ l_{ef} / (1 + l_{ef}) \quad (9)$$

Acc. to prEC 5 (2021), the characteristic joint capacity, $F_{t,90,prEN,k}$, is given acc. to Eq. (10), which considers the material factor k_{mat} and the density factor k_G acc. to Eq. (11) and the effective width b_{ef}, which was interpreted by the authors in analogy to glued-in rods and acc. to Eq. (8).

$F_{t,90,prEN,k} = k_{mat}\ k_G\ b_{ef}\ (h_e / (1 - h_e / h))^{0.5}$ (10)

with k_{mat} = {0.6 for ST; 0.8 for GLT; 1.0 for parallel LVL}; $k_G = (0.05\ \rho_k + 2)$ (11)

Following the proposal for the block shear failure mechanism of Blaß et al. (2019), the lateral resistance of the joint volume against rolling shear stresses can be calculated acc. to Eq. (12), again with l_{ef} substituted by l_p.

$F_{r,90,Blaß} = 2\ l_p\ (1.5\ l_p + (r - 1)\ a_1\ b / (b - (s - 1)\ a_2)\ f_r$ (12)

In general, also row shear might become a relevant failure mechanism. As this failure mechanism was neither observed in joints tested acc. to the geometric conditions in EC 5 (2014) nor ETAs, it is not considered further.

3 Results and Discussion

3.1 Data sets

For the validation of the proposed block shear model, meanwhile, a valuable amount of experimentally determined data sets is available, which comprises configurations with near, in-between and distant supports, done by Plieschounig (2010), Schoenmakers (2010), Mahlknecht (2011), Mahlknecht and Brandner (2013), Mahlknecht and Brandner (2019), Ringhofer and Schickhofer (2015) and Mahlknecht et al. (2022). As already stated earlier, not all tests featured 1st failures. In such cases $R_{90,test} = F_{1st}$ applies. Data sets of Koch (2018), as presented in Blaß and Flaig (2019), are listed as well, although they don't fulfil the geometric minimum conditions acc. to EC 5 (2014) or various ETAs. Furthermore, they used beech-LVL instead of a steel plate as outer member and analysed only the maximum load from their tests. From the corresponding test curves, however, load-drops prior reaching the maximum load could be observed similar to own test experiences and the load corresponding to this first failure is evaluated. In the following, only data sets, which fulfil the required geometric conditions acc. to EC 5 (2014) or various ETAs are considered. Outcomes from testing screws of three producers featuring the same joint design and test setup (series s15_A; s15_B) are summarised to two series. Data sets featuring withdrawal or steel failure mechanism in experiments and model predictions are omitted. For these data sets a congruent and safe prediction is concluded.

3.2 Evaluation of the model

Table 3.3 lists per series the settings of the main parameters {l_{emb}; l_{ef}; d; a_1; a_2; n} and classifies the support distance and the observed failure mechanisms together with the number of observations. Furthermore, corresponding capacities $F_{1st,mean}$ and $F_{1st,min}$ or $F_{1st,05}$, last in case of > 8 # replicants per failure mechanism, are specified. Based on the stochastic-mechanical model mean and 5 %-quantile values are provided: (i) for the relevant single screw failure mechanism, min {$n\ F_{ax,sgl}$; $n\ F_{tens,sgl}$}, (ii) the resistance against block shear $F_{BS,1st}$ acc. to Section 2.2, (iii) the resistance against tension perpendicular-to-the-grain $F_{t,90,Blaß}$ acc. to Eq. (5), and (iv) the resistance against rolling shear $F_{r,90,Blaß}$ acc. to Eq. (12). For (iii) and (iv) the strength values are taken out of the stochastic modelled material properties. A view on the resulting strength values as well as the reference and block shear failure plane dimensions areas as basis for the corresponding strengths is given in Table 3.1. In Table 3.3, the bold ratios/values are derived from min $R_{90,pred(r,t)}$ = {n F_{slg}; $F_{t,90,Blaß}$; $F_{r,90,Blaß}$}. Underlined ratios/values are derived from $R_{90,pred(BS)}$ = min {n F_{slg}; $F_{BS,1st}$}.

Table 3.1 Range of area dimensions, reference areas for determination of strength values acc. to EN 408 (2012) and range in statistics (mean and 5 %-quantile values) of strength from stochastic-mechanically modelled test series; $f_{t,90}$ and f_v in dependence of the area of the affected plane.

area [mm²]	A_{ref} [N/mm²]	mean values [N/mm²]	5 %-quantile values [N/mm²]	timber product
$3,600 \leq A_{t,90} \leq 25,200$	3,150	$1.4 \leq f_{t,90,mean} \leq 2.0$	$0.9 \leq f_{t,90,05} \leq 1.3$	solid timber
$567 \leq A_{t,90} \leq 18,432$	25,000	$1.3 \leq f_{t,90,mean} \leq 2.6$	$0.9 \leq f_{t,90,05} \leq 1.7$	glulam
$4,800 \leq A_{sr} \leq 27,600$	–	$f_{r,mean} = 1.9$	$f_{r,05} = 1.3$	solid timber; glulam
$4,800 \leq A_{ss} \leq 14,400$	9,600	$6.7 \leq f_{v,mean} \leq 8.5$	$5.2 \leq f_{v,05} \leq 6.6$	solid timber
$1,440 \leq A_{ss} \leq 15,872$	–	$5.8 \leq f_{v,mean} \leq 9.4$	$4.5 \leq f_{v,05} \leq 7.4$	glulam

3.2.1 Mean value

In Figure 3.1 mean values from the tests including the 95 % confidence interval CI_{95} are compared with: (left) the suggested mean model predictions $R_{90,pred(BS),mean}$ and (right) the model predictions $R_{90,pred(r,t),mean}$ following the proposal of Blaß et al. (2019). If the predicted match with the mainly observed failure mechanism, the data points are additionally marked. As at tests of two series the main crack pattern and load-deformation curves indicates a mixed failure mechanism, tension perpendicular-to-the-grain and block shear (TB, series h21_E) or withdrawal and block shear (WB, series BS11), they were assigned to block shear as well. $R_{90,pred(r,t),mean}$ covers block shear either by the tension perpendicular-to-the-grain or the rolling shear failure. But, as this failure mechanisms are independently from each other and additionally observed in diverse test series, in Figure 3.1 (left) $R_{90,pred(r,t),mean}$ doesn't mark the block shear matches.

For all the series, which failed mainly in block shear also block shear as failure is predicted at $R_{90,pred(BS),mean}$ together with a resistance which is estimated somewhat conservatively in total ($F_{BS,1st,mean}$ / $R_{90,test,mean} \geq 0.7$); average bias of all data ($R_{90,pred(BS),mean}$ / $R_{90,test,mean}$): mean | CoV = 0.9 | 0.16. The outcome for$R_{90,pred(BS),mean}$ clearly demonstrates that the supposed model is able to predict average resistances and failure mechanisms reliable for the majority of test series. The outcome for $R_{90,pred(r,t),mean}$ demonstrates a widely similar prediction quality of the resistance, however, predict for 36 % of the series, which failed mainly in block shear single screw failure; average bias of all data ($R_{90,pred (r,t),mean}$ / $R_{90,test,mean}$): mean | CoV = 1.13 | 0.19.

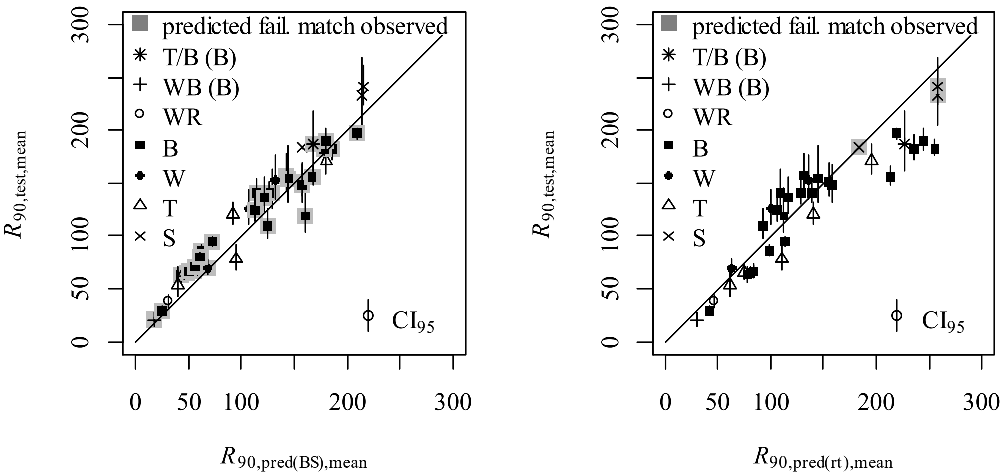

Figure 3.1 mean values $R_{90,test,mean}$ and corresponding confidence intervals (CI_{95}) vs. mean values $R_{90,pred,mean}$ predicted from supposed models: (left) $R_{90,pred(BS),mean}$; (right) $R_{90,pred(r,t),mean}$.

3.2.2 Coefficients of variation from experiments and model predictions

Before analysing 5 %-quantiles, the coefficients of variation CoV of all available test series with at least eight repetitions and all apart maximum one specimen failing in block shear, with $R_{90,\text{test}} = F_{\text{BS,1st,test}}$, are compared to that of the stochastic-numerical model, CoV[$F_{\text{BS,1st,pred}}$]; see Table 3.2. All tests were done with self-tapping screws in solid timber (C24 acc. to EN 338, 2016) or glulam (GL 24h acc. to EN 14080, 2013) and fulfil the geometric conditions acc. to EC 5 (2014) or various ETAs. More details of each series are provided in Table 3.3. In the residual series, experiments featuring other failure mechanisms than block shear are treated as right-censored; corresponding statistics for these series are estimated by means of the maximum likelihood method for right censored, lognormally distributed data.

Looking at Table 3.2, the values 0.04 ≤ $\text{CoV}_{\text{MLE}}[R_{90,\text{test}}]$ ≤ 0.12 for glulam appear rather low compared to the resistance associated with other brittle timber failure mechanisms; even the coefficients of variation for the rather brittle timber strengths, e.g. CoV[f_i] ≥ 0.15 in Table 2.2, are much higher. In contrast, the values of CoV[$F_{\text{BS,1st,pred}}$] are by a factor 1.5 to 3 higher and somewhat better agree with the expectations. Those test series with unexpected low values of $\text{CoV}_{\text{MLE}}[R_{90,\text{test}}]$ show also rather low variations in the density with CoV[ρ] ≤ 5 %. This indicates a very homogeneous material, used for those test series. This circumstance is further strengthened by positioning screw groups in almost only knot free solid timber in series s10 and s11 (to prevent force concentrations in knots), by using almost only knot free lamellas for the glulam specimens in series s15 and by producing specimens out of only a limited number of glulam beams (≤ 5) with length 12.5 m in series f13. Consequently, the applied sampling procedures led to very homogeneous but less representative test series in respect to variations in test outcomes. The comparable higher coefficients of variation in simulated series appear rather realistic but lead to more conservative results for quantiles of p < 50 %.

Table 3.2 Coefficient of variation $CoV_{MLE}[R_{90,test}]$ of test series with ≥ 8 replicates, all apart maximum one failing in block shear, compared to model predictions $CoV[F_{BS,1st,pred}]$.

series	s10 C	s10 D	s11 H	s11 I	s11 J	s12 K	s15 A	s15 B	s15 E	s15 G	s15 H	s15 I	f13 K	f13 I	f13 J
failures a)	9 10	10 10	9 9	10 10	9 9	8 8	30 30	29 30	10 10	10 10	10 10	10 10	10 10	13 15	15 15
$CoV_{MLE}[R_{90,test}]$	0.18	0.27	0.19	0.17	0.14	0.10	0.08	0.10	0.04	0.09	0.07	0.09	0.08	0.07	0.09
$CoV[F_{BS,1st,pred}]$	0.16	0.16	0.25	0.25	0.26	0.15	0.25	0.26	0.13	0.20	0.20	0.26	0.20	0.20	0.20
$CoV[\rho]$	0.15	0.09	0.10	0.08	0.11	0.03	0.03	0.04	0.02	0.07	0.04	0.03	0.04	0.05	0.05
timber product	ST	ST	ST	ST	ST	GLT	GLT	GLT	GLT	GLT	GLT	GLT	GLT	GLT	GLT
knot free zone	✓	✓	✓	✓	✓	–	✓	✓	✓	✓	✓	✓	–	–	–
≤ 5 raw glulam beams (12.5 m)	–	–	–	–	–	–	–	–	–	–	–	–	✓	✓	✓

a) the upper value indicates the no. of block shear failures, the lower the total no. of tests per series

3.2.3 5 %-quantiles from experiments and model predictions

Analogue to the mean values in Figure 3.1, Figure 3.2 compares the 5 %-quantile values from test series, $R_{90,test,05}$, based on a lognormal distribution, vs. the 5 %-quantile values from the model predictions $R_{90,pred,05}$ (with $F_{BS,1st,05}$*). As for the mean values, the outcomes of the supposed model, $R_{90,pred(BS),05}$ in Figure 3.2 left, predict pretty well the per series dominating failure mechanisms and the corresponding resistances are overall somewhat conservative in trend, which, as discussed in Section 3.2.2, was expected. For all of the series, which failed mainly in block shear also block shear is predicted at $R_{90,pred(BS),05}$. $R_{90,pred(r,t),05}$ in Figure 3.2 right appears partly less conservative and for 64 % matches brittle timber failure for observed mainly block shear mechanism. The number of withdrawal failure predictions, although the main observed mechanism was block shear, will increase by following the rules in EC 5 (2014) and various ETAs, because in the made comparison $n_{ef} = n$.

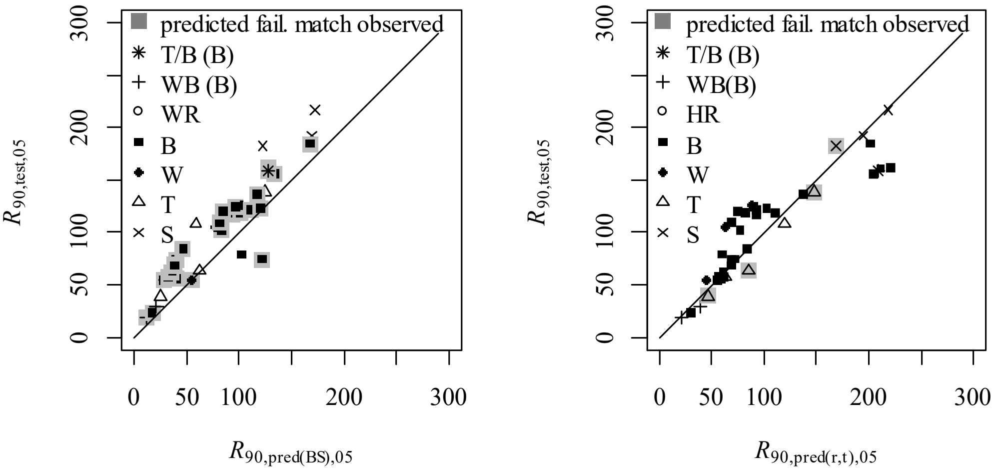

Figure 3.2 5 %-quantil values $R_{90,test,05}$ vs. 5 %-quantil values $R_{90,pred,05}$, both based on lognormal distribution, predicted from suppposted models: (left) $R_{90,pred(BS),05}$ and (right) $R_{90,pred(r,t),05}$

Table 3.3. Statistics of test results and model predictions from series dominated by / solely featuring block shear failures

<table>
<tr><th>series</th><th>$(l_{emb}+l_{ef} \mid a_1 \mid a_2) / d; n$</th><th>failure$_{no. of replicants}$</th><th>$R_{90,test,05}$ a) [kN]</th><th>$R_{90,test,mean}$ [kN]</th><th>$n F_{sgl,mean}$ b) / $R_{90,test,mean}$</th><th>$F_{r,90,Blaß,mean}$ / $R_{90,test,mean}$</th><th>$F_{t,90,Blaß,mean}$ / $R_{90,test,mean}$</th><th>$F_{BS,1st,mean}$ / $R_{90,test,mean}$</th><th>$n F_{sgl,05}$ b) [kN]</th><th>$0.9\ n F_{sgl,05}$ b) [kN]</th><th>$n_{ef,EC5} F_{sgl,05}$ b) [kN]</th><th>$F_{r,90,05}$ [kN]</th><th>$F_{t,90,Blaß,05}$ [kN]</th><th>$F_{BS,1st,05}$ [kN]</th></tr>
<tr><td colspan="15">solid timber C24 acc. to EN 338 (2016); screws with d = 6 mm, near support</td></tr>
<tr><td>s10_B</td><td>2+11.3 | 5 | 5; 9</td><td>W_6
B_4</td><td>64
54</td><td>70</td><td>0.98</td><td>0.91</td><td>1.12</td><td>1.27</td><td>55</td><td>50</td><td>44</td><td>45</td><td>52</td><td>67</td></tr>
<tr><td>s10_C</td><td>2+11.3 | 5 | 5; 16</td><td>W_1
B_9</td><td>133
104 a)</td><td>110</td><td>1.16</td><td>0.93</td><td>0.85</td><td>1.13</td><td>102</td><td>92</td><td>77</td><td>72</td><td>60</td><td>95</td></tr>
<tr><td>s10_D</td><td>2+11.3 | 5 | 5; 25</td><td>B_{10}</td><td>110 a)</td><td>119</td><td>1.74</td><td>1.54</td><td>0.95</td><td>1.35</td><td>153</td><td>136</td><td>109</td><td>131</td><td>72</td><td>122</td></tr>
<tr><td>s11_C</td><td>25.7 | 5 | 5; 16
h = 252 mm</td><td>S_3
B_2</td><td>239
191</td><td>234</td><td>1.10</td><td>1.32</td><td>1.30</td><td>0.92</td><td>199</td><td>176</td><td>149</td><td>217</td><td>195</td><td>169</td></tr>
<tr><td>s11_D</td><td>25.7 | 5 | 5; 16
h = 163 mm</td><td>S_4
B_1</td><td>246
215</td><td>242</td><td>1.07</td><td>1.28</td><td>38.1</td><td>0.89</td><td>206</td><td>182</td><td>154</td><td>218</td><td>5916</td><td>172</td></tr>
<tr><td>s11_H</td><td>4+11.3 | 7.5 | 3.5; 25</td><td>B_9</td><td>134 a)</td><td>141</td><td>1.30</td><td>0.77</td><td>0.97</td><td>0.91</td><td>146</td><td>131</td><td>106</td><td>77</td><td>87</td><td>83</td></tr>
<tr><td>s11_I</td><td>4+11.3 | 10 | 3.5; 25</td><td>B_{10}</td><td>151 a)</td><td>157</td><td>1.18</td><td>0.84</td><td>0.99</td><td>0.91</td><td>148</td><td>133</td><td>107</td><td>93</td><td>100</td><td>93</td></tr>
<tr><td>s11_J</td><td>4+11.3 | 12.5 | 3.5; 25</td><td>B_9</td><td>146 a)</td><td>151</td><td>1.21</td><td>1.02</td><td>1.15</td><td>1.04</td><td>146</td><td>131</td><td>106</td><td>110</td><td>112</td><td>101</td></tr>
<tr><td colspan="15">glulam GL 24h acc. to EN 14080 (2013); data of Koch (2018)/Blaß and Flaig (2019); geometric conditions acc. to EC 5 (2014) or var. ETAs not fulfilled; near support</td></tr>
<tr><td>BS11</td><td>9 | 4 | 4; 4; d = 6 mm</td><td>WB_5
WR_1</td><td>18.6
21.8</td><td>21</td><td>1.47</td><td>1.42</td><td>4.42</td><td>0.82</td><td>26</td><td>22</td><td>23</td><td>21</td><td>59</td><td>12</td></tr>
<tr><td>BS12</td><td>9 | 4 | 4; 8; d = 6 mm</td><td>B_5
WB_1</td><td>25.6
24.0</td><td>29</td><td>2.06</td><td>1.44</td><td>4.24</td><td>0.87</td><td>50</td><td>45</td><td>41</td><td>30</td><td>80</td><td>17</td></tr>
<tr><td>BS21</td><td>9 | 4 | 4; 4; d = 8 mm</td><td>WR_6</td><td>31.5</td><td>38</td><td>1.23</td><td>1.47</td><td>8.44</td><td>0.83</td><td>39</td><td>35</td><td>34</td><td>39</td><td>205</td><td>21</td></tr>
<tr><td>BS22</td><td>9 | 4 | 4; 8; d = 8 mm</td><td>B_5</td><td>55.2</td><td>63</td><td>1.56</td><td>1.23</td><td>7.16</td><td>0.67</td><td>82</td><td>74</td><td>67</td><td>56</td><td>293</td><td>28</td></tr>
<tr><td>BS31</td><td>14 | 4 | 4; 8; d = 6 mm</td><td>B_5</td><td>60.9</td><td>65</td><td>1.34</td><td>1.24</td><td>12.1</td><td>0.76</td><td>73</td><td>65</td><td>59</td><td>57</td><td>528</td><td>37</td></tr>
<tr><td>BS32</td><td>14 | 4 | 5; 8; d = 6 mm</td><td>B_6</td><td>58.2</td><td>66</td><td>1.35</td><td>1.26</td><td>12.4</td><td>0.82</td><td>75</td><td>67</td><td>61</td><td>59</td><td>534</td><td>40</td></tr>
<tr><td colspan="15">glulam GL 28h acc. to EN 14080 (2013); data of Schoenmakers (2010) ; distant support</td></tr>
<tr><td>Sc_c</td><td>8 | 8 | 8; 6; d = 8 mm</td><td>T_5</td><td>45.4</td><td>54</td><td>1.13</td><td>2.81</td><td>1.35</td><td>0.74</td><td>51</td><td>46</td><td>43</td><td>105</td><td>47</td><td>25</td></tr>
<tr><td>Sc_d</td><td>14 | 8 | 8; 6; d = 8 mm</td><td>T_5</td><td>69.3</td><td>78</td><td>1.42</td><td>4.49</td><td>1.70</td><td>1.22</td><td>94</td><td>85</td><td>79</td><td>246</td><td>86</td><td>63</td></tr>
<tr><td>Sc_g</td><td>5 | 8 | 8; 6; d = 12 mm</td><td>T_5</td><td>56.6</td><td>65</td><td>1.53</td><td>1.91</td><td>1.58</td><td>0.70</td><td>63</td><td>56</td><td>52</td><td>88</td><td>66</td><td>29</td></tr>
<tr><td>Sc_h</td><td>9 | 8 | 8; 6; d = 12 mm</td><td>T_5</td><td>107.5</td><td>121</td><td>1.53</td><td>2.29</td><td>1.53</td><td>0.76</td><td>119</td><td>108</td><td>100</td><td>197</td><td>120</td><td>59</td></tr>
<tr><td colspan="15">glulam GL 24h acc. to EN 14080 (2013); near support</td></tr>
<tr><td>s12_C</td><td>28.3 | 10 | 2.5; 12;
d = 6 mm</td><td>S_4
B_1</td><td>184
182</td><td>184</td><td>1.00</td><td>1.90</td><td>2.10</td><td>0.86</td><td>169</td><td>152</td><td>132</td><td>248</td><td>251</td><td>123</td></tr>
<tr><td>s12_K</td><td>17.8 | 7.5 | 3.5; 12;
d = 6 mm</td><td>B_8</td><td>123 a)</td><td>141</td><td>1.28</td><td>1.23</td><td>0.91</td><td>0.81</td><td>154</td><td>139</td><td>120</td><td>124</td><td>83</td><td>88</td></tr>
</table>

series	$(l_{emb}+l_{ef} \mid a_1 \mid a_2) / d; n$	failure$_{\text{no. of replicants}}$	$R_{90,test,05}$ a) [kN]	$R_{90,test,mean}$ [kN]	$n\,F_{sgl,mean}$ b) / $R_{90,test,mean}$	$F_{r,90,Blaß,mean}$ / $R_{90,test,mean}$	$F_{t,90,Blaß,mean}$ / $R_{90,test,mean}$	$F_{BS,1st,mean}$ / $R_{90,test,mean}$	$n\,F_{sgl,05}$ b) [kN]	$0.9\,n\,F_{sgl,05}$ b) [kN]	$n_{ef,EC5}\,F_{sgl,05}$ b) [kN]	$F_{r,90,05}$ [kN]	$F_{t,90,Blaß,05}$ [kN]	$F_{BS,1st,05}$ [kN]
s12_L	17.8 | 10 | 3.5; 12; d = 6 mm	B_7 W_1	130 164	141	1.28	1.38	0.99	0.90	153	138	120	136	90	97
s12_M	17.8 | 5 | 5; 12; d = 6 mm	B_1 W_4	124 154	153	1.17	1.30	0.88	0.86	153	138	119	140	88	102
s12_N	17.8 | 7.5 | 5; 12; d = 6 mm	B_2 W_2 c)	126 156	155	1.20	1.45	0.94	0.93	159	143	124	160	93	111
s12_O	17.8 | 10 | 5; 12; d = 6 mm	B_3 W_2 c)	130 148	148	1.24	1.71	1.06	1.06	156	140	122	178	102	120
s12_S	14.2 | 5 | 5; 12; d = 6 mm	B_2 W_3	112 129	126	1.13	1.10	0.80	0.84	119	107	93	98	63	77
s12_T	14.2 | 7.5 | 5; 12; d = 6 mm	B_5	109	124	1.13	1.26	0.85	0.91	118	106	92	111	69	81
s12_U	14.2 | 10 | 5; 12; d = 6 mm	B_2 W_2	123 134	137	1.08	1.33	0.85	0.89	123	111	96	129	75	84
s15_A	8.8 | 5 | 5; 9; d = 8 mm	B_{30}	69 a)	71	1.24	1.23	1.60	0.80	73	66	59	61	73	36
s15_G	8.8 | 5 | 5; 12; d = 8 mm	B_{10}	84 a)	86	1.35	1.16	1.53	0.73	97	87	76	68	85	40
s15_B	8.8 | 7 | 5; 9; d = 8 mm	B_{29} W_1	79 a) 97	80	1.07	1.21	1.52	0.73	73	66	58	69	80	39
s15_H	8.8 | 7 | 5; 12; d = 8 mm	B_{10}	93 a)	94	1.20	1.26	1.61	0.77	95	86	74	84	98	46
s15_I	8.8 | 10 | 2.5; 9; d = 8 mm	B_{10}	65 a)	67	1.25	1.32	1.89	0.75	70	63	56	62	81	32
s15_E	24.8 | 7 | 5; 9; d = 8 mm	B_{10}	195 a)	197	1.11	2.50	2.08	1.07	202	182	162	348	267	168
glulam GL 24h acc. to EN 14080 (2013); screws with d = 8 mm; distant support														
f13_N	18.5 | 10.5 | 5; 8	B_3 T_5 R_2	127 165 167	171	1.14	2.29	1.32	1.05	168	151	137	273	147	124
f13_K	18.5 | 5.3 | 5; 10	B_{10}	153 a)	156	1.47	2.31	1.36	1.07	198	178	157	256	137	117
f13_O	18.5 | 5.3 | 5; 10	B_6 T_1 R_3	162 169 155	183	1.29	1.98	4.23	1.02	204	184	162	255	502	133
f13_I	18.5 | 7.9 | 3.3; 10	B_{13} R_2	182 a) 172	183	1.40	1.86	4.09	0.97	221	199	175	241	497	128
f13_J	18.5 | 5.3 | 5; 10	B_{15}	186 a)	190	1.29	1.82	3.97	0.95	211	190	168	246	483	128
h21_E	31.5 | 10 | 2.5; 6	TB_4	164	187	1.21	2.98	2.01	0.90	209	188	175	398	243	128

W … withdrawal; B … block shear; T … tension perpendicular-to-the-grain; S … screw tension; R … rolling shear; mixed failure: TB … block shear / tension perpendicular-to-the-grain, WB … withdrawal / block shear, WR … withdrawal / rolling shear; a) for ≤ 8 # replicants $F_{1st,min}$; b) $F_{tens,sgl}$ only if relevant, otherwise $F_{ax,sgl}$; c) one test failed by screw tension

4 Simplified block shear model

The proposed block shear model in its comprehensive version might be probably too cumbersome for the daily practice. Furthermore, material parameters as implemented in this model are usually not available for the designers, which have to rely on characteristic properties tabulated in product and design standards. With focus on ease-of-use, the aim is to elaborate a simplified version. Therefore, some additional boundary conditions and limits are set:

- In view of typical practical applications, only distant support conditions are considered. Resulting from this: $C_{t,90} = 0.5$; $C_t = C_s = C_r = 1.0$; $X_r = 2.5\ d$; $X_s = (10 - 5\ l_p / h)\ d$
- So far, rolling shear properties are only provided for glulam in EN 14080 (2013), with $G_{r,mean} = 65$ N/mm² and $f_{r,k} = 1.2$ N/mm². These values are clearly different to $G_{r,mean} = 100$ N/mm² and $f_{r,k} = 1.3$ N/mm² used so far in the model. To adjust the currently regulated properties to currently proposed values, the factors $k_{r,G} = 1.5$ and $k_{r,f} = 1.1$ apply in the simplified model; see Eq. (16) and (17).
- For all softwood solid timber strength classes acc. to EN 338 (2016) $f_{t,90,k} = 0.4$ N/mm², and for classes higher than C22 $f_{v,k} = 4.0$ N/mm² apply. EN 14080 (2013) gives constant strength values $f_{t,90,k} = 0.5$ N/mm² and $f_{v,k} = 3.5$ N/mm² for all glulam strength classes. These values are again clearly below the more realistic material properties used so far in the model (see Table 3.1). Current regulations also not account for size effects, i.e. the dimension of $A_{t,90}$ and $A_{s,s}$. As $f_{t,90}$ turned out to be the dominating property for the block shear resistance adequate basic values and their adjustment to $A_{t,90}$ are mandatory. In respect to the latter, the size effect can be regulated analogue to the volume factor k_{vol} of EC 5 (2014) or similar to the model of $F_{t,90,Blaß}$ via $(A_{t,90,ref} / A_{t,90})^{0.2}$. As the depth of the failure plane is clearly defined in case of block shear, i.e. at the screw tips, for solid timber and glulam the same properties apply which are set acc. to Ehlbeck et al.(1989). To adjust them accordingly to characteristic properties currently regulated in EN 338 (2016) and EN 14080 (2013) following applies: $k_{t,90} = 2.4\ (3{,}150 / A_{t,90})^{0.2}$ for solid timber and $k_{t,90} = 3.0\ (3{,}150 / A_{t,90})^{0.2}$ for glulam. An analogue size effect applies also for the shear strength with $k_v = 1 / f_{v,k} \min\{4.0\ (150 / h_b)^{0.2}; 4.5\}$ for solid timber and $k_v = 1 / f_{v,k} \min\{3.5\ (600 / h_b)^{0.2}; 4.0\}$ for glulam acc. to Brandner et al. (2012); see Eq. (17).

Consequently, Eqs. (13) to (17) summarise the simplified block shear model.

$$A_{t,90} = (r-1)\ a_1\ (s-1)\ a_2;\ A_{s,s} = (s-1)\ a_2\ h_b;\ A_{s,r} = (r-1)\ a_1\ h_b \quad \text{with } h_b = 0.5\ l_{emb} + l_{ef} \tag{13}$$

$$K_{t,90} = 2\ E_{t,90,mean}\ A_{t,90} / h_b \tag{14}$$

$$K_s = G_{0,mean}\ A_{s,s} / X_s + E_{t,90,mean}\ A_{t,s} / (10\ h_b) \quad \text{with } A_{t,s} = (s-1)\ a_2\ X_s \text{ and } X_s = (10 - 5\ l_p / h)\ d \tag{15}$$

$$K_r = 0.4\, k_{r,G}\, G_{r,mean}\, A_{s,r} / d + E_{t,90,mean}\, A_{t,r} / (10\, h_b), \text{ with } A_{t,r} = 2.5\, d\, (r-1)\, a_1 \qquad (16)$$

$$F_{BS,05} = (K_{t,90} + 2\, K_s + 2\, K_r) \min \{k_{t,90}\, f_{t,90,k}\, A_{t,90} / K_{t,90};\, k_v\, f_{v,k}\, A_{s,s} / K_s;\, k_{r,f}\, f_{r,k}\, A_{s,r} / K_r\} \qquad (17)$$

Figure 4.1 compares the block shear test data of series done in glulam with close (s15), in-between (f13, BS) and distant (h21) support, with single resistance $F_{sgl,05}$ considering n, 0.9 n and n_{ef} acc. to EC 5 (2014), the simplified block shear resistance $F_{BS,05}$, min ($F_{r,90,Blaß,05}$; $F_{t,90,Blaß,05}$) and with both resistances regulated for beams/hangers against tension perpendicular-to-the-grain, $F_{t,90,prEN,k}$ and $F_{t,90,SIA,k}$, by means of f_i acc. to EN 14080 (2013); all values referenced to $n\, F_{sgl,05}$.

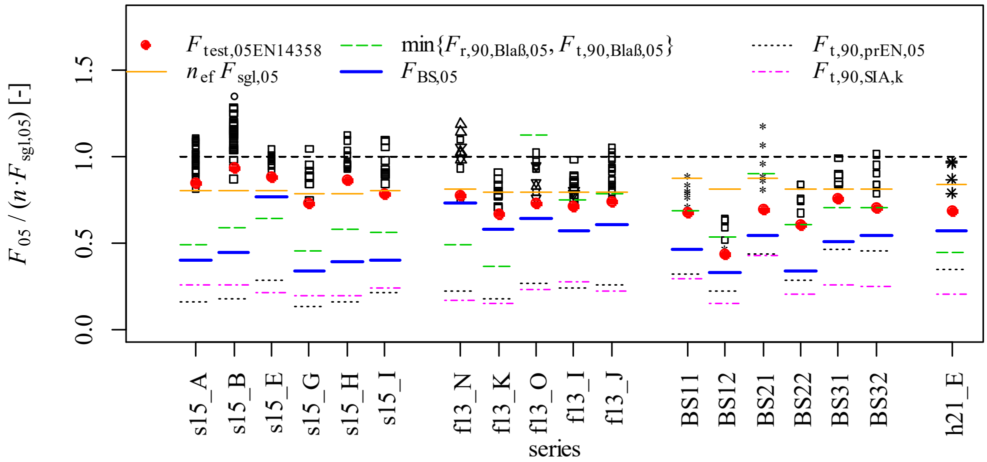

Figure 4.1 comparison of test data from series in glulam with close (s15), in-between (f13, BS) and distant support (h21), which failed solely or primary in block shear with various model predictions on characteristic (5 %-quantile) level.

The comparison outlines the necessity to consider brittle timber failure modes, even for joints which fulfil the conditions acc. to EC 5 (2014) and various ETAs (s15_, f13_ and h21_E). Regarding the block shear model predictions of Blaß et al. (2019), with $R_{90,05}$ = min {$n_{ef}\, F_{sgl,05}$, $F_{r,90,Blaß,05}$; $F_{t,90,Blaß,05}$}, the results are shortly progressive; however, considering realistically a higher scatter they become even more. This is especially apparent for series featuring $l_p > 0.7\, h$ (e.g. series f13_O, f13_I and f13_J). The simplified block shear model, with $R_{90,05}$ = min {$n_{ef}\, F_{sgl,05}$, $F_{BS,05}$}, gives results on the safe side, which, considering the area of application of this model, are consistent for series featuring in-between and distant support conditions. The model is somewhat conservative for the near supporting (s15) and for series with $l_p < 0.7$. The models acc. to prEC (2021) and SIA (2021) give overall very conservative results.

5 Conclusions

Generally, the aim to end up in joint failure mechanisms whose properties are well-known from single screws and easy to determine has clearly the benefit of ease-of-use. For axially-loaded screw groups in softwood Mahlknecht and Brandner (2019) noted: (i) for l_{ef} up to 20 d withdrawal is usually the leading failure mechanism as long as the spacing complies with EC 5 (2014) and the number of screws in a row in grain is $r \leq 3$, and (ii) for screw groups prone to fail in steel, the current regulation $a_1\, a_2 \geq 25\, d^2$ can be applied as long as $a_1 \geq 5\, d$ and $a_2 \geq 3.5\, d$ and $F_{model} > (1.05\, n\, F_{tens})$

are fulfilled. Mahlknecht et al. (2021) confirm these principle findings also for applications in hardwoods. If the recommendations cannot be followed, there might be a risk for brittle timber failure mechanisms. This was demonstrated for various group parameter settings which lead to failure in block shear or tension perpendicular-to-the-grain, even at penetration lengths $l_p > 0.7\ h$. The rule to be safe from brittle timber failure mechanisms in joints featuring $l_p > 0.7\ h$ in the national annexes of Austria (ÖNORM B 1995-1-1, 2019) and Germany (DIN EN 1995-1-1/NA, 2013) is seen critically. Anyhow, this recommended penetration length should be applied also in joints with axially-loaded screws.

The advantage of the proposed block shear model is its flexibility in respect to material properties and group dimensions. Even joints with >> $a_{2,CG}$, as e.g. wind bracing joints situated on member's side-face can be represented accordingly. Additionally, the proposed block shear model predicts the experimentally observed failure mechanism with high accuracy. The simplified model on the characteristic (5 %-quantile) level adapts standardized characteristic properties to realistic ones (evident by a large amount of experimental test results) in an explicit, comprehensible manner and thus enables an objective adjustment of any pre-factors and formulations in the event of changes in these. The model gives safe predictions for all available series, especially for series with $l_p > 0.7\ h$. The models acc. to prEC (2021) and SIA (2021) for the resistance of joints in beams/hangers loaded perpendicular-to-the-grain give overall very conservative predictions.

6 Acknowledgements

The current investigations are part of the European Research Area Networking (ERA-NET) project FOREST VALUE hardwood_joint project with funding by European Union. Thank goes to the scientific project partners of Karlsruhe Institute of Technology (KIT; leader) in Germany, Linneaus University in Sweden, Universite de Lorraine in France and commercial partners Schmid Schrauben Hainfeld GmbH, Adolf Würth GmbH & Co. KG, Pollmeier Furnierwerkstoffe GmbH and Hasslacher Group for their valuable input. Preceded work took place in the extent of the FFG projects BRIDGE-SCREWS (2010–2012; No. 824929) at Graz University of Technology and COMET-K “focus_sts” (2013–2016; No. 836619) at holz.bau forschungs gmbh in Graz.

7 References

Blaß HJ, Ehlbeck J, Schmid M (1998) Ermittlung der Querzugfestigkeit von Voll- und Brettschichtholz. Technical Report, Universität Karlsruhe, Germany (in German).

Blaß HJ, Flaig M (2019) Blockscheren von Holzbauteilen im Verbindungsbereich axial beanspruchter Vollgewindeschrauben. Karlsruher Berichte zum Ingenieurholzbau, Band 35, KIT, Germany (in German).

Blaß HJ, Flaig M, Meyer N (2019) Row shear and block shear failure of connection with axially loaded screws. INTER/52-07-6, Tacoma, USA.

Brandner R (2012) Stochastic system actions and effects in engineered timber products and structures. Dissertation, TU Graz, Austria.

Brandner R, Gatternig W, Schickhofer G (2012) Determination of shear strength of structural and glued laminated timber. CIB-W18/45-12-2, Växjö, Sweden.

Carradine DM, Newcombe MP, Buchanan AH (2009) Using screws for structural applications in laminated veneer lumber. CIB-W18A/42-7-7, Duebendorf, Switzerland.

Dietsch P, Brandner R (2015) Self-tapping screws and threaded rods as reinforcement for structural timber elements – A state-of-the-art report. Constr Build Mater 97, pp. 78-89.

DIN EN 1995-1-1/NA:2013 Nationaler Anhang – National festgelegte Parameter – Eurocode 5: Bemessung und Konstruktion von Holzbauten – Teil 1-1: Allgemeines – Allgemeine Regeln und Regeln für den Hochbau. DIN.
EC 5 (2014) – EN 1995-1-1:2004 + AC:2006 + A1:2008 + A2:2014 Eurocode 5: Design of timber structures – Part 1-1: General – Common rules and rules for buildings. CEN.
Ehlbeck J, Görlacher R, Werne H (1989) Determination of perpendicular-to-grain tensile stresses in joints with dowel-type fasteners. CIB-W18A/22-7-2, Berlin, Germany.
Ehrhart T, Brandner R (2018) Rolling shear: test configurations and properties of some European soft- and hardwood species. Eng Struct 172, pp. 554-572
EN 338 (2016) Structural timber – Strength classes. CEN.
EN 408 (2010+A1) Timber structures – Structural timber and glued laminated timber – Determination of some physical and mechanical properties. CEN
EN 14080 (2013) Timber structures – Glued laminated timber and glued solid timber - Requirements. CEN.
EN 14358 (2016) Timber structures – Calculation and verification of characteristic values. CEN.
JCSS (2006) JCSS probabilistic model code – Part 3: resistance models – 3.5 properties of timber. Joint Committee on Structural Safety.
Koch E (2018) Blockscheren von Holzbauteilen. Master Thesis, KIT, Germany (in German).
Krenn H (2017) Die Stahlblech-Holz-Laschenverbindung mit schrägen Schrauben. Dissertation, TU Graz, Austria (in German).
Leijten AJM, Jorissen A (2001) Splitting strength of beams loaded by connections perpendicular to grain, model validation. CIB-W18/34-7-1, Venice (I)
Mahlknecht U (prospective 2023) Blockscheren am Queranschluss einer axial beanspruchten Schraubengruppe. Dissertation, TU Graz, Austria (in German).
Mahlknecht U, Brandner R (2013) focus_sts 3.1.2 Untersuchungen des mechanischen Verhaltens von Schrauben – Verbindungsmittelgruppen in VH, BSH und BSP – Forschungsbericht. HBF gmbh and TU Graz, Austria (in German).
Mahlknecht U, Brandner R (2019) Block shear failure mechanism of axially-loaded groups of screws. Eng Struct 183(2019) 220-242.
Mahlknecht U, Brandner R, Augustin M (2016) Block shear failure mode of axially loaded groups of screws. WCTE 2016, Vienna, Austria.
Mahlknecht U, Brandner R, Ringhofer A (2021) Minimum geometric and execution conditions for axially loaded groups of screws in hardwood. INTER/54-07-7, online.
Mahlknecht U, Brandner R, Ringhofer A (2022) Queranschluss mit axial beanspruchten Schraubengruppen am Einfeldträger aus Laubholz und Fichte. Technical Report, TU Graz, Austria (in German).
Mahlknecht U, Brandner R, Ringhofer A, Schickhofer G (2014) Resistance and failure modes of axially loaded groups of screws. RILEM Bookseries, Springer, 1 ed., Vol. 9.
Mayer N, Blaß HJ (2018) Connections with glued-in rods in trusses made of beech-LVL. WCTE 2018, Seoul, Republic of Korea.
ÖNORM B 1995-1-1:2019 Eurocode 5: Design of timber structures – Part 1-1: General – Common rules and rules for buildings – Consolidated version. ASI.
Plieschounig S (2010) Ausziehverhalten axial beanspruchter Schraubengruppen. Master Thesis, TU Graz, Austria (in German).
prEC 5 (2021) prEN 1995-1-1:2021 Comment: Consolidated draft prEN 1995-1-1, informal enquiry, Eurocode 5: Design of timber structures – Common rules and rules for buildings – Part 1-1: General. CEN.
Ringhofer A, Schickhofer G (2015) Ausziehprüfungen von Schraubengruppen in Anlehnung an das EAD 130015-00-0603, Abschnitt 2.2.1210 zur Bestimmung der Mindestabstände a_1 und a_2, Test Report Nr. PB15-471-1-01. Lignum Test Center (LTC), TU Graz, Austria (in German).
Ringhofer A, Brandner R, Schickhofer G (2015) A universal approach for withdrawal properties of self-tapping screws in solid timber and laminated timber products. INTER/48-7-1, Sibenik, Croatia.
Schoenmakers JCM (2010) Fracture and failure mechanisms in timber loaded perpendicular to the grain by mechanical connections. Dissertation, Eindhoven University of Technology, Netherlands.
SIA 265:2021 Timber Structures, Schweizerischer Ingenieur- und Architektenverein.
Zarnani P, Quenneville P (2012) Predictive analytical model for wood capacity of rivet connections in glulam an LVL. WCTE 2012, Auckland, New Zealand.

DISCUSSION

The paper was presented by U Mahlknecht

T Tannert and U Mahlknecht discussed that shear perpendicular to grain failure did not happen, but the mechanical model considered load sharing and stress redistribution offered by the material in shear perpendicular to grain with their stiffness values coming from CLT documents.

JM Cabrero asked how the stress concentration factor was developed. U Mahlknecht responded that they were obtained from FEM analysis with parametric studies (0.8 to 1.).

S Winter and U Mahlknecht discussed the failure did not occur as a real block failure but with two main failure planes. S Aicher added that contribution of failure can be observed with saw cutting of the specimen.

R Jockwer questioned whether distribution of screws over the surface can help avoid this failure. U Mahlknecht replied that different arrangements of screw groups could help but one needs to be careful to avoid tension perpendicular to grain failures.

A Frangi and U Mahlknecht discussed what might be the volume of the block shear mode if inclined screws were used.

Brittle failures of connections with self-tapping screws on CLT plates

José M. Cabrero, ONESTA Wood Chair. University of Navarra, 31009 Pamplona, Spain. jcabrero@unav.es

Jan Niederwestberg, University of Alberta, Faculty of Engineering, Edmonton, AB T6G 2R3, Canada. niederwe@ualberta.ca

Boris Azinović, Slovenian National Building and Civil Engineering Institute (ZAG Ljubljana), 1000 Ljubljana, Slovenia. boris.azinovic@zag.si

Henrik Danielsson, Lund University, Faculty of Engineering LTH, 221 00 Lund, Sweden. henrik.danielsson@construction.lth.se

Ying Hei Chui, University of Alberta, Faculty of Engineering, Edmonton, AB T6G 2R3, Canada. yhc@ualberta.ca

Tomaž Pazlar, Slovenian National Building and Civil Engineering Institute (ZAG Ljubljana), 1000 Ljubljana, Slovenia. tomaz.pazlar@zag.si

Chun Ni, FPInnovations, Canada, chun.ni@fpinnovations.ca

Keywords: Timber connection, Brittle failure, Cross Laminated Timber, Parallel-to-grain, Self-tapping screws, Eurocode 5 , CSAO86

1 Introduction

Cross Laminated Timber (CLT) has become a popular product in current timber construction. However, several features set it aside from typical timber products, namely due to its crosswise layer arrangement. Regarding its failure response, the perpendicular layers are supposed to provide dimensional stability and reinforcement. Hence, it is sometimes assumed that brittle failure may be greatly reduced.

However, as shown in previous works by *Zarnani and Quenneville* (2015) and *Asgari et al.* (2022), this is not necessarily the case.

In the European context, as CLT is not yet included as a product in the current Eurocode 5, CLT connection design is yet to be included. Practitioners (*Schenk et al.*, 2022) use several manuals (*Wallner-Novak et al.*, 2014; *Borgström and Fröbel*, 2019; *Bogensperger et al.*, 2010) and ETAs from CLT and fastening manufacturers (*ETA 12-0347*, 2020; *ETA 14-0349*, 2020).

CLT design is already taken into account in the US (*ASTM D5457-21a*, 2021) and Canadian regulations (*CSA O86-09*, 2019). In the latter, as pointed out by *Asgari et al.* (2022), a statement is given where row shear and group tear out (block or plug shear) are explicitly dismissed in CLT connections. On the other hand, in the current Eurocode 5 draft, a note regarding the possibility of brittle failure was discussed in the commenting process, but no guidance is eventually given.

Brittle failure in connections could become a problem if the designer is not able to consider it, for two main reasons: reduction of ductility in cases where the structural design demands it, or reduction of estimated load-carrying capacity.

Current existing brittle failure models are mainly developed for timber products such as glulam and LVL (*Cabrero and Yurrita*, 2018; *Yurrita, Cabrero, and Moreno-Zapata*, 2021; *Yurrita and Cabrero*, 2020). Due to the load distribution between adjacent layers within a CLT element, i.e. through cross-layer reinforcements, these models cannot be applied directly to CLT. *Zarnani and Quenneville* (2015) made some modifications to their original model (*Zarnani and Quenneville*, 2014) to adapt it for CLT, and verified the new approach for rivetted CLT connections.

The typical connection in CLT structures is a 3D steel plate (ie, hold-down or steel angle bar) connected to the CLT elements using small diameter fasteners, such as screws, anchor bolts or rivets. Thus, the expected brittle failure mode is plug shear, defined by three different planes: head tensile, lateral shear and bottom shear, determined by the boundary of the connection area.

Zarnani and Quenneville (2015) defined six different modes for plug shear in CLT, as shown in Figure 1. They were distinguished since different load distribution phenomena and considerations have to be introduced in the model, based on the considered penetration of the fastener in the layers.

Other failure modes different from plug shear may also appear: step shear, in which the torn block corresponds to the entire width of the panel, and the net tension failure of the complete CLT cross-section (Figure 1).

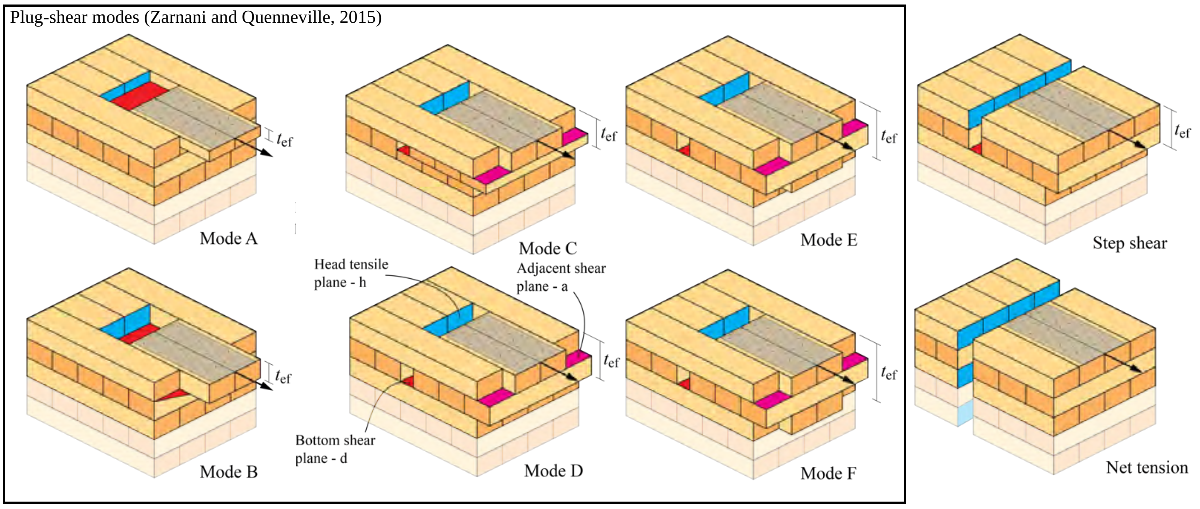

Figure 1. Typical brittle failure modes in CLT, with failure planes depicted. Plug-shear modes A-F correspond to those defined by Zarnani and Quenneville (2015).

The current paper describes two different experimental campaigns, which were carried out independently in Europe and Canada, on connections with self-tapping screws subjected to tensile loads parallel to the outer layer of the CLT. Both experimental campaigns, the obtained results and observed failure modes are described in Section 2. Sect. 3 describes briefly the existing model, its application to the performed tests and the obtained results.

2 Experimental campaigns

2.1 Europe

The European connections consisted of a single steel plate attached to both ends of a CLT element (single shear plane). It comprised ten different sets of tests (see Table 1) which differed in terms of CLT type, CLT width (*w*), and fastener length (ℓ_f = 40, 60, and 100 mm). Fully threaded screws with a diameter of 8 mm ($M_{y,k}$ = 20Nm according to the producer (*ETA 11-0284*, 2019)) and steel plates with dimensions 208 × 800 × 8 mm (steel grade S355) were used, with the hole pattern designed according to the provisions of Eurocode 5 (Fig. 2a). Some additional specimens (not described in this paper) were tested with the outer layer oriented perpendicular to the applied load. The interested reader may find them in the related paper (*Azinović et al.*, 2022).

The denomination of the different test series was related to the penetration of the fastener into the layers and the failure modes denomination by *Zarnani and Quenneville* (2015) (Fig. 1). Therefore, in AB specimens only the first layer is penetrated, while in CD and EF the second and third, respectively.

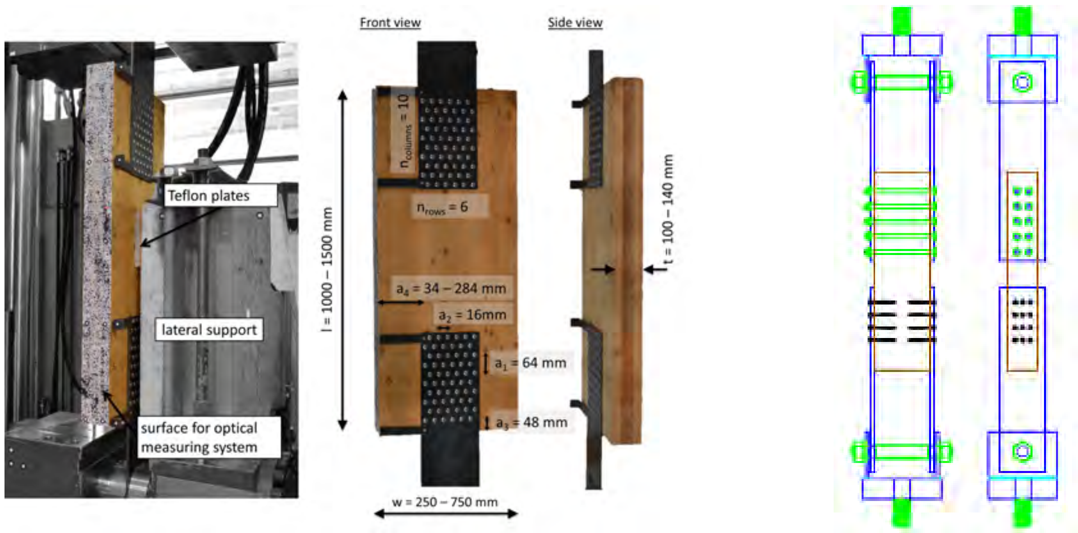

(a) Europe *(b) Canada*

Figure 2. Tests setup and used denomination for the geometrical features.

The connections were tested using a tensile test configuration (Fig. 2a) with nominally equal connections on both sides of the specimen and a displacement control protocol according to *EN 26891* (1992). The relative displacement of each connection was determined as the difference between the displacement of the steel plate and the displacement at the centre of the CLT specimen.

2.2 Canada

The Canadian data set consisted of nine steel-wood-steel connections with steel plates on both sides of the CLT element (double shear plane) with self-tapping screws (STS) (see Table 1), from the same type and manufacturer as the European ones (*ETA 11-0284*, 2019). Specimens consisted of an element of CLT, two identical STS connections and one stronger bolted connection (Fig. 2b). Bolted connections were over-designed in order to prevent their failure. All specimens were loaded parallel to the grain of the outer layers of the CLT. The spacing, end and edge distances of the STS groups followed the proposed design prescriptions.

The CLT was of V2M1.1 grade from Structurlam using SPF #2 and better lumber in all layers. The steel plates used in the tests had a thickness of 12.5 mm and a grade of 300W. The plates had pre-drilled holes in accordance with the spacings presented in Table 1. Holes for STS and bolt connections were drilled prior to installation of the steel plates. For STS connections, holes were drilled at 70% of the nominal diameter (0.7d) of the respective screws.

Additionally, nine different steel-to-glulam (GLT) connections were tested, but not described in this paper. The reader is referred to the full report for further details

Table 1. Basic characteristics of the specimens used in the experiments.

Test series	n [-]	w [mm]	t [mm]	ℓ [mm]	d_f [mm]	ℓ_f [mm]	n_r [-]	n_c [-]	a_1 [mm]	a_3 [mm]	a_2 [mm]	a_4 [mm]	CLT layers [mm]
Europe													
AB1	6	245	142	1 228	8	40	6	10	64	48	16	34	40-20-20-20-40
AB2	6	250	142	1 498	8	40	6	10	64	48	16	37	33-20-33-20-33
CD1	7	250	101	988	8	40	6	10	64	48	16	37	20-20-20-20-20
CD2	7	251	101	1 201	8	60	6	10	64	48	16	37	30-40-30
CD3	6	500	101	1 199	8	60	6	10	64	48	16	162	30-40-30
CD4	6	743	101	1 198	8	60	6	10	64	48	16	283	30-40-30
CD5	6	250	140	1 200	8	60	6	10	64	48	16	35	33-20-33-20-33
EF1	4	250	100	1 000	8	100	6	10	64	48	16	35	20-20-20-20-20
EF2	6	250	140	1 200	8	100	6	10	64	48	16	35	33-20-33-20-33
EF3	3	500	140	1 200	8	100	6	10	64	48	16	165	33-20-33-20-33
Canada													
CA4	3	420	175	588	8	80	5	3	40	96	24	20.5	35-35-35-35-35
CA5	3	420	175	588	8	80	5	3	40	96	24	20.5	35-35-35-35-35
CA6	3	140	175	588	8	80	5	3	40	96	24	20.5	35-35-35-35-35
CA10	3	420	175	588	8	120	5	3	40	96	24	20.5	35-35-35-35-35
CA11	3	420	175	588	8	120	5	3	40	96	24	20.5	35-35-35-35-35
CA12	3	140	175	588	8	120	5	3	40	96	24	20.5	35-35-35-35-35
CA16	3	420	175	588	12	100	3	3	60	144	36	34	35-35-35-35-35
CA17	3	420	175	588	12	100	3	3	60	144	36	34	35-35-35-35-35
CA18	3	140	175	588	12	100	3	3	60	144	36	34	35-35-35-35-35

Legend: *n, number of replicates (in the case of the European data, the actual number of tested connetions is 2n); w, t, ℓ, width, thickness and length of the CLT panel; d_f, ℓ_f, diameter and length of the self-tapping screw; n_r, n_c, number of rows (parallel to grain) and columns (perp. to grain); a_1, a_3, spacing and end distance in the parallel direction; a_2, a_4, spacing and edge distance in the perpendicular direction.*

(*Ni and Niederwestberg*, 2022). Original denominations of the test campaign have been respected in this work for consistency with the full report.

2.3 Results

Table 2 summarises the results of the tests from both campaigns. Mean $F_{t,mean}$ and characteristic $F_{t,char}$ tensile maximum loads are given, accompanied by the corresponding coefficient of variation CoV. In the case of the European campaign, since two nominally identical connections were tested simultaneously for each specimen, but only one failed, a probabilistic model based on the Weibull distribution was used to obtain the mean and coefficient of variation (CoV). The characteristic load-bearing capacity values were calculated according to the recommendations in *EN 14358* (2016), with a normal distribution assumed. This characteristic value is highly penalised in the case of the Canadian dataset due to the low number of replicates, so they may be considered as less reliable.

Furthermore, the table presents evaluated average stiffness values obtained according to *EN 26891* (1992) as secant stiffness between 10% and 40% of the ultimate load for the specimen, and the ductility index D_f as defined in *EN 12512*

Table 2. Test results.

Test series	$F_{t,mean}$ [kN]	CoV [%]	$F_{t,char}$ [kN]	F_{yield} [kN]	u_{yield} [mm]	k_{10-40} [kN/mm]	CoV [%]	D_f [-]	CoV [%]	Failure mode [-]
Europe										
AB1	260.8	8.9	200.7	247	7.8	64.7	17.3	1.5	10.0	PS/RS
AB2	236.7	8.8	181.5	199.1	6.4	66.7	27.5	1.4	29.0	PS/RS
CD1	190.2	4.4	103.7	175.7	3.9	96.4	12.1	1.5	12.8	PS
CD2	246.7	6.7	173.5	246.7	4.1	124.1	24.4	1.5	15.0	PS
CD3	304.6	8.3	229.6	267.7	4.3	146.1	12.4	1.5	6.1	PS/RS
CD4	358.1	8.8	274.3	313.5	4.5	134.3	15.8	1.5	5.8	PS/RS
CD5	224.2	5.7	143.1	200.6	3.8	112.3	8.3	1.5	4.9	PS/RS
EF1	224.9	4.9	124.2	224.9	3.4	166.2	20.6	1.4	13.5	NT
EF2	269.1	8.6	205.1	246.0	4.0	110.5	7.0	1.6	19.7	PS/RS
EF3	286.7	11.7	229.7	282.5	4.1	173.5	27.7	2.3	44.1	PS/RS
Canada										
CA4	213.0	4.1	185.3	177.0	9.0	22.7	10.0	2.5	22.7	EYM
CA5	220.0	5.0	185.1	189.0	6.4	35.6	18.3	2.0	38.8	PS
CA6	203.0	4.7	172.6	174.0	6.5	26.7	9.8	2.6	45.4	SS
CA10	309.0	0.8	301.2	167.0	6.8	26.5	18.0	3.8	11.5	EYM
CA11	297.0	10.8	195.2	197.0	6.3	21.1	13.3	2.8	31.7	EYM
CA12	228.0	16.3	111.0	172.0	6.7	25.8	16.8	1.8	27.9	SS
CA16	236.0	4.1	205.3	273.0	149	27.3	14.9	5.0	25.5	EYM
CA17	254.0	7.7	192.1	242.0	137	24.2	15.2	5.9	18.9	EYM
CA18	253.0	8.6	184.4	275.0	143	27.4	11.4	4.4	34.9	EYM

Legend: $F_{t,mean}$, $F_{t,char}$, *mean and characteristica maximum load;* F_{yield}, u_{yield}, *yield load and corresponding displacement;* k_{10-40}, *connection stiffness;* D_f, *connection ductility; CoV, coeffficient of variation.*
Failure modes: *PS, plug shear; RS, row shear (tearing); NT, net tension; SS, step shear; EYM, yielding of the fastener. Where two are indicated, both are observed in some specimens of the series.*

(2016). Yield loads and associated deformations are based on the 5% stiffness offset method based on *ASTM D5764-97a* (2018). In this method, the stiffness of the load-deformation curve is determined within the linear range first, and then a line with the same slope is shifted (offset) at a displacement equal to 5% of the fastener diameter. The yield load is then determined as the load at the intersection of the 5% offset curve and the load-displacement curve or ultimate load, whatever is critical.

Table 2 also presents the associated failure mode. In some cases, a secondary failure mode is presented that was observed during the tests (sometimes failure modes differed among similar specimens).

Yield loads are lower than the ultimate load capacity in most specimens. Hence, plastic deformation of the screws occurs prior to failure in most test series, although most specimens tested eventually failed in a brittle manner. This was shown to be the case also in test campaigns for self-tapping screw connections on glulam and LVL in the past (*Yurrita and Cabrero*, 2021).

(a) Europe. AB1. *(b) Europe. CD3* *(c) Europe. EF2*

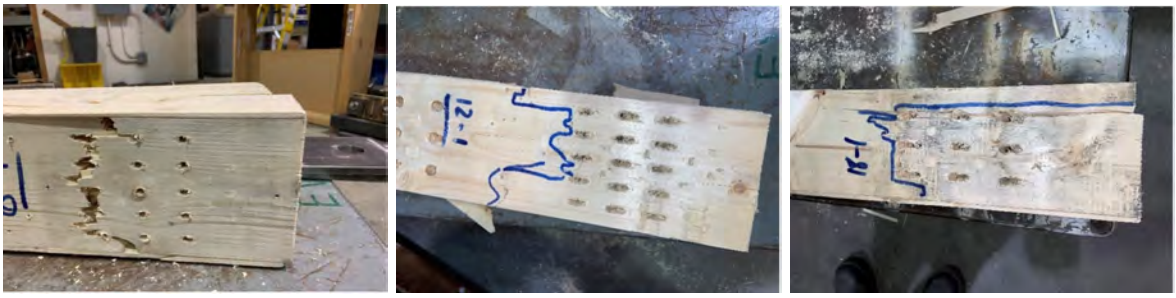

(d) Canada. CA6 *(e) Canada. CA12* *(f) Canada. CA18*

Figure 3. Failures of specimens

Plug shear was the most representative failure mode, but sometimes in combination with row tearing of the screws (e.g., specimen EF2 in Fig.3c). In the case of the test series with reduced width (i.e., CA6 and CA12), due to their narrow width, the typical failure was step shear. In series EF1, net tensile failure of the CLT cross-section occurred. In the case of the Canadian dataset, some specimens eventually failed in a brittle manner, but after a significant deformation, as shown by the higher obtained ductility values. Their failure mode is marked as EYM in Table 2.

An increased specimen width increases the load-bearing capacity, while elastic stiffness does not change significantly. It is clearly observed when comparing specimens CD2 (250 mm) and CD4 (750 mm), with an increase of 45% in capacity, and a stiffness increase of only 8%. The same trend may be observed between C10 and C12 (35% capacity increase in the mean load-bearing capacity values —up to 270% at the characteristic level—, only 2% stiffness increase).

In most cases, there is a direct relationship between the fastener penetration depth and the resulting stiffness (70% increase between CD1 and EF1, with 40 mm and 100 mm). However, this trend is not so clear in the Canadian set. The increase in load capacity between comparable series with different penetration depths is not so remarkable. Although the failed timber plug is deeper for deeper fasteners, there is no significant capacity increase (e.g., AB2 and CD5).

The influence of different layups was analysed only in the case of the European campaign. No significant changes in stiffness are observed (e.g., 3% difference between AB1 and AB2, 10% between CD2 and CD5). There was a more direct influence on the resulting load capacity, mostly dependent on the penetration of the screw with respect to the individual layers.

There are significant differences in ductility between the European and Canadian series. In the case of Europe, the mean ductility was around 1.5, while it was higher in the Canadian tests, where even some tests eventually failed in a ductile way, with ductility values higher than 4 (whose failure mode is reported as EYM). One reason for this difference is response may be related to the lower number of fasteners in the Canadian set (15 screws in comparison to 60 in the European one).

3 Model verification

3.1 Model description

The model from *Zarnani and Quenneville* (2015) originates from their plug shear proposal for small diameter timber fasteners for solid wood products (*Zarnani and Quenneville*, 2014), modified to consider the crosswise layer arrangement of the CLT plates. It is a stiffness-based model, in which the total load carrying capacity is obtained by considering the stiffness of each failure plane. Hence, for every failure plane, both stiffness and capacity are defined.

The plug shear failure is defined by the failure onset of three different planes (depicted in previous Fig. 1): bottom (failing in shear), head (parallel tension) and lateral (shear). However, in the case of CLT, the lateral planes are dismissed, since in most cases boards are not laterally glued, and the position of the joints is undetermined.

In the case of the bottom plane, two different independent contributions are considered: the adjacent shear planes (*a*) between the top and below layers, and the bottom shear plane (*d*). The formulation of the bottom plane takes into account the reinforcement effect of the cross-layers that contributes to the load transfer to adjoining outer and inner parallel laminations. Due to the different occurring load distributions in relation to the fastener relative layer depth penetration, they established a set of different failure modes as shown in previous Figure 1.

After a first run of the model, a re-run to obtain the remaining capacity from the not-yet failed planes has to be additionally performed, to verify that the remaining

Table 3. Used material properties at the characteristic level (ETA 12-0347, 2020; ETA 14-0349, 2020; CSA O86-09, 2019).

Campaign	Lamination strength class	ρ_m [kg/m^3]	$E_{0,m}$ [MPa]	G_m [MPa]	$G_{m,r}$ [MPa]	$f_{t,0,k}$ [MPa]	$f_{t,90,k}$ [MPa]	$f_{v,k}$ [MPa]	$f_{v,r,k}$ [MPa]
Europe	C24	380	12 000	690	50	14	0.12	4	1.8
Canada	V2M1.1	450	10 000	600	60	19.55	0.98	2.01	0.67

capacity is not higher than the initial one. Moreover, when the fastener penetrates the second layer (Mode C), if the failure is due to the head plane, an additional resisting mechanism is defined as a virtual connection between the failed timber plug. It is obtained from the rolling shear in the bottom plane and the yielding of the fastener.

3.2 Model results

Used timber material properties are given in Table 3, obtained from typical design literature in both regions (*ETA 12-0347*, 2020; *ETA 14-0349*, 2020; *CSA O86-09*, 2019). The tensile values in the case of Canada were taken from comparable glulam values since the original ones for CLT were extremely low in comparison (for CLT, $f_{t,0,k} = 6.3$ MPa).

Obtained results are given in Table 4, which contains not only the prediction of the load capacity but also the predicted mode (based on the penetration of the fastener, given by the effective thickness t_{eff}) and the plane which produced the failure. Additionally, the load capacity obtained for the ductile mechanism is given as well, considering ($F_{EYM,Rope}$) and not considering (F_{EYM}) the rope effect. The ductile failure model (European Yield Model, EYM) is based on proposals from the practice literature (*Wallner-Novak et al.*, 2014; *Borgström and Fröbel*, 2019; *Bogensperger et al.*, 2010). The required embedment strength values are obtained from the declared characteristic density, and assumed the same for all layers, regardless of the angle between the force and the direction of the fibre.

Figure 4 presents a comparison of the model results with the experimental results. The figure shows the whole range of experimental results and the load capacities predicted from the brittle and ductile (without rope effect —yielding onset— and with rope effect —increased capacity after large displacements—) models. It has to be considered that in most of the tests, the yielding of the fastener was observed prior to the eventual brittle failure.

Statistical analyses using various metrics were performed as well (Table 5). The metrics are those used by *Cabrero and Yurrita* (2018) and allow a comprehensive

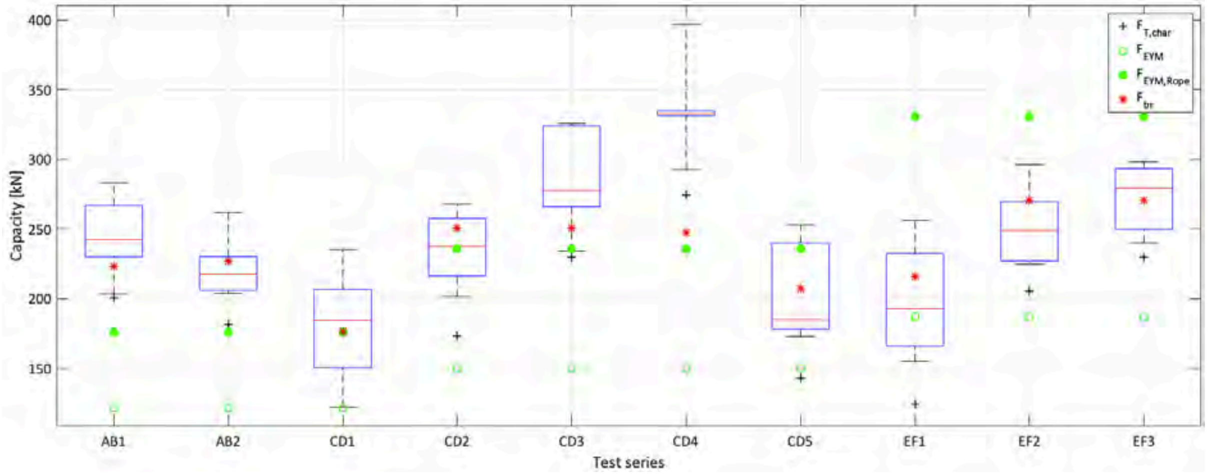

(a) Europe

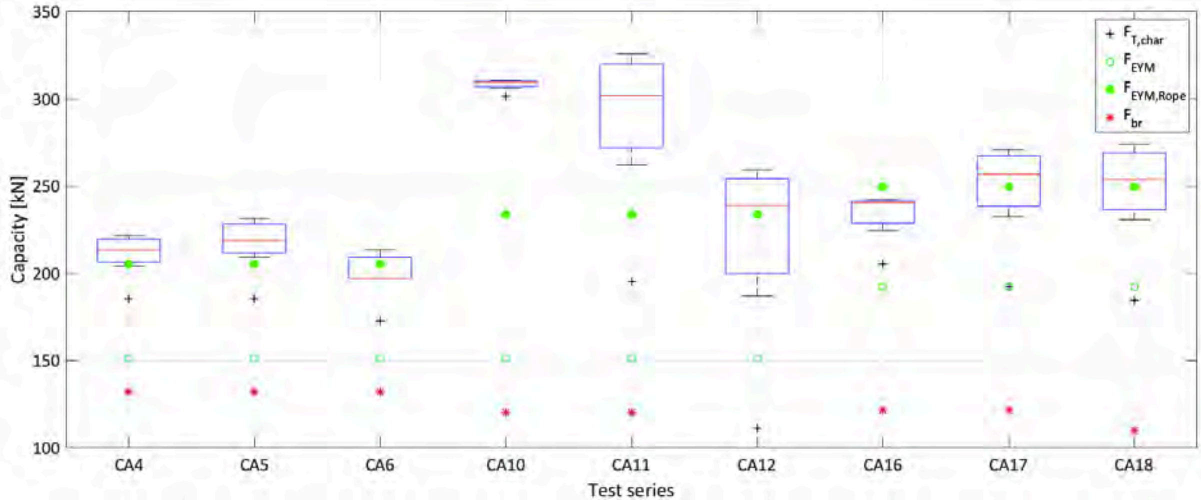

(b) Canada

Figure 4. Results from the models in comparison to the experimental results.

analysis of the model's response in different aspects. The overall performance is analyzed by the determination coefficient Q^2 (*Steyerberg et al.*, 2010; *Chirico and Gramatica*, 2011) (reliable threshold value 0.70, best values closest to 1) and the concordance correlation coefficient *CCC* (*Chirico and Gramatica*, 2011; *Chirico and Gramatica*, 2012; *Gramatica and Sangion*, 2016) (again, values close to 1 are best, recommended threshold value of 0.85). *CCC* is used as an alternative measure to Q^2, whose reliability has been questioned previously (*Golbraikh and Tropsha*, 2002; *Alexander et al.*, 2015). The ability to provide good correlation (without quantitative prediction) is assessed using the rank correlation coefficient *c* (*Alexander et al.*, 2015) (values closer to 1 are the best) and slope *m* of the linear fitting through the origin. In addition, mean relative error MRE (about 10% to be acceptable values) and associated standard deviation SD are observed.

Regarding the brittle model, the obtained values greatly differ between both test

Table 4. Results from the model and comparison to experimental results at the characteristic level (in brackets, corresponding ratio vs. experimental result).

Test	Experiment		Brittle model				EYM no rope	EYM + rope eff.
	$F_{t,k}$ [kN]	Fail.M.	F_{br} [kN]	Mode	Plane	t_{eff} [mm]	F_{EYM} [kN]	$F_{EYM,Rope}$ [kN]
Europe								
AB1	200.7	PS/RS	223.1 (1.11)	A	D	30.2	121.3 (0.60)	176.1 (0.88)
AB2	181.5	PS/RS	226.8 (1.25)	A	D	30.2	121.3 (0.67)	176.1 (0.97)
CD1	103.7	PS	176.4 (1.70)	C	D	30.2	121.3 (1.17)	176.1 (1.70)
CD2	173.5	PS	250.9 (1.45)	C	YR	44.8	150.0 (0.86)	235.9 (1.36)
CD3	229.6	PS/RS	250.9 (1.09)	C	YR	44.8	150.0 (0.65)	235.9 (1.03)
CD4	274.3	PS/RS	247.3 (0.90)	C	D	44.8	150.0 (0.55)	235.9 (0.86)
CD5	143.1	PS/RS	207.2 (1.45)	C	D	44.8	150.0 (1.05)	235.9 (1.65)
EF1	124.2	NT	215.7 (1.74)	E	YR	44.8	186.9 (1.50)	330.6 (2.66)
EF2	205.1	PS/RS	270.9 (1.32)	E	YR	64.0	186.9 (0.91)	330.6 (1.61)
EF3	229.7	PS/RS	270.9 (1.18)	E	YR	64.0	186.9 (0.81)	330.6 (1.44)
Canada								
CA4	185.3	EYM	132.1 (0.71)	C	YR	56.0	151.2 (0.82)	205.5 (1.11)
CA5	185.1	PS	132.1 (0.71)	C	YR	56.0	151.2 (0.82)	205.5 (1.11)
CA6	172.6	SS	132.1 (0.77)	C	YR	56.0	151.2 (0.88)	205.5 (1.19)
CA10	301.2	EYM	120.3 (0.40)	C	YR	68.7	151.2 (0.50)	233.8 (0.78)
CA11	195.2	PS	120.3 (0.62)	C	YR	68.7	151.2 (0.77)	233.8 (1.20)
CA12	111.0	SS	79.6 (0.72)	C	D	68.7	151.2 (1.36)	233.8 (2.11)
CA16	205.3	EYM	121.5 (0.59)	C	YR	64.0	192.4 (0.94)	249.4 (1.21)
CA17	192.1	EYM	121.5 (0.63)	C	YR	64.0	192.4 (1.00)	249.4 (1.30)
CA18	184.4	EYM	110.0 (0.60)	C	D	64.0	192.4 (1.04)	249.4 (1.35)

Failure modes: *PS, plug shear; RS, row shear (tearing); NT, net tension; SS, step shear; EYM, yielding of the fastener. Where two are indicated, both are observed in some specimens of the series.*
Mode (bottom failure plane location): *A, first layer; C, second layer; E, third layer.*
Plane legend*: D, bottom plane; YR, yielding of fastener + rolling shear; H, head plane.*

Table 5. Statistical analysis of the obtained results

	Overall performance		Correlation		Error	
	Q^2	*CCC*	*m*	*c*	*MRE*	*SD*
All tests	-1.21	0.18	0.90	0.22	0.33	0.19
Europe	-0.35	0.39	1.20	0.75	0.28	0.13
Canada	-2.34	0.09	0.59	0.05	0.38	0.23

campaigns. In the case of the European campaign, they are within the range of the obtained experimental values (Fig.4a), but fall outside and are much lower in the Canadian tests (Fig.4b). While the model overpredicts the European characteristic value, it clearly underpredicts the Canadian ones.

This different trend may be explained by two different aspects. The low number of replicates in the Canadian set may reduce the obtained characteristic value. However, this approach was preferred to apply those material properties used in practice. Additionally, the much different material values recommended in the literature (Table 3). Especially in the case of the shear strengths, both of which control the brittle capacity in the bottom plane or yielding rolling mechanism, the Canadian properties are lower (half or even more) than the European values.

As mentioned above, the applied Canadian properties were those for glulam since the Canadian values for CLT are even lower. If CLT values were applied, the reported brittle capacities would even be much lower (15% to 50% lower than those shown in Table 4, with ratios ranging from 19% to 53% of the experimental values). Moreover, having such a low tensile strength, the predicted failure plane changes: the head plane becomes the main failure mechanism, followed by the bottom plane.

The resulting failure mechanisms are either the bottom plane or the yielding-rolling limit mechanism. The latter is the most represented failure mode in the Canadian set (possibly due to the low rolling shear strength), while they are quite homogeneously reported in the European tests. No failure is related to the adjacent plane.

Most of the Canadian tests showed large ductilities, though they eventually failed in a brittle manner after a significant deformation. Unexpectedly, when assessing the models, the resulting brittle capacities are lower than the ductile values. Based on this, brittle failure would be expected, though it is not the case. Again, the low shear strengths in the standard may explain this fact.

As shown in Table 5, the prediction ability is quite low (negative Q^2, and very low *CCC* values). Although the quantitative prediction is poor (as shown by the performance and error metrics), the correlation of the model (that is, the ability to capture the trend) is quite good in the case of the European set. All the metrics worsen in the Canadian set which mostly failed with increased ductilities.

4 Conclusions

This work describes several tests on connections with laterally-loaded self-tapping screws on CLT plates subjected to parallel tension. This type of connection and internal force would be typical in the case of hold-downs, for example. It presents research carried out independently on the same topic in Europe and Canada, and thus allows for a more comprehensive perspective on the topic.

It was found that brittle failure typically occurs after the yielding of the fastener has already started. Quite low ductility values are typically observed, in the range of 1.5-2.5, which would make these types of connections not appropriate for their use in seismic areas, where higher local ductility would be desirable. However, it has been shown in the Canadian set how also ductile failure with ductility values over 4 can be reached as well. For connections with a reduced number of fasteners (as it is the case of the Canadian set), yield modes seem to govern.

The existing model, developed by *Zarnani and Quenneville* (2015), obtained quite scattered results in this work. One main reason is the noticeable differences among declared material properties between both regions. It must be stressed how the need for reliable material properties becomes (as always) a major task. Moreover, they should be obtained from tests in conditions comparable to those assumed in the model. Moreover, shown trends may be affected by the reliability of the characteristic level, due to the low number of replicates in the Canadian case.

Although the brittle model's prediction ability is quite low, its correlation is good, mostly in the case of the European set, which features most of the brittle failures with low ductility values. As it is a stiffness-based model and considers a main and a secondary failure mechanism, it becomes quite cumbersome. It demands the use of dedicated software (in our case, a MatLab script was produced, and validated with the original paper (*Zarnani and Quenneville*, 2015)). The development of simpler design models for practice is advisable.

CLT has become a major product in current timber construction. However, our current design methods for connections still demand improvements. Further work should be done to obtain a better prediction of both yield and brittle load-bearing capacities of CLT connections.

Acknowledgments

The European research has received support within ERA-NET Cofund ForestValue by MIZŠ, VINNOVA, FORMAS, STEM, BMLFUW, FNR and MINECO-AEI and has received funding from the European Union's Horizon 2020 research and innovation program under grant agreement N° 773324. The financial support provided by the Spanish Ministerio de Ciencia, Innovación y Universidades – Agencia Estatal de Investigación under contract PCI2019-103591 AEI is gratefully acknowledged.

This Canadian project was financially supported by the Canadian Forest Service of Natural Resources Canada, the Natural Sciences and Engineering Research Council of Canada and all industry partners of the Industrial Research Chair for Advanced Research in Timber Systems.

5 References

Alexander, D. L., A. Tropsha, and D. A. Winkler (2015). "Beware of R^2: Simple, Unambiguous Assessment of the Prediction Accuracy of QSAR and QSPR Models." In: *Journal of Chemical Information and Modeling* 55.7, pp. 1316–1322. DOI: 10.1021/acs.jcim.5b00206.

Asgari, H., T. Tannert, and C. Loss (2022). "Block tear-out resistance of CLT panels with single large-diameter connectors." In: *European Journal of Wood and Wood Products*. DOI: 10.1007/s00107-022-01809-3.

ASTM D5457-21a (2021). *Standard Specification for Computing Reference Resistance of Wood-Based Materials and Structural Connections for Load and Resistance Factor Design*.

ASTM D5764-97a (2018). *Standard Test Method for Evaluating Dowel-Bearing Strength of Wood and Wood-Based Products*. ASTM.

Azinović, B., J. M. Cabrero, H. Danielsson, and T. Pazlar (2022). "Brittle failure of laterally loaded self-tapping screw connections for cross-laminated timber structures." In: *Engineering Structures* 266, p. 114556. DOI: https://doi.org/10.1016/j.engstruct.2022.114556.

Bogensperger, T., T. Moosbrugger, and G. Schickhofer, eds. (2010). *BSPhandbuch, Holz- Massivbauweise in Brettsperrholz*. Verlag der Technischen Universität Graz.

Borgström, E. and J. Fröbel, eds. (2019). *The CLT Handbook*. First. Stockholm, Sweden: Swedish Wood.

Cabrero, J. M. and M. Yurrita (2018). "Performance Assessment of Existing Models to Predict Brittle Failure Modes of Steel-to-Timber Connections Loaded Parallel-to-Grain with Dowel-Type Fasteners." In: *Engineering Structures* 171. **(INTER paper 51-7-12)**, pp. 895–910. DOI: 10.1016/j.engstruct.2018.03.037.

Chirico, N. and P. Gramatica (2012). "Real External Predictivity of QSAR Models. Part 2. New Intercomparable Thresholds for Different Validation Criteria and the Need for Scatter Plot Inspection." In: *Journal of Chemical Information and Modeling* 52.8, pp. 2044–2058. DOI: 10.1021/ci300084j.

Chirico, N. and P. Gramatica (2011). "Real External Predictivity of QSAR Models: How to Evaluate It? Comparison of Different Validation Criteria and Proposal of Using the Concordance Correlation Coefficient." In: *Journal of Chemical Information and Modeling* 51.9, pp. 2320–2335. DOI: 10.1021/ci200211n.

CSA O86-09 (2019). *Engineering Design in Wood*. Canadian Standards Association.

EN 12512 (2016). *EN 12512:2005, Timber Structures - Test Methods - Cyclic Testing of Joints Made with Mechanical Fastener*. CEN.

EN 14358 (2016). *Timber Structures - Calculation and Verification of Characteristic Values*. Tech. rep. CEN.

EN 26891 (1992). *Timber Structures -Joints Made with Mechanical Fasteners - General Principles for the Determination of Strength and Deformation Characteristics*.

ETA 11-0284 (2019). *Screws for Use in Timber Construction*.

ETA 12-0347 (2020). *Solid Wood Slab Element to Be Used as a Structural Element in Buildings*.

ETA 14-0349 (2020). *Solid Wood Slab Element to Be Used as a Structural Element in Buildings*.

Golbraikh, A. and A. Tropsha (2002). "Beware of Q^2!" In: *Journal of Molecular Graphics and Modelling* 20.4, pp. 269–276. DOI: 10.1016/S1093-3263(01)00123-1.

Gramatica, P. and A. Sangion (2016). "A Historical Excursus on the Statistical Validation Parameters for QSAR Models: A Clarification Concerning Metrics and Terminology." In: *Journal of Chemical Information and Modeling* 56.6, pp. 1127–1131. DOI: 10.1021/acs.jcim.6b00088.

Ni, C. and J. Niederwestberg (2022). *Investigation of brittle failure modes in self-tapping screw steel to wood connections parallel to the grain*. Tech. rep. 301014606. FPInnovation.

Schenk, M., C. Hübner, and J. M. Cabrero (2022). "Cross-Laminated Timber: A Survey on Design Methods and Concepts in Practice." In: *CivilEng* 3.3, pp. 610–629. DOI: 10.3390/civileng3030036.

Steyerberg, E. W., A. J. Vickers, N. R. Cook, T. Gerds, M. Gonen, N. Obuchowski, M. J. Pencina, and M. W. Kattan (2010). "Assessing the Performance of Prediction Models." In: *Epidemiology* 21.1, pp. 128–138. DOI: 10.1097/EDE.0b013e3181c30fb2.

Wallner-Novak, M., J. Koppelhuber, and K. Pock (2014). *Cross-Laminated Timber Structural Design*. proHolz Austria.

Yurrita, M. and J. M. Cabrero (2020). "New Design Model for Brittle Failure in the Parallel-to-Grain Direction of Timber Connections with Large Diameter Fasteners." In: *Engineering Structures* 217. **(INTER paper 52-7-7)**, p. 110557. DOI: 10.1016/j.engstruct.2020.110557.

Yurrita, M. and J. M. Cabrero (2021). "Experimental analysis of plug shear failure in timber connections with small diameter fasteners loaded parallel-to-grain." In: *Engineering Structures* 238. **(INTER paper 53-7-6)**, p. 111766. DOI: https://doi.org/10.1016/j.engstruct.2020.111766.

Yurrita, M., J. M. Cabrero, and E. Moreno-Zapata (2021). "Brittle Failure in the Parallel-to-Grain Direction of Timber Connections with Small Diameter Dowel-Type Fasteners: A New Design Model for Plug Shear." In: *Engineering Structures* 241. **(INTER paper 54-7-10)**, p. 112450. DOI: 10.1016/j.engstruct.2021.112450.

Zarnani, P. and P. Quenneville (2015). "New Design Approach for Controlling Brittle Failure Modes of Small-Dowel-Type Connections in Cross-laminated Timber (CLT)." In: *Construction and Building Materials* 100. **(INTER paper 47-7-3)**, pp. 172–182. DOI: 10.1016/j.conbuildmat.2015.09.049.

Zarnani, P. and P. Quenneville (2014). "Wood Block Tear-out Resistance and Failure Modes of Timber Rivet Connections: A Stiffness-Based Approach." In: *Journal of Structural Engineering* 140.2. **(CIB-W-18 paper 45-7-1)**, p. 04013055. DOI: 10.1061/(ASCE)ST.1943-541X.0000840.

DISCUSSION

The paper was presented by J M Cabrero

P Dietsch commented that the input properties in the model for different countries are very different. There is a need to harmonize how to measure these properties. JM Cabrero agreed as the brittle failure model relies on input parameters and stiffness information is also important.

T Tannert asked about the eccentricity in the test set up. JM Cabrero said lateral support was provided to counter this.

H Blass asked if slender fasteners also only have failure planes at the fastener tips. JM Cabrero replied mostly in the tip. H Blass commented that in EC5 the thickness of block for shear is different for shear and tension. JM Cabrero said this is a model assumption and seems to work.

S Aicher commented that looking at different scenarios with the variety of layups, engineers would not have control of the laminate thickness, width, etc. JM Cabrero agreed in general; however, this information is needed in advance in terms of where the lamination is with respect to the screws.

A Frangi received confirmation that the connections were originally designed to fail in brittle mode.

G Doudak asked if the observed failure modes agreed with the predicted ones. JM Cabrero said it was difficult to distinguish through observation the exact brittle failure mode.

M Fragiacomo asked if it would be appropriate to use the solid wood approach in EC5 with a statement that this would be a conservative approach. JM Cabrero said this would be too conservative by a factor of 2.

T Demscher and JM Cabrero discussed the contribution of the lateral shear plane.

Low cycle ductility of self-tapping screws

Michael Steilner, Karlsruhe Institute of Technology

Henning Kunkel, Karlsruhe Institute of Technology

Carmen Sandhaas, Karlsruhe Institute of Technology

Keywords: self-tapping screws, timber, wood, low cycle ductility

1 Introduction

In principle, timber structures show an excellent behaviour in the event of earthquakes. The positive ratio of strength and mass leads to lower seismic loads. Traditionally, many slender metallic fasteners are used in timber structures, e.g., in timber frame construction. Joints using such dowel-type fasteners generally behave ductile and thus dissipate energy.

With the advent of massive timber construction using materials such as CLT, the individual elements have larger formats and are stiffer than in traditional timber frame construction. Additionally, whereas timber frame construction makes use of many, small-diameter joints distributed over the whole structure, fewer and more discrete joints are needed in massive timber construction. Consequentially, earthquake loads increase, leading also to higher forces in the joints. Self-tapping timber screws are suitable for the transmission of large forces. However, they are usually made of hardened carbon steel, which fails brittle. By means of special hardening processes, the screws are treated in such a way that they remain ductile to a certain extent. For earthquake design, however, a secure ductile behaviour is required, which means that screws must be able to form plastic hinges.

prEN 14592 Annex E (2017) introduces a new test method that divides fasteners into so-called "low cycle ductility classes" to describe the ductile behaviour of fasteners. This new test method shall guarantee that the fasteners are able to form plastic hinges under reversed loading without failure resp. to classify the screws in dependence of their plastic deformation capacity. The aim of this work is to investigate if the proposed classification depends on the test setup parameters and if it is possible to divide screws directly into low cycle ductility classes by more simple tests according to EN 409 (2009), with which the yield moment of fasteners is determined. Both test methods, prEN 14592 and EN 409, however, encompass tests using only the fasteners. Therefore, this work moreover investigates if tests with only fasteners deliver significant results also for joints, where a system of fastener and timber must behave ductile. For this scope, quasi-static reversed cyclic tests on timber-to-timber joints with screws according to EN 12512 (2005) are carried out, using screws assigned to different low cycle ductility classes. The focus here is on self-tapping timber screws from different manufacturers and different diameters. The new test method from prEN 14592 Annex E, EN 409 and EN 12512 for the determination of the ductility and the cyclic behaviour of joints are considered.

2 State of the art

Self-tapping timber screws can be arranged differently in timber joints. If they are axially loaded, they can activate their high stiffness and load-carrying capacity. However, these joints fail in a rather brittle manner. If the screws in the joint are laterally loaded, they exhibit a more ductile behaviour and can also dissipate energy under cyclic loads (Hossain et. al, 2018).

Ductile behaviour in timber construction is hence mainly created in joints with laterally loaded dowel-type fasteners by the formation of plastic hinges in the metallic fasteners and the embedding strength of the timber components. The timber components themselves fail brittle, especially under tensile and bending loads (Jorissen and Fragiacomo, 2011; Ottenhaus et. al., 2021). The steel properties of the fasteners influence the ductility of a joint. Hardened fasteners fail brittle compared to unhardened ones. In most cases, several fasteners are arranged in a row and are thus exposed to different loads. Ductile fasteners are advantageous here because they can redistribute stresses (Geiser et. al, 2021). The ductility of an entire joint depends not only on the fastener itself, but also on the geometry of the joint, such as fastener spacing. To determine the ductility of entire joints, test standards are available, such as EN 12512 and ASTM E2126 (Casagrande et. al, 2020).

Concerning joints with laterally loaded screws, the screws must be able to withstand reversed cyclic bending to dissipate energy under cyclic loads. Concerning a screw’s bending capacity, the current certification of screws in accordance with EN 14592 (2017) and EAD 130118-01-0603 (2019) so far is only based on monotonic tests with screws (EN 409). As a robustness criterion, a certain bending angle depending on the screw diameter must be achieved during the test. To be able to make a statement about the cyclic properties of fasteners, prEN 14592 contains a test method that divides the dowel-type fasteners into different “low cycle ductility” classes with respect to their low cycle behaviour. Initial studies have shown that the test method allows the classification into classes for commercially available timber screws (Izzi and Polastri, 2019; Cervio and Muciaccia, 2020).

3 Test in accordance with prEN 14592:2017 Annex E

3.1 Normative requirements and their implementation

To classify a screw in a low cycle ductility class, three tests under cyclic load and three tests under monotonic load are necessary, where only the screw itself and not a whole joint is tested. The cyclic test encompasses three fully reversed cycles up to a bending angle α_c and a final monotonic loading to determine the residual bending moment capacity. Two criteria must be met for the screw to be classified in a low cycle ductility class. For ***criterion 1*** (see (Figure 3), screws with diameters up to 8 mm must reach a minimum bending angle during monotonic loading of at least 45° respectively 30° for screws with larger diameters, where the standard is unclear if this applies to both the monotonic tests and the final monotonic loading during the cyclic tests. At KIT, both curves must reach the minimum bending angles. If the residual bending moment capacity after three fully reversed cycles reaches at least 80 % of the moment capacity under monotonic load, the screw passes the test, ***criterion 2*** (see Figure 3). Three different low cycle ductility classes are defined where for the higher classes providing more energy dissipation capacity, larger bending angles α_c must be reached during the cyclic test. This means that the bending angle α_c must be defined beforehand in order to apply the correct deformations during the cycles and if the test failed, a new test with a lower bending angle α_c is necessary. The bending angles α_c for the classification into the three low cycle ductility classes are defined for the low cycle ductility class S1 as $\alpha_c = \alpha$, S2 as $\alpha_c = 1.5\alpha$ and S3 as $\alpha_c = 2\alpha$. For this, α can be calculated by the formula $\alpha = 45°/d^{0.7}$, with d being the nominal diameter of the screw.

Annex E of prEN 14592 furthermore describes a test setup for the determination of the low cycle ductility classes. Figure 1 shows the principal test setup from prEN 14592. Figure 2 shows the implementation in the laboratory of the KIT Research Centre for Steel, Timber, and Masonry. Using this test setup, the monotonic and the cyclic tests (including a final monotonic loading) are carried out.

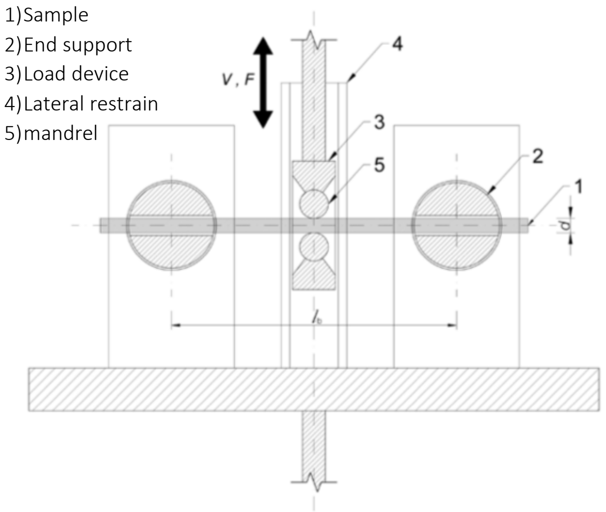

"The length of the support, l_b shall be less than 16d. The diameter of the mandrel which the sample is bent over shall be 2d ± 0.5d. The end supports shall allow for axial displacements and free rotations of the sample. The sample shall be laterally restrained in order to prevent out of plane rotations." Annex E to prEN 14592

Figure 1: Test setup and requirements given in prEN 14592 Annex E, there Figure E.1

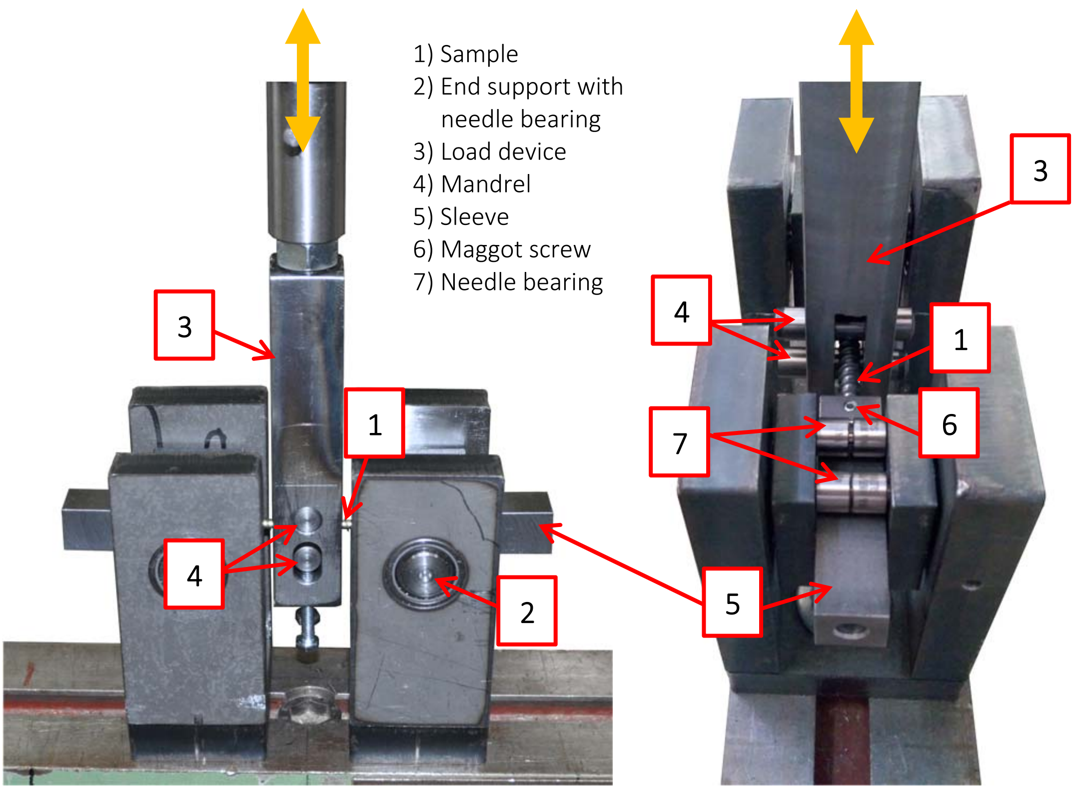

Figure 2: Implemented experimental setup at KIT

The dowel-type fastener is inserted in two sleeves (5) and fixed with two maggot screws (6) per sleeve. The fixation prevents lateral movement of the fastener under alternating load. Eight needle bearings (7) in turn hold one sleeve per support side to ensure free movement in the axial direction of the fastener, which prevents normal forces in the fastener. The needle bearings are connected to steel plates, which are held vertically via further needle bearings (2), allowing for rotation. The fastener is attached to the load device (3) via two mandrels (4). With a vertical shift of the load device, the fastener is loaded with a moment and a shear force. The test device is installed in a universal testing machine, a vertical displacement is applied via the load device and the associated force and displacement are measured.

From the measured forces and displacements, the moment and the bending angle are calculated. In Figure 3, such a moment-bending angle diagram is shown. The black curve shows the monotonous test of a screw up to the bending angle α_{max} = 45°. The blue curve shows the three cycles of a test up to the bending angle α_c and then the red curve shows the final monotonic loading up to the bending angle α_{max}. Due to the change of load direction, a force-free displacement in the zero crossing is created due to the backlash between mandrel and fastener.

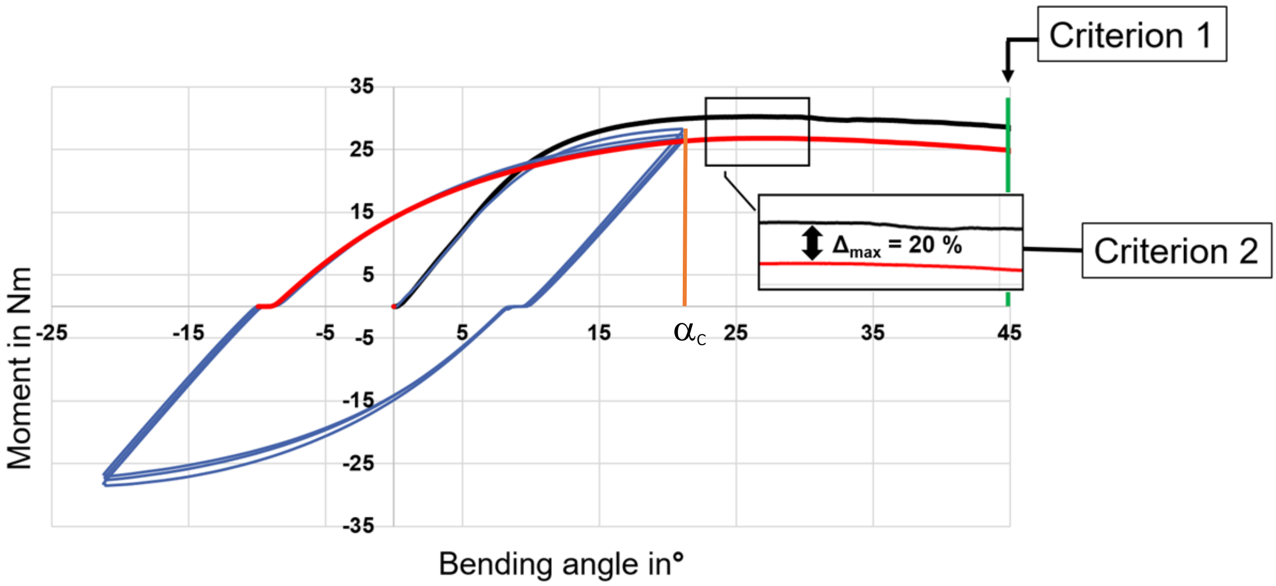

Figure 3: Moment-bending-angle-diagram of cyclic test in accordance with prEN 14592 and the criteria 1 and 2

3.2 Variation of test parameters and their effect on the test result

The test procedure in prEN 14592 is new and there is little knowledge about the influence of test parameters, which can in parts be chosen freely. For this reason, extensive tests with variations of these three parameters were carried out:

- Testing time
- Mandrel diameter *D*
- Support distance l_b

The prescribed testing time seems with t = 300 s ± 60 s very long compared to a real cyclic load due to earthquakes. Therefore, the normative testing time was compared with a significantly shorter testing time. Kuck and Sandhaas (2022) have shown that tests according to EN 409 lead to different results when varying the free bending length. They have shown that a variation of the free bending length has an influence on the stiffness and the maximum yield moment. The smaller the free length is chosen, the more critical the test is in terms of ductility, i.e., the more likely an early failure is to be expected, as bending radii decrease. This behaviour was also expected in the tests for the classification of the screws into the low cycle ductility classes according to prEN 14592. It was expected that the same influence can be shown by variation of the mandrel diameter which influences the radius of the plastic hinge, and by varying the support distance.

Seven different screws with diameters from 5 mm to 12 mm were tested. All screws were fully threaded with exception of one screw, which was partially threaded. It is expected that the influence of the three parameters is greater in the higher low cycle ductility classes since the deformations are then at their maximum. For this reason, the screws were tested in the highest low cycle ductility class S3.

3.2.1 Influence of testing time

prEN 14592 specifies a possible test duration of t = 300 s ± 60 s. The specified average test duration of t = 300 s was selected as reference. In order to show the greatest possible influence, the standard specification was largely reduced and a test duration of one tenth, i.e. t = 30 s, was chosen. Five different types of screws with diameters from 5 to 12 mm was examined. 10 test series with 3 cyclic and monotonic tests per series were carried out.

Screws that already show a significant drop in moment load-carrying capacity during the final monotonic loading after the cyclic loads with a test duration of t = 300 s also show this with a test duration of t = 30 s, only that the drop in moment load-carrying capacity is greater and occurs at smaller bending angles (red rectangles in Figure 4). In the case of screws that showed no drop in moment load capacity, no influence of the different loading rates could be determined. Figure 4 shows an example of a comparison of the two load rates for screws where a drop in the moment carrying capacity could be observed.

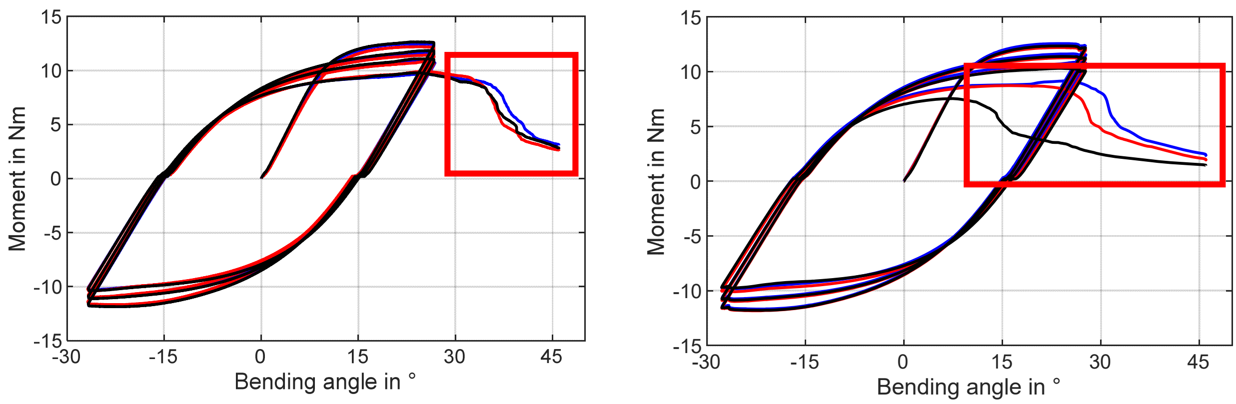

Figure 4: Influence of time - left side t = 300 s and right side t = 30 s, screw with d = 6 mm

3.2.2 Influence of mandrel diameter

prEN 14592 specifies a possible margin for the diameter of the mandrel from $2d \pm 0.5\ d$, over which the fasteners must be bent. Two mandrels with a diameter D of 12 mm and 18 mm were available for the investigations. Screws with diameters of 6 mm, 6.5 mm and 7.5 mm were tested. The ratio of mandrel diameter and screw diameter was between 1.6 d and 3.0 d with a mean difference of about 1.0 d. A total of six series with 3 cyclic tests each were carried out.

An increase in the mandrel diameter led to a slight improvement of the test result, i.e. the achievement of a greater bending angle during the final monotonic loading without failure. However, as in the tests with different loading rates, this also only occurred with screws that proved to be critical in the final monotonic loading. Figure 5 exemplifies the influence on the variation of the mandrel diameter, which shows a small increase in the bending angle up to rupture.

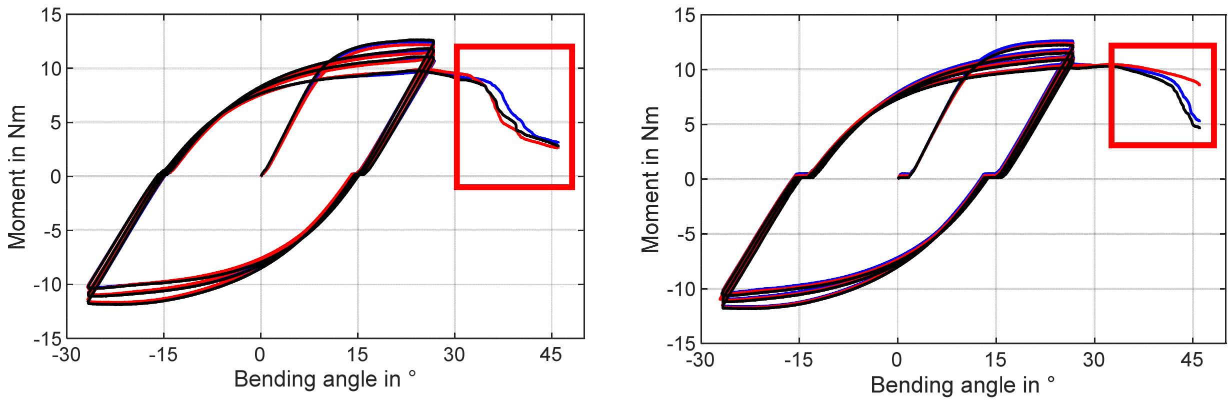

Figure 5: Influence of mandrel diameter – left side D = 12 mm and right side D = 18 mm, screw with d= 6 mm

3.2.3 Influence of the support distance l_b

prEN 14592 specifies a support distance of $l_b \leq 16\ d$, but no lower limit. Since the support distance has an influence on the elastic part of the bending angle, tests were carried out on screws with diameters of 6 to 12 mm. The support distance was chosen between a maximum distance of $l_b = 16\ d - 1$ mm and a distance of $l_b = 10\ d$. Due to the test device, this could not be reduced further than 10 d. In addition, the plastic bending angle β of each tested fastener was determined and documented after carrying out the test. All screws have been tested in their highest possible low cycle ductility class. An overview of the test results can be found in Table 1. It shows that for both the monotonic and the cyclic tests, the plastic bending angle β increased with decreasing the support distance l_b. This led to larger plastic deformations in the screw. A steady increase in moment capacity under monotonic loading (M_m) was also observed, confirming the increase in plastic bending angles β. On the other hand, the residual capacity of the bending moment after the cyclic tests (M_c) showed only slightly increased or even reduced values. This can be explained by increased alternating stress/fatigue. In the case of the criteria for classification into the low cycle ductility class, there is no influence of the support distance for criterion 2. For criterion 1, in which a bending angle of 45° or 30° must be achieved, it can be seen that this is not achieved with small support distances. This shows that small support distances and large plastic bending angles are the critical parameters for the classification into the low cycle ductility classes. From this, it could be assumed that a monotonic test with a small contact distance and a large plastic bending angle can potentially replace the cyclic tests.

Table 1: Test results of support distance l_b

d in mm	support distance l_b in mm	Low cycle ductility class	Monotonic Tests		Cyclic Tests		Criterion 1	Criterion 2
			M_m in Nm	β_m in °	M_c in Nm	β_c in °	min. bend. angle	Δ M_m to M_c $\leq 20\,\%$
6	16 d - 1	S2	12.2	34.8	11.5	34.3	pass	pass
	13 d	S2	13.0	36.5	10.9	38.2	fail	pass
6.5	16 d - 1	S2	-	-	24.8	34.5	fail	-
	16 d - 1	S1	26.7	34.5	26.3	34.3	pass	pass
	13 d	S1	27.2	39.3	26.6	39.3	fail	pass
7.5	16 d - 1	S2	21.5	33.7	21.3	34.2	pass	pass
	13 d	S2	22.7	36.7	22.1	38.7	pass	pass
	11 d	S2	23.3	38.3	20.8	41.5	fail	pass
9	16 d - 1	S3	37.4	20.5	35.8	20.3	pass	pass
	13 d	S3	38.7	22.0	36.8	21.8	pass	pass
	10 d	S3	41.2	24.5	38.7	24.7	fail	pass
12	16 d - 1	S3	89.6	17.5	81.3	19.0	pass	pass
	13 d	S3	86.2	19.5	90.0	19.5	pass	pass
	10 d	S3	92.2	21.8	85.0	21.3	pass	pass
12	16 d - 1	S3	77.0	18.3	75.1	19.0	pass	pass
	13 d	S3	80.3	21.5	73.1	21.5	pass	pass
	10 d	S3	81.4	24.3	71.3	26.3	fail	pass

M_m: Mean bending moment under monotonic load / M_c: mean bending moment after cyclic load
β: Mean measured plastic bending angle of screw after testing under monotonic or cyclic load

4 Comparative tests between EN 409 and prEN 14592

4.1 Test setup

EN 409 describes a test method for determining the yield moment M_y of dowel-type fasteners. Here, a pure moment is applied to the fastener by carrying out a four-point bending test. During the test, the moment and the bending angle are measured. The bending angle, at which the yield moment is determined, corresponds to $45/d^{0.7}$ according to EN 14592 (2012). However, during the test, the fastener is usually bent far above 45°and the moment is recorded. The free bending length in the test is limited to a maximum of 3 *d*, resulting in a small support distance and a large plastic bending angle. Therefore, based on the results from section 3.2.3, it should now be checked if a classification into the low cycle ductility classes can be made using this (critical) test setup.

Comparative tests according to EN 409 and cyclic tests according to prEN 14592 were hence carried out on 27 different screws made of carbon steel and eight different screws made of stainless steel. The different screws were fully threaded as well as partially threaded with nominal diameters ranging from 5 mm to 12 mm. Per series, three tests were carried out.

In the test setup according to prEN 14592, a support distance of $l_b = 16\,d – 1$ mm was selected, and a mandrel diameter D = 12 mm was used for screws with diameters $d \leq 8$ mm and D = 18 mm for screws with diameters $d > 8$ mm.

In the tests according to EN 409, the screws were bent up to a bending angle of 60° if they did not fail beforehand and the moment and the angle were measured.

4.2 Results and discussion

Figure 6 shows three normalised moment-bending angle curves of tests according to EN 409. It can be seen that the three curves show different moment-bending angle behaviour, which leads to a possible classification of the screws in classes F1 to F3. Curve F1 shows an almost ideally plastic behaviour of the screw, whereas the moment bending angle curves of class F2 screws decrease after having reached a maximum. The screw of curve F3, finally, fails before reaching a bending angle of 60°. Based on these three typified curves, the tested screws were divided into the corresponding classes F1 to F3 based on their moment-bending angle curves.

Class F1 screws can be accepted as ductile and class F3 screws as quite brittle. The curves of class F2 screws indicate that the cross-section was damaged, reducing the moment capacity.

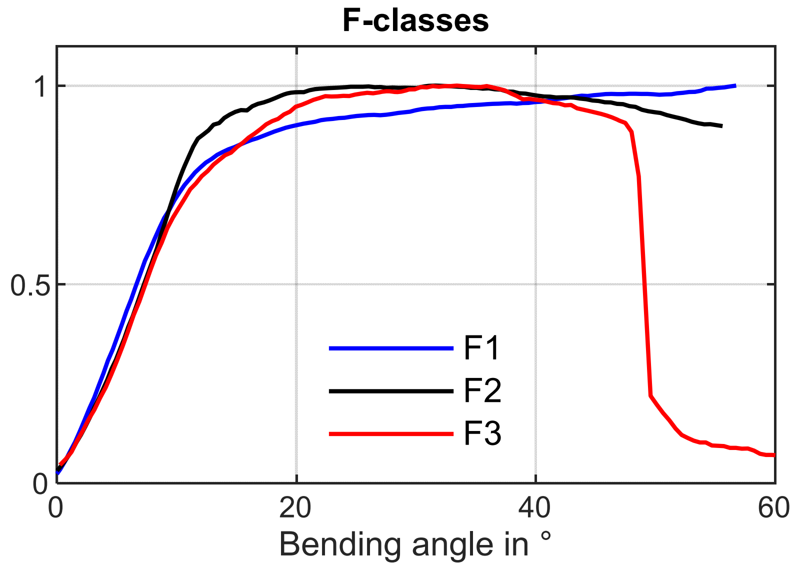

Figure 6: Exemplary curves of the different classes F1, F2, F3.

The cyclic tests according to prEN 14592 were carried out as described in section 3.1 and the screws were classified into the corresponding low cycle ductility classes.

Figure 7 shows the assignment of the determined values of the low cycle ductility classes according to prEN 14592 to the classes F1 to F3. With 24 out of 35 screws, most of them could be classified in class F1. As expected, most of them, 21 screws, can be classified in low cycle ductility class S3. But one screw was classified in low cycle ductility class S1 and two in class S2. Classes F2 and F3 do not show a clear trend that this classification corresponds to the classification of the low cycle ductility classes. One screw each from classes F2 and F3 could not even be classified in the lowest low cycle ductility class S1 because it did not meet the criteria. However, it can be clearly seen that most of the screws were classified in the low cycle ductility class S3 and the number of screws in the other classes was small. However, this shows that commercially available screws can usually reach class S3.

The results show that screws that are classified into F3 tend not to be able to be classified into low cycle ductility class S3 and screws that are classified into F1 are more likely to reach class S3. But it cannot be safely assumed that screws that have been classified into F1 can be safely classified into the low cycle ductility class S3. In other words, tests according to EN 409 cannot replace tests according to prEN 14592.

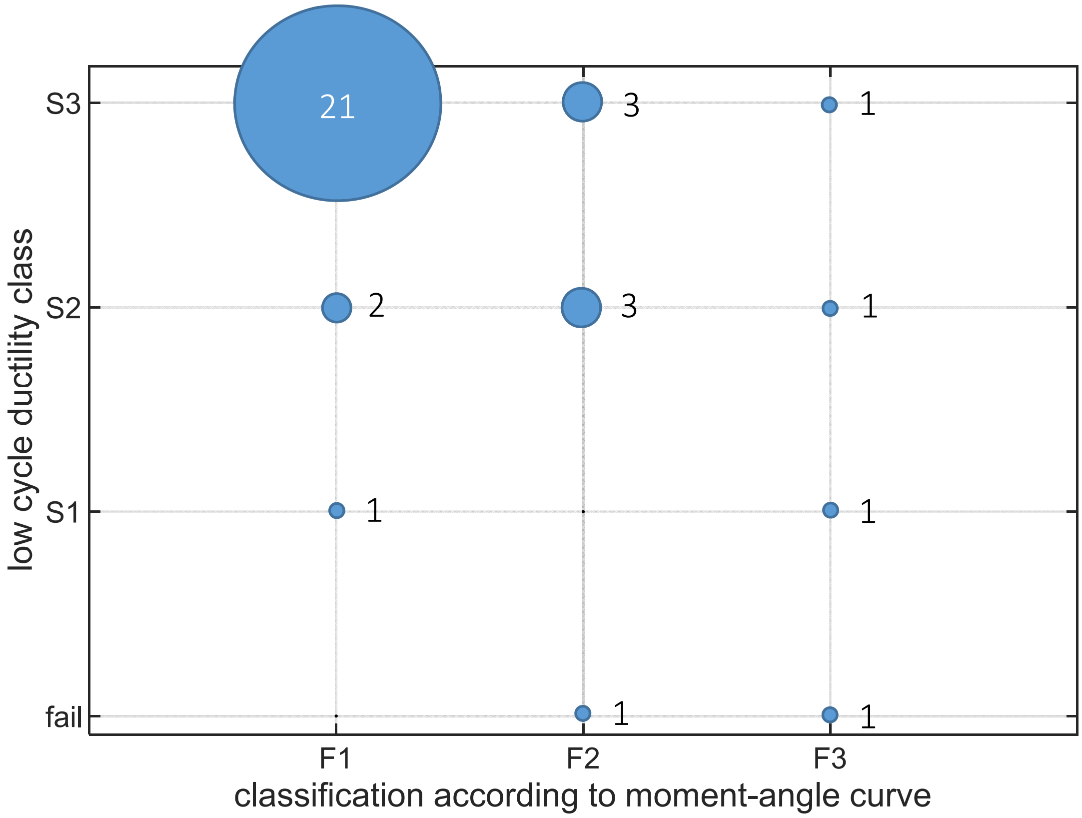

Figure 7: Assignment of the low cycle ductility classes to the classes F1 to F3 (The numbers indicate the number of associated screws)

5 Tests in accordance with EN 12512

Based on prEN 14592, screws can be divided into three different low cycle ductility classes. Investigations that verify this classification with actual cyclic tests on timber joints are not yet available. To gain initial insights into this, screws tested according to prEN 14592 were selected, which achieved both the highest classification S3 as well as the lowest S1. These screws were then used for cyclic tests according to EN 12512 on timber-to-timber joints. The aim of the investigation was to evaluate if joints with screws with different classifications in the low cycle ductility classes show different behaviour under cyclic loading of the joints.

To carry out the tests in accordance with EN 12512, the focus was placed on ductile joint behaviour, testing a joint with only one screw. For this reason, the timber cross-sections as well as the end and edge distances were chosen to be very large in order to prevent early timber failure. Two different timber materials were used, spruce (Picea abies) and laminated veneer lumber made of beech (beech LVL). In Figure 8, the test setup and the test procedure can be seen. Tests with two different fully threaded screws were carried out, where the specimen layout was symmetric, testing two joints with one screw per shear plane. The screws classified in low cycle ductility class S1 had a diameter of 6.5 mm and for the screws classified in class S3, the diameter was 8 mm. A total of nine tests were carried out.

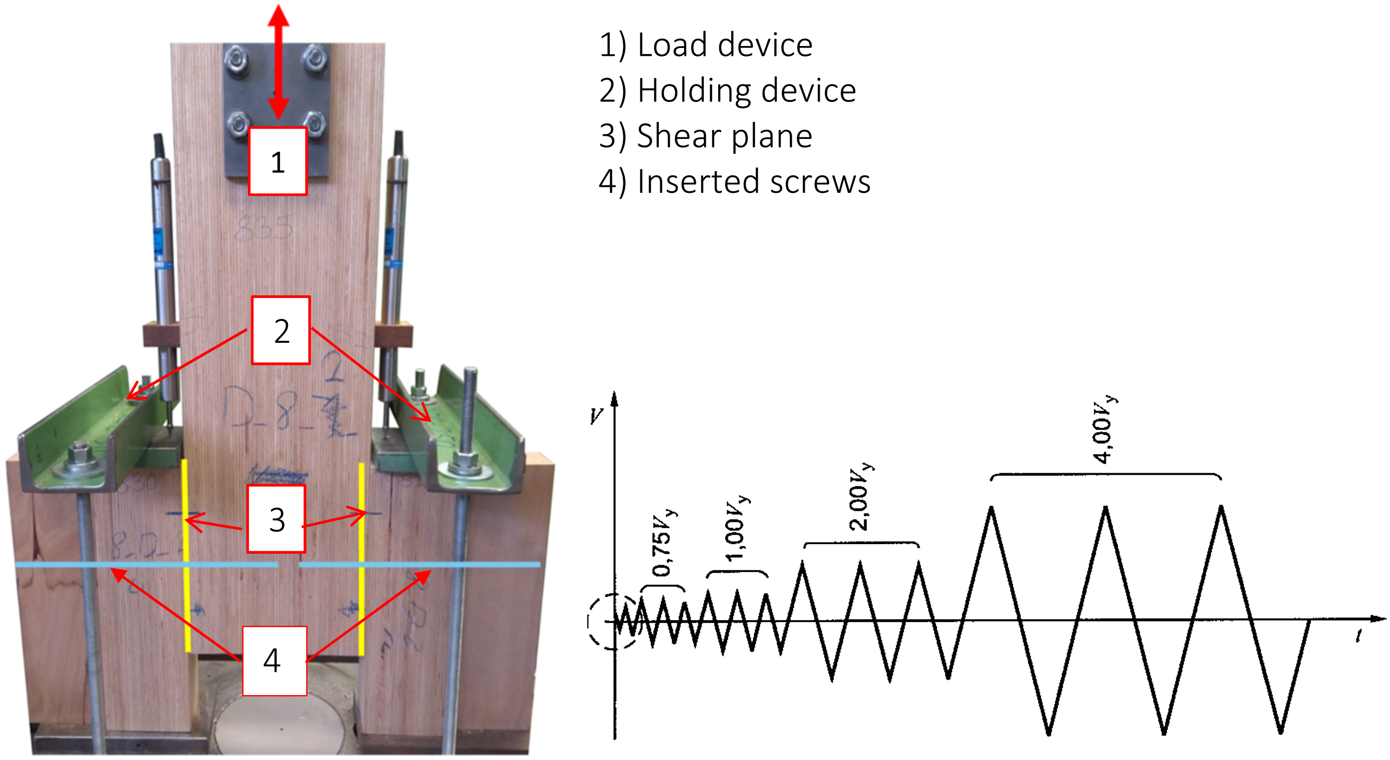

Figure 8: Left: Test setup. Right: Test procedure according to EN 12512

Figure 9 and Figure 10 show the load-displacement curves of joints with beech LVL and softwood. On the left side, the joint with S1-classified screws is shown (d = 6.5 mm), and on the right side, the joint with S3-classified screws (d = 8 mm). The joints with the S1-classified screws failed at a number of cycles that the S3-classified screws could go through without failure. The reason for failure was the breaking off of the S1-classified screws.

It is striking that the shape of both curves for each wood type is almost identical although both diameters differ by 1.5 mm. This suggests a stronger hardening, which could explain the lower classification in S1. Summarising, the joint with S3-classified screws shows a more ductile behaviour compared to the joint with S1-classified screws, which confirms the differentiation in classification of the screws according to prEN 14592.

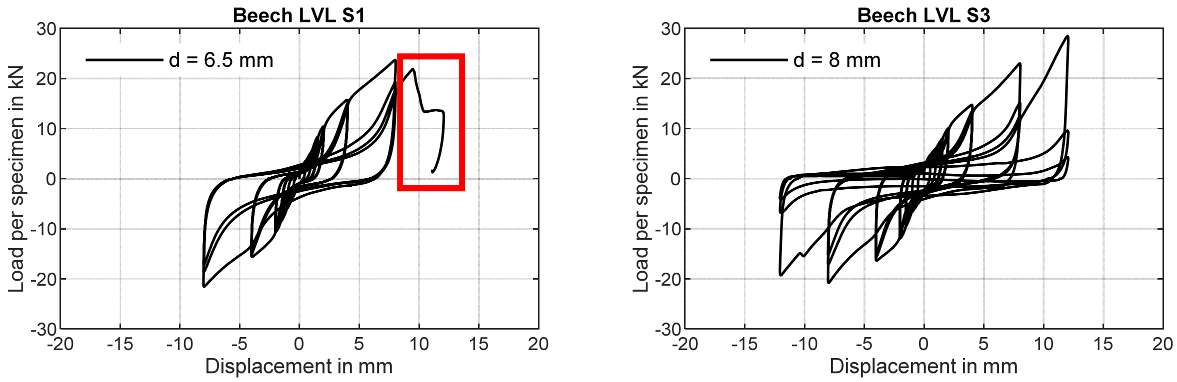

Figure 9: Load-displacement curves for tests according to EN 12512 in beech LVL; left side: S1-classified screw, right side: S3-classified screw

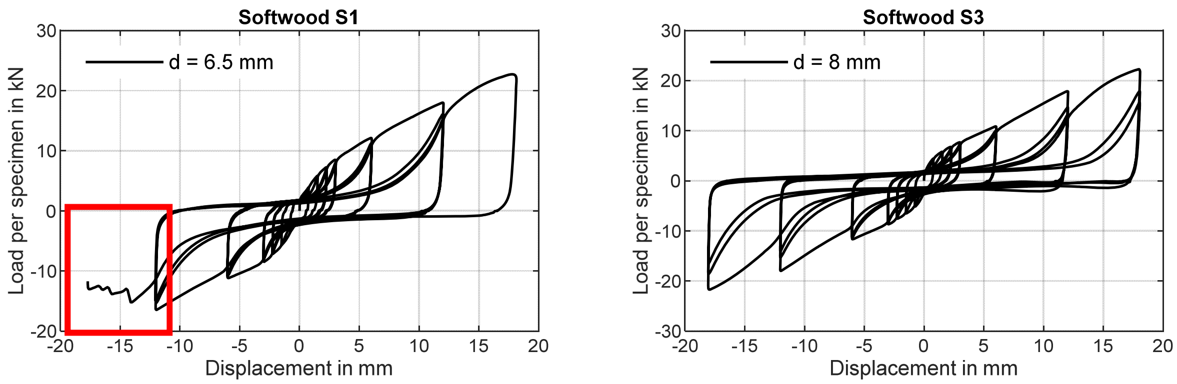

Figure 10: Load-displacement curves for tests according to EN 12512 in softwood; left side: S1-classified screw, right side: S3-classified screw

6 Conclusion and outlook

Tests were carried out on screws according to the test procedure in prEN 14592 for classification into low cycle ductility classes. The parameters testing time, diameter of the mandrel and support distance were examined and discussed for their influence on the results of tests according to prEN 14592. It was found that the support distance l_b has the greatest influence on the test results. In the standard, this parameter only has an upper limit. However, a more precise definition of the support distance is required, in particular to be able to compare test results between different test laboratories.

Furthermore, the relationship between monotonic bending tests according to EN 409 and cyclic tests according to prEN 14592 was examined. It could be shown that although there is a tendency that fasteners with ductile behaviour according to EN 409 can be classified in a high low cycle ductility class according to prEN 14592, this cannot be determined with certainty. Therefore, the tests according to prEN 14592 cannot be replaced by purely monotonic tests according to EN 409.

Finally, tests were carried out on timber-to-timber joints according to EN 12512 with screws classified in low cycle ductility classes S1 and S3, to evaluate the influence of screw classification on cyclic behaviour of joints. The tests were carried out on beech joints and softwood joints, each with one screw per shear plane. In these tests, a tendency can be seen that S3 screws lead to improved cyclic behaviour than S1 screws, especially in beech joints. However, a joint with only one screw with a very large edge and end distance was selected for the tests. Real joints, however, consist of several screws, with smaller distances. Further tests are therefore necessary to investigate the influence of the low cycle ductility classification of the screws on the cyclic behaviour of more realistic joints, including tests on steel-to-timber joints.

7 References

Casagrande D, Bezzi S, D'Arenzo G, Schwendner S, Polastri A, Seim W, Piazza M (2020) A methodology to determine the seismic low-cycle fatigue strength of timber connections *Construction and Building Materials* 231: 117026
doi: 10.1016/j.conbuildmat.2019.117026

Cervio M, Muciaccia G (2020) Low-cycle behavior of wood screws under alternating bending *European Journal of Wood and Wood Products* 78/1: 41-52
doi: 10.1007/s00107-019-01484-x

EAD 130118-01-0603 (2019) *Screws and threaded rods for use in timber constructions.* European Assessment document, EOTA, Brussels, Belgium.

EN 12512 (2001) + A1 (2005) *Timber structures – Test methods – Cyclic testing of joints made wiht mechanical fasteners.* Comité Européen de Normalisation (CEN), Brussels, Belgium.

EN 14592 (2012) *Timber structures – Dowel-type fasteners – Requirements.* Comité Européen de Normalisation (CEN), Brussels, Belgium.

prEN 14592 (2017) *Timber structures – Dowel-type fasteners – Requirements.* Comité Européen de Normalisation (CEN), Brussels, Belgium.

EN 409 (2009) *Timber structures – Test methods – Determination of the yield moment of dowel type fasteners.* Comité Européen de Normalisation (CEN), Brussels, Belgium; Belgium.

Jorissen A, Fragiacomo B (2011) General notes on ductility in timber structures. *Engineering Structures* 33: 2987-2997.
doi: 10.1016/j.engstruct.2011.07.024

Geiser B, Bergmann M, Follesa M (2021) Influence of steel properties on the ductility of doweled timber connections. *Construction and Building Materials* 266: 121152.
doi: 10.1016/j.conbuildmat.2020.121152

Hossain A, Popovski M, Tannert T (2018) Cross-laminated timber connections assembled with a combination of screws in withdrawal and screws in shear. *Engineering Structures* 168: 1-11.
doi: 10.1016/j.engstruct.2018.04.052

Izzi M, Polastri A (2019) Low cycle ductile performance of screws used in timber structures *Construction and Building Materials* 217: 416-426
doi: 10.1016/j.conbuildmat.2019.05.087

Kuck E, Sandhaas C (2022) Load-bearing behaviour of partially threaded screws in hardwood *Wood Material Science & Engineering*: 1-16
doi: 10.1080/17480272.2022.2084453

Ottenhaus L-M, Jockwer R, van Drimmelen D, Crews K (2021) Designing timber connections for ductility – A review and discussion *Construction and Building Materials* 304: 124621
doi: 10.1016/j.conbuildmat.2021.124621

DISCUSSION

The paper was presented by M Steilner

F Lam commented that this issue is also important in steel-wood-steel connections.

M Fragiacomo commented that it is nice to confirm cyclic tests versus static tests. Tests according to EN 12512 should be revised. One should consider preparing a proposal revision for EN 12512. M Steilner agreed.

Fatigue Behaviour of Notched Connections for Timber-Concrete Composite Bridges – Failure Modes and Fatigue Verification

Simon Mönch, M.Sc., Scientific Researcher

Prof. Dr.-Ing. Ulrike Kuhlmann, Head of Institute

Institute of Structural Design, University of Stuttgart, Germany

Keywords: Timber-Concrete Composite Bridges, Notched Connections, Fatigue

1 Introduction

Timber-concrete composite bridges (TCC bridges) are based on the combination of timber and concrete and thus enable economical bridge constructions. In case of typical single-span TCC bridges subjected to bending, the timber cross-section is placed in the tension area and the concrete cross-section in the compression area. This allows for the use of both materials according to their advantageous properties. However, connectors between timber and concrete with high strength and stiffness are required.

In the case of covered wooden bridges, which were built more and more often in Europe from the 13th century and onwards, a roof served as protection against the weather. Figure 1.1 (left) shows an example of a covered pedestrian bridge over the river Saane near Gümmenen (CH).

Figure 1.1. Timber bridge with roof near Gümmenen (CH), built in the 15th century (Gerold (2007)) (left) and TCC bridge across the river Agger in Lohmar with 28 m midspan, built in 2014 (Miebach et al. (2018)) (right).

For innovative TCC bridges, the concrete deck, which extends sideways over the timber cross-section, acts as structural timber protection (see Figure 1.1 (right)). Kerbs, roadway expansion joints and railings can be designed by using common constructional details of concrete bridges. For the first TCC road bridge for heavy traffic loading in Germany, built at Wippra in 2008 (Rautenstrauch & Müller (2012)), the composite action is achieved by notches with inserted steel plates with welded-on shear studs (see also Müller (2014)). To achieve the composite action for the TCC road bridge in Lohmar (see Figure 1.1 (right)) the HBV system according to Bathon & Bletz-Mühldorfer (2014) was used, where a design approval (Z-9.1-557 (2015)) also for cyclic loading exists.

Due to their high values of strength and stiffness, notches form ideal connectors between timber and concrete for TCC bridges. Figure 1.2 shows a notched connection with the relevant geometrical parameters. For road bridges, however, the verification of sufficient fatigue strength under frequently recurring traffic loads is required.

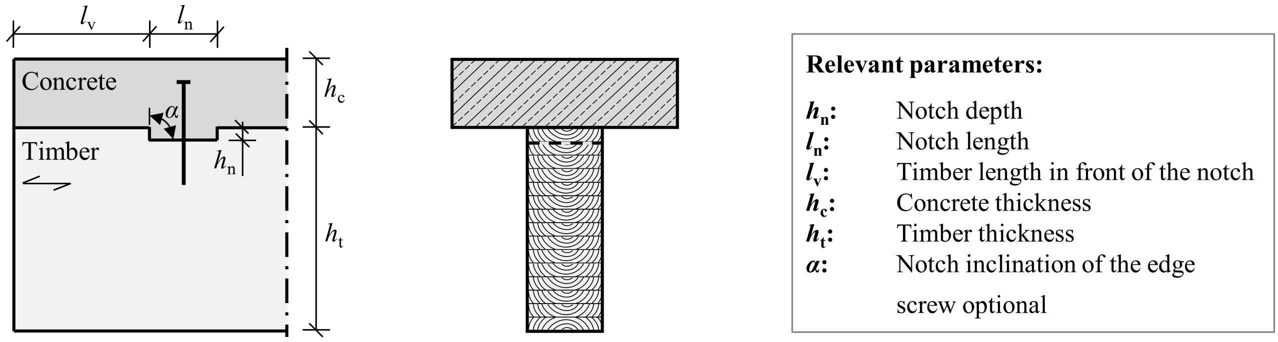

Figure 1.2. Drawing of a notched connection with geometrical parameters: side view (left) and cross section (right) (Mönch (2023)).

Within the framework of the DFG research project (Kuhlmann et al. (2021)), a total of 36 symmetrical push-out tests and 9 TCC-beam tests were conducted as cyclic tests as well as static reference tests. Part of the outcome has been reported in (Mönch & Kuhlmann (2020)). In the meantime, additional tests series have been conducted. Based on fatigue investigations on threaded screws (SPAX) with cylinder head according to ETA-12/0114 (2017) by the project partners at the Technical University of Braunschweig (Germany), also a series of tests on notched connections were conducted at the University of Stuttgart, where the timber in front of the loaded edge of the notch was reinforced by these fully threaded screws. And most important, TCC beams with notched connections were tested measuring 4 m in length with a stress ratio of R = 0.4, that resembles more the actual loading and geometry of real TCC bridges in practice.

In this contribution, first an overview on the current state of research and standardization is given including a summary of the rules of notched connections according to the Technical Specification CEN/TS 19103 (2021) “Design of Timber Structures – Structural design of timber-concrete composite structures”. Subsequently, the results of the experimental programme on the fatigue behaviour of notched connections (Kuhlmann et al. (2021)) on push-out tests together with tests on TCC beams are presented in order to derive *S-N* curves for the fatigue verification and confirm the fatigue rules given in EN 1995-2 (2004) in view of the future application in prEN 1995-1-1 (2021).

As the test results underline the importance of the different failure modes of notched connections for the static and fatigue resistance, observations on the influences for the different failure modes are discussed in principal and by a numerical study by means of a Finite Element Model (FE model) which has been validated by test results. Thereby, conclusions on the effects of the notch geometry and material properties on the stiffness, load bearing capacity and failure modes are drawn that may clarify the application of future code rules.

2 State of the art

CEN/TS 19103 (2021), a European Technical Specification (TS) for the design of timber-concrete composite structures was published in November 2021 and it will be applied as a future standard for provisional application. The aim is to subsequently transfer the CEN/TS into a part of Eurocode 5. Rules in the CEN/TS are partially based on results of extensive static TCC push-out and beam tests with notched connections, carried out by the Institute of Structural Design at the University of Stuttgart in recent years, (see Kudla (2017), Kuhlmann & Mönch (2018), Mönch & Kuhlmann (2020) and Kuhlmann et al. (2021)). Among others, results obtained from extensive investigations on notched TCC-connections by Boccadoro (2016), Simon (2008), Schönborn (2006), Grosse (2005) and Dias (2005) contributed to the current version of the CEN/TS 19103 (2021). As a result, TCC elements can safely be designed as economical, wide-span slabs for multi-storey and industrial buildings and are already used more often. In addition to values for the notch stiffness K_{ser}, the European Technical Specification CEN/TS 19103 (2021) for the design of timber-concrete composite structures also includes a verification procedure for the load-carrying capacity for all four possible failure modes in the area of the notch. Figure 2.1 summarizes the verification procedure and gives all required equations and input values.

For TCC bridges (especially subjected to road traffic) a verification of sufficient fatigue strength under frequently recurring traffic loads is required. Currently, design rules for the fatigue verification of TCC bridges and of appropriate connectors are not given in the standard.

In the current version of EN 1995-2 (2004), a fatigue verification for pure timber structures is given. The timber strength is reduced by the coefficient k_{fat} as a function of the number of load cycles. This coefficient also includes the stress ratio R, which is the ratio of the numerically smallest to the numerically largest design stress ($\sigma_{d,min}$ / $\sigma_{d,max}$) due to relevant fatigue loading. At present, it has only been partially investigated to what extent the k_{fat} verification also applies to TCC structures and, in particular, to notches as shear connectors.

Verification of the load-carrying capacity of notched connections
(According to CEN/TS 19103:2021, section 10.3.4.3.)

Verification: $F_{v,Ed} \leq F_{Rd}$

$$F_{Rd} = \min \begin{cases} f_{vcd} \cdot b_n \cdot l_n & \text{a) shear of concrete} \\ f_{cd} \cdot b_n \cdot h_n & \text{b) crushing of concrete} \\ k_{cr} \cdot f_{v,t,d} \cdot b_n \cdot l_{min} & \text{c) shear of timber} \\ f_{c,0,d} \cdot b_n \cdot h_n & \text{d) crushing of timber} \end{cases}$$

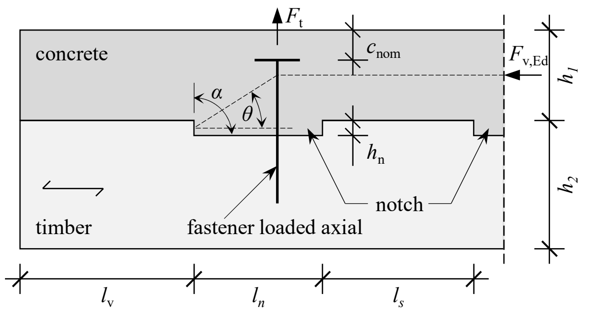

with $l_{min} = 8 \cdot h_n$ $\quad f_{vcd} = \dfrac{v \cdot f_{cd}}{(\cot\theta + \tan\theta)}$ $\quad v = 0.6 \cdot \left(1 - \dfrac{f_{ck}}{250}\right)$ $\quad \theta = \max\left\{\arctan\dfrac{0.5 \cdot (h_c + h_n)}{(l_n + l_s)}\ ;\ \arctan\dfrac{h_n}{l_n}\right\}$

where
- $F_{v,Ed}$ is the design shear force between the timber and the concrete cross-section;
- F_{Rd} is the design load-carrying capacity for the notched connections;
- f_{vcd} is the effective design shear strength of the concrete member;
- b_n is the notch width;
- l_n is the notch length;
- f_{cd} is the design compressive strength of the concrete member;
- h_n is the notch depth;
- k_{cr} is the crack factor and may be obtained from EN 1995-1-1;
- $f_{v,t,d}$ is the design shear strength of the timber member;
- l_{min} is the minimal shear length of the timber;
- $f_{c,0,d}$ is the design compression strength of the timber member parallel to the grain;
- l_v is the length of timber in front of the end notch;
- l_s is the distance between notches;
- v is a strength reduction factor for concrete crack in shear;
- θ is the angle of the concrete strut between the maximum values given in EN 1992-1-1 and the minimum value of the equation above
- f_{ck} is the characteristic compressive strength of the concrete member;
- h_c is the height of the concrete without the depth of the notch.

NOTE The design values of the timber material properties are determined using k_{mod}

Figure 2.1. Verification of the load-carrying capacity of notched connections summarized and redrawn (Mönch (2023)) according to CEN/TS 19103 (2021).

Initial tests on notches under cyclic loading were conducted by Kuhlmann & Aldi (2010). Simon (2008) also conducted a small cyclic test series. However, due to low maximum loads, some run-outs occurred (no failure appeared after more than 2 million load cycles). The tests were stopped and the results consequently could not be used to derive *S-N* curves. However, they showed tendencies to high fatigue strength in the range of low maximum loads.

3 Static and cyclic TCC push-out and beam tests

3.1 Introduction

Within the DFG research project (Kuhlmann et al. (2021)) extensive static and cyclic tests with notched connections were conducted, namely 36 push-out tests in a total of 13 test series over a period of three years. Figure 3.1 (left) shows the push-out test setup with timber shear failure in front of the loaded edge of the notch. Based on the push-out test series in single amplitude load spectrum with a stress ratio of $R = 0.4$, subsequent 9 TCC beam tests (see Figure 3.1 (right)) were performed in a total of 3 test series (one static and two cyclic series) as 4 m long 3-point bending tests in 2021.

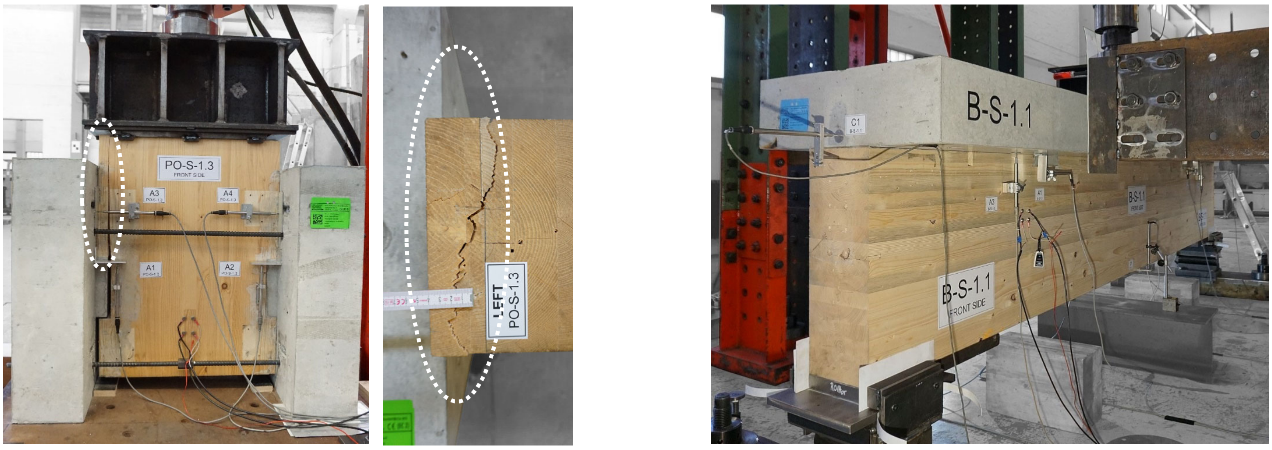

Figure 3.1. Push-out test specimen PO-S-1.3 after timber shear failure in front of the notch as front view (left), PO-S-1.3 specimen timber shear failure top view (middle) and TCC beam specimen B-S-1.1 test setup at the MPA Stuttgart (right).

In comparison to push-out tests, the geometry of TCC beam test specimens is more similar to real TCC bridge constructions. A stress ratio of $R = 0.4$ represents a typical stress ratio for TCC road bridges under traffic load in practice. Thus, the cyclic TCC beam series were tested with a stress ratio of $R = 0.4$. These investigations aimed to confirm the results obtained from the push-out test series tested with the same stress ratio R and to derive even more accurate and meaningful *S-N* curves based on the extended database.

3.2 Geometry, material and load protocol of the TCC push-out and beam tests

All test specimens were made of glued-laminated timber out of spruce of quality GL 28h according to EN 14080 (2013) and concrete of quality C 30/37 according to EN 1992-1-1 (2004). Material tests for timber and concrete were conducted parallel to the TCC push-out and beam tests and showed relatively high values for both materials. For example, the mean value of the Young's modulus of the timber lamellae used to manufacture the glulam elements for the push-out tests resulted in 14,209 N/mm² with a coefficient of variation of 18.4%. Concrete cube compression tests showed a mean value of 65.0 N/mm² with a coefficient of variation of 6.2%. For all specimens, the notch depth h_n was chosen to 40 mm, which is a common dimension in bridge construction (cf. multi-storey buildings: usually $h_n = 20$ mm). The timber length in front of the loaded edge of the notch l_v was always 400 mm (corresponding to $10 \cdot h_n$). For all conducted TCC push-out and beam tests the geometry of the notch was identical. Further information on the push-out test specimens, test series and results can be found in Mönch & Kuhlmann (2020). The measurement devices on the TCC beam test specimens are shown in Figure 3.2. In principle, a ductile failure is preferable, because deformations are recognized before fracture. However, to derive *S-N* curves from cyclic tests for the most critical situation, a clear timber shear failure was aimed at. In order to achieve a timber shear failure, the timber length in front of the loaded edge of the notch was chosen to $10 \cdot h_n$ for all TCC test series. The mean value of the carrying capacity F_{ult} determined from the static TCC beam tests of series B-S-1 was used as reference for determining the maximum loads F_{max} of the cyclic tests of series B-C-1 ($F_{max} = 0.75 \cdot F_{ult}$) and B-C-2 ($F_{max} = 0.60 \cdot F_{ult}$).

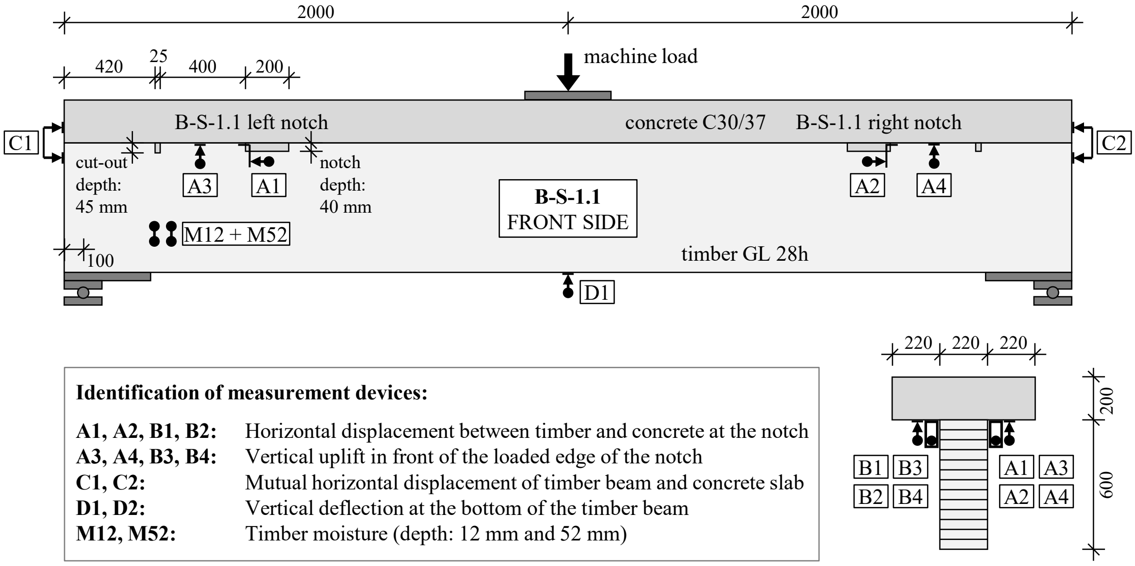

Figure 3.2. TCC beam test specimen with measurement devices: front view (top) and cross section (bottom right), dimensions in mm (Mönch (2023)).

All cyclic tests were first statically preloaded up to the mean load of the cyclic load protocol (shown in Figure 3.3 (left)). The resulting cyclic load protocol for the cyclic TCC beam test series is shown in Figure 3.3 (right).

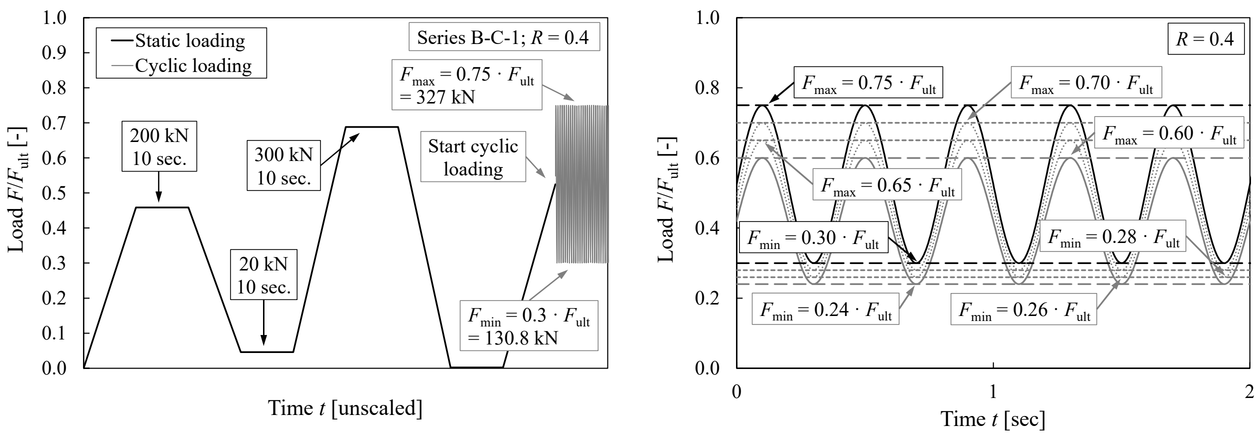

Figure 3.3. Static preloading together with the start of the cyclic loading for test series B-C-1 (left) and load protocols of the cyclic loadings of the TCC beam test series with a stress ratio of R = 0.4 (right).

3.3 Results of test series with single amplitude load spectrum on TCC push-out and beam tests and derived *S-N* curves for a stress ratio of $R = 0.1$ and $R = 0.4$

For almost all conducted 36 push-out tests, the failure occurred as brittle timber shear failure in front of the loaded edge of the notch (see Figure 3.1 (left)). However, 2 push-out tests failed due to concrete cam shear failure, in one case after initial timber compression failure. Two static push-out test series were conducted. Series PO-S-1 was fabricated without reinforcement of the timber in front of the notch, which represents the standard case for almost all conducted cyclic TCC push-out and beam test series.

For test series PO-S-2 threaded screws (SPAX) with cylinder head according to ETA-12/0114 (2017) were used to reinforce the timber in front of the notch. However, the reinforced specimens showed similar results in regard to stiffness, load bearing capacity and failure mode as well as for the number of load cycles in subsequent conducted cyclic test series. 7 out of 8 specimens of test series PO-S-1 and PO-S-2 failed due to timber shear failure. Only one specimen of series PO-S-2 failed due to concrete cam shear failure (see Figure 5.2). The second concrete cam shear failure within the 36 push-out tests occurred during the application of the static preloading protocol on a cyclic test. Nevertheless, for all TCC beam tests the failure occurred as timber shear failure. Chapter 4 will focus on different failure modes of notched connections. The number of load cycles before failure (timber shear failure in front of the loaded edge of the notch), was determined by means of cyclic tests with single amplitude load spectrum for varied maximum loads F_{max}. Subsequent *S-N* curves were derived. Figure 3.4 (left) shows *S-N* curves with a stress ratio of $R = 0.1$ obtained from own push-out tests together with similar tests conducted by Kuhlmann & Aldi (2010). Results obtained from cyclic push-out test series for a second stress ratio of $R = 0.4$, together with results obtained from TCC beam tests, are shown as *S-N* curves in Figure 3.4 (right).

The longest running push-out test specimen showed a brittle timber shear failure after 3.4 million load cycles. However, one cyclic TCC beam test within the test series with a relatively small maximum load of $F_{max} = 0{,}60 \cdot F_{ult}$ showed a long crack in the timber in front of the loaded edge of the notch after more than 6 million load cycles, but no brittle failure occurred. Considering a frequency of $F = 2.5$ Hz, this corresponds to a test period of more than 27 days. For that reason, the maximum load was first increased to $0.65 \cdot F_{ult}$ and finally to $0.70 \cdot F_{ult}$ (see Figure 3.3 (right)) until, after a total of 7.19 million load cycles, a brittle timber shear failure in front of the loaded edge of the notch occurred. This procedure also had to be applied to another test within this TCC beam test series. Both run-outs could not be used for deriving the *S-N* curves (but are shown in Figure 3.4 (right)). They confirm the tendency to high fatigue strength in the range of small maximum loads, as already observed by Simon (2008).

Figure 3.4 shows the *S-N* curves derived from the mean values (MV) of the tests for the relevant failure mode (timber shear failure) as well as the resulting statistically evaluated *S-N* curve (5% fractile values) for both investigated stress ratios *R*. For both stress ratios *R* the mean value *S-N* curves as well as the 5% fractile value *S-N* curves are located above the resulting *S-N* curves for timber in shear according to EN 1995-2 (2004), A3. Therefore, the verification of the notches in shear according to the current rules proves to be on the safe side.

Further information on the test evaluation and the statistical analysis can be found in Mönch & Kuhlmann (2020) or Mönch (2023). This also includes the test series with various amplitude load spectrum, which gives a positive indication that the interpolated mean value corresponding to the linear damage accumulation hypothesis according to the Palmgren and Miner rule (see Miner (1945)) is below the actual average of load cycles before failure in test series PO-C-6 and thus on the safe side.

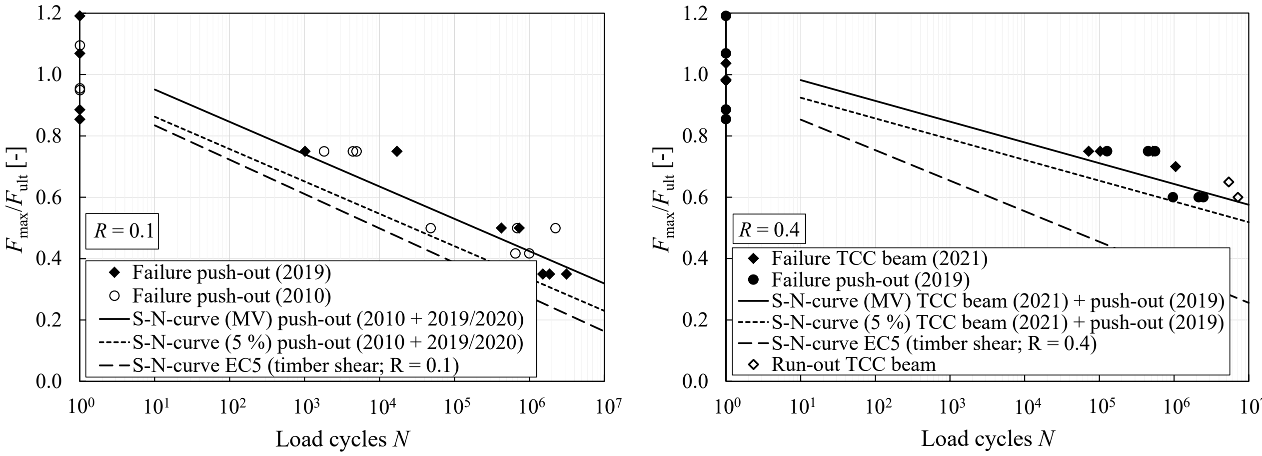

Figure 3.4. S-N curves for a stress ratio of R = 0.1 derived from push-out tests in 2019 and 2020 together with test results from Kuhlmann & Aldi (2010) (left) and S-N curves for a stress ratio of R = 0.4 derived from TCC push-out and beam tests with marked run-outs (right) (Mönch (2023)).

A closer comparison between the *S-N* curve derived from EN 1995-2 (2004), A.3 and the *S-N* curves derived from the tests with a stress ratio of $R = 0.4$ (Figure 3.4 (right)) shows that the distance is even larger than for the *S-N* curves with $R = 0.1$ shown in Figure 3.4 (left). This indicates that the test results with a stress ratio of $R = 0.4$, which is more realistic in practice for TCC bridges, show an even higher fatigue strength compared to EN 1995-2 (2004), A.3. This confirms the already standardized fatigue verification (decrease of strength by k_{fat}) given in EN 1995-2 (2004), A.3 for timber in shear also for the verification of the timber in front of the loaded edge of the notch in TCC systems. Based on the test results, it is suggested to allow the k_{fat} verification of timber on shear also for the verification of TCC notches. Within the future generation of the Eurocodes, the k_{fat} procedure will be maintained (see prEN 1995-1-1 (2021)), but based now on a more elaborated background.

4 Failure modes of notched connections

4.1 Overview on possible failure modes

In principle four different failure modes can occur in the area of a notched connection of TCC elements (see Figure 4.1). Timber can fail due to shear failure of the timber element in front of the loaded edge of the notch as well as due to compression. Concrete can fail due to concrete cam shear failure as well as due to compression.

Different types of failure modes observed in previous tests at the University of Stuttgart are shown in Figure 4.2. Within four static test series (conducted in 2017) with a constant notch dept of $h_n = 20$ mm and constant concrete cam length of $l_n = 160$ mm ($l_n = 8 \cdot h_n$), among other parameters, the timber length in front of the loaded edge of the notch l_v was varied (see Kuhlmann & Mönch (2018)). For a relative long timber length in front of the loaded edge of the notch ($l_v = 15 \cdot h_n = 300$ mm) all specimens failed due to a ductile timber compression failure (see Figure 4.2 (left)). A shorter timber length in front of the loaded edge of the notch ($l_v = 8 \cdot h_n = 160$ mm) resulted in a brittle timber shear failure.

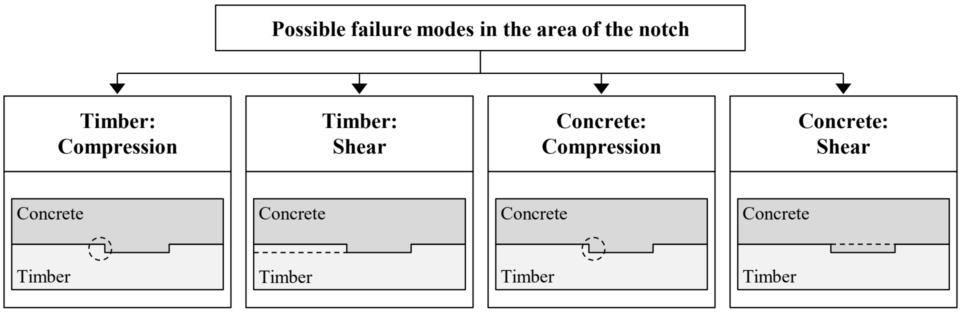

Figure 4.1. Possible failure modes in the area of the notch for timber-concrete composite structures (Mönch (2023)).

All static and cyclic TCC push-out and beam tests discussed in chapter 3 were fabricated with a notch depth of $h_n = 40$ mm, a timber length in front of the loaded edge of the notch of $l_v = 10 \cdot h_n = 400$ mm and a concrete cam length of $l_n = 200$ mm ($l_n = 5 \cdot h_n$). In total 34 out of 36 push-out tests (conducted in 2019 and 2020) as well as all 9 TCC beam tests (conducted in 2021) showed a brittle timber shear failure in front of the loaded edge of the notch (see Figure 4.2 (middle)). However, two push-out tests showed a concrete cam shear failure (see Figure 4.2 (right)), in one case after an initial timber compression failure.

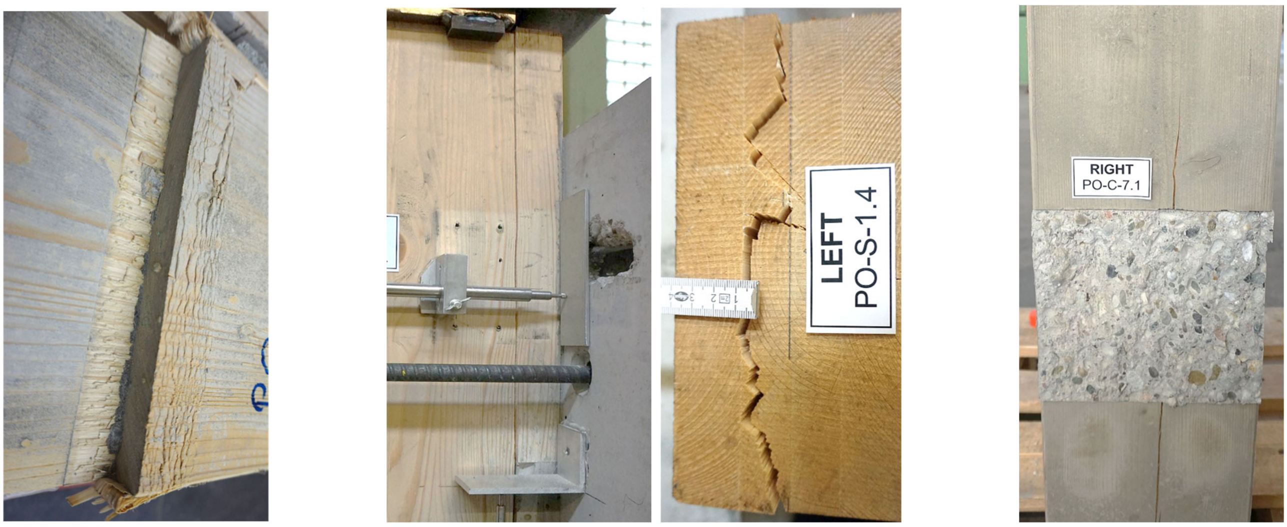

Figure 4.2. Failure modes occurred on tests conducted at the University of Stuttgart: Timber compression failure at push-out tests conducted in 2017 with $h_n = 20$ mm; $l_n = 160$ mm; $l_v = 300$ mm (left), timber shear failure (middle) and concrete shear failure (right) both at tests conducted in 2019 and 2020 with $h_n = 40$ mm; $l_n = 200$ mm; $l_v = 400$ mm.

Further studies on the influence of the ratio between the notch depth h_n and the timber length in front of the loaded edge of the notch l_v or the concrete cam length l_n will be discussed in chapter 5.

4.2 Verification procedure in the area of the notch according to Technical Specification CEN/TS 19103

For the notch geometric parameters of the tests discussed in chapter 3, a parametrical study on characteristic level, using the verification procedure according to CEN/TS 19103 (2021) was carried out, based on the values obtained from the mentioned concrete material tests and for a shear strength for timber of $f_{v,k}$ = 3,5 N/mm² and k_{cr} = 1.0. It became apparent, that the theoretical load-bearing capacities of three possible failure modes (shear of concrete, shear of timber and crushing of timber) are within a closely narrow range (≤ 4%). This indicates that the used material grades and geometric parameters could lead to both, either timber shear or concrete shear failure. This could be a reason why, in addition to the dominating timber shear failure (for 34 push-out and 9 TCC beam test specimens), for two push-out specimens a concrete shear failure occurred. Only for the theoretical failure mode "crushing of concrete" twice the load-bearing capacity were calculated. And indeed, this failure mode never occurred in any test.

As the type of failure in static as well as in fatigue tests seem to be determined by geometric and material parameter, in the following a numerical study is realised to identify possible limiting values.

5 Numerical study on the effects of the notch geometry and material properties on the stiffness, load bearing capacity and failure modes

5.1 Overview on the FE model and implemented material models

In order to carry out further studies on the influence of the notch geometry and material properties, a numerical model was developed in ANSYS workbench 19.2. Figure 5.1 shows the geometry, area of loading, supports and measuring points of displacement. The material models and fracture criteria for timber and concrete applied in the FE model are able to simulate all four possible failure modes (see Figure 4.1).

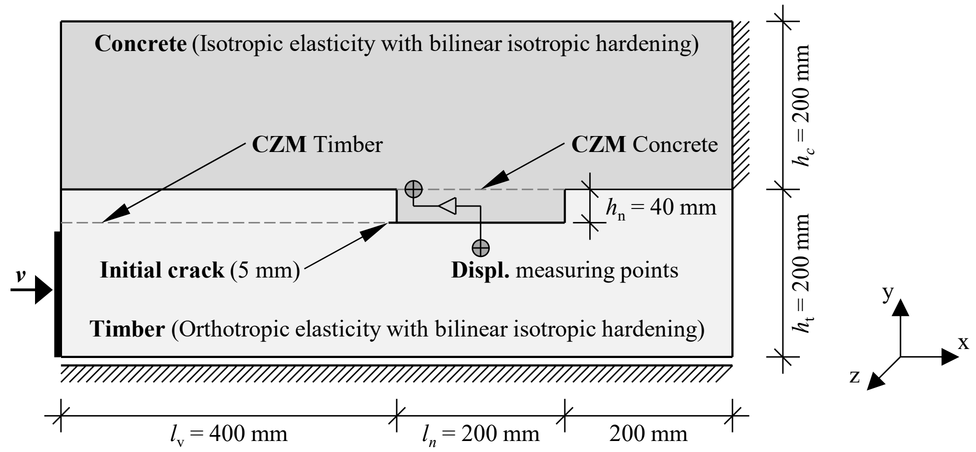

Figure 5.1. Notched connection with relevant parameters for the FE model study (Mönch (2023)).

A bilinear material model with orthotropic elasticity and isotropic hardening was implemented for the timber elements. For the concrete elements, a bilinear material model with isotropic elasticity and isotropic hardening was used. This allows for a reliable modelling of a possible compression failure of timber or concrete in the area of the loaded edge of the notch. In order to allow for a timber shear failure in front of the loaded edge of the notch or a concrete cam shear failure, fracture criteria were defined in the corresponding areas (see Figure 5.1). Therefore, bilinear Cohesive Zone Material models (CZM) according to Alfano & Crisfield (2001) were implemented. Since for the test specimens a small crack was observed at the loaded edge of the notch before loading, an initial crack (5 mm) was also considered in the FE model (see Figure 5.1). In the area of the loaded edge of the notch and in the area close to the implemented CZM zones, a mesh size of 1 mm was chosen. In the areas without significant stresses, the mesh size was chosen to 5 mm or 20 mm (see Figure 5.3). The FE model was realized by means of hexahedron elements and a mesh size in z-direction equal to the smallest mesh size of 1 mm.

5.2 Validation of the FE model and comparison to push-out tests

All material models and fracture criteria were verified on small size patch-tests. Subsequently, the FE model was calibrated against the conducted push-out tests (see chapter 3). The values used for the material models of timber and concrete were based on conducted material tests (see section 3.2). Since a timber moisture content of around 20% was measured in the area of the loaded edge of the notch during the tests, in this local area the material model for timber was modified by reducing the Young's modulus by 15% and the yield strength by 5%. For the Cohesive Zone Material (CZM) of the timber shear zone the maximum equivalent tangential contact stress was calibrated to $\tau_{max,t}$ = 4.1 N/mm². Brandner et al. (2012) showed, that the shear strength is located in this range or even higher. For the CZM of the concrete shear zone a calculation using the equations given in CEN/TS 19103 (2021) was conducted and finally calibrated to $\tau_{max,c}$ = 6.1 N/mm².

Figure 5.2 shows the load-displacement curves for push-out test series PO-S-1 (see chapter 3) together with results obtained from a similar static test series PO-S-2 in which screws as reinforcement of the timber in front of the loaded edge of the notch were arranged. Since series PO-S-2 showed similar results in regard to stiffness, load bearing capacity and failure mode, these tests were also considered for the validation of the FE model. In Figure 5.2 the load-displacement curve of the FE model is shown as "FEM, $E_{x,t}$ = 14,209 N/mm²". Since the glulam lamellae material tests showed a relatively high coefficient of variation (18.4% for the Young's modulus, see section 3.2) Figure 5.2 also shows results obtained from studies using a longitudinal timber Young's modulus of 11,500 N /mm² and 17,000 N/mm², which may represent this scatter.

Table 5.1 shows the stiffness K_{ser}, the maximum load at failure F_{max}, the measured displacement at failure and the failure mode for the push-out tests of series PO-S-1 and PO-S-2 together with results obtained by the FE model.

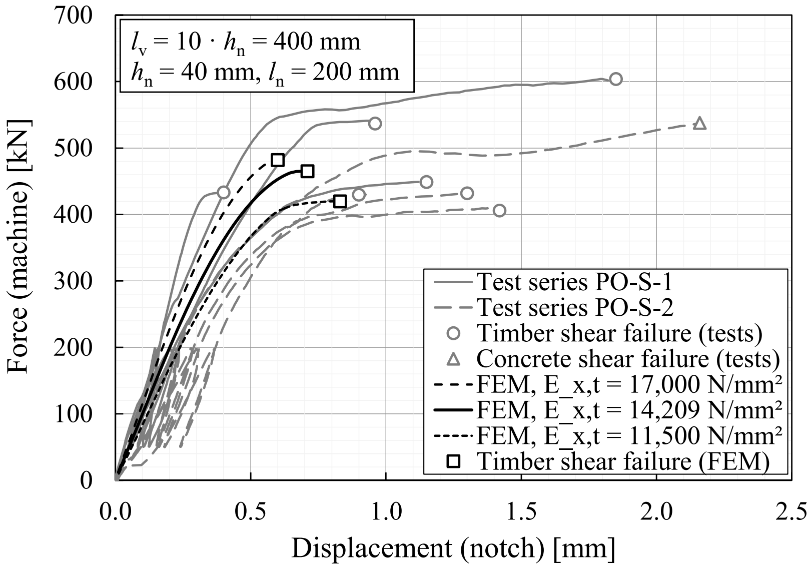

Figure 5.2. Results of static test series PO-S-1 and PO-S-2 together with the FE model with varied longitudinal timber Young's modulus ($E_{x,t}$) (Mönch (2023)).

The numerical model allows for a good estimation of the maximum load at failure F_{max} as well as the failure mode (timber shear failure with initial timber compression). However, the stiffness K_{ser} is slightly overestimated.

Table 5.1. Results of push-out test series PO-S-1 and PO-S-2 together with values of the FE model.

Series number	K_{ser} [kN/mm/m]	F_{max} [kN]	Displ. at failure [mm]	Occurred failure modes
Test series PO-S-1	2,269	507.0	1.20	Timber shear failure (for all 4 test)
Test series PO-S-2	1,608	452.4	1.21*	Timber shear failure (3 tests) Concrete shear failure (1 test)
MV test series	1,891	479.7	1.20*	Timber shear failure (7 tests) Concrete shear failure (1 test)
FE model	2,488	465.2	0.71	Timber shear failure

** For the given displacements at failure only tests with timber shear failure are considered*

5.3 Evaluation and parameter studies

Figure 5.3 (left) shows the equivalent stress distribution at a time step equivalent to 40% of the estimated maximal Load F_{max}. The displacements to calculate the stiffness K_{ser} based on the numerical study (measuring points, see Figure 5.1) were captured in the same area as in the conducted tests (see chapter 3) and calculated between 10% and 40% of F_{max}. Figure 5.3 (right) shows the deformations after the final timber shear failure occurred (see highlighted timber shear plain after failure). Both figures also show the chosen graded mesh sizes already described in section 5.3.

A parameter study was carried out to investigate the influence of a varied notch depth h_n on the maximum load F_{max}, the governing failure mode and the resulting stiffness K_{ser}. Figure 5.4 shows the load-displacement curves for a varied notch depth h_n between 15 mm and 50 mm.

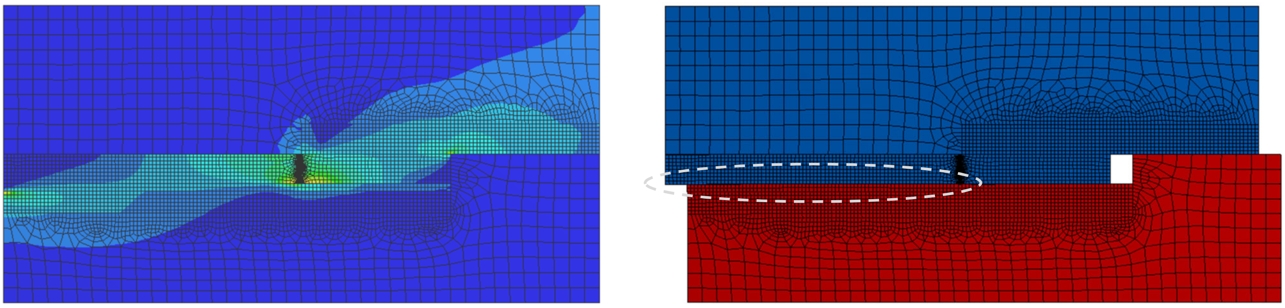

Figure 5.3. Equivalent stress distribution at time step equivalent to 40% of F_{max} (left) and deformations after final timber shear failure (for better illustration shown as 15 times superextended deformations) (right).

The curve for a geometry similar to the conducted tests discussed in chapter 3 (h_n = 40 mm) is highlighted in bold. For this study, the timber length in front of the loaded edge of the notch l_v was always adjusted to 10 times the notch depth h_n, while the concrete cam length l_n was kept constant at 200 mm.

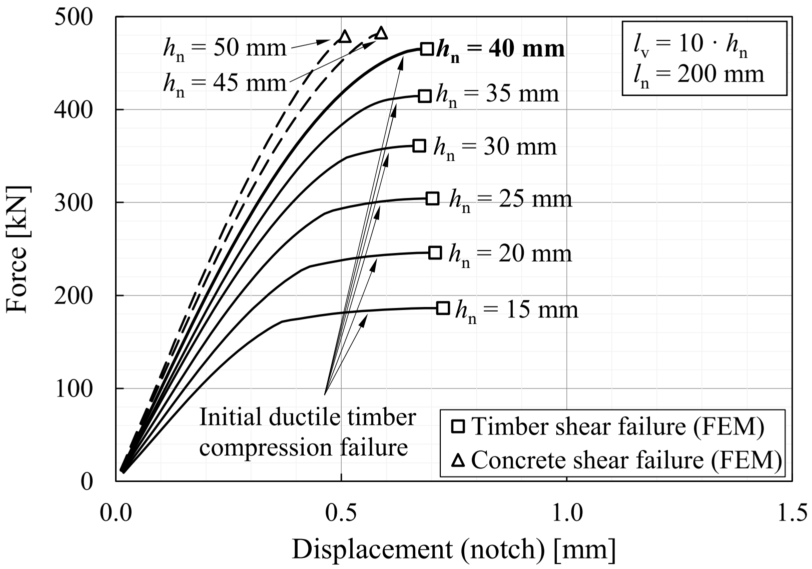

Figure 5.4. Results of a numerical study with varied notch depth h_n between 15 mm and 50 mm and marked failure modes (Mönch (2023)).

As a conclusion: for a notch depths h_n up to 40 mm the final failure always occurred as timber shear failure. For deeper notches (h_n = 45 mm and 50 mm), the final failure occurred as concrete cam shear failure. In addition, an initial ductile timber compression failure at the loaded edge of the notch could be observed with increasing ductile displacement for lower notch depths h_n.

For a ratio of the notch length l_n to the notch depth h_n between l_n / h_n = 200 mm / 15 mm = 13.3 up to a ratio of l_n / h_n = 200 mm / 40 mm = 5.0 always a timber shear failure occurred. However, for the smaller ratios (l_n / h_n = 200 mm / 45 mm = 4.4 and l_n / h_n = 200 mm / 50 mm = 4.0) always a concrete cam shear failure occurred. This confirms the assumption that the geometry chosen in the tests discussed in chapter 3 (ratio l_n / h_n = 200 mm / 40 mm = 5.0) may be located just at the borderline between timber and concrete shear failure.

Four test series conducted in 2017 (see INTER paper: Kuhlmann & Mönch (2018)) with a notch depth of h_n = 20 mm and a notch length of l_n = 160 mm were fabricated with a ratio of l_n / h_n = 160 mm / 20 mm = 8.0. Also, Kudla (2017) conducted five push-out test series in 2015. All specimens had a notch depth of h_n = 20 mm and the ratio of the test series with the shortest concrete cam length l_n resulted in l_n / h_n = 120 mm / 20 mm = 6.0. All tests failed due to timber shear- or/and timber compression failure. No concrete cam shear failure occurred for any of these tests, which support the above-mentioned observation.

Within a further parametric study, the timber length l_v in front of the loaded edge of the notch was varied between 320 mm and 600 mm, while the notch depth h_n was kept constant at 40 mm. The study was conducted for three different concrete cam lengths l_n between 180 mm and 220 mm. Table 5.2 shows the resulting final failure modes. The values and the result for a geometry similar to the conducted tests discussed in chapter 3 (l_n = 200 mm and l_v = 400 mm) are highlighted in bold. Obviously, for a slightly longer concrete cam length l_n a concrete cam shear failure does not occur, even for longer timber lengths l_v. However, for a slightly shorter concrete cam length of l_n = 180 mm a concrete cam shear failure occurs for almost all varied timber lengths in front of the loaded edge of the notch l_v.

Table 5.2. Failure modes (T = timber shear failure, C = concrete shear failure) depending on a varied timber length l_v in front of the loaded edge of the notch as well as a varied length of the concrete cam l_n (with constant notch depth of h_n = 40 mm).

Concrete cam length l_n [mm]	Timber length l_v [mm] in front of the loaded edge of the notch							
	320	360	**400**	440	480	520	560	600
180	T	C	C	C	C	C	C	C
200	T	T	**T**	C	C	C	C	C
220	T	T	T	T	T	T	T	T

The numerical study showed, that the geometry chosen in the conducted tests (see Chapter 3) with a concrete cam length l_n to notch depth h_n ratio of l_n / h_n = 200 mm / 40 mm = 5.0 may be located just at the borderline between timber and concrete shear failure. To avoid a concrete cam shear failure, a ratio of the concrete cam length l_n to the notch depth h_n of l_n / h_n > 5.0 should be realized.

6 Summary and Outlook

In this contribution experimental investigations on static and cyclic TCC push-out and beam test specimens with notched connections were discussed. The tests were conducted at the University of Stuttgart from 2019 to 2021 and showed that the fatigue verification (decrease of strength by k_{fat}) for timber in shear, already implemented in EN 1995-2 (2004), A.3, may also be applied with sufficient safety for the fatigue verification of notched connections in TCC bridges. A closer comparison of test results with a stress ratio of R = 0.1 and R = 0.4 indicates that for the test results with a stress ratio of R = 0.4, which is more realistic in practice for TCC bridges, an even higher fatigue strength compared to EN 1995-2 (2004), A.3. exists. Within the future generation of the Eurocodes, the k_{fat} procedure will be maintained, but based now on a more elaborated background. Consequently, TCC bridges with notched connections subjected to recurring traffic loads may be designed economically and safely.

Whereas most of the realised static and cyclic tests failed by the most critical timber shear failure, some other failure modes such as timber compression failure or concrete shear failure were also observed. In order to identify the geometrical and material parameters that influence the failure modes, a study was conducted analysing also the failure modes, which had occurred in various test series at the University of Stuttgart in recent years. Almost all tests showed a final timber failure (timber shear- or timber compression failure). However, very few tests failed due to concrete cam shear failure. Analytical and numerical parameter studies showed that concrete cam shear failure should be avoided by realizing a ratio of the concrete cam length l_n to the notch depth h_n of l_n / h_n > 5.0. A more brittle timber shear failure instead of a timber compression failure may be initiated by a sufficiently long concrete cam length (l_n / h_n > 5.0). CEN/TS 19103 (2021) states that the concrete cam length l_n must be at least 150 mm. Thus, in particular, the ratio l_n / h_n is relevant for greater notch depths ($h_n \geq 30$ mm). However, timber shear failure is covered by the fatigue verification as could be demonstrated within the various test series.

The use of timber as a regenerative building material significantly reduces the total weight of the bridge compared to conventional concrete constructions. A high degree of prefabrication of the timber elements also allows for a significant reduction in construction time. The shown investigations and results enable to expand the use of sustainable TCC structures not only in multi-story buildings, but also in bridge construction. The spread of knowledge and a new codification based on CEN/TS 19103 (2021) and the results of these investigations will allow for an increase in the use of sustainable timber constructions for bridges.

7 Acknowledgements

The investigations are funded by the German Research Foundation (DFG) – project number 397985109. This support is gratefully acknowledged.

We extend our appreciation to our DFG project partner, the Institute of Building Construction and Timber Structures at the Technical University of Braunschweig (Prof. Dr.-Ing. Mike Sieder and Peter Niebuhr, M.Sc.) for the good collaboration.

Moreover, we thank SPAX International GmbH & Co. KG for providing screws for the specimens and MPA Stuttgart for their great support in conducting the tests.

8 References

Alfano, G.; Crisfield, M. A. (2001): Finite element interface models for the delamination analysis of laminated composites: mechanical and computational issues. In: International Journal for Numerical Methods in Engineering 50 (2001), S. 1701-1736.

Bathon, L.; Bletz-Mühldorfer, O. (2014): Fatigue Design of Wood-Concrete-Composite System. In: World Conference on Timber Engineering, WCTE (Québec City, Canada).

Boccadoro, L. (2016): Timber-concrete composite slabs made of beech laminated veneer lumber with notched connection. ETH Zürich, Switzerland, PhD thesis, 2016.

Brandner, R.; Gatterning, W.; Schickhofer, G. (2012): Determination of shear strength of structural and glued laminated timber. In: International Council for Research and Innovation in Building and Construction, Working Commission W18 – Timber Structures, Paper No. CIB-W 18/45-12-2, Växjö, Sweden, August 2012.

CEN/TS 19103 (2021) Eurocode 5: Design of Timber Structures – Structural design of timber-concrete composite structures – Common rules and rules for buildings. Technical Specification, CEN European Committee for Standardization, Nov. 2021.

Dias, A. (2005): Mechanical Behaviour of Timber-Concrete Joints. Technical University of Delft, Netherlands, PhD thesis, 2005.

EN 1995-2 (2004): Eurocode 5: Design of timber structures – Part 2: Bridges. European Committee for Standardization (CEN), Brussels.

EN 14080 (2013): Timber structures – Glued laminated timber and glued solid timber – Requirements. European Committee for Standardization (CEN), Brussels.

EN 1992-1-1 (2004): Eurocode 2: Design of concrete structures – Part 1-1: General rules and rules for buildings. European Committee for Standardization (CEN), Brussels with corrections and amendments + AC:2010.

ETA-12/0114 (2017): European Technical Assessment ETA-12/0114 of 12/10/2017. SPAX self-tapping screws – Screws for use in timber constructions, ETA-Denmark.

prEN 1995-1-1 (2021): Eurocode 5: Design of timber structures – Common rules and rules for buildings – Part 1-1: General (Consolidated draft for informal enquiry). CEN/TC 250/SC 5 N 1488.

Gerold, M. (2007): Holzbrücken am Weg (in German). Self-published, ISBN: 978-3-00-023624-2, Karlsruhe, Germany.

Grosse, M. (2005): Zur numerischen Simulation des physikalisch nichtlinearen Kurzzeittragverhaltens von Nadelholz am Beispiel von Holz-Beton-Verbundkonstruktionen (in German). Institute of Structural Engineering, Bauhaus-Universität Weimar, PhD thesis, 2005.

Kudla, K. (2017): Kerven als Verbindungsmittel für Holz-Beton-Verbundstraßenbrücken (in German). Institute of Structural Design, University of Stuttgart, Mitteilung No. 2017-02, PhD thesis, 2017.

Kuhlmann, U.; Aldi, P. (2010): Fatigue strength of timber-concrete-composite bridges: Determination of a S-N-line for the grooved connection and the „X-connector“. In: World Conference on Timber Engineering, WCTE, Trento, Italy, 20-24. June 2010.

Kuhlmann, U.; Mönch, S. (2018): Design Parameters of Notched Connections for TCC Structures as Part of Eurocode 5. In: International Network on Timber Engineering Research, Paper No. 51-7-8, Tallinn, Estonia, 13.-16. August 2018.

Kuhlmann U., Sieder M., Mönch S., Niebuhr P. (2021): Ermüdungsverhalten von Kerven und selbstbohrenden Vollgewindeschrauben für die Anwendung als Verbindungsmittel bei Holz-Beton-Verbundträgern (Fatigue behaviour of notches and self-drilling screws for the application as connectors in TCC beams), (in German). University of Stuttgart, Institute of Structural Design and Technical University Braunschweig, Institute of Building Construction and Timber Structures, DFG-Research-Project, Project number: 397985109, 2018-2021.

Miebach, F.; Niewerth, D.; Wolf, F; Laraki, J. (2018): Holz-Beton-Verbundbrücken – Erfahrungen und Perspektiven (in German). Qualitätsgem. Holzbrückenbau e.V.

Miner A. (1945): Cumulative Damage in Fatigue. In: Journal of Applied Mechanics 12 (1945), pp. 159-164.

Mönch, S. (2023): Performance of Notched Connections under Static and Cyclic Loading for Timber-Concrete Composite Systems. Institute of Structural Design, University of Stuttgart, PhD thesis, in preparation.

Mönch, S.; Kuhlmann, U. (2020): Fatigue Behaviour of Notched Connections for Timber-Concrete-Composite Bridges. In: International Network on Timber Engineering Research, Paper No. 53-7-7, Online-meeting, 17.-19. August 2020.

Müller, J. (2014): Trag- und Verformungsverhalten spezieller Verbundelemente für Holz-Beton-Verbundstraßenbrücken unter Kurzzeit-, Ermüdungs- und Langzeitbeanspruchung (in German), Institut für Konstruktiven Ingenieurbau, Bauhaus-Universität Weimar, PhD thesis, 2014.

Rautenstrauch, K.; Müller, J. (2012): Trag-, Verformungs- und Ermüdungsverhalten spezieller Verbundelemente für Holz-Beton-Verbundstraßenbrücken (in German). Forschungsvorhaben AiF/iVTH 16266 BR, Bauhaus Universität Weimar, Report.

Schönborn, F. (2006): Holz-Beton-Fertigteilelemente (in German). Leopold-Franzens-Universität Innsbruck, PhD thesis, 2006.

Simon, A. (2008): Analyse zum Trag- und Verformungsverhalten von Straßenbrücken in Holz-Beton-Verbundbauweise (in German). Institute of Structural Engineering, Bauhaus-Universität Weimar, PhD thesis, 2008.

Z-9.1-557 (2015): Allgemeine bauaufsichtliche Zulassung Z-9.1-557: Holz-Beton-Verbundsystem mit eingeklebten HBV-Schubverbindern (in German). Deutsches Institut für Bautechnik, Berlin.

DISCUSSION

The paper was presented by S Mönch

A Frangi and S Mönch discussed that the safety margins are not consistent. The TCC bridge is only a small part of a larger project. Furthermore, the length of the notch relative to the geometry of concrete can control the failure. A Frangi said material properties of concrete are optimistic (compression and tension strength of 65 MPa and 6 MPa, respectively). S Mönch said test results show even higher values.

M Fragiacomo asked if k_{fat} *for notch can be adjusted and whether there is any clear proposal for change. S Mönch said adjustment of* k_{fat} *for the notch can be considered as a possibility. The fatigue work is aimed at verification only.*

H Blass asked about the screw producer. He commented that the inclined compression strut will result in tension force. This is already an issue for the static case as the screw head is embedded in the concrete but is worst for the fatigue case. He said that the failure mode of screws should be considered. U Kuhlmann said partners tested fatigue of screws.

H Kreuzinger discussed the availability of only a small test database including fatigue. He asked, if k_{mod} *and* k_{fat} *should be used in combination.*

A Frangi commented that in Switzerland there are TCC applications in commercial building showing good results even without the screw.

Design of moment loaded steel contact connections at the narrow face and side face of CLT panels

Michael Schweigler, Thomas K. Bader, Stephen Sabaa

Department of Building Technology, Linnaeus University, Växjö, Sweden

Keywords: cross-laminated timber , moment loading , contact connections , engineering design

1 Introduction

Load transfer between structural elements in cross-laminated timber (CLT) structures is either established through shear, embedment and withdrawal loading of dowel-type fasteners, or by contact pressure in the narrow face or the side face of CLT panels. Load transfer through contact forces is especially important in platform-type building systems, where the load takedown essentially relies on transferring loads in compression perpendicular to the grain of CLT. Gravity loads, like the self-weight of the structure, cause uniformly distributed compressive forces in the connection's contact surface. Possible asymmetries in the geometry and the load dispersion, e.g. at the connection of a CLT floor to an outer wall, are usually neglected in the design. However, additional lateral forces on structural elements, like wind loads on walls or live loads on the floor, can lead to bending moments in the contact surfaces of the connection, and thus, to a non-uniform distribution of compressive forces perpendicular to the grain of the CLT element's side face. In addition, the narrow face of CLT elements can be exposed to non-uniform compressive loading because of a contact connection transferring moment loading. The connection of balcony railings, mounted on the side face or the narrow face of CLT panels is a prime example for this type of load transfer mechanism with compression perpendicular to the grain in CLT and tension and shear in mechanical fasteners. These forces are caused by a combination of bending moment/shear force as a result of lateral forces acting on the railing.

Research, design rules and testing standards almost exclusively focused on loading situations with uniformly distributed compressive forces in solid timber, glued-laminated timber (glulam) and CLT. Among others, *Thelandersson and Mårtensson* (1997) and

Blaß and Görlacher (2004) studied uniform loading of solid timber perpendicular to the grain, and proposed design concepts. Uniform compression perpendicular to the grain loading situations at the CLT side face were e.g. investigated by *Serrano and Enquist* (2010), *Brandner* (2018), and *Akter et al.* (2021). In these studies, among other influence parameters, different load configurations as regards deck-layer orientation and positions of the load introduction plate were investigated. Less investigated is the load introduction via compressive forces on the CLT narrow side. *Flaig et al.* (2019) studied the compressive strength and stiffness of end grain contact connections in glulam and CLT. Connections with end grain to end grain, and steel plate to end grain contact were recently investigated in *Totsuka et al.* (2022). In this study, a damage zone below steel loading plates that influences the compressive properties of glulam parallel to the grain was defined.

Moment transfer in steel-to-CLT contact connections was however hardly investigated. *Schweigler et al.* (2021) presented an experimental-numerical study for contact connections at the side face of CLT. The current design concepts (e.g. Eurocode 5 (*EN 1995-1-1*, 2004), Swedish CLT handbook (*The CLT handbook*, 2019)), and test standards exclusively focus on uniform loading cases, and load introduction perpendicular to the grain of timber and to the CLT side face, respectively. No information for non-uniform loading, and for load introduction at the CLT narrow face can be found in design standards/handbooks and testing standards. Thus, the purpose of this paper is to facilitate the understanding of CLT contact connections under moment loading, with the aim to propose rules for the design and testing of such connections. The objectives of this paper are to

- present experimental results, by means of stiffness and strength parameters of steel-to-CLT contact connections at the side face and the narrow face of CLT, exposed to moment loading,
- propose engineering design concepts for CLT contact connections under moment loading, and to
- propose test evaluation methods for CLT loaded by non-uniform distributed compressive forces.

2 Experimental work

Steel-to-CLT connections under predominant moment loading, mounted on the side face (*Schweigler et al.*, 2021) and on the narrow face of CLT, were investigated. The goal was to determine moment-rotation curves from the experiments, which gave access to the connection's stiffness and strength. In addition, measurement data allowed to calculate the contact surface of the steel plate with the CLT as a function of the loading.

2.1 Test setups and series

2.1.1 Side face connection

For the side face connection (index ”s”), a balcony railing, consisting of a steel post and a steel base-plate connected to the CLT-surface via two M16 steel rods, was chosen (Figure 1(a)). The steel post was loaded in its transverse direction at a distance of 400 mm from the base-plate, which caused a bending moment, M, and a shear force, V, in the interface between base-plate and CLT-surface. The bending moment was transferred to the CLT by a pair of forces, i.e., by a tension force in the steel rods and contact stresses between steel base-plate and CLT. The steel rods were anchored at a steel plate on the back side of the CLT-specimen, transferring the force via contact pressure. The applied shear force was transmitted through the shear capacity of the steel rods and by embedment pressure into the CLT-specimen. The CLT-specimen itself was held in place by clamps on the upper and lower side of the specimen (see Figure 1(a)).

Two different positions of the steel plate on the CLT panel (edge and center), with moment loading in two different orientations with respect to the grain orientation of the deck-layer were studied. Thus, in total four different load configurations were tested, namely for loading in center position along the fiber (AL_S) and across the fiber (AC_S), and for loading in edge position along the fiber (AL_C_S) and across the fiber (AC_C_S), see Figure 1(a). In addition, different CLT-plate thicknesses and CLT-layups were investigated, which are however not presented in this study. More information about the experiments can be found in *Schweigler et al.* (2021).

In total, 29 tests were carried-out on a 3-layered spruce CLT-plate with a symmetric layup of 30-40-30 mm and a total thickness of 100 mm. The average CLT-plate density, ρ_{CLT}, amounted to 477 kg/m^3 (CV=2.9 %, n=29). In addition, compression tests on prismatic specimens (*EN 16351*, 2015) on the same CLT material were carried-out to gain the reference compression strength perpendicular grain $f_{c,90}$ (mean ρ_{CLT}=502 kg/m^3, CV=8.0 %, n=9). Prior to testing, CLT-specimens were stored at 20 °C and 65 % relative humidity, resulting in an average moisture content (*MC*) of 11.89 % (CV=7.6 %, n=11), determined by the kiln-drying method. Specimens for AL_S and AC_S tests had a length (along the grain) of 453 mm, and a width (across the grain) of 389 mm. For AL_C_S and AC_C_S tests, the larger dimension was equal to the corresponding AL_S and AC_S specimens, while the smaller dimension was equal to the width of the steel base-plate, b_{base}=165 mm. The length of the base-plate amounted to, l_{base}=150 mm (=dimension along the load application direction).

2.1.2 Narrow face connection

For the narrow face connection (index ”n”), a similar test setup as for the side face connection was used. However, the steel base-plate, welded to the steel post at its length side, was connected to the narrow face of the CLT-panel (Figure 1(b)). The connection to

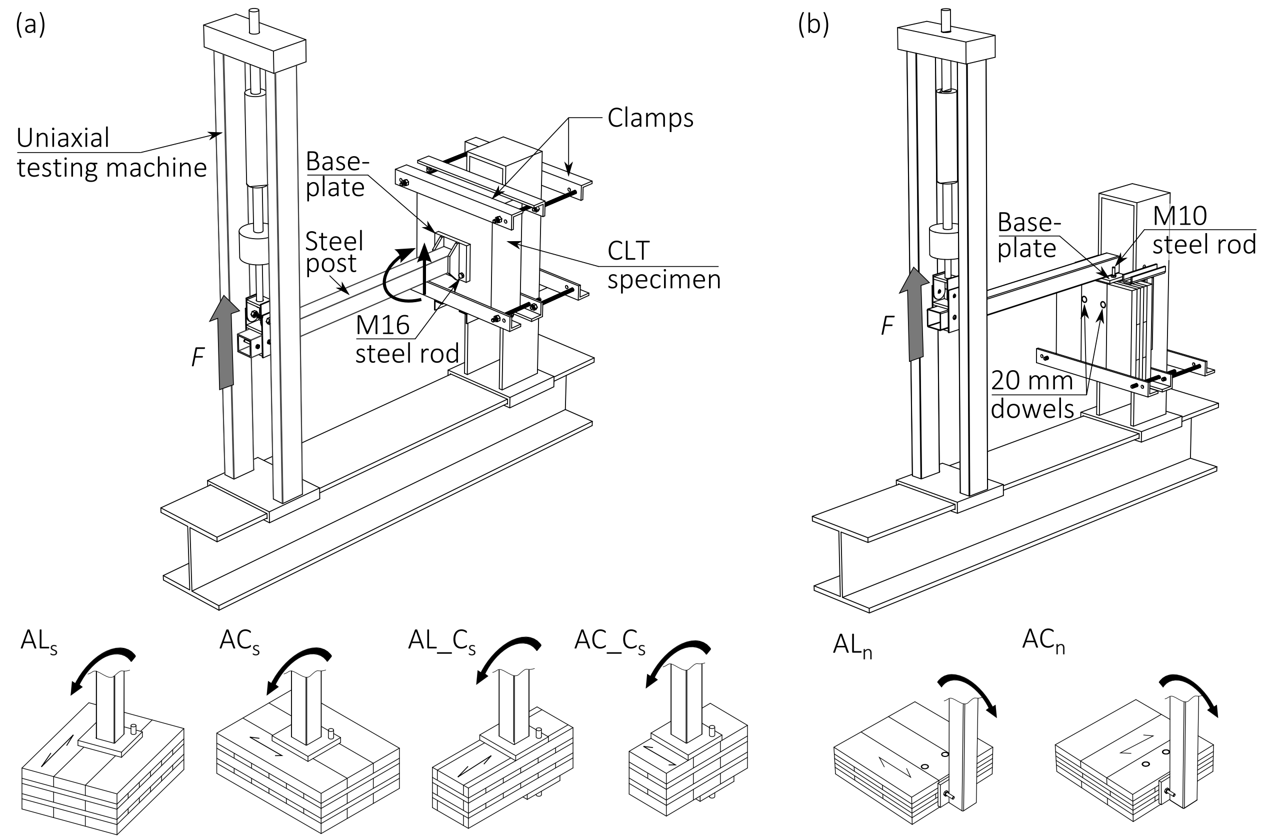

Figure 1. (a) Side face connections, and (b) Narrow face connections - experimental setup, and load configurations regarding deck-layer orientation and base-plate position.

the CLT was established by two M10 steel rods, anchored into two steel dowels with a diameter d=20 mm, inserted from the side face of the CLT panel (Figure 1(b)). Moment loading was established in the same way as for the side face connection, by applying a transverse load at the steel post at a distance of 800 mm from the M10 steel rods. As for the side face connection, a pair of forces, i.e., a tensile force in the steel dowel anchored steel rods and a compression force through contact pressure transfers the moment load to the CLT.

Two different positions of the connection with respect to the deck-layer orientation of the CLT-panel and the two narrow faces, i.e., deck-layer along (AL_n) and across (AC_n) the fiber were tested. In both cases, the steel base plate was centered on the CLT narrow face (Figure 1(b)). The influence of different parameters, i.e., the dowel edge distance, CLT-plate thickness, mounting torque, dowel borehole play and steel base-plate height on the connection behavior was investigated. Herein, only the reference series is presented.

For the reference series, 18 tests were carried-out on a 5-layered spruce CLT-plate with a symmetric layup of 30-20-20-20-30 mm, giving a total thickness of 120 mm. An edge distance of the steel dowel of 80 mm (=4d), mounting torque of 35 Nm, dowel borehole play of 2 mm was chosen. The average CLT-plate density, ρ_{CLT}, amounted to 474 kg/m^3 (CV=2.0%, n=18). Prior to testing, CLT-specimens were stored at 20 °C and 65 % relative humidity, resulting in an average moisture content (MC) of 12.24 % (CV=5.4 %, n=125), determined by the kiln-drying method. For all specimens equal specimen length and width of 400 mm was used. For the steel base plate the length amount to l_{base}=100 mm (=dimension along the load application direction), while the width was equal to b_{base}=150 mm. The 20 mm steel dowels were made of a declared steel grade S355 with a tensile strength, f_u=675 MPa, in the corresponding product specifications.

2.2 Measurement technique and test evaluation

For both connection types, side and narrow face, the reaction force, F, as a result of the applied transverse displacement loading of the balcony railing, was directly measured by the load cell of the testing machine (see Figure 1). The relative displacement of the connection between the balcony-railing base-plate and CLT-surface was measured by four displacement transducers (potentiometers) fixed at the corners of the steel base-plate (Figure 2).

The base-plate rotation, φ, which is equal to the rotation of the balcony railing steel post at its base, was then calculated by

$$\varphi = \tan^{-1} \frac{|\ u_{t,pot}\ | + |\ u_{c,pot}\ |}{l_{ref}}, \tag{1}$$

with $u_{t,pot}$ and $u_{c,pot}$ as the average relative displacement of the potentiometers at the tension and compression side of the base-plate, respectively (Figure 2). l_{ref} is the distance between the potentiometers at the compression and tension side (side face: l_{ref}=142 mm, narrow face: l_{ref}=122 mm).

The moment acting on the connection, M, was defined as the measured force at the loading point, F, times the distance between the loading point and contact connection, e (side face: e=400 mm, narrow face: e=800 mm). Calculation of φ and M for every load increment gives access to the nonlinear moment-rotation curve of the connection. Based thereon, stiffness and moment capacity properties were determined following the definitions of *EN 16351* (2015) and *EN 408* (2010), respectively, regarding compression perpendicular to the grain loading.

In *EN 408* (2010), compression strength is defined as the intersection of the 1 %-offset of the line connecting stress points on the stress-strain curve at 10 % and 40 % of the strength. The stiffness is defined as the inclination of this line. In this study, non-uniform loading of CLT is investigated, which requires adaption of the evaluation procedure. Since a moment-rotation curve is used instead of a stress-strain curve, the strength is expressed as moment capacity, $M_{0.01}$, and the stiffness as moment per rotation, C_{elast}. The stiffness C_{elast}, is defined as the inclination of the line connecting the points on the moment-rotation curve at 10 % and 40 % of the moment capacity (for narrow face connection). For the side face connection the first stress point was increased to 15 % compared to *EN 408* (2010), since it was seen that the point at 10 % of the moment

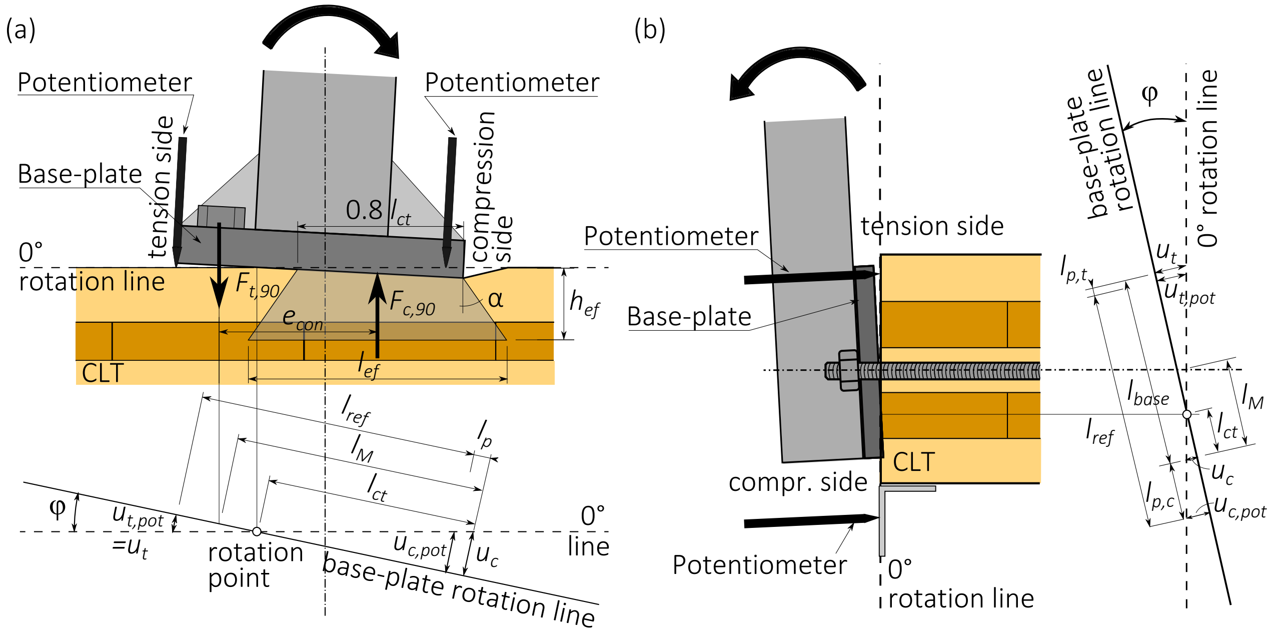

Figure 2. Definition of connection geometry, and experimentally measured displacements and calculated base plate rotation, for (a) side face connection, and (b) narrow face connection.

capacity included still deformations from the initial softer, nonlinear part of the curve. For the connection capacity, $M_{0.01}$, the offset-method, as in *EN 408* (2010), was applied. However, an absolute offset of 1 mm displacement below the compression edge of the balcony railing base-plate (u_c) was used instead of the relative strain offset defined for uniform compressive loading in *EN 408* (2010).

In addition, the relative contact length, l_{ct}/l_M, in the interface between steel base plate an CLT was calculated as

$$\frac{l_{ct}}{l_M} = \frac{u_c}{\tan\varphi \cdot l_M}, \tag{2}$$

with l_{ct} as the contact length between steel base-plate and CLT, and l_M as the distance between the compression edge and the fastener (steel rods) axis taking the tensile forces of the connection (side face: l_M=128 mm, narrow face: l_M=50 mm).

2.3 Test results

The relative contact length, l_{ct}/l_M, illustrated in Figure 3(a) (side face) and Figure 7(a) (narrow face), gives important information for the development of engineering design concepts of moment loaded contact connections in CLT. The change in l_{ct}/l_M with φ reflects the change in stiffness properties of the anchoring tensile element (steel rods), and the contact compression element (CLT in compression) with increasing load. For side face connections AL_s and AC_s similar trends were seen, with a relative contact length of about 75 to 80 % when $M_{0.01}$ is reached. For the narrow face connections AL_n and AC_n, the contact length for AC_n (about 60%) was almost double as compared to AL_n (about 30%), which reflects the different stiffness properties in the contact zone. Interestingly,

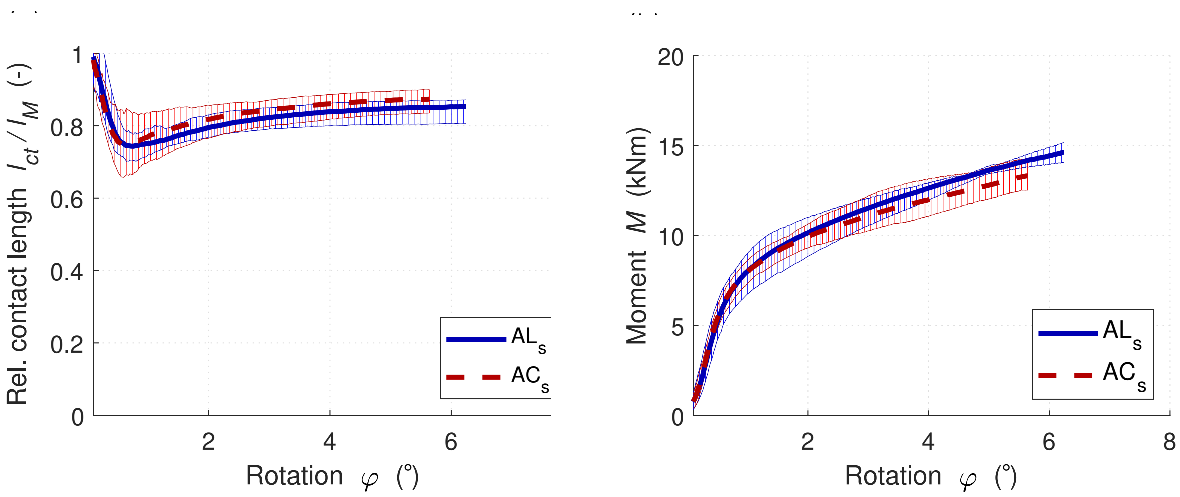

Figure 3. Side face connection, (a) relative contact length, l_{ct}/l_M, plotted over the connection rotation, φ,and (b) moment-rotation curves for experiments from load configuration AL_s and AC_s (mean values).

AL_n and AC_n showed an almost constant contact length for a relative rotation higher than ca. 1.5°.

Moment-rotation curves in Figure 3(b) (side face) and Figure 7(b) (narrow face) show a pronounced ductile behavior, with substantial increasing moment capacity after yielding of the connection. The corresponding moment capacities, $M_{0.01}$, and connection stiffnesses, C_{elast}, are given in Table 1.

For the side face connections, almost the same moment-rotation behavior, i.e., similar moment capacities and stiffnesses, were found for the AL_s, AC_s, and AL_C_s load configurations. Significantly smaller moment capacity (-15%) and stiffness (-20%) was seen for the AC_C_s configuration (Table 1). Thus, test results for the side face indicated an almost deck-layer orientation independent connection behavior, as long as the wood fibers of the deck-layers are continuing over the edge of the steel base-plate, and thus allow for load-distribution in fiber direction and development of the rope effect. Compression tests on prismatic specimens resulted in an average compression strength, $f_{c,90}$, of 3.91 MPa (CV=7.7%, n=9). For more details the reader is referred to *Schweigler et al.* (2021).

Narrow face connections showed considerably lower capacities and strengths as compared to the side face connections (Table 1). This can be explained by different connection geometries used in the experiments, resulting in a smaller distance between compression edge and anchoring steel rods, and thus by a smaller lever arm for the moment transfer. For moment loading along the deck-layer orientation (AL_n) an about 65 % higher strength, and an about 70 % higher stiffness as compared to loading across the deck-layer (AC_n) was found. This can be explained by load transfer in grain direction at the steel base-plate compression edge for AL_n, instead of load transfer perpendicular to the grain at the compression edge, as it was the case for AC_n.

Table 1. Experimentally determined moment capacity, $M_{0.01}$ (kNm) and stiffness, C_{elast} (kNm/°), including the coefficient of variation, CV (%), and number of experiments , n, for side face connections AL_S, AL_C_S, AC_S and AC_C_S, and for narrow face connections AL_n and AC_n .

	AL_S		AL_C_S		AC_S		AC_C_S		AL_n		AC_n	
	mean	CV	mean	CV	mean	CV	mean	CV	mean	CV	mean	CV
$M_{0.01}$	9.02	10.5	8.62	12.1	8.66	6.1	7.64	12.1	3.39	4.4	2.06	8.7
C_{elast}	12.53	10.2	12.06	16.9	13.32	9.2	9.56	13.0	3.70	22.6	2.25	26.1
n	6		6		8		9		10		8	

3 Engineering design concepts

3.1 Side face connection

For moment loaded contact connections at the side face of CLT panels, the design concept of the EC5-draft (*prEN 1995-1-1*, 2022) for uniform compression loading perpendicular to the grain could be applied, reading as

$$\sigma_{c,90,d} = \frac{F_{c,90,d}}{b_{c,90} \cdot l_{c,90}} \leq k_{mat} \cdot k_{c,90,CLT} \cdot k_{mod} \cdot \frac{f_{c,90,k}}{\gamma_M}, \tag{3}$$

with k_{mat} as the factor accounting for the material behaviour and degree of compressive deformation perpendicular to grain, and $f_{c,90,k}$ as the characteristic compressive strength perpendicular to grain of CLT. This concept is based on a stress dispersion model as proposed by *Brandner* (2018) for the application on CLT. The stress dispersion below the contact area is considered by the so-called stress spreading factor, $k_{c,90,CLT}$, defined as

$$k_{c,90,CLT} = \sqrt{\frac{b_{ef} \cdot l_{ef}}{b_{c,90} \cdot l_{c,90}}} \leq 4, \tag{4}$$

with $b_{c,90}$ and $l_{c,90}$ as the dimensions of the loaded contact area across and along the grain, respectively. Corresponding effective spreading dimensions b_{ef} and l_{ef}, can be calculated for uniform compressive loading by assuming a spreading gradient, α, equal to 35°, and an effective depth, h_{ef}, which depends on the loading situation and CLT-plate thickness, t_{CLT}. However, for non-uniform loading situations (NuCL) in moment loaded contact connections, it was seen that h_{ef} seems to be independent from t_{CLT}, see also *Schweigler et al.* (2021). Thus, it is proposed to define h_{ef} for NuCL by absolute values, which can be calculated based on the experimental findings presented in Section 2.3, by inserting Equation (4) into Equation (3), and solving them for h_{ef}.

To define h_{ef} for NuCL, mean values from experiments were used. Hence, in Equation (3), the partial safety factor, γ_M, and the modification factor, k_{mod}, were assumed to be equal to 1. For $f_{c,90,k}$ the mean value of the strength from corresponding compression tests on CLT prisms was taken (see Section 2.3). Case A according to EC5-draft was assumed, resulting in k_{mat} equal to 1.4. The contact width, $b_{c,90}$, was assumed equal to the base plate with, b_{base}, of 150 mm. Fully-plastic compression stress distribution is assumed in the contact area. Thus, the contact length, $l_{c,90}$, was defined based on the relative contact length, l_{ct}/l_M, equal to 0.75 (Figure 3(a)), which was further reduced to 80 % in order to consider the nonlinear stress distribution in the contact area, resulting in $l_{c,90}$ equal to 77 mm. With this assumption, the lever arm, e_{con}, and thus the compressive load, $F_{c,90,d}$ can be calculated as the ratio of the moment bearing capacity, $M_{0.01}$, and e_{con}. For AL_S and AC_S, a stress spread in the CLT at all four sides of the steel plate is assumed, while for AL_C_S and AC_C_S a stress spread is only in moment loading direction possible. For all cases, α equal to 35° is assumed. Based on this assumptions, effective depths, h_{ef}, were calculated and are summarized in Table 2.

Table 2. Proposed effective depths, h_{ef}, for moment contact connections on the CLT side face. h_{ef} in (mm) is calculated based on mean values.

	AL_S	AL_C_S	AC_S	AC_C_S
h_{ef}	34.5	50.7	30.0	28.0

For the ultimate limit state (ULS) verification, it is proposed to use the design concept of the EC5-draft (*prEN 1995-1-1*, 2022), for uniform compression loading perpendicular to the grain as given in Equation (3). For k_{mat}, k_{mod}, γ_m, and $f_{c,90,k}$ values from EC5 and corresponding product standards shall be taken. The contact area width, $b_{c,90}$, shall be assumed equal to the steel plate width, while for $l_{c,90}$ it is proposed to use $0.8 \cdot l_{ct}$, with $l_{ct} = 0.75 \cdot l_M$ (see Figure 2(a) and 3(a)). For connections in the center of CLT-plates, a stress spread in the CLT at all four sides of the steel plate is assumed, while for connections close to the edge(s) of CLT-plates, no stress spread is considered at the corresponding steel plate side(s). As a simplification on the conservative side, it is proposed to use an effective depth, h_{ef} of 25 mm for all connections, independent from their position on the CLT-plate. h_{ef} was determined based on mean values from experiments in this study. In *Schweigler et al.* (2022), it was shown for uniform compression loading perpendicular to the grain that the determination of design parameters based on characteristic values from experiments yielded similar results as the determination based on mean values.

3.2 Narrow face

Moment loaded contact connections at the narrow face of CLT panels are characterized by a load transfer in the layered structure of CLT, resulting in alternating contact stiffness properties of 0° and 90° layers in the interface between CLT and steel plate. This fact makes it more challenging in defining engineering design concepts for this connection type. In this study, a nonlinear spring model (Section 3.2.1) is proposed, which can be used to predict the connection capacity and stiffness, and serves as basis for simplified engineering models (Section 3.2.2), suitable for engineering design.

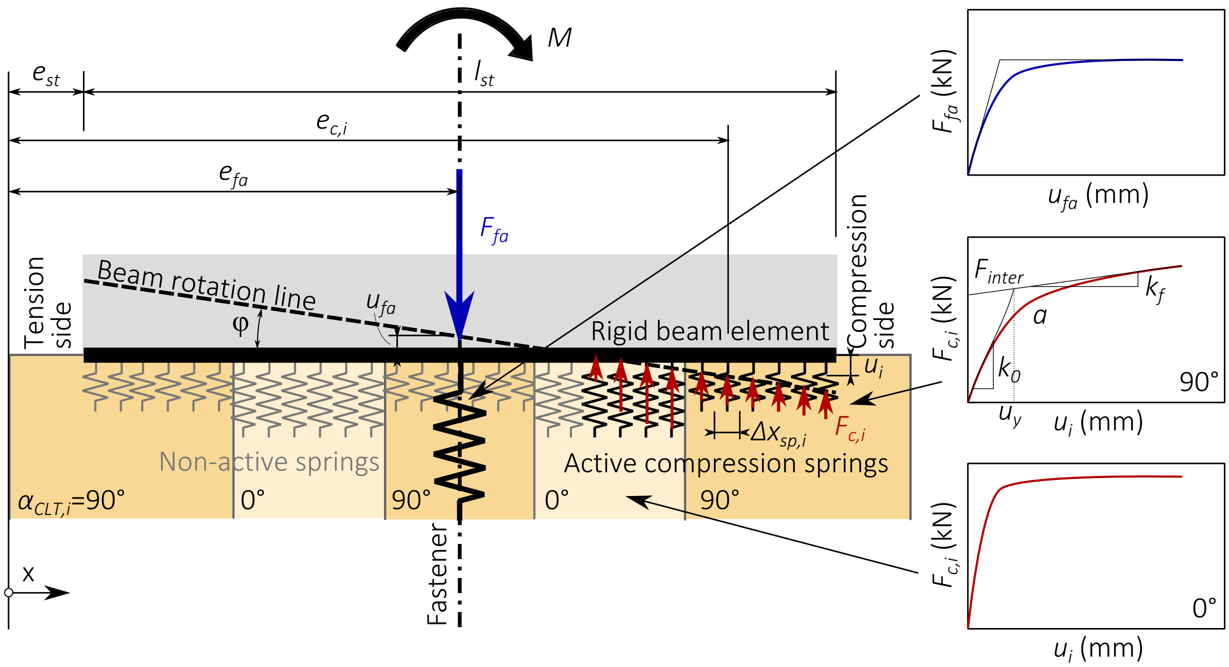

Figure 4. Nonlinear spring model for narrow face connections, illustrating the model components and nonlinear spring definitions.

3.2.1 Nonlinear spring model

The nonlinear spring model applies nonlinear springs for the contact elements (CLT) and the anchoring tension element (fastener), supporting the steel plate of the contact connection, which is assumed to act as rigid beam element (Figure 4). Thus, a rigid beam-on-nonlinear foundation model (rBOF) is applied.

For the nonlinear behavior, the mathematical function from Richard/Abbott was used as proposed in *Schweigler et al.* (2018), giving the reaction force, F, as a function of the applied displacement, u, as

$$F(u) = \frac{(k_0 - k_f) \cdot u}{\left[1 + \left[\frac{(k_0 - k_f) \cdot u}{F_{inter}}\right]^{a}\right]^{\frac{1}{a}}} + k_f \cdot u, \tag{5}$$

where k_0 and k_f are the gradient of the initial and end tangent of the curve, representing the elastic and plastic stiffness, respectively. The parameter F_{inter} describes the intersection between the end tangent and the y-axis (force axis), and thus represents the strength of the contact element. Furthermore, the parameter a controls the transition characteristic between the initial and end tangent of the curve (see exemplary Figure 4).

For the fastener, acting as anchoring tensile element in the moment loaded contact connection, the parameter k_0 could be chosen as the elastic stiffness, K_{ser} for laterally loaded connections, or K_{ax} for axially loaded connections, from corresponding design standards or product declarations. The parameter F_{inter} can be defined by the capacity of the fastener, while k_f can consider a possible strength hardening of the fastener after yielding, if applicable for the fastener type. For the compression contact elements, representing the CLT layers, a segmentation of the single CLT-layers in stripes of e.g. $\Delta x_{sp,i}$ =1 mm is done. Thus, each spring element is related to a certain contact area, $A_{sp,i}$, defined by $\Delta x_{sp,i}$ times the steel plate width b_{st}. The capacity of the contact spring (F_{inter}) can then be defined by the product of $A_{sp,i}$ and the corresponding material strength, i.e. $f_{c,0}$ (0° layers) or $f_{c,90}$ (90° layers). For the latter, $k_{c,90}$ for structural timber with the possibility of load dispersion could be consider as multiplying factor. The elastic stiffness, k_0, can be defined as quotient of the yield capacity, F_y, and yield displacement, u_y. With k_f, strength hardening of the material can be considered. Parameters u_y and k_f can be taken from literature. The parameters F_y and F_{inter} are equal for k_f =0.

The geometry of the connection needs to be defined by the position of the CLT-layers, $x_{CLT,i}$, and their corresponding grain orientations, $\alpha_{CLT,i}$. Furthermore, the steel plate length, l_{st}, and its position from the CLT edge, e_{st}, as well as the position of the fastener, e_{fa}, from the CLT edge need to be specified.

The reaction moment, M, for a certain applied rotation, φ, can be calculated by moment equilibrium as

$$M = F_{fa}(u_{fa}) \cdot e_{fa} - \sum_{i=0}^{n} F_{c,i}(u_i) \cdot e_{c,i}, \tag{6}$$

with $F_{fa}(u_{fa})$ as the tensile force in the fastener at the fastener displacement u_{fa}, resulting from the applied rotation φ. Furthermore, $F_{c,i}(u_i)$ stands for the compression force at compression spring element i, which depends on the applied displacement u_i and the corresponding layer orientation (0° or 90°), defined by the position of the spring element e_i. In this study, tension forces are defined positive, while compression forces are defined negative.

Simultaneously force equilibrium of the components needs to be satisfied, giving

$$F_{fa}(u_{fa}) = -\sum_{i=0}^{n} F_{c,i}(u_i). \tag{7}$$

To satisfy the criterion in Equation (7), an iterative procedure is applied. The rotation, φ, is adjusted until force equilibrium is reached. Thereafter, the reaction moment, M, can be calculated according the Equation (6).

To get access to the moment-rotation curve of the contact connection, the procedure defined by Equations (6) and (7) is repeated j-times for a desired set of rotations, φ_j. Consequently, connection capacity, $M_{0.01}$, and stiffness, C_{elast}, as well as the relative contact length, l_{ct}/l_M, can be calculated from the moment-rotation curve as defined in Section 2.2. Pre-tensioning of the connection, as a result of e.g. mounting the fastener with a certain mounting torque (see Section 2.1.2), can be considered by applying an initial pre-tensioning force at the fastener.

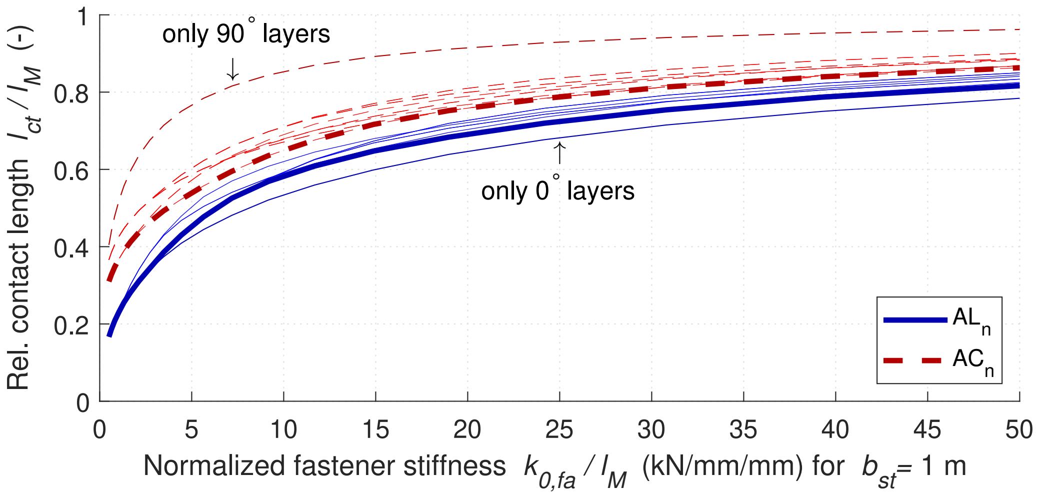

Figure 5. Design chart for moment loaded contact connection at the narrow face. Relative contact length, l_{ct}/l_M plotted over the normalized fastener stiffness, $k_{0,fa}/l_M$ defined per 1 m steel plate width. Based on connection properties given in Section 3.2.1.

Definition of design charts

The nonlinear spring model can be used to create design charts suitable for engineering design. The connection behavior depends on the mechanical properties of the CLT and the anchoring fastener as well as on the connection geometry. For a certain type of CLT, e.g. commercial spruce CLT, the relative contact length, l_{ct}/l_M, can be defined by the ratio of fastener stiffness, $k_{0,fa}$, and the distance between fastener and compression edge, l_M, for a connection width, b_{st}, of 1 m . The relative contact length can then be used in a limit state approach to calculate the connection moment capacity (see Section 3.2.2).

To create a design chart the nonlinear spring model is applied for a set of fastener stiffness, $k_{0,fa}$, in combination with a set of commercial CLT-layups. This allows to define lower limit curves for loading along (AL_n) and across (AC_n) the grain of the CLT deck-layer. An example of a design chart can be seen in Figure 5.

Model input parameters

To create the design chart in Figure 5, eleven different CLT-layups with different combinations of 20, 30, and 40 mm layers were used. In addition, the extreme case of uniaxial fiber orientation in all layers are included (indicated by: only 0° layers, only 90° layers in Figure 5). All layups were loaded along and across the grain of the deck-layer, amounting to in total 24 cases. The design chart is defined for a connection with a steel plate width, b_{st}, of 1 m. The position of the steel plate from the CLT-plate edge, e_{st}, was chosen to 10 mm. No pre-tensioning of the connection was considered.

The parameters defining the nonlinear springs for the CLT-layers are given in Table 3. For the 0° layers, data from experiments on end grain contact joints in glulam (Table 4 and Figure 7 in *Flaig et al.* (2019)) were used. Values for 90° layers are based on compression perpendicular to the grain test on prismatic CLT-specimens in *Schweigler et al.* (2022). In addition, F_{inter} is multiplied with $k_{c,90}$ equal to 1.8.

Table 3. Parameters for the nonlinear spring definitions of the CLT-layers used for creation of the design chart and verification example. Parameters are based on mean values.

	F_{inter} (MPa)	u_y (mm)	k_f (MPa/mm)	a (-)
0° layer	34.5	0.4	0	5
90° layer	3.56	1.0	0.1	3

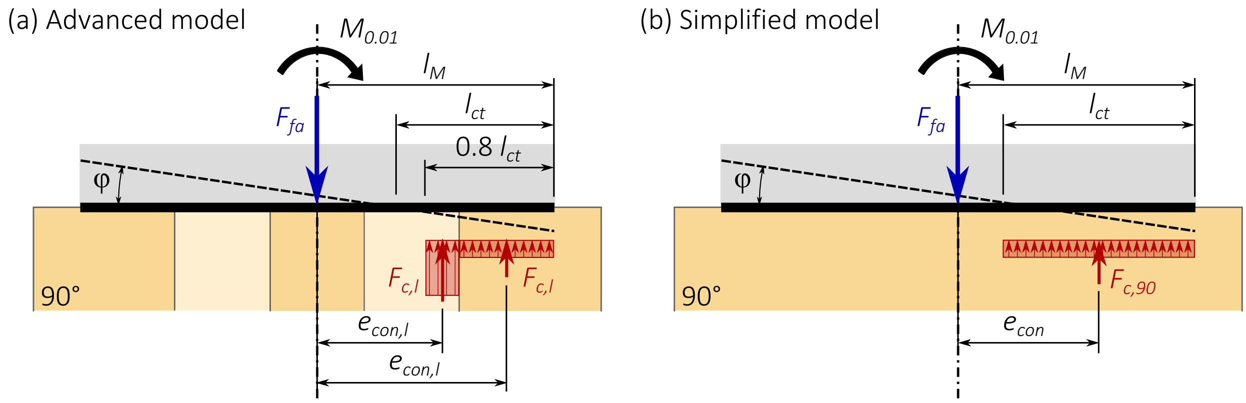

Figure 6. Engineering models for narrow face connections, (a) advanced model, considering the CLT-layup, and (b) simplified model, assuming only 90° layers.

For the verification example, the fastener parameters are calculated according to EC5 (*EN 1995-1-1*, 2004), based on the fastener properties given in Section 2.1.2. The fastener capacity is defined by the minimum of the yield strength of the steel rods and the shear capacity of the steel dowels, which amounts to F_{inter}=88.4 kN. The elastic fastener stiffness is defined by the elastic stiffness of the steel rod in combination with the elastic stiffness of the dowel (defined by K_{ser}), resulting in k_0=59.0 kN/mm. A plastic stiffness of k_f=0 kN/mm, and the parameter a=3 is assumed. The connection geometry and CLT-layup is defined as given in Section 2.1.2.

3.2.2 Engineering models

For engineering design, an advanced and a simplified engineering model, based on the design chart as described in Section 3.2.1 is proposed. The design chart given in Figure 5 can be used for commercial spruce CLT (C24), with common lay-ups. Furthermore, elastic fastener behavior needs to be ensured. Otherwise, a reduced elasto-plastic stiffness of the fastener needs to be considered in the design chart.

In the advanced engineering design model, the alternating CLT layers (0° and 90° layers), the loading direction with respect to the deck-layer's grain orientation (along or across), and the relative contact length from the design chart (Figure 5) are considered. Together with the steel plate position, e_{st}, and the position of the fastener, e_{fa}, on the CLT narrow face, contact forces, $F_{c,l}$, of each layer, l, in the steel plate-CLT interface can be calculated (see Figure 6(a)). For determination of the relative contact length, l_{ct}/l_M, it is proposed to use the AL_n-limit curve and AC_n-limit curve from Figure 5 (bold lines), respectively.

Full plasticity for $F_{c,l}$ is assumed in each layer. However, it is proposed to reduce the contact length to 80 % of l_{ct}, in order to consider the nonlinear stress distribution in the contact area. The contact forces, $F_{c,l}$, correspond to the layer's grain orientation (0° and 90°). Thus, the design connection capacity, $M_{0.01,d}$, can be calculated as

$$M_{0.01,d} = \sum_{l=1}^{n} F_{c,l,d} \cdot e_{con,l}, \tag{8}$$

with

$$\begin{aligned} F_{c,l,d} &= k_{mod} \cdot \frac{f_{c,0,k}}{\gamma_m} \cdot t_l \cdot b_{st} && \text{for} \quad 0° \text{ layers, and} \\ F_{c,l,d} &= k_{mod} \cdot k_{mat} \cdot k_{c,90} \cdot \frac{f_{c,90,k}}{\gamma_m} \cdot t_l \cdot b_{st} && \text{for} \quad 90° \text{ layers.} \end{aligned} \tag{9}$$

The lever arm, $e_{con,l}$, defines the distance between the anchoring fastener and the position of the resultant contact force, $F_{c,l,d}$, in each layer, l (see Figure 6(a)). Characteristic compressive strength values, $f_{c,0,k}$, and $f_{c,90,k}$, modification factor, k_{mod}, modification factor for material and compressive deformations, k_{mat}, and stress spreading factor, $k_{c,90}$, can be taken from corresponding design and product standards for structural timber (e.g. *EN 338* (2016) and *prEN 1995-1-1* (2022)). Parameters t_l and b_{st} correspond to the layer thickness and steel plate width, respectively.

Furthermore, the moment connection capacity, $M_{0.01,d}$, needs to be limited by the anchoring fastener capacity, $F_{fa,d}$, by definition of the following inequality

$$F_{fa,d} \geq \sum_{l=1}^{n} F_{c,l,d}. \tag{10}$$

If the inequality in Equation (10) is not fulfilled, the anchoring fastener capacity, $F_{fa,d}$, either needs to be increased, or the connection capacity $M_{0.01,d}$ needs to be limited by reducing $F_{c,l,d}$ to fulfill Equation (10).

In the simplified engineering design model, only the connection geometry, i.e. fastener position and steel plate dimensions, but not the CLT-layup and loading direction, is considered (Figure 6(b)). The simplified approach is especially suitable for early stage design, at which the CLT-layup might be unknown. As a lower limit approach, it is assumed that all layers are loaded perpendicular to the grain (90°).

The relative contact length, l_{ct}/l_M, can be assumed as

$$\begin{aligned} \frac{l_{ct}}{l_M} &= 0.8 && \text{for} \quad \frac{k_{0,fa}}{l_M} \geq 10\,\text{kN/mm/mm, and} \\ \frac{l_{ct}}{l_M} &= 0.4 + \frac{0.8-0.4}{10} \cdot \frac{k_{0,fa}}{l_M} && \text{for} \quad \frac{k_{0,fa}}{l_M} < 10\,\text{kN/mm/mm,} \end{aligned} \tag{11}$$

where $k_{0,fa}/l_M$ is defined per 1 m steel plate width.

The design connection capacity, $M_{0.01,d}$, can be calculated assuming full-plasticity of the timber in the connection interface as

$$M_{0.01,d} = F_{c,90,d} \cdot e_{con}, \tag{12}$$

with

$$F_{c,90,d} = k_{mod} \cdot k_{mat} \cdot k_{c,90} \cdot \frac{f_{c,90,k}}{\gamma_m} \cdot \frac{l_{ct}}{l_M} \cdot l_M \cdot b_{st}, \quad \text{and} \quad e_{con} = l_M - \frac{1}{2}\frac{l_{ct}}{l_M} \cdot l_M. \tag{13}$$

In addition, the connection capacity, $M_{0.01,d}$, needs to be limited by the anchoring fastener capacity, $F_{fa,d}$, as defined in Equation (10). Properties, $f_{c,90,k}$, k_{mod}, k_{mat} and $k_{c,90}$, can be taken from corresponding design and product standards for structural timber (e.g. *EN 338* (2016) and *prEN 1995-1-1* (2022)). For connections at the narrow face of CLT, no reduction of the contact area due to a nonlinear compression stress distribution in the contact area is proposed. Connections close to the intersection of two narrow faces of the CLT-panel shall be avoided. Otherwise, it is proposed to use a $k_{c,90}$ equal 1, since no load distribution effects can be activated.

3.2.3 Model validation

Experimental results, presented in Section 2.3, are compared with results from the nonlinear spring model (Section 3.2.1) and the engineering models (Section 3.2.2). The model input parameters can be found in Section 3.2.1 and 2.1.2, respectively. For the engineering models, the design chart given in Figure 5 is applied. The validation is carried-out based on mean values from experiments and models, by using k_{mod} and γ_m equal to 1. For the nonlinear spring model, the case without (circular markers in Figure 7) and with pre-tensioning (squared markers in Figure 7) of the anchoring fastener is investigated. The pre-tensioning force is assumed to 20 kN. The normalized fastener stiffness, $k_{0,fa}/l_M$, amounts to 7.87 kN/mm/mm for loading across the grain of the deck-layer (AC_n). For loading along the grain (AL_n), the fastener starts to yield before the connection capacity, $M_{0.01}$, is reached, and thus a reduced stiffness of 3.41 kN/mm/mm is used.

Relative contact length-rotation curves in Figure 7(a), show a good agreement between experimental findings and predictions from the nonlinear spring model for larger rotations, φ. Considering a pre-tensioning force at the fastener allows for appropriate prediction of the the relative contact length even for small connection rotations. Comparison of the relative contact length, l_{ct}/l_M, at connection capacity (Table 4), shows an overestimation of the experiments of less than 28 % by the nonlinear models. This indicates, that the fastener stiffness might be overestimated, or the CLT contact stiffness might be underestimated in the spring models. Contact lengths, estimated from the design chart, used in the advanced engineering model show a good agreement with the

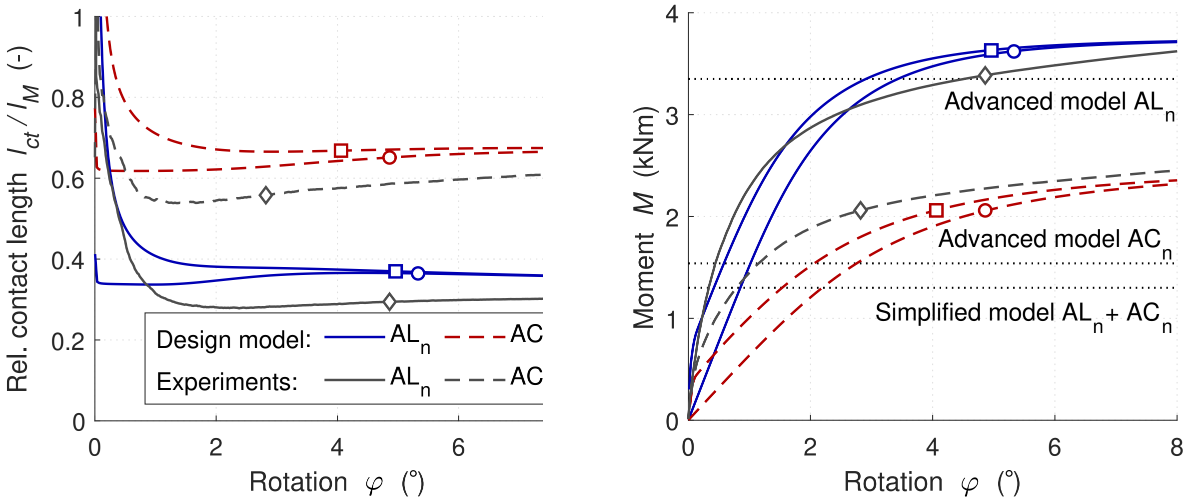

Figure 7. Narrow face connection, (a) relative contact length, l_{ct}/l_M, plotted over the connection rotation, φ, and (b) moment-rotation curves, for load configuration AL_n (continues lines) and AC_n (dashed lines). Experiments (gray lines, diamond marker), the nonlinear spring model (colored lines, without pre-tensioning: circular marker, and with pre-tensioning: squared marker), and engineering design models are based on mean values. Markers indicate the rotation at connection capacity.

Table 4. Comparison of moment capacity, $M_{0.01}$ (kNm), stiffness, C_{elast} (kNm/°), and relative contact length at connection capacity, l_{ct}/l_M (-) from experiments and design models, for AL_n and AC_n connections (mean values).

		Experiments	Nonlinear model		Engineering model	
			no pretension	with pret.	advanced	simplified
AL_n	$M_{0.01}$	3.39	3.62 (+7 %)	3.63 (+7 %)	3.35 (-1 %)	1.30 (-62 %)
	C_{elast}	3.70	1.51 (-59 %)	1.78 (-52 %)	-	-
	l_{ct}/l_M	0.29	0.36 (+24 %)	0.37 (+28 %)	-	-
AC_n	$M_{0.01}$	2.06	2.06 ($\pm$0 %)	2.06 ($\pm$0 %)	1.54 (-25 %)	1.30 (-7 %)
	C_{elast}	2.25	0.63 (-72 %)	0.76 (-66 %)	-	-
	l_{ct}/l_M	0.56	0.65 (+16 %)	0.67 (+20 %)	-	-

experimental findings. A considerable larger contact length needs to be used for the simplified engineering models, since pure loading perpendicular to the grain is assumed.

Moment-rotation curves in Figure 7(b), reflect the good correlation of the contact lengths from experiments and model predictions. However, simulations from the nonlinear spring model without pre-tensioning of the fastener show a pronounced underestimation (up to 72 %) of the elastic connection stiffness, C_{elast}, which can be minimized when considering a pre-tension force (Table 4). The connection capacity, $M_{0.01}$, from the nonlinear spring model and the advanced engineering model show only minor differences (less than 7 %) to the experimental findings, except for loading across the grain (AC_n) modeled by the advance engineering model (-25 %). This can be explained by the conservative approach of reducing the contact length to 80 % of the estimated length from the design chart. Furthermore, it can be seen that the limit state approach in the simplified engineering model considerably underestimates the connection capacity (up to 62 %).

4 Conclusions

From experiments on moment loaded contact connections at the CLT side face it was shown, that the deck-layer orientation has almost no influence on the connection capacity and stiffness, as long as a certain distance of the loading plate from the CLT-panel edge is ensured. For connections on the CLT narrow face, a distinct difference between loading along and across the deck-layer fiber orientation was seen. Loading along the grain gave about 65 % higher capacity, and about 70 % higher connection stiffness.

For test evaluation of moment loaded contact connections in CLT, it is proposed to adapted the current method for uniform compressive loading perpendicular to the grain in *EN 408* (2010). For strength and stiffness determination, an absolute offset of 1 mm displacement at the compression edge of the connection steel base-plate, instead of the the 1 % strain-offset from *EN 408* (2010) could be used. For measurement of the connection rotation, it is proposed to use a minimum of four displacement transducer, mounted at the steel plate edge, measuring relatively to the CLT surface. The same test procedure and evaluation method can be used for side face and narrow face connections.

The engineering design concept proposed in *prEN 1995-1-1* (2022) for uniform loading perpendicular to the grain can be used for side face connections, by assuming a contact length of 75 % of the distance between anchoring fastener and compression edge in combination with an absolute effective depth, h_{ef}, independent from the CLT-plate thickness. It is proposed to use h_{ef} equal to 25 mm for all loading positions on the CLT side face. For narrow face connections, an advanced and a simplified engineering design model for the connection capacity, considering the stiffness of the anchoring fastener loaded in tension is proposed. Design charts, as proposed in this contribution, can be used to define the contact length of the connection and based thereon the connection capacity. In the advanced model, accurate prediction of the connection capacity is possible by considering the CLT layup, while in the simplified model, connection capacity is substantially underestimated, since a limit state approach by considering only 90° layers is used. Strength and stiffness properties for the connection components can be taken from current design and product standards.

The proposed rigid beam-on-nonlinear foundation model showed promising results in predicting connection capacity and contact length. It can not only be used for preparation of design tables for engineering design, but also for prediction of connection capacity and stiffness in software supported design.

5 Acknowledgments

This research work was funded by the Knowledge Foundation through the project ‘Improving the competitive advantage of CLT-based building systems through engineering design and reduced carbon footprint’ (20190026).

6 References

Akter, S. T., M. Schweigler, E. Serrano, and T. K. Bader (2021). “A Numerical Study of the Stiffness and Strength of Cross-Laminated Timber Wall-to-Floor Connections under Compression Perpendicular to the Grain.” In: *Buildings* 11.10, p. 442.

Blaß, H. J. and R. Görlacher (2004). “Compression perpendicular to the grain.” In: *Proceedings of the 8th World Conference on Timber Engineering (WCTE), Lahti, Finland*. Vol. 2. 435-440.

Brandner, R. (2018). “Cross laminated timber (CLT) in compression perpendicular to plane: Testing, properties, design and recommendations for harmonizing design provisions for structural timber products.” In: *Engineering Structures* 171, pp. 944–960.

EN 16351 (2015). “Timber structures- Cross laminated timber- Requirements.” In: *CEN, Brussels, Belgium*.

EN 408 (2010). “Structural Timber and Glued Laminated Timber. Determination of Some Physical and Mechanical Properties.” In: *CEN, Brussels, Belgium*.

EN 1995-1-1 (2004). “Eurocode 5: Design of timber structures – Part 1-1: General – Common rules and rules for buildings.” In: *CEN, Brussels, Belgium*.

EN 338 (2016). “Structural timber–strength classes.” In: *CEN, Brussels, Belgium*.

Flaig, M., T. Schmidt, and H. J. Blass (2019). “Compressive strength and stiffness of end grain contact joints in glulam and CLT.” In: *Proceedings of the International Network on Timber Engineering Research (INTER)*. Vol. 52. Tacoma USA, pp. 313–325.

prEN 1995-1-1 (2022). “Eurocode 5: Design of timber structures – Common rules and rules for buildings – Part 1-1: General.” In: *CEN/TC 250/SC 5 N1616 (2022-09-12)*.

Schweigler, M., S. T. Akter, N. Ncube, S. Sabaa, T. Johansson, and T. K. Bader (2021). “Non-uniform compressive loading of cross-laminated timber (CLT) perpendicular to the grain.” In: World Conference on Timber Engineering (WCTE), Santiago, Chile.

Schweigler, M., S. T. Akter, S. Sabaa, and T. K. Bader (2022). “An experimental study of the stiffness and strength of cross-laminated timber wall-to-floor connections under compression perpendicular to the grain.” In: *Engineering Structures* 271, p. 114850.

Schweigler, M., T. K. Bader, G. Hochreiner, and R. Lemaitre (2018). “Parameterization equations for the nonlinear connection slip applied to the anisotropic embedment behavior of wood.” In: *Composites Part B: Engineering* 142, pp. 142–158.

Serrano, E. and B. Enquist (2010). “Compression strength perpendicular to grain in cross-laminated timber (CLT).” In: *Proceedings of World Conference on Timber Engineering (WCTE), Riva del Garda, Italy*.

The CLT handbook (2019). “CLT structures- facts and planning.” In: *Svenskt Trä*.

Thelandersson, S. and A. Mårtensson (1997). “Design principles for timber in compression perpendicular to grain.” In: *CIB-W18, 30-20-1, Vancouver, Canada*.

Totsuka, M., R. Jockwer, H. Kawahara, K. Aoki, and M. Inayama (2022). “Experimental study of compressive properties parallel to grain of glulam.” In: *Journal of Wood Science* 68.1, pp. 1–14.

DISCUSSION

The paper was presented by y M Schweigler

S Winter was critical about the robustness of CLT in balconies and said reasonable protection to ensure durability is needed. M Schweigler agreed but replied the method is general and can be applied to other applications. S Winter commented that distribution of stresses perpendicular to grain will change. M Schweigler said this will be researched in future.

E Serrano asked about the stiffness of the steel plate and said that different products will have different stiffness of the lever arm. M Schweigler replied that the steel plate was considered stiff.

G Doudak questioned if the model fits when the plate is not centred and thicker CLT plates are used. M Schweigler replied additional tests showed no influence.

A Frangi commented that this work should not be considered as part of a standard. He asked about moment/shear interaction. M Schweigler replied other work is studying this aspect and no influence can be observed because shear forces are carried by the connectors.

S Franke questioned why the arrangement of connectors between narrow and wide face was changed. M Schweigler replied this was recommended by the commercial partner.

S Franke and M Schweigler discussed evaluation of influence of stiffness by use of nonlinear spring models.

T Demschner discussed possibilities of other applications and the shear force when the steel plate was installed on the edge of the panel and the possibility of development of tensile stress perpendicular to grain. He also commented that engineers would not know the CLT layup a priori. M Schweigler did not think CLT layup is an issue and only small shear force needs to be considered.

P Dietsch commented that the load dispersion concept into CLT using $k_{c,90}$ was not intended for this use.

D Glasner commented that one needs to be careful to account for prestressing effects.

Reinforced Rigid Glulam Joints with Glued-in Rods subjected to Axial and Lateral Force Action

Kai Simon; Simon Aicher
Materials Testing Institute, University of Stuttgart

Keywords: glued-in rods, axial and lateral force action, reinforced connections, beam and cantilever tests, bonded panel reinforcement, screw reinforcement, end-grain bonding, combined moment and shear force action

1 Motivation

The potential of rigid joints in glulam and LVL by means of glued-in rods is evident from numerous research work, increasing numbers of use in timber construction works and hence its consideration in the presently drafted new Eurocode 5-1-1 (2021). The assets of axially loaded steel rods glued-in parallel or inclined to wood fiber direction is widely acknowledged and sufficiently covered by commonly agreed on design rules. However, in moment rigid joints, e.g. at a clamped column basis lateral rod forces and their interaction with axial forces has to be considered, too. Lateral rod forces induce tensile stresses perpendicular to grain in the end grain region, which lead to crack formation parallel to the rod axis. The lateral force resistance of glued-in rods, as addressed now in (Eurocode 5 draft, 2021), clearly represents a rather worst-case scenario of a rod positioned very close to the loaded edge. A previous more plausible and economic design approach has been dropped (Blaß & Laskewitz, 2001). In addition, the proposed linear interaction of axial and lateral forces has been shown experimentally and analytically being utmost conservative (Aicher & Simon, 2021). Irrespective hereof the mentioned tests have clearly revealed, that the joint capacity could be significantly increased by apt reinforcement perpendicular to grain. This conclusion states the motivation of tests on reinforced glued-in rod joints.

The research work reports on a test program with cantilever- and beam-type GLT-specimens with joints by glued-in rods reinforced by alternate methods in order to prevent premature splitting mainly due to lateral forces. Three major alternatives for reinforcement, shown schematically in Figure 1 have been investigated: i) self-tapping screws, ii) laterally glued-on plywood strips and iii) a plywood plate bonded at the end grain face of the connection. Within each alternative a specific sensible configuration was investigated which may not represent the absolute optimal solution. In order to assess the reinforcement effects best possible the same specimen sizes and test configurations as used in the previous investigations with unreinforced joints (Aicher & Simon, 2021) was used. Due to time and funding restrictions only a limited number of specimens per configuration was investigated. This affects the derivation of characteristic values, however not the assessment of the principle capacity potential of the reinforcements. In order to assess the reinforcement effects with regard to of prevention of pre-peak crack formation best possible, the loading scheme was predominantly quasi static reversed.

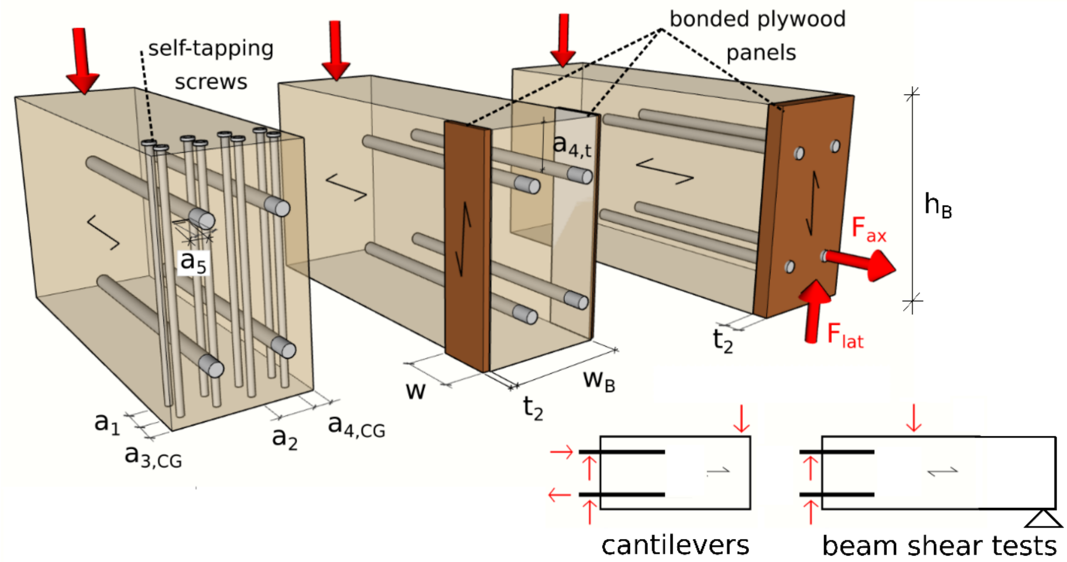

Figure 1.1: Investigated reinforcement alternatives

2 Test program

2.1 GLT, steel rod, adhesive and rod placement

All test specimens were made from spruce GLT of strength class GL30h according to EN 14080 (2013) with a height of h_B = 280 mm and widths of w_B = 80 mm and 160 mm, respectively. The length of the beams varied from 600 mm to 1200 mm depending on the investigated loading configurations given below. In the beam shear tests with single rods these were placed as in (Aicher & Simon, 2021) at two different distances $\alpha = a_{4,t} / h$ vs. the loaded edge, with values of $\alpha_1 = 0{,}23$ and $\alpha_2 = 0{,}77$. Further shear tests were performed two rods along height placed at $\boldsymbol{\alpha_1}$ and $\boldsymbol{\alpha_2}$ and this configuration was also used in the cantilever tests. In case of GLT beam widths of 80 mm throughout one rod was placed along width and in case of GLT widths of 160 mm two rods were placed along width.

The glued-in metrically threaded rods with a diameter of d = 16 mm conformed to strength class 8.8 acc. to EN ISO 898-1 (2013). The characteristic yield strength of the steel rod is $f_{y,k}$ = 640 N/mm² and the nominal stress area is A_s = 157 mm². This results in a rod yield capacity of

$$F_{t,k} = 640 \frac{N}{mm^2} \cdot 157\, mm^2 = 100{,}5\, kN.$$

The bonded-in length l_b was 320 mm (20·d) for all test specimens. The rods were glued into GLT holes with diameter d_{drill} = 20 mm. The adhesive used was an epoxy resin (EP

32 S with hardener B 22 TS, company WEVO Chemie, Ostfildern-Kemnat) acc. to German National Technical Approval (Z-9.1-705, 2021) and conforming to EN 17334 (2021). Using the characteristic bond strength value specified in the approval $f_{k1,k}$ = 4,4 N/mm² the resulting axial withdrawal capacity of the glued-in rod is

$$F_{b,k} = \pi \cdot 16\,mm \cdot 320\,mm \cdot 4{,}4\,\frac{N}{mm^2} = 70{,}8\,kN.$$

2.2 Screw reinforcement

Fully-threaded screws with a nominal diameter of 8 mm and a length of 280 mm of type *Würth Assy plus VG 4 CH,* conforming to European Technical Approval (ETA-11/0190, 2018) were used. In case of the reinforcement by self-tapping screws the distance between the screw axis and the end grain face as well as the distance a_5 between glued-in rod and reinforcing screw have to be minimized. To achieve the best effect of the screw-reinforcement the distances to the edges and to the next screw were slightly reduced compared to the minimum distances specified in the screw ETA.

Table 1 shows the realized spacings and edge distances altogether with the ETA specified values; the spacing notations are shown in Figure 1.1. The screw holes were predrilled with a diameter of 5,0 mm to prevent splitting of the GLT at insertion of the screws.

Table 1. Spacings and edge distances of investigated screw reinforcement

self-tapping screws	**spacings and edge distances**				
	a_1	a_2	$a_{3,CG}$	$a_{4,CG}$	a_5
	[mm] (x·d for d = 8 mm)				
test configuration	32 (4·d)	40 (5·d)	28 (3,5·d)	20 (2,5·d)	10 (1,2·d)
ETA-11/0190	(5·d)	(2,5·d)	(5·d)	(3·d)	-

2.3 Reinforcement with lateral or end-grain bonded plywood strips

The reinforcement panels consisting of beech plywood, acc. to EN 636 (2015), had thicknesses of 15 mm and 20 mm in case of lateral and end-grain reinforcement, respectively. The plates were bonded either to both GLT wide sides, immediately adjacent to the clamped beam end or to the GLT end-grain face. The fiber direction of the outer panel plies was oriented perpendicular to the grain direction and the height of the GLT beams. The dimensions of the plates are given in Table 2.
The end-grain bonding of the plates was throughout performed with a gap filling type I phenol resorcinol PRF adhesive acc. to EN 301 (2018) also covered by German National Technical Approval Z-9.1-840 (2019) which is suitable for a glue line thickness up to 1,5 mm. In case of the laterally bonded plates either the mentioned PRF was used or a gap-filling type I melamine urea formaldehyde MUF adhesive covered by EN 301 and

approval Z-9.1-823 (2020). The cramping pressure was exerted by screw-gluing with self-tapping screws of diameter 5,0 mm and a length of 80 mm. The nominal pressure was about 0,5 N/mm² obtained by a rather narrow screwing pattern.

Table 2. Dimensions of glued-on plywood reinforcement strips

bonding position	h	w	t_2	material	no. of plies
		[mm]			
side	280	80	15	plywood, beech	7
end-grain	280	80 / 160	20	plywood, beech	9

2.4 Test configurations

To obtain the load-carrying behavior of the reinforced connections separately for axial and lateral forces as well as for moment and shear force interaction, the following three types of tests were performed: i) pure axial rod loading, ii) shear force tests with very small / neglectable moment interaction and iii) cantilever tests with a moment and shear force rigid clamped end.

The investigations addressing the pure shear capacity were carried out as single-span beams with a length of 1200 mm, as shown in Figure 2.1. The tests with the moment and shear force rigid joints were performed with cantilever type specimens and loaded by a single vertical force at the unsupported cantilever end (Figure 2.1 and 2.3). Two significantly different global moment / shear force ratios of M/V = 0,55 and M/V = 1,15 were realized by cantilever lengths of effectively 550 mm and 1150 mm. Tables 3 and 4 contain a compilation of the test program for shear and cantilever tests, respectively.

Besides the tests with glued-in rod connections embedment tests parallel to spruce fiber direction were performed acc. to EN 383 (2007) with steel dowels of 16 mm and 20 mm diameter, representing the diameter of the glued in steel rod and the adhesive filled drill hole, respectively. Further, the bond strength and integrity of the bond-line between beech plywood panel and GLT end-grain surface, unknown today, was investigated by block shear tests with and without water-boil treatment acc. to EN 14374, Annex B (2005).

Table 3: Compilation of test program for the shear force tests

designation of test	type of reinforcement	GLT width and height	position of rod along beam height	number of tests	specimen notation
S1	none	80 mm x 280 mm	near (α_1)	4	S1_α_1
			far (α_2)	3	S1_α_2
			near + far (α_1=0,23)	3	S1_α_{1+2}
S1_screw	self-tapping screws		near (α_1)	2	S1_screw_α_1
			far (α_2)	1	S1_screw_α_2
			near + far (α_1=0,23)	1	S1_screw_α_{1+2}
S1_end	bonded end-grain plate		near (α_1)	3	S1_end_α_1
			far (α_2)	2	S1_end_α_2
			near + far (α_1=0,23)	3	S1_end_α_{1+2}
S3	none	160 mm x 280 mm	near (α_1)	2	S3_α_1
			far (α_2)	2	S3_α_2
			near + far (α_1=0,23)	2	S3_α_{1+2}
S3_end	bonded end-grain plate		near (α_1)	1	S3_end_α_1
			far (α_2)	1	S3_end_α_2

Table 4: Compilation of test program for the cantilever tests

designation of test and M/V ratio	type of reinforcement	length of GLT	GLT width and height	position of rod along beam height	number of tests
C1 (0,55)	none	60	80 x 280	near + far (α_1 and α_2)	6
C2 (1,15)		120			7
C1_screw (0,55)	self tapping screws	60			3
C2_screw (1,15)		120			3
C1_lateral (0,55)	bonded lateral plate	60			3
C2_lateral (1,15)		120			3
C1_end (0,55)	bonded end-grain plate	60			2
C2_end (1,15)		120			3
C5 (0,55)	none	60	160 x 280	near + far (α_1 and α_2)	5
C6 (1,15)		120			5
C5_screw (0,55)	self screws	60			3
C6_screw (1,15)		120			2
C5_lateral (0,55)	bonded lateral plate	60			2
C5_lateral (1,15)		120			2
C5_end (0,55)	bonded end-grain plate	60			2
C6_end (1,15)		120			2
C7 (1,95)	none	200	80 x 280	near + far (α_1 and α_2)	4
C8 (1,95)			280		3

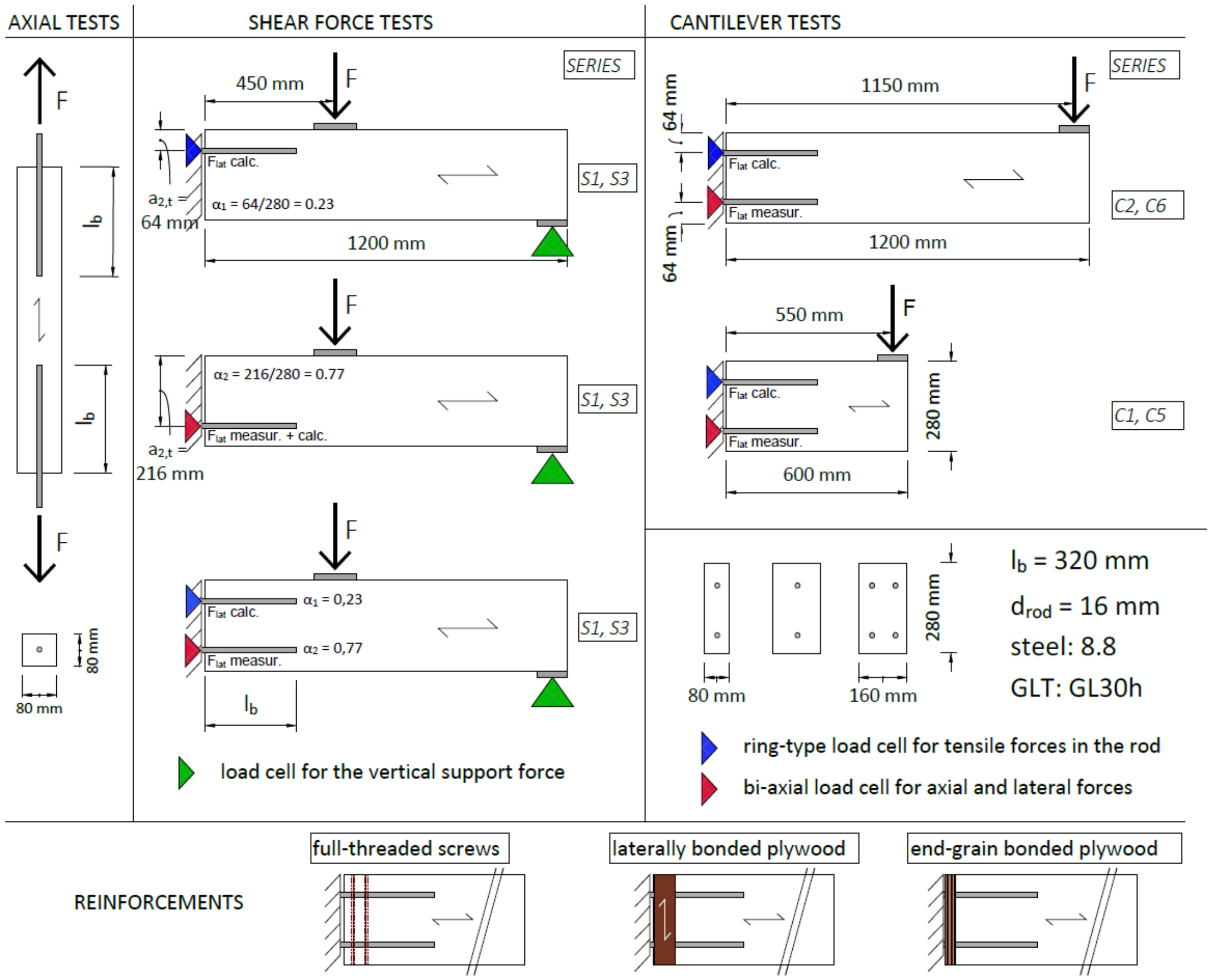

Figure 2.1: Investigated test configurations: axial tests, shear force tests, cantilever tests, cross-sections and types of reinforcement

2.5 Test set-up and procedure

A special steel frame, then clamped to the test machine, was manufactured to enable i) a rigid connection of the test specimen and ii) a proper installation of the force and displacement measurement equipment. The steel frame, shown in Figure 2.2, allows a reversed loading for cantilever type beams. It contains special adapter plates which enable the fixation of 1D and 3D load cells for measurement of the rod forces. In order to allow in the tests for large deflections and beam inclinations at the loaded beam end a special load application kit was conceived suitable for large rotations in reversed loading. Figure 2.3 shows a photograph of a cantilever specimen with lateral bonded strip reinforcement mounted in the test machine and the force application kit for reversed loading.

The loading of the test specimens was performed displacement controlled. The shear beam specimens were throughout loaded monotonic. Most of the cantilever beams were loaded reversed to observe the improved behavior vs. an unreinforced column or beam which has a perpendicular to grain crack at one rod and is then loaded from the opposite direction. A loading scheme for a test with reversed loading is given in Figure 2.4.

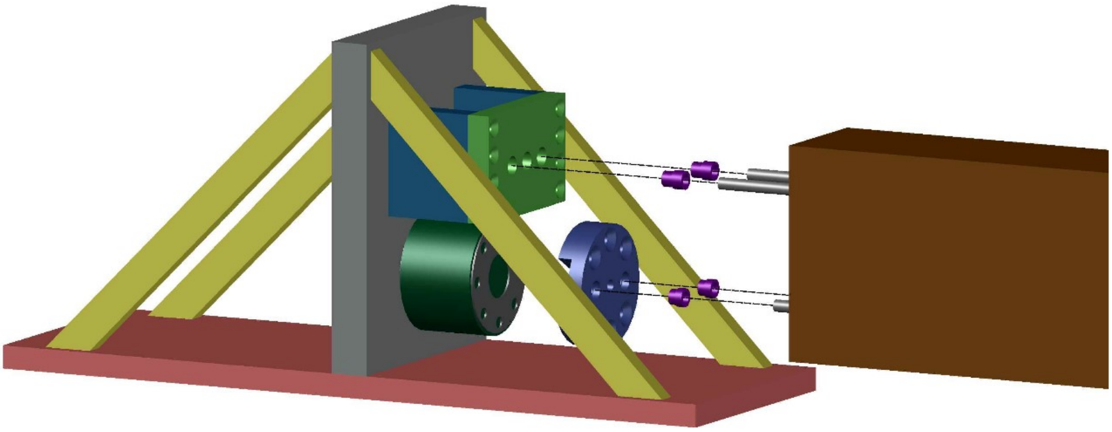

Figure 2.2: Steel frame and installation principle of the test specimens, here for a test beam of width w = 160 mm with two rods along width

Figure 2.3: cantilever test specimen C2_lateral_01 with laterally bonded strip reinforcement mounted in the test machine

The measurement of the axial and lateral forces of the rods at the cantilever tests conformed to the procedure described in detail in (Aicher & Simon, 2021). In case of the pure lateral shear force tests the force at the end support was measured by two parallelly arranged load cells to allow a calculation of the total shear force acting at the clamped joint at one or both rods. The principle location of the load cells is given in the configuration overview in Figure 2.3.

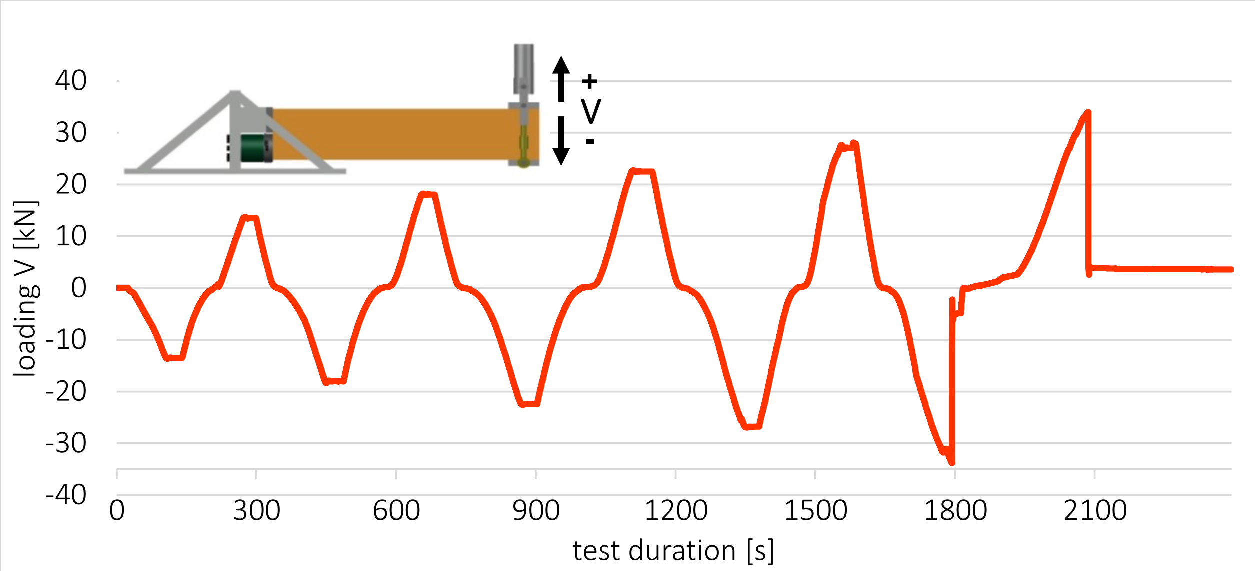

Figure 2.4: Loading scheme of cantilever test C2_lateral_01 with reversed loading

3 Results for joints with lateral loading

The entity of shear capacity results of the reinforced joint configurations are given in Table 5. The mean values are illustrated in Figure 3.1 where the results for identic configurations without reinforcement, given previously in (Aicher & Simon, 2021), are shown, too. In order evaluate the effect of reinforcement with a decent number of specimens the results of series S1 (one rod per width) and series S3 (two rods per width) were merged to one sample; hereby the results for the S3 series were divided by a factor of 2.

Very sensible the reinforcement gain is highest in case of a single rod placed close to the loaded edge (α_1 = 0,23). Here screw and end-grain plate reinforcements deliver capacity increases on the mean load level by factors of 3 and 5,2 respectively. The splitting failure mode observed in the unreinforced specimens can be prevented entirely by the reinforcement.

For the case of α_2 = 0,77, i.e. a rod at a very large distance from the loaded edge the capacity gains of the reinforcements are smaller but still amounts at the mean level to factors of 1,7 and 2,1 in case of screws and end-grain plates.
In case of two rods placed close and far from the loaded edge (α_1 and α_2), i.e. representing a cantilever joint loaded in lateral shear exclusively, the capacity increases amount to factors of 1,8 and 2,6 in case of screws and end-grain reinforcement, respectively. Not revealed graphically in this paper the test set-up enables the separation of the shear forces of the cantilever type joints. These measurements show that comparable reinforcement increases are obtained as specified for the single rod configurations.

Figure 3.2 shows selected load displacement curves of the pure shear force tests with either unreinforced and reinforced specimens. The shown lateral displacements u refer to the upper edge of the beam immediately besides the clamped edge. Curve 1 shows the force displacement behavior of a joint with a rod with a large distance $\alpha_2 = 0{,}77$ from the loaded edge. Curve 2, being very similar to curve 1, represents the situation of a rod placed very close to the loaded edge ($\alpha_1 = 0{,}23$) but reinforced by screws. Curve 3 represents the F_{lat}-u relationship of a rod placed at α_2, reinforced with screws. Finally Curve 4 revealing the most stiff behavior up to a very high load represents again a rod placed at α_2, now reinforced by an end-grain bonded plate.

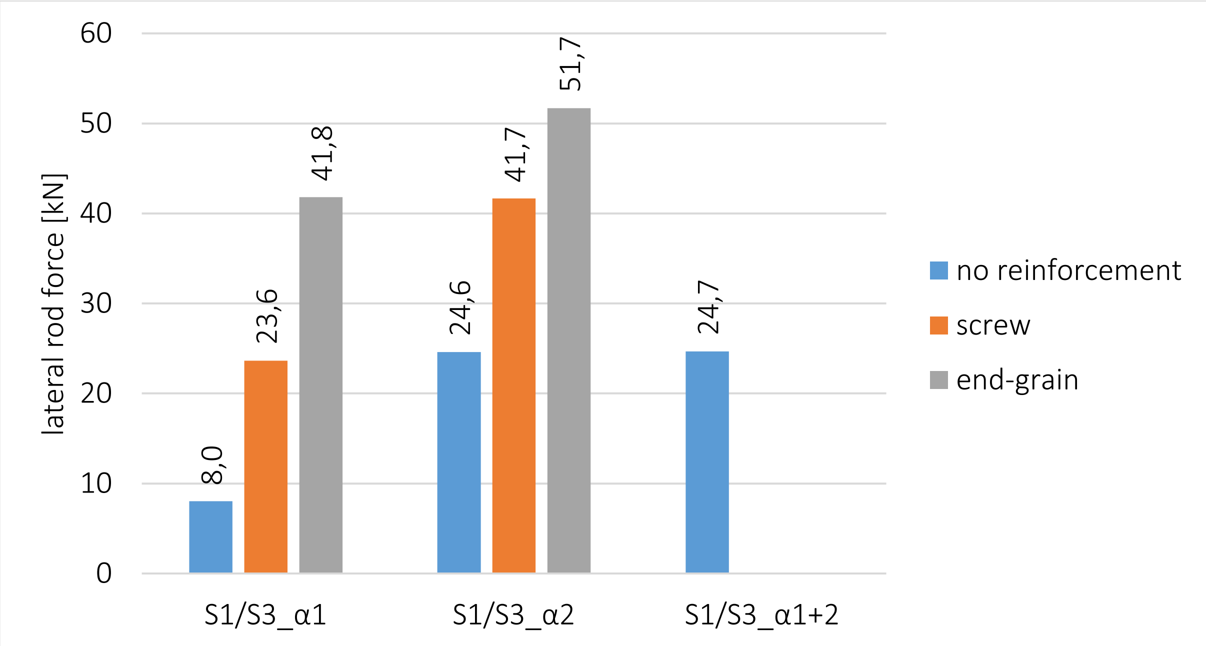

Figure 3.1: mean capacities of lateral force tests (configurations S1 and S3)

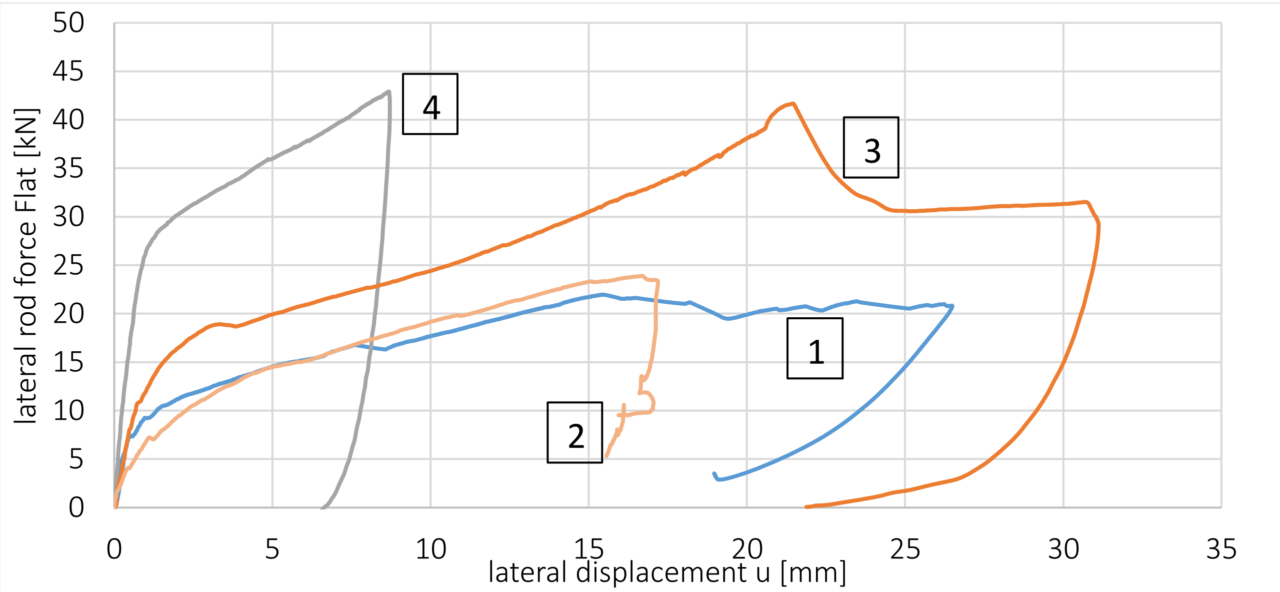

Figure 3.2: typical load displacement curves of unreinforced and screw / end-grain reinforced lateral force tests

Table 5: Compilation of test results for joints with lateral loading

specimen configuration [test designation]	**No.**	**beam loading V = F** F_u [kN]	**measured rod forces shear forces** $F_{\alpha1,u,lat}$ [kN]	$F_{\alpha2,u,lat}$ [kN]	**vertical displacement** u [mm]	
S_α₁ [S1+S3]	_01	13,2	8,6		1,8	
	_02	12,3	7,8		0,3	
	_03	11,6	7,6		1,7	
	_04	18,1	10,1		3,0	
	_01	11,7	7,5		2,3	
	_02	10,5	6,6		3,1	
	mean (COV)	**12,9 (19%)**	**8,0 (14%)**		**2,0**	
S_screw_α₁ [S1 + S3]	_01	42,6	23,5		17,0	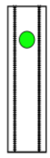
	_02	42,7	23,8		21,3	
	mean (COV)	**42,7 (0%)**	**23,6 (0%)**		**19,2**	
S_end-grain_ α₁ [S1 +S3]	_01	68,6	39,3		6,2	
	_02	76,8	43,8		7,4	
	_03	76,1	43,2		9,0	
	_01	71,8	41,0		8,1	
	mean (COV)	**73,3 (5%)**	**41,8 (4%)**		**7,7**	
S_α₂ [S1+S3]	_01	44,4		23,8	16,0	
	_02	44,7		23,8	16,4	
	_03	31,6		19,3	18,7	
	_01	51,9		28,5	19,8	
	_02	51,4		27,6	18,9	
	mean (COV)	**44,8 (16%)**		**24,6 (13%)**	**17,9**	
S_screw_α₁ [S1]	_01	86,8		41,7	22,7	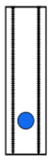
S_end-grain_α₁ [S1 + S3]	_01	76,2		48,9	8,7	
	_02	75,8		58,1	9,0	
	_01	81,0		48,2	14,2	
	mean (COV)	**77,6 (3%)**		**51,7 (9%)**	**10,6**	
S_α₁₊₂ [S1 + S3]	_01	36,1	3,2	18,6	17,7	
	_02	46,5	8,9	19,6	16,2	
	_03	35,3	6,5	16,1	14,8	
	_01	38,5	7,8	14,8	17,0	
	_02	47,8	9,5	18,4	9,2	
	mean (COV)	**40,9 (13%)**	**7,2 (31%)**	**17,5 (10%)**	**15,0**	
S_screw_α₁₊₂ [S1]	_01	78,2	18,0	25,4	17,3	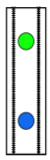
S_end-grain_α₁₊₂ [S1]	_01	110,0	23,5	46,1	3,2	
	_02	92,7	20,2	37,0	1,8	
	mean (COV)	**101,3 (9%)**	**21,8 (7%)**	**41,5 (11%)**	**2,5**	

4 Results for joints with combined axial and lateral forces

The results of the cantilever tests with combined moment and lateral force action on the glued-in rods are shown graphically in Figure 4.1 for the mean ultimate load level. In order evaluate the effect of reinforcement with a decent number of specimens the results of series C1 (one rod per 80 mm GLT width) and series C5 (two rods per width) were merged to one sample; hereby the result for the C5 series was divided by a factor of 2. The same applies for test series C2 and C6.

In a first comparison of reinforced vs. unreinforced specimens no differentiation is made between the different reinforcement types. Doing so, the reinforcement increase is denoted by factors of 1,7 and 1,8 for F_{ax} and F_{lat}, respectively, when regarding the short cantilever beams (configurations C1 / C5). In case of the long cantilever beams (C2 / C6) the reinforcement gains are significantly lower with a factor of 1,3 equally for F_{lat} and F_{ax}. The smaller reinforcement gain in case of the long cantilevers is sensible as the reinforcement, which provides primarily an increased shear force capacity, cannot increase the longitudinal capacity beyond an interface glued-in rod bond strength of about 7 N/mm² which can be calculated form the average F_{ax} load of the reinforced specimens. In this context it should be recalled that 7 N/mm² is already a rather high shear strength value for small clear wood specimens.

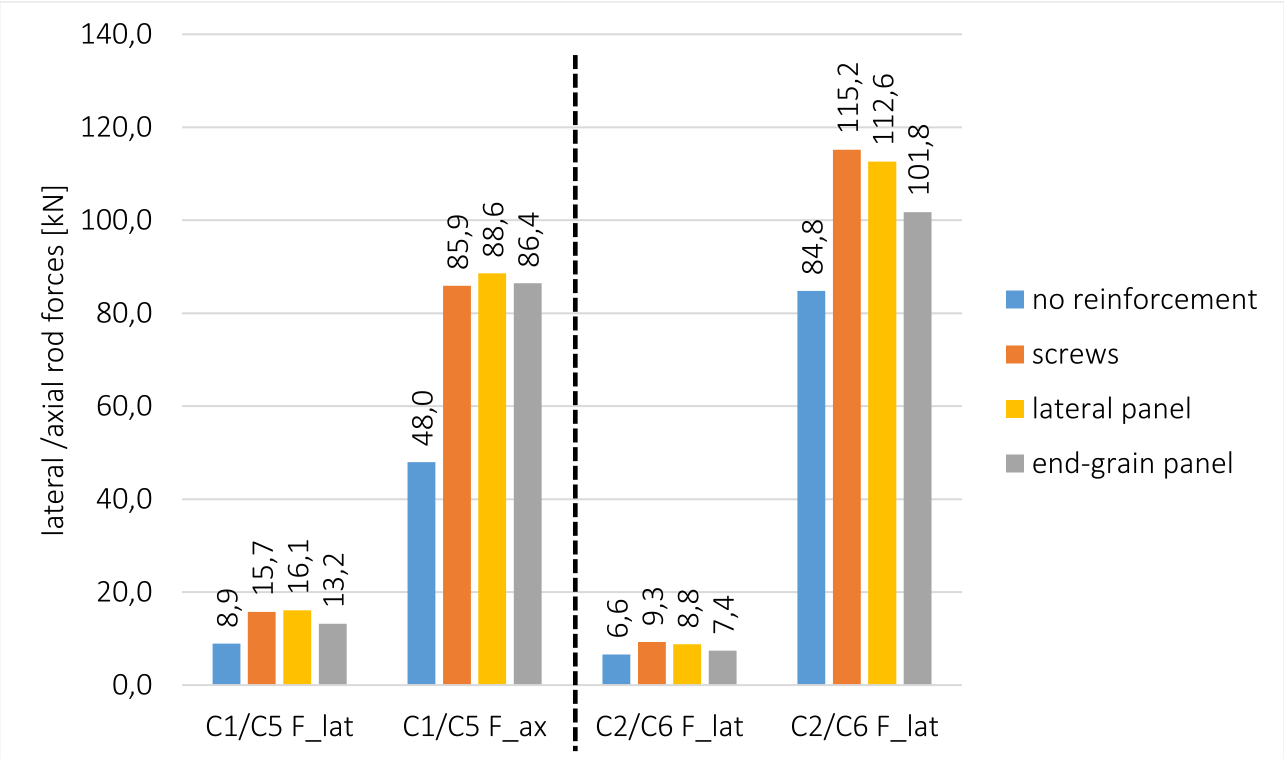

Figure 4.1: Mean axial and lateral force capacities F_{lat} and F_{ax} per rod of cantilever tests C1 / C5 (M/V = 0,55) and C2 / C6 (M/V =1,15)

Contrarily, in case of the short cantilevers the capacity of the joint is not limited to the same extent by the F_{ax} value which in case of the reinforced specimens is related in average to a bond shear strength of 5,4 N/mm². Hence the shear force increases are much higher as compared to the long cantilevers. Very obvious a more expressed interaction of F_{ax} and F_{lat} is experienced for the short cantilevers.
Regarding the effect of the different reinforcements hereby summarizing the short and long cantilevers no significant differences can be stated on the mean level. However, the screwed reinforcements showed a much higher scatter, with a COV of 24% vs. 9% for glued panels in case of the short cantilevers where the interaction capacity is more influenced by the lateral force capacity / reinforcement.

5 Interaction relationship of F_{ax} and F_{lat}

Figure 5.1 shows the force interaction relationship whereby ordinate and abscissa show the pure axial and lateral capacities. Also given are tentatively quadratic interaction curves related to mean and minimum values of panel reinforced joints. Furthermore, the interaction capacity of unreinforced glued-in rods acc. to (Eurocode 5, 2010) and (Eurocode 5 / NA, 2013), valid for the characteristic strength level is presented (see also (Aicher & Simon, 2021)). The graph and the comparison with the EC5-design curve evidences the enormous capacity gains resulting from the investigated reinforcements. In this context it has to be recalled that the draft EC5 design curve for glued-in rods was found much to conservative already at unreinforced joints (Aicher & Simon, 2021).

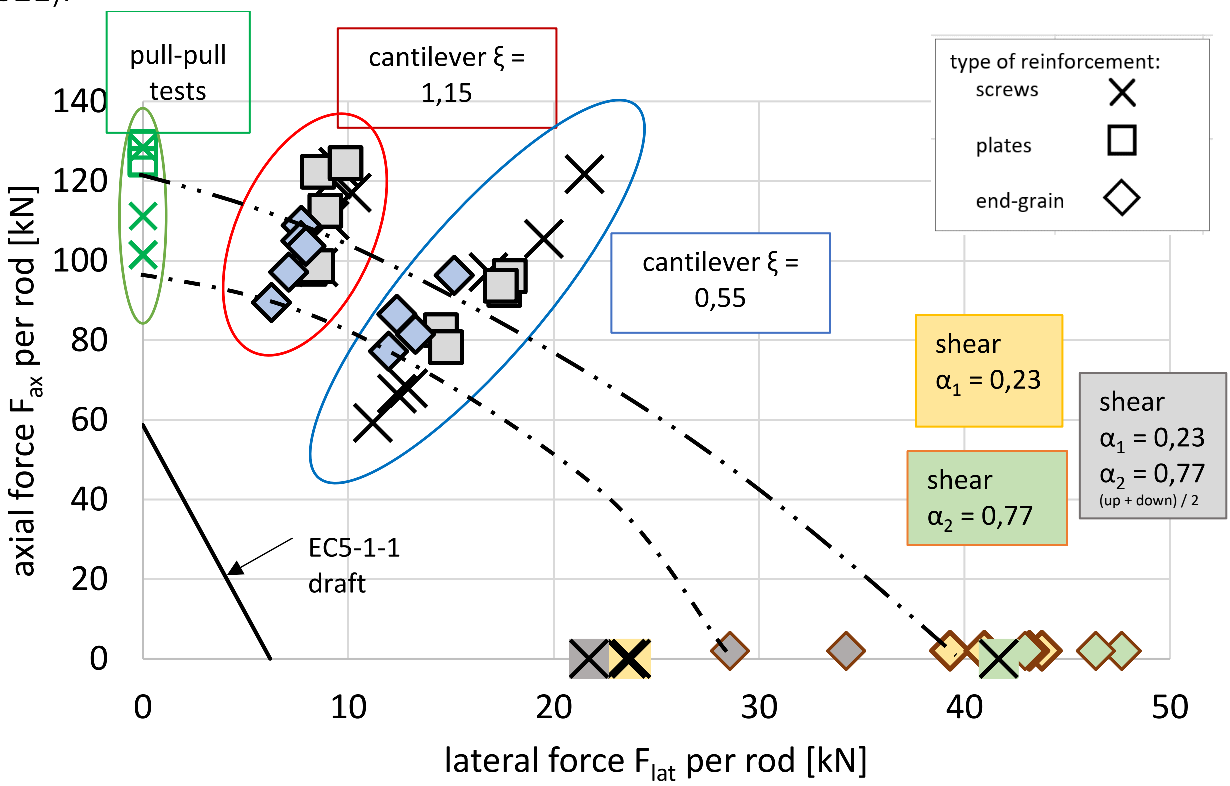

Figure 5.1: Interaction relationship of axial and lateral forces at joint failure for glued-in rod joints with different reinforcements

6 Design Approach

6.1 End-grain bonded plate

Riberholt (1986) and (1988) holds the merit for firstly presenting experimental tests with rods glued-in parallel to grain and loaded laterally as well as by combined moment and shear force action. He observed splitting as a weakness of the joints when either the beams were very slim or the rod was close to the loaded beam edge. To overcome this joint deficiency, he firstly investigated a reinforcement by a 9 mm birch plywood panel glued-on the GLT end-grain. Based on the test results the lateral rod capacity of unreinforced joints and for an eccentricity of e = 0 mm was then proposed (1986) as

$$F_{lat,Rk,unreinf} = f_{h1,k} \cdot d \cdot \sqrt{\frac{2 \cdot M_{y,Rk}}{f_{h1,k} \cdot d}} = \sqrt{2} \cdot \sqrt{f_{h1,k} \cdot d \cdot M_{y,Rk}} \qquad \text{Eq. (1)}$$

This Equation (1) is similar to equation 8.9 (b) given in the present EC5-1-1 (2010) and draft EC5 (2021).

Equation (1) was then extended (Riberholt, 1986) to the case of an end-grain reinforcement as (see Figure 6.1)

$$F_{lat,Rk,reinf} = \left[\left(\sqrt{\left(\frac{2 \cdot M_{y,Rk}}{f_{h1,k} \cdot d}\right) - t^2 \cdot \left(\frac{f_{h2,k}}{f_{h1,k}} - 1\right)} - t\right) \cdot f_{h1,k} + t \cdot f_{h2,k}\right] \cdot d. \qquad \text{Eq. (2a)}$$

where

- $f_{h1,k}$ embedment strength of spruce (rod parallel to grain and loaded lateral as $f_{h1,k} = 0{,}125 \cdot 0{,}082 \cdot (1 - 0{,}01 \cdot d) \cdot \rho_{k,GLT}$ (EC5 eq. 8.16)
- $f_{h2,k}$ embedment strength of beech plywood in N/mm²
  as $f_{h2,k} = 0{,}11 \cdot (1 - 0{,}01 \cdot d) \cdot \rho_{k,plywood}$ (EC5 eq. 8.36)
- d steel rod diameter in mm
- $M_{y,Rk}$ yield moment of the steel rod in Nmm
  $M_{y,Rk} = 0{,}3 \cdot f_{u,k} \cdot d^{2{,}6}$ (EC5 eq. 8.14)
- t thickness of the plywood plate

Equation (2a) describes a failure mode of a single plastic hinge in the GLT or of two yield hinges in case the glued-on end-grain panel is thick. If the embedment strength of the GLT parallel to grain is neglected ($f_{h1,k} = 0$) in a conservative design approach, the lateral capacity results simply in

$$F_{lat,Rk,reinf,2} = f_{h2,k} \cdot d \cdot t. \qquad \text{Eq. (2b)}$$

For the investigated specimens the lateral force resistances result in
$F_{lat,Rk,unreinf}$ = 6,2 kN, $F_{lat,Rk,reinf}$ = 23,4 kN and $F_{lat,Rk,reinf,2}$ = 20,7 kN
(with $f_{h1,k}$ = 3,7 N/mm²; $f_{h2,k}$ = 65 N/mm²; $M_{y,Rk}$ = 324 kNmm; d = 16 mm; t = 20 mm). The characteristic capacities obtained for the end-grain plate reinforcement are still rather conservative in compare to the test results.

Such a design proposal for joints with glued-in rods containing an end-grain reinforcement is presently not given in the Eurocode 5.

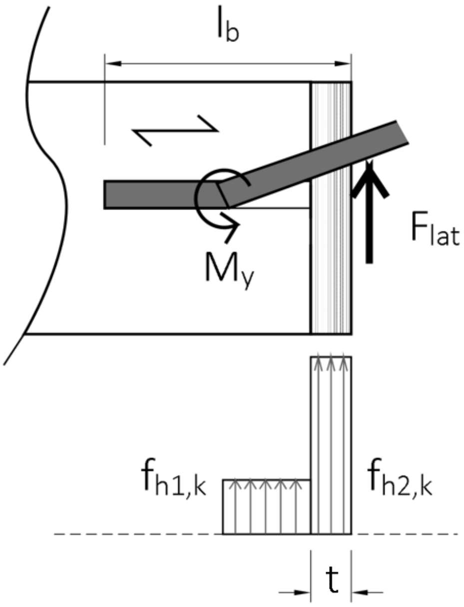

Figure 6.1: Lateral force capacity model for a glued-in rod with a bonded end-grain plate

In the addition to the embedment / plastic hinge resistance capacity of the end-grain plate the shear force transfer of the plate bonded to the GLT end-grain face has to be verified for the bond line interface. The characteristic shear capacity is then determined by the total bonding area, here $h_p \cdot w_p$. In general, the end-grain plate will cover the total GLT end-grain face, hence $h_p = h_B$ and $w_p = w_B$. In case of a cantilever situation the characteristic lateral capacity is given by

$$F_{lat} \cdot n_{rod} \leq h_p \cdot w_p \cdot f_{v,b,end-grain} \qquad \textit{Eq. (3)}$$

where

$f_{v,b,end-grain,k}$ characteristic bond line shear strength of GLT vs. plywood panel

As no values for $f_{v,b,end-grain}$ can be found in literature some tests were performed resulting for the used PRF-adhesive in mean and minimum values of 5,0 N/mm² and 4,2 N/mm², respectively.

Further the tension capacity of the panel / strip cross-section parallel to direction of shear force, being in general parallel to beam height, has to be verified as

$$F_{lat} \cdot n_{rod} \leq t_p \cdot (w_p - d_{drill}) \cdot f_{t,plate}. \qquad \textit{Eq. (4)}$$

6.2 Laterally bonded plates

For the case of reinforcements with laterally bonded plates an appropriate design of joint situations with one or two glued in rods along width is analogous to the reinforcement of notches and holes with lateral plates. The characteristic shear capacity of the panel reinforcement is determined by the bonding area $a_{4,t} \cdot w_p$ between rod and the closer beam edge. In case of a cantilever situation the characteristic lateral capacity is given by

$$F_{lat} = 2 \cdot (2 \cdot w \cdot a_{4,t} \cdot f_{v,k1}) \qquad \textit{Eq. (5)}$$

where $f_{v,k1}$ is the interface bond shear strength between the plywood and the GLT beam which represents a rolling shear situation. In the present German National Application Document DIN EN 195-1-1/NA (2013) and alike in draft EC5-1-1 (2021) the characteristic value of $f_{v,k1}$ = 0,75 N/mm² is specified with regard to the uneven bond shear stress distribution. Tests reported in (Aicher, 2011) have shown that this value is extremely conservative and a value of $f_{v,bond,k}$ = 1,0 - 1,5 N/mm² could be safely proposed which is on the medium / upper end of characteristic rolling shear strength of

CLT with softwood adherends (here hardwood-softwood interface).. Further the net tensile capacity of the plywood strip has to be verified analogous to 6.1. For the investigated case of the specimens in configuration S1 (with two rods) and C1 / C2 a characteristic lateral force capacity of 15,4 kN per rod is obtained.

6.3 Screws

The screw design is analogous to the design for laterally bonded plates, i.e.

$$F_{lat} = n_{ef} \cdot d \cdot a_{4,t} \cdot f_{ax,k} \qquad \textit{Eq. (6)}$$

For the investigated case of specimens with the screw reinforcement of the joint this results in a characteristic lateral force capacity of 19,6 kN per rod (with $n_{ef} = 4^{0,9} = 3,5$ and $f_{ax,k} = 11$ N/mm² acc. to ETA-11/0190 (2018)).

7 Conclusions

The performed investigations of glued-in rod joints reinforced by three alternative methods have shown that the load capacity of such joints subjected to either pure lateral force or, technically much more important, to combined axial and lateral force can be increased significantly vs. unreinforced joints. As reinforcements self-tapping screws and laterally or end-grain bonded plywood plates were considered. The effects of the reinforcement are deduced from comparison with test results of geometrically identic unreinforced configurations presented in a previous paper (Aicher & Simon, 2021). In a very general statement it can be said that the axial capacity of the glued-in rod joint cannot be increased in substantial manner by lateral reinforcement provided sufficient edge distance exists, what is sensible. However, the lateral capacity of the joint can be increased significantly due to restriction of premature splitting parallel to grain. The experimentally obtained resistance increases range from 1,8 to 5,2 depending on placement and number of the glued-in rods and reinforcement type. In the pure lateral force tests the end-grain reinforcements by a glued-on plywood plate proved much higher capacity gains as compared to screws.

Regarding combined moment (M) and shear force (V) actions occurring in a cantilever situation, building relevant tests with two significantly different moment shear force ratios were performed. Hereby the capacity gains vs. the unreinforced situations have to be differentiated between low and high M/V ratios. For a high M/V ratio (1,15) the capacity gains for the axial and lateral resistances revealed on the mean capacity level in average a factor of 1,3 vs. the unreinforced configurations. Contrary hereto for low M/V ratios (0,55), i.e. with a higher shear force contribution, in average the capacity gains for lateral and axial rod resistances showed factors of 1,7 and 1,8 on the mean level. The reason for lower capacity gains for the longer cantilevers with very dominant axial forces is constituted by the fact that the axial resistance can be hardly increased by the reinforcement. In the cantilever tests capacity-wise the different reinforcement types provide rather similar results on the mean level, however, the scatter is much higher in case of screw reinforcement.

A further significant asset of all investigated reinforcement alternatives is constituted by the fact that undamaged reversed loading of the joint is possible until ultimate load. This is in general not possible for unreinforced glued-in rod joints where cracking occurs premature at the rod close to the loaded edge. Regarding seismic actions it is noteworthy that the reinforcement by end-grain plates shows no pinching effect which is quite pronounced in case of screw reinforcement. Not investigated in depth here but noteworthy is that climate changes and direct water impact do not cause a noticeable crack formation in case of end-grain plates and laterally bonded strips.

8 Acknowledgements

The partial support of the ongoing research by the Deutsche Forschungsgemeinschaft (DFG, German Research Foundation) under Germany´s Excellence Strategy – EXC 2120/1 – 390831618, Excellence Cluster IntCDC, is gratefully acknowledged.

9 References

Aicher, S. (2011). Glulam beams with internally and externally reinforced holes - tests, detailing and design. In *International Council for Research and Innovation in Building and Construction, paper 44-12-4, CIB Meeting 44.* Alghero, Italy.

Aicher, S., & Simon, K. (2021). Rigid Glulam Joints with Glued-in Rods subjected to Axial and Lateral Force Action, paper 54-7-3. In *Proceedings International Network on Timber Engineering Research (INTER), Meeting 54* (S. 113-128). Online.

Blaß, H.-J., & Laskewitz, B. (2001). *Glued-in Rods for Timber Structures – Effect of distance between rods and between rods and timber edge on the axial strength.* Germany: Versuchsanstalt für Stahl, Holz und Steine, Abteilung Ingenieurholzbau, Universität Fridericiana Karlsruhe.

EN 14080 (2013). *EN 14080:2013-09: Timber structures - Glued laminated timber and glued solid timber - Requirements;.* Brussels, Belgium: CEN.

EN 14374 (2005). *Timber structures - Structural laminated veneer lumber - Requirements.* Brussels, Belgium: CEN.

EN 17334 (2021). *N 17334:2021-06: Glued-in rods in glued structural timber products - Testing, requirements and bond shear strength classification.* Brussels, Belgium: CEN.

EN 301 (2018). *Adhesives, phenolic and aminoplastic, for load-bearing timber structures - Classification and performance requirements.* Brussels, Belgium: CEN.

EN 314 (2005). *Plywood - Bonding quality - Part 1: Test methods; German version EN 314-1:2004.* Brussels, Belgium: CEN.

EN 383 (2007). *Timber Structures - Test methods - Determination of embedment strength and foundation values for dowel type fasteners.* Belgium, Brussels: CEN.

EN 636 (2015). *EN 636:2015-05: Plywood - Specifications.* Brussels, Belgium: CEN.

ETA-11/0190 (2018). *Self-tapping screws for use in timber constructions, Adolf Würth GmbH & Co. KG, Künzelsau, Germany.* Berlin, Germany: DIBt.

Eurocode 5 / NA (2013). *DIN EN 1995-1-1/NA:2013-08: National Annex - Nationally determined parameters - Design of timber structures - Part 1-1: General - Common rules and rules for buildings.* Berlin, Germany: DIN.

Eurocode 5 (2010). *EN 1995-1-1:2010-12: Design of timber structures - Part 1-1: General - Common rules and rules for buildings.* Brussels, Belgium: CEN.

Eurocode 5 draft (2021). *informal enquiry: prEN 1995-1-1: Design of timber structures - Part 1-1: General and rules for buildings (CEN/TC 250/SC 5 N 1488).* Brussels, Belgium: CEN.

ISO 898 (2013). *ISO 898-1:2013-01: Mechanical properties of fasteners made of carbon steel and alloy steel - Part 1: Bolts, screws and studs with specified property classes - Coarse thread and fine pitch thread.* Geneva, Switzerland: ISO.

Riberholt, H. (1986). *Glued bolts in glulam. Serie R, No 210.* Department of Structural Engineering, Technical University of Denmark.

Riberholt, H. (1988). Glued bolts in glulam- Proposals for CIB Code. In *International Council for Building Research, Studies and Documentation, Working Commission W18A Timber Structures, Meeting 21.* Parksville, Canada: CIB.

Z-9.1-705 (2021). *2K-EP-Adhesive WEVO special resin EP 32 S with WEVO hardener, valid until 26/11/2022, WEVO-CHEMIE GmbH, Ostfildern-Kemnat, Germany.* Berlin, Germany: DIBt.

Z-9.1-823 (2020). *Melamine-urea resin adhesive Kauramine Glue 683 with Kauramine Hardener 686 for the Production of bonded joints with thick adhesive joint thickness (in German).* Berlin, Germany: DIBt.

Z-9.1-840 (2019). *Production of load-bearing wood components and bonding of joints with thick adhesive joint thickness using the phenolic resorcinol resin adhesive Prefere 4094 with the hardener Prefere 5827 (in German).* Berlin, Germany: DIBt.

DISCUSSION

The paper was presented by K Simon

F Lam received confirmation that the glue was phenolic based.

P Dietsch asked why the edge distances were reduced compared to the ETA. K Simon replied that he wanted to use this according to EC proposal.

P Dietsch asked about the long-term performance of unreinforced end grain case. K Simon replied few EN 408 tests were prepared and seems to be okay, but more tests are needed.

T Tannert received confirmation that the intended failure mode was observed in the unreinforced cases.

S Franke suggested that more tests should be conducted with deeper beams.

S Winter asked why high CV was observed for the reinforced beam. K Simon said it could be density of the wood and failure mode of the wood. S Winter asked what would happen if you do a pure bending case, would the stiffness of the glued in rod also participate in splitting. K Simon replied that in pure bending the rod will pull out.

E Serrano received clarification on the test set up with contact in compression at the end grain. Also the use of 3D load cell provided information on shear force.

R Jockwer commented that with different potential failure modes, embedment strength information from EC5 should fit well. K Simon stated that embedment strength values in EC5 seem to be much conservative. R Jockwer commented that relative edge distance information is useful and asked which interaction proposal should be made for the unreinforced case. K Simon replied that linear interaction.

T Demschner, K Simon and S Aicher discussed load transfer mechanisms in the test set up which may result in increase in measured axial capacity of the bond strength.

F Lam received confirmation that there was no splitting.

A Frangi commented on shear transfer mechanisms of the end grain reinforcement such that even if the bonding is durable the shear transfer is not.

E Serrano commented that it is important to add information on the failure mode of different tests.

Proposed design approach for lateral stability of timber beams

Ghasan Doudak, Professor, University of Ottawa, Canada

Magdi Mohareb, Professor, University of Ottawa, Canada

Yang Du, Technical Service Specialist, Canadian Wood Council, Canada

Keywords: lateral stability, timber beams

1 Introduction

Lateral-torsional buckling is an important design consideration for beams with relatively long spans under the action of transverse loads. The compression side of the beam has a tendency to buckle, similar to a column under compression, while the tension side acts as a restraint against buckling. Failure in lateral-torsional buckling is characterized by a lateral displacement u and an angle of twist (or torsion) θ about the beam longitudinal axis. For an idealized beam without initial out-of-straightness, Figure 1 illustrates different stages of deformations under a transverse load inducing bending about the beam strong axis. First, the beam is assumed to undergo a transverse deformation v from Configuration 1 to 2 under the transverse load q. The applied load is then increased by a factor λ so that the load is λq at the onset of buckling in Configuration 3. At that stage, the transverse deformation increases proportionally to λv assuming a linearly elastic response. Under the critical load λq, the beam undergoes lateral-torsional buckling in Configuration 4 manifested by a lateral displacement u and an angle of twist θ.

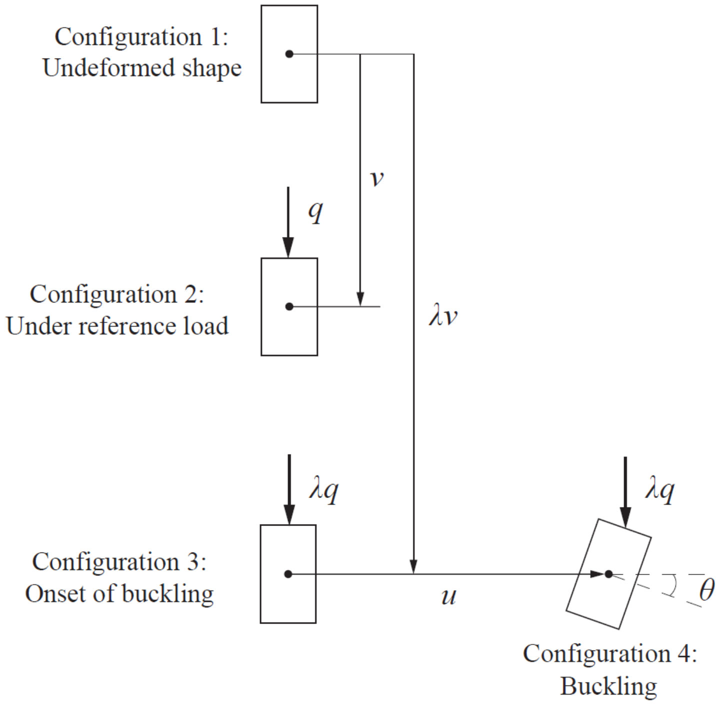

Figure 1. Different stages of beam deformations.

In wood design standards, the ratio of the critical moment obtained from a buckling analysis to the moment resistance based on material failure is commonly referred to as the lateral stability factor. A ratio below 1.0 means the beam resistance is governed by a lateral-torsional buckling failure, whereas a ratio equal to 1.0 means the failure is controlled by material strength. Lateral-torsional buckling can be further divided into two subcategories. The first category is elastic buckling which tends to govern the capacity of beams with high depth-to-width ratios and long spans. The second category is inelastic buckling linked to beams with intermediate depth-to-width ratios and spans. The critical moment for elastic buckling depends solely on the material stiffness properties (i.e., the relevant modulus of elasticity E and shear modulus G). In comparison, the inelastic buckling is influenced by both stiffness and material strength and is typically represented by an empirical formula that depends upon the elastic critical moment and the moment resistance due to material failure.

2 Literature Review

Analytical lateral-torsional buckling solutions for beams under constant moment were presented in classical references (e.g., Vlasov 1961, Timoshenko and Gere 1961). The solutions assume simply supported boundary conditions for lateral displacement and torsion. It is applicable to beams where the major moment of inertia I_x is significantly higher than the minor axis I_y. Flint (1952) modified the classical solution to accommodate beams with less slender cross-sections by accounting for the pre-buckling effect. Based on this theoretical study, Hooley and Madsen (1964) proposed approximate solutions for lateral-torsional buckling of wood beams both in the elastic and inelastic ranges. The effective length approach presented in the paper provided solutions for simply supported, single-span beams and fixed-free cantilevers under transverse loads. The solutions adjust, in an approximate manner, for the effects of load height and partial (or non-rigid) torsional restraints at beam ends. This study formed the basis for the lateral stability provisions in wood design standards in U.S. (AWC, 2018) and Canada (CSA O86, 2019). AWC (2003) summarized analytical studies on lateral stability of wood beams and introduced an adjustment factor for the load height effect in single-segment and fixed-free cantilevers. Sahraei et al. (2018) developed energy-based lateral-torsional buckling solutions for rectangular beams that capture effects of moment gradient, partial twist end restraints, load height and pre-buckling deformation for simply supported, single-span beams and fixed-free cantilevers. The predicted lateral-torsional buckling capacities were in close agreement with results obtained from experimental testing and 3D finite element modelling (Xiao et al. 2017). Hu et al. (2017a and 2017b) developed energy-based solutions for the lateral-torsional buckling analysis for beams with flexible mid-span lateral braces and investigated the bracing height effect. Du et al. (2016, 2019, and 2020) examined the effects of continuous partial torsional restraints provided by wood decking on the lateral-torsional buckling capacity of timber beams. The studies investigated non-sway beam-deck systems in which the beam top face is continuously restrained laterally (2016), laterally-free systems that are rigidly connected to decking (2019) and with partial rotational connections between the beams and decking (2020).

Experimental studies on lateral torsional buckling of wooden beams include the work of Hooley and Madsen (1964) who conducted lateral stability tests on glulam beams under concentrated loads. For experimental testing on lumber products, Xiao (2014) and Xiao et al. (2017) investigated the lateral-torsional buckling of visually graded lumber while Hindman et al. (2005a) focused on machine stressed-rated (MSR) lumber and structural composite lumber (SCL). Hindman et al. (2005b), Burow et al. (2005, 2006), St-Amour and Doudak (2018) and Pelletier and Doudak (2019) conducted experimental testing on lateral-torsional buckling of engineered wood I-joists. The experimental results from the abovementioned studies are, in general, consistent with analytical solutions, thus validating the lateral-torsional buckling theory for wood members characterized by orthotropic material properties.

3 Limitations in Current Lateral Stability Provisions

Wood design standards in Canada (CSA O86, 2019), U.S. (AWC, 2018), and Europe (Eurocode 5, 2004) all consider lateral-torsional buckling as a possible failure mode for bending members. This failure mode is accounted for by applying a lateral stability factor to relate the buckling capacity to the bending moment resistance based on material failure.

The lateral stability factor in the elastic range is determined by the elastic lateral-torsional buckling capacity, while the stability factor for the inelastic range is influenced by both the elastic buckling capacity and material strength. In general, the capacity in the inelastic buckling range is represented by an approximate transition curve connecting the buckling capacity in the elastic region and the flexural resistance in the material strength region. However, the curves estimating the effects of material strength and elastic buckling differ in magnitude between standards.

In terms of the design capabilities, the U.S., Canadian and European standards can all predict the lateral stability factors for fixed-free cantilevers and single-span, single-segment beams. In addition, the American and Canadian standards can also handle single-span, single-segment beams with additional intermediate lateral braces. However, multi-span, multi-segment beams are currently beyond the scope of all three standards. In the following, a “span” is defined as the distance between two boundary points providing transverse supports and a “segment” refers to the distance between two boundary points providing both lateral and torsional restraints. The two definitions separate the “segment” relating exclusively to lateral stability from the “span” used in other flexural design considerations, such as bending moments about the major axis and transverse deflections.

Regarding the design limitations, except for the European standard, there are no solutions available for beams subject to transverse loads applied offset from the top face. Even for the European standard where the load height effect is captured, the empirical solution, which increases the effective length by two times the member depth for top loading and decreases by half the member depth for bottom loading, is an approximation. In addition, except for the European standard, the lateral stability provisions are derived from an assumed E/G ratio of 16, whereas the ratio can vary from 2 to 32 across different wood species (AWC, 2003). Another limitation is that the effect of partial torsional restraints at beam ends due to imperfect wood connections are not adequately considered. In the U.S. and Canadian standards, the effect of partial torsional restraint is accounted for in an approximate manner by imposing a prescriptive 15% increase to the effective lengths (Hooley and Madsen, 1964), while in Europe the effect is ignored altogether. Finally, the American and Canadian standards consider the pre-buckling deformation effect in an approximate manner while such effect is conservatively ignored in the European standard.

Table 1 summarizes the capabilities and limitations of the three design standards discussed above. While the limitations allow for relatively simple format for effective lengths in wood standards, they inevitably sacrifice accuracy and transparency in terms of the types of effects being considered or ignored. Within the above context, a new solution is introduced in the next section to address the limitations in the current wood standards.

Table 1. Design features and limitations in wood standards and the proposed solution.

Design features	U.S.	Canada	Europe	Proposed solution
Single-span beams	✓	✓	✓	✓
Single-span beams with intermediate lateral braces	✓	✓	X	✓
Fixed-free cantilevers[(1)]	✓	✓	✓	(✓)
Multi-span beams	X	X	X	✓
Load height effect	X	X	✓	✓
Generic *E/G* material ratio	X	X	✓	✓
Partial torsional restraint	✓	✓	X	✓
Pre-buckling deformation effects	✓	✓	X	✓

Note: (1) While the present study does not present solutions to fixed-free cantilevers, it is possible to expand the proposed solution for cantilevers, as shown in Sahraei et al. (2018).

4 Proposed Lateral Stability Solution

4.1 Elastic lateral-torsional buckling capacity

The general expression for the proposed elastic critical moment of a wooden beam with a rectangular section takes the form presented in Eq. (1) (Sahraei et al., 2018).

$$M_{cr} = C_r C_b C_l C_p M_u \tag{1}$$

where $M_u = (\pi / L_u)\sqrt{EI_y GJ}$ is the classical lateral-torsional buckling solution from Timoshenko and Gere (1961) for the hypothetical case of a beam with an unbraced segment L_u with lateral displacement and twist restraints at both ends under uniform moment. In the classical solution, E is the modulus of elasticity in beam in longitudinal direction, I_y is the moment of inertia about the beam weak axis, G is the shear modulus and J is the Saint-Venant torsional constant. The reference moment M_u does not account for effects such as partial twist restraint, moment gradient, load height, or pre-buckling deformation. Such effects are accounted for separately through the modifiers C_r, C_b, C_l and C_p, respectively (Sahraei et al., 2018).

The C_r coefficient characterizes the reduction in critical moment due to partial twist restraint provided at the ends of beam segment and is given by

$$C_r = \sqrt{\frac{1}{1+\alpha\beta_z}} \tag{2}$$

in which the torsional stiffness ratio is given as $\alpha = (GJ/L_u)/R$, where R is the torsional stiffness provided by the detailing at the end of beam segment (e.g., beam hangers) and GJ/L_u is an indicator of the torsional stiffness of the beam section.

Therefore, the torsional stiffness ratio α is indicative of the torsional stiffness of the beam relative to the torsional stiffness of the end restraints.

Coefficient β_z depends on the transverse moment distribution $M(z)$ along the beam segment and is expressed as

$$\beta_z = \left\{ \frac{\pi \int_0^{L_u} M(z) \left[\left(\frac{\pi}{L_u} \right)^2 \sin\left(\frac{\pi z}{L_u} \right) \right] dz}{2 \int_0^{L_u} M(z) \left[\left(\frac{\pi}{L_u} \right)^2 \sin^2\left(\frac{\pi z}{L_u} \right) \right] dz} \right\}^2 \quad (3)$$

It is noted that the above formula is applicable only to single-span, single-segment beams subject to loads that are symmetric relative to the mid-span point. Table 2 provides coefficient β_z for common loading conditions based on Eq. (3). For the purpose of code/standard development, β_z for other loading conditions can be derived and adopted, while the more elaborate expression in Eq. (3) can be referred to in an appendix or in the research paper.

Table 2. Coefficient β_z for single-span beams.

Load case	β_z
Uniform moment	4.00
Concentrated load at mid-span	3.28
Concentrated loads at 1/3 points	3.42
Concentrated loads at 1/4 points	3.45
Uniformly distributed load	3.48

As expected, when the torsional stiffness R approaches infinity, Eq. (2) yields $C_r = 1.0$ which corresponds to no reduction in critical moment due to partial torsional restraint. When the torsional stiffness R is unavailable, coefficient C_r can be estimated from experimental results. For example, Hooley and Madsen (1964) proposed a 15% increase in the effective length to account for partial torsional restraint, which corresponds to $C_r = 1/1.15 = 0.87$. This 15% increase is currently already incorporated into the CSA O86 (2019) and AWC (2018).

The moment gradient factor C_b is intended to adjust the reference uniform moment loading in the classical solution to other moment distributions. The moment gradient factor was adopted in the America Wood Council's TR-14 report (AWC, 2003) and has also been widely adopted in steel design standards (CSA S16, 2019, Eurocode 3, 2005 and AS-4100, 1998). Sahraei et al. (2018) compared different moment gradient equations from the abovementioned sources for single-span, single-segment glulam beams subject to various loading conditions and recommended the Australian formula

$$C_b = \frac{1.7M_{\max}}{\sqrt{M_a^2 + M_b^2 + M_c^2}} \tag{4}$$

The expression can also be applied to beams with multiple segments. In comparing the moment gradient approach against the effective length approach that forms the basis of the current wood standards, the latter is not able to provide a simple solution for multi-segment, multi-span beams. This limitation is directly tied to the disadvantage of the effective length approach which requires devising an effective length L_e for each loading case and boundary condition. There exist no simple expressions to accurately predict the effective length for various loading and boundary conditions.

The load height coefficient C_l accounts for the effect of the load application position on the critical moment when no torsional restraint is provided at point of loading. For a single-segment beam subject to a uniformly distributed load q and/or a series of equidistant point loads of equal magnitude P, the load height factor C_l takes the form

$$C_l = \sqrt{1+\eta^2} - \eta \tag{5}$$

where η is given by

$$\eta = \frac{\pi}{2L_u \int_0^{L_u} M(z) \left[\left(\frac{\pi}{L_u} \right)^2 \sin^2\left(\frac{\pi z}{L_u} \right) \right] dz} \left\{ P y_p \left[\sum_i^{n_p} \sin^2\left(\frac{\pi z_i}{L_u} \right) \right] + \frac{q L_u y_q}{2} \right\} \sqrt{\frac{EI_y}{GJ}} \tag{6}$$

where $M(z)$ is the beam moment distribution within the segment, n_p is the number of equidistant point loads $i = 1,2...n_p$ located at a longitudinal distance z_i from the beam end acting at a distance y_p relative to the beam shear centre. Similarly, y_q is the transverse distance between the height of the uniformly distributed load q and the shear centre. As a sign convention, the transverse distances y_p and y_q are taken as positive when gravity-induced (downward) loads are applied above the beam shear centre. Conversely, the sign is negative when either the applied load is in uplift direction or act below the shear centre. For the special case of a single-span, single-segment beam subject to either a uniformly distributed load or a series of equidistant point loads applied at the beam top face, Eq. (6) simplifies to

$$\eta = \left(ky/L_u \right) \sqrt{EI_y / GJ} \tag{7}$$

where y is the load height relative to the shear centre and takes the value $y = d/2$ when gravity loads are applied to the top face. Parameter k is determined from Eq. (6) based on the loading type. Values of k for a few common loading types are provided in Table 3 and can be expanded for other load types for adoption in the code/standard development. For gravity loads applied above the shear centre, the values of k from Table 3 and η from Eq. (7) are both positive, leading to a load height coefficient $C_l < 1.0$ and reflecting the destabilizing effects for gravity load applied at the beam top.

Table 3. Load height parameter k for a beam subject to top face loading.

Load case	k
Concentrated load at mid-span	1.81
Concentrated loads at 1/3 points	1.60
Concentrated loads at 1/4 points	1.54
Uniformly distributed load	1.46

For single- and multi-segment beams subject to other load conditions, closed-form solutions for the load height coefficient C_l cannot be readily formulated. As an alternative, the present study develops simple and conservative load-height factors obtained numerically from the finite element analysis. The analysis indicates that coefficient C_l is sensitive to the load types, the beam E/G ratio and the ratio L_u/y of the unbraced segment length L_u to load height ($-d/2 \le y \le d/2$). To develop the C_l factors, a mid-segment point load is chosen because it represents the lower-bound solution since a load application point at the beam mid-segment is the farthest from the end, and hence is associated with a larger angle of twist, resulting in a more pronounced load height effect. Table 4 provides the load height factors C_l for single- and multi-segment beams under any loading types applied at a height h above the shear centre for beam segments with L_u/y ratios ranging from 10 to 60, based on an assumed E/G ratio of 16. This table is recommended for code/standard adoption given the relatively simple format and the versatility in terms of providing load height factors to various loading and boundary conditions.

Table 4. Load height factor C_l for single- and multi-segment beams under gravity load applied at a distance y above beam shear centre.

Number of unbraced segments in the beam	L_u/y					
	10	20	30	40	50	60
Single	0.7	0.83	0.88	0.91	0.92	0.94
Multiple	0.56	0.72	0.8	0.85	0.87	0.89

The pre-buckling coefficient C_p is a magnification factor to be applied to the critical moment to account for the pre-buckling deformation. Based on previous studies (e.g., Flint 1952), the C_p factor takes the form for a beam segment under uniform moments

$$C_p = \frac{1}{\sqrt{1 - I_y/I_x}} = \frac{1}{\sqrt{1-(b/d)^2}} \tag{8}$$

Sahraei et al. (2018) verified the applicability of the above expression as an accurate approximation for other loading conditions.

4.2 Lateral stability factor

For lateral-torsional buckling in the elastic range, the critical moment M_{cr} of a laterally unbraced segment expressed in Eq. (1) is modified to the design-level 5th percentile critical moment $M_{cr,05}$ as

$$M_{cr,05} = \gamma C_r C_b C_l C_p \frac{\pi}{L_u} \sqrt{E_{05} I_y G_{05} J} \tag{9}$$

where E_{05} and G_{05} are the 5th percentile modulus of elasticity and shear modulus, respectively. Coefficient γ is a calibration constant introduced here in the context of the Canadian standards to maintain the same level of safety as that in current Canadian design standards. Generally, however, the γ constant is expected to vary depending on the code or standard potentially adopting a similar procedure.

The general critical moment expression for elastic buckling in Eq. (9) can be substituted into the existing lateral stability approach in each design standard to improve accuracy and transparency, while maintaining the same general approach for continuity. As an example, the following demonstrates the application of Eq. (9) into the lateral stability approach in the Canadian standard. The beam slenderness ratio λ as defined in a manner consistent with the present Canadian standard is

$$\lambda = \sqrt{L_u d \Big/ \left(C_r C_b C_l C_p b^2\right)} \tag{10}$$

Also, the threshold slenderness delineating elastic and inelastic LTB is determined from

$$\lambda_e = 3\sqrt{\left(\gamma\pi\sqrt{E_{05} I_y G_{05} J}\right) \Big/ \left(b^3 d F_b\right)} \tag{11}$$

Following the current Canadian approach in defining the lateral stability factor in the elastic/inelastic/material strength regions and the associated delineation points, the revised lateral stability factor K_L is then defined as

$$K_L = \begin{cases} 1.0 & \lambda \le 10 & \text{material strength resistance} \\ 1 - \dfrac{1}{3}\left(\lambda/\lambda_e\right)^4 & 10 < \lambda \le \lambda_e & \text{inelastic LTB resistance} \\ M_{cr,05}/F_b S & \lambda_e < \lambda \le 50 & \text{elastic LTB resistance} \end{cases} \quad (12)$$

where $S = bd^2/6$ is the beam section modulus and F_b is the specified bending strength of the material. The following section provides design examples using the proposed solution and compares results against the current Canadian standard to showcase its advantages.

5 Examples

5.1 Example 1: Single-span, single-segment beam

Calculate the lateral stability factor for a Canadian D. Fir-L 24f-EX glulam beam subject to a uniformly distributed load (UDL) applied at the beam top face. The beam is simply supported transversely and laterally at both ends with partial torsional restraints provided by beam-to-column connections. The beam span is 7 m with a 130 × 570 mm cross-section. From the Canadian standard, the bending strength F_b is 30.6 MPa and the modulus of elasticity E is 12800 MPa with the 5th percentile E_{05} taken as $0.87E$. The shear modulus G is assumed to be 800 MPa ($E/16$), with G_{05} taken as $0.87G$.

<u>Proposed solution</u>

The calibration constant is taken as $\gamma = 0.6$ for glulam beams. In the absence of information suggesting otherwise, the partial twist coefficient is taken as $C_r = 0.87$ in a manner consistent with the Canadian standard. The moment gradient factor as determine from Eq. (4) is $C_b = 1.17$ for UDL. The pre-buckling coefficient as determined from Eq. (8) is $C_p = 1.03$.

For the load height coefficient C_l, parameter k is taken as 1.46 from Table 3 for UDL. Substituting $I_y = 1.04 \times 10^8$ mm^4 and $J \approx (1 - 0.63b/d)b^3d/3 = 3.57 \times 10^8$ mm^4 into Eq. (7), one obtains $\eta = 0.128$ which corresponds to a load height coefficient $C_l = 0.880$. Alternatively, the C_l factor can be conservatively estimated from Table 4 through linear interpolation of the tabulated L_u/y ratios, yielding a slightly lower value of $C_l = 0.853$.

Based on the above, the critical moment as determine from Eq. (9) is $M_{cr,05} = 133$ kNm. The beam slenderness ratio as determined from Eq. (10) is $\lambda = 16.0$ and the threshold slenderness ratio between elastic and inelastic buckling from Eq. (11) is

$\lambda_e = 15.4$. Since $\lambda_e < \lambda \leq 50$, the beam resistance is governed by elastic buckling and the lateral stability factor as calculated from Eq. (12) is $K_L = 0.618$.

FEA Solution

A 3D finite element analysis (FEA) based on the commercial software Abaqus (2021) has been developed to conduct a linearized eigen-value buckling analysis for the beam under consideration. The 8-node brick element C3D8 is chosen from the Abaqus library to mesh the beam. The element has 8 nodes, each with 3 translational degrees of freedom (DOF), resulting in a total of 24 DOFs per element. This element was successfully used (e.g., Xiao et al. 2017, Hu et al. 2017a and 2017b) to investigate the lateral-torsional buckling behaviour of wood beams.

Based on the mesh sensitivity analysis conducted by Xiao (2014) for C3D8 elements, the element dimensions used in the FEA are chosen as 10 mm × 10 mm × 20 mm, which results in 13 elements in the beam lateral direction, 57 elements in the transverse direction and 350 elements in the longitudinal direction.

Regarding the material constitutive model, wood is characterized as a cylindrically orthotropic material with varying material properties in the longitudinal (L), tangential (T) and radial (R) directions. Yet, the orthotropic constitutive model available in Abaqus is defined along a Cartesian coordinate system rather than a cylindrical coordinate system. Due to the proximity of wood properties along the tangential and radial directions (FPL,2010), the properties along these directions can be conservatively taken as the lower of the two without introducing significant errors in the predicted buckling capacity. This simplification enables the cylindrically orthotropic wood constitutive behaviour to be approximated by the Abaqus Cartesian orthotropic model characterized by different material defined along the longitudinal, transverse, and lateral directions. In the following, these three directions are referred to by subscripts *1*, *2* and *3*, respectively.

The Cartesian orthotropic model requires nine independent parameters, i.e., three moduli of elasticity, three shear moduli and three independent Poisson's ratios. Under the approximation of equal material properties along the transverse and lateral directions, the number of independent parameters is reduced to six, i.e., E_1, $E_2 = E_3$, $G_{12} = G_{13}$, G_{23}, $\nu_{12} = \nu_{13}$, and ν_{23}. Xiao (2014) conducted a lateral torsional buckling sensitivity analysis on the six parameters and concluded that only the longitudinal modulus of elasticity E_1 and the shear moduli $G_{12} = G_{13}$ have a significant impact on the beam buckling capacity while other parameters have nearly no influence.

In the present FEA model, E_1 is taken as E_{05} = 11136 MPa and $G_{12} = G_{13}$ are taken as G_{05} = 696 MPa. The magnitudes of the remaining material parameters have minor impact on the predicted buckling capacity, and are obtained from FPL (2010) as follows: $E_2 = E_3$ = 557 MPa, G_{23} = 78 MPa, $\nu_{12} = \nu_{13}$ = 0.292 and ν_{23} = 0.390.

With equal material properties in the transverse and lateral directions, the constitutive model is essentially simplified to transverse isotropy in the transverse-lateral plane. From classical mechanics, the shear modulus G_{23} in the 2-3 plane of isotropy can be related to E_2=E_3 through the expression $G_{23} = E_2 / \left[2\left(1+\nu_{23}\right) \right]$. This would yield a G_{23} value of 230 MPa which is 2.9 times higher than that obtained from FPL (2010). However, this discrepancy has nearly no impact on the predicted critical moment since the buckling capacity was observed to be non-sensitive to G_{23}.

A reference UDL with a magnitude of q (kN/m) is applied to the centreline of the top face as a series of nodal forces. The boundary conditions in the FEA are modelled to emulate simply supported conditions at both ends with respect to vertical and lateral displacements and torsion. While it is possible to model the partial twist restraint in the FEA model to provide an independent assessment of the C_r expression proposed in Eq. (5), such a verification has been conducted Sahraei et al. (2018) and is not repeated in the present study. Instead, the adjustment needed to account for partial torsional restraint will be made by applying the coefficient $C_r = 0.87$, as discussed in Section 4.1.

To simulate the simply-supported boundary condition, a set of restraints are enforced at both ends of the beam, as illustrated by Figure 2a at one end and Figure 2b at the opposite end. At both ends, restraints are placed along the Lines *AB* and *A'B'* and Lines *CD* and *C'D'* passing through the centroid. The transverse displacements are restrained at the nodes along Lines *AB* and *A'B'*. In addition, the lateral displacements are restrained at nodes along Lines *CD* and *C'D'*. One end of the beam is also longitudinally restrained at the cross-section centroid, while the centroid of the other end is allowed to move freely in the longitudinal direction. The above restraints prevent displacements along the longitudinal, lateral and transverse directions and rotation about the longitudinal axis, while allowing rotations about the lateral and transverse axes.

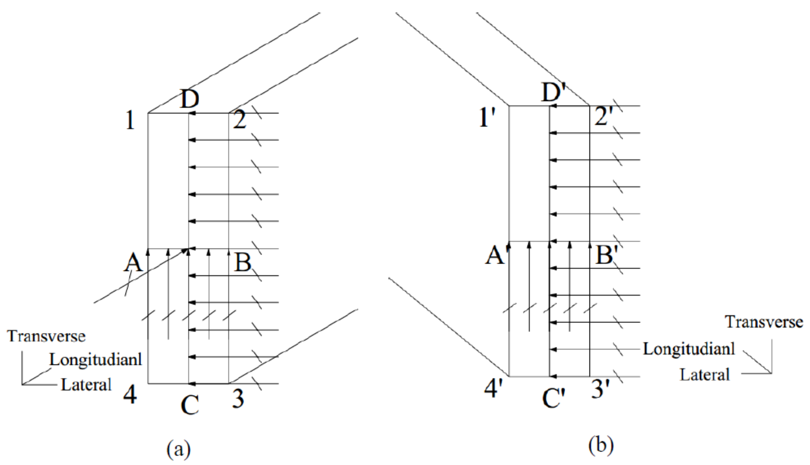

Figure 2. Simply-supported boundary conditions for rectangular sections (Xiao 2014).

Upon running the FEA in ABAQUS, the first reported eigen-value that corresponds to a lateral-torsional buckling mode is q = 38.1 kN/m, which leads to a nominal elastic critical moment = $qL_u^2/8$ = 233 kNm. Applying the same calibration constant $\gamma = 0.6$, partial twist coefficient $C_r = 0.87$ (to account for partial twist restraints) and pre-buckling coefficient $C_p = 1.03$, one obtains the 5th percentile critical moment $M_{cr,05}$ = 125 kNm. By rearranging the terms in Eq. (9), one obtains $C_r C_b C_l C_p = M_{cr,05} / \left(\gamma\pi \sqrt{E_{05} I_y G_{05} J} / L_u \right) = 0.864$. Substituting into Eq. (10) yields the beam slenderness ratio $\lambda = 16.5 > \lambda_e = 15.4$. Therefore, the beam is governed by elastic lateral-torsional buckling and the lateral stability factor as calculated from Eq. (12) is $K_L = 0.581$. A summary of key adjustment factors and results from the proposed solution and FEA are provided in Table 5.

The lateral stability factor as determined from the proposed procedure is 0.618. This value compares 0.581 based on the FEA and 0.602 based on the present Canadian standard. Hence, the proposed solution is 6.3% higher than the FEA solution while the Canadian standard yields a prediction that is 3.6% higher.

5.2 Example 2: Two-span, two-segment beam

Determine the lateral stability factor for a 20 m long beam subject to a uniformly distributed load (UDL) applied at the beam shear centre. Transverse, lateral and partial torsional restraints are provided at the beam ends and mid-length. Beam cross-section and material properties are identical to those defined in Example 1.

Proposed solution

The proposed solution follows a similar calculation procedure as in Example 1. For simplicity, the adjustment factors and slenderness ratio calculations applied to Example 2 are tabulated in Table 5, which yields a lateral stability factor K_L = 0.854.

FEA solution

The specifics of FEA model are similar to those outlined in Example 1 while increasing the number of C3D8 elements along the beam span from 350 to 1000 elements, to accommodate the change of beam length from 7 m to 20 m while preserving a comparable aspect ratio for the elements. Also, the boundary conditions as specified at the beam end with restraints along Lines *A'B'* and *C'D'* are replicated at beam mid-span. The nominal elastic critical moment for the two-span, two-segment beam is found to be 440 kNm.

The procedure to convert the nominal critical moment as obtained from Abaqus to the lateral stability factor is similar to that presented in Example 1. For simplicity, Table 5 summarizes the modification factors applicable to FEA and slenderness ratio calculations. It is noted that the lateral stability factor as determined from FEA is 0.876, which is only 2.6% higher than that of the proposed solution. This compares to K_L = 0.420 based on CSA O86-19 provisions, highlighting the high level of conservatism implied in the current CSA O86-19 standard for multi-span beams with loads that are offset from the beam top face.

5.3 Example 3: Single-span, two-segment beam

Calculate the lateral stability factor for the beam defined in Example 2 when transverse restraints are provided only at beam ends but not at mid-span (Note: while a 20 m span beam might fail under bending or may violate deflection requirements, this example is intended to provide a direct comparison with Example 2 by removing the transverse restraint in the middle).

Proposed solution

Following the same calculation procedure as detailed in Example 1, Table 5 summarizes the adjustment factors and slenderness ratio calculations which results in K_L = 0.583.

FEA Solution

The FEA model is similar to that in Example 2, expect that only lateral restraints along Line *C'D'* are provided at the beam mid-span, to provide lateral and torsional restraints without restraining transverse movement. The nominal elastic critical moment for the two-span, two-segment beam is found to be 258 kNm.

Following a similar conversion procedure as in Example 1 with adjustment factors from Table 5, one obtains K_L = 0.640. In comparison, K_L = 0.583 from the proposed solution is 8.9% lower while K_L = 0.420 based on the Canadian standard is 34.4% lower.

When comparing the results of Example 2 and Example 3, it is noted that the CSA O86 standard predicts the same K_L factor irrespective of the presence/absence of a transverse support in the beam mid-span. In contrast, both the proposed solution and FEA account for the different support conditions, yielding a significantly different stability factor.

Table 5. Summary of modification factors and calculations from Examples 1, 2 and 3.

Example No.	Solution type	Modification factors γ	C_r	C_b Eq.(4)	C_l Eq.(7)	C_p Eq.(8)	$M_{cr,05}$ Eq.(9)	λ Eq.(10)	λ_e Eq.(11)	K_L Eq.(12)
1	Proposed	0.60	0.87	1.17	0.880	1.03	133	16.0	15.4	0.618
	FEA			-	-		125	16.5	15.4	0.581
2	Proposed			2.40	1		217	12.5	15.4	0.854
	FEA			-	-		237	12.0	15.4	0.876
3	Proposed			1.39	1		126	16.5	15.4	0.583
	FEA			-	-		139	15.7	15.4	0.640

6 Conclusion

The present study introduces a comprehensive solution to address lateral-torsional buckling in both the elastic and inelastic regions, while expanding the applicability of the provisions beyond those currently available in the wood design standards in U.S., Canada and Europe. The main focus of the study is to introduce a general expression for the critical moment for elastic lateral torsional buckling (i.e., Eq. (9)) that can be applied to beams in both single and multi-segment applications, while accounting for the effects of partial twisting restraint, moment gradient, load height and pre-buckling deformation in a transparent format through separate modification factors. The proposed elastic buckling expression can be subsequently substituted into the existing lateral stability approach defining elastic/inelastic buckling and material failure in a design standard, thus enhancing the accuracy and transparency of the standard while maintaining the same general approach for continuity. An example of utilizing the proposed elastic buckling expression into the Canadian standard has been presented in Section 4.2.

For single-segment beams, the proposed solution for the Canadian standard is observed to predict lateral stability factors that are similar to those from the standard and FEA. For multi-segment beams, the stability factors from the proposed solution, while consistent with FEA, are significantly higher than those based on the present Canadian standard. The study highlights the need for improvements to the current lateral stability provisions in Canada and, possibly, in other countries.

7 References

ABAQUS (2021). [Computer software]. Providence, RI, Dassault Systèmes Simulia.

American Wood Council (2003): Designing for lateral-torsional stability in wood members. AFPA Technical Report 14. Washington, DC, USA.

American Wood Council (2018): National design specification (NDS) for wood construction. Leesburg, VA, USA.

AS-4100 (1998): Steel structures. Sydney, Australia.

Burow, JR *et al.* (2005): Lateral stability considerations for composite wood I-joists. In ASAE Annual International Meeting.

Burow JR *et al.* (2006): Lateral stability of composite wood I-Joists under concentrated-load bending. Transactions of the ASABE, 49(6), 1867-1880.

Canadian Standard Association (CSA) (2019): Engineering design in wood O86-19. Toronto, Ontario, Canada.

Canadian Standard Association (CSA) (2019): Design of steel structures S16-19. Toronto, Ontario, Canada.

Du, Y *et al.* (2016): Nonsway model for lateral torsional buckling of wooden beams under wind uplift. Journal of Engineering Mechanics;142:04016104.

Du, Y *et al.* (2019): Sway model for the lateral torsional buckling analysis of wooden twin-beam-deck systems." Structures, vol. 19, pp. 19-29.

Du, Y *et al.* (2020): Effect of beam-deck connection flexibility on lateral torsional buckling strength of wooden twin-beams. Engineering Structures, 207, p.110226.

Eurocode 3 (2005): Design of steel structures - Part 1-1: General rules and rules for buildings. CEN. (EN 1993-1-1).

Eurocode 5 (2004): Design of timber structures - Part 1-1: General and rules for buildings. CEN. (EN 1995-1-1).

Flint, AR (1952): The lateral stability of unrestrained beams. Engineering, Vol 173, 65-67.

Forest Products Laboratory (FPL) (2010): Wood handbook - Wood as an Engineering Material. Madison, U.S.

Hindman, DP *et al.* (2005a): Measurement and prediction of lateral torsional buckling loads of composite wood materials: rectangular sections. Madison, WI, ETATS-UNIS: Forest Products Society.

Hindman, DP *et al.* (2005b): Measurement and prediction of lateral torsional buckling loads of composite wood materials: I-joist sections. Forest Products Journal;55(10):43–8.

Hooley, RF & Madsen, B (1964): Lateral stability of glued laminated beams. Journal of the Structural Division 90:201–18.

Hu, Y *et al.* (2017a): Effect of eccentric lateral bracing stiffness on lateral torsional buckling resistance of wooden beams. International Journal of Structural Stability and Dynamics;1850027.

Hu Y *et al.* (2017b): Lateral torsional buckling of wooden beams with midspan lateral bracing offset from section midheight. Journal of Engineering Mechanics;143:04017134.

Pelletier, B & Doudak, G (2019): Investigation of the lateral-torsional buckling behaviour of engineered wood I-joists with varying end conditions. Engineering Structures 187: 329-340.

Sahraei, A *et al.* (2018): Simplified expressions for elastic lateral torsional buckling of wooden beams. Engineering Structures 174: 229-241.

St-Amour, R & Doudak, G (2018): Experimental and numerical investigation of lateral torsional buckling of wood I-joists. Canadian Journal of Civil Engineering 45.1: 41-50.

Timoshenko, S & Gere, J (1961): Theory of elastic stability, 2nd ed. New York: McGraw-Hill.

Vlasov, VZ (1961): Thin-walled elastic beams. 2nd. ed. Israel Program for Scientific Translations, Jerusalem.

Xiao, Q *et al.* (2014): Lateral torsional buckling of wood beams: FEA modelling and sensitivity analysis. World conference on timber engineering. Quebec City, Canada.

Xiao, Q *et al.* (2017): Numerical and experimental investigation of lateral torsional buckling of wood beams. Engineering Structures 151:85–92.

DISCUSSION

The paper was presented by G Doudak

H Blass stated that the original bucking equation is based on constant or uniform moment. He asked about the effect of different length factor (US 1.84, Canada 1.92 and EU 1.0). G Doudak replied that load applied on top of the beam is the reason. H Blass said that load cannot be applied on top of the beam if there is a uniform moment. Further E in the wide direction could be different from E in the narrow face and mentioned that the product E · G is taken as mean value in EC 5..

A Frangi stated that the proposal is complicated and asked about imperfections. G Doudak said the equation in the current standard is not usable for many load and support conditions. He said geometric nonlinearity is important but is not considered here.

H Kreuzinger received clarification that it is necessary to run a model to go from unbraced length to obtain effective length.

M Schenk asked if is this needed in the code as there are many cases in the code where solutions are not available. He queried whether this should be part of education for background rather than a code provision. M Schenk and G Doudak discussed the need of information for stiffness and imperfection. There were further comments on how much mechanics is needed in design standards with calculation methods existing outside the code.

U Kuhlmann and G Doudak discussed the differences between European and Canadian approaches with proposal focusing on the buckling range.

G Hochreiner asked about the combined loading case. G Doudak said the Canadian code considers this aspect.

P Dietsch mentioned that a large part of the given systems are already covered in e.g. the German National Annex to EC5 and suggested to study also European literature on this item.

Shear stiffness and strength of European ash glued laminated timber

Pedro Palma, Empa – Swiss Federal Laboratories for Materials Science and Technology, Structural Engineering Research Laboratory, Switzerland

René Steiger, Empa – Swiss Federal Laboratories for Materials Science and Technology, Structural Engineering Research Laboratory, Switzerland

Thomas Strahm, neue Holzbau AG, Switzerland

Ernst Gehri, Prof. emeritus ETH Zürich, Switzerland

Keywords: shear strength, shear modulus, glued laminated timber, hardwood, experimental research, size effect

1 Introduction

1.1 Background

The determination of shear properties, namely the shear modulus *G* and shear strength f_v, has been the focus of decade-long discussions at CIB-W18 and INTER Meetings (Foschi and Barrett 1980; Madsen 1995; Lam et al. 1997; Riyanto and Gupta 1998; Yeh and Williamson 2001; Brandner et al. 2007; Steiger and Gehri 2011; Brandner et al. 2012). In the ongoing revision of EN 1995-1-1:2004 *Eurocode 5*, the determination of shear strength has also been under active discussion, namely regarding conversion factors required to convert results from small-scale tests into values that represent the behaviour of the material in a structure. As pointed out, e.g., by Ehrhart et al. (2020), the main issues with the experimental determination of the shear strength parallel to the grain are the: i) influence of perpendicular-to-the-grain stresses; ii) influence of volume- and geometry-related parameters and; iii) incidence of unrelated failure modes.

Regarding the influence of perpendicular-to-the-grain stresses, on small-scale specimens the presence of tensile perpendicular-to-the-grain tensile stresses reduces the shear strength, whereas the presence of low perpendicular-to-the-grain compressive stresses increases (or at least it does not decrease) the shear strength (Mistler 1979; Spengler 1982). Most of these tests, however, were carried out on small clear specimens (Sandhaas 2012). The incidence of unrelated failure modes, namely in bending and compression perpendicular-to-the-grain arises mostly in tests on large-scale specimens and is due to the test and load-application configurations. Finally, the influence of volume-related parameters arises from shear being a brittle failure mode and, therefore, dependent on the theoretical higher probability of a strength-reducing feature occurring in a larger stressed volume.

1.2 Full-scale beam tests

Previous studies have concluded that realistic values of shear strength cannot be based on tests on small-scale specimens, such as those prescribed by EN 408:2010, but should instead be based on full-scale beam tests (Schickhofer 2001; Yeh and Williamson 2001; Klöck 2005; Gehri 2010; Aicher and Ohnesorge 2011). Shear failures are brittle and, therefore, the shear strength depends on the stressed volume. In this cases, it is common to relate the strength to a reference volume V_{ref} (or dimension) in the form of a power law $(V/V_{\mathrm{ref}})^{-k}$. Stress states of pure shear are difficult to materialise experimentally and hardly occur in real structures, therefore the test configurations should mostly aim to represent the conditions to which the material is subjected in reality. As already mentioned, an issue with using bending tests to determine the shear strength has been the high number of bending failures that tend to occur. To overcome this, beams with I-shaped cross sections have been used and at a certain point they were even included in the draft amendment to EN 408:2007/prA1:2007, even though they were finally not adopted. The main shortcomings of these beams are the bigger preparation effort, a more complicated calculation of shear stresses and shear modulus, and stress concentrations in the web-flange transition.

Gehri (2010) proposed the test configuration in Figure 1.1. This configuration comprises a simple three-point bending test and a beam with rectangular cross-section, allowing for an easy determination of shear strength and shear modulus. To ensure that the shear stresses are as constant as possible over the entire shear field, without significant perpendicular-to-the-grain stresses, the applied forces are introduced using glued-in rods (GiRs), namely the GSA® system developed by *neue Holzbau* AG, and not through "conventional" compressive perpendicular-to-the-grain stresses (Steiger and Gehri 2011). Since the shear strength of hardwood is higher than that of softwood glued laminated timber (GLT), the requirements for the load-transfer system are also higher, otherwise the shear strength of hardwood could not be captured experimentally. The shear fields proposed by Gehri (2010) have a ratio $\alpha = L_v/h = 1.75$, avoiding the bending failures that come with high values of α and still remaining within the classical beam theory with $\alpha > 1.5$.

Ehrhart (2019) performed shear tests under an asymmetric four-point bending configuration, based on a test configuration developed by Basler et al. (1960), on beams with an I-shaped cross section (Figure 1.2). In comparison with 3-point bending tests, this configuration allows for longer shear fields for the same beam height and bending moment, which gives the possibility to study the influence of the various geometric parameters over broader ranges.

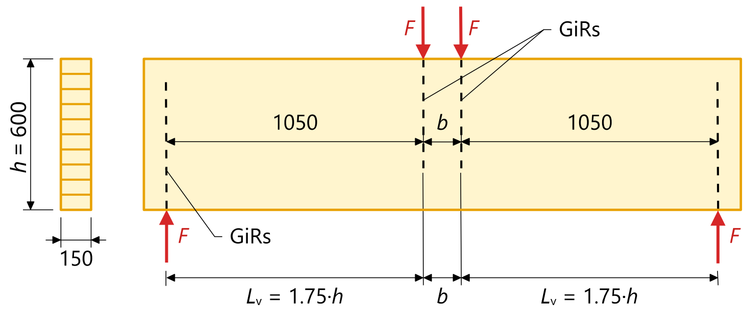

Figure 1.1. Three-point bending tests configuration proposed by Gehri (2010) for the determination of shear properties.

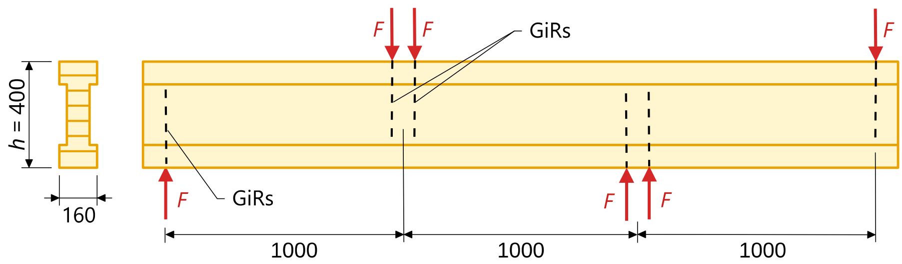

Figure 1.2. Asymetric four-point bending tests performed by Ehrhart (2019) for the determination of shear properties.

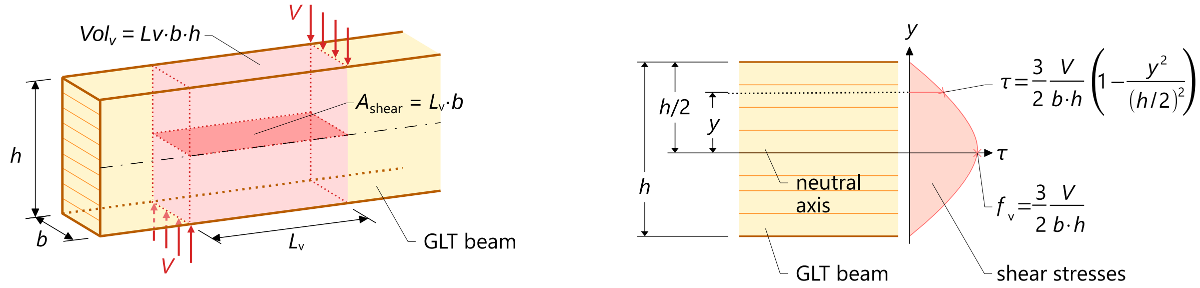

Figure 1.3. Geometric parameters and distribution of shear stresses.

For structural engineering practice, the values of shear strength must be adjusted for the actual climatic and loading conditions and geometry of the structural member. It is therefore of interest to study the influence of geometric parameters on the shear strength (Figure 1.3), namely those that are easily available to the designer, since the shear strength of GLT is not correlated (or slightly negatively correlated) to the strength classes (EN 14080:2013). The most straightforward parameter is the beam height h, since the volume under the higher shear stresses around the neutral axis is correlated to the beam height. The shear length L_v is also a parameter of interest, since it is proportional to the shear crack area. The volume of the shear field Vol_v is also a relevant parameter, but it is not always easy to determine, since it depends on the loading configuration and might be disturbed by perpendicular-to-the-grain stresses. Therefore, test configurations should ensure that shear stresses are as constant as possible over the entire shear field, without significant perpendicular-to-the-grain stresses. This is possible if the applied forces are introduced using GiRs, as mentioned above.

1.3 Objectives and scope

The objectives of the study presented in this paper were to:

- obtain knowledge on the influence of the member size (geometrical parameters) and of the test configuration on the shear strength of softwood (spruce) and hardwood (ash) GLT;
- develop tests methods for the experimental determination of the shear stiffness and strength parallel to the grain of GLT beams for two fields of application:
    - research – where it is important to obtain only shear failures and where it is possible to implement more complicated test set-ups and use advanced measurement methods (e.g. digital image correlation);
    - GLT production – where simple test set-ups (e.g. 3-point bending tests) and measurement and evaluation methods are required;
- define the reference dimensions for cross-sections that meet the requirements for the two abovementioned fields of application;
- propose simple relationships to account for size effects in design standards (SIA 265:2021 and EN 1995-1-1:2004)

The experimental research presented in this paper was conducted on full-scale glued laminated timber (GLT) beams made of European ash (*Fraxinus excelsior* L.). For comparison purposes, tests were also performed on GLT made of Norway spruce (*Picea abies* (L.) H. Karst.).

2 Experimental research

2.1 Three-point bending tests on spruce GLT

2.1.1 Materials and methods

The company *neue Holzbau AG* performed preliminary 3-point bending tests on spruce (*Picea abies* (L.) H. Karst.) GLT beams (Figure 2.1 and Table 2.2). The test specimens were made from spruce GLT of strength class GL28c, with T14 inner laminations and T26 outer laminations. The lower outer laminations of specimens FI-2.2-4 had no finger joints. To homogenise the inner zone, the T14 laminations were limited to MOEs between 9000 and 13000 $N{\cdot}mm^{-2}$ and densities between 380 and 450 $kg{\cdot}m^{-3}$. The load-application zones were reinforced with the GiRs (GSA® system).

The tests were performed under force control. The shear modulus G was determined based on the shear field method, with square measurement fields with side lengths $h/2$. The shear strength f_v was calculated as $f_v = 3/2{\cdot}F/(b{\cdot}h)$.

2.1.2 *Results*

The results of the 3-point bending tests on spruce GLT are presented in Table 2.2 and Figure 2.2. The mean shear modulus was G_{mean} = 603 N·mm^{-2} (4% coefficient of variation) and showed no size dependency. The global mean shear strength was $f_{v,mean}$ = 4.0 N·mm^{-2} (18% coefficient of variation), but the shear strength showed a clear size dependency that can be described as a function of the beam height h by

$$f_v = 511 \cdot h^{-0.76} = \underbrace{4.0}_{\frac{511}{600^{0.76}}} \left(\frac{600}{h}\right)^{0.76} \tag{1}$$

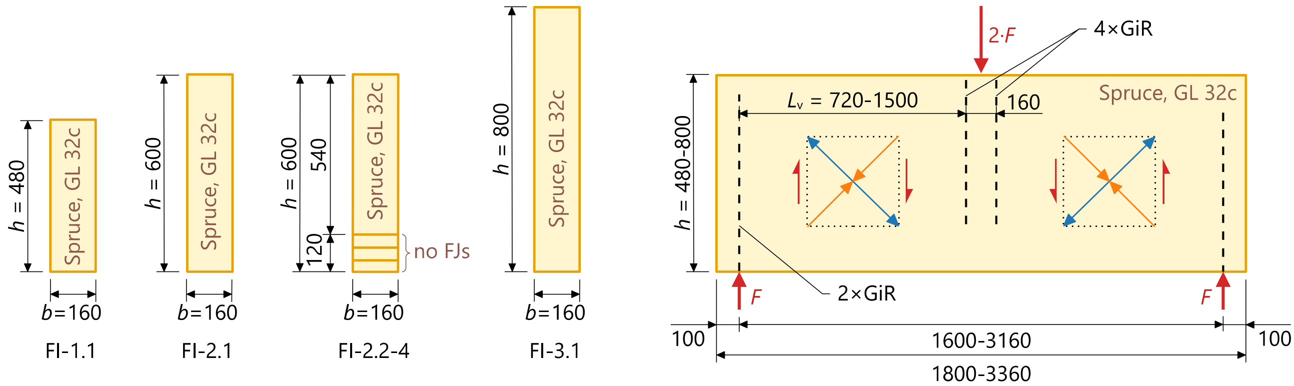

Figure 2.1. Three-point bending tests on spruce GLT: geometry of test specimens and test configuration.

Table 2.1. 3-point bending tests on spruce GLT: geometry of test specimens and test configuration.

Test configuration		Cross-section Width b [mm]	Height h [mm]	Shear field Length L_v [mm]	Ratio $\alpha = L_v/h$ α [mm·mm^{-1}]	Area A_{shear} [mm^2]	Volume Vol_v [m^3]
FI-1.1	(n=3)	160	480	768	1.6	122880	0.059
FI-2.1	(n=3)	160	600	960	1.6	153600	0.092
FI-2.2	(n=1)	160	600	720	1.2	115200	0.069
FI-2.3	(n=1)	160	600	1200	2.0	192000	0.115
FI-2.4	(n=1)	160	600	1500	2.5	240000	0.144
FI-3.1	(n=3)	160	800	1280	1.6	204800	0.164

Table 2.2. Results of the 3-point bending tests on spruce GLT.

Test configuration		Shear modulus G_{mean} [N·mm^{-2}]	CoV [ ]	Shear strength $f_{v,mean}$ [N·mm^{-2}]	CoV [ ]
FI-1.1	(n=3)	611	3%	5.1	8%
FI-2.1	(n=3)	616	5%	3.8	13%
FI-2.2	(n=1)	587	n.a.	4.2	n.a.
FI-2.3	(n=1)	567	n.a.	3.2	n.a.
FI-2.4	(n=1)	627	n.a.	3.9	n.a.
FI-3.1	(n=3)	592	2%	3.4	3%
All	(n=12)	603	4%	4.0	18%

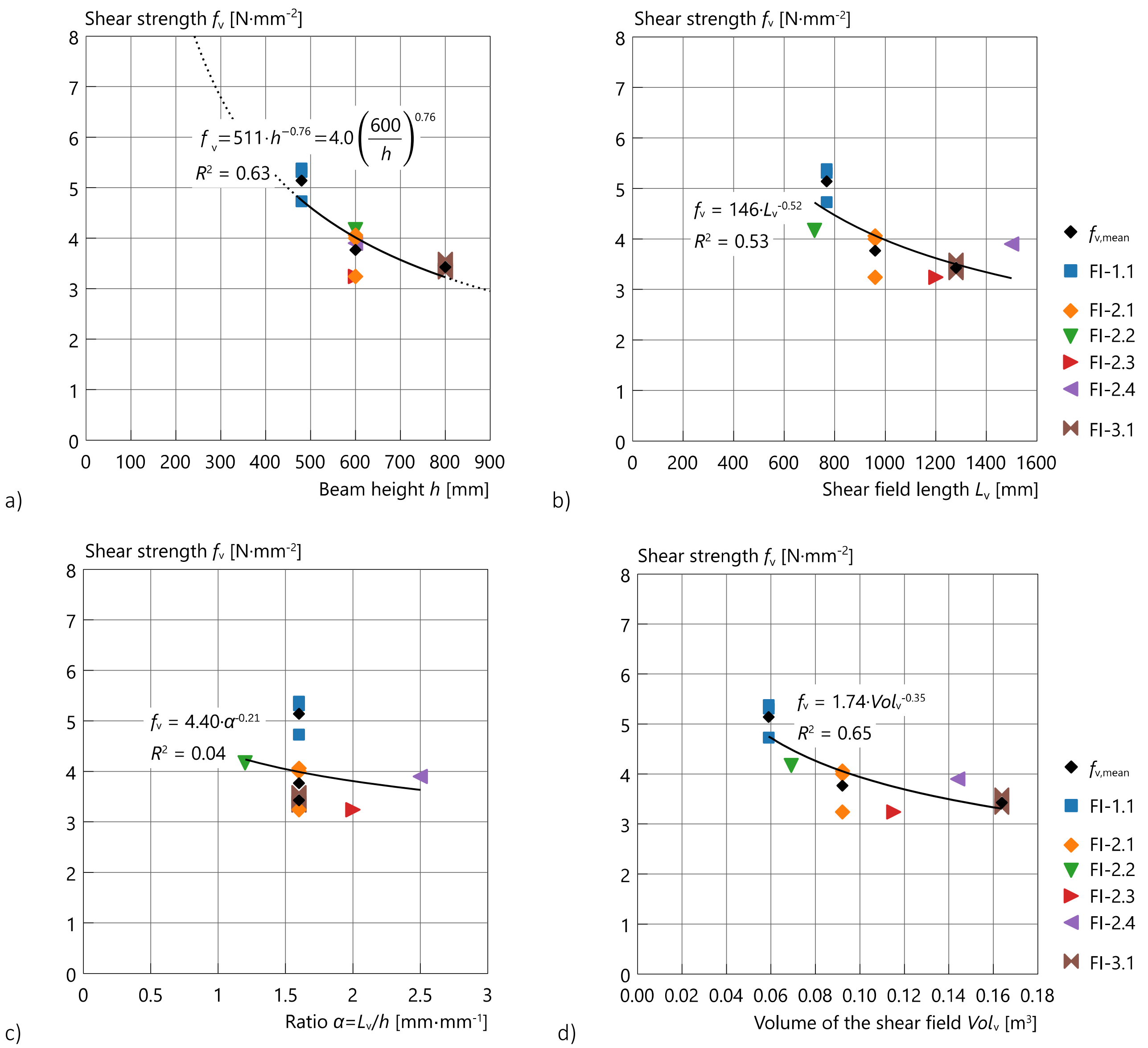

Figure 2.2. Results of the 3-point bending tests on spruce GLT. Shear strength f_v as a function of the: a) beam height h; b) length of the shear field L_v; c) ratio $\alpha=L_v/h$; and d) volume of the shear field Vol_v.

2.2 Three-point bending tests on ash GLT

2.2.1 Materials and methods

The 3-point bending tests on European ash (*Fraxinus excelsior* L.) GLT beams (Figure 2.3 and Table 2.3) were performed at the Structural Engineering Research Lab of Empa. The test specimens were made from ash GLT of strength class GL48c "special", with T33 laminations and three T50 outer laminations, without finger joints, in the tension zone. The mean density of the test specimens was 640 kg·m^{-3} (3% coefficient of variation). The load-application zones were reinforced with GiRs (GSA® system).

The tests were performed under force control. The shear modulus G was determined based on the shear field method, with square measurement fields with side lengths $h/2$. The shear strength f_v was calculated as $f_v = 3/2 \cdot F/(b \cdot h)$.

2.2.2 Results

The results of the 3-point bending tests on ash GLT are presented in Table 2.4 and Figure 2.5. The mean shear modulus was G_{mean} = 1162 N·mm^{-2} (6% coefficient of variation) and showed no size dependency (Figure 2.4). The global mean shear strength was $f_{v,mean}$ = 10.2 N·mm^{-2} (14% coefficient of variation). Some size-dependency of the shear strength can be observed at the mean-value level, but the scatter of the results

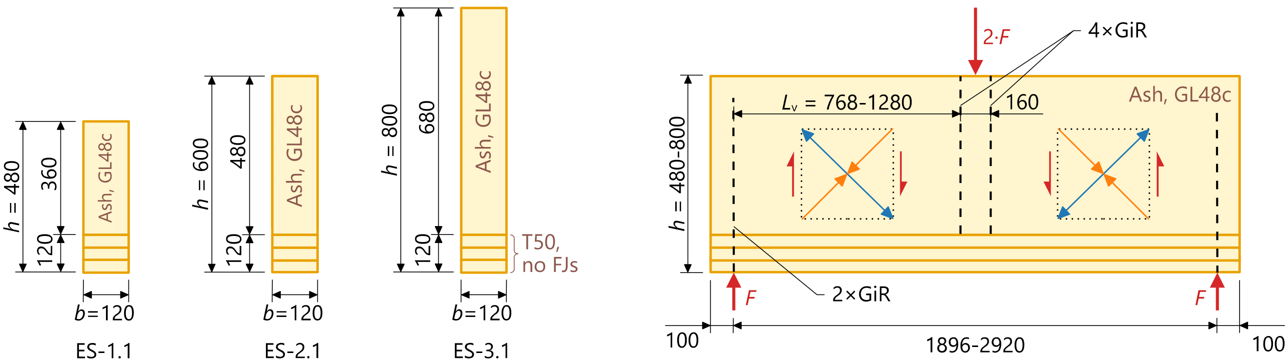

Figure 2.3. Three-point bending tests on ash GLT: geometry of test specimens and test configuration (dimensions in mm, drawing not to scale).

Table 2.3. Three-point bending tests on ash GLT: geometry of test specimens and test configuration.

Test configuration		Cross-section		Shear field			
		Width	Height	Length	Ratio $\alpha = L_v/h$	Area	Volume
		b	h	L_v	α	A_{shear}	Vol_v
		[mm]	[mm]	[mm]	[mm·mm^{-1}]	[mm^2]	[m^3]
ES-1.1	(n=3)	120	480	768	1.6	92160	0.044
ES-2.1	(n=3)	120	600	960	1.6	115200	0.069
ES-3.1	(n=3)	120	800	1280	1.6	153600	0.123

make it less clear than for the equivalent spruce GLT beams. The shear strength can be described as a function of the beam height h by

$$f_v = 34 \cdot h^{-0.19} = 10.2 \left(\frac{600}{h}\right)^{0.19} \quad (2)$$

The position of the longitudinal shear cracks in the beam height was above the neutral axis in approximately 70% of the tests and below in approximately 30% of the tests (Figure 2.10). For beam heights h = 480 and 600 mm, the shear cracks occurred within 25% of the beam height above the neutral axis (i.e. in the zone under longitudinal compressive stresses), which corresponds to shear stresses higher than $0.75 \cdot \tau_{max}$, with $\tau_{max} = 1.5 \cdot V/(b \cdot h)$. For the three beams with height h = 800 mm, the shear cracks occurred within 15 and 20% of the beam height above and below the neutral axis, respectively, which corresponds to shear stresses higher than $0.84 \cdot \tau_{max}$, with $\tau_{max} = 1.5 \cdot V/(b \cdot h)$.

The mean maximum bending stresses reached when the shear failures occurred were $\sigma_{m,max,mean}$ = 70.9 N·mm^{-2} (15% coefficient of variation) and no bending failures happened.

Table 2.4. Results of the 3-point bending tests on ash GLT.

Test configuration		Shear modulus G_{mean} [N·mm^{-2}]	CoV [ ]	Shear strength $f_{v,mean}$ [N·mm^{-2}]	CoV [ ]
ES-1.1	(n=3)	1228	19%	10.7	18%
ES-2.1	(n=3)	1117	15%	10.4	16%
ES-3.1	(n=3)	1132	8%	9.6	10%
All	(n=12)	1162	15%	10.2	14%

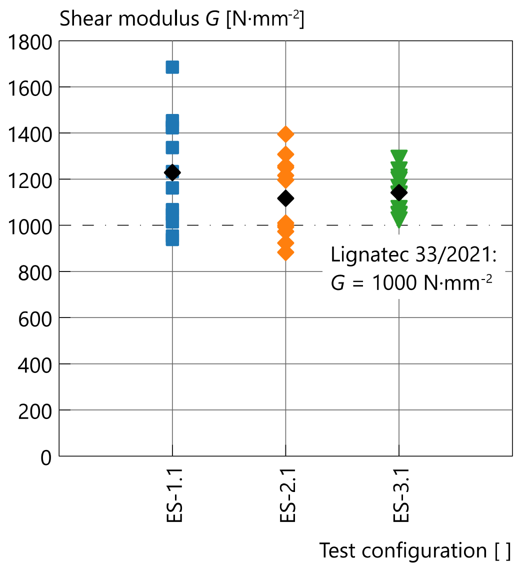

Figure 2.4. Results of the 3-point bending tests on spruce GLT – shear modulus G for the different test configurations.

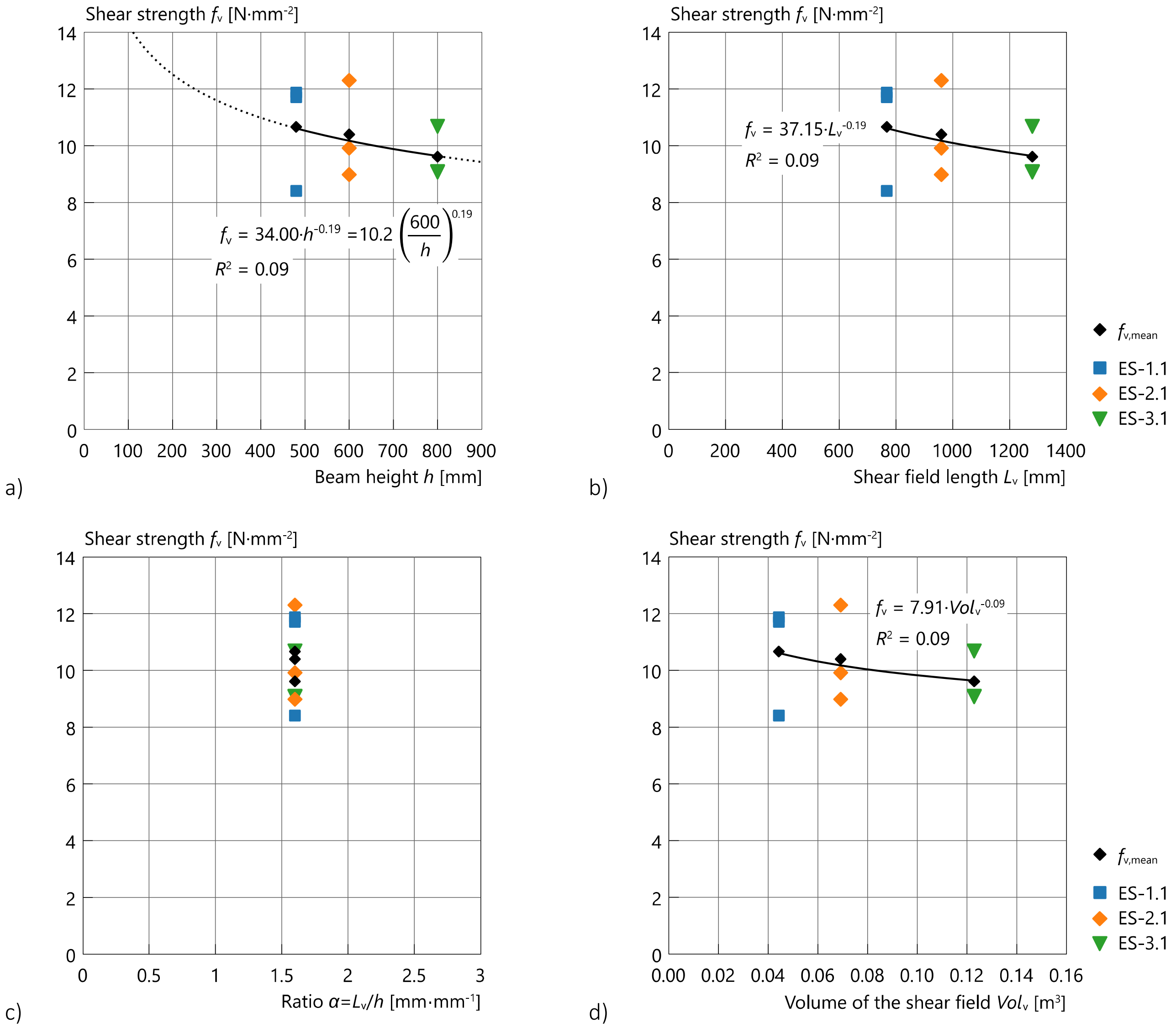

Figure 2.5. Results of the 3-point bending tests on spruce GLT – shear strength f_v as a function of the: a) beam height h; b) length of the shear field L_v; c) ratio $\alpha = L_v/h$; and d) volume of the shear field Vol_v.

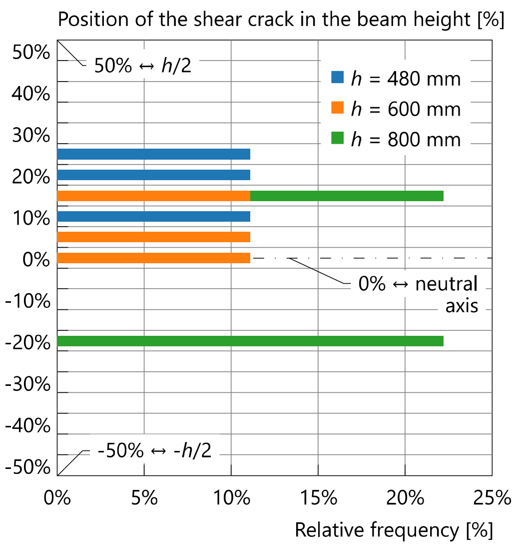

Figure 2.6. Results of the 3-point bending tests on spruce GLT – Histograms of the position of the longitudinal shear crack in the beam height, grouped by the beam height h.

2.3 Asymmetric 4-point bending tests on ash GLT

2.3.1 Materials and methods

The asymmetric 4-point bending tests on ash (*Fraxinus excelsior* L.) GLT beams were also performed at the Structural Engineering Research Lab of Empa. The test specimens (Figure 2.7 and Table 2.5) were made from ash GLT of strength class GL40c, except test specimens ES-2.5, which were made from ash GLT of strength class GL48c "special", with T33 inner laminations and three T50 outer laminations, without finger joints, in the tension zones. The mean density of the test specimens was 664 kg·m^{-3} (3% coefficient of variation). The load-application zones were reinforced with GiRs (GSA® system).

The tests were performed under force control. This test configuration was more difficult to implement, namely because both reaction forces (supports 1 and 2) had to be

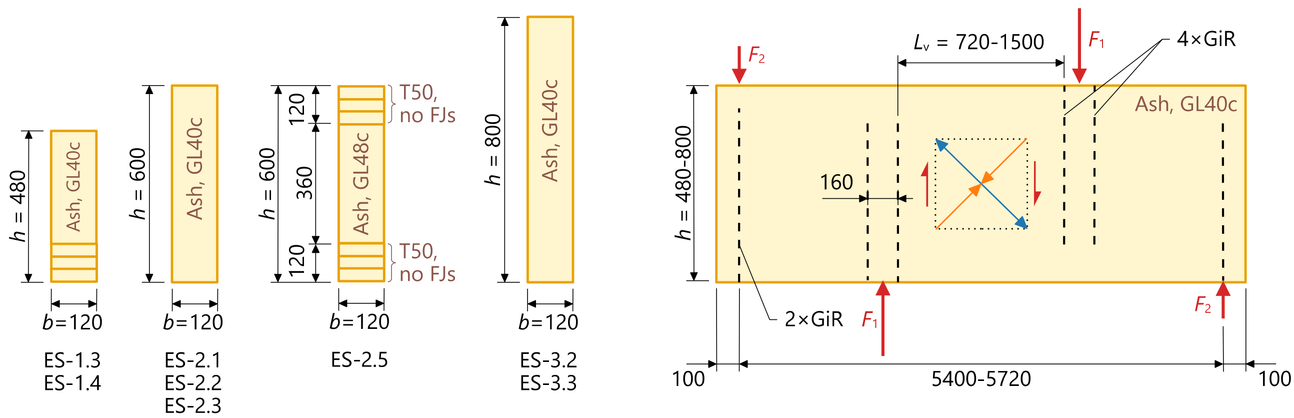

Figure 2.7. Asymmetric 4-point bending tests on ash GLT: geometry of test specimens and test configuration (dimensions in mm, drawing not to scale).

Table 2.5. Asymmetric 4-point bending tests on ash GLT: geometry of test specimens and test configuration.

Test configuration		Cross-section Width b [mm]	Height h [mm]	Shear field Length L_v [mm]	Ratio $\alpha = L_v/h$ α [mm·mm^{-1}]	Area A_{shear} [mm^2]	Volume Vol_v [m^3]
ES-1.3	(n=3)	120	480	768	1.6	92160	0.044
ES-1.4	(n=3)	120	480	960	2.0	115200	0.055
ES-2.2	(n=3)	120	600	720	1.2	86400	0.052
ES-2.3	(n=5)	120	600	960	1.6	115200	0.069
ES-2.4	(n=3)	120	600	1200	2.0	144000	0.086
ES-2.5	(n=3)	120	600	1500	2.5	180000	0.108
ES-3.2	(n=3)	120	800	960	1.2	115200	0.092
ES-3.3	(n=3)	120	800	1280	1.6	153600	0.123

measured and vertical displacements of both load-application points had to be the same, to ensure symmetry of applied loads and support reactions. The shear modulus *G* was determined based on the shear field method, with square measurement fields with side lengths $h/2$. The shear strength f_v was determined calculated as $f_v = 3/2 \cdot (F_1 - F_2)/(b \cdot h)$ (see Figure 2.7).

2.3.2 Results

The results of the asymmetric 4-point bending tests on ash GLT are presented in Table 2.6. The mean shear modulus was $G_{mean} = 1120$ N·mm^{-2} (6% coefficient of variation) and showed no size dependency (Figure 2.8). The global mean shear strength was $f_{v,mean} = 12.2$ N·mm^{-2} (15% coefficient of variation). Some size-dependency of the shear strength can be observed at the mean-value level, but the scatter of the results make it less clear than for the equivalent spruce GLT beams. The shear strength can be described as a function of the beam height *h* by

$$f_v = 127 \cdot h^{-0.37} = 12.2 \left(\frac{600}{h}\right)^{0.37} \tag{3}$$

The position of the longitudinal shear cracks in the beam height was above the neutral axis in approximately 60% of the tests and below in approximately 40% of the tests (Figure 2.10). All but one shear crack occurred within ±20% of the beam height from the neutral axis, which corresponds to shear stresses higher than $0.84 \cdot \tau_{max}$, with $\tau_{max} = 1.5 \cdot V/(b \cdot h)$

The mean maximum bending stresses reached when the shear failures occurred were $\sigma_{m,max,mean} = 47.3$ N·mm^{-2} (29% coefficient of variation) and no bending failures happened.

Table 2.6. Results of the asymmetric 4-point bending tests on ash GLT.

Test configuration		Shear modulus G_{mean} [N·mm^{-2}]	Shear modulus *CoV* [ ]	Shear strength $f_{v,mean}$ [N·mm^{-2}]	Shear strength *CoV* [ ]
ES-1.3	(*n*=3)	1097	5%	11.5	13%
ES-1.4	(*n*=3)	1108	4%	12.3	12%
ES-2.2	(*n*=3)	1105	4%	13.9	10%
ES-2.3	(*n*=5)	1124	12%	13.9	12%
ES-2.4	(*n*=3)	1124	4%	12.6	10%
ES-2.5	(*n*=3)	1092	3%	12.5	4%
ES-3.2	(*n*=3)	1172	6%	9.8	3%
ES-3.3	(*n*=3)	1134	5%	10.3	11%
All	(*n*=26)	1120	6%	12.2	15%

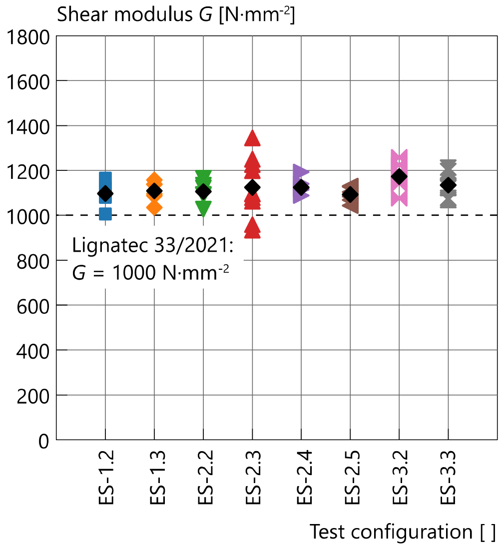

Figure 2.8. Results of the asymmetric 4-point bending tests on ash GLT – shear modulus G for the different test configurations.

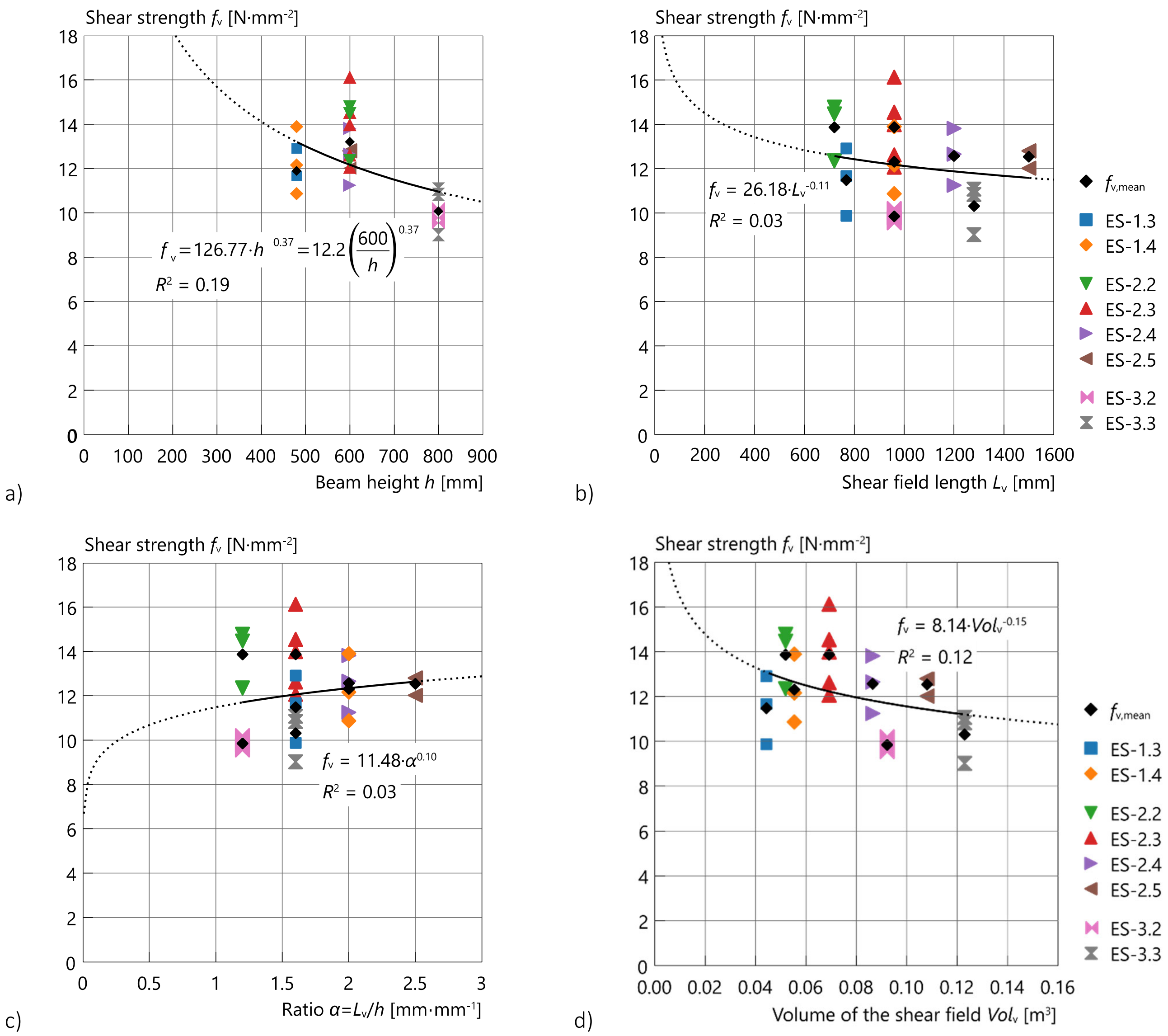

Figure 2.9. Results of the asymmetric 4-point bending tests on ash GLT – shear strength f_v as a function of the: a) beam height h; b) length of the shear field L_v; c) ratio $\alpha = L_v/h$; and d) volume of the shear field Vol_v.

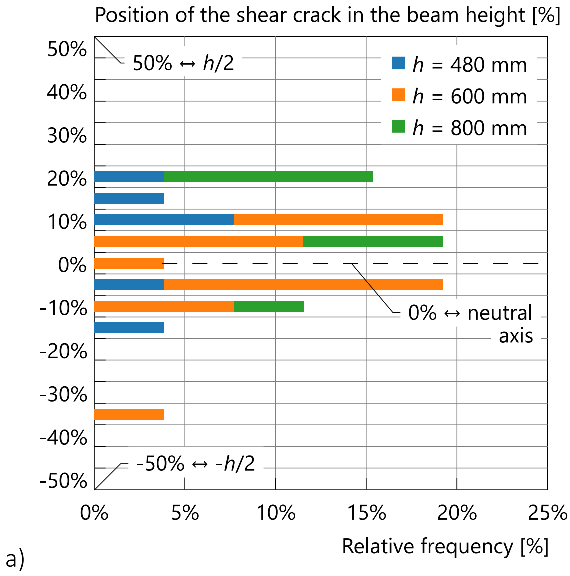

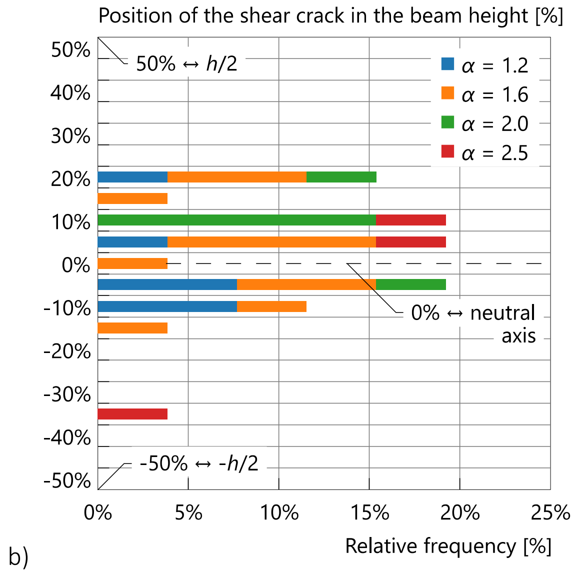

Figure 2.10. Results of the asymmetric 4-point bending tests on ash GLT – histograms of the position of the longitudinal shear crack in the beam height: a) results grouped by the beam height h; b) results grouped by the ratio $\alpha = L_v/h$.

3 Discussion and conclusions

3.1 Test configurations

From a quality-control point of view, e.g. to check if a specified or declared material property (which in effect means a system value linked to a controlled procedure) is met, the simpler 3-point bending test configuration is adequate. The asymmetric 4-point bending test allows for a broader range of geometric parameters, namely higher $\alpha = L_v/h$ ratios, given the higher shear forces for the same bending moment. It is better suited to study the shear behaviour of timber beams but it is also significantly more complicated to perform. Reinforcement with GiRs is necessary to ensure a uniform shear field and to apply the required forces, in particular for hardwood GLT.

3.2 Reference size of test specimens

The test results showed that it is possible to test beams with cross-sectional dimensions of up to 160×800 mm^2 for spruce GLT and 120×800 mm^2 for ash GLT, but the applied forces are quite high (up to 550 and 1150 kN, respectively). Since the bending properties are given for a reference beam height h = 600 mm (e.g. EN 14080:2013, SIA 265:2021), it makes sense to adopt this dimension as the reference height, i.e. h_{ref} = 600 mm.

3.3 Shear modulus *G*

The shear modulus showed no size dependency. The stiffness of the tension and compression diagonals in the shear fields showed, however, some dependency on the ratio $\alpha = L_v/h$. The obtained mean values were G_{mean} = 1162 (CoV 6%) and 1120 N·mm^{-2} (CoV 6%), for the 3-point and asymmetric 4-point bending tests, respectively. This is in good agreement with the value G_{mean} = 1000 N·mm^{-2} specified in the publication Lignatec 33/2021.

3.4 Shear strength f_v

The obtained shear strengths had mean values $f_{v,mean}$ = 10.2 (CoV 14%) and 12.2 N·mm^{-2} (CoV 15%), for the 3-point and asymmetric 4-point bending tests, respectively (Figure 3.1). The test configuration showed a marked influence on the shear strength and on the position of the failures cracks. Failure cracks in the 4-point bending tests were evenly distributed within ±0.2·*h* from the neutral axis, whereas in the 3-point bending tests the failure cracks occurred mostly within 0.25·*h* above the neutral axis.

The shear strength also showed some size dependency (obtained strength modification factors presented in Figure 3.2), even though not as evident as in the preliminary tests on spruce GLT. The exponent *k* of the strength modification factor $(h/600)^{-k}$ for the 3- and asymmetric 4-point bending tests is *k* = 0.19 and 0.37, respectively. The latter is close to the value *k* = 0.4 proposed by Ehrhart (2019) for beech GLT, but that was based on 3-point bending tests on beams with I-shaped cross sections and h_{web} < 240 mm. The publication Lignatec 33/2021 specifies a value of *k* = 0.25 for beech and ash GLT, which is approximately the average of the *k* values determined in the 3– and asymmetric 4-point bending tests. The same publication also specifies a conservative reference design shear strength $f_{v,d}$ = 3.2 N·mm^{-2} for *h* = 600 mm and all strength classes.

3.5 Size effects in design standards

In Eurocode 5 (EN 1995-1-1:2004), the design shear strength is based on the characteristic 5th-percentile values derived from tests according to EN 408:2010 and prescribed, e.g. for softwood GLT, in EN 14080:2013 as $f_{v,g,k}$ = 3.5 N·mm^{-2} for all strength classes. As already mentioned, the strength values derived from EN 408:2010 are not adequate for typical structural applications and a strength modification factor k_{cr} was introduced already in the first Amendment to Eurocode 5 (EN 1995-1-1:2004/A1:2008). This modification factor was supposed to account for the negative influence of "cracks" and the recommended value was k_{cr} = 0.67. Since it was a "nationally determined parameter", countries were able to set their own values of k_{cr}, which led to widely varying approaches. During the systematic reviews of EN 1995-1-1, there were many comments and requests regarding clarification and harmonisation of k_{cr}, namely to discretise it into more well-defined factors accounting for the influence of specific parameters on the shear strength. A revision of the verification of shear strength is ongoing within Working Group 3 of CEN/TC 250/SC 5 *Eurocode 5: Design of timber structures*. The latest draft of the revised verifications (CEN/TC 250/SC 5/WG 3 N388) includes a modification factor to account for the effect of size on the shear strength of softwood GLT that is a function of $(600/h)^{-0.2}$, i.e. sets $k = 0.2$ as proposed by Brandner et al. (2012) (based on 3-point bending tests on spruce beams with I-shaped cross sections and $h_{web} < 300$ mm). That value is in good agreement with the value $k = 0.19$ determined in the 3-point bending tests on ash GLT.

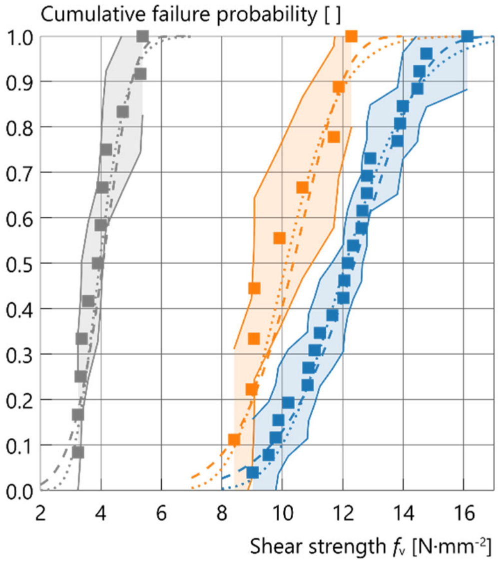

Test config.	Mean value $f_{v,mean}$ [N·mm^{-2}]	Coef. of variation $CoV(f_v)$ [ ]	5%-percentile: Empirical 5-th percentile $f_{v,0.05}$ [N·mm^{-2}]	5%-percentile: Weibull distribution $f_{v,0.05,Weibull}$ [N·mm^{-2}]	5%-percentile: Lognormal distribution $f_{v,0.05,Lognormal}$ [N·mm^{-2}]
FI-3P	4.0	19%	3.2	2.6	2.9
ES-3P	10.2	14%	8.6	7.6	8.0
ES-4P	12.2	15%	9.6	8.8	9.5

Figure 3.1. Cumulative failure distributions of the shear strength in the 3-point bending tests on spruce GLT, 3-point bending tests on ash GLT, and asymmetric 4-point bending tests on ash GLT.

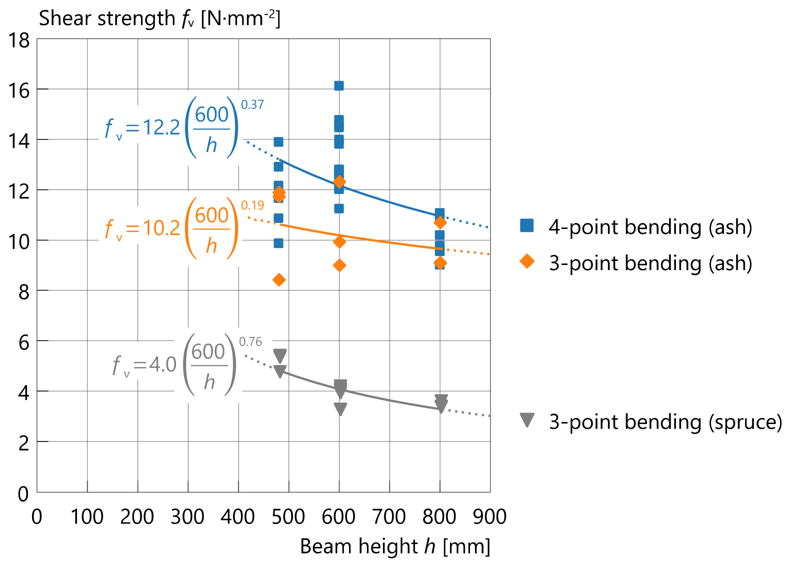

Figure 3.2. Shear strength as a function of the beam height h of the cross section for the 3-point bending tests on spruce GLT, 3-point bending tests on ash GLT, and 4-point bending tests on ash GLT.

Acknowledgments

The authors gratefully acknowledge financial support from the *Wald- und Holzforschungsförderung Schweiz* (WHFF-CH) of the Swiss *Federal Office for the Environment* (FOEN).

References

Aicher, S., and D. Ohnesorge. 2011. “Shear strength of glued laminated timber made from European beech timber.” *Eur. J. Wood Wood Prod.*, 69 (1): 143–154. https://doi.org/10.1007/s00107-009-0399-9.

Basler, K., B.-T. Yen, J. A. Mueller, and B. Thürlimann. 1960. *Web buckling tests on welded plate girders.* Technical Report. Fritz Engineering Laboratory, Lehigh University.

Brandner, R., W. Gatternig, and G. Schickhofer. 2012. “Determination of shear strength of structural and glued laminated timber.” *Proc. CIB-W18 Meet. 45*, 45-12–2, 16 p. Växjö, Sweden: CIB.

Brandner, R., E. Gehri, T. Bogensperger, and G. Schickhofer. 2007. “Determination of modulus of shear and elasticity of glued laminated timber and related examinations.” *Proc. CIB-W18 Meet. 40*. Bled, Slovenia.

Ehrhart, T. 2019. “European beech glued laminated timber.” Doctoral Thesis. Zurich, Switzerland: ETH Zurich.

Ehrhart, T., R. Steiger, M. Lehmann, and A. Frangi. 2020. “European beech (Fagus sylvatica L.) glued laminated timber: Lamination strength grading, production and mechanical properties.” *Eur. J. Wood Wood Prod.*, 78 (5): 971–984. https://doi.org/10.1007/s00107-020-01545-6.

EN 408:2007/prA1:2007. *Timber structures. Structural timber and glued laminated timber. Determination of some physical and mechanical properties*. 2007. 32. Brussels: European Committee for Standardization (CEN).

EN 408:2010+A1:2012. *Timber structures. Structural timber and glued laminated timber. Determination of some physical and mechanical properties*. 2012. 38. Brussels: European Committee for Standardization (CEN).

EN 1995-1-1:2004. *Eurocode 5: Design of timber structures – Part 1-1: General – Common rules and rules for buildings*. 2004. 123. Brussels: European Committee for Standardization (CEN).

EN 1995-1-1:2004/A1:2008. Eurocode 5: Design of timber structures – Part 1-1: General – Common rules and rules for buildings. 2008. 16. Brussels: European Committee for Standardization (CEN).

EN 14080:2013. *Timber structures – Glued laminated timber and glued solid timber – Requirements*. 2013. 106. Brussels: European Committee for Standardization (CEN).

Foschi, R., and J. Barrett. 1980. "Consideration of size effects and longitudinal shear strength for uncracked beams." *Proc. CIB-W18 Meet. 13*, 13-6–2, 9 p. Otaniemi, Finland.

Gehri, E. 2010. "Shear problems in timber engineering – Analysis and solutions." *Proc. 11th World Conf. Timber Eng. WCTE2010*, 6. Trentino, Italy.

Klöck, W. 2005. "Statistical analysis of the shear strength of glued laminated timber based on full-size flexure tests." *Otto-Graf-J.*, 16: 225–244.

CEN/TC 250/SC 5/WG 3 N 388. *Revised INF ENQ Draft clauses: Verification of shear strength*. 2022-06-17. Kupferle, F. CEN.

Lam, F., H. Yee, and J. D. Barrett. 1997. "Shear strength of Canadian softwood structural lumber." *Can. J. Civ. Eng.*, 24 (3): 419–430. NRC Research Press Ottawa, Canada. https://doi.org/10.1139/l96-119.

Lignatec 33/2021. Verklebte Laubholzprodukte für den statischen Einsatz. 2021. Zürich, Schweiz: Lignum, Holzwirtschaft Schweiz.

Madsen, B. 1995. "Shear strength of Douglas Firs timbers." *Proc. CIB-W18 Meet. 28*, 28-6–2, 37 p. Copenhagen, Denmark.

Mistler, H.-L. 1979. *Die Tragfähigkeit des am Endauflager unten rechtwinklig ausgeklinkten Brettschichtträgers*. 112. Karlsruhe, Germany: Technische Hochschule Karlsruhe.

Riyanto, D., and R. Gupta. 1998. "A comparison of test methods for evaluating shear strength of structural lumber." *For. Prod. J.*, 48 (2): 83–90.

Sandhaas, C. 2012. "Mechanical behaviour of timber joints with slotted-in steel plates." Doctoral thesis. Delft, Netherlands: Delft University of Technology (TU Delft).

Schickhofer, G. 2001. "Evaluation of glulam shear strength using a full-size four-point test method." *Proc. CIB-W18 Meet. 34*, 34-12–6, 383–409. Venice, Italy.

SIA 265:2021. *Holzbau*. 2021. 114. Zurich, Switzerland: SIA.

Spengler, R. 1982. *Festigkeitsverhalten von Brettschichtholz unter zweiachsiger Beanspruchung - Teil 1 - Ermittlung des Festigkeitsverhaltens von Brettelementen aus Fichte durch Versuche*.

Steiger, R., and E. Gehri. 2011. "Interaction of shear stresses and stresses perpendicular to the grain." *Proc. CIB-W18 Meet. 44*, 44-6–2, 14 p. Alghero, Italy.

Yeh, B., and T. Williamson. 2001. "Evaluation of glulam shear strength using a full-size four-point test method." *Proc. CIB-W18 Meet. 34*, 34-12–2, 13 p. Venice, Italy.

DISCUSSION

The paper was presented by P Palma

P Dietsch asked why k is different for Spruce and Ash. P Palma replied that he is also surprised by the findings of the Spruce results; with decrease in CV one expects decrease in size effect. P Dietsch commented that with the aspect ratio of the specimens, they look more like a diaphragm rather than a beam; however, the beam formula was used. P Palma agreed.

R Jockwer asked if the proposal for EC with k factor of 0.2 only applies to Glulam and if it can be applied to other products such as LVL. Palma said this is for Glulam only. P Dietsch commented that the range of application should be limited.

S Aicher commented that the exponent for Beech Glulam is similar.

F Lam commented that size effect for shear design of glulam in Canadian code is volume dependent with a reference volume of 2 m^3 and k of 0.18. F Lam asked whether the width b being a parameter of study. P Palma agreed but will not examine this now.

C Sandhaas asked if there is any issue of getting Ash. P Palmar said 20% of forest resource in Switzerland is Ash.

Size effect of glulam made of oak wood under consideration of the finite weakest link theory

Cristóbal Tapia, Materials Testing Institute, University of Stuttgart

Simon Aicher, Materials Testing Institute, University of Stuttgart

Keywords: glulam, size effect, quasibrittle behavior, stochastic strength model, oak wood

1 Introduction

The material phenomenon known as *size effect* which predicts the decrease in nominal strength with increasing size of the element, is a widely acknowledged characteristic of all brittle and quasibrittle materials. It has been verified experimentally for ceramics, concrete, timber (firstly by *Barrett*, 1974) and derived bonded wooden members subjected to bending, such as glulam (GLT) in a multiplicity of investigations (e.g. *Moody* et al. (1990), *Frese* & *Blaß* (2009), *Lam* (2011), and *Blank* et al. (2017) for GLT). The size effect was first mathematically described for perfectly brittle materials by *Weibull* (1939), in what has come to be known as the *weakest link theory*. In its most general form the concept considers a weighting of the volume subjected to tensile stresses, thus producing a dependency with the considered loading case. However, for the special case of a purely geometrical scaling, the change in nominal tensile strength is fully explained by the change in nominal size and is described by a power law. This concept has been adopted in many timber design standards, albeit with some differences in the implementation. For example, the present European timber design code EN 1995-1-1 (2010), considers a modification factor for the bending strength according to

$$k_h = \min\left\{1.1;\ \left(\frac{600}{h}\right)^{0.1}\right\} \quad , \tag{1}$$

which allows for an increase in strength for cross-sectional depths h smaller than the reference depth, yet not demanding a strength reduction for $h > 600\,\mathrm{mm}$. The latter has been changed in the new draft of prEN 1995-1-1 (2021), where k_h is applicable throughout. However, the new Eurocode 5 still differs to the more conservative approach adopted in the US (ASTM D 3737, 2018), where all three dimensions depth, d, length, L, and width, b, of the GLT element are simultaneously considered for the modification factor as

$$K_Z = \left(\frac{b_0}{b} \cdot \frac{d_0}{d} \cdot \frac{L_0}{L}\right)^{1/k} \leq 1 \quad , \tag{2}$$

where k is the species-dependant size effect exponent in the range of 8–20 and the subindices “0” denote reference values for the width, depth and length of the beam. In this case, an increase of the strength is not allowed for volumes, V, smaller than the reference volume $V_0 = b_0 \times d_0 \times L_0$, but a reduction of strength is considered for $V > V_0$, being experimentally well supported by *Lam* (2011). The Canadian size effect factor for bending is $K_{Zbg} = 1.03 \cdot (bL)^{-0.18}$, where the depth of the beam is not considered, as it is assumed that the strength is determined by the outermost lamination in tension (*Lam*, 2011). It is evident then, that although the concept of size effect has influenced many timber design standards worldwide, an overarching consensus around the issue has not yet been achieved despite several deepened theoretical and experimental investigations on the issue (e.g. *Lam* (2011), *Blank* et al. (2017), and *Frese* & *Blaß* (2009, 2016)). On the one hand, a consequent consideration of the weakest link approach demands the penalization of large GLT elements as done in the US and Canada. On the other hand, large penalizations with the current design concepts translate in rather uneconomical designs, reducing the competitiveness of GLT. The question is then whether these two issues of safety and economical viability can be reconciled to some degree under a solid theoretical framework.

The main problem with the standardized approaches to consider the size effect in glulam members stems from the rigorous assumption of Weibull theory of weakest link, thus intrinsically assuming perfect brittle behavior of the material. However, it is known (see e.g. *Brandner* et al., 2007) that wood exhibits a quasibrittle failure behavior, which is associated to a different scaling law. In fact, in recent years, a new approach for the statistical characterization of the failure behavior of quasibrittle materials has been developed in a series of works i.a. by *Bažant* & *Pang* (2007), known as the *Finite Weakest Link Theory* (FWLT). This theory is based on the concept of a *Representative Volume Element* (RVE), which is defined as the smallest volume of material whose failure will trigger the collapse of the whole structure. The strength distribution of such an RVE can be described by the so-called Weibull-Gaussian distribution, which is a Gaussian distribution with a Weibull distribution grafted at the far lower tail (*Bažant* & *Pang*, 2007). The higher the number of RVE’s present in a system (larger structures), the more relevant becomes the Weibull portion of the strength distribution of the whole structure. Eventually, the Weibull distribution dominates and brittle behavior can be assumed. The FWLT considers the cases where a relatively low number of links (RVEs) is present, and fills the gap between perfectly brittle and perfectly ductile materials (*Bažant* & *Le*, 2017), revealing a more complex but—for design purposes—potentially more convenient size effect law. Considering the above, it is reasonable to assume that the currently implemented scaling laws for glulam beams is based on wrong assumptions, presenting the opportunity to introduce a more refined and theoretically sound scaling law.

This paper is set to reanalyze experimental data for GLT beams made of oak wood subjected to pure bending and tension conditions under the scope of the finite weakest link theory. By means of stochastic simulations with a glulam strength model and using material strength distributions according to the FWLT as input parameters, it will be shown that the scaling of GLT beams can only be approximated by a power law within a certain size range. Outside this range the size effect slowly decreases, following the general tendency known from quasibrittle materials. This has the potential of drastically reducing the number and sizes of required glulam experiments for certification purposes. By focusing on an accurate characterization of boards and finger-joints according to the FWLT, a more reliable prediction can be expected from glulam simulation models.

2 Materials and methods

2.1 Materials and test configurations

This study presents experimental data of oak boards and GLT beams tested under the scope of an European Technical Approval (ETA-13/0642, 2013), also presented in *Aicher* & *Stapf* (2014). The oak wood material (*Quercus robur*, *Quercus petraea*) originates form France and was classified in strength grades LS10 and LS13 according to DIN 4074-5 (2008). All experiments were carried out in a non-climatized environment with a temperature of about 20 °C.

2.1.1 Experimental tests of oak boards and finger-joints

A total of 100 boards (50×LS10 and 50×LS13) with a planed cross-section of 100 × 20 mm^2 were tested in tension according to EN 408 (2013). The average moisture content of the boards, measured with the oven drying method, was 11 % and the measured density was 735 kg/m^3. The free length was 9 × $b = 900$ mm.

For the experiments with finger-joints the same cross-section of 100 × 20 mm^2 was used. A total of 98 finger-joints were tested (49×LS10 and 49×LS13). The average moisture content was 11 % and the measured density was 739 kg/m^3. All tensile tests were carried out in a displacement-controlled manner with a servo-hydraulic machine (maximum load capacity of 600 kN). The measured mean and standard deviation for the tensile strength of the LS10 and LS13 boards were (45.1 ± 14.4) MPa and (55.1 ± 16.9) MPa, respectively. For the finger-joints the measured tensile strengths were (44.6 ± 10.0) MPa and (42.4 ± 10.0) MPa for jointed boards of grades LS10 and LS13, respectively.

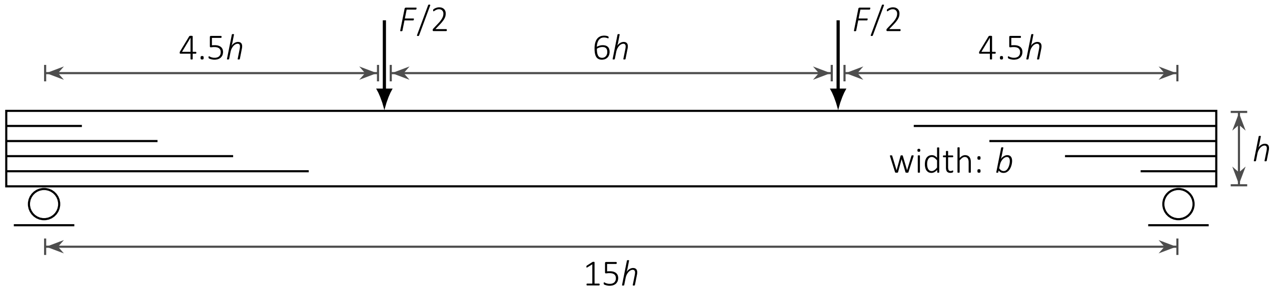

(a)

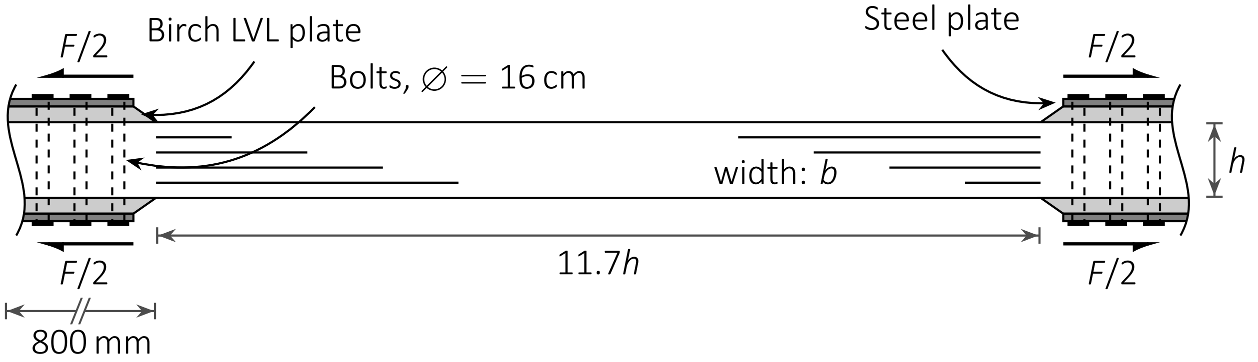

(b)

Figure 1. Experimental configurations for the (a) four-point bending and (b) tensile tests on GLT beams

2.1.2 *Experimental tests of glulam made of oak*

The GLT beams were tested both in four-point bending and tension tests. For the bending configurations three different cross-sections with width × depth of 100 × 120 mm^2, 100 × 200 mm^2 and 100 × 300 mm^2 were considered, each consisting of a total of ten specimens. The tension tests were performed with a homogeneously built-up cross-section of 100 × 120 mm^2. Each bending member cross-section was built-up inhomogeneously considering boards of the strength grade LS13 for regions located at the outer one-sixth of the cross-sectional depth, h, and LS10 boards for the inner region. The lamination thickness was throughout 20 mm and the average length of boards (inter-finger-joint distance) was about 450 mm. The average moisture content for all GLT beams was 13 % and the measured density was 740 kg/m^3.

The four-point bending tests were performed according to EN 408 (2013) with a total span length of 15h. The two loading points were placed at a distance 4.5h from the support points, leaving a central, constant moment region of 6h in length (see Fig. 1a). A total of ten beams per cross-section were loaded until failure in a constant, quasi-load-controlled regime, such that maximum load was achieved at (300 ± 120) s.

For the tension tests a free length of 1400 mm ($\approx$ 11.7h) was used. The ends of the beam were attached to two hinged steel plates, fixed to the servo-hydraulic testing machine by means of twelve bolts of 16 mm in diameter. The clamping region—about 800 mm in length—was reinforced with birch LVL plates glued onto each side, in order to reduce the chance of failure due to the splitting of the cross-section caused by the dowel-type fasteners (see Fig. 1b). For further details regarding the test configurations and experimental results, see *Aicher* & *Ruckteschell* (2011).

2.2 Scaling according to Weibull's weakest link theory

The weakest link theory was introduced by *Weibull* (1939) to describe the strength distribution and size effect of perfect brittle materials. The theory assumes that the failure of the whole structure is triggered by the weakest element (link), thus no load sharing is allowed to stronger links. Weibull noticed that the left tail of the strength distribution follows a power law, which lead to the now well-known Weibull failure probability integral (*Bažant* & *Le*, 2017, p. 24):

$$P_f = 1 - \exp\left[\int_V - \left(\frac{\sigma\left(\underline{x}\right)}{s}\right)^m dV\right] \quad , \tag{3}$$

where s is the scale parameter, $\sigma(\underline{x})$ is the *tensile* stress ($\sigma \geq 0$) at each point $\underline{x}$ and m is the so-called Weibull modulus, which is associated to the magnitude of the size-effect. When comparing different structures, it is common to define a nominal strength, σ_N, which is a maximum load parameter (*Bažant* & *Le*, 2017). In this manner, the stress field can be defined as $\sigma(\underline{x}) = \sigma_N \cdot \bar{\sigma}(\underline{\xi})$, where $\bar{\sigma}(\underline{\xi})$ is the dimensionless stress field, dependent on the dimensionless coordinate system $\underline{\xi} = \underline{x}/D$, and D is the characteristic length of the structure. These definitions allow to express Eq. (3) as

$$F(\sigma_N) = 1 - \exp\left[-\left(\frac{\sigma_N}{s}\right)^m \cdot D^{n_d} \cdot \Psi\right] \quad , \tag{4}$$

where n_d is the relevant number of dimensions of the structure (1, 2 or 3) and the factor Ψ considers the effect of the geometry and stress distribution, and is defined as

$$\Psi = \int_V \bar{\sigma}\left(\underline{\xi}\right)^m dV\left(\underline{\xi}\right) \quad . \tag{5}$$

For the case of two structures A and B, each with a different value Ψ_A and Ψ_B, a relation between their nominal strength (size effect) can be derived by applying Eq. (4) to both structures at any probability level and then equating both expressions. This results in the following scaling rule:

$$\sigma_{N_A} = \sigma_{N_B} \left(\frac{D_B}{D_A}\right)^{n_d/m} \left(\frac{\Psi_B}{\Psi_A}\right)^{1/m} \tag{6}$$

The value of Ψ for the studied bending configuration Ψ_b can be analytically derived as

$$\Psi_b = \frac{4.5}{(m+1)^2} + \frac{3}{m+1} \quad , \tag{7}$$

allowing the computation of the equivalent size of the tension specimen with regard to the bending specimen. Regarding the scaling of the nominal strength under different loading modes see also *Colling* (1986).

2.3 Finite weakest link theory

The Finite Weakest-Link theory deals with the statistical characterization of the failure behavior of quasibrittle materials, and was developed in a series of works i.a. by *Bažant* & *Pang* (2007) and *Le* et al. (2011). The theory describes the transition zone between ductile and brittle behavior by considering a power law in the lower tail of the strength distribution (brittle failure) combined with a normally distributed core (ductile failure). Such behavior is accurately represented by the so-called "grafted Weibull-Gaussian" distribution (*Bažant* & *Le*, 2017) defined as

$$F(\sigma) = \begin{cases} 1 - \exp\left[-\left(\frac{\sigma}{s}\right)^m\right] & , \sigma \leq \sigma_{\mathrm{gr}} \\ F_{\mathrm{gr}} + \frac{r_{\mathrm{f}}}{\delta\sqrt{2\pi}} \int_{\sigma_{\mathrm{gr}}}^{\sigma} \exp\left[-\left(\frac{y-\mu}{2\delta}\right)^2\right] dy & , \sigma > \sigma_{\mathrm{gr}} \end{cases} , \tag{8}$$

where σ_{gr} is the grafting point, m and s are the shape and scale parameters of the two-parameter Weibull distribution, μ and δ are the mean and standard deviation of the Gaussian core. (m is commonly referred to as the Weibull modulus.) The grafting probability, $F(\sigma_{\mathrm{gr}}) = F_{\mathrm{gr}}$, is defined as

$$F_{\mathrm{gr}} = 1 - \exp\left[-\left(\frac{\sigma_{\mathrm{gr}}}{s}\right)^m\right] \quad . \tag{9}$$

To ensure that $F(x)$ does not exceed 1, the factor r_f is used to scale the Gaussian distribution (*Bažant* & *Pang*, 2007) as

$$r_f = \frac{1 - F_{\mathrm{gr}}}{1 - \Phi_{\mathrm{gr}}(\mu, \delta)} \quad , \tag{10}$$

where $\Phi_{\mathrm{gr}}(\mu, \delta)$ is the Normal distribution $\mathcal{N}(\mu, \delta)$ evaluated at the grafting point. To ensure continuity of the PDF at σ_{gr} the condition $f\left(\sigma_{\mathrm{gr}}^-\right) = f\left(\sigma_{\mathrm{gr}}^+\right)$ must hold.

A cornerstone in this theory is the concept of representative volume element (RVE). A RVE can be defined as the smallest volume whose failure triggers the collapse of the whole structure (*Pang* et al., 2008), i.e. the weakest link in a (finite) chain. In the present

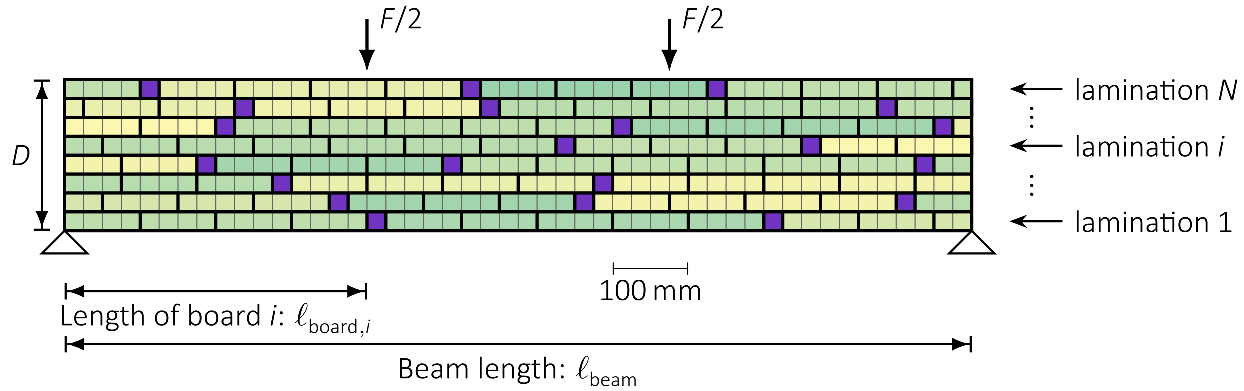

Figure 2. Illustration of geometric parameters, cell definition and distribution of material properties in the developed finite element model

work, no effort is made in trying to find the *real* RVE of the studied material. Instead, the 100 mm cells are assumed to work as RVEs, as discussed by *Tapia* & *Aicher* (2022). It should be clear though, that each cell should be thought of as a hierarchical model of links connected in series and parallel. This means that local failures may occur within this RVE prior to achieving ultimate load, as load sharing occurs internally.

2.4 Stochastic glulam strength model

A finite element (FE)-based stochastic glulam strength model was implemented in the Julia programming language (*Bezanson* et al., 2017) using the FE toolbox Ferrite.jl (*Carlsson* et al., 2022). The implementation is similar as that presented in *Tapia* (2022), where the variation of mechanical properties of boards is discretized in cells of 100 mm in length according to a vector autoregressive model, as described in *Tapia* & *Aicher* (2021, 2022). The failure of the board material and finger-joints is considered by means of an energy-based softening (see below).

2.4.1 Finite element model

The 2D FE model uses plane stress, linear quadrilateral elements with full integration and considers an orthotropic behavior for the material constitutive law. Each lamination of the GLT beam is represented by one row of elements with aspect ratio close to 1:1. Material properties for modulus of elasticity parallel to grain, $E_{0,\text{cell}}$, and tensile strength, $f_{t,0,\text{cell}}$, are assigned to each element according to the respective cell (100 mm) in which they are located (see Fig. 2). At the end of each board a finger-joint is simulated by a single element with a tensile strength value taken from the corresponding probability distribution, and an MOE value equal to the average of the two corresponding connecting board cells. The stiffness properties for the direction perpendicular to the grain and shear are assigned to each element based on the corresponding ratio $\alpha = E_{0,\text{cell}}/E_0^*$ as $E_{90,\text{cell}} = E_{90}^* \cdot \alpha$ and $G_{\text{cell}} = G^* \cdot \alpha$, with E_0^*, E_{90}^* and G^* as the respective reference values.

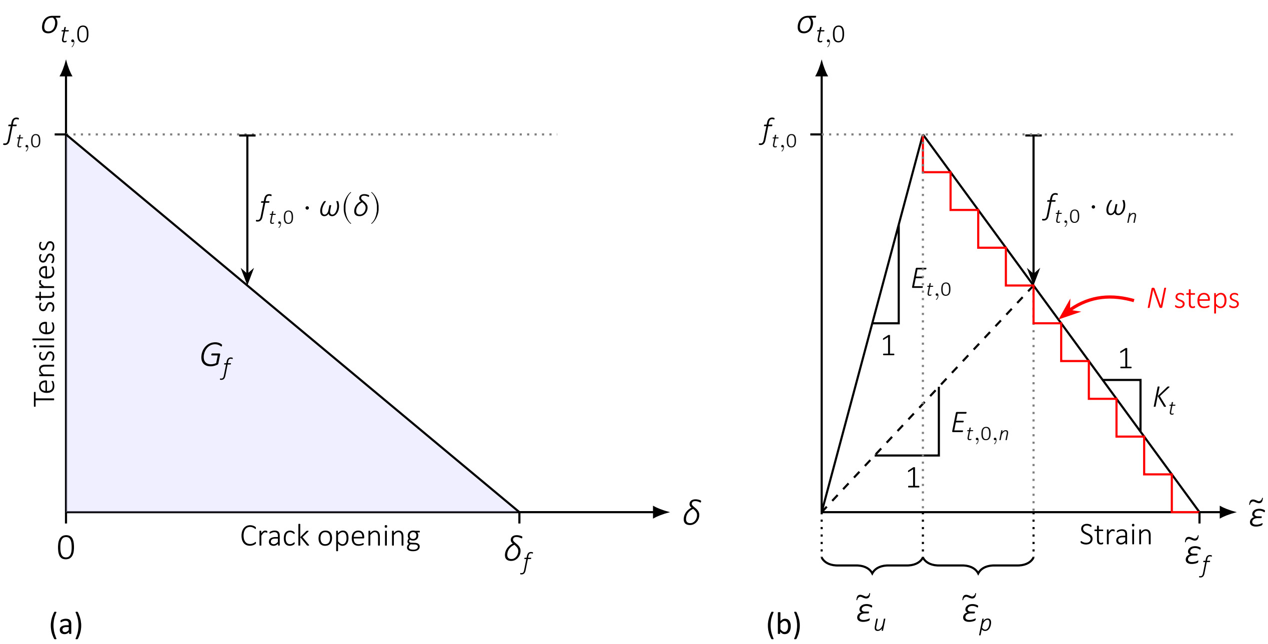

Figure 3. Illustration of fracture energy, G_f, and discretized softening curve

2.4.2 *Consideration of softening*

It has been shown in previous investigations that the consideration of softening behavior is necessary to correctly simulate the bending strength of GLT beams, as otherwise the obtained strengths are far too low (see e.g. *Blank* et al. (2017), *Tapia* (2022), and *Vida* et al. (2022)). In this study the softening is considered as in *Blank* et al. (2017), where the concept of a *smeared crack* is used. In order to avoid convergence problems during the solving of this highly non-linear problem, the system was solved considering the softening in a discrete manner as proposed by *Rots* & *Invernizzi* (2004) and also implemented by *Luo* & *Bažant* (2018). This means that the system is solved linearly for an arbitrary load, F_0, which is then scaled by a factor λ, such that $\lambda \cdot \sigma_{t,0,i}/f_{t,0,i} = 1$ for at least one element, where $\sigma_{t,0,i}$ is the maximum of the stresses evaluated at each integration point and $f_{t,0,i}$ is the corresponding strength of the element. The updated tensile strength for the next step n is computed as $f_{t,n} = f_{t,0} \cdot (1 - \omega_n)$, where ω_n is the discrete damage variable denoting the current relative position along the softening curve (see Fig. 3b). For this study the softening curve was discretized in $N = 20$ steps, which is regarded as a good compromise between accuracy and computational time according to *Luo* & *Bažant* (2018). The modulus of elasticity is modified at each step according to

$$E_{t,n} = \frac{f_{t,n}}{\tilde{\varepsilon}_u + \tilde{\varepsilon}_p} \quad , \tag{11}$$

where $\tilde{\varepsilon}_u$ can be deduced from Fig. 3 as the strain at $f_{t,0}$ and $\tilde{\varepsilon}_p = -\omega_n \cdot f_{t,0}/K_t$ with K_t as the tangent stiffness of the softening branch (see *Blank* et al. (2017) for details on computation of this value).

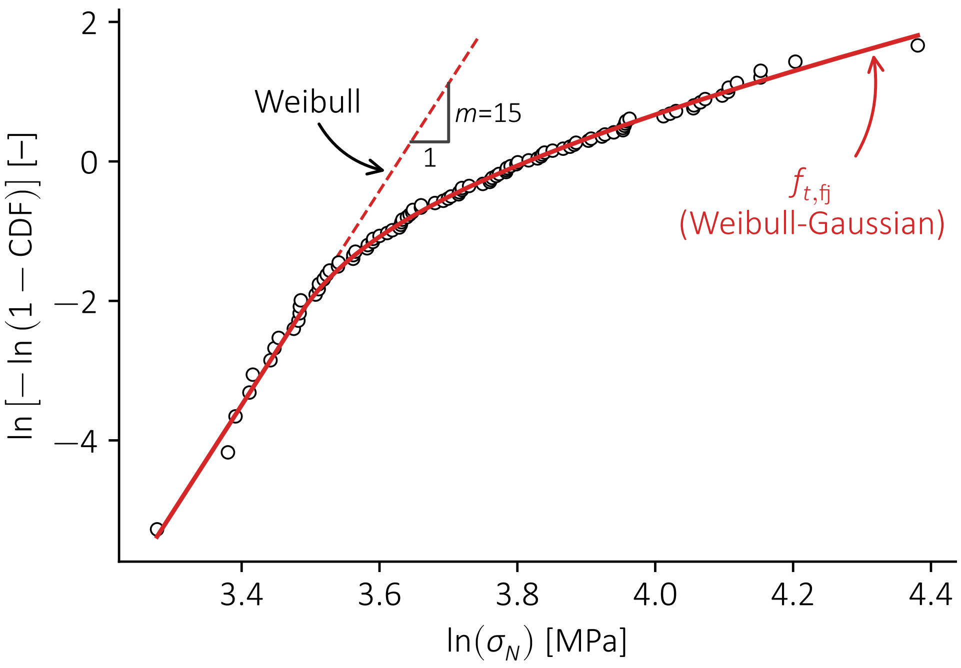

Figure 4. Tensile strength distribution of finger-joints in oak boards and fitted Weibull-Gaussian distributions

3 Statistical strength distributions of finger-joints and boards

3.1 Strength distribution of finger-joints

The empirical tensile strength distribution of the finger-joints between the regarded oak boards is shown in Fig. 4 in the so-called Weibull scale. In this scale, a dataset that follows the Weibull distribution will exhibit a linear trend, where the slope is the Weibull exponent. It is evident that the experimental results do not follow a Weibull distribution throughout the whole strength range, but only on the lower tail. This is in agreement with the behavior expected for quasibrittle materials (*Bažant* & *Le*, 2017). Therefore, a grafted Weibull-Gaussian distribution can be fitted as shown in Fig. 4. The fitting was done by first determining the parameters of the Weibull part using the first ten datapoints and then fitting the parameters σ_{gr}, and μ and σ of the Gaussian part by the maximum likelihood method. The fitted parameters are presented in Table 1. For this analysis, finger-joints belonging to both strength grades LS10 and LS13 were considered together, as there is no reason to assume large differences in joint strengths as a consequence of the grading process. This was also confirmed by the experimental data.

3.2 Strength distribution of boards

The tensile strength distributions for boards of strength grades LS10 and LS13 are presented separately in Fig. 5a in the Weibull scale. There are two main aspects about these

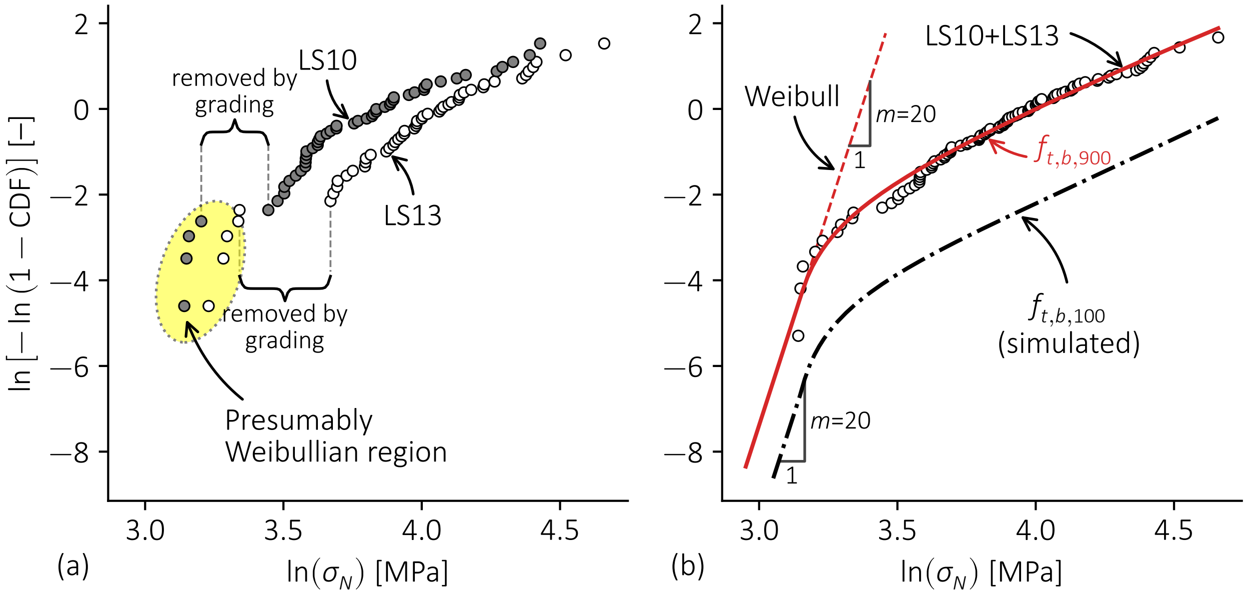

Figure 5. Tensile strength distributions of oak boards of grades LS10 and LS13; (a) experimental data for LS10 and LS13, (b) experimental LS10+LS13, fitted distribution and simulated results for cell length of 100 mm

data. Firstly, a Weibull region can be presumed at the lower tail of both distributions. This can be recognized by a rather sharp change in slope in the Weibull plot. Although not so clear as for the case of finger-joints (Fig. 4), this behavior is assumingly owed to the fact of wood being a quasibrittle material. (Note: that the larger the RVE (i.e. fewer RVEs in a given volume), the less pronounced is the Weibull region. Therefore, Fig. 5b suggests that the RVE of the oak boards is relatively large.) The second aspect relates to the fact that the classification process effectively removes a large portion of the lower tail. However, it seems that is not possible to fully remove the Weibull part, at least for the tested board length of $9 \cdot b = 900$ mm. For the strength grades LS10 and LS13 the removed strength ranges are 24.6–31.4 MPa and 28.3–39.3 MPa, respectively.

Figure 5b shows the strength distribution of all boards (LS10+LS13) in the Weibull plot, where a *smoother* distribution can be observed, as compared to the distributions for each strength grade separately. Since there are not enough data in the Weibullian region (lower tail) a Weibull modulus of $m = 20$ was assumed in order to fit the WG distribution (see Fig. 5b). The fitted parameters are given in Table 1 labeled as $f_{t,b,900}$ to denote that these correspond to a board length of 900 mm. In a previous study on a different dataset of oak boards a value $m = 10$ was proposed based on a survival anal-

Table 1. Parameters fitted to the Weibull-Gaussian distribution for the strength distributions of finger-joints ($f_{t,fj}$), boards ($f_{t,b,900}$) and 100 mm board cells ($f_{t,b,100}$)

variable	m	s	μ	δ	σ_{gr}
$f_{t,\mathrm{fj}}$	15.4	37.6	32.1	15.8	32.5
$f_{t,b,900}$	20.0	29.1	45.6	19.8	23.5
$f_{t,b,100}$	20.0	32.5	99.2	38.9	23.4

ysis of tensile strength tests (*Tapia* & *Aicher*, 2022). In general, the Weibull modulus, m, varies between 10–50, which is determined by the sequential rising of the exponent by each parallel statistical coupling, starting with $m = 1$ at the atomic scale (*Bažant* & *Pang*, 2007). For example, experiments have determined a value $m = 26$ for an asphalt mixture (*Le* et al., 2013) and $m = 24$ for concrete (*Bažant* & *Le*, 2017). The value $m = 20$ used here was chosen as it better fits the data. However, in order to accurately determine the Weibull modulus for oak boards, a larger number of specimens needs to be tested, which allows for a better resolution in the lower tail of the distribution.

3.3 Simulation of strength distributions for 100 mm cells

The FE model described in Section 2.4 assigns material properties on cells of 100 mm in length, however, the tensile strength distribution for boards was determined for a length of 900 mm. Assuming that a board behaves like a (finite) chain of links, the strength distribution for cells of 100 mm in length, $f_{t,b,100}$, can be derived from $f_{t,b,900}$ by means of order statistics. If the distribution for $f_{t,b,900}$ (F_{900}) is known, then the distribution for $f_{t,n,100}$ (F_{100}) can be derived (*Castillo* et al., 2005) as

$$F_{100}(\sigma) = 1 - [1 - F_{900}(\sigma)]^9 \,. \tag{12}$$

Eq. (12) was applied to the CDF of the fitted WG distribution, which was then fitted to a new WG distribution by means of the maximum likelihood method. The obtained distribution can be seen in Fig. 5b, whilst the fitted parameters are presented in Table 1. Notice that the Weibull modulus, m, remains the same for $f_{t,b,900}$ and $f_{t,b,100}$, which is in agreement with the finite weakest link theory. For the FE simulations the distribution $f_{t,b,100}$ is used with additional considerations to imitate the grading process (see below).

4 Statistical strength distribution of GLT

4.1 General remarks on performed simulations

A series of stochastic FE simulations were performed with the model described in Section 2.4. For each experimental configuration (bending and tension) a total of 10^3 simulations were made. The fracture energy was chosen as $G_f = 1000\,\mathrm{J/m^2}$ (10 N/mm) based on prior numerical investigations with the model, being very close to the value $G_f = 1100\,\mathrm{J/m^2}$ obtained for a previous implementation of the model in Abaqus (*Tapia*, 2022). The material for the oak boards was taken from the distribution of $f_{t,b,100}$. For simplicity reasons, only the material corresponding to the strength grade LS13 was considered, as it is the material subjected to the higher stresses, and whose failure leads to the global failure of the GLT elements. However, the consideration of different material regions is trivial and will be implemented in a future version of the model. In order to correctly consider the strength distribution of boards, the effect of the grading process

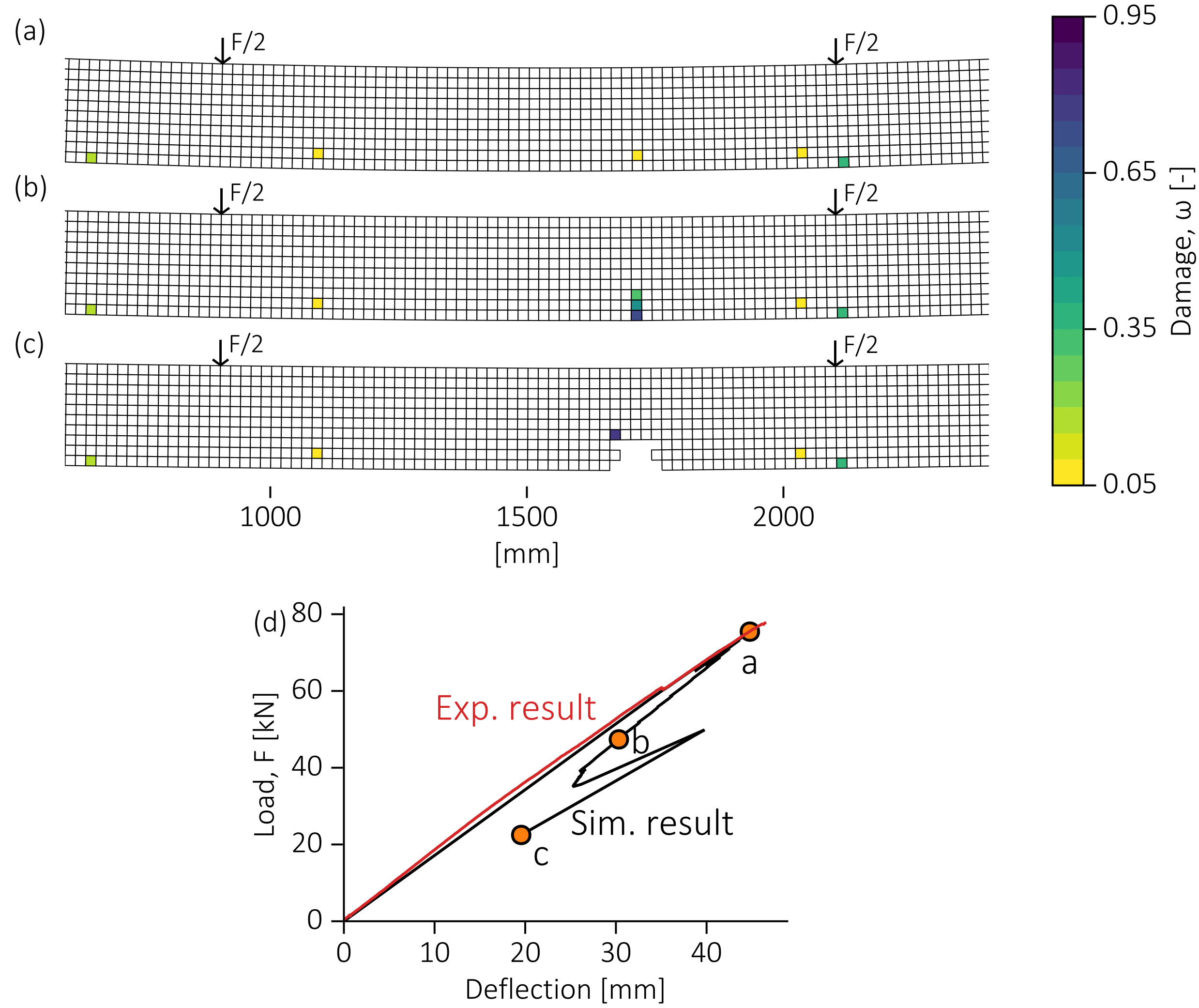

Figure 6. Example of typical simulation of one GLT beam in four-point bending ($D = 200$ mm): (a) maximum load; (b) failure of finger-joint; (c) further failing of oak wood elements; (d) Load-displacement curve. The red curve depict the results of one of the experimentally tested beams.

as shown in Fig. 5a must be taken into account. To this end, all simulated boards with a minimum strength value $f_{t,b,\min} < 39$ MPa were discarded. According to Fig. 5a the values $f_{t,b,\min} < 28$ MPa could have been included, too, however this was not done here. The reasoning for not including values with $f_{t,b,\min} < 28$ MPa is the following: the boards used in the investigated GLT elements are rather short, presenting a mean length of about 450 mm, which is owed to the consequent removal of any segment with knots or fiber deviations regarded as detrimental for the strength of the board. Thus, it can be assumed that the observed lower strengths on the Weibull region are effectively removed. This is also supported by the fact that most of the failure in the tested GLTs can be attributed to a failure in a finger-joint. However, a definitive answer can only be provided by performing tensile tests on similarly short boards.

An example of a typical GLT bending capacity simulation is presented in Fig. 6 at three loading stages. The load-displacement curve shown in Fig. 6d evidences the highly non-linear nature of this problem. Figure 6a depicts the damage level, ω, of each element at the maximum load ($F = 75.5$ kN), where an initial damage at various points along the

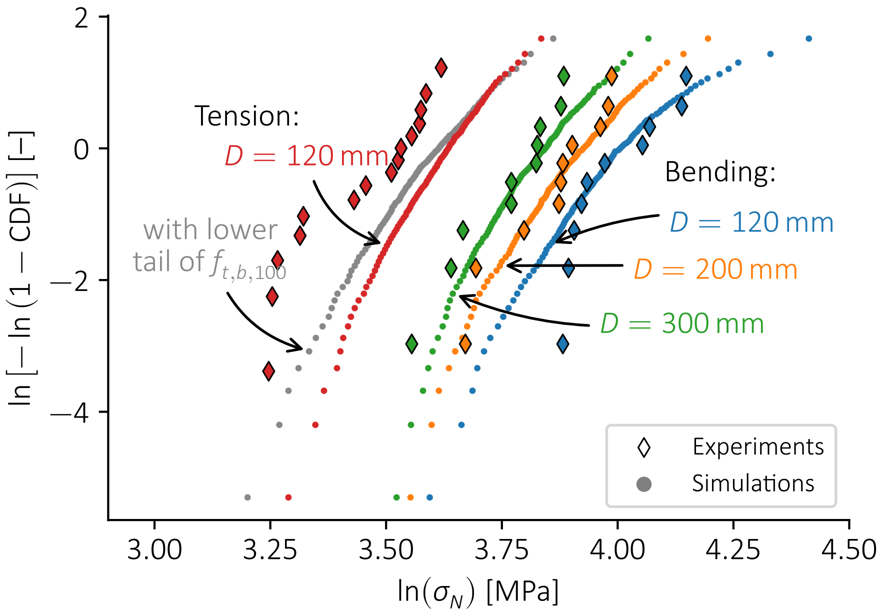

Figure 7. Experimental and simulated nominal strength distributions, σ_N, for GLT beams tested in four-point bending and tension configurations, presented in the Weibull scale. (Each simulated result shown represents the average of 10 simulations.)

two lowest laminations can be appreciated (see yellow and light green elements). From this point on a snap-back behavior is observed, where the damage further increases in the central region, forming a damage concentration zone (Fig. 6b), until finally the elements in this region fail and are then removed from the model (Fig. 6c). The logic of element removal considers the deletion of the two neighbouring elements at each side of the failed element in the same lamination for the case of board elements, such that the whole cell of 100 mm is removed. For the case that a finger-joint element fails, only one element at each side is removed. Figure 6d also presents an experimentally determined load-displacement curve, where a similar behavior can be observed—including small non-linearities previous to the maximum load. This example evidences the redundancy supplied by the fracture energy, as it allows to redistribute stresses before complete failure of the element occurs.

4.2 Simulations of nominal strengths in GLT

The results of the Monte-Carlo simulations for GLT beams loaded in bending and tension are presented in the Weibull scale in Fig. 7 alongside the experimental results. It can be seen that the general trend of the simulations agrees with the experimental results to a large degree. The major discrepancies are observed for the tension results ($d = 120$ mm), where the simulated strengths are considerably shifted to higher values as compared to the experiments. Considering the lower tail of $f_{t,b,100}$ (previously disregarded) the values are reduced, but remain rather high. This indicates that the model still needs some refinement regarding the failure criterion, as it seems to be too redundant under tension loading.

In the Weibull plot the experimental results are difficult to interpret, as no clear trend is seemingly present. The CDF curves show neither a perfect Weibull nor a Weibull-Gaussian behavior. Furthermore, a rather marked discontinuity can be discerned at a probability level of about 0.3–0.4, which is present in all four test series. This discontinuity might be related to the above-mentioned rigorous grading system applied to the boards composing the studied GLT, however, it is out of the scope of this paper to investigate this in further detail.

Considering the complex behavior of the strength distribution, the simulation results coupled with the understanding of FWLT offer a rational framework to make sense of the experimental data. For example, alone from the shape of the CDF curves in the Weibull plot it can be inferred that the nominal strength is not described by a Weibull distribution. The immediate consequence of this is that the scaling rule cannot be described by a simple power law, as such behavior is intrinsically linked to the Weibull theory of weakest link. Although it is evident from the previous sections that some input parameters—such as the exact distribution of $f_{t,b,100}$—require further refinements, the general principles considered for the characterization of the material (FWLT) must apply. Therefore, the above-derived conclusion regarding the size effect must hold. This will be further explored in the following section.

4.3 Size effect of GLT in bending

In the previous section it was hypothesized that the scaling behavior of the studied GLT beams should not follow a power law due to the evident absence of a Weibull distribution. This idea was numerically tested by simulating two additional beam sizes in bending with depths of 600 mm and 1000 mm. A total of 10^3 simulations were performed for each size. The results of these simulations are shown in Fig. 8 in the log-log scale for the mean and 5%-quantile levels.

A scaling rule described by a power law defines a straight line in the log-log plot of nominal strength, σ_N vs. characteristic length, D. As evidenced by Fig. 8 the size effect described by the simulations presents a varying slope, thus not following a power law. The simulated size effect is rather low compared to the experiments, however, by means of a better characterization of the input materials, a closer fit with the empirical data might be achieved. The relevant point here is the general evolution of the size effect. This simulation-based curve resembles the typical curve of quasibrittle materials described by the FWLT (see e.g. *Le* et al., 2013), although the range is too short to observe whether a Weibull limit is present for large sizes. Actually, due to the mechanical behavior of the model, this curve probably shares more in common with the scaling law derived from Fishnet Statistics, as described in *Luo* & *Bažant* (2017), where softening and load sharing are taken into account. In this theory, not the weakest, but the n^{th} weakest link determines the nominal strength, which better suits the rather redundant system defined by a GLT beam. In general terms, it can be argued that this curve can

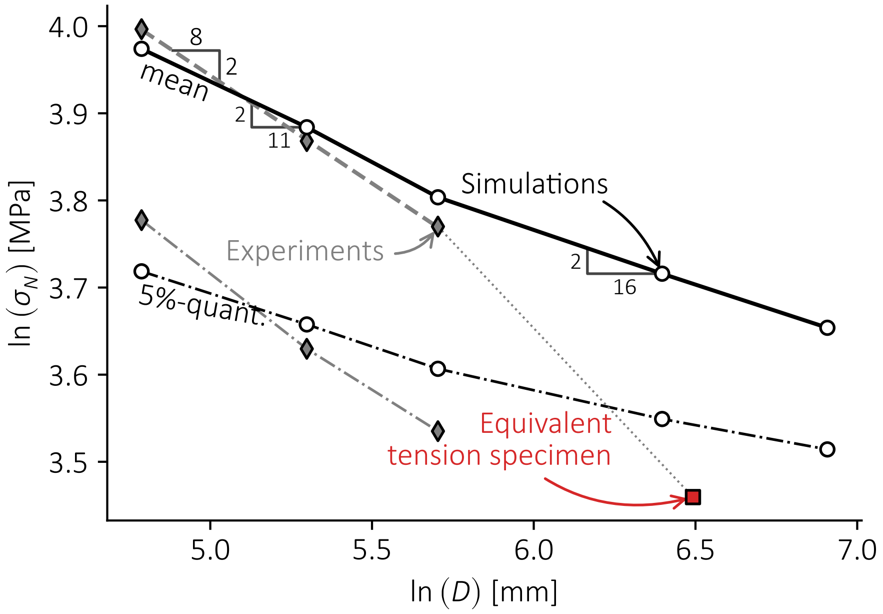

Figure 8. Experimental and simulated size effect of the nominal strength on the mean and 5%-quantile levels for oak GLT in bending

be approximated by a power law, as the experimental curves also suggest. However, this would probably only work for the studied range of depths, and may present large discrepancies for larges nominal sizes.

An additional analysis can be made by using the experimental results for the oak GLT specimen tested in tension. These results can be assigned to the corresponding equivalent characteristic size, D_{eq}, in bending by applying Eq. (6). The required Weibull modulus was taken from the slope of the experimental scaling curve as $m = 8$ (see Fig. 8), resulting in $D_{\mathrm{eq}} = 660$ mm. By adding this additional point to the plot, it can be seen that the size effect seems to increase slightly. In fact, this is most probably only the result of applying the Weibull theory under wrong assumptions, i.e. the assumption that σ_N follows a Weibull distribution for the studied specimens, which was shown above to be unlikely.

5 Conclusions

The study of the size effect on bending strength of GLT beams has been an important research topic in the last decades. Indeed, an accurate representation of the scaling effect has very practical consequences for the timber industry due to the economical impact associated to the requirement of larger or smaller cross-sections. Although the relevance of considering the quasibrittle behavior of wood has been mentioned in the literature previously (e.g. *Brandner* et al., 2007; *Blank* et al., 2017), no consequent effort known to the authors has been pursued to analyze the implications of this assumption in the size effect of GLT and the behavior of its constituent parts: boards and finger-joints. Based on the experimental and numerical results presented in this paper, the following conclusions can be stated:

- Tensile strength of finger-joints of oak boards present a clear quasibrittle behavior that can be described by a Weibull-Gaussian distribution with a Weibull modulus $m = 15$.
- Oak boards, being a quasibrittle material, exhibit a Weibullian region on the lower tail of the strength distribution. However, the grading limits remove a large part of it, which leaves mostly a truncated Gaussian distribution for the rather short boards used in the studied GLT beams.
- The size effect of GLT assembled from the quasibrittle boards, here characterized by a truncated Gaussian distribution, cannot follow a power law—currently assumed in most standards—, as this implies Weibullian-type perfect brittle behavior. The fact that an accurate modelling of GLT relies on load redistribution through energy dissipation suffices to discard the latter assumption. In fact, the size effect of GLT is more complex, as the softening-induced stress redistribution enables global failures triggered not by the weakest link, but by the 2$^{\text{nd}}$, 3$^{\text{rd}}$ or in general n^{th} weakest link. This in addition to the quasibrittle nature of the material, which does present a power law in the lower tail of the strength distribution.
- The fact that a power law scaling seems to explain the experimental data correctly might be related to the typical tested sizes being too small. Larger cross-sections of up to 2 m in depth—although commonly used in the practice—are much too costly to be experimentally tested in full size. However, by applying the power law fitted from small specimens the material is probably strongly penalized.
- Finally, in order to improve the prediction accuracy of the model applied to oak or any other wood species (soft- or hardwood), the size of the respective RVE must be determined, as this defines the size of the used *cells* in the FE model.

6 References

Aicher, S. & N. Ruckteschell (2011). *VIGAM-Glued laminated timber from European oak (in German)*. Tech. rep. 901 4329 000_1. Stuttgart, Germany: Materials Testing Institute, University of Stuttgart.

Aicher, S. & G. Stapf (2014). “Glulam from European white oak: finger joint influence on bending size effect. Recent Developments of Technology.” In: *Materials and Joints in Timber Structures*. RILEM Bookseries 9. Springer, pp. 641–656.

ASTM D 3737 (2018). *Standard Practice for Establishing Allowable Properties for Structural Glued Laminated Timber (Glulam)*. West Conshohocken, Pa: American Society for Testing Materials.

Barrett, J. D. (1974). “Effect of size on tension perpendicular-to-grain strength of douglas-fir.” In: *Wood and Fiber Science* 6.2, pp. 126–143.

Bažant, Z. P. & J.-L. Le (2017). *Probabilistic mechanics of quasibrittle structures: strength, lifetime, and size effect*. Cambridge University Press. DOI: 10.1017/9781316585146.

Bažant, Z. P. & S.-D. Pang (2007). "Activation energy based extreme value statistics and size effect in brittle and quasibrittle fracture." In: *Journal of the Mechanics and Physics of Solids* 55.1, pp. 91–131. DOI: 10.1016/j.jmps.2006.05.007.

Bezanson, J.; A. Edelman; S. Karpinski & V. B. Shah (2017). "Julia: A Fresh Approach to Numerical Computing." In: *SIAM Review* 59.1, pp. 65–98. DOI: 10.1137/141000671.

Blank, L.; G. Fink; R. Jockwer & A. Frangi (2017). "Quasi-brittle fracture and size effect of glued laminated timber beams." In: *European Journal of Wood and Wood Products* 75.5, pp. 667–681. ISSN: 1436-736X. DOI: 10.1007/s00107-017-1156-0.

Brandner, R.; T. Bogensperger; G. Jeitler & G. Schickhofer (2007). "Size effect considerations for linear structural elements of timber." In: *COST E55 – Modelling of the performance of timber structures – 2nd Workshop and 4th MC Meeting*. Eindhoven University of Technology, Netherlands.

Carlsson, K.; F. Ekre & Contributors (2022). *Ferrite.jl*. Version 0.3.7. URL: https://github.com/Ferrite-FEM/Ferrite.jl.

Castillo, E.; A. S. Hadi; N. Balakrishnan & J. M. Sarabia (2005). *Extreme value and related models with applications in engineering and science*. Hoboken, N.J. : Wiley. ISBN: 0-471-67172-X.

Colling, F. (1986). "Influence of volume and stress distribution on the strength of a beam with rectangular cross section – Derivation of a general relationship with the help of a 2-parameter Weibull-distribution." In: *European Journal of Wood and Wood Products* 44.4. (In German), pp. 121–125.

DIN 4074-5 (2008). *Strength grading of wood – Part 5: Sawn hard wood*. Berlin, Germany: Deutsches Institut für Normung.

EN 1995-1-1 (2010). *Eurocode 5: Design of timber structures – Part 1-1: General – Common rules and rules for buildings*. Brussels, Belgium: European Committee for Standardization.

EN 408 (2013). *Timber structures – Glued laminated timber and glued solid timber – Requirements*. Brussels, Belgium: European Committee for Standardization.

ETA-13/0642 (2013). *European Technical Approval, "VIGAM – Glued laminated timber of oak"*. Vienna, Austria: Österreichisches Institut für Bautechnik.

Frese, M. & H. J. Blaß (2009). "Bending strength of spruce glulam." In: *European Journal of Wood and Wood Products* 67, pp. 277–286. ISSN: 0018-3768.

Frese, M. & H. J. Blaß (2016). "Reliability of large glulam members- Part 1: Data for the assessment of partial safety factors for the bending strength." In: *Proceedings of the International Network on Timber Engineering Research – Meeting 49*. Graz, Austria, pp. 331–344.

Lam, F. (2011). "Size Effect of Bending Strength in Glulam Beams." In: *Proceedings of the International Council for Research and Innovaition in Builing and Construction (CIB) – Working Commission W18 – Timber Structures – Meeting 44*. Alghero, Italy: Karlsruhe Instutute of Technology, pp. 44–5.

Le, J.-L.; Z. P. Bažant & M. Z. Bažant (2011). “Unified nano-mechanics based probabilistic theory of quasibrittle and brittle structures: I. Strength, static crack growth, lifetime and scaling.” In: *Journal of the Mechanics and Physics of Solids* 59.7, pp. 1291–1321. DOI: 10.1016/j.jmps.2011.03.002.

Le, J.-L.; A. C. Falchetto & M. O. Marasteanu (2013). “Determination of strength distribution of quasibrittle structures from mean size effect analysis.” In: *Mechanics of Materials* 66, pp. 79–87. DOI: 10.1016/j.mechmat.2013.07.003.

Luo, W. & Z. P. Bažant (2017). “Fishnet statistics for probabilistic strength and scaling of nacreous imbricated lamellar materials.” In: *Journal of the Mechanics and Physics of Solids* 109, pp. 264–287. DOI: 10.1016/j.jmps.2017.07.023.

Luo, W. & Z. P. Bažant (2018). “Fishnet model with order statistics for tail probability of failure of nacreous biomimetic materials with softening interlaminar links.” In: *Journal of the Mechanics and Physics of Solids* 121, pp. 281–295. DOI: 10.1016/j.jmps.2018.07.023.

Moody, R.; R. Falk & T. Williamson (1990). “Strength of glulam beams – Volume effects.” In: *Proc. Int. Timber Engineering Conf.* Vol. 1. Tokyo, Japan, pp. 176–186.

Pang, S.-D.; Z. P. Bažant & J.-L. Le (2008). “Statistics of strength of ceramics: finite weakest-link model and necessity of zero threshold.” In: *International Journal of Fracture* 154.1-2, pp. 131–145. DOI: 10.1007/s10704-009-9317-8.

prEN 1995-1-1 (2021). *Consolidated draft, Eurocode 5: Design of timber structures – CEN/TC 250/SC5 N1488*. Brussels, Belgium: European Committee for Standardization.

Rots, J. G. & S. Invernizzi (2004). “Regularized sequentially linear saw-tooth softening model.” In: *International Journal for Numerical and Analytical Methods in Geomechanics* 28.78, pp. 821–856. DOI: 10.1002/nag.371.

Tapia, C. & S. Aicher (2021). “Simulation of the Localized Modulus of Elasticity of Hardwood Boards by Means of an Autoregressive Model.” In: *Journal of Materials in Civil Engineering* 33.6. DOI: 10.1061/(asce)mt.1943-5533.0003696.

Tapia, C. & S. Aicher (2022). “Survival Analysis of Tensile Strength Variation and Simulated Length–Size Effect along Oak Boards.” In: *Journal of Engineering Mechanics* 148.1. DOI: 10.1061/(asce)em.1943-7889.0002006.

Tapia, C. (2022). “Variation of mechanical properties in oak boards and its effect on glued laminated timber – Application to a stochastic finite element glulam strength model.” PhD thesis. Materials Testing Institute, University of Stuttgart. DOI: 10.18419/OPUS-12111.

Vida, C.; M. Lukacevic; J. Eberhardsteiner & J. Füssl (2022). “Modeling approach to estimate the bending strength and failure mechanisms of glued laminated timber beams.” In: *Engineering Structures* 255, p. 113862. DOI: 10.1016/j.engstruct.2022.113862.

Weibull, W. (1939). *A statistical theory of the strength of materials*. 151. Stockholm, Sweden: Royal Swedish Institute for Engineering Research.

DISCUSSION

The paper was presented by C Tapia

E Serrano received clarification about the numerical model. In the FEM mesh, a 100 mm cell has 5 FEs lengthwise and one in the depth direction. Gauss integration for each element was performed with an average value taken. Influence of element size was not considered but should be mesh independent. When one element fails, the 100 mm section was removed.

R Brandner and C Tapia discussed the representativeness of the length of 100 mm. In past work on MOE versus strength, a 80 mm volume was found in the literature. R Brandner questioned that the distance between the knots is larger than 100 mm. C Tapia said smaller knots exists and that a representative length 2 or 3 times the size of the large knots would be appropriate. R Brandner asked if other distributions were tried. C Tapia said other distributions have not been tried as the chosen distribution needs to have a theoretical base.

H Blass and C Tapia discussed about RVE versus the size with tests at different lengths.

S Franke received clarification about model correlations.

R Jockwer asked about the tension tests of laminate in relation to the relatively small beam height. He suggested that bending laminate tests are needed for calibration. C Tapia disagreed as the difference is the number of finger joints in small beams.

F Lam commented that the AR approach that assumes statistical dependency with a certain lag, but the Weibull approach is based on statistical independency between elements. This contradiction should be noted. F Lam received clarification about poor tension fit being presented and suggested that clear explanations are needed in the text.

H Danielson and C Tapia discussed that fracture energy in the paper was assumed to be 500 N mm/mm^2 based on fitting.

P Dietsch commented that a load deformation curve based on load control is closer to reality. C Tapia agreed.

Size Effect of Large Glued Laminated Timber Beams – Contribution to the Ongoing Discussion

Christoffer Vida, Markus Lukacevic, Georg Hochreiner, and Josef Füssl

Institute for Mechanics of Materials and Structures, TU Wien

Keywords: size effect, global failure criterion, glued laminated timber, XFEM

1 Introduction

The effect of the size of large glued laminated timber (GLT) beams on the bending strength is a matter of debate among experts. For smaller beams with depths of up to 600 mm, the so-called size effect was studied with four-point bending tests (*Aasheim and Solli*, 1995; *Kandler et al.*, 2018a; *Schickhofer*, 1996). The identified size effect can be applied by the commonly used factor k_h in conjunction with a characteristic reference bending strength $f_\mathrm{b,k,ref}$. An arbitrary sized GLT beam has then the characteristic bending strength $f_\mathrm{b,k}$ defined as:

$$f_\mathrm{b,k} = f_\mathrm{b,k,ref} \cdot k_\mathrm{h} \,. \tag{1}$$

According to *DIN EN 1995-1-1* (2010), k_h describes a strength increase that can be applied to GLT beams with depths h smaller than the reference depth h_ref of 600 mm:

$$k_\mathrm{h} = \min\begin{cases} \left(\frac{600}{h}\right)^{0.1} \\ 1.1 \end{cases} \quad \text{for} \quad h \leq 600\,\mathrm{mm}\,. \tag{2}$$

The increase is limited by 10 %. The characteristic reference bending strength $f_\mathrm{b,k,ref}$ is defined in *DIN EN 14080* (2013) ($f_\mathrm{m,g,k}$) for individual strength classes.

Generally, this concept is consistent with the one for wooden members presented by *Bohannan* (1966) based on Weibull's strength theory (*Weibull*, 1939). The same basis was used by *Colling* (1986) for proposing a concept that considers the volume V instead of only the depth h and additionally accounts for the loading situation. There, the influence of the volume V, compared to the reference volume V_{ref}, reads as:

$$k_{\mathrm{h}} = \left(\frac{V_{\mathrm{ref}}}{V}\right)^{\frac{1}{m}} \quad . \tag{3}$$

Figure 1 shows the test setup, where the total beam length ℓ_{tot} depends on the depth h (*DIN EN 408*, 2012). The distance between the two loading points ℓ is defined by the fixed dimensional ratio: ℓ/h = 6.0. Together with the assumption of a constant beam width b, Eq. (3) reduces to:

$$k_{\mathrm{h}} = \left(\frac{h_{\mathrm{ref}}}{h}\right)^{\frac{2}{m}} = \left(\frac{h_{\mathrm{ref}}}{h}\right)^{\frac{1}{m^*}} \quad , \tag{4}$$

where $m = 2\,m^*$.

However, experimental testing of larger GLT beams involves a tremendous effort. Thus, such tests were hardly conducted. Numerical simulation campaigns represent an alternative, but they are heavily influenced by the modeling strategy. Therefore, results from the literature (*Fink et al.*, 2015; *Frese and Blaß*, 2015) present a different influence of the beam depths on the bending strength. To predict the size effect, we carried out a simulation campaign covering 8840 GLT beams ranging from 165 mm to 3300 mm in depth, using advanced modeling concepts including discrete cracking and plasticity.

This paper presents excerpts of our modeling strategy and findings regarding the size effect to contribute to the ongoing discussion. A computational modeling approach to estimate the bending strength of GLT beams subjected to four-point bending tests has already been published (*Vida et al.*, 2022a), and regarding the size effect, two manuscripts are currently in preparation (*Vida et al.*, 2022b; *Vida et al.*, 2022c).

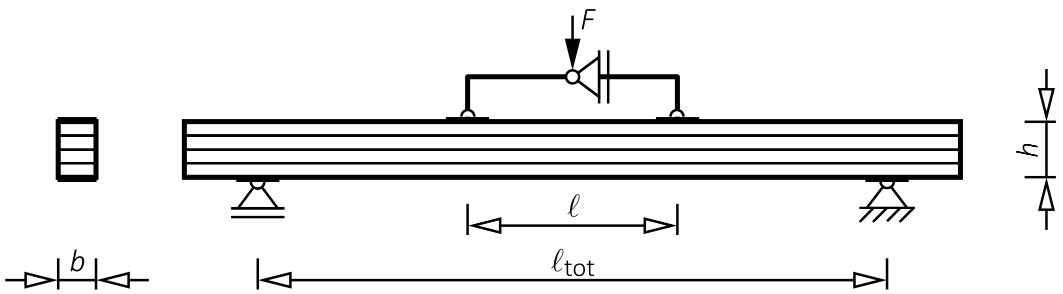

Figure 1. Four-point bending test setup for a GLT beam with the span ℓ_{tot}, depth h, and width b, loaded by a constant bending moment over the length ℓ. Redrawn from Vida et al. (2022c)

2 Modeling strategy

2.1 Wooden boards

We build up GLT beams using replications of boards based on real wooden boards. The deterministic estimation of the material properties is based on the procedure presented by *Kandler et al.* (2018b). The virtually reconstructed board is parted in sections i that either refer to defect-free wood, so-called clear wood, or to sections with single large knots or knot clusters, referred to as knot sections. The length of a section is defined by the configuration of knots in the real wooden boards and, thus, is of individual size. To each section, constant material properties are assigned, i.e., the longitudinal modulus of elasticity (MOE) $E_{L,i}$ and the tensile strength $f_{t,i}$ in fiber direction (Fig. 2a,d). Two strength classes, T14 and T22, were considered. An overview of the boards' properties is given by *Vida et al.* (2022a).

In total 140 boards of each strength class are available. The length of a board is 5400 mm, the width is 90 mm, and the thickness is 33 mm. The longitudinal MOE of an entire

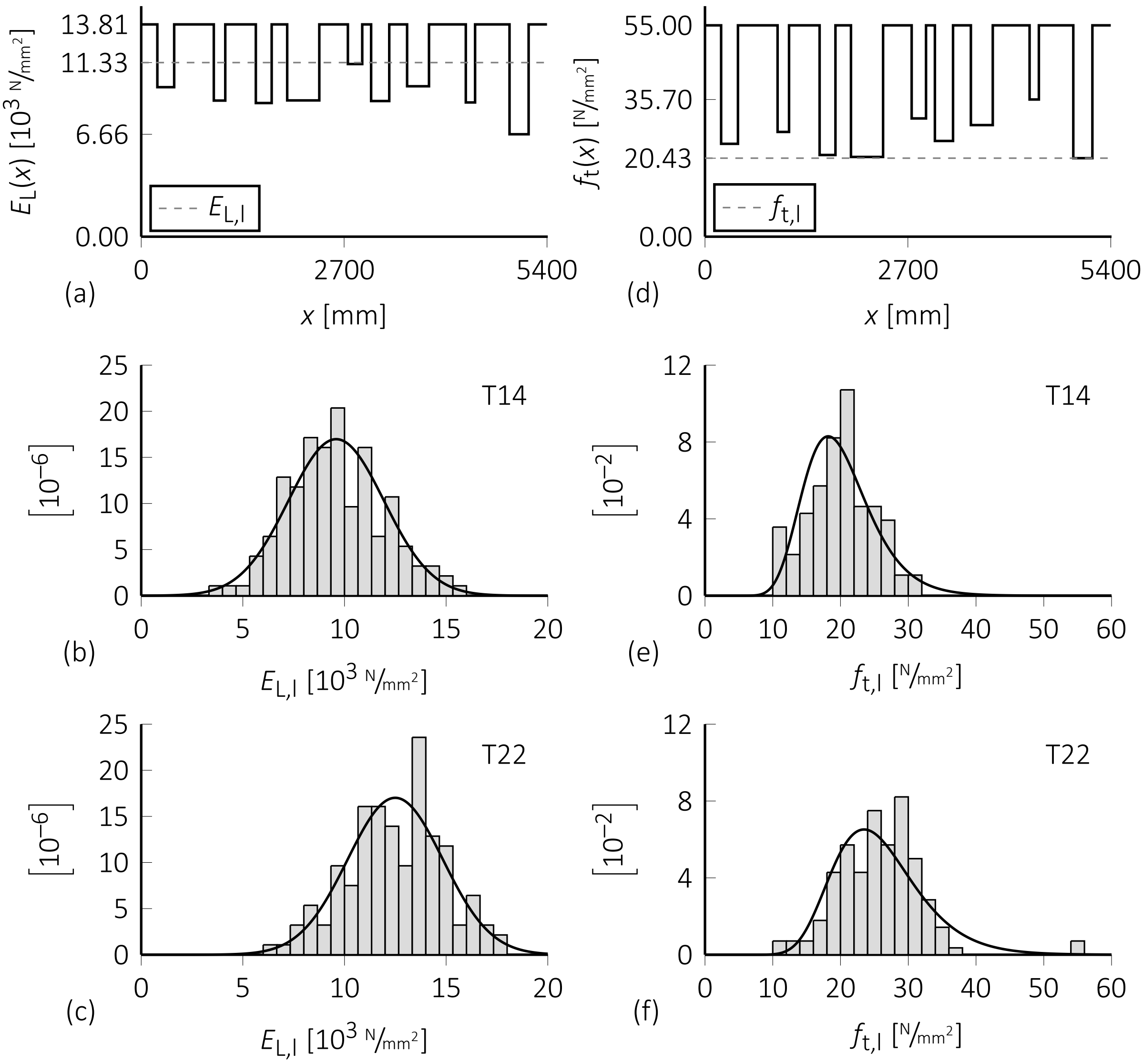

Figure 2. Example of a board's property profiles providing (a) the effective longitudinal stiffness $E_L(x)$ and (d) the effective tensile strength $f_t(x)$ as well as histograms considering all boards and distributions for (b,c) the stiffness $E_{L,I}$ and (e,f) the tensile strengths $f_{t,I}$, separated for both strength classes T14 and T22. Redrawn from Vida et al. (2022a)

Table 1. Comparison of the mean and characteristic values of the histograms in Fig. 2b–c,e–f to values according to DIN EN 14080 (2013). (Vida et al., 2022a)

Strength class	$E_{\mathrm{L,l,mean}}$ [a] $[\mathrm{N/mm^2}]$	$E_{\mathrm{t,0,l,mean}}$ [b] $[\mathrm{N/mm^2}]$	$f_{\mathrm{t,l,k}}$ [a] $[\mathrm{N/mm^2}]$	$f_{\mathrm{t,0,l,k}}$ [b] $[\mathrm{N/mm^2}]$
T14	9592	11 000	11.6	14.0
T22	12 497	13 000	16.6	22.0

[a] Simulation based values (board length of 5400 mm).
[b] Values according to *DIN EN 14080* (2013) (board length of $\geq$ 810 mm according to *DIN EN 408* (2012)).

board $E_{\mathrm{L,l}}$ considers all sections i of the board as a chain of linear springs:

$$E_{\mathrm{L,l}} = \frac{\ell_{\mathrm{tot}}}{\sum_i \frac{\ell_{\mathrm{s},i}}{E_{\mathrm{L},i}}} \quad \text{with} \quad \ell_{\mathrm{tot}} = \sum_i \ell_{\mathrm{s},i} \,. \tag{5}$$

where $\ell_{\mathrm{s},i}$ is the length corresponding to the section-wise constant $E_{\mathrm{L},i}$ from its stiffness profile (Fig. 2a). Figure 2b,c shows the histograms and the fitted normal distributions of $E_{\mathrm{L,l}}$ according to Eq. (5) for both strength classes T14 and T22, respectively. The board tensile strength $f_{\mathrm{t,l}}$ is assumed as the lowest strength $f_{\mathrm{t},i}$ of a section i within the strength profile of the considered board (Fig. 2d):

$$f_{\mathrm{t,l}} = \min_i \left\{ f_{\mathrm{t},i} \right\} \,. \tag{6}$$

Figure 2e,f shows the histograms and the fitted log-normal distributions of $f_{\mathrm{t,l}}$ according to Eq. (6) also for both strength classes, respectively. A comparison of the characteristic tensile board strength and the mean longitudinal board MOE to the values according to *DIN EN 14080* (2013) is given in Tab. 1. Generally, the simulated values are lower than those specified in the standard. The underestimation could be due to different board lengths in the test setup, especially for the strengths.

2.2 Modeling approach

In the test setup, a constant bending moment acts on the GLT beam between the two loading points (Fig. 1), representing the section of the beam with the maximum load. With our modeling approach, we focus on this GLT beam section by directly applying a constant bending moment (Fig. 3). This saves computational costs and allows to efficiently conduct extensive and advanced simulation campaigns. The approach is based on the model and findings presented by *Vida et al.* (2022a) and considers local failure by allowing discrete cracking in two directions, as schematically illustrated in Fig. 3. The simulations of GLT beam sections are performed by using the finite element software *Abaqus* (2021). Finally, we calculate the effective bending strength f_{b} from the maximum bending moment M_{max} applied during the simulation.

The length ℓ to depth h ratio of the GLT beam section (Fig. 3) is kept constant for the

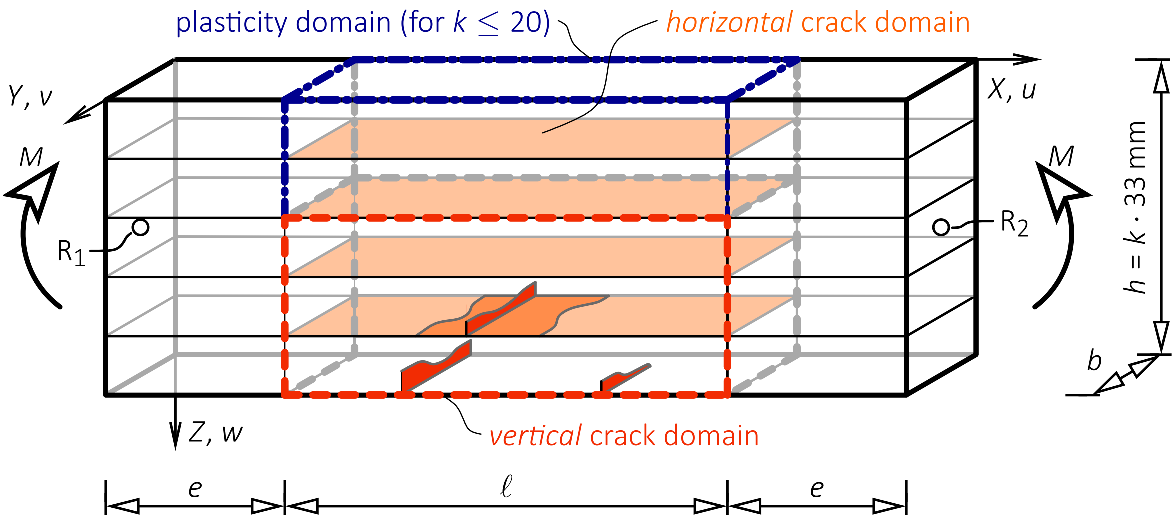

Figure 3. Representative GLT beam section of length ℓ as used for the numerical simulations with k lamellas resulting in the depth h. The constant bending moment M and the bearing is applied at the reference points R_1 *and* R_2*. Redrawn from Vida et al. (2022c)*

majority of the simulations to investigate the influence of the beam depth h. Additionally, the constant length e of 100 mm is added on both ends to avoid disturbing the area of interest by load application effects. The layout of all beam sections is homogeneous, meaning that only boards of one strength class were randomly arranged. The GLT beams correspond to strength class GL 24h and GL 30h using the boards of strength class T14 and T22, respectively. Each placed lamella is selected by a uniformly distributed pseudo-random process consisting of the following steps:

1. Random picking of a full-length board from the entire pool of virtual boards.
2. Random longitudinal displacement of the board within the GLT beam section to define the start and end positions of the lamella.
3. Random choice of the lamella's orientation in the GLT beam layout.

GLT typically includes finger joints (FJs) to overcome restrictions on the length of individual boards. In contrast to growth-related defects such as knots, which generally have low stiffness and strength, FJs are characterized by high stiffness due to their positioning in clear wood and potentially low strength due to flaws in production. Although failure of FJs is commonly observed in experiments, experimental studies (*Aasheim and Solli*, 1995; *Pischl et al.*, 1995) found that the bending strength of GLT beams, generally corresponding to lower strength classes, is basically independent of whether failure occurs in the FJ or lamination. This led to the conclusion that the effect of FJs on global failure is similar to that of natural weak points. Therefore, we assume that the random allocation of lamellas with all their weak points is a reasonable representation of random GLT beam sections. Nevertheless, a future implementation of FJs in the model would be useful and would allow further studies, e.g., the effect of different FJ qualities on the bending strength.

The two failure modes are implemented for either vertical or horizontal discrete cracks (Fig. 3). Vertical cracks are realized with the extended finite element method as proposed by *Tapia Camú and Aicher* (2018), and horizontal ones with cohesive failure surfaces. Together, both modes are able to cover the effect of cracks interacting over multiple laminations. For example, the horizontal cracking allows two vertical cracks with a horizontal offset in adjacent laminations to become one continuous crack. The implementation is described in detail by *Vida et al.* (2022a). The applied fracture energy was 30 N mm/mm^2 for the implementation of vertical cracks and 0.6 N mm/mm^2 for the horizontal ones, which additionally use assigned strength and stiffness properties. Those properties were assumed as constants because of the lack of available data. The formation of vertical cracks is the dominate failure mechanism governing the simulated bending strength.

The general material behavior is prescribed as linear elastic. An experimental study on GLT beams *Kandler et al.* (2018a) found that plastic deformations might occur in the zone of compressive stresses. These deformations are assumed to be relevant for small beams and high strength classes. Therefore, we implemented ideal plasticity with a multisurface failure criterion (*Lukacevic et al.*, 2015; *Lukacevic et al.*, 2017; *Pech et al.*, 2021) in the upper beam half for simulations of small beams with a maximum of 20 lamellas corresponding to a depth of 660 mm (with the upper two laminations for beam sections consisting of five lamellas; Fig. 3).

The three-dimensional model is discretized by eight-node hexahedron elements in conjunction with tri-linear shape functions. To reduce the model size, symmetry characteristics in the width direction are exploited. In the zone of tensile stresses, the cross-section has two element layers over the lamination depth and three element layers over the lamination width (exploiting symmetry). There, the element length is generally defined as 16.5 mm but adapts to the partition of the sections.

Global failure of the GLT beam section is defined by the first 3 % drop of the bending moment M in relation to the maximum observed bending moment M_{max}, which defines the reached load-bearing capacity. Herein, we refer to this criterion as *load drop criterion*. According to beam theory the effective bending strength f_{b} reads as:

$$f_{\text{b}} = \frac{6\,M_{\text{max}}}{bh^2}\,, \tag{7}$$

where the dimensions b and h can be found in Fig. 3.

The approach simulates beam sections having a specific depth to length ratio ℓ/h. The bending strength was validated with experiments, and additionally, the influence of plastic material behavior and different mesh sizes was investigated by *Vida et al.* (2022c).

2.3 Consideration of different dimensional ratios

It can be assumed that the beam length to depth ratio ℓ/h, which is also referred to as dimensional ratio, influences the structural response. In order to estimate the extent of this influence, 1400 simulations were carried out with modeled sections having a ratio ℓ/h of 6.0 and 4800 simulations with a ratio ℓ/h of 1.5. Both ratios covered beam depths h of 165 mm, 330 mm, and 660 mm. The resulting bending strengths f_b were comprised by two-parameter log-normal distributions, which were fitted to the entire sample by maximum likelihood estimations.

The resulting probability distribution functions (PDFs) are given in Fig. 4a–c for the three different beam depths, where the PDFs for the two different dimensional ratios and strength classes are plotted against each other. It is obvious that the bending strength f_b heavily depends on the dimensional ratio. This poses a problem because as the model

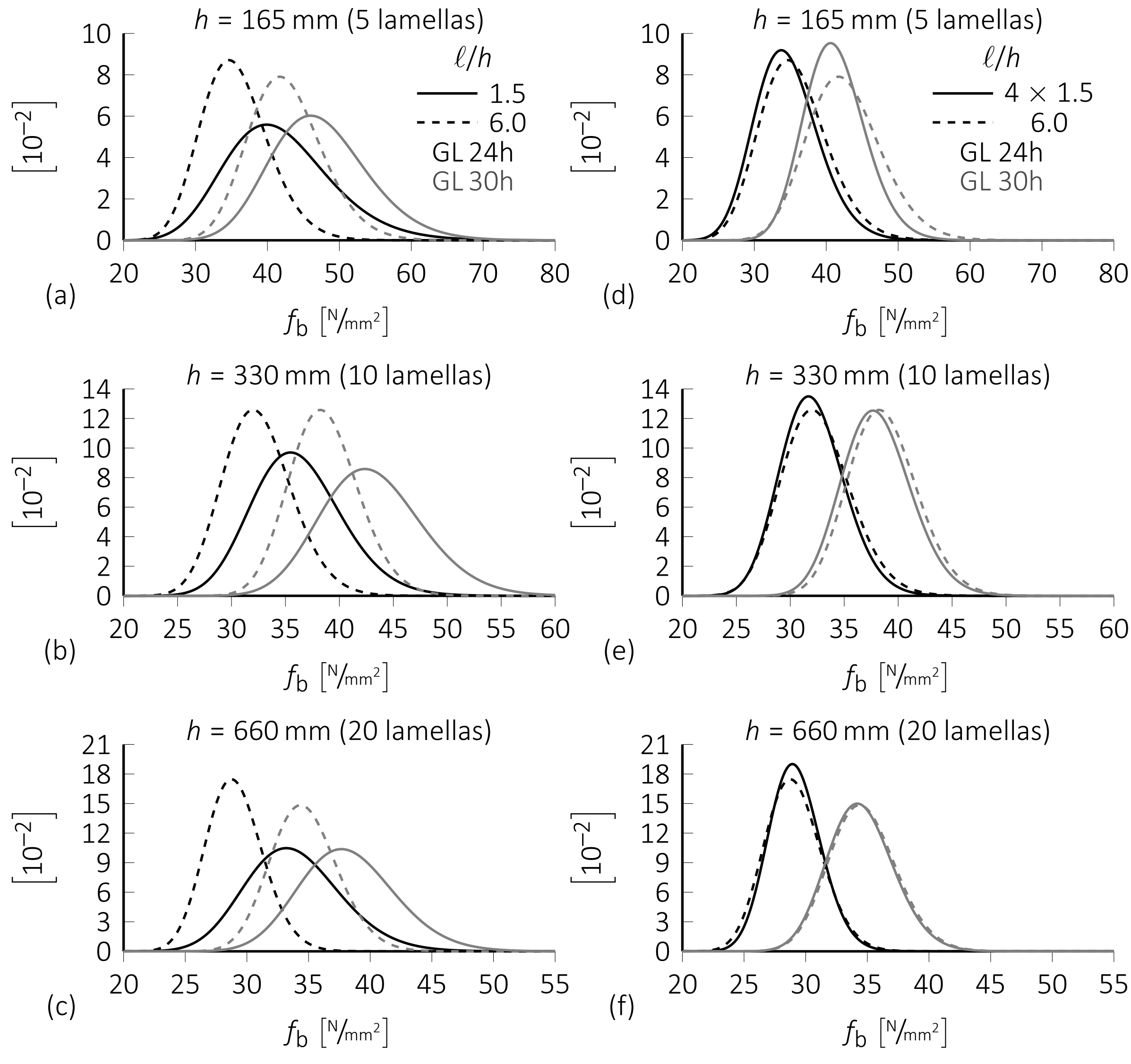

Figure 4. Probability distribution functions for the bending strength f_b obtained from simulations with a ratio (a–c) of 1.5 or (d–f) of 4×1.5 compared to a ratio of 6.0 covering both strength classes and three beam depths: 165 mm, 330 mm, and 660 mm. Redrawn from Vida et al. (2022c)

size increases with increasing dimensional ratio, the nonlinear calculations to determine the bending strength become very time consuming. For this reason, it would be very valuable to predict the bending strength for different dimensional ratios only based on the results of the finite element models with a ratio of 1.5.

This was achieved by combining the n simulation results for the dimensional ratio of 1.5 to estimate results for larger dimensional ratios $p \times 1.5$ in the following way:

$$f_{b,i} = \min\left(f_{b,(i-1)\cdot p+1}, f_{b,(i-1)\cdot p+2}, \ldots, f_{b,(i-1)\cdot p+p}\right) , \tag{8}$$

with $i \in \{1, \ldots, \lfloor n/p \rfloor\}$, where $\lfloor \cdot \rfloor$ denotes the floor function that rounds the included number to the nearest smaller integer.

This method could be roughly validated by evaluating it for $p = 4$ before making the comparison with the available simulation results having a dimensional ratio of 6.0 (Fig. 4d–f). Considering the simplicity of Eq. (8), the agreement with the simulation results is surprisingly good, with a maximum deviation of the mean bending strength of 3.3 % and the characteristic bending strength of 2.2 %. For this reason, this method can be used to estimate the influence of different dimensional ratios.

3 Size effect

3.1 Extent of the simulation campaign

We carried out an extensive simulation campaign covering beams in the standardized test setup *DIN EN 408* (2012) with depths ranging from 165 mm up to 3300 mm, corresponding to two common strength classes GL 24h and GL 30h. The number of simulations performed depended on the beam size but was the same for both strength classes (Tab. 2). All models had a dimensional ratio of 1.5 and were generated by random assembly of the 140 virtually reconstructed wooden boards of each strength class.

Table 2. Studied beam depths with the corresponding number of lamellas and simulations. (Vida et al., 2022c)

Depth h [mm]	Lamellas k [–]	Sample size[a] [–]
165	5	1600
330	10	400
660	20	400
1320	40	400
1980	60	300
2640	80	200
3300	100	200

[a] For each strength class with $\ell/h = 1.5$.

3.2 Beam sections with fixed dimensional ratio

The effective bending strengths, obtained by our simulations, decrease for both strength classes with increasing beam size (Fig. 5). According to *DIN EN 408* (2012), the test setup requires a dimensional ratio ℓ/h of 6.0, which defines the length ℓ, where a constant bending moment exists, as six times the beam depth h. The required dimensional ratio was achieved by applying Eq. (8). The PDFs used to describe the results were again two-parameter log-normal distributions fitted to the entire sample by maximum likelihood estimations. The mean and characteristic values were derived from these distributions. The decrease of the mean values, with increasing beam depth, is larger than for the characteristic values. This is due to the concurrent reduction of the variance.

This size effect becomes even more obvious when looking at the trend of the characteristic strength values normalized to the characteristic reference strength (Fig. 6a). We analytically describe k_h with Eq. (1) in conjunction with Eq. (4). To this end, the characteristic reference bending strength $f_{b,k,ref}$ and power law parameter m^* are fitted to our simulation results in the sense of the least squares method. The reference beam depth h_{ref} for Eq. (4) was 600 mm. The characteristic reference bending strengths $f_{b,k,ref}$ found through fitting overestimate the values provided by *DIN EN 14080* (2013) by about 7 % and 4 % for GL 24h and GL 30h, respectively (Tab. 3). The found parameter m^* is quite similar for both strength classes, which basically describes the same extent of

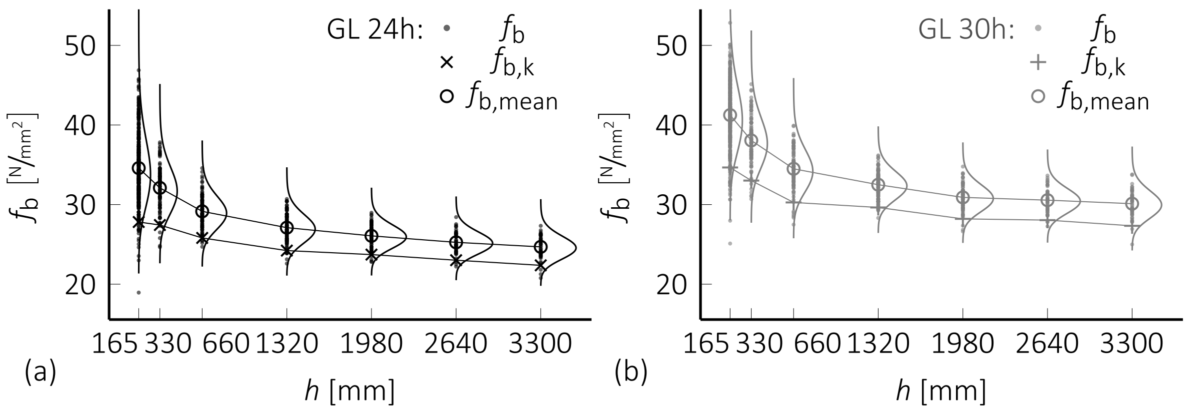

Figure 5. Bending strength f_b values and distributions obtained from simulations with the beam depth h and dimensional ratio of 4×1.5 *for strength classes (a) GL 24h and (b) GL 30h. Redrawn from Vida et al. (2022c)*

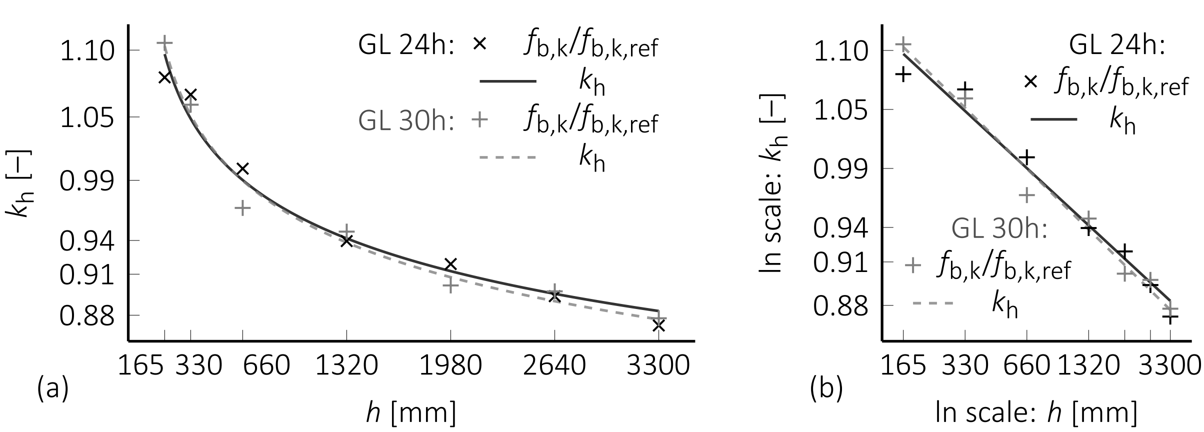

Figure 6. The factor k_h, commonly describing the size effect, for GLT beams having a depth h of up to 3300 mm in (a) linear scale and (b) ln scale. Redrawn from Vida et al. (2022c)

Table 3. Characteristic reference bending strength $f_{\mathrm{b,k,ref}}$ and power law parameter m^* fitted to our simulation results. (Vida et al., 2022c)

Criterion	GL 24h		GL 30h	
	$f_{\mathrm{b,k,ref}}$ $[\mathrm{N/mm^2}]$	m^* $[-]$	$f_{\mathrm{b,k,ref}}$ $[\mathrm{N/mm^2}]$	m^* $[-]$
Load drop	25.74	13.50	31.23	12.69

decrease (Tab. 3). The mean value of m^* is 13.1. The suitability to describe k_{h} for different beam depths h by a power law can be seen in a ln–ln plot, where a straight line represents the simulation results very well (Fig. 6b).

Our predicted size effect k_{h} quantifies the strength decrease also for large GLT beams. As the parameter m^* governs the decrease, the quite similar results of both strength classes lead to a decrease of basically the same extent. As a result, the characteristic bending strengths $f_{\mathrm{b,k}}$ of large beams with a depth of 3300 mm decreases of about 12 % compared to $f_{\mathrm{b,k,ref}}$ (Fig. 6). For smaller beam depths than h_{ref}, the herein predicted k_{h} agrees well with the modification according to Eq. (2) from *DIN EN 1995-1-1* (2010). Additionally, our results agree very well with two experimental studies from the literature testing beams with depths of about 300 mm and 600 mm. *Schickhofer* (1996) identified k_{h} as 1.04 and *Aasheim and Solli* (1995) as 1.07. In comparison, our approach predicts k_{h} to be 1.05 for the same beam depths by employing Eq. (4) with the parameter m^* as the mean value of both strength classes.

3.3 Beam sections with different dimensional ratios

The bending strength seems to depend heavily on the dimensional ratio of the beam (Fig. 4). Thus, an appropriate formulation is needed to determine realistic bending strengths for different dimensional ratios. This is efficiently enabled by the procedure proposed in Section 2.3 using only the simulation results of the model with a dimensional ratio of 1.5. With this procedure, we analyze the estimated bending strengths of GLT sections of all seven depths h and of five different lengths to depth ratios ℓ/h, ranging from 1.5 to 9.0.

The obtained characteristic bending strengths $f_{\mathrm{b,k},h,\ell/h}$ are then normalized by the result $f_{\mathrm{b,k},h,6.0}$ of the corresponding beam depth h with a ratio ℓ/h of 6.0 (4×1.5). This normalized value is denoted as $k_{\ell/h}$ and is plotted for all simulated beam depths h in Fig. 7. There, the influence of different beam lengths, based on the five ratios, is illustrated for all beam depths individually. The beam length for a specific ratio is thus different for each beam depth.

Generally, when focusing on an individual beam depth h, the characteristic bending strength decreases with increasing dimensional ratio (beam length). This effect is more pronounced for smaller beam depths, especially smaller than 660 mm. Above 660 mm the factor $k_{\ell/h}$ stays almost constant with increasing h for each dimensional ratio. This

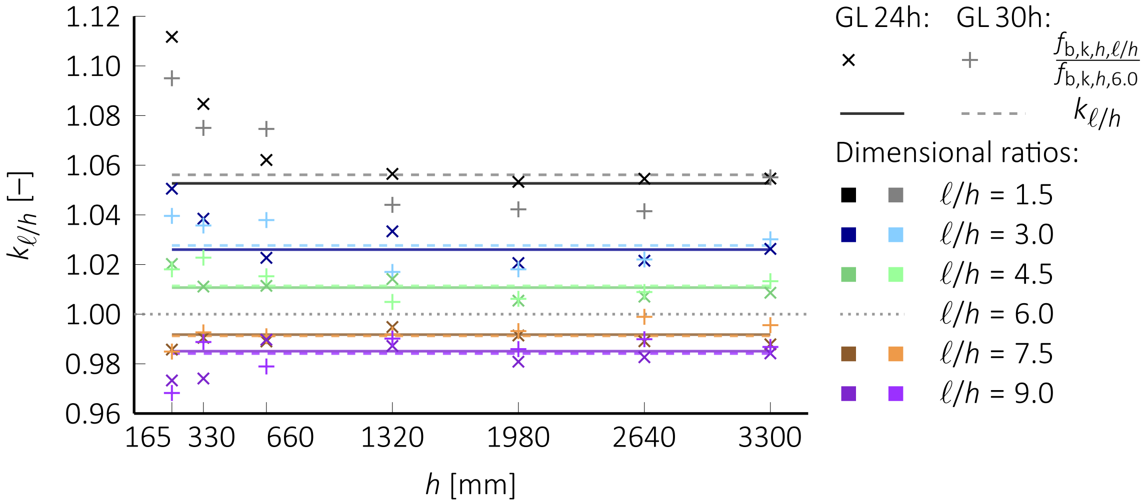

Figure 7. Comparison of the normalized values $k_{\ell/h}$ of each individual beam depth h: the scatters refer to the simulated results obtained by using Eq. (8), and the horizontal lines are according to Eq. (10). Redrawn from Vida et al. (2022c)

effect can be described quite adequately with the general relation according to Eq. (3) (Fig. 7, horizontal lines).

To this end, Eq. (3) is specified for beams with a constant width, dimensional reference ratio of 6.0, and reference depth of 600 mm:

$$k_h = \left(\frac{6.0 \cdot 600^2}{\ell/h \cdot h^2}\right)^{\frac{1}{m}} , \tag{9}$$

where ℓ/h denotes the specific dimensional ratio with the length ℓ and depth h. Finally, the factor k_h can be normalized by dividing Eq. (9) with itself specified for the dimensional reference ratio ℓ/h = 6.0, giving the factor $k_{\ell/h}$:

$$k_{\ell/h} = \left(\frac{6.0 \cdot 600^2}{\ell/h \cdot h^2}\right)^{\frac{1}{m}} / \left(\frac{6.0 \cdot 600^2}{6.0 \cdot h^2}\right)^{\frac{1}{m}} = \left(\frac{6.0}{\ell/h}\right)^{\frac{1}{m}} . \tag{10}$$

The parameter m can be determined by simulations, but m^* was already fitted based on the realized simulations representing the dimensional ratio ℓ/h of 6.0 (Fig. 5). The relation of the two parameters m and m^* was given in Eq. (4). Thus, m equals $2\,m^*$ with m^* according to Tab. 3 for the corresponding strength class.

3.4 Influence of the applied global failure criterion

The numerical studies presented by *Fink et al.* (2015) and *Frese and Blaß* (2015) applied different global failure criteria. The present approach and the ones from the literature all follow different modeling strategies. The applied global failure criterion defines the simulated load-bearing capacity M_{max} that is used to further calculate the corresponding bending strength f_b of the beam sections. We have tried to replicate their criteria, and apply them within our modeling approach to investigate potential differences. Our approach allows us to do this because we simulate the entire load–displacement curve, illustrated in Fig. 8 as the relation between the bending moment and the rotation.

Additional to our already presented *load drop criterion*, we apply the following global failure criteria to study their influence on the bending strength:

- The *system stiffness reduction criterion*, which is met by the first global stiffness reduction of at least 1 % compared to the initial global stiffness obtained from the first loading increment. In each increment, the system stiffness is calculated with the current bending moment and rotation. The load-bearing capacity is then the maximum load during the loading before the criterion is fulfilled. This implementation is similar to the criterion applied by *Fink et al.* (2015).
- The *first crack initiation criterion* focuses only on the initiation of the first crack in the outermost tensile lamination to identify the load-bearing capacity, which is then the maximum bending moment observed during the simulation up to this point. During the loading process, an arbitrary number of cracks can occur within the beam. This criterion is comparable with the one used by *Frese* (2016) and *Frese and Blaß* (2015).

Figure 8 shows the load–displacement curves with the obtained global failure points according to the criteria for three exemplary GLT beams with different depths. As illustrated, the simulated load-bearing capacity of an individual beam can heavily depend on the applied global failure criterion. During the simulation, the beam's structure is damaged by the initiation and progression of local failure mechanisms, which are summarized below.

A vertical crack is initiated when the tensile stress in the element's centroid exceeds the assigned strength. After the initiation, the crack surfaces are still able to transfer stresses according to a traction–separation law. With increasing separation of the crack

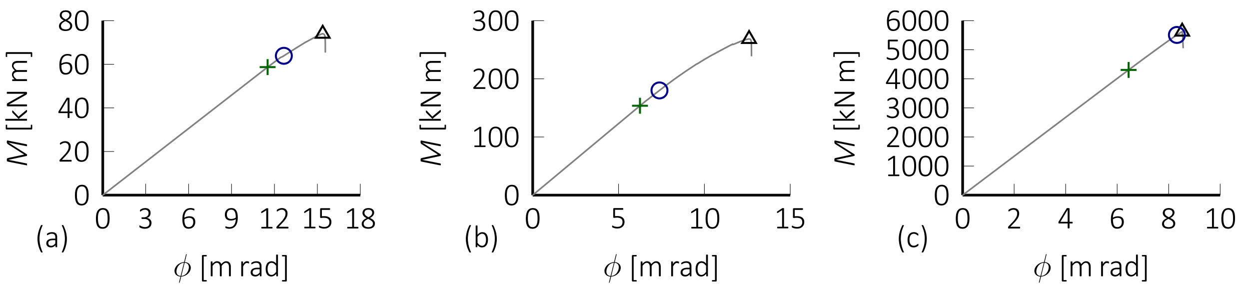

Figure 8. Exemplary load–displacement curves, with bending moment M and rotation ϕ, for beams of strength class GL 30h with a depth h of (a) 330 mm, (b) 660 mm, and (c) 3300 mm. Marking the three global failure criteria: (i) the first crack initiation in the outermost tensile lamella criterion with a green plus, (ii) the system stiffness reduction criterion with a blue circle, and (iii) the load drop criterion with a black triangle. Redrawn from Vida et al. (2022b)

surfaces the transferred stresses are degraded until the two surfaces can move freely. The vertical cracks are able to form continuous crack patterns over multiple laminations with the implementation of horizontal cracks between the laminations. Additionally, for beams of up to 660 mm depth, plastic deformations in the compressive zones are considered with a multisurface failure criterion. All these local failure mechanisms affect the load-bearing behavior described by the load–displacement curves (Fig. 8).

The GLT beam stiffness obtained by simulations is influenced by the initiated and progressing damage, which causes the non-linear behavior and the abrupt load drop (Fig. 8). Experimentally, the non-linearity was also observed by *Kandler et al.* (2018a), *Fink et al.* (2013), and *Ehlbeck et al.* (1984). Generally, *Fink et al.* (2013) observed a less pronounced non-linear behavior.

Regarding the first crack initiation in the outermost tensile lamination, the present approach allows for a brittle crack initiation only over a part of the lamination depth, e.g., in only one finite element. In contrast, the criterion applied by *Frese* (2016) and *Frese and Blaß* (2015) accounts for brittle failure of the entire outermost tensile lamination. There, a two-dimensional finite element approach was applied with one element over the lamination depth. However, the brittle crack initiation in an element over the entire lamination or only a part of the cross-section is linked by the stress distribution gradient. The gradient depends on the beam depth according to beam theory. With increasing depth, the gradient and the difference between the two cases decrease. Thus, our comparable criterion delivers a closely related result that features the original brittle behavior without prior damaging the outermost tensile lamination.

To the entire simulated sample of each beam depth, PDFs were fitted by maximum likelihood estimations (Fig. 9). The two-parameter log-normal distribution was used for the results estimated by the system stiffness reduction criterion. For the results obtained by the first crack initiation criterion, the four-parameter beta distribution was applied for the set strength range of 0 N/mm^2 to 100 N/mm^2. The mean and characteristic values were taken from the probability distributions.

Depending on the applied global failure criterion, the PDFs of the bending strengths show different characteristics. Generally, both strength classes share the same characteristics. The results obtained by the system stiffness reduction criterion have a decreasing mean value with increasing beam depth, but the characteristic value hardly changes due to a reduction of the variation (Fig. 9a,b). Those characteristics were also found by *Fink et al.* (2015). The first crack initiation criterion result in mainly constant COVs for different beam sizes (Fig. 9c,d). Thus, the mean and characteristic values decrease about the same for beams with increasing depth. In contrast to the almost constant COVs, *Frese and Blaß* (2016) found a decreasing COV for increasing beam depths. Generally, the strengths obtained by the first crack initiation criterion are lower than the results obtained by the other two criteria (Fig. 9).

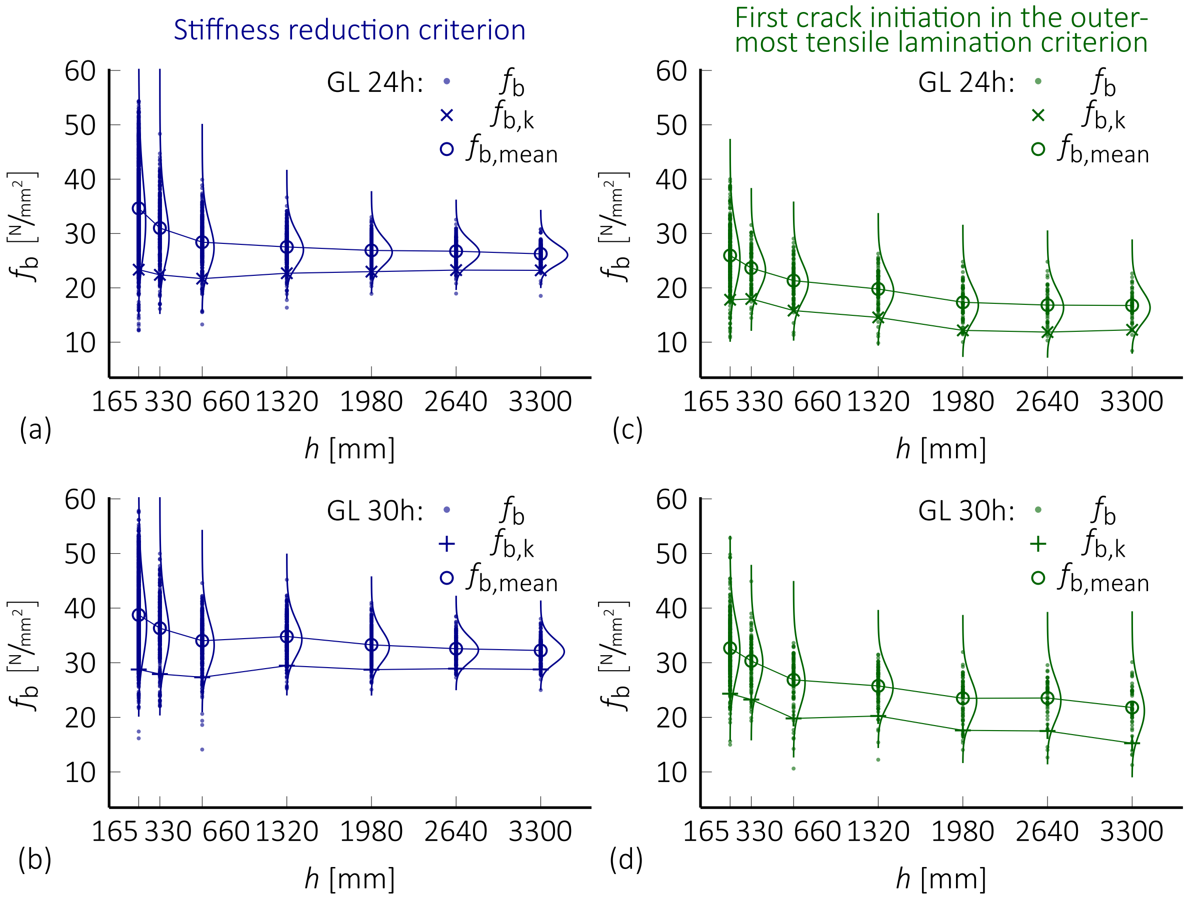

Figure 9. Bending strength f_b values and distributions obtained from simulations with the beam depth h employing the (a,b) system stiffness reduction criterion (dimensional ratio of 1.5*) and the (c,d) first crack initiation criterion (dimensional ratio of* 4 × 1.5*) for both strength classes. Redrawn from Vida et al. (2022b)*

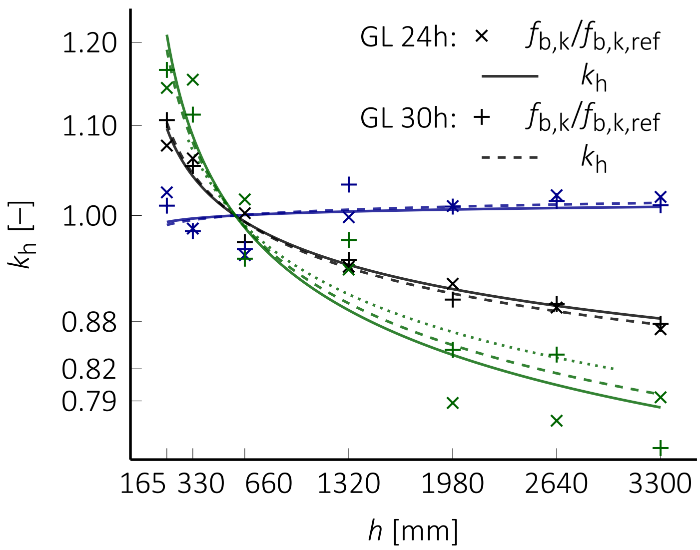

Figure 10. k_h factor according to Eq. (4), obtained with simulations based on three different global failure criteria: (i) the load drop criterion in black*, (ii) the system stiffness reduction criterion in* blue*, and (iii) the first crack initiation in the outermost tensile lamination criterion in* green *compared to (iv) the proposed result by Frese and Blaß (2015) with the dotted line in* green*. Redrawn from Vida et al. (2022b)*

The observed size effect, expressed by k_h, heavily depends on the applied global failure criterion (Fig. 10). For the analytically description of k_h, we again use Eq. (1) in conjunction with Eq. (4) to fit $f_{b,k,ref}$ and m^* (Tab. 4). Now, we compare the two additional criteria to the already presented results obtained by the load drop criterion (Fig. 10, denoted in *black*). In comparison, the system stiffness reduction criterion shows a basically constant characteristic bending strength for all beam sizes (Fig. 10, denoted in *blue*). The same trend was found by *Fink et al.* (2015). The results obtained by the first crack initiation criterion suggest a greater decrease of the characteristic bending strength (Fig. 10, denoted in *green*). The more pronounced trend agrees with the findings presented by *Frese and Blaß* (2015) (Fig. 10, denoted with the dotted line in *green*).

Table 4. Characteristic reference bending strength $f_{b,k,ref}$ and power law parameter m^* fitted to our simulation results. (Vida et al., 2022b)

Criterion	GL 24h $f_{b,k,ref}$ $[N/mm^2]$	GL 24h m^* $[-]$	GL 30h $f_{b,k,ref}$ $[N/mm^2]$	GL 30h m^* $[-]$
System stiffness reduction	22.73	−171.94	28.44	−117.81
First crack initiation[a]	15.53	6.83	20.84	7.39

[a] In the outermost tensile lamination.

4 Conclusion

Based on a comprehensive simulation campaign, the size effect could be predicted qualitatively as well as quantitatively for beam depths ranging from 165 mm to 3300 mm using the load drop criterion. For the characteristic strength values, a decrease of up to about 12 % was observed compared to the reference depth of 600 mm. Simultaneously with the characteristic strength decrease, the variation of simulated strengths significantly decreased with increasing beam depths. We found that additional to the beam depth also the beam length influences the characteristic bending strength. This effect can be described very well with the concept proposed by *Colling* (1986), at least for beams with depths greater than 660 mm. We could successfully reproduce different global failure criteria from the literature, which heavily influence the observed size effect.

In the opinion of the authors, the size effect on the characteristic bending strength is also present for large GLT beams. Although results obtained by numerical simulations heavily depend on the modeling strategy, the presented advanced simulations seem to be a promising way to achieve reasonable predictions. Nevertheless, the authors recommend further test series on GLT beams with different dimensions. This would allow simulation concepts to be validated and their informative value to be strengthened. Large parameter studies of different kind, which can be performed efficiently with simulations, would gain in value and could be used as a basis for standardization.

5 References

Aasheim, E. and K. H. Solli (1995). Size factor of Norwegian glued laminated beams. *CIB-W18 Meeting 28*. Paper CIB-W18/28-12-2. Copenhagen, Denmark.

Abaqus (2021). Abaqus 2021 HF5. Dassault Systèmes Simulia Corp. Providence, RI, USA.

Bohannan, B. (1966). Effect of size on bending strength of wood members. Research Paper FPL-56. Madison, WI, USA: U.S. Department of Agriculture, Forest Service, Forest Products Laboratory.

Colling, F. (1986). Einfluß des Volumens und der Spannungsverteilung auf die Festigkeit eines Rechteckträgers: Herleitung einer allgemeinen Beziehung mit Hilfe der 2-parametrigen Weibull-Verteilung. *Holz als roh- und werkstoff* 44(4): 121–125.

DIN EN 14080 (2013). Holzbauwerke – Brettschichtholz und Balkenschichtholz – Anforderungen; Deutsche Fassung EN 14080:2013. Berlin, Germany: DIN.

DIN EN 1995-1-1 (2010). Eurocode 5: Bemessung und Konstruktion von Holzbauten – Teil 1-1: Allgemeines – Allgemeine Regeln und Regeln für den Hochbau; Deutsche Fassung EN 1995-1-1:2004 + AC:2006 + A1:2008. Berlin, Germany: DIN.

DIN EN 408 (2012). Holzbauwerke – Bauholz für tragende Zwecke und Brettschichtholz – Bestimmung einiger physikalischer und mechanischer Eigenschaften; Deutsche Fassung EN 408:2010+A1:2012. Berlin, Germany: DIN.

Ehlbeck, J., F. Colling, and R. Görlacher (1984). Einfluß keilgezinkter Lamellen auf die Biegefestigkeit von Brettschichtholzträgern. Forschungsbericht. Karlsruhe, Germany: Versuchsanstalt für Stahl, Holz und Steine, Abt. Ingenieurholzbau und Baukonstruktionen, Universität Fridericiana Karlsruhe.

Fink, G., A. Frangi, and J. Kohler (2015). Probabilistic approach for modelling the load-bearing capacity of glued laminated timber. *Engineering structures* 100: 751–762.

Fink, G., J. Kohler, and A. Frangi (2013). Bending tests on glued laminated timber beams with well-known material properties: Test report. Report. Zurich, Switzerland: Institut für Baustatik und Konstruktion, ETH Zürich.

Frese, M. (2016). Computergestützte verfahren zur pragmatischen beurteilung der tragwiderstände von brettschichtholz: zusammenfassung exemplarischer simulationsstudien. Karlsruhe, Germany: KIT Scientific Publishing.

Frese, M. and H. J. Blaß (2015). Numerical description of size and load configuration effects in glulam structures. *Proceedings of the 12th International Conference on Applications of Statistics and Probability in Civil Engineering (ICASP12)*. Vancouver, Canada.

Frese, M. and H. J. Blaß (2016). Reliability of large glulam members Part 1: Data for the assessment of partial safety factors for the bending strength. *INTER Meeting 49*. Paper INTER/49-17-1. Graz, Austria.

Kandler, G., M. Lukacevic, and J. Füssl (2018a). Experimental study on glued laminated timber beams with well-known knot morphology. *European journal of wood and wood products* 76(5): 1435–1452.

Kandler, G., M. Lukacevic, C. Zechmeister, S. Wolff, and J. Füssl (2018b). Stochastic engineering framework for timber structural elements and its application to glued laminated timber beams. *Construction and building materials* 190(5): 573–592.

Lukacevic, M., J. Füssl, and R. Lampert (2015). Failure mechanisms of clear wood identified at wood cell level by an approach based on the extended finite element method. *Engineering fracture mechanics* 144: 158–175.

Lukacevic, M., W. Lederer, and J. Füssl (2017). A microstructure-based multisurface failure criterion for the description of brittle and ductile failure mechanisms of clear-wood. *Engineering fracture mechanics* 176: 83–99.

Pech, S., M. Lukacevic, and J. Füssl (2021). A robust multisurface return-mapping algorithm and its implementation in Abaqus. *Finite elements in analysis and design* 190: 103531.

Pischl, R., G. Schickhofer, C. Seiner, A. Steinberger, E. Gehri, and R. Mauritz (1995). Entwicklung leistungsfähiger Holzleimbauteile: Zusammenfassender Bericht zum FFF-Forschungsprojekt. FFF-Forschungsprojekt. Graz/A – Zürich/CH – Wien/A.

Schickhofer, G. (1996). Development of efficient glued laminated timber. *CIB-W18 Meeting 29*. Paper CIB-W18/29-12-1. Bordeaux, France.

Tapia Camú, C. and S. Aicher (2018). A stochastic finite element model for glulam beams of hardwoods. *Proceedings of the 2018 World Conference on Timber Engineering (WCTE 2018)*. Seoul, Republic of Korea.

Vida, C., M. Lukacevic, J. Eberhardsteiner, and J. Füssl (2022a). Modeling approach to estimate the bending strength and failure mechanisms of glued laminated timber beams. *Engineering structures* 255: 113862.

Vida, C., M. Lukacevic, and J. Füssl (2022b). Size effect of glued laminated timber predicted by simulation concepts – Influence of global failure criterion definition on bending strength and failure mechanism. (manuscript in preparation).

– (2022c). Size effect on bending strength of glued laminated timber predicted by a numerical simulation concept including discrete cracking (manuscript in preparation).

Weibull, W. (1939). A statistical theory of the strength of materials. Handlingar Nr. 151. Stockholm, Sweden: Ingeniörsvetenskapsakademiens, Generalstabens litografiska anstalts förlag.

DISCUSSION

The paper was presented by C. Vida

H Blass stated that the cited GLT bending tests were conducted by other institutes such as in Scandinavia. He asked if detailed information on the bending tests and failure modes were considered. C Vida stated that the data was informative. H Blass commented that in bending tests of GLT, finger joint failures would typically also influence the failure of beams. C Vida said that the model did not consider finger joints as the boards in the model were 5.4 m long. Also the model assumed that finger joints were stronger than boards because knots were cut out before finger jointing. H Blass said that this is a rough assumption and stated that also clear wood stiffness is lower than finger joint stiffness, hence finger joints would attract higher loads.

F Lam agreed with H Blass comments on importance of considering finger joints in models. The UBC database on GLT beams (including 1.2 m deep 21 m long beams) showed that finger joints often govern beam capacity. The CV of these large beams is consistent with the smaller beams. F Lam stated that it would be better to show cumulative probability distributions with data points rather than probability density functions when verifying models. He questioned the assumption of the factor m being size dependent as this contradicts Weibull weakest link theory which is the basis of the size effect model. C Vida said that at the end the size effect provision is based on power law fitting not Weibull.

S Aicher stated that finger joint strengths have large variations and can have an influence on beam bending strength. He asked how MOE's were considered and if there was any correlation between MOE and strength. C Vida replied that KAR was used to determine tensile strengths and was correlated via regression from a different distribution.

C Tapia stated that the size effect curves presented cannot be easily assessed and suggested log-log plots would show clearer trends. Also showing cumulative distributions would be clearer. C Vida replied that rough evaluation with long beam sections were considered, and the model fitted well with characteristic bending strength based on log-normal distribution. Other distributions might have different results. Also 400 simulations with large size beams were conducted.

A Frangi stated that the benchmarking would have a bias if not compared with other data. He stated that he was surprised by such a large difference between the different failure criteria. C Vida replied that the model could have a bias and that he was also surprised by the difference offered by the failure criterions. He stated that with smaller dimension beams, beam theory was used and failure was only depended on bending moments.

P Palma received clarification that in fitting of distributions C Vida did not fit to different ranges.

R Brandner received confirmation that the simulation data base had 140 boards and the simulated 3 m high beams used all these boards. Also most of the boards did not contribute to failure. He stated that a bigger database is needed to be representative, also for width effect considerations.

P Dietsch stated that the model results seemed to show unrealistic lag between occurrence of first crack until final failure. He stated there are large data sets on glulam bending tests in Europe and they should be mirrored in the results of the model. He also questioned whether the minimum CV of 6% for 3 m beams is appropriate. C Vida said that the 1st crack may not correspond to tensile failure of the outer lamina. P Dietsch stated that in this case the model does not represent Frese's failure criterion as stated in the paper. They also discussed the influence of dynamic impact in failure. Both agreed that industry should invest in testing larger GLT beams to clarify the issue.

E Serrano questioned benchmarking a model that does not consider finger joints to models that do consider the influence of finger joints. E Serrano also received confirmation that the model can consider finger joints if data was available.

A Frangi received confirmation that Fink's failure criterion based on stiffness reduction was not used here.

S Aicher stated that the GLT model must consider finger joint failure and its variability. He also mentioned that finger joint failure can have larger variability than knots, as shown in reports of factory production control. MPA Stuttgart has also datasets on large beams. S Aicher stated that one should also examine the N. American data base on GLT beam tests and check N. American m-values.

S Winter stated that size effect in GLT is needed to be considered and asked, if this was common understanding in the group.

Design of timber trusses with dowelled steel-to-timber connections

Stephan Schilling[1)], Nadja Manser[2) 1)], Pedro Palma[2)], René Steiger[2)], Andrea Frangi[1)]

[1)] ETH Zürich, Institute of Structural Engineering, Switzerland

[2)] Empa – Swiss Federal Laboratories for Materials Science and Technology, Structural Engineering Research Laboratory, Dübendorf, Switzerland

Keywords: Design parameters, trusses, dowelled steel-to-timber connections, stiffness, load-deformation behaviour, load-carrying capacity

1 Introduction

Timber trusses with dowelled steel-to-timber connections with slotted-in steel plates are commonly used in large-span roof structures and bridges, and lately even as mega-frames for the lateral stiffening of high-rise timber buildings. The layout of timber trusses has not changed significantly since around 1800, even though the connection technologies have undergone significant developments (Möhler 1966, Gehri et al. 1979). Dowelled connections began to be used around 1900, but nailed connections and split ring connectors became more popular for some decades. The main reason for this dominance of nailed over dowelled connections was the too favourable testing conditions of nailed connections (Gehri et al. 1979, Gehri 1980). Until the 1960s, sufficient load-carrying capacity was ensured by applying global safety factors, alongside small truss slenderness ratios (i.e. truss height-to-span ratios) which were recommended in order to limit deflections (Möhler 1966). No requirements were imposed on the connection stiffness. Over the years, the construction of more slender timber trusses became popular and studies on their behaviour were conducted (Möhler 1966). Since the 1980s, connections with dowel-type fasteners became the most popular. Parallel to this development, solid timber members were replaced by engineered wood products, namely glued laminated timber (GLT) (Gehri et al. 1979, Dubas et al. 1981). Contrary to traditional timber-to-timber connections with single split ring connectors or nailed connections, dowelled connections do exhibit considerable bending stiffness, especially if assembled with slotted-in steel plates (Dubas et al. 1981). Therefore, the axial, lateral and rotational stiffnesses of the connections in joints of modern trusses depend on construction detailing. Due to this and because the chords of these trusses are usually continuous members, the requirements for application of the ideal-truss theory (Culmann 1866) during design are not met. Various investigations were conducted considering modelling approaches for truss joints and their connections and to derive adequate design rules (Gehri et al. 1979, Gehri 1980, Scheer & Golze 1981, Dubas et al. 1981, Gehri et al. 1982, Gehri & Fontana 1983, Fontana 1984).

In design standards, i.e. EN 1995-1-1:2004 and SIA 265:2021, it is stated that timber trusses shall be modelled and designed as frame structures and hence, that the connection stiffness should be considered. There are, however, additional simplified design rules in both standards, valid within specified boundaries, which allow assuming axially and laterally rigid and rotationally pinned connections in the design. This assumption leads to having only axial forces acting in the members but not bending moments. Additional reduction factors and limits on allowable deflections are imposed to account for the modelling simplifications. These simplified design rules date back to a time when the use of computational models was not as widespread as it is today. Nevertheless, current design guidance for trusses with dowelled steel-to-timber connections in EN 1995-1-1:2004 and SIA 265:2021 does not allow for an easy design of these structures as frames. Such trusses inherit parasitic bending moments due to non-negligible rotational stiffness in the connections which limit the connections' axial load-carrying capacity. Furthermore, the accurate modelling of the truss joints and the consideration of the load-deformation behaviour of the connections (including axial, lateral, and rotational stiffnesses) is complex.

In this publication, (i) the above-mentioned truss design rules from the design standards are reviewed; (ii) the relevant parameters for the design of timber trusses with dowelled steel-to-timber connections are identified; (iii) different aspects of the load-deformation behaviour of such connections are discussed and compared to collected data; and (iv) the influence of eccentric loading on the load-carrying capacity of dowelled steel-to-timber connections is investigated based on collected data.

2 Truss design

2.1 Review of approaches for the design of trusses

According to EN 1995-1-1:2004, the analysis of assemblies shall be carried out by static models that consider the behaviour to an acceptable level of accuracy. Further, it is specified that frame models should be applied or, in the special case of trusses with punched metal plate fasteners, a simplified analysis can be carried out when strict geometric conditions are fulfilled. The models that shall be applied for the design of these frame structures are further specified and it is pointed out that next to precise support conditions the deformations of the members and joints are to be considered when determining the member forces and moments. With respect to connection modelling, it is recommended that their location coincides as closely as possible with the actual joint configuration and their stiffness should correspond to the actual connections. Their rotational stiffness may be assumed stiff or pinned in dependence of the expected effect on the member forces and moments.

SIA 265:2021 provides less details but in principle states the same requirement that the section forces and deformations of trusses shall be determined by means of adequate frame models and hence, that the detailing of the truss joints shall consider the corresponding normal and shear forces and bending moments. In contrast to EN 1995-1-1:2004, in SIA 265:2021 a simplified analysis is provided which is not limited to a specific connection type. Likewise, strict geometric conditions have to be fulfilled if the simplified analysis is applied. Its derivation for the first implementation in Swiss standard for the design of timber structures SIA 164:1981 clearly shows a background in trusses with nailed connections (Dubas et al. 1981). In the current version SIA 265:2021, an expansion for the consideration of the non-negligible rotational stiffness of dowelled steel-to-timber connections is included. The derivation of the reduction factor (set to 0.75) for the connections' load-carrying capacity under consideration of parasitic bending moments dates back to Gehri (1980) and Gehri et al. (1982).

The main principle of both design standards require the practitioners using accurate models for the joints and subsequently also for the connections. Despite general awareness of complex interrelations of several parameters (Sec. 2.2), simplified truss joint models and connection models are used widely. Both simplified design rules from the design standards are based on pure truss theory according to Culmann (1866) with pinned connections at all beam nodes (Figure 1b) and provide correction factors to account for the applied simplifications. When using more accurate models, commonly axial springs or both axial and rotational springs (Figure 1c) are added at the end of web members and the continuity of the chords is considered. Such models were also applied in the derivation of the simplified design rules in the SIA standards (Dubas et al. 1981). However, truss joints typically consist of three connections and not only of the two that are located at the end of web members. It was shown that the third connection, which is located in the chords, has an influence on the system deflection that is in the same order of magnitude as the web member end springs. Subsequently, the bending moments in the continuous chords determined with the model shown in Figure 1c are underestimated and the bending moments in the web members are inaccurate (Schilling 2022). In accordance with the detailed modelling prescriptions in EN 1995-1-1:2004, a joint model was developed by (Schilling 2022) which includes all connections and their correct location by introducing beams representing the steel plates (Figure 1d).

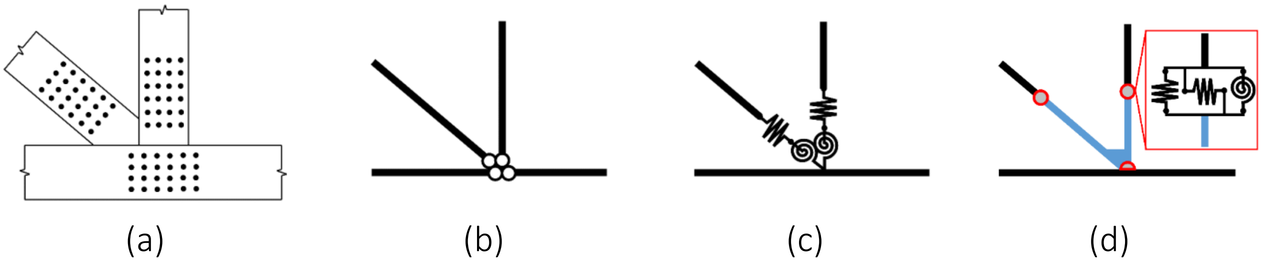

Figure 1: Truss joint with three dowelled steel-to-timber connections with slotted-in steel plates and corresponding modelling approaches based on the schematic example (a); (b) ideal truss model with pinned connections; (c) model which considers the continuity of the chords and uncoupled axial and

rotational springs at the end of the web members; and (d) model which considers the continuity of the chords, all three connections with springs for all degrees of freedom in-plane and their correct location by introducing beams representing the steel plates.

With respect to the connection modelling, the stiffness of the single dowels per shear plane under service load is the only quantity provided in the design standards. EN 1995-1-1:2004 further specifies a generalised factor of 2/3 for the conversion of the stiffness under service load to ultimate loading conditions and a factor of 2.0 for steel-to-timber connections. Schweigler et al. (2018) showed that the in-plane degrees of freedom (DoF) are actually coupled and developed a calculation procedure to determine the connection stiffness. EN 1995-1-1:2004 provides two options: (i) an accurate model for all DoF is applied or (ii) the rotational DoF is modelled pinned and rigid to get approximate lower and upper limits of the bending moments. To make the first option feasible, it is recommended to apply a parametrised finite element model, including the model developed by Schweigler et al. (2018) as a subroutine (Schilling 2022). However, for both options a more detailed model for the load-deformation behaviour of a single dowel per shear plane should be provided in the design standards. For option (i), this information is needed for all load-to-grain angles while for option (ii) it is sufficient doing so for the axial displacements.

Both standards EN 1995-1-1:2004 and SIA 265:2021 provide an approach for determining the load-carrying capacity of dowelled steel-to-timber connections that are loaded uniformly in any load-to-grain angle. However, bending moments cannot be considered. The approach to design moment resisting connections by Racher (1995) requires larger dowel spacings than provided in EN 1995-1-1:2004 and assumes that all dowels can be considered independently (no group effect). In Pedersen et al. (2001), it can be seen that a fairly ductile connection under pure lateral loading shows a brittle failure under combined or dominating moment loading even though Racher's minimal spacings are met. Therefore Racher's approach is questionable. Further, Schweigler et al. (2018) criticised Racher's approach with respect to the possibly non-conservative load-distribution due to negligence of the interaction of internal forces. Subsequently, a major prerequisite for proper connection detailing is missing in both design codes and inside the framework of Eurocode 5 and SIA 265 it has to be relied on simplified design approaches such as the one provided by SIA 265:2021.

2.2 Relevant parameters for the design of trusses

In truss design, the outer geometry, i.e. span-width, height and shape, is the most decisive property with respect to the system stiffness and inner force flow (Gehri 1983). The inner geometry, i.e. the partition of the truss members, their layout and subsequently, their inclination, influences the inner force flow as well, but is of secondary importance for the truss stiffness (Gehri 1983, Schilling 2022). As common in timber structures, the connections between the truss members are crucial. Their loading is primarily depending on the combination of outer and inner geometry (Gehri 1983). From a theoretical point of view, ideal timber trusses are built as static determined structures with large slenderness ratios (i.e. truss height-to-span ratios), leading to a dominant truss action according to Culmann (1866). Nevertheless, most connections and especially dowelled steel-to-timber connections introduce non-negligible rotational stiffness between the truss members, leading to a certain frame action in the trusses. Subsequently, bending moments occur not only in the chords, which are typically continuous, but also in the web members (Gehri 1980, Schilling 2022). Hence, the member's cross-section, their materialisation and the connection dimensions (Figure 2) influence the inner force flow (Gehri 1983). Furthermore, the axial stiffness of the connections directly influences the system stiffness and thereby indirectly the internal forces that depend on the frame action (Schilling 2022). Compared to other connections traditionally applied in trusses, steel-to-timber connections bring the advantage that the inner force flow from the truss action, i.e. the normal forces, can be perfectly centred in the joints by appropriate design – meaning that no systematic eccentricities have to be considered in the design (Dubas et al. 1981). Additionally to their influence on the force flow, dowelled steel-to-timber connections influence the stability of truss members. On the one hand, due to the stiffness of the connection, buckling lengths of truss members in-plane are reduced compared to pinned connections. On the other hand, the slots for the steel plates weaken the member cross-sections with respect to the out-of-plane buckling behaviour (Dubas et al. 1981, Schilling 2022).

In actual design situations, many of the above-listed relevant parameters cannot be chosen freely. Therefore, unfavourable conditions leading to severe frame action are common and hence, the properties of connections are of utmost importance. The behaviour of the connections themselves depends on various geometric and material parameters such as number of dowels, their spacing, the timber member thickness and the material properties (EN 1995-1-1:2004).

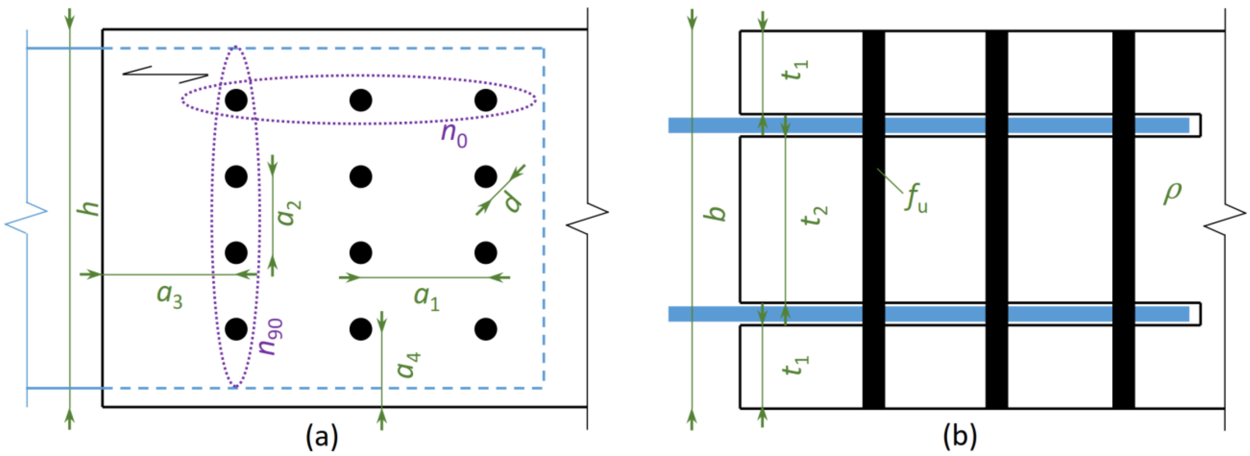

Figure 2: Dowelled steel-to-timber connection in (a) side view and (b) section view along a dowel row with the parameters: number of dowel rows n_0 parallel to grain, number of dowel rows n_{90} perpendicular to grain, dowel diameter d, tensile strength f_u, timber density ρ, side member thickness t_1, middle member thickness t_2, spacing between dowel in grain direction a_1, spacing between dowel perp. to grain direction a_2, end spacing in grain direction a_3, end spacing in perp. to grain direction a_4.

3 Load-deformation behaviour of steel-to-timber connections

If non-ductile failure modes are prevented, the load-deformation behaviour of a dowelled steel-to-timber connection can be described based on the load-deformation behaviour of single dowels (Schweigler et al. 2018). There are different approaches available to address the non-linearity in the load-deformation behaviour of single fasteners. In this paper, the approach by Richard & Abott (1975) is used (Figure 3). It is defined by the initial stiffness K_1 in the domain of the serviceability limit state, the reduced stiffness K_2 in the domain of the ultimate limit state, the intersection F_0 of K_2 with the y-axis, the deformation w_{int} at the point of reaching the load-carrying capacity and α_{RA}, a measure of how fast the curve transitions from the initial stiffness K_1 to the reduced stiffness K_2. For further investigations, this approach has been extended by three more parameters, the decreasing stiffness K_3, the deformation at the intersection of reduced and decreasing stiffness w_{int} and the ultimate deformation w_{ult}.

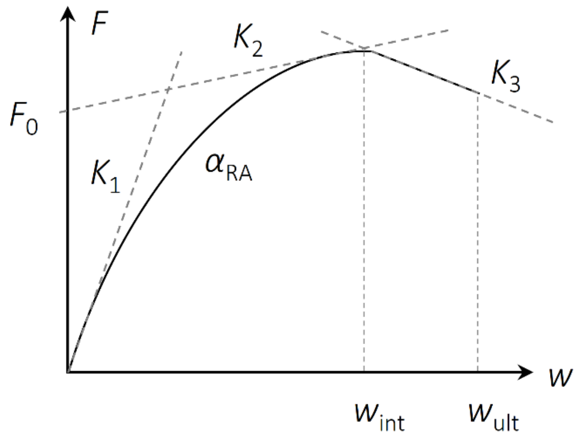

Figure 3: Approach to parametrize the load-deformation curve of a single dowel connection proposed by Richard & Abott (1975), extended with a decreasing branch.

EN 1995-1-1:2004 only defines the initial stiffness K_1, i.e. K_{ser}, per shear plane and dowel and the load-carrying capacity of single dowels and full connections. For K_{ser}, a dependence on the dowel diameter and the timber density is assumed in EN 1995-1-1:2004 and SIA 265:2021, but the formulae (1) and (2) are different with respect to factor, exponents and quantile value (mean and characteristic level) of the density:

$$K_{\text{ser,EC5}} = \frac{2}{23} \cdot d \cdot \rho_{\text{mean}}^{1.5} \tag{1}$$

$$K_{\text{ser,SIA}} = 6 \cdot d^{1.7} \cdot \rho_{\text{k}}^{0.5} \tag{2}$$

Based on existing experimental data (Table 1), the load-deformation behaviour along the grain is discussed and an enhanced approach for modelling is presented. The analysed experiments involve dowels with diameters between 6.3 and 12 mm and tensile strengths between 390 and 1390 N/mm^2. All specimens were made of Norway spruce (*picea abies*), most of glued laminated timber and some of solid timber. Many experimental sub-series were conducted in order to investigate specific parameters, such as the influence of the number of dowels in a row. Subsequently, properties like the number of dowels, member thickness and dowel spacing were varied throughout the experiments and studies.

Collecting all parameters depicted in Figure 2 for every experiment, the load-deformation curve has been evaluated per shear plane and dowel. The curve of each experiment has been parametrized using the approach described in Richard & Abbott (1975) (Figure 3), extended by a third, decreasing stiffness K_3 (Manser 2021).

Table 1: Overview of the experimental data used for the investigation of the load-deformation behaviour of a single dowel per shear plane and dowel in a dowelled steel-to-timber connection.

Source	Dowel properties		Timber	Number of tests
	d [mm]	f_u [N/mm^2]	(Norway spruce)	
Mischler (1998)	6.3	650	GLT	139
		390		12
Van Groesen and Kranenburg (2007)	8.0	1240	C24	32
Langedijk (2007)	8.0	1240	C24	11
Erchinger (2009)	6.3	600	GL24h	15
		640		10
Sandhaas (2012)	12.0	590	GL28h	15
		1390		10

In Figure 4, K_{ser} determined in every experimental configuration is compared to K_{ser} resulting when applying Formulae (1) & (2) to the data. To compare the ability of the design formulae to describe the collected values of K_{ser}, the coefficient of determination R^2 is used. For EN 1995-1-1:2004, the respective R^2 value is 0.19 and for SIA 265:2021 a value of 0.63 was determined (Manser 2021). Hence, both models predict K_{ser} of the database with insufficient precision. A possible explanation of the higher R^2 value found when applying Formula (1) is that the latter is based on experimental investigations of connections with small dowel diameters and the majority of the data analysed consists of experiments on dowels of small diameters.

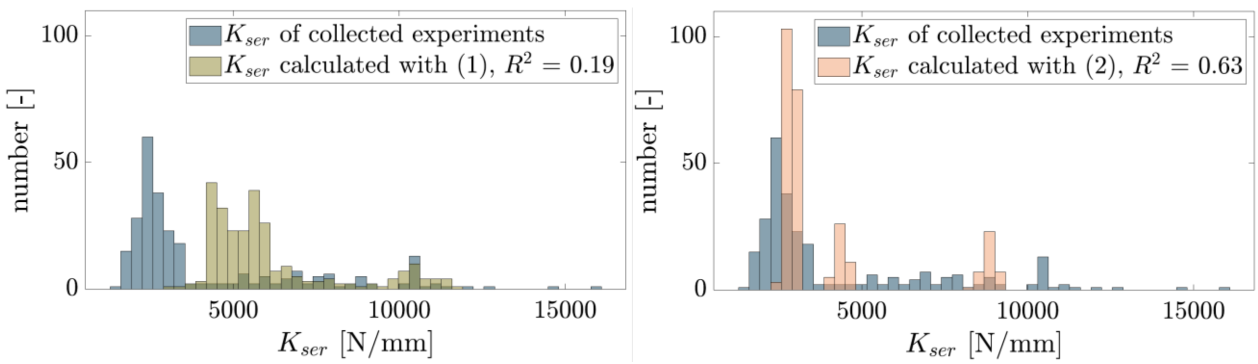

Figure 4: Comparison of K_{ser} of the collected experiments and the results obtained when calculating K_{ser} for each experimental setup acc. to Formula (1) (left) and Formula (2) (right).

To evaluate the influence of the tensile strength of the dowel, the number of dowel rows parallel and perpendicular to the grain and the geometric parameters normalized by the dowel diameter (Figure 2), a non-linear regression model with a power function of the form $A \cdot d^B \cdot \rho^C \cdot par^D$ was applied to the collected values of K_{ser}. The coefficients of determination R^2 of these regressions resulted in values between 0.65 and 0.75 (Manser 2021). The R^2 value of the function including the number of dowels parallel to the grain is the highest, meaning that beside the dowel diameter and the timber density, this particular parameter has the largest influence on the load-deformation behaviour of a single dowel. The regression model does not reveal a distinctive second-best parameter, since the R^2 values of all other evaluated parameters are similar.

A study by Jockwer and Jorissen (2018) confirmed the correctness of the formulae in the design standards to calculate K_{ser} of dowelled timber-to-timber connections as power functions, but they included the dowel diameter, the number of dowels perpendicular and parallel to the grain and the timber thickness normalized by the dowel diameter in their model. They did not take the influence of the timber density and the tensile strength of the dowel into account, as there was no significant variation in these parameters in the database. The collected data of the study described in the present paper shows a significant variation in the timber density and the dowel tensile strength. Subsequently, these two parameters have additionally been included in the non-linear regression. Furthermore, the middle member thickness normalized by the dowel diameter has been accounted for in the regression model (Formula 3), resulting in a R^2 value of 0.85 (Manser 2021). Using this regression model, the collected values of K_{ser} can be predicted with much higher accuracy than when using Formula (1) or Formula (2).

$$K_{\mathrm{ser}} = A \cdot n_{90}^{B} \cdot n_{0}^{C} \cdot d^{D} \cdot f_{\mathrm{u}}^{E} \cdot \rho^{F} \cdot \left(\frac{t_1}{d}\right)^{G} \cdot \left(\frac{t_2}{d}\right)^{H} \tag{3}$$

To further increase the accuracy, all geometric and material specific parameters have been included in the regression model (Formula (4)), resulting in a R^2 value of 0.92 (Manser 2021).

$$K_{ser} = A \cdot n_{90}^{B} \cdot n_{0}^{C} \cdot d^{D} \cdot f_{\mathrm{u}}^{E} \cdot \rho^{F} \cdot \left(\frac{t_1}{d}\right)^{G} \cdot \left(\frac{t_2}{d}\right)^{H} \cdot \left(\frac{a_1}{d}\right)^{I} \cdot \left(\frac{a_2}{d}\right)^{K} \cdot \left(\frac{a_3}{d}\right)^{L} \cdot \left(\frac{a_4}{d}\right)^{M} \tag{4}$$

Applying regression models similar to Formula (4), i.e. replacing K_{ser} with respective parameters, a model for all curve characterizing parameters of the load-deformation curve (Figure 3) has been evaluated (Manser 2021). The resulting coefficients of determination R^2 are listed in Table 2.

Table 2: Coefficients of determination R^2 for all curve-characterizing parameters of the load-deformation curve of a single dowel connection (Manser 2021).

	F_0	K_1	K_2	K_3	w_{int}	w_{ult}	α_{RA}
R^2	0.98	0.92	0.81	0.24	0.71	0.59	0.26

The regression model (4) is not suitable to accurately describe α_{RA}. The scattering of α_{RA} around the mean value is small and mostly independent of the configuration and therefore it was decided to set α_{RA} constant, i.e. to take its mean value. The regressions of the parameters describing the curve up to the load-carrying capacity (F_0, K_1, K_2, w_{int}) have R^2 values between 0.71 and 0.98 and hence, describe the parameters sufficiently accurately. For the parameters describing the post-peak behaviour (K_3, w_{ult}) the regressions show low R^2 values.

Overall, from the regression analyses it can be concluded that the approach of applying various connection parameters in a power-function is appropriate to describe the first part of the extended Richard & Abbott (1975) curve accurately, in case the transition parameter α_{RA} is set constant. The post-peak behaviour cannot be described sufficiently accurately but is generally less important. To improve the model and to be able to better identify and exclude irrelevant parameters, more data should be collected, in particular data with systematic changes in all parameters.

To describe the load-deformation behaviour of arbitrarily loaded dowelled steel-to-timber connections, the load-deformation behaviour per shear plane and dowel must be available for all load-to-grain angles. However, hardly any tests on full connections conducted in load-to-grain angles other than parallel-to-grain are available. When bending moments are acting in the tested connection, the evaluation per shear plane and dowel is difficult. Therefore, single dowel connection tests conducted on spruce LVL along and perpendicular to the grain with the same connection configuration had been analysed by Eschmann (2021). For the parameters needed to describe the curve in its rising branch (Figure 3), conversion factors k_{conv} were determined (Table 3) (Manser 2021). By multiplying the parameters of the load-deformation curve per dowel and shear plane for 0° with these conversion factors, the behaviour for 90° load-to-grain angles can be estimated. For arbitrary load-to-grain angles, it is recommended to interpolate between 0 and 90° load-to-grain angles applying the approach developed by Hankinson (1921). The conversion factor of the initial stiffness is smaller than the one applied in SIA 265:2021 where it is 0.5. EN 1995-1-1:2004 only provides one value for all load-to-grain angles.

Table 3: Conversion factors k_{conv} to estimate selected parameters of the load-deformation curve of single-dowel connections perp.-to-grain based on values parallel-to-grain ($par_{90°,i} = k_{conv} \cdot par_{0°,i}$) (Manser 2021).

	F_0	K_1	K_2	w_{int}	α_{RA}
k_{conv}	0.61	0.33	2.0	1.4	1.4

4 Connection load-carrying capacity under complex loading

Dowelled steel-to-timber connections provide resistance in all degrees of freedom but so far, no model is available to determine the load-carrying capacity under complex multiaxial loading (Section 2). Due to the high stiffness of dowelled connections, in the joints not only axial forces are acting, but also shear forces and bending moments. In trusses, normal forces dominate and shear forces are small enough to be neglected. The influence of the "parasitic" bending moments on the load-carrying capacity has been investigated by Gehri (1980). The experimental setup used by Gehri is schematically shown in Figure 5. The investigated bending moments were introduced by an eccentrically applied normal force. One single connection configuration (Figure 7) was tested without and with three different values of eccentricity. Each of the tests was repeated twice, resulting in eight tests, whereby only the mean values were provided. A linear regression has been drawn using the mean values of each value of eccentricity (solid blue line in Figure 8).

Based on the experimental data published by Gehri (1980), Mischler (1998) and Pedersen et al. (2001), the impact of the eccentricity of the tensile force in the truss member on the load-carrying capacity of the connection can be investigated. Mischler (1998) tested a connection configuration (Figure 7) using the same test setup as Gehri (1980) (Figure 5) five times without eccentricity and three times with eccentricity, for two different eccentricities. Pedersen et al. (2001) investigated the influence of moments acting in the connection using a beam simultaneously loaded axially and perpendicular at mid span (Figure 6). Two connection configurations (Figure 7) with different timber thicknesses were tested, without and with different magnitudes of perpendicular force, repeating each test four times. The magnitudes of the applied perpendicular force ranged between 5% and 33% of the applied axial force.

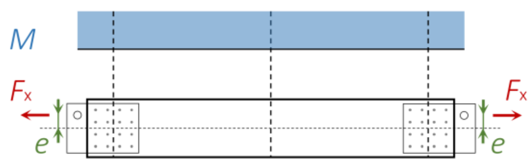

Figure 5: Experimental setup used by Gehri (1980) and Mischler (1998). The axial force F_x is applied with an eccentricity e with respect to the neutral axis. The resulting bending moment distribution is shown in blue.

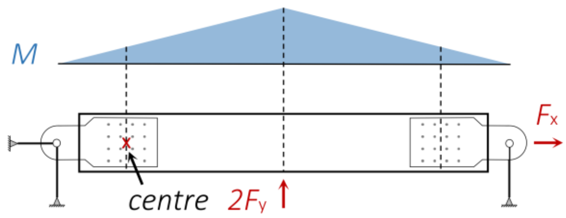

Figure 6: Experimental setup used by Pedersen et al. (2001). The beam is loaded applying a combination of axial force F_x and perpendicular force F_y. The resulting bending moment distribution is shown in blue.

In order to be able to use the results from both test setups in a combined analysis, the results determined by Pedersen et al. (2001) were adapted (Manser 2021). First, the bending moment acting in the centre of the connection was calculated. The bending moment induced by the eccentricity of axial force with respect to the neutral axis in the deformed shape was neglected, since the deformations in the centre of the connection are assumed to be small. The bending moment acting in the centre of the connection was set equal to the moment induced by the normal force, acting with a virtual eccentricity. The resulting shear force in the connection was neglected, which is rated to be conservative. The applied perpendicular and axial forces are negatively correlated, since more perpendicular force enlarges the bending moment and hence, the axial load-carrying capacity is reduced.

The same absolute value of eccentricity induces a smaller relative bending moment in a large connection compared to a small connection. Since the sizes of the connections tested by Gehri, Mischler and Pedersen et al. are strongly different, the eccentricity was normalized by dividing it by the height of the connection, which was defined as the distance between the outermost dowel rows (Figure 7) (Manser 2021).

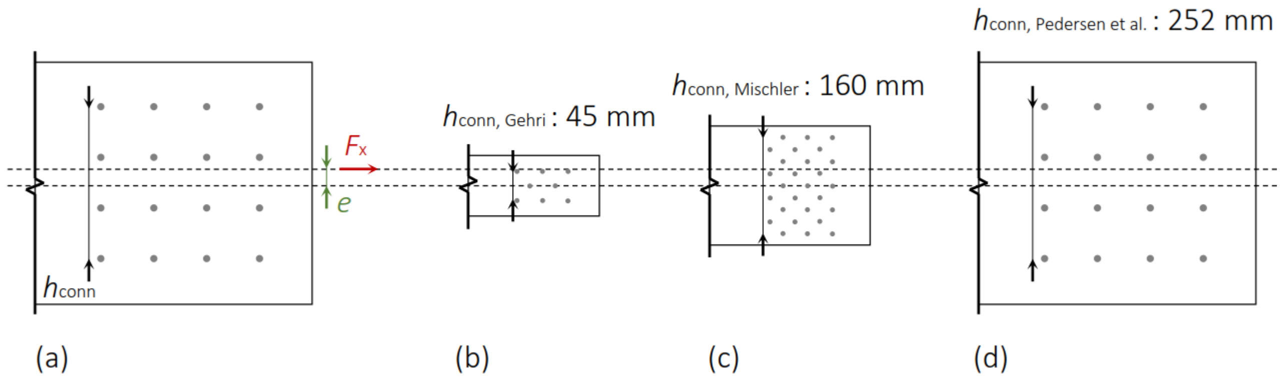

Figure 7: Height h_{conn} of a connection loaded with an eccentricity e (a) and connection configuration tested by Gehri (1980) (b), Mischler (1998) (c) and Pedersen et al. (2001) (d).

When exclusively considering the results of the tests by Gehri (1980) and Mischler (1998) (dashed blue line in Figure 8) and comparing them to the regression model proposed by Gehri (solid blue line in Figure 8), the model proposed by Gehri is only conservative up to a normalized eccentricity of about 22%. When exclusively considering the data published by Pedersen et al. (2001) (dotted line in Figure 8) the proposed model by Gehri is not conservative for any normalized eccentricity. When taking into account all collected data and applying a non-linear regression, the reduction in load-carrying capacity depending on the normalized eccentricity can be described with Formula 5 (Manser 2021).

$$k_{\mathrm{e}} = \frac{F_{\mathrm{u,e}}}{F_{\mathrm{u,0}}} = 1 - 1.56\left(\frac{e}{h_{\mathrm{conn}}}\right)^{1.25} \qquad R^2 = 0.88 \qquad (5)$$

Comparing this regression (dash-dotted blue line in Figure 8) to the reduction factor of 0.75 (rose line in Figure 8) for calculating the load-carrying capacity of eccentrically loaded connections according to SIA 265:2021, it can be stated that the reduction factor is conservative up to a normalized eccentricity of about 23%. Using these 23% and knowing the geometric dimension of a given connection it can be calculated, for which magnitude of bending moment the SIA 265:2021 reduction factor is conservative.

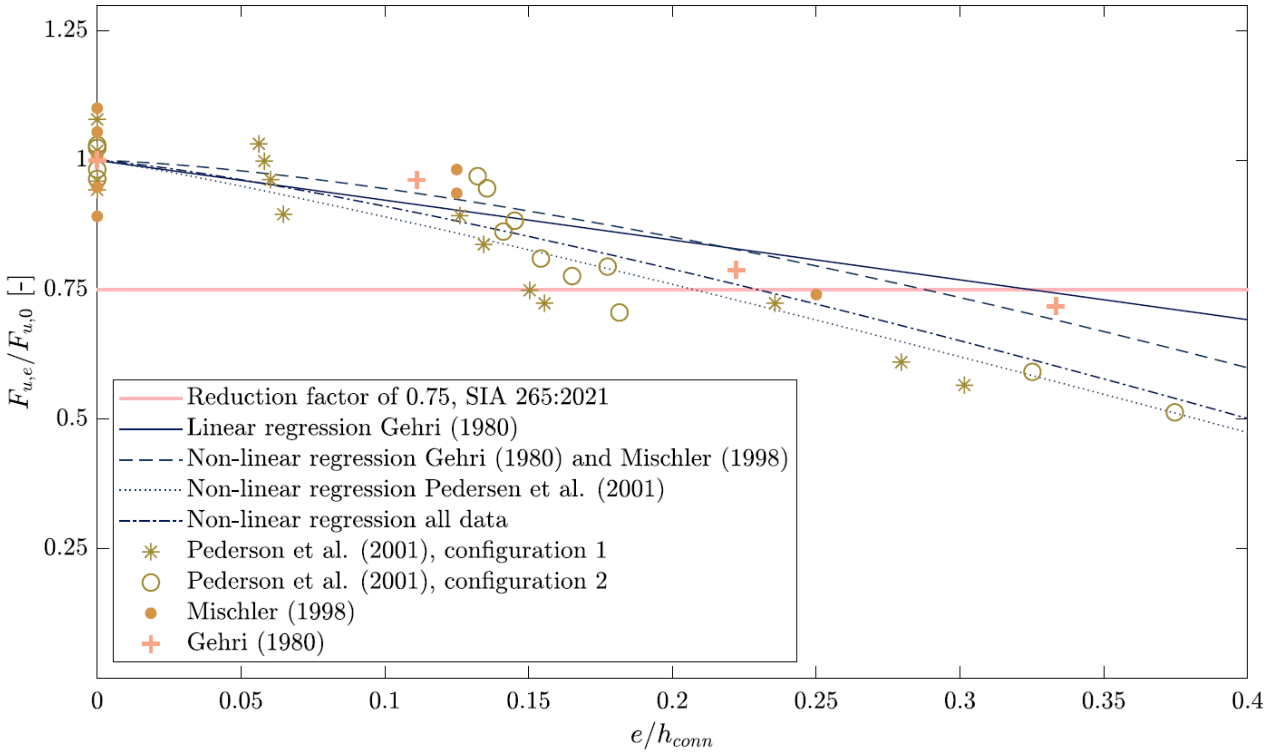

Figure 8: Reduction of the load-carrying capacity of eccentrically loaded dowelled steel-to-timber connections in dependence of the normalized eccentricity.

5 Conclusions & outlook

From the conducted evaluations and discussions, the following can be concluded:

- The principle truss design rules in EN 1995-1-1:2004 and SIA 265:2021, that a truss shall be designed like a frame structure with accurate joint models, can hardly be followed. The modelling is demanding and important sub-models are missing in the design standards.
- A parametrisation approach with an enhanced connection subroutine to fulfil these principle truss design rules was made available (Schilling 2022).
- The available specifications in EN 1995-1-1:2004, SIA 265:2021 and information in literature on the load-deformation behaviour of single dowels and full dowelled steel-to-timber connections is scarce.
- The provisions for the stiffness under service load K_{ser} in EN 1995-1-1:2004 and SIA 265:2021 are different and inaccurate when comparing to collected test data. This conclusion agrees with the conclusions expressed by Jockwer & Jorissen (2018) for dowelled timber-to-timber connections.
- An approach similar to the one applied by Jockwer & Jorissen (2018), but for steel-to-timber connections and including more regression parameters for K_{ser} revealed promising results.
- Despite the limited available data, the curve parametrisation approach for the load-deformation behaviour is feasible at least up to the load-carrying capacity.
- Both standards EN 1995-1-1:2004 and SIA 265:2021 are lacking a resistance model for considering complex multi-axial loading of dowelled steel-to-timber

connections. For the simple case of dominant normal forces with additional bending moments, a regression model for a corresponding reduction factor of the load-carrying capacity was provided.

6 Acknowledgements

The authors gratefully acknowledge the financial support from the Swiss National Science Foundation (project no. 200021_175821/1). Dr.ir. Carmen Sandhaas, from the Karlsruhe Institute of Technology (KIT), is gratefully acknowledged, for kindly providing the two bachelor theses that she supervised.

7 References

Culmann C (1866): Die graphische Statik. Zurich, Switzerland: Meyer & Zeller. https://doi.org/10.3931/e-rara-20052

Dubas P, Gehri E, Steurer A (1981): Einführung in die Norm SIA 164 (1981) Holzbau - Autographie zum Fortbildungskurs für Bauingenieure. Zurich, Switzerland: Lehrstuhl für Baustatik und Stahlbau ETH Zürich.

EN 1995-1-1:2004. Eurocode 5: Design of timber structures - Part 1-1: General - Common rules and rules for buildings. Brussels, Belgium: European Committee for Standardization CEN.

Erchinger C-D (2009): Zum Verhalten von mehrschnittigen Stahl-Holz-Stabdübelverbindungen im Brandfall. Doctoral Thesis. ETH Zurich, Switzerland. https://doi.org/10.3929/ethz-a-005774542

Eschmann L (2021): Neue Prüfmethode zur Bestimmung der Lochleibungseigenschaften von Holz. Master Thesis. ETH Zurich, Switzerland.

Fontana M (1984): Festigkeits- und Verformungsverhalten von hölzernen Fachwerkträgern unter besonderer Berücksichtigung der Knotenausbildung. Doctoral Thesis. ETH Zurich, Switzerland.

Gehri E, Vogel H, Menig W, Häring C, Bannholzer H, Blumer H (1979): Entwurf und Bemessung von Schnittholz-Konstruktionen mit neuzeitlichen Verbindungen. Zürich, Switzerland: Schweizerische Arbeitsgemeinschaft für Holzforschung.

Gehri E (1980): Betrachtungen zum Tragverhalten von Bolzenverbindungen im Holzbau. Schweizer Ingenieur und Architekt 51-52/80:1336–44.

Gehri E, Steurer A, Fontana M (1982): Fachwerkträger aus Buche und Fichte mit Stahlknotenplatten in eingeschlitzten Hölzern. ETH Zurich, Switzerland.

Gehri E, Fontana M (1983): Betrachtungen zum Tragverhalten von Passbolzen in Holz-Holz-Verbindungen. ETH Zurich, Switzerland.

Hankinson R L (1921): Investigation of crushing strength of spruce at varying angles of grain. Air service information circular 3/259:3-15.

Jockwer R, Jorissen A (2018): Load-deformation behaviour and stiffness of lateral connections with multiple dowel type fasteners. Paper INTER/51-7-7. INTER Meeting 51. Tallinn, Estonia.

Langedijk A (2007): Houtverbindingen met hoge sterkte staal. Bachelor Thesis. TU Delft, The Netherlands.

Manser N (2021): Sensitivity studies of dowelled timber connections. Master Thesis. ETH Zurich, Switzerland.

Mischler A (1998): Bedeutung der Duktilität für das Tragverhalten von Stahl-Holz-Bolzenverbindungen. Doctoral Thesis. ETH Zurich, Switzerland.

Möhler K (1966): Spannungen und Durchbiegungen parallelgurtiger Fachwerkträger aus Holz. Bauen mit Holz 4:155–61.

Pedersen MBU, Damkilde L, Hoffmeyer P (2001): Dowel type timber connections strength modelling. Lyngby, Denmark: Technical University of Denmark (DTU). https://backend.orbit.dtu.dk/ws/portalfiles/portal/5275951/Martin.pdf

Racher, P (1995): Moment resisting connections. Timber Engineering – STEP 1. Almere, The Netherlands: Centrum Hout.

Richard RM, Abbott, BJ (1975): Versatile Elastic-Plastic Stress-Strain Formula. Journal of the Engineering Mechanics Division 101/4:511-515. https://doi.org/10.1061/JMCEA3.0002047

Sandhaas C (2012): Mechanical behviour of timber joints with slotted-in steel plates. Doctoral Thesis. Technical University Delft, The Netherlands.

Scheer C, Golze B (1981): Berechnung von Fachwerkkonstruktionen unter Berücksichtigung des durchlaufenden Ober- und Untergurts. Bauen mit Holz 7:155-56.

Schilling S (2022): Structural behaviour and reliability of timber trusses with dowelled steel-to-timber connections. Doctoral Thesis. ETH Zurich, Switzerland. https://doi.org/10.3929/ethz-b-000538109

Schweigler M, Bader TK, Hochreiner G (2018): Engineering modeling of semi-rigid joints with dowel-type fasteners for nonlinear analysis of timber structures. Engineering Structures 171:123–39. https://doi.org/10.1016/j.engstruct.2018.05.063

SIA 265:2021. Holzbau. Zurich, Switzerland: Schweizerischer Ingenieur- und Architektenverein SIA.

Van Groesen J, Kranenburg M (2007): Houtverbindingen met hoge sterkte staal. Bachelor Thesis. TU Delft, The Netherlands.

DISCUSSION

The paper was presented by S Schilling

R Jockwer asked are you designing for nonlinearity. S Schilling replied non-linear information is for research only.

M Fragiacomo asked about the difference in stiffness between SIA and EC5 models as it should be a constant. S Schilling said the EC5 model is currently the one and the new version of EC5 will not change. P Dietsch commented that the EC5 model is intended for a single fastener. There may be a need to consider alternatives for connections.

S Aicher asked about the difference between K_{ser} in parallel and perpendicular directions. S Schilling said tests are only for perpendicular to grain direction and a $k_{parallel}$ to $k_{perpendicular}$ factor of 3 was found. SIA has a factor of 2.

G Hochreiner commented that in the level of normal design maybe a more sophisticated approach is needed.

P Dietsch commented that S Egner at KIT is working on combination of loads in connections.

Multilinear load-displacement relationship of LFT shearwalls based on code regulations

Sascha Schwendner, University of Kassel

Werner Seim, University of Kassel

Giuseppe D'Arenzo, University of Kassel

Keywords: light frame timber shearwall, ductility, stiffness, mean values, push-over

1 Introduction and state of the art

Different methods are available in code regulations and the literature to design and verify a structure against earthquake actions. Force-based seismic design (FBSD) is typically used in engineering practice, while experimental test results together with more complex models and sophisticated calculation tools are required for non-linear time history analyses. Compared to these two methods, displacement-based seismic design (DBSD) is a powerful methodology which works with comparatively simple assumptions. In DBSD, the overall behavior of the structure is described by the capacity curve, which accounts for both the elastic and plastic behavior of the structure.

Capacity design is used nowadays to design building structures in seismic prone areas, due to its simplicity and effectiveness, in counteracting the random nature of earthquake actions. According to this design strategy, structural components with ductile behavior are chosen to undergo large nonlinear deformation under seismic actions, while structural components with brittle or non-ductile behavior are overdesigned to remain in the elastic field. This design strategy was firstly developed for concrete and steel structures and is, therefore, available in many codes and regulations concerning these structural materials today. The application of capacity design principles to timber structures is much younger, and applications of this methodology to these structural typologies emerged only in the last decade, which explains why no detailed capacity design prescriptions for timber structures are addressed in the seismic codes of many advanced countries today.

However, capacity design principles are also available and regulated for timber structures in the new generation of Eurocodes, specifically in the new Eurocode 8 (*prEN 1998-1-2*, 2022). Moreover, the latter provides an analytical approach to calculate the elastic-plastic load-displacement relationship of the components with dissipative behaviour, offering the advantage that DBSD can also be used for timber structures without reference to experimental tests of the ductile components.

The trilinear load-displacement curve adopted in *prEN 1998-1-2* (2022) and the relationships for calculation of the relevant parameters of this curve are shown in Equation 1 - 3 and Figure 1. The curve parameters can be calculated based on the stiffness, the load-carrying capacity and the ductility of the ductile component considered. While the stiffness and load-carrying capacity can be calculated by adopting empirical and mechanics-based formulas given in the new Eurocode 5 (*prEN 1995-1-1*, 2021), the use of ductility values given in *prEN 1998-1-2* (2022) is recommended.

$$F_{\mathrm{max,prEN}} = F_{\mathrm{v,Rk}} \cdot k_{\mathrm{mod}} \cdot 1.35 \tag{1}$$

$$F_{\mathrm{y,prEN}} = F_{\mathrm{v,Rk}} \cdot k_{\mathrm{mod}} \cdot 1.35 \cdot 0.90 \tag{2}$$

$$F_{\mathrm{ult,prEN}} = F_{\mathrm{v,Rk}} \cdot k_{\mathrm{mod}} \cdot 1.35 \cdot 0.80 \tag{3}$$

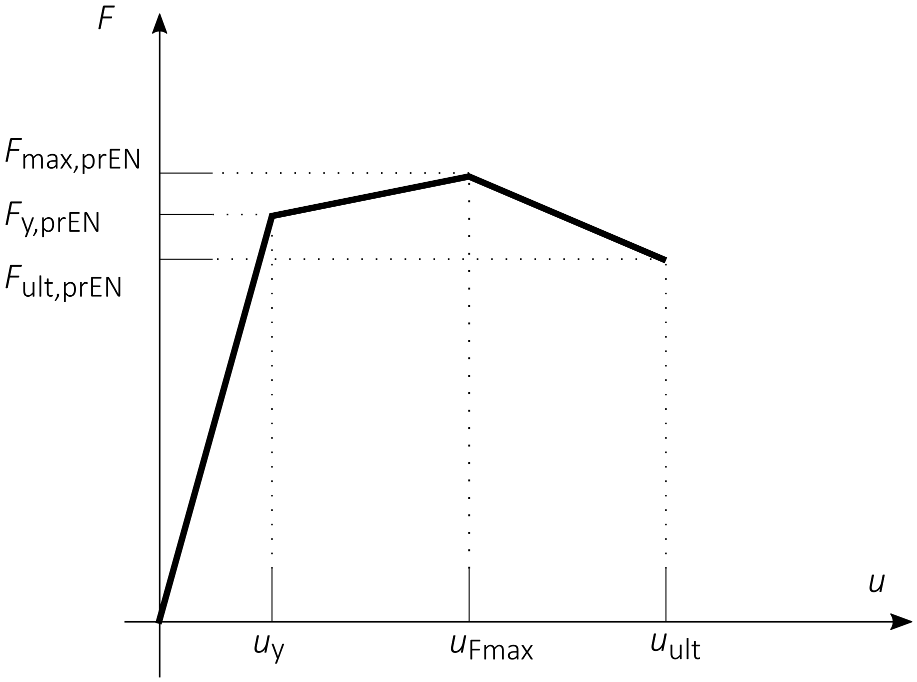

Figure 1. Load-displacement relationship to be used in DBSD according prEN 1998-1-2 (2022)

Mean values of the curve parameters should be adopted in DBSD and formulas for the calculation of the load-carrying capacity given in standards predict characteristic values, therefore, factors are used to increase the load-carrying capacity of the load-displacement relationship from the characteristic to the mean values, while mean stiffness values according to standard prescriptions and minimum ductility values according to Eurocode 8 prescriptions are used. The approach given in *prEN 1998-1-2* (2022) is general and can be adopted to describe the behavior of a generic ductile component of any timber structure.

The objective of this paper is to challenge and discuss the load-displacement relationship proposed in *prEN 1998-1-2* (2022) to be adopted in more complex systems made of different structural parts, such as light-frame timber (LFT) shearwalls. An alternative load-displacement relationship to be used for LFT shearwalls based on the principle of energy equivalence will be presented and compared with the methodology proposed in *prEN 1998-1-2* (2022). The novelty of this proposal relies on the definition of α-factors, which are statistically derived based on a large amount of experimental data taken from the literature to be applied to the curve parameters in order to obtain energy equivalent load-displacement curves.

Firstly, the methodologies to calculate the curve parameters (k, F, μ) will be shown in Section 2. In Section 3, the experimental data and the methodology used to calculate the mechanical parameters of the experimental curves will be discussed. Section 4 will present the α-factors and the load-displacement relationship proposed in this study. The main results of the study are shown and discussed in Section 5, while Section 6 reports the main conclusions of this study.

2 Analytical calculation of LFT shearwalls

The nonlinear lateral behavior of LFT shearwalls can be described through equivalent bilinear or trilinear load-displacement curves, which depend on three major mechanical properties: the lateral load-carrying capacity, $F_{\mathrm{v,Rk}}$, the lateral elastic stiffness, k_{W}, and the ductility, μ. A brief state of the art is reported in the further course of this section which summarizes how these properties can be calculated according to current code regulations or technical standards.

2.1 Lateral load-carrying capacity

The characteristic lateral load-carrying capacity $F_{\mathrm{v,Rk}}$ of a LFT shearwall can be calculated according to Equation 4, as defined in *EN 1995-1-1* (2010). This expression is derived from a mechanical model, in which studs and rails are assumed to be rigid, while a plastic behavior is assumed for the sheathing-to-frame connections. In Equation 4, $F_{\mathrm{F,Rk}}$ is the load-carrying capacity of one sheathing-to-frame connector, L is the length of the shearwall, a_{v} is the spacing of the sheathing-to-frame connectors and c is a factor considering the geometry of the LFT shearwall.

$$F_{\mathrm{v,Rk}} = \frac{1.2 \cdot F_{\mathrm{F,Rk}} \cdot L \cdot c}{a_{\mathrm{v}}} \tag{4}$$

The load-carrying capacity of the sheathing-to-frame connector, $F_{F,Rk}$, can be calculated according to the European Yield Model prescribed in *EN 1995-1-1* (2010), which considers both the shear capacity (Johansen component) and the rope effect of the connection.

The design value of the load-carrying capacity $F_{v,Rd}$ can be calculated according to

$$F_{v,Rd} = \frac{F_{v,Rk} \cdot k_{mod}}{\gamma_m} \tag{5}$$

where k_{mod} is a factor that takes into account the serviceability class and load duration, and γ_m is the safety factor. In order to reach design values in earthquake design, k_{mod} is set to 1.1 and γ_m is set to 1.0 for timber structures.

2.2 Stiffness

The lateral elastic stiffness k_W of a LFT shearwall can be calculated with Equation 6, in which F represents the lateral force applied at the head of the shearwall and u is the total corresponding horizontal elastic displacement.

$$k_W = \frac{F}{u} \tag{6}$$

The displacement can be calculated as the sum of six different deformation parts (*NZS 3603-1993* (1996), *Hummel et al.* (2016) or *prEN 1995-1-1* (2021)), see Equation 7 - 12. The horizontal deformation includes the displacement due to the sheathing-to-frame connection u_{CON}, the deformation of the sheathing panel u_{SH}, the displacement of an LFT shearwall due to the elongation of the studs u_{FR}, the displacement of an LFT shearwall due to the compression perpendicular to the grain in the bottom rail u_{C90}, the displacement due to the uplift of the anchoring under tension u_{HD} and the deformation due to the sliding of the shearwall, u_{AB}.

The horizontal displacement due to the sheathing-to-frame connection can be calculated as

$$u_{CON} = \left(2 + n_b \cdot 2\frac{H}{L} + 2\frac{H}{L}\right) \frac{a_V \cdot F}{k_F \cdot L \cdot n_B} \tag{7}$$

where n_b is the number of joints between the sheathing panels, H is the height of the wall element, L is the length of the wall element, a_V is the spacing of the fasteners, F is the horizontal load, k_F is the stiffness of a single fastener and n_B considers one-sided or double-sided sheathing.

The horizontal deformation of the sheathing panel itself can be calculated as

$$u_{\mathrm{SH}} = \frac{F \cdot H}{L \cdot G \cdot t \cdot n_{\mathrm{B}}} \tag{8}$$

where G is the shear modulus and t is the thickness of the sheathing board.

The horizontal displacement of an LFT shearwall due to the elongation in the studs and in the rail can be calculated as

$$u_{\mathrm{FR}} = \frac{2 \cdot F}{3 \cdot EA} \left[L + \frac{H^3}{L^2} \right] \tag{9}$$

where E is the Young's modulus of the studs material and A is the cross section of the studs.

The horizontal displacement of an LFT shearwall due to the compression perpendicular to the grain in the bottom rail can be estimated as

$$u_{\mathrm{C90}} = \frac{H}{L} \cdot \nu_{90} \cdot \frac{\eta_{\mathrm{c,90}}}{1,2} \tag{10}$$

where ν_{90} is set as 1 mm for the deformation perpendicular to the grain and $\eta_{\mathrm{c,90}}$ is the ratio between the stress applied and the maximum stress according to *EN 1995-1-1* (2010) perpendicular to the grain.

The horizontal displacement due to the uplift of the anchoring under tension can be calculated as

$$u_{\mathrm{HD}} = \frac{H}{L \cdot k_{\mathrm{HD}}} \left(\frac{H \cdot F}{L} - \frac{q \cdot b_{\mathrm{r}}}{2} \right) \tag{11}$$

where q is the constant vertical load on top of the wall element, b_{r} is the spacing of the inner studs and k_{HD} is the stiffness of the tension anchorage.

The horizontal deformation due to the sliding of the shearwall can be calculated as

$$u_{\mathrm{AB}} = \frac{F}{k_{\mathrm{AB}}} \tag{12}$$

where k_{AB} is the stiffness of the anchorage against horizontal forces.

The geometry of the LFT shearwall, the Young's modulus of the materials and the stiffness of the fasteners are normally required to be inserted into these equations. However, many studies agree that the most significant displacement contribution is given by the sheathing-to-frame connections and the deformation of the connections at the base of the shearwall.

2.3 Ductility

In contrast to the calculation of the load-carrying capacity and the stiffness, no methodologies are currently available for the calculation of either the ductility or the ultimate displacement of timber structural components with ductile behavior. That is another difference compared to the methodologies available for concrete structures.

Therefore, *prEN 1998-1-2* (2022) prescribes using minimum ductility values for different structural types and ductility classes. Table 1 reports these values for LFT elements in the case of medium (DCM) and high (DCH) ductility class for connections and shearwalls. It is noteworthy to mention that these values are significantly different from those reported in the current version of *EN 1998-1-1* (2010).

Table 1. Ductility values for LFT shearwalls according to prEN 1998-1-2 (2022)

	shearwalls	connection
DCM	2,2	3,5
DCH	3,5	5,5

3 Post-processing of experimental data

3.1 Data set of experimental tests

The dataset of experimental tests used for comparison with analytical predictions is introduced and documented in this section. In order to cover a wide range of most adopted solutions used in practice for LFT walls, four shearwall categories different for sheathing panel material and sheathing-to-frame connection were considered, namely Na-OSB, Na-GFB, St-OSB and St-GFB, where Na and St refer to the fasteners in the sheathing-to-frame connection with nails and staples, respectively, and OSB (oriented strand board) and GFB (gypsum fiber board) refer to the sheathing panel material. Table 2 shows the experimental campaigns taken from the literature forming the data set.

A total of 62 experimental tests formed the statistical basis for the data post-processing. The data set covers all the shearwall categories targeted in the study and considers 24 experimental tests of Na-OSB shearwalls, 4 of Na-GFB shearwalls, 19 of St-OSB shearwalls and 15 of St-GFB shearwalls. In all cases, test results from the positive and negative quadrant were used, that leads to a data set of 124 backbone curves which were subsequently evaluated.

Table 2. Overview of the experimental campaigns taken from the literature

	Na-OSB	Na-GFB	St-OSB	St-GFB	Total
Seim et al. (2014)	9	-	-	9	18
Schwendner et al. (2020)	3	-	4	-	7
Seim et al. (2013)	-	4	-	4	8
Wilden and Hoffmeister (2021)	-	-	3	-	3
Becker and Zeitter (1992)	-	-	7	-	7
Gattesco et al. (2012)	3	-	-	-	3
Rädel (2018)	-	-	5	1	6
Grossi et al. (2015)	9	-	-	1	10
Total	24	4	19	15	62

3.2 Linearization of experimental load-displacement curves

The lateral behavior of timber connections is also characterized by nonlinearity at early stages of deformation, therefore, standardized methods are used to derive the relevant mechanical parameters of the load-displacement relationship of these components from the experimentally determined backbone curves, aiming for a simplified multi-linear description.

An overview of these methods is given by *Muñoz et al.* (2008), with *EN 12512* (2005) being the reference most used in Europe. These methodologies allow one specifically to calculate the stiffness, yielding displacement and ultimate displacement and differ one from another for the criteria used for the calculation of these parameters. In this study, a bilinear approximation is chosen for a first step, in which the prescriptions given in *EN 12512* (2005) are used to determine the elastic stiffness, while an energy equivalence approach is followed to calculate the energy equivalent lateral load-carrying capacity and the ductility of the equivalent bilinear curves obtained from the experimental data set described in the previous section, see Figure 2.

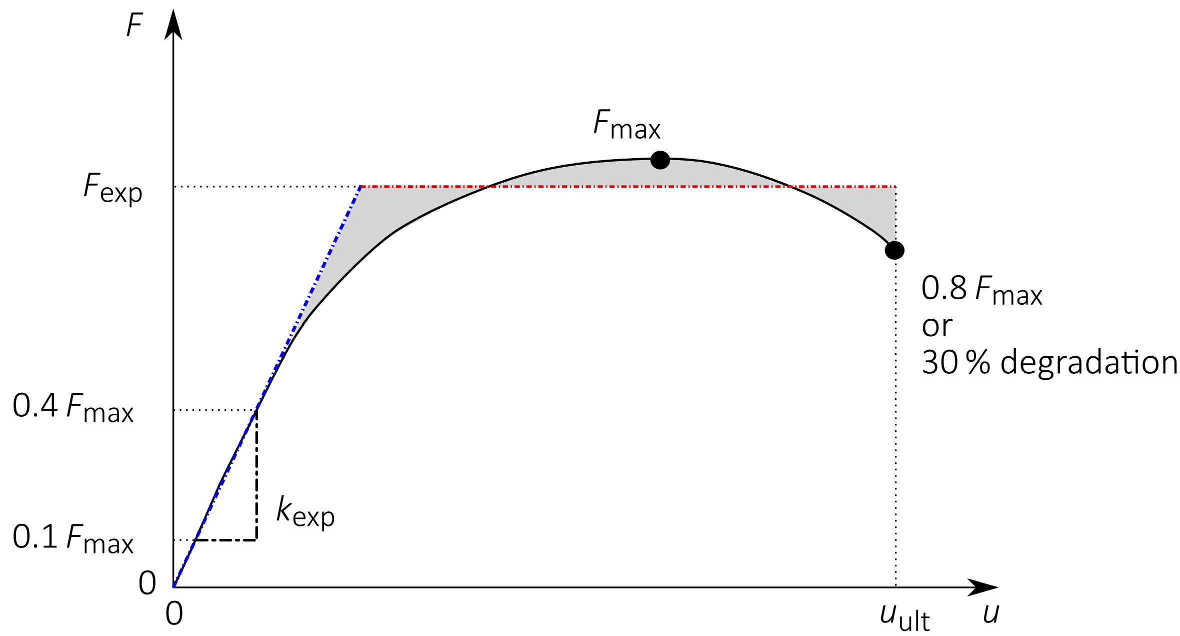

Figure 2. Bilinearization of the backbone curves taken from the experimental test

As shown in Figure 2, the elastic stiffness is calculated as the secant line between the points with ordinates 0.1 F_{max} and 0.4 F_{max} of the backbone curve, according to *EN 12512* (2005). The ultimate displacement $u_{ult,exp}$ is determined by considering the most stringent condition between a reduction of the maximum load of 20 % or a force degradation of 30 % between the 1st and the 3rd envelope curve. The yielding force is calculated by considering an energy equivalence between the experimental and bilinear curve. In this way, the characterizing parameters k_{exp}, F_{exp} and μ_{exp} can be derived from experimental test results for each backbone curve.

4 Load-displacement relationship of LFT shearwalls

4.1 Determination of α-factors

The relationship between the experimentally determined and analytically calculated mechanical properties is used in this section for the definition of factors (α-factors) to be used later for the scaling of the code-based properties. The α-factors can be defined, in general terms, as the ratio between the experimental and analytical results and can be calculated for the elastic stiffness, load-carrying capacity and ductility.

$$\alpha_{k,exp} = \frac{k_{exp}}{k_W} \tag{13}$$

$$\alpha_{F,exp} = \frac{F_{exp}}{F_{V,Rk} \cdot k_{mod}} \tag{14}$$

$$\alpha_{\mu,exp} = \frac{\mu_{exp}}{\mu_{EC8}} \tag{15}$$

4.2 Linearization used in DBSD

In this section, a new trilinear load-displacement relationship based on the adoption of the α-factors is proposed. This approach, called the α-approach, is based on the analytical models and standard prescriptions given in Section 2 and the α-factors according to the previous paragraph and allows one to define theoretically energy-equivalent load-displacement relationships. This is reached by considering the product between generically calculated mechanical properties and its related α-factor, see Equation 16 - 19. The factors 0.8 and 1.1 in Equation 16, 17 and 19 result from an energy-equivalent transfer from bi- to tri-linearity. The trilinear load-displacement relationship of the α-approach is shown in Figure 3.

$$F_{max,\alpha} = 1.1 \cdot \alpha_F \cdot F_{v,Rk} \cdot k_{mod} \tag{16}$$

$$F_{y,\alpha} = 1.1 \cdot 0.8 \cdot \alpha_F \cdot F_{v,Rk} \cdot k_{mod} \tag{17}$$

$$k_\alpha = \alpha_k \cdot k_W \tag{18}$$

$$\mu_\alpha = 1.1 \cdot \alpha_\mu \cdot \mu \tag{19}$$

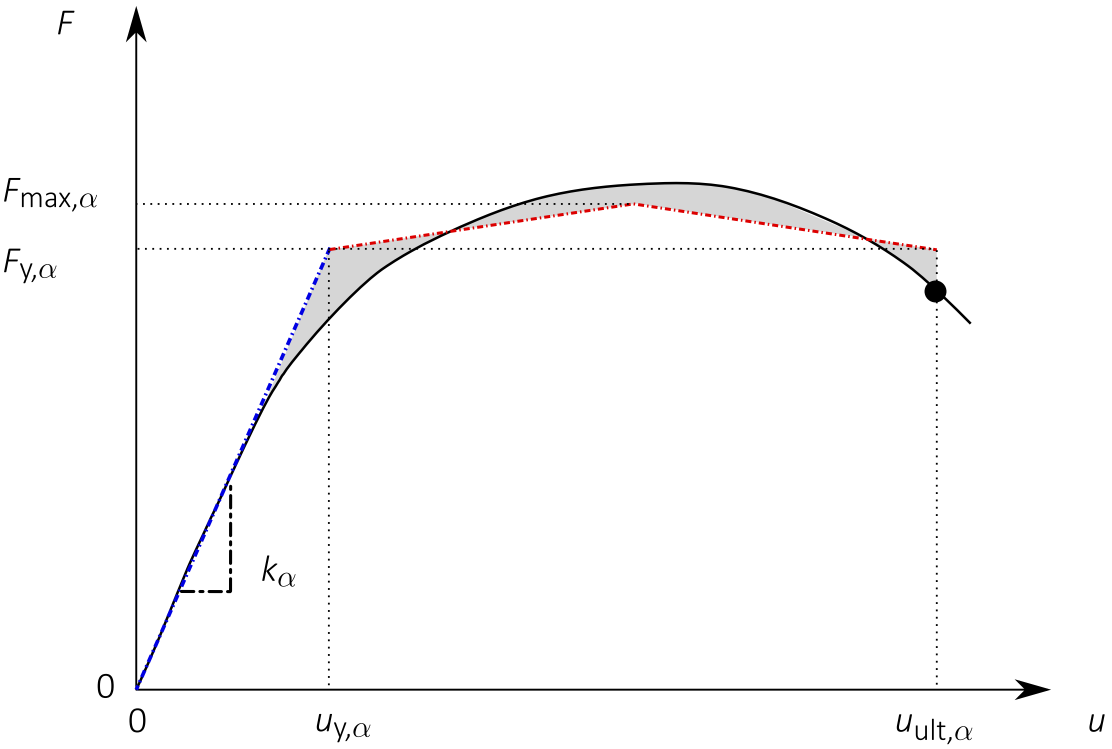

Figure 3. Trilinear load-displacement relationship following the α-approach

Based on Equation 16 - 19, the yielding displacement and the deformation capacity can be calculated according to Equation 20 and 21.

$$u_{y,\alpha} = \frac{F_{y,\alpha}}{k_\alpha} \tag{20}$$

$$u_{ult,\alpha} = \mu_\alpha \cdot u_{y,\alpha} \tag{21}$$

It is relevant to mention that the factor 0.8 is a value chosen by the authors *a priori* to ensure that ultimate displacement occurs at 80 % of the maximum force, while the factor 1.1 was calculated to ensure energy equivalence between the trilinear curve proposed and the bilinear curve shown in Figure 2.

5 Results and discussion

5.1 α-factors

The α-factors for the capacity, stiffness and ductility were calculated for each experimental test of the data set with Equation 13 - 15. The mean values α_{mean} and the coefficient of variations (*CoV*) were evaluated for each shearwall category, see Table 3, in which n is the number of investigated backbone curves. the ductility values of the sheathing-to-frame connections with GFB and nails and staples are larger than 6 (*ETA-03/0050*, 2022), thus, all the LFT shearwalls analyzed in this study were considered in DCH according to Table 1.

Table 3. Statistical evaluation of α-factors

Cartegory	n	Capacity		Stiffness		Ductility	
		$\alpha_{\mathrm{F,mean}}$	CoV	$\alpha_{\mathrm{k,mean}}$	CoV	$\alpha_{\mu,\mathrm{mean}}$	CoV
Na-OSB	48	1.27	19.8	0.81	29.1	1.00	33.6
Na-GFB	8	1.29	15.5	0.78	14.8	1.02	9.7
St-OSB	38	1.27	33.2	1.30	20.7	0.89	23.6
St-GFB	30	1.24	14.8	1.00	25.9	0.89	33.6

The α_{mean}-factors are rounded to the nearest 0.05 to be used in practice. The final α-factors proposed for all categories are given in Table 4.

Table 4. Proposed α-factors

Category	α_{F}	α_{k}	α_{μ}
Na-OSB	1.25	0.80	1.00
Na-GFB	1.25	0.80	1.00
St-OSB	1.25	1.30	0.90
St-GFB	1.25	1.00	0.90

5.2 Comparison between experimental results and analytical calculation

In this section, the analytical parameters of the α-approach and those of the *prEN 1998-1-2* (2022) are compared with the experimental data set presented in Section 3. A full documentation of the geometrical and mechanical properties used in the analytical calculation can be found in *Schwendner* (2022). The comparison between the values calculated and the results from experimental tests are presented in Figures 4 and 5, in which the horizontal axis shows the results from analytical calculations and the vertical axis, the experimental test results. Each graph contains 124 points together with the regression line for each calculation method, which provides an understanding about the quality of the prediction. The best prediction is generally achieved when the regression line corresponds to the bisector of the quadrant, namely, when the slope of the regression line, m, is equal to 1 and the line passes through the origin.

5.2.1 Load-carrying capacity and stiffness

It can be observed from Figure 4 a, that the maximum lateral load-carrying capacity of LFT shearwalls can be predicted very well with both methods — the proposal according to *prEN 1998-1-2* (2022) and the α-approach. Here, the maximum lateral load-carrying capacity of each trilinear approximation is compared with the maximum resistance taken from the experimental test results.

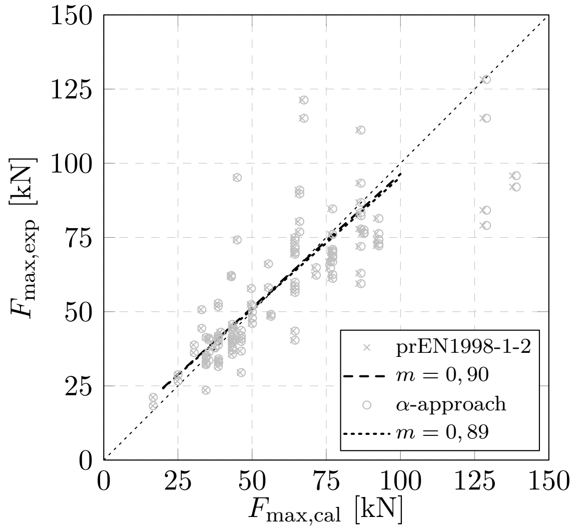

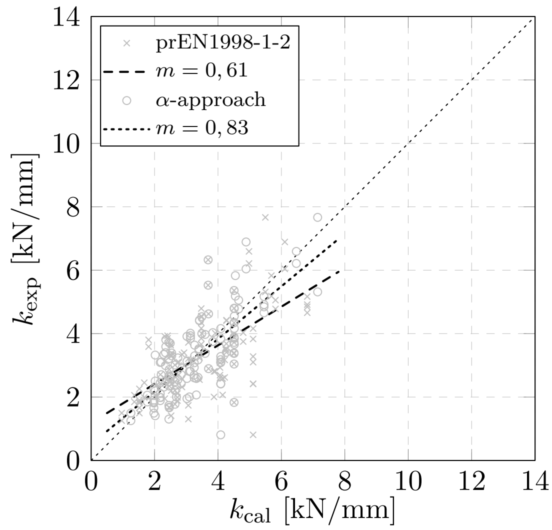

(a) *(b)*

Figure 4. Comparison of experimental and analytical results for the (a) lateral load-carrying capacity and (b) elastic stiffness

In the case of the elastic stiffness (Figure 4 b), the best prediction is provided by the α-approach, while the proposal given in the *prEN 1998-1-2* (2022) on average overestimates the elastic stiffness values.

5.2.2 Ductility and ultimate displacement

The comparison between the experimental and the calculated ductility for the four shearwall categories considered in this study is shown in Figure 5 (a). The graph shows the value of ductility taken from the *prEN 1998-1-2* (2022) and the α-approach compared to mean values taken from the experimental test results considering energy equivalence. It can be seen that the ductility values can be predicted with good agreement even if the values given in the *prEN 1998-1-2* (2022) are minimum required ductility values.

The structural deformation capacity, which is associated to the ultimate displacement, is relevant in DBSD, therefore, the prediction of the latter was considered as well, see Figure 5 (b). The ultimate displacement is calculated based on the ductility value and the yielding displacement, which, in turn, depends on the load-carrying capacity and stiffness. Figure 5 (b) shows the comparison between the experimental and calculated ultimate displacement. It is possible to observe that the *prEN 1998-1-2* (2022) provides a much lower agreement with the experimental data compared to the α-approach, where multiplicative factors modify the stiffness and ductility values in addition to the modification of the load-carrying capacity.

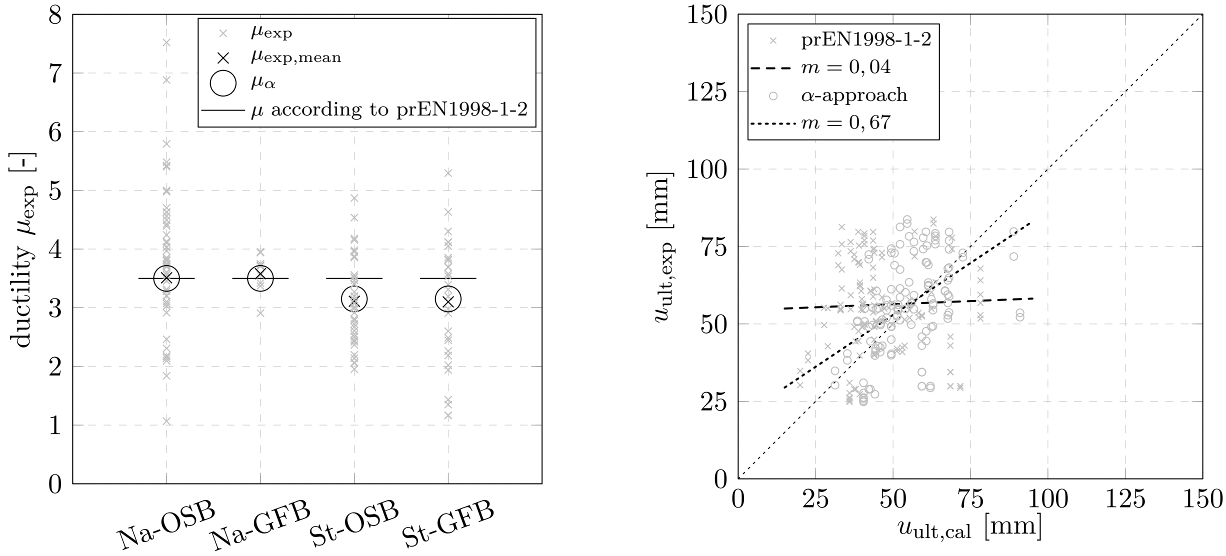

(a) *(b)*

Figure 5. Comparison of experimental and analytical results for the (a) ductility values and (b) deformation capacity

6 Conclusion

A simplified bi- or trilinear load-displacement relationship for single shearwall elements forms the basis for DBSD, which is a promising calculation method in earthquake engineering. It is necessary to define the bi- or trilinear load-displacement relationship based on parameters and properties which are available from code regulations or technical approvals to generalize this methodology to a certain level. Factors have been derived for typical types of LFT shearwalls to predict mean values related to a trilinear load-displacement relationship. The necessary adjustment factors have been derived based on data of experimental test results post-processing. The data post-processing and the transfer from bi- to trilinear load deformation was carried out consequently on the basic principle of energy equivalence. The findings can be summarized as follows:

- The *prEN 1998-1-2* (2022) and the α-approach predict the maximum load-carrying capacity of an LFT shearwall very well for all configurations. The factor proposed in *prEN 1998-1-2* (2022) to transfer characteristic to mean values could be confirmed.
- The stiffness of LFT shearwalls is well predicted by the definitions according to *prEN 1998-1-2* (2022) for the category St-OSB.
- A modification factor to predict the stiffness of LFT shearwalls should be used for the categories Na-OSB, Na-GFB and St-GFB.
- The ductility values taken from the *prEN 1998-1-2* (2022) fit very well with the mean ductility values achieved in experimental tests for LFT shearwalls with OSB as the sheathing material, whereby in the case of GFB as the sheathing material, a reduction of ductility is proposed according to the α-approach. This based on the

assumption that LFT shearwalls can generally be attributed to DCH. The assumption differs from the provision of *prEN 1998-1-2* (2022), where LFT shearwalls with GFB and/or staples should be attributed to DCM.

- The deformation capacity predicted with the α-approach is in a good agreement with the experimental test results.

7 References

Becker, K. and H. Zeitter (1992). “Untersuchung der dynamischen und duktilen Eigenschaften von mechanischen Verbindungsmitteln im Hinblick auf die Beschreibung in den europäischen Regelwerken (EC 8).” Research report. Stuttgart.

EN 12512 (2005). *Timber structures — Test methods — Cyclic testing of joints made with mechanical fasteners; EN 12512:2001 + A1:2005*.

EN 1995-1-1 (2010). *Design of timber structures – Part 1-1: General and rules for buildings*. EN 1995-1-1. European Committee for Sandardization.

EN 1998-1-1 (2010). *Eurocode 8: Design of structures for earthquake resistance-part 1: general rules, seismic actions and rules for buildings*.

ETA-03/0050 (2022). *fermacell Gypsum fibre boards — Gypsum fibre boards for planking and lining of building components*.

Gattesco, N., A. Dudline, and R. Franceschinis (2012). “Experimental investigation on the seismic behavior of timber shear walls with particle boards.” In: *Proc., 12th World Conf. on Timber Engineering: WCTE 2012, Auckland, New Zealand*, pp. 310–318.

Grossi, P., T. Sartori, and R. Tomasi (2015). “Tests on timber frame walls under in-plane forces: part 1.” *Proc. Institution of Civil Engineers — Structures and Buildings* 168.11, pp. 826–839. ISSN: 0965-0911. DOI: 10.1680/stbu.13.00107.

Hummel, J., W. Seim, and S. Otto (2016). “Steifigkeit und Eigenfrequenzen im mehrgeschossigen Holzbau.” *Bautechnik* 93.11, pp. 781–794.

Muñoz, W., W. Mohammad, A. Salenikovich, and P. Quenneville (2008). “Need for a harmonized approach for calculations of ductility of timber assemblies.” *CIB-W18Paper*, pp. 41–15.

NZS 3603-1993 (1996). *NZS 3603:1993: Timber Structures Standard*.

prEN 1995-1-1 (2021). *Eurocode 5: Consolidated version of EN 1995-1-1 dated June 2021*.

prEN 1998-1-2 (2022). *Eurocode 8: - Design of structures for earthquake resistance - Part 1-2: Rules for new buildings; Draft of EN 1998-1-2 from 2022-05-31*.

Rädel, P. (2018). “Ein Beitrag zum erdbebensicheren Konstruieren mit gipsgebundenen Plattenwerkstoffen im Holzbau.” Dissertation. TU Darmstadt.

Schwendner, S. (2022). “Ein einheitlicher Ansatz der Last-Verformungsbeziehung aussteifender Wandscheiben im Holzbau.” Dissertation, reviewed and accepted. University of Kassel.

Schwendner, S., W. Seim, and G. D'Arenzo (2020). "Entwicklung einer Methode für die zuverlässige und einfache Bewertung der Erdbebensicherheit ein- bis viergeschossiger Holzbauten sowie einfacher Hallentragwerke in Zonen geringer und mittlerer Seismizität — OptimberquakeCheck." Research report. Universität Kassel.

Seim, W., M. Fragiacomo, J. Hummel, B. Parmentier, T. Vogt, M. Schick, and A. Skowron (2014). "Optimierung mehrgeschossiger Holzbauten gegen Erdbebeneinwirkungen — Optimberquake." In: Fachgebiet Bauwerkserhaltung und Holzbau.

Seim, W., H. Ulrich, T. Vogt, and G. Höflich (2013). "Holzrahmenwände mit Gipsfaserplatten unter zyklischer Belastung." Fachgebiet Bauwerkserhaltung und Holzbau.

Wilden, V. and B. Hoffmeister (Jan. 2021). "Experimental analyses of innovative wood-shear walls under seismic loads." *IABSE Congress, Christchurch 2021: Resilient technologies for sustainable infrastructure*, pp. 1222–1229. DOI: 10.2749/christchurch.2021.1222.

DISCUSSION

The paper was presented by S Schwendner

M Fragiacomo asked about the prediction of stiffness from experimental results. EC results were based on predictions. α factor was not used for prediction of strength where K_m factors were used. S Schwendner said $\tau\eta\varepsilon$ α factor can be easily applied, and ductility is the important aspect for consideration.

D Casagrande asked about the stiffness of the hold-down and angle bracket. How would α change if connection stiffness are considered in future codes. S Schwendner responded that the α approach can be established for connections but database for connections are needed. D Casagrande commented that nail properties can be improved. S Schwendner said nail properties cannot be used directly for stiffness of assembly.

A Frangi questioned α factors for staples. S Schwendner agreed that more refinements can be made.

G Doudak expressed concerns that explanations were not given why values were adjusted. Adjustment of code to match test results without explanations may be a concern. S Schwendner agreed as the finding were simply based on 50 or so test results from literature.

A proposal for evaluating the lateral displacements of multi-storey CLT Lateral Load Resisting Systems

Daniele Casagrande, National Research Council of Italy (Italy)
Giuseppe D'Arenzo, University of Kassel (Germany)
Igor Gavric, InnoRenew CoE & University of Primorska (Slovenia)
Ghasan Doudak, University of Ottawa (Canada)

Keywords: Cross Laminated Timber, displacement, lateral load, shear-wall

1. Introduction

Lateral Load Resisting Systems (LLRSs) in Cross Laminated Timber (CLT) platform type buildings are typically composed of single- or multi-panel shear-walls. The major deformation contributions of CLT shear-walls with no openings can mainly be attributed to the flexibility of the mechanical anchors (e.g. hold-downs and angle brackets), used to connect the CLT shear-walls to the foundation or to the storey below, and the mechanical fasteners along the vertical panel-to-panel joints. Analytical models are currently available in the literature for the evaluation of the elastic lateral displacement for single-storey CLT shear-walls (e.g. Lukacs et al., 2019). The proposed methods differ from one-another mainly in the calculation of the lever arm used in calculating the compressive deformations at the wall panel edge in the rocking kinematic mode, as well as the assumptions related to assigning uni- or bi-directional behavioural characteristics to the mechanical anchors. For multi-panel shear-walls, most analytical proposals have been developed for two-panel CLT shear-walls (Gavric et al., 2015; Flatcher & Schickhofer, 2016) while a more general approach involving *m*-panels was developed by Casagrande et al. (2018). Proposals accounting for multi-storey effects have been very limited.

The current paper aims to present a general analytical approach to be implemented in design to calculate the lateral displacements of multi-storey shear-walls (Figure 1) consisting of single- or multi-panel walls and including consideration for the angle bracket to behave in uni or bi-directional behaviour. The proposal is a culmination of available literature and forms the basis for a potential code change proposal for Eurocode 5 as well as the CSA O86. Additionally, a cantilevered beam model is also presented as a simplified alternative to the proposed analytical methodology for the evaluation of lateral displacements of a LLRS.

2. Calculation of lateral displacements of an isolated multi-storey CLT shear-wall

In this section, an analytical methodology for the calculation of the lateral displacements of an isolated multi-storey platform-type CLT shear-wall is presented, as shown in Figure 1. The total lateral displacement of the shear-wall at the k^{th} storey, d_k, may be calculated as the cumulative inter-storey lateral displacements, δ_i, from the 1st to the k^{th} storey, as presented in Equation (1).

$$d_{\mathrm{k}} = \sum_{i=1}^{k} \delta_{\mathrm{i}} \tag{1}$$

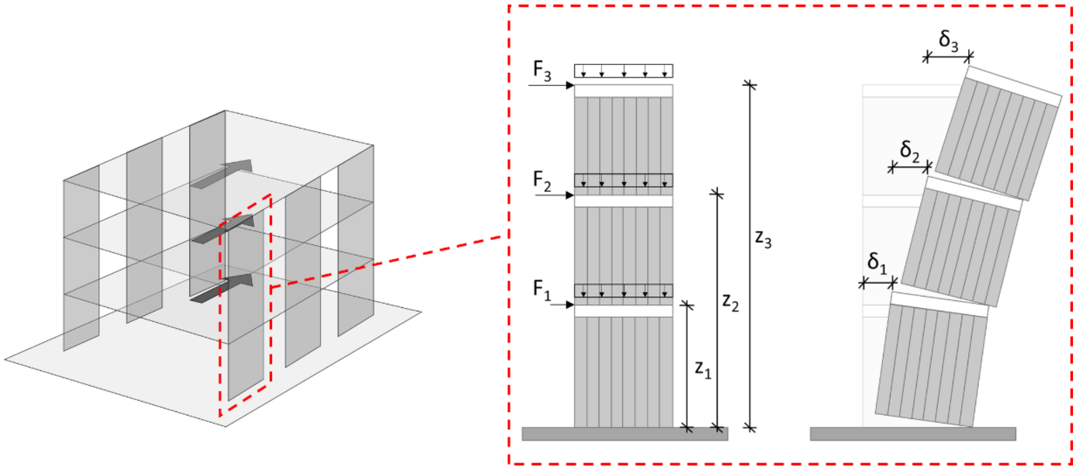

Figure 1: Isolated multi-storey CLT shear-wall subjected to lateral loads

The inter-storey lateral displacement, δ_i, may be taken as the sum of five main displacement contributions (Equation (2)), namely: i) panel shear deformation $\delta_{S,i}$, ii) panel bending deformation $\delta_{B,i}$, iii) rigid body sliding of the shear-wall related to the lateral-shear flexibility of the mechanical anchors $\delta_{A,i}$, iv) rigid body rocking of the shear-wall related to the flexibility of vertical joints (for multi-panel shear-walls) and the vertical-tensile flexibility of the mechanical anchors $\delta_{R,i}$, and v) the lateral displacement due to the rotation at the top of the shear-wall below the wall under consideration – namely, the wall at the *(i-1)^th^* storey, $\delta_{\theta,i}$. The five displacement contributions are shown in Figure 2 (b-f).

$$\delta_{\mathrm{i}} = \delta_{\mathrm{S,i}} + \delta_{\mathrm{B,i}} + \delta_{\mathrm{A,i}} + \delta_{\mathrm{R,i}} + \delta_{\theta,\mathrm{i}} \tag{2}$$

The analytical methodology is presented for single-panel and multi-panel CLT shear-walls with no openings. The following symbols are used throughout the paper and represent variables at the inter-storey levels: h_{i} is the inter-storey height of the shear-wall; B_{i} is the total length of the shear-wall; V_{i} is the total design shear load acting on the shear-wall due to lateral loads; N_{i} is the total axial compressive load acting on the shear-wall due to gravity loads; $M_{\mathrm{i,top}}$ is the total design moment acting at the top of the shear-wall due to lateral loads; M_{i} is the total design moment acting at the bottom of the shear-wall due to lateral loads.

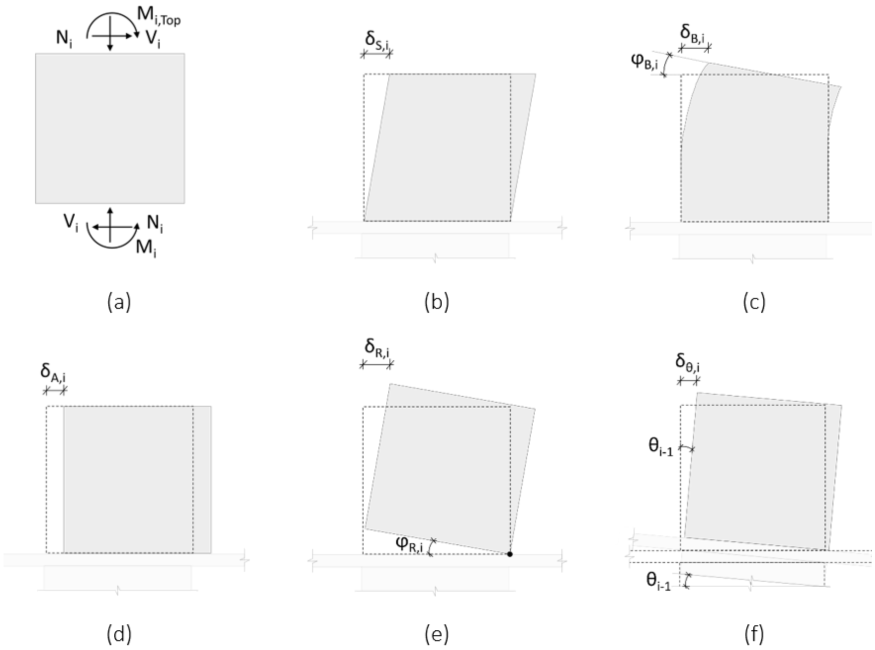

Figure 2: Inter-storey lateral displacement contributions: (a) internal forces acting on an undeformed CLT panel; (b) panel shear deformation; (c) panel bending deformation; (d) rigid body sliding; (e) rigid body rocking; (f) rotation of the shear-wall below

2.1 Single-panel CLT shear-walls

According to Hummel et al. (2016), Gavric et al. (2015) and Flatscher & Schickhofer (2016) the inter-storey lateral displacement due to panel shear deformation, $\delta_{S,i}$, can be calculated as provided by Equation (3):

$$\delta_{\mathrm{S,i}} = \frac{V_{\mathrm{i}} \cdot h_{\mathrm{i}}}{G_{xy,i} t_{\mathrm{i}} \cdot B_i} \tag{3}$$

where t_{i} is the total thickness of the CLT panel at the *i^th^* storey and $G_{xy,i}$ is the effective in-plane shear modulus calculated according to Brandner et al. (2017) as:

$$G_{\mathrm{xy,i}} = \frac{G_0}{1+6\cdot\alpha\cdot\left(\frac{t_{mean}}{w}\right)^2} \tag{4}$$

where G_0 is the in-plane shear modulus of the laminations, w is the width of the laminations, t_{mean} is the mean value of the thickness of laminations and α is calculated as $p \cdot \left(\frac{t_{mean}}{w}\right)^{-0.79}$ where values of p are taken equal to 0.535 and 0.425 for a three- and five-layer panel, respectively.

The inter-storey lateral displacement due to panel bending deformation, $\delta_{B,i}$, can be calculated according to the beam theory as:

$$\delta_{\mathrm{B,i}} = \frac{M_{\mathrm{i,top,}} \cdot {h_{\mathrm{i}}}^2}{2\cdot(EI)_{\mathrm{eff,i}}} + \frac{V_{\mathrm{i}} \cdot {h_{\mathrm{i}}}^3}{3\cdot(EI)_{\mathrm{eff,i}}} \tag{5}$$

where $(EI)_{eff,i}$ is the effective bending stiffness of the CLT panel at the i^{th} storey calculated as $\frac{E_0 \cdot t_{\mathrm{z,i}} \cdot B_i{}^3}{12}$, where E_0 is the modulus of elasticity parallel to the grain and $t_{z,i}$ is the total thickness of vertical layers of the CLT panel.

The inter-storey lateral displacement due to the rigid body sliding of the wall, $\delta_{A,i}$, may be calculated using Equation (6):

$$\delta_{\mathrm{A,i}} = \frac{V_{\mathrm{i}}}{K_{\mathrm{A,i}}} \tag{6}$$

where $K_{A,i}$ is the stiffness in the direction of wall sliding of the shear-wall at the i^{th} storey, which can be calculated as the sum of the lateral-shear stiffness of all the mechanical anchors, namely $K_{A,i} = \sum_r K_{a,x,r}$. The displacement contribution of the floor at the i^{th} storey to the $(i\text{-}1)^{th}$ storey wall connection, assuming in-plane rigid diaphragm, may be considered as $\frac{V_{\mathrm{i,tot}}}{K_{\mathrm{f,i,tot}}}$, where $V_{i,tot}$ is the total design shear load acting on the i^{th} storey due to lateral action and $K_{f,i,tot}$ is the total shear stiffness of the connection between the floor and the wall in the $(i\text{-}1)^{th}$storey.

Several proposals have been presented in literature for the calculation of the deformation contribution related to the rocking $\delta_{R,i}$ of single-panel CLT shear-walls (e.g. Pei et al., 2012; Tomasi, 2014; Gavric et al., 2015; Casagrande et al., 2016; Reynolds et al., 2017;; Lukacs et al., 2019). In this study, a modified version of the proposal presented by Gavric et al. (2015) is adopted.

The inter-storey lateral displacement due to the rocking kinematic mode of the wall, $\delta_{R,i}$ can be calculated in accordance with Equation (7) as the difference between the inter-storey lateral displacement due to the overturning bending moment caused by lateral loads, $\delta_{R,M,i}$, and the lateral displacement due to the stabilizing effect of the total vertical load, $\delta_{R,N,i}$:

$$\delta_{\mathrm{R,i}} = \delta_{\mathrm{R,M,i}} - \delta_{\mathrm{R,N,i}} \geq 0; \tag{7}$$

The inter-storey lateral displacement due the overturning bending moment caused by lateral loads, $\delta_{R,M,i}$, can be calculated as expressed by Equation (8).

$$\delta_{\mathrm{R,M,i}} = \varphi_{R,\mathrm{M},i} \cdot h_{\mathrm{i}} \tag{8}$$

where $\varphi_{R,M,i}$ is the inter-storey rotation due to the overturning bending moment caused by lateral loads which can be calculated as:

$$\varphi_{R,M,i} = \frac{M_{\mathrm{i}}}{K_{\mathrm{R,i}}} \tag{9}$$

$K_{R,i}$ is the rocking stiffness of shear-wall at the i^{th} storey due to the vertical-tensile stiffness calculated according to Equation (10).

$$K_{\mathrm{R,i}} = \sum_r \left[K_{\mathrm{a,z,r}} \cdot \left(s_{a,r} - b_{c,i} \right)^2 \right] \tag{10}$$

where $K_{a,z,r}$ is the vertical-tensile stiffness of the r^{th} mechanical anchor (e.g. hold-down, angle bracket, etc.) subjected to uplift, $s_{a,r}$ is the distance of the r^{th} mechanical anchor from the shear-wall edge and $b_{c,i}$ is the length of the contact region between the shear-wall and the ground or the floor below (Figure 3).

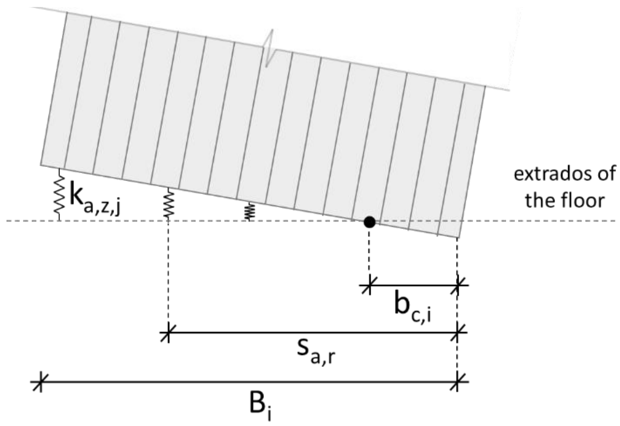

Figure 3: Rocking kinematic mode for a monolithic CLT shear-wall

The value of $b_{c,i}$ may be considered in a simplified way, according to Casagrande et al. (2016), equal to the 10% of the shear-wall length B_i or calculated by considering the deformation contribution related to the contact of the panel with either the foundation or the timber floor panel underneath (Tamagnone et al., 2018).

The lateral displacement due to the stabilizing effect of the total vertical load, $\delta_{R,N,i}$ can be calculated as expressed in Equation (11):

$$\delta_{\mathrm{R,N,i}} = \varphi_{R,\mathrm{N},i} \cdot h_{\mathrm{i}} \tag{11}$$

where $\varphi_{R,N,i}$ is the inter-storey rotation due the stabilizing effect of the total vertical load and can be calculated as:

$$\varphi_{R,N,i} = \frac{N_{\mathrm{i}} \cdot (0.5B_i - b_{c,i})}{K_{\mathrm{R,i}}} \tag{12}$$

Defining the total inter-storey rocking rotation $\varphi_{R,i}$ as $\frac{\delta_{\mathrm{R,i}}}{h_{\mathrm{i}}}$ and substituting Equations (8) and (11) in Equation (7), one obtains:

$$\varphi_{R,i} = \frac{\delta_{\mathrm{R,i}}}{h_{\mathrm{i}}} = \varphi_{R,M,i} - \varphi_{R,N,i} \geq 0 \tag{13}$$

In order to take into account the cumulative rotation due to the bending and rocking deformation contribution of the storey below, the inter-storey lateral displacement $\delta_{\theta,i}$ due to the rotation at the top of the shear-wall at the *(i-1)*th storey can be calculated as:

$$\delta_{\mathrm{\theta,i}} = \theta_{i-1} \cdot h_{\mathrm{i}} \qquad \text{for} \quad i \geq 1 \tag{14}$$

where θ_{i-1} is the rotation at the top of the shear-wall at the *(i-1)*th storey calculated as provided in Equation (15).

$$\theta_{i-1} = \theta_{i-2} + \varphi_{B,i-1} + \varphi_{R,i-1} \tag{15}$$

where θ_{i-2} is the rotation at the top of the shear-wall at the *(i-2)*th storey, $\varphi_{B,i-1}$ is the rotation due to the panel bending deformation at the top of shear-wall at the *(i-1)*th storey calculated as given by Equation (16) and $\varphi_{R,i-1}$ is the rotation contribution due to the rocking of the shear-wall at the *(i-1)*$^{\text{th}}$ storey calculated as given by Equation (13) where index *i* is replaced with index *i-1*.

$$\varphi_{\mathrm{B,i-1}} = \frac{M_{\mathrm{i-1,top,}} \cdot h_{\mathrm{i-1}}}{(EI)_{\mathrm{eff,i-1}}} + \frac{V_{\mathrm{i-1}} \cdot h_{\mathrm{i-1}}{}^{2}}{2 \cdot (EI)_{\mathrm{eff,i-1}}} \tag{16}$$

θ_0 accounts for the rotation of substructure below the shear-wall at the ground level and can be assumed to be equal to zero when substructure deformation contribution can be neglected.

2.2 Multi-panel CLT shear-walls

In this section, the deformation contributions related to the inter-storey displacement at the *i*th storey for a CLT shear-wall composed of m panels with the same length b_i are defined.

The governing kinematic mode is expected to play a key role in the displacement of multi-panel CLT shear-walls. In general, three different rocking kinematic modes may occur, depending on the relative stiffness of the hold-down to that of vertical joints, including Coupled-Panel (CP), Single-Wall (SW) and Intermediate (IN) kinematic mode, as shown in Figure 4.

Coupled-Panel) kinematic mode corresponds to each panel being in contact with the foundation (or the floor underneath) and having a well-defined centre of rotation, Figure 4(a). Single-Wall kinematic mode corresponds to having a single centre of rotation for the entire shear-wall, which behaves mostly like a monolithic wall, Figure 4(c). Coupled-Panel and Single-Wall kinematic modes are achieved in case of a relatively rigid and flexible hold-down, respectively. Intermediate (IN) kinematic mode corresponds to having only some panels in contact with ground, as shown in Figure 4(b).

According to Casagrande et al. (2018) if the multi-panel shear-wall is anchored against uplift at the corners and the vertical-tensile stiffness of the shear connections is neglected, the CP, IN or SW kinematic modes are achieved if Equations (17) to (19), respectively, are satisfied:

$$\frac{K_{\mathrm{hd,i}}}{K_{\mathrm{v,i}}} \geq \frac{1-\widetilde{N_\iota} \cdot \frac{3m-2}{\mathrm{m}^2}}{1-\widetilde{N_\iota} \cdot \frac{m-2}{\mathrm{m}^2}} \qquad \text{CP kinematic mode} \tag{17}$$

$$\frac{1-\widetilde{N_\iota}}{1+\widetilde{N_\iota} \cdot (\mathrm{m}-2)} < \frac{K_{\mathrm{hd,i}}}{K_{\mathrm{v,i}}} < \frac{1-\widetilde{N_\iota} \cdot \frac{3m-2}{\mathrm{m}^2}}{1-\widetilde{N_\iota} \cdot \frac{\mathrm{m}-2}{\mathrm{m}^2}} \qquad \text{IN kinematic mode} \tag{18}$$

$$\frac{K_{\mathrm{hd,i}}}{K_{\mathrm{v,i}}} \leq \frac{1-\widetilde{N_\iota}}{1+\widetilde{N_\iota} \cdot (m-2)} \qquad \text{SW kinematic mode} \tag{19}$$

where $K_{hd,i}$ is the vertical-tensile stiffness of the hold-down placed at the corner of the shear-wall at the *i*th storey, $K_{\mathrm{v,i}}$is the vertical-shear stiffness of the vertical joint at the i^{th} storey, $\widetilde{N_i}$ is the dimensionless vertical load on the shear-wall at the i^{th} storey and may be obtained according to Equation (20).

$$\widetilde{N_i} = \frac{N_{\mathrm{i}} \cdot m \cdot b_i}{2 \cdot M_{\mathrm{i}}} \tag{20}$$

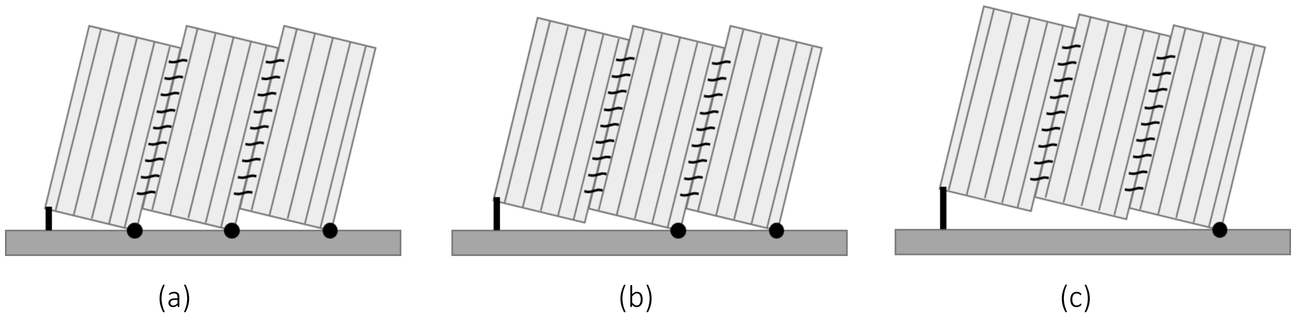

Figure 4: Rocking kinematic modes for a multi-panel CLT shear-wall: Coupled-Panel (CP) kinematic mode; (b) Intermediate (IN) kinematic mode; (c) Single-Wall (SW) kinematic mode

The inter-storey lateral displacement due to the panel shear deformation, $\delta_{S,i}$, can be calculated in a similar manner as presented for single-panel shear-walls according to Equation (2), where B_i is the total length of the shear-wall, namely equal to $m \cdot b_i$. The inter-storey lateral displacement due to the panel bending deformation $\delta_{B,i}$, can be determined by means of Equation (5) where $(EI)_{eff,i}$ represent the total bending stiffness of the entire multi-panel shear-wall. Similar to composite elements, the bending stiffness should be calculated by considering the stiffness and spacing of the connections between the panels. Such stiffness is expected to range between the value of bending stiffness related to m separate panels $(EI)_{0,i}$ and the value related to an equivalent single-panel shear-wall $(EI)_{\infty,i}$, as expressed by Equation (21).

$$(EI)_{0,\mathrm{i}} = m \cdot \frac{E_0 \cdot t_{\mathrm{z,i}} \cdot {b_i}^3}{12} \leq (EI)_{\mathrm{eff,i}} \leq (EI)_{\infty,\mathrm{i}} = \frac{E_0 \cdot t_{\mathrm{z,i}} \cdot {B_i}^3}{12} \tag{21}$$

The inter-storey lateral displacement due to the rigid body sliding of the wall, $\delta_{A,i}$, may be calculated consistently with the approach for a single-panel shear-wall according to Equation (6).

The analytical methodology developed by Casagrande et al. (2018) is adopted in this proposal for the evaluation of the rotation due to the rocking of the shear-wall, $\varphi_{R,i}$, for CP and SW modes as expressed in Equations (22) and (23). The contribution due to the vertical-tensile stiffness of the shear connections is neglected in these equations. Analytical expressions which take into account the contribution of angle-brackets to the rocking behaviour of a multi-panel CLT shear-walls are available in literature (Masroor et al., 2020).

$$\varphi_{\mathrm{R,i}} = \varphi_{R,M,i,CP} - \varphi_{R,N,i,CP} \geq 0 \qquad \text{for CP mode} \tag{22}$$

$$\varphi_{\mathrm{R,i}} = \varphi_{R,M,i,SW} - \varphi_{R,N,i,SW} \geq 0 \qquad \text{for SW mode} \tag{23}$$

where $\varphi_{R,M,i,CP}$ and $\varphi_{R,M,i,SW}$ are the inter-storey rotation due to the overturning bending moment caused by lateral loads for the CP and SW mode, respectively (Equations (24) and (25)), whereas $\varphi_{R,N,i,CP}$ and $\varphi_{R,N,i,SW}$ are the inter-storey rotation due the stabilizing effect of the total vertical load for the CP and SW mode, respectively (Equations (26) and (27)):

$$\varphi_{R,M,i,CP} = \frac{M_i}{K_{R,i,CP}} \tag{24}$$

$$\varphi_{R,M,i,SW} = \frac{M_i}{K_{R,i,SW}} \tag{25}$$

$$\varphi_{R,N,i,CP} = \frac{N_i \cdot b_i}{2 \cdot K_{R,i,CP}} \tag{26}$$

$$\varphi_{R,N,i,SW} = \frac{N_\mathrm{i}}{2 \cdot K_\mathrm{hd,i} \cdot B_i} \tag{27}$$

In Equations (24) to (26), $K_{R,i,CP}$ and $K_{R,i,SW}$ represent the rocking stiffness of shear-wall at the *i^th^* storey in case of CP and SW kinematic mode, calculated according to Equation (28) and (29), respectively.

$$K_{R,i,CP} = \frac{[K_\mathrm{hd,i} + (m-1) \cdot K_\mathrm{v,i}]}{m^2} \cdot {B_i}^2 \tag{28}$$

$$K_{R,i,SW} = \left[\frac{1}{K_\mathrm{hd,i}} + \frac{(m-1)}{K_\mathrm{v,i}}\right]^{-1} \cdot {B_i}^2 \tag{29}$$

The inter-storey lateral displacement due to the rocking kinematic mode of the wall, $\delta_{R,i}$, can be calculated as provided by Equation (30).

$$\delta_\mathrm{R,i} = \varphi_\mathrm{R,i} \cdot h_i \geq 0 \tag{30}$$

Analytical expression for the calculation of the rocking rotation for the IN mode can be found in Casagrande et al. (2018).

The inter-storey lateral displacement due to the cumulative rotation of the shear-walls underneath may vary depending on the kinematic modes of the shear-walls. Due to the nature of different possible kinematic mechanisms, these rotations are expected to be lower for CP kinematic mode and larger for SW kinematic mode. However, very few studies investigated this issue so far (D'Arenzo et al., 2021), and no analytical expressions for calculation of this this displacement contribution are currently available. Based on the observations from previous experimental studies on full-scale CLT buildings and multi-storey CLT walls (Popovski et al., 2010; Popovski and Gavric, 2016), when the CP kinematic mode occurs at the shear-wall at the *i-1^th^* storey, the contribution due to the cumulative rotation at the *i^th^* storey may be neglected, assuming $\delta_{\theta,i} = 0$. Conversely, the inter-storey lateral displacement due to the rotation at the top of the shear-wall below the wall under consideration may be calculated as given by Equations (13)-(16) when either SW or IN kinematic mode occurs.

3. Implementing the proposed procedure at the LLRS level

The lateral displacement of a LLRS composed of M_S isolated multi-storey walls can be analytically obtained by means of a matrix formulation as discussed in this Section.

3.1. Matrix formulation for an isolated CLT shear-wall

The analytical methodology outlined in Section 2 for an isolated shear-wall is presented in this section through an analytical matrix formulation expressed by Equation (31):

$$\{d_S\} = [K_S]^{-1}\{F_S\} - \{d_{S,N}\} \tag{31}$$

where $\{d_S\}$ is the lateral displacement array, $\{F_S\}$ is the applied lateral load array, $[K_S]$ is the matrix stiffness and $\{d_{S,N}\}$ is the array representing the equivalent lateral displacement due to the vertical loads. The latter component represents the reduction in rocking displacement due to the stabilizing effect of the vertical loads as discussed in the previous section.

The stiffness matrix of an isolated multi-storey shear-wall, $[K_S]$, can be obtained as the inverse of the flexibility matrix $[U_S]$, namely $[K_S] = [U_S]^{-1}$, where the generic element $U_{S,i,j}$ represents the lateral displacement at the i^{th} storey due to a unit lateral force applied at the j^{th} storey.

The analytical expressions for the calculation of $U_{S,i,j}$ are based on an extension of the analytical methodology presented in Section 2 and developed by considering the five inter-storey drift contributions. All contributions related to the vertical load are neglected ($\delta_{\mathrm{R,N,i}} = 0$; $\varphi_{R,\mathrm{N},i} = 0$) in the calculation of $U_{S,i,j}$, since the stabilizing effect due to the vertical load is already included in the term $\{d_{S,N}\}$ of Equation (31).

In this formulation, an isolated N_s-storey shear-wall with the same inter-storey height h at all storeys and with a unit lateral load $F_{S,j} = 1$ applied at the j^{th} storey, is considered. The total shear load V_i , total overturning moment acting at the bottom M_i, and the total overturning moment acting at the top of $M_{i,top}$ the i^{th} storey can be obtained according to Equations (32) to (34), respectively.

$$V_{\mathrm{i}} = \begin{cases} 1 & for\ i \le j \\ 0 & for\ j < i < N_s \end{cases} \tag{32}$$

$$M_{\mathrm{i}} = \begin{cases} 1 \cdot [j - (i-1)] \cdot h & for\ i \le j \\ 0 & for\ j < i \le N_s \end{cases} \tag{33}$$

$$M_{\mathrm{i,top}} = \begin{cases} 1 \cdot (j - i) \cdot h & for\ i < j \\ 0 & for\ j \le i \le N_s \end{cases} \tag{34}$$

The lateral displacement $U_{S,1,j}$ at the *1st* (*i=1*) storey due to a unit lateral force applied at the j^{th} storey can be calculated according to Equation (2) as presented in Equation (35).

$$U_{S,1,j} = \delta_{\mathrm{S,1,j}} + \delta_{\mathrm{B,1,j}} + \delta_{\mathrm{S,1,j}} + \delta_{\mathrm{R,M,1,j}} + \delta_{\mathrm{\theta,1,j}} \tag{35}$$

where $\delta_{\mathrm{\theta,1,j}}$ can be assumed to be equal to zero if the rotation at the bottom of the shear-wall can be neglected. For single-panel CLT shear-walls, by substituting Equations (3), (5), (6), (7), (14) and (32) to (34) into Equation (35), one obtains:

$$U_{S,1,j} = \frac{h}{G_{xy,1} \cdot t_1 \cdot B_1} + \left[\frac{(j-1) \cdot h^3}{2 \cdot (EI)_{eff,1}} + \frac{h^3}{3 \cdot (EI)_{eff,1}}\right] + \frac{1}{K_{A,1}} + \frac{j \cdot h}{K_{R,1}} \cdot h \tag{36}$$

The equivalent displacement due to the vertical loads at the 1st storey $d_{S,N,1}$ can be calculated according to Equation (37) by considering the inter-storey rocking rotation due to vertical load (Equations 11 and 12).

$$d_{S,N,1} = \varphi_{R,N,1} \cdot h = \frac{N_1 \cdot (0.5B_1 - b_{c,1})}{K_{R,1}} \cdot h \tag{37}$$

Similarly, the lateral displacement at the 2nd storey due to unit lateral force applied at the *j*th storey $U_{S,2,j}$ can be expressed as:

$$U_{S,2,j} = U_{S,1,j} + \delta_{\mathrm{S,2,j}} + \delta_{\mathrm{B,2,j}} + \delta_{\mathrm{S,2,j}} + \delta_{\mathrm{R,M,2,j}} + \delta_{\mathrm{\theta,2,j}} \tag{38}$$

Substituting Equations (3), (5), (6), (7), (14) and (32) to (34) into Equation (38) for single-panel CLT shear-walls, one obtains:

$$U_{S,2,j} = U_{S,1j} + \frac{h}{G_{xy,2} \cdot t_2 \cdot B_2} + \left[\frac{(j-2) \cdot h^3}{2 \cdot (EI)_{eff,2}} + \frac{h^3}{3 \cdot (EI)_{eff,2}}\right] + \frac{1}{K_{A,2}} + \frac{(j-1) \cdot h}{K_{R,2}} \cdot h + \theta_{1,j} \cdot h \tag{39}$$

where $\theta_{1,j}$ is calculated according to Equations (15) and (16) as presented in Equation (40).

$$\theta_{1,j} = \theta_0 + \varphi_{B,1,\mathrm{j}} + \varphi_{R,\mathrm{M},1,\mathrm{j}} = 0 + \frac{(\mathrm{j}-1) \cdot h^2}{(EI)_{eff,1}} + \frac{h^2}{2 \cdot (EI)_{eff,1}} + \frac{j \cdot h}{K_{R,1}} \tag{40}$$

Substituting Equation (40) into Equation (39), $U_{S,2,j}$ can be calculated as:

$$U_{S,2,j} = U_{S,1j} + \frac{h}{G_{xy,2} \cdot t_2 \cdot B_2} + \left[\frac{(j-2) \cdot h^3}{2 \cdot (EI)_{eff,2}} + \frac{h^3}{3 \cdot (EI)_{eff,2}}\right] + \frac{1}{K_{A,2}} + \frac{(j-1) \cdot h}{K_{R,2}} \cdot \mathrm{h} + \left(\frac{(\mathrm{j}-1) \cdot h^2}{(EI)_{eff,1}} + \frac{h^2}{2 \cdot (EI)_{eff,1}} + \frac{j \cdot h}{K_{R,1}}\right) \cdot \mathrm{h} \tag{41}$$

The rotation at the top of the 2nd storey $\theta_{2,j}$ is calculated according to Equation (15) and (16) as expressed by Equation (42):

$$\theta_{2,j} = \theta_{1,j} + \varphi_{B,2,\mathrm{j}} + \varphi_{R,M,2,\mathrm{j}} = \theta_{1,j} + \frac{(j-2) \cdot h^2}{(EI)_{eff,2}} + \frac{h^2}{2 \cdot (EI)_{eff,2}} + \frac{(j-1) \cdot h}{K_{R,2}} \tag{42}$$

The displacement due to the vertical loads $d_{S,N,2}$ can be calculated by considering the rocking displacement $d_{S,N,1}$ (Equation (37)) and the rocking rotation of the shear-wall below $\varphi_{R,N,1}$ (Equations (11)-(12)) due to the vertical loads, as expressed in Equation (43).

$$d_{S,N,2} = d_{S,N,1} + \left(\varphi_{R,N,1} + \varphi_{R,N,2}\right) \cdot h = d_{S,N,1} + \left(\frac{N_1 \cdot (0.5B_1 - b_{c,1})}{K_{R,1}} + \frac{N_2 \cdot (0.5B_2 - b_{c,2})}{K_{R,2}}\right) \cdot h \tag{43}$$

At the i^{th} storey, and where $i \leq j$, Equations (41) and (42) can be generalized as expressed by Equations (44) and (45), respectively.

$$U_{S,i,j} = U_{S,i-1,j} + \frac{h}{G_{xy,i} \cdot t_i \cdot B_i} + \left[\frac{(j-i) \cdot h^3}{2 \cdot (EI)_{eff,i}} + \frac{h^3}{3 \cdot (EI)_{eff,i}}\right] + \frac{1}{K_{A,i}} + \frac{(j-i+1) \cdot h}{K_{R,i}} \cdot \mathrm{h} + \theta_{i-1} \cdot \mathrm{h} \tag{44}$$

$$\theta_{i,j} = \theta_{i-1,j} + \varphi_{B,i,j} + \varphi_{R,M,i,j} = \theta_{i-1,j} + \frac{(j-i) \cdot h^2}{(EI)_{eff,i}} + \frac{h^2}{2 \cdot (EI)_{eff,i}} + \frac{(j-i+1) \cdot h}{K_{R,i}} \tag{45}$$

Alternatively, for the i^{th} storey, where $j < i \leq N_s$, since the shear and bending moment are equal to zero, $U_{S,i,j}$ and $\theta_{i,j}$ can be obtained as expressed in Equations (46) and (47), respectively:

$$U_{S,i,j} = U_{S,j,j} + \theta_{j,j} \cdot (i-j) \cdot h \tag{46}$$

$$\theta_{i,j} = \theta_{j,j} \tag{47}$$

The generic element $U_{S,i,j}$ of the flexibility matrix $[U_S]$ can hence be expressed as:

$$U_{S,i,j} = \begin{cases} U_{S,i-1,j} + \frac{h}{G_{xy,i} \cdot t_i \cdot B_i} + \left(\frac{(j-i) \cdot h^3}{2 \cdot (EI)_{eff,i}} + \frac{h^3}{3 \cdot (EI)_{eff,i}}\right) + \frac{1}{K_{A,i}} + \frac{(j-i+1) \cdot h}{K_{R,i}} \cdot \mathrm{h} + \theta_{i-1,j} \cdot \mathrm{h} & for\ i \leq j \\ U_{S,j,j} + \theta_{j,j} \cdot (i-j) \cdot h & for\ j < i \leq N_s \end{cases} \tag{48}$$

The displacement due to the vertical loads $d_{S,N,i}$ can be generalized as expressed by Equation (49).

$$d_{S,N,i} = d_{S,N,i-1} + \sum_{r=1}^{i} \varphi_{R,N,\mathrm{r}} \cdot h = d_{S,N,i-1} + \sum_{r=1}^{i} \frac{N_r \cdot (0.5B_r - b_{c,r})}{K_{R,r}} \cdot h \tag{49}$$

3.2. Matrix formulation for a 2-D CLT LLRS

The analytical methodology outlined in the previous section for an isolated shear-wall is extended in this section to a 2-D LLRS composed of M_s isolated shear-walls. Horizontal truss elements are assumed to connect the shear-walls to each other at each storey in order to simulate the effect of the diaphragm (Figure 5). The bending stiffness of the floor as well as any interaction between floors and walls or between lintels, parapets and wall segments are neglected in this formulation.

The matrix formulation for the generic j^{th} isolated shear-wall can be written by rearranging Equation (31), as expressed in Equation (50):

$$\{F_S\}_j = [K_S]_j \left(\{d_S\}_j + \{d_{S,N}\}_j\right) \tag{50}$$

Due to the assumed in plane rigidity of the floor diaphragm, the lateral displacement array for the *j*[th] shear-wall $\{d_S\}_j$ can be assumed equal to the lateral displacement array of the LLRS $\{d_{LLRS}\}$, namely:

$$\{d_S\}_j = \{d_{LLRS}\} \tag{51}$$

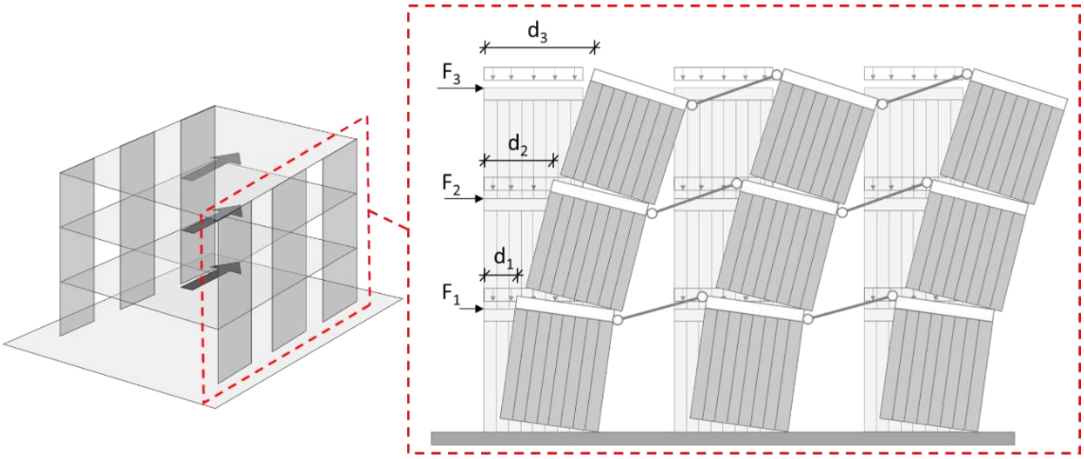

Figure 5: CLT LLRS subjected to lateral loads

Equation (50) can hence be rewritten as:

$$\{F_S\}_j = [K_S]_j \left(\{d_{LLRS}\} + \{d_{S,N}\}_j\right) \tag{52}$$

By considering equilibrium of the lateral loads acting on the LLRS $\{F_{LLRS}\}$ and on each shear-wall $\{F_S\}_j$ one obtains:

$$\{F_{LLRS}\} = \sum_{j=1}^{M_s} \{F_S\}_j \tag{53}$$

Substituting Equations (52) into Equation (53) yields:

$$\{F_{LLRS}\} = \sum_{j=1}^{M_s} [K_S]_j \{d_{LLRS}\} + \sum_{j=1}^{M_s} [K_S]_j \{d_{S,N}\}_j \tag{54}$$

which can be rewritten as:

$$\{F_{LLRS}\} = [K_{LLRS}]\{d_{LLRS}\} + \{F_{LLRS,N}\} \tag{55}$$

where $[K_{LLRS}]$ is the LLRS stiffness matrix and $\{F_{LLRS,N}\}$ is the LLRS equivalent lateral force array related to the vertical loads, which can be obtained as presented in Equations (56) and (57), respectively:

$$[K_{LLRS}] = \sum_{j=1}^{M_s} [K_S]_j \tag{56}$$

$$\{F_{LLRS,N}\} = \sum_{j=1}^{M_s} [K_S]_j \cdot \{d_{S,N}\}_j \tag{57}$$

By rearranging Equation (50) the lateral displacements of the LLRS can be calculated as expressed in Equation (57):

$$\{d_{LLRS}\} = [K_{LLRS}]^{-1} \cdot \left(\{F_{LLRS}\} - \{F_{LLRS,N}\}\right) \tag{58}$$

A similar approach can be adopted for the case of a 3D LLRS, where the position of shear-walls as well as the torsional effect and influence of perpendicular walls can be taken into account.

3.3. Rocking displacement consistency

The lateral displacements obtained from Equation (58) might not be consistent with the initial conditions assumed for the system. In fact, the formulation described in the previous two sections is based on the assumption that rocking occurs in each shear-wall and at each storey. However, this may not be the case when the overturning moment is lower than the stabilizing moment due to the vertical loads. A verification on the rocking displacement consistency is therefore needed.

Knowing the lateral displacements from Equation (58), the lateral force array acting on each isolated shear-wall $\{F_S\}_j$ can be calculated according to Equation (52) from which the overturning moment action at the bottom of the *i*th storey $M_{i,j}$ can be calculated as expressed by Equation (59):

$$M_{\mathrm{i,j}} = \sum_{r=i}^{n} F_{S,r,j} \cdot (r - i + 1) \cdot h \tag{59}$$

The stabilizing moment of the *j*th isolated shear-wall can be calculated using Equation (60).

$$M_{\mathrm{stab,i,j}} = N_{i,j} \cdot \frac{b}{2} \tag{60}$$

The condition for the activation of the rocking mechanism at the *i*th storey of the *j*th shear-wall can be expressed as reported in Equation (61).

$$\Delta M_{\mathrm{i,j}} = \left|M_{\mathrm{i,j}}\right| - \left|M_{\mathrm{stab,i,j}}\right| \tag{61}$$

If $\Delta M_{\mathrm{i,j}} > 0$, the rocking mechanism is activated as assumed in the initial condition of the analysis. If $\Delta M_{\mathrm{i,j}} < 0$, the rocking mechanism is not activated and the whole analysis on the LLRS should be reiterated. This implies that the matrix stiffness and the vertical load array of the *j*th shear-wall have to be recalculated by assuming that the rocking deformation contribution at the *i*th storey is neglected, namely $K_{\mathrm{R,i,j}} \to \infty$.

4. Cantilevered beam model for CLT LLRS

As an alternative to the analytical methodology presented in the two previous sections, a simplified finite element modelling strategy is proposed for the calculation of lateral displacements of a CLT LLRS based on an equivalent cantilevered beam approach.

4.1 Model definition

An isolated multi-storey CLT shear-wall is modelled by means of vertically aligned frame elements connected to each other using pins and rotational springs, as illustrated in Figure 6.

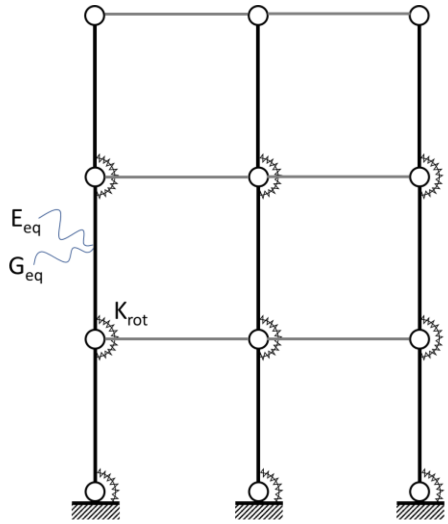

Figure 6: Multi-storey cantilevered beam model with rotational springs

4.1.1 Single-panel CLT shear-walls

The thickness, t_{cb}, and the width, w_{cb}, of the cross section of the cantilever beam element at the *i*th storey are equal to the total thickness, t_i, and the length, B_i, of the CLT shear-wall. The effective modulus of elasticity, $E_{eff,cb,i}$, of the frame element at the *i*th storey is equal to the effective in-plane modulus of elasticity of the panel along the major (i.e. vertical) axis, as reported in Equation (62).

$$E_{eff,cb,i} = \frac{t_{\mathrm{z,i}}}{t_{\mathrm{i}}} \cdot E_0 \tag{62}$$

The effective shear modulus, $G_{eff,cb,i}$, of the frame element at the *i*th storey can be calculated with Equation (63) by considering the in-plane shear deformation contribution of the panel as well as the flexibility along the lateral-shear direction of the mechanical anchors due to sliding.

$$G_{eff,cb,i} = \frac{1.2}{\frac{1}{G_{\mathrm{xy,i}}} + \frac{B_i \cdot t_i}{K_{\mathrm{A,i}} \cdot h_i}} \tag{63}$$

The stiffness of the rotational spring, $K_{rot,i}$, at the base of each frame element at the *i*th storey can be calculated as:

$$K_{rot,i} = K_{\mathrm{R,i}} \tag{64}$$

where $K_{\mathrm{R,i}}$ is the rocking stiffness of the wall at the *i*th storey, as presented in Equation (10).

4.1.2 Multi-panel CLT shear-walls

Similar to the case of single-panel shear-wall, the effective shear modulus $G_{eq,cb}$ can be defined by considering the in-plane shear deformation contribution of all panels through the effective in-plane shear modulus, $G_{xy,i}$, as well as the flexibility along the lateral-shear direction of all mechanical anchors due to the lateral-sliding.

The effective modulus of elasticity, $E_{eq,cb,i}$, of the frame element at the *i*th storey can be calculated using Equation (65).

$$E_{eff,cb,i} = \frac{12 \cdot (EI)_{\mathrm{eff,i}}}{t_i \cdot B_i{}^3} \tag{65}$$

where $(EI)_{eff,i}$ can be calculated as discussed in Section 2.2 and Equation (21).

The stiffness of the rotational spring, $K_{rot,i}$, at the base of each frame element at the *i*th storey can be calculated as:

$$K_{rot,i} = K_{R,i,SW} \qquad \text{for SW mode} \tag{66}$$

where $K_{R,i,SW}$ is the rocking stiffness of the wall at the *i*th storey for SW mode, as expressed previously in Equation (29).

When the CP kinematic mode occurs and the contribution due to the cumulative rotation at the *(i-1)*th storey may be neglected, the rocking deformation contribution should be included in the calculation of the effective shear modulus whereas the rotational springs should be fixed ($K_{rot,i} \to \infty$). The effective shear modulus, $G_{eff,cb,i}$ can be obtained as presented in Equation (67):

$$G_{eq,cb,i} = \frac{1.2}{\frac{1}{G_{\mathrm{xy,i}}} + \frac{B_i \cdot t_i}{K_{\mathrm{A,i}} \cdot h_i} + \frac{B_i \cdot t_i \cdot h_i}{K_{\mathrm{R,i}}}} \tag{67}$$

4.2 Load applications and lateral displacements

The cantilevered model presented in the previous section is a linear model, in which the binary rocking behaviour of the wall (activated or not activated) cannot directly be taken into account. To consider this aspect and hence reflect the real behaviour of the LLRS, it is suggested to consider the effects of the overturning and stabilizing moments in the model separately, and then using the superposition principle. To this purpose, two different load conditions are defined, as highlighted in Figure 7. In the first condition (Figure 7a), the lateral loads are applied in order to only calculate the overturning moments and the effects (displacement and internal forces) due the lateral loads. In the second condition, the stabilizing effect of the vertical loads is considered by applying an equivalent stabilizing moment $M_{N,i,j}$, at the top of each frame element:

$$M_{\mathrm{N,i,j}} = \left(N_{i,j} - N_{i-1,j}\right) \cdot \frac{B_{i,j}}{2} \tag{68}$$

From the superimposition of the two load conditions, the internal actions on each frame element and the lateral displacement of the LLRS can be calculated.

Analogously to the analytical matrix formulation presented in the Section 3, an iterative procedure may be required in order to satisfy the rocking displacement consistency condition. In this case, when $\Delta M_{\mathrm{i,j}} = \left|M_{\mathrm{i,j}}\right| - \left|M_{\mathrm{stab,i,j}}\right| > 0$ the rocking contribution is activated as assumed in the initial condition of the analysis and the model can be considered consistent. Where $\Delta M_{\mathrm{i,j}} < 0$, the rocking mechanism is not activated, and the analysis should be reiterated by assuming that the relevant rotational spring as fixed.

The lateral displacements and the internal actions are obtained from the superimposition of the two load conditions.

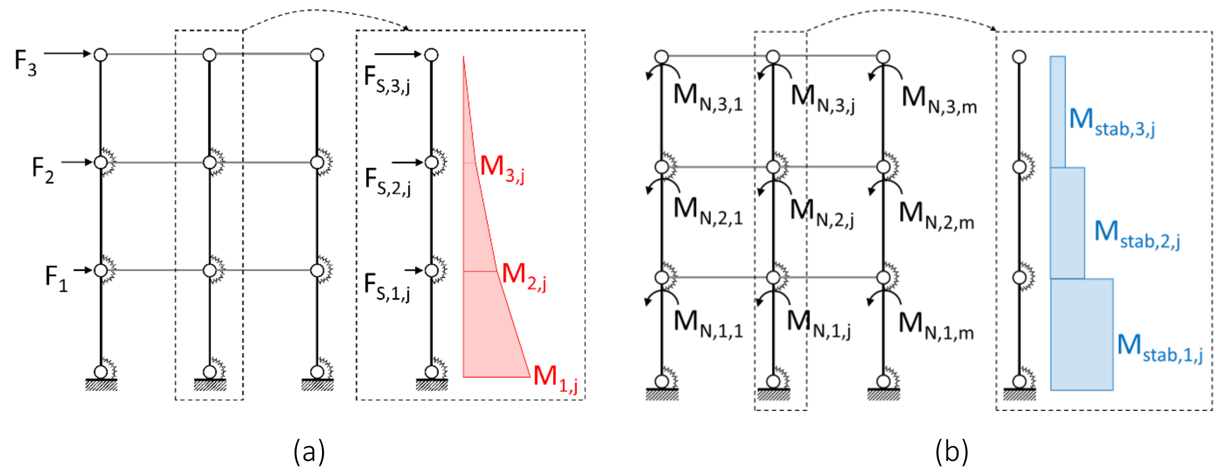

Figure 7: Multi-storey cantilevered beam model for calculation of (a) overturning moments and (b) stabilizing moments.

5. Conclusions

This paper presented an analytical approach for the calculation of the lateral displacements of multi-storey CLT shear-walls in both single-panel and multi-panel configuration. The proposed analytical approach is the culmination and extension of available literature and forms the basis for a potential code change proposal for Eurocode 5 as well as the CSA O86.

Analytical formulas for the calculation of the bending and shear panel, sliding, rocking and cumulative rotational displacements based on the elastic properties of CLT panels and wall base connections are provided for both cases of single and multi-panel shear-wall. In the case of rocking displacement of multi-panel shear-walls, both Coupled Panel and Single Wall kinematic behaviours are considered.

The expressions for the calculation of lateral displacements of the single wall at the i^{th} storey are then used to generalize the calculation of displacements for a LLRS through a matrix approach. The flexibility matrix of the isolated multi-storey shear-walls is defined based on the expressions for calculation of lateral displacements of the single wall and then used for the calculation of the stiffness matrix of the isolated multi-storey shear-walls and laterally aligned multi-storey shear-walls. In addition, a simplified finite element modelling strategy is proposed for the calculation of lateral displacements of a CLT LLRS based on an equivalent cantilevered beam approach.

The proposed study is intended to provide a relatively simple and easy-to-use approach, which can be used by practitioners for the calculation of lateral displacements of CLT buildings.

6. References

Brandner R, Dietsch P, Droscher J, Schulte-Wrede M, Kreuzinger H, Sieder M. (2017) Cross laminated timber (CLT) diaphragms under shear: Test configuration, properties and design. Constr Build Mater; (147):312–27.

Casagrande D, Rossi R, Sartori T, Tomasi R. (2016) Proposal of an analytical procedure and a simplified numerical model for elastic response of single-storey timber shear-walls, Constr Build Mater, Volume 102, Part 2, Pages 1101-1112, ISSN 0950-0618, https://doi.org/10.1016/j.conbuildmat.2014.12.114.

Casagrande D, Doudak G, Mauro L, and Polastri A. (2018) Analytical approach to establishing the elastic behavior of multipanel CLT shear-walls subjected to lateral loads. J. Struct. Eng. 144 (2): 04017193.

D'Arenzo G, Schwendner S, Seim W. (2021) The effect of the floor-to-wall interaction on the rocking stiffness of segmented CLT shear-walls, Engineering Structures, Volume 249, 113219, ISSN 0141-0296, https://doi.org/10.1016/j.engstruct.2021.113219.

Flatscher G, Schickhofer G. (2016) Displacement-based determination of laterally loaded Cross Laminated Timber (CLT) wall systems. Proceedings of the 3rd INTER Meeting - INTER/49-12-1, Graz.

Gavric I, Fragiacomo M, Ceccotti A. (2015) Cyclic behaviour of CLT wall systems: experimental tests and analytical prediction models. J Struct Eng 2015;141.

Hummel J, Seim W, Otto S. (2016) Steifigkeit und Eigenfrequenzen im mehrgeschossigen Holzbau. Bautechnik, 93: 781-794. https://doi.org/10.1002/bate.201500105.

Lukacs I, Björnfot A, Tomasi R. (2019) Strength and stiffness of cross-laminated timber (CLT) shear-walls: State-of-the-art of analytical approaches (2019) Engineering Structures, 178.

Masroor M, Doudak G, Casagrande D. (2020) The effect of bi-axial behaviour of mechanical anchors on the lateral response of multi-panel CLT shear-walls, Engineering Structures, Volume 224, 111202, ISSN 0141-0296, https://doi.org/10.1016/j.engstruct.2020.111202.

Pei S, Popovski M, Van De Lindt J.W. (2012) Seismic design of a multi-story cross laminated timber building based on component level testing. World Conference on Timber Engineering 2012, WCTE 2012, 2, pp. 244-252.

Popovski M, Schneider J, Schweinsteiger M. (2010) Lateral load resistance of cross-laminated wood panels) 11th World Conference on Timber Engineering 2010, WCTE 2010, 4, pp. 3394-3403.

Popovski M, Gavric I. (2016) Performance of a 2-Story CLT House Subjected to Lateral Loads, Journal of Structural Engineering (United States), 142 (4), art. no. E4015006. doi: 10.1061/(ASCE)ST.1943-541X.0001315.

Reynolds T, Foster R, Ramage M, Bregulla J., Chang W-S, and Harris R. (2017) Lateral-load resistance of cross-laminated timber shear-walls. J. Struct. Eng. 143 (12): 06017006. https://doi.org/10.1061/(ASCE)ST.1943-541X.0001912.

Tamagnone G, Rinaldin G, Fragiacomo M. (2018) A novel method for non-linear design of CLT wall systems, Engineering Structures, Volume 167, Pages 760-771, ISSN 0141-0296, https://doi.org/10.1016/j.engstruct.2017.09.010.

Tomasi R. (2014) CLT course at FPS COST Action FP1004 – Enhance mechanical properties of timber, engineered wood products and timber structures. CLT Training School, University of Trento; 15–17 April 2014.

DISCUSSION

The paper was presented by G D'Arenzo

P Dietsch and G D'Arenzo discussed the analytical and cantilever approach giving largest contributions from sliding and rocking. Panel deformation may be considered relatively small especially for common hold-downs and angle brackets.

T Tannert commented about cumulative overturning that assumed floor and diaphragm can rock individually. G D'Arenzo is aware of this aspect and the model has a limitation. Further work is needed.

T Tannert stated in most tests angle brackets tested may have different boundary conditions for the single storey case versus a multi-storey case as multi-storey wall systems have more degrees of freedom. G D'Arenzo said the paper has information that the model can address this aspect.

S Winter stated that timber concrete floors tend to be more rigid. He received clarification of the deformation mechanism of multiple walls.

S Winter asked what is the recommendation for practice. G D'Arenzo said more dissipative elements may be desirable. D Casagrande added elastic behaviour is considered here whereas seismic cases need to consider yielding, energy dissipation and ductility.

H Blass commented that buckling of CLT elements may be important with large vertical loads. G D'Arenzo responded that boundary conditions are an adjustment factor that can be used and agreed that vertical loads in tall building can lead to CLT deformations.

T Demscher has concerns about having to model this in FEM. G D'Arenzo responded that the plan is to generalize the analytical approach to buildings.

Rocking capacity model of CLT walls with openings and timber plasticization

Yuri De Santis, Department of Civil, Building-Construction and Environmental Engineering, University of L'Aquila, 67100 L'Aquila, Italy

Angelo Aloisio, Department of Civil, Building-Construction and Environmental Engineering, University of L'Aquila, 67100 L'Aquila, Italy

Martina Sciomenta, Department of Civil, Building-Construction and Environmental Engineering, University of L'Aquila, 67100 L'Aquila, Italy

Massimo Fragiacomo, Department of Civil, Building-Construction and Environmental Engineering, University of L'Aquila, 67100 L'Aquila, Italy

Keywords: Cross-Laminated Timber, Capacity model, Inelastic behaviour, Finite Element modelling

1 Introduction

The scientific literature presents two approaches for predicting the lateral capacity of CLT panels (Franco et al., 2019). The former is entirely analytical and originates from the solution of the equilibrium equations of a CLT panel. The latter one is based on Finite Element modelling and aims at reducing the number of assumptions related to the former approach.

Simplified capacity models predict the CLT wall ultimate rocking capacity by multiplying the overturning restraint strength by its distance from the compressive stress resultant, often assumed coincident with the panel edge. However, timber plasticization at the interface with the foundation and in-plane deformability induced by openings can significantly affect the lever arm of the hold down reaction.

In predicting the rocking capacity Tomasi R. (2014) neglect the contribution of angle brackets and assumes a rectangular stress block distribution in the compression zone, with size 0.8*x* where *x* is the compressed zone length. Wallner-Novak et al. (2013) proposes a model similar to Harris, R. & van de Kuilen J. W. (2016), but with compression zone equals to 0.25*l*. Pei et al. (2013), Reynolds et al. (2017), Gavric and Popovski (2014) presented models that include the tensile contribution of angle brackets. Pei et al. (2013) assumes an elastic triangular distribution of tensile forces by considering the rigid body rotation around one edge of the shear wall. Reynolds et al. (2017) presented three different models, which all include the presence of a compression zone, but differ in the size of that zone and the distribution of tensile forces between angle brackets and hold-down. Gavric and Popovski (2014) presents a model similar to Gavric and Popovski (2014), but considers the interaction between horizontal and vertical forces on the angle brackets. Aloisio et al., (2021) discussed a simplified capacity model that is valid for both LTF and CLT walls based on equilibrium equations.

Some papers also consider the effects of the openings on the ultimate capacity of CLT walls. In past years, Dujic et al. (2007 and 2008) addressed the issue of CLT panels with openings by providing analytical estimates of strength and stiffness reduction related to the openings aspect ratios, based on non-linear static pushover analyses. Awad et al. (2017) carried out experimental tests on CLT walls with openings. Based on FE numerical analyses, the proposed analytical models estimate the lateral capacity and the expected failure mechanism. However, to the authors knowledge, no scholar attempted to estimate the effects of the openings on the dimensionless lever arm to be used in an elementary capacity model of the CLT wall.

The investigation herein presented leads to a hybrid capacity model. The structure of the capacity equation derives from the panel equilibrium, while the empirical equation of the dimensionless lever arm derives from the linear fitting of the FE results. The authors investigated two limit cases, a CLT wall on a rigid concrete foundation and a CLT wall on a deformable foundation, representative of the timber floor in platform frame buildings. In platform frame buildings CLT panels are prone to rocking, particularly at higher stories, and consequently are subjected to local timber plasticization. Local plasticization of the timber floor panel occurs at the attainment of its low strength in perpendicular to grain direction Serrano E. & Enquist B. (2010).

Practitioners and codes demand elementary but accurate formulations for predicting the lateral capacity of CLT wall panels. In the current draft revision of the Eurocode 8, the stress-block formulation is suggested (Tomasi R., 2014) to determine the rocking strength to be used in the capacity-based design of non-dissipative connections like joints between floors and supporting walls underneath and joints between orthogonal walls joints. These connections should be capacity designed by means of an overstrength ratio that is the minimum between shear strength-design force ratio and the rocking strength-design force ratio (if unidirectional behavior of the shear and overturning connections is assumed).

According to the draft revision of Eurocode 8 the overturning restraints should be placed at wall ends, adjacent to door openings, and at opening ends when the ratio between the area of the window opening and the area of the wall panel exceeds 0,50.

In this way it is assumed a priori that even for shaped CLT walls, that are those in which the opening is obtained by cutting a portion of the panel and therefore in which the mechanical continuity is preserved, they behave as two separate panels regarding to the rocking behavior. In other words, it is assumed that the portion above the door-type openings is unable to ensure the coupling necessary for the rocking of the wall as a whole. In this way there is a risk of underestimating the rocking capacity to be used in the capacity-based design.

This paper investigates the rocking of walls on rigid and concrete foundations with window and door openings and proposes an extended version of the current Eurocode 8 formula for the prediction of the rocking capacity, based on parametric finite element analyses that take into account the plasticization at the base of the panel, the in-plane deformability and which is suitable for perforated walls which exhibit overall rocking.

2 Mechanical model

Assuming a unidirectional behaviour of the shear connections and the connections against overturning so that shear connections and the connections against overturning are only considered effective along the shear-horizontal and tensile-vertical direction, respectively, the rocking behaviour of CLT walls is governed by the hold-down connections only and therefore the contribution of angle brackets is neglected.

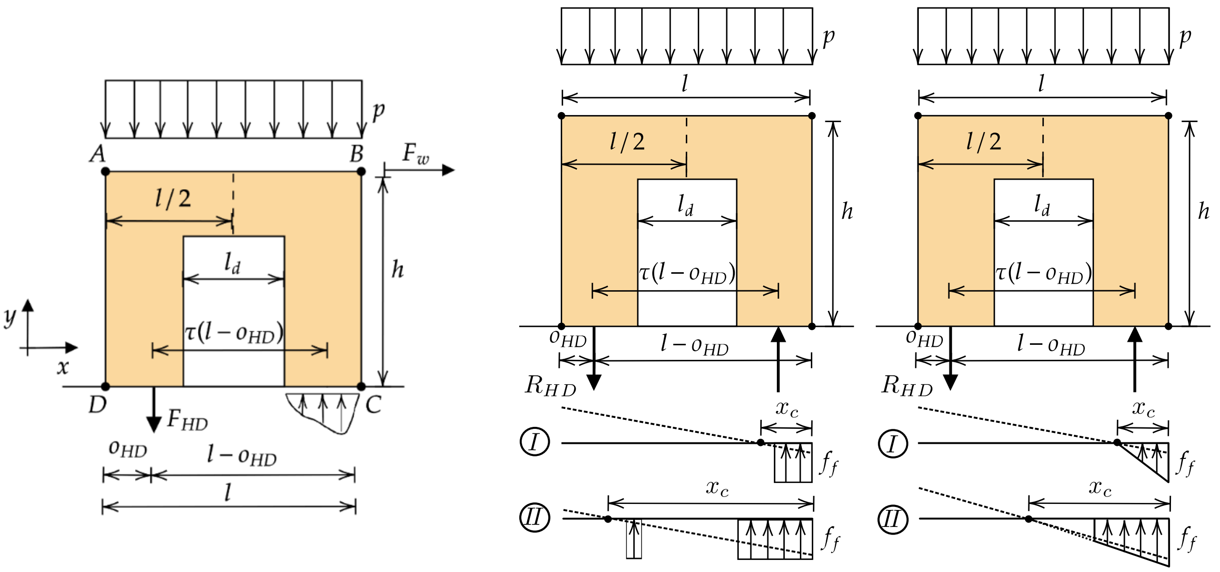

Figure 1. Mechanical model of the shear wall (left), base stress distribution assumptions as a function of neutral axis position: Stress-block (centre), Triangular (right).

The equilibrium to the vertical translation of the panel can be written as:

$$\sum_i F_{y,i} = 0 \Rightarrow -pl - F_{HD} + F_{Ti} = 0 \quad (1)$$

where $F_{y,i}$ is the *i-th* horizontal force, p is the vertical load, l and h are the length and height of the panel, F_{HD} is the hold down resisting force, and F_{Ti} is the resultant of the compression stresses. The equilibrium to the rotation around the position of the resultant of the compression stresses can be written as:

$$\sum_i M_{r,i} = 0 \Rightarrow pl\left[o_{HD}+\tau(l-o_{HD})-\frac{l}{2}\right]-F_W h+F_{HD}\tau(l-o_{HD})=0 \qquad (2)$$

where F_W is the horizontal force acting on the top of the panel, and o_{HD} is the distance between the hold-down reaction force and the closest edge of the panel, $\tau(l-o_{HD})$ is the distance between the reaction force of the hold down and the compression force.

By solving Eq. (2), the expression of τ when the hold-down reaches failure ($F_{HD} = R_{HD}$) can be written as shown in Eq. (3):

$$\tau=\frac{-plo_{HD}+pl^2/2+R_W h}{(pl+R_{HD})(l-o_{HD})} \qquad (3)$$

By solving Eq. (2), the expression of R_W when the hold-down reaches failure can be written as shown in Eq. (4):

$$R_W=\frac{pl}{h}\left[o_{HD}+\tau(l-o_{HD})-\frac{l}{2}\right]+R_{HD}\frac{\tau(l-o_{HD})}{h} \qquad (4)$$

2.1 Analytical formulas for the dimensionless lever arm τ

Assuming an arbitrary distribution of the stresses at the base of the panel, the position of the resultant of the compressive stresses that balances the hold-down force at failure is known a priori or can be calculated by static equivalence.

Below are listed the expressions of the equivalent arm corresponding to two different hypotheses very recurrent in the literature. The well-known expressions have been extended to the case of panels with a centred door.

2.1.1 Stress-block

Assuming the planarity of the base section which means implicitly assuming a rigid panel behaviour and substituting the real non-linear stress distribution with a rectangular distribution of extension equal to 80% of the length of the compressed zone:

For $x_c \leq \frac{1}{0.8}\frac{l-l_d}{2}$ (I, Figure 1 centre):

$$\tau = 1 - \frac{1}{2}\;\frac{R_{HD}+pl}{n_l\, t_l\,(l-o_{HD})f_f} \qquad (5)$$

For $x_c > \frac{1}{0.8}\left(\frac{l-l_d}{2}+l_d\right)$ (II, Figure 1 centre):

$$\tau = 1 - \frac{1}{2}\ \frac{n_l\, t_l\, f_f \left(l_d\, l - \left(\frac{R_{HD} + p\, l + n_l\, t_l\, f_f}{n_l\, t_l\, f_f} \right)^2 \right)}{-(R_{HD} + pl)(l - o_{HD})} \qquad (6)$$

2.1.2 Triangular

Assuming the planarity of the base section and assuming that at the hold-down failure, the stress distribution is triangular with incipient compression failure of the timber on the edge of the wall:

For $x_c \leq \frac{l - l_d}{2}$ (I, Figure 1 right):

$$\tau = 1 - \frac{2}{3}\ \frac{R_{HD} + pl}{n_l\, t_l\, (l - o_{HD})\, f_f} \qquad (7)$$

For $x_c > \frac{l - l_d}{2}$ (II, Figure 1 right):

$$\tau = 1 - \frac{1}{24}\ \frac{(l - l_d)\left(8 + \frac{(l_d - l)\, n_l\, t_l\, f_f}{R_{HD} + pl} \right)}{(l - o_{HD})} \qquad (8)$$

The Eqs. (5-8) allow together with Eq. (4) to estimate the rocking capacity of a wall with or without holes.

2.2 Finite element model

The aim of the paper is to determine the capacity of a rocking CLT panel accounting for the in-plane panel deformability and non-linear base stress distribution. If the wall were a rigid panel without holes, the problem would be almost trivial as seen in Par. 2.1. The position of the neutral axis could be estimated from the equilibrium to the translation, and consequently, the arm of the internal forces. The problem grows in complexity when the in-plane panel stiffness lowers, as occurring in the case of CLT panels with large openings, see Figure 7. Therefore, it is necessary to carry out a Finite Element analysis to assess the contribution of the panel deformability to the lateral capacity of the panel.

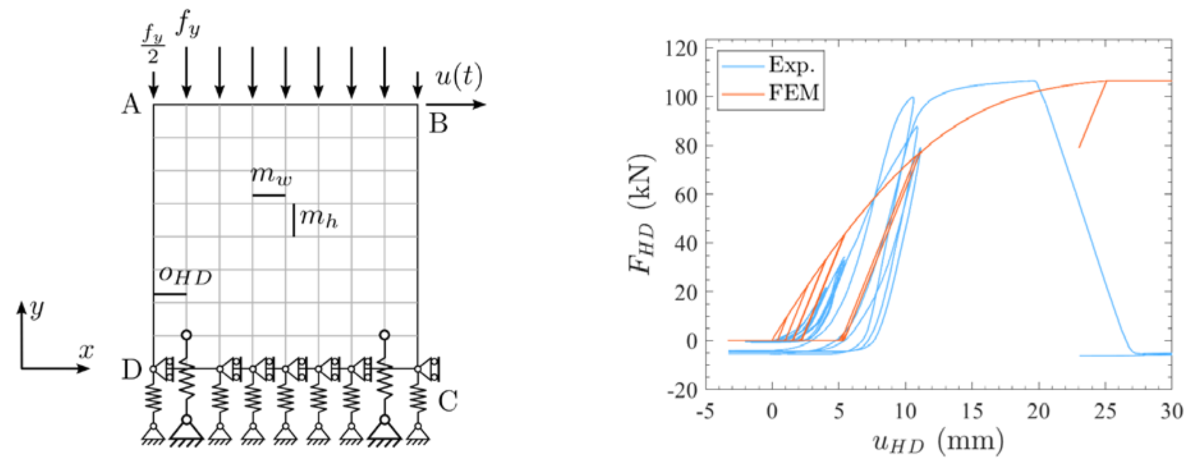

Figure 2. Finite element model representation (left) and fitted hold-down constitutive law (right).

The rocking behaviour of the CLT wall has been schematized through a 2D model consisting of an assembly of two-dimensional elements representing the CLT panel and elastic–plastic springs representing the overturning restraints and the panel-underlying structure interaction (Figure 2 left).

The CLT panel is modelled via S4R 4-node general-purpose shell elements (ABAQUS/Standard library), with elastic orthotropic behaviour. The shell thickness is assumed equal to the actual panel thickness t_p and the in-plane elasticity modules were calculated according to the well-known approach from the literature (Brandner R. et al., 2017):

$$E_x=\frac{\sum_{i=1}^{n_{lx}} E_0 t_{x,i}+\sum_{i=1}^{n_{ly}} E_{90} t_{y,i}}{t_p} \quad (9)$$

$$E_y=\frac{\sum_{i=1}^{n_{ly}} E_0 t_{y,i}+\sum_{i=1}^{n_{lx}} E_{90} t_{x,i}}{t_p} \quad (10)$$

The in-plane shear module for CLT elements without lateral gluing interfaces at the narrow faces can be calculated according to the formula given by Bogensperger T. et al. (2010):

$$G_{xy}=\frac{G_{0,90}}{1+6\alpha(t_m/w_l)^2} \quad (11)$$

The panel has been discretized by means of square elements (*m_w=m_h=50 mm*). In order to induce pure rocking behaviour, the base nodes translation in *x* direction were restrained (u_x=0 on CD, Figure 2 left). The typical simulation consisted in a static incremental, geometrical linear, displacement-controlled analysis.

Regarding the wall-panel-base interaction both the case of a wall on a rigid base and the case of a wall on CLT floor were considered. In the first case the interaction was modelled by means of compression-only rigid-plastic springs representing the rigid behaviour of the base and the plastic behaviour of the wall. The springs yield stress was determined assuming *y*-oriented layers only as resistant and considering their compression strength parallel to grain. In the second case the interaction was modelled by means of compression-only elastic–plastic springs representing the behaviour of the underlying CLT panel. The yield stress was assumed equal to the compression strength of the floor panel perpendicular to grain. The springs stiffness k_s was calculated:

$$k_s = k_f = \frac{E_{f,90}}{t_f} \tag{12}$$

where$E_{f,90}$ is the mean modulus of elasticity perpendicular to grain direction and t_f is the floor CLT panel thickness.

The hold-down behaviour including its interaction with the panel through the nailed connection is modelled via a two nodes connector element with elastic–plastic behaviour. The elastic component of the hold-down displacement has been related to the force with the following:

$$F_{HD}(u_{el}) = K_0 u_{el} \tag{13}$$

The plastic component of the hold-down displacement has been related to the force with the following:

$$F_{HD}(u_{pl}) = F_{HD,0} + a\left(1 - e^{-bu_{pl}}\right) \tag{14}$$

By imposing $b = 0.25$, the analytical constitutive law thus defined is able to describe the displacement-force relation of any hypothetical hold-down of assigned strength and stiffness with a good approximation (Figure 2 right), thus allowing to carry out parametric analyses without having a large number of experimental hold-down tests.

2.3 FEM derived empirical formulation of the dimensionless lever arm τ

The finite element model was used to derive an empirical formulation of the dimensionless arm τ which implicitly takes into account the deformability of the wall and the effective distribution of the stresses at the base of the panel.

A multidimensional dataset of significant input parameters uniformly distributed in the domain of practical interest (Table 3) was generated (2625 configurations) and the corresponding solution in terms of non-dimensional equivalent arm τ was calculated by Eq. (3) with the FEM derived wall capacity R_W.

The exact solution of the FEM model in terms of τ was interpolated using a trial function similar to the solution obtained for the stress-block assumption (Eq.5)

Best fit coefficient has been determined (Eq. 16, with coefficient of determination R^2= 0.75 and Root Mean Square Error RMSE = 0.04) and a cross-validation was carried out on two datasets of uniformly distributed pseudo-random inputs.

Defined $F_{HD,lim}$ as the strength of the area of timber base between the hold-down and the edge of the panel:

$$F_{HD,lim} = n_l t_l \left(l - l_d - o_{HD} \right) f_f - pl \tag{15}$$

The proposed formulas can be written as:

$$\tau = 1 - \frac{1}{2}\ \frac{R_{HD}}{F_{HD,lim}} + \frac{l_d}{7\,l} \qquad (16)$$

For 90% of the cross-validation configurations with window opening, the percent deviation between τ determined with the interpolation law and the FEM derived $\boldsymbol{\tau}$ is between −2.08% and +3.13%. The corresponding values for the configurations with door opening are −6.23% and +6.38%.

3 Comparisons

In this paragraph the results of the analytical formulas for the calculation of τ, based on the assumptions of triangular (Eqs.5-6) and stress-block stress distribution (Eqs.7-8), the results of the formula implicitly included in Eurocode 8 (Eq.7), and the proposed formula (Eq.16) results are compared with the exact results of the finite element model.

A multidimensional dataset of input parameters randomly distributed in the domain of practical interest (Table 3) was generated (1000 configurations for each opening type - foundation type combination) and the corresponding solution in terms of non-dimensional equivalent arm τ was calculated by Eq. (3) with the FEM derived wall capacity R_w.

Table 3. Parameters domain of comparison configurations.

	l (m)	h (m)	l_{op}/l	h_{op}/h	CLT class	nl (n°)	K_{HD} (kN/mm)	$R_{HD}/F_{HD,lim}$*3 (kN/mm)	P (kN/m)
Lower	1	2.5	0	0.4*1	C14	3	6.5	0.1-0.4	0
Upper	5	5	0.6	0.8*2	C50	7	13	0.2-0.8	40

*1 Window opening heigh ratio, *2 Door opening heigh ratio, *3 Rigid foundation-CLT foundation

3.1 Wall on rigid foundation

The analyses carried out for the walls with window-type openings with hole area percentages lower than 48% show an excellent correspondence between the results of the analytical formulations and the results obtained from the finite element analyses (Figure 3 left).

Hold-down strength between 10% and 20% of the strength of the timber side (Eq.15) were considered with the aim of limiting the investigation to the domain of overturning restraint strength achievable with current technologies (50kN -2800kN, Tannert (2022)). In the domain of the considered parameters, the analyses return τ values between 0.9 and 0.98, thus confirming the validity of the assumption of pivot point positioned at the wall edge even in the case of walls with window type openings of limited area (Figure 3 left).

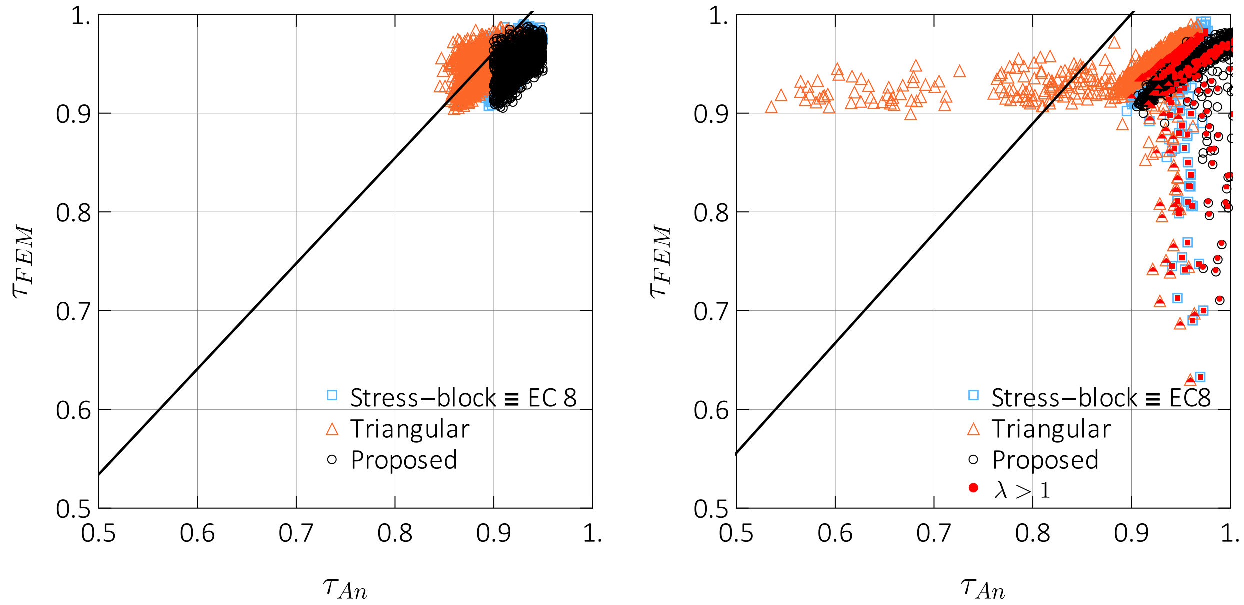

Figure 3. FEM derived vs analytically predicted τ: wall on rigid foundation with window openings (left) and door openings (right).

Note for door openings: The stress-block and EC8 formulations coincides due to the chosen input parameters ($x_c \leq (l-l_d)/2$ always with stress-block)

The analyses carried out on walls with door-type openings revealed two possible qualitatively different wall behaviors:

• When the lintel above the door is slender compared to the portions of the wall on the sides of the door, the wall tends to exhibit an individual rocking behavior: the two portions rotate independently of each other, each showing a compressed zone and a zone raised from the foundation (Figure 7 left)

• When the lintel above the door is squat compared to the portions of the wall on the sides of the door, the wall tends to exhibit an overall rocking behavior: the perforated wall rotates as a whole, the base section of the wall approximately retains the planarity (Figure 7 right)

As a first approximation, the transition between the two qualitative behaviors can be characterized through a critical value of the ratio between the slenderness of the lintel and the slenderness of the portions of the wall on the door side (Figure 1).

$$\lambda = \frac{l_l / h_l}{l_{sw} / h_{sw}} = \frac{l_d / (h-h_d)}{h_d / 0.5(l-l_d)} \tag{17}$$

Sensitivity studies identified λ= 1 as the critical value. The transition from overall rocking to individual rocking is clearer for rigid foundation walls compared to the case of wall on CLT floor (Figure 4).

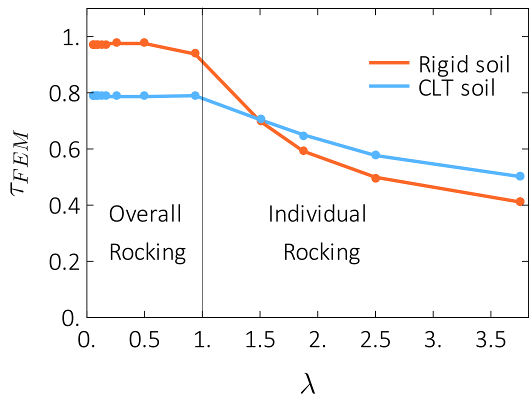

Figure 4. Dimensionless equivalent arm τ as a function of the slenderness ratio λ.

In the comparisons, an overall rocking was assumed a priori. The stress-block and proposed interpolating formula show an excellent correspondence with the numerical result with the exception of cases characterized by individual rocking, marked in red in Figure 3 (right).

The assumption of triangular distribution leads to a considerable underestimate of the dimensionless equivalent arm for wall on rigid foundation with door type-openings when $x_c \geq (l-l_d)/2 + l_d$ (Figure 1 right).

3.2 Wall on CLT floor

Due to the reduced compressive strength of the CLT floor, to grant the equilibrium of the forces in the vertical direction (Eq. 1), a compressed area of greater length is required compared to the case of a wall on a rigid foundation. The analyses were performed assuming hold-down strengths between 40% and 80% of the compressive strengths on the timber side (R_{hd} = 20kN -500kN).

As can be seen from Figures 5, in the case of window-type openings and in the absence of vertical load, the Eurocode formula (stress-block assumption) coincides with the proposed formula and with the finite element results. From the comparisons made on the random configurations emerged that the proposed formula and the Eurocode formula both provide results characterized by extremely limited deviations from the FEM (less than ±5% and R^2=0.96 in both cases, Figure 6). The dimensionless equivalent arm deriving from the assumption of triangular stress distribution is suitable for describing only the configurations characterized by hold-downs that are not very resistant with respect to timber ($R_{hd}/F_{hd,lim} < 0.1$, Figure 5) which correspond to values of τ greater than 0.8.

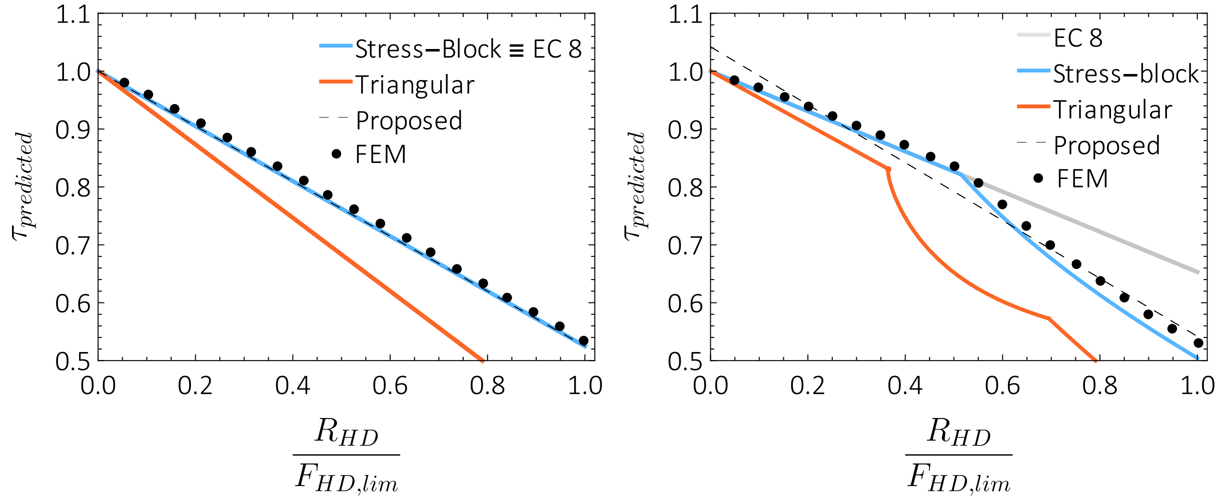

Figure 5. Dimensionless equivalent arm τ as a function of the hold-down – timber strength ratio: wall with window openings (left) and wall with door openings (right).

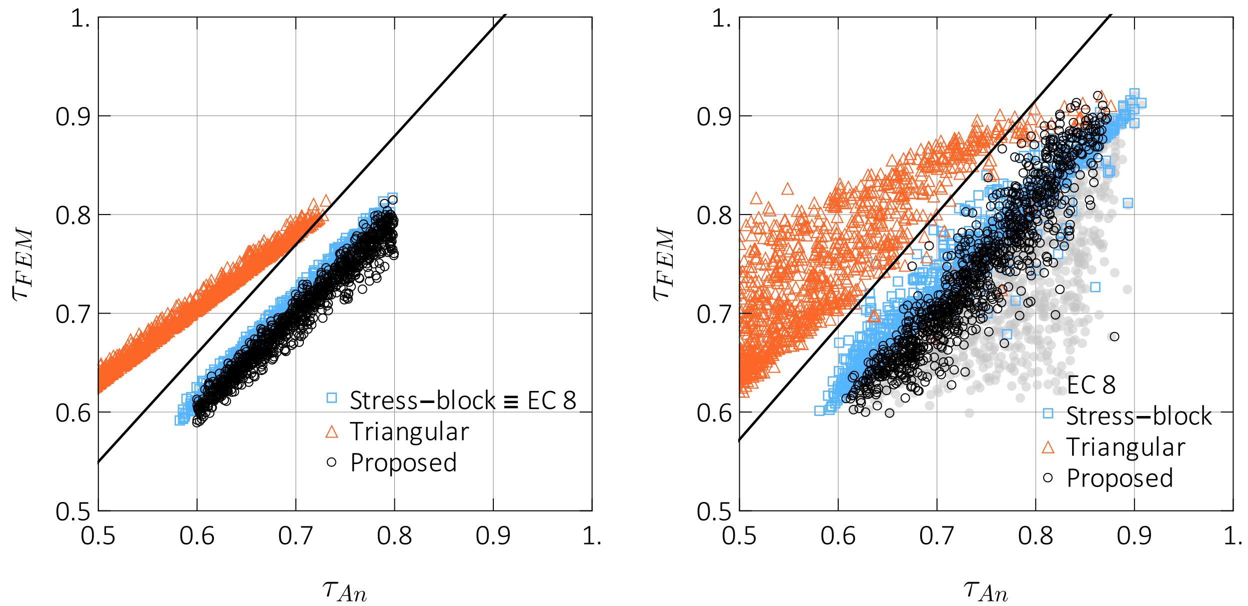

Figure 6. FEM derived vs analytically predicted τ : wall on CLT floor with window openings (left) and door openings (right).

Due to the greater deformability of the wall support, the individual rocking of walls with door opening of CLT floor is less frequent than in the case of walls on a rigid foundation. Consequently, the proposed analytical formula and the stress-block formula extended to the case of walls with door-type openings are reliable in almost all cases (Figure 6 right). The Eurocode formulation that does not contemplate the possibility of door type openings is significantly overestimating in all cases in which overall rocking occurs and the neutral axis pass the door hole ($0.8\ x_c \geq (l\text{-}l_d)/2 + l_d$) (Figures 5 and 6 right).

It is worth noting that the proposed formula, despite its simplicity, well approximates the τ value in both field I and field II (fields definition in Figure 1) (Figure 5 right). The expression of τ associated with the hypothesis of triangular stress is also in this case reliable only for walls with low strength hold-downs.

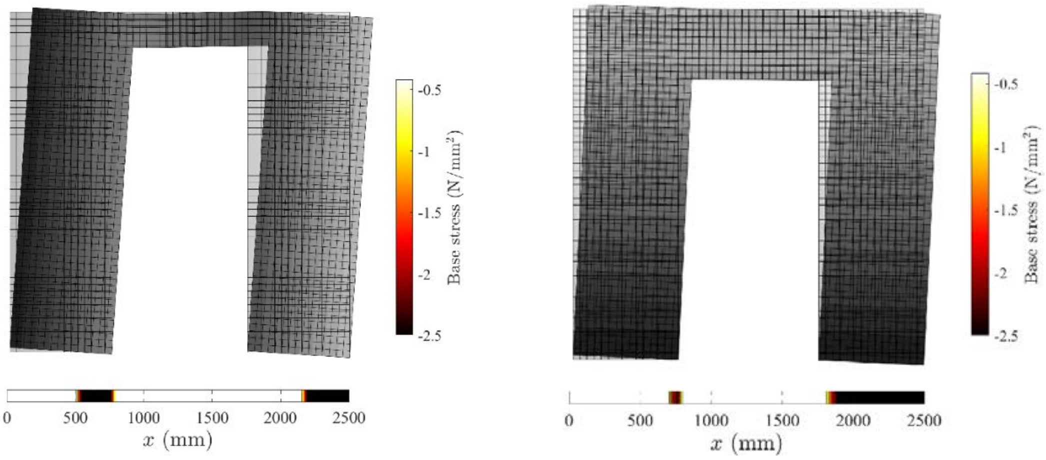

Figure 7. FEM derived deformed shape of wall on CLT floor with: individual rocking behaviour (left) and overall rocking behaviour (right).

4 Conclusions and proposal

The analyses carried out have shown that overall rocking behaviour is possible for walls with doors openings and squat lintels. When this occurs, even if the wall is equipped with both wall end hold-downs and door sides hold-downs, only one of the four hold downs is in tension and therefore active (Figure 7 right). The overall rocking causes the wall to exhibit higher rocking capacity than the capacity associated with the individual rocking of the two portions of the panel on the sides of the door.

The current draft revision of Eurocode 8 prescribes the insertion of hold-downs at the ends of door-type opening and imposes checks for capacity design by means of an overstrength factor (Ω) dependent on the rocking capacity of the wall without specifying whether in the case of shaped panels, the check should be performed for the individual portions of the panel or for the panel in its entirety.

In order to avoid that the brittle failures or that the failure of connections involved in the box-like behaviour can anticipate the ductile failure mechanisms (e.g., failure of the corner joint before the failure of the hold down) it is considered to be necessary to prescribe the calculation of the overstrength factor Ω considering the “overall rocking” of the panel even in the case of door openings.

The formulation included in the current draft revision of Eurocode 8 for calculating the rocking capacity (Eq.18) is not suitable for describing the case of overall rocking of walls with door-type openings resulting significantly overestimated (Figure 8). A new formulation suitable for both cases of intact panel and panel perforated by door and window openings is proposed (Eq.19). Eq.19 descends from the equilibrium equation Eq.4 by assuming the FEM derived expression for τ (Eq. 16), using the same symbols as in the Eurocode 8 draft and assuming $B_{\mathrm{N,CLT,i,j}} = B_{\mathrm{CLT,i,j}} - c_{\mathrm{hd}}$.

$$M_{\mathrm{Rd,rock,i,j}} = F_{\mathrm{Rd,hd,i,j}}\left(\frac{B_{\mathrm{CLT,i,j}}}{2} - c_{\mathrm{hd}}\right) + \frac{N_{\mathrm{Ed,i,j}}+F_{\mathrm{Rd,hd,i,j}}}{2}\left(B_{\mathrm{CLT,i,j}} - \frac{N_{\mathrm{Ed,i,j}}+F_{\mathrm{Rd,hd,i,j}}}{f_{\mathrm{c,eff,CLT.i,j}}\, t_{\mathrm{eff,CLT.i,j}}}\right) \tag{18}$$

$$M_{\mathrm{Rd,rock,i,j}} = N_{\mathrm{Ed,i,j}}\left(c_{\mathrm{hd}} - \frac{B_{\mathrm{CLT,i,j}}}{2}\right) + B_{\mathrm{N,CLT,i,j}}\left(N_{\mathrm{Ed,i,j}} + F_{\mathrm{Rd,hd,i,j}}\right)\left(1 + \frac{B_{\mathrm{D,i,j}}}{7\,B_{\mathrm{CLT,i,j}}} + \frac{F_{\mathrm{Rd,hd,i,j}}}{2(N_{\mathrm{Ed,i,j}} - (B_{\mathrm{N,CLT,i,j}} - B_{\mathrm{D,i,j}}) f_{\mathrm{c,eff,CLT.i,j}}\, t_{\mathrm{eff,CLT.i,j}})}\right) \tag{19}$$

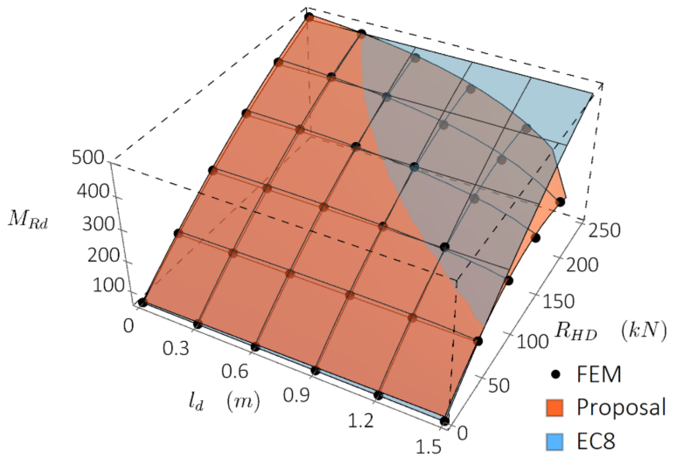

Figure 8. Design rocking strength as a function of the door opening length and hold-down strength. Proposal vs current formula (overall rocking).

5 References

Franco, L., Pozza, L., Saetta, A., Savoia, M., & Talledo, D. (2019). Strategies for structural modelling of CLT panels under cyclic loading conditions. Engineering Structures, 198, 109476.

Tomasi, R. (2014). CLT course at FPS COST Action FP1004–Enhance mechanical properties of timber, engineered wood products and timber structures. *CLT Training School, University of Trento. (2014 April 15-17).*

Wallner-Novak, M., Koppelhuber, J., & Pock, K. (2013). Brettsperrholz Bemessung: Grundlagen für Statik und Konstruktion nach Eurocode: Informationen für die Berechnung und konstruktive Gestaltung von Holztragwerken. ProHolz Austria.

Harris, R., & van de Kuilen, J. W. (2016). Enhance mechanical properties of timber, engineered wood products and timber structures. Special Issue based upon work from COST Action FP1004, supported by COST (European Cooperation in Science and Technology). European Journal of Wood and Wood Products, 74(3), 281-283.

Pei, S., van de Lindt, J. W., & Popovski, M. (2013). Approximate R-Factor for Cross-Laminated Timber Walls in Multistory Buildings. Journal of Architectural Engineering, 19(4), 245–255.

Reynolds, T., Foster, R., Bregulla, J., Chang, W. S., Harris, R., & Ramage, M. (2017). Lateral-load resistance of cross-laminated timber shear walls.

Gavric I, Popovski M. (2014). Design models for CLT shearwalls and assemblies based on connection properties. In: Proceedings of international network on timber engineering research, INTER/47-15-4. 2014.

Reynolds, T., Foster, R. M., Bregulla, J., Chang, W., Harris, R., & Ramage, M. (2017). Lateral Load Resistance of Cross-laminated Timber Shear Walls. Journal of Structural Engineering-Asce, 143, 6017006.

Aloisio, A., Boggian, F., Tomasi, R., & Fragiacomo, M. (2021). The role of the hold-down in the capacity model of LTF and CLT shear walls based on the experimental lateral response. Construction and Building Materials, 289, 123046.

Dujic, B., Klobcar, S., & Zarnic, R. (2007). Influence of openings on shear capacity of wooden walls. 40th CIB-W18 Meeting, Bled, Slovenia. Paper 40-15-6.

Dujic B, Klobcar S, Zarnic R. (2008). Shear capacity of cross-laminated wooden walls. Proceedings of the 10th world conference on timber engineering, Miyazaki, Japan.

Awad, V., Giresini, L., Koshihara, M., Puppio, M. L., & Sassu, M. (2017). Experimental analyses and numerical models of CLT shear walls under cyclic loading. Wood in Civil Engineering, 223.

Serrano, E., & Enquist, B. (2010). Compression strength perpendicular to grain in cross-laminated timber (CLT). In WCTE2010.

Eurocode 8 draft (2022): Design of structures for earthquake resistance — Part 1-2: Buildings. CEN.

Brandner, R., Dietsch, P., Dröscher, J., Schulte-Wrede, M., Kreuzinger, H., & Sieder, M. (2017). Cross laminated timber (CLT) diaphragms under shear: Test configuration, properties and design. Construction and Building Materials, 147, 312–327.

Bogensperger T, Moosbrugger T, Silly G. Verification of CLT-plates under loads in plane. In: World conference on timber engineering. 2010, p. 1–9, 11th World Conference on Timber Engineering, WCTE 2010; Conference date: 20-06-2010 Through 24-06-2010.

Brandner, R., Dietsch, P., Dröscher, J., Schulte-Wrede, M., Kreuzinger, H., & Sieder, M. (2017). Cross laminated timber (CLT) diaphragms under shear: Test configuration, properties and design. Construction and Building Materials, 147, 312–327.

Tannert, T., & Loss, C. (2022). Contemporary and Novel Hold-Down Solutions for Mass Timber Shear Walls. Buildings, 12(2), 1–14.

DISCUSSION

The paper was presented by Y De Santis

G Hochreiner and Y De Santis discussed limitations of the model which considers central openings only.

G Doudak received clarification that the existing EC model does not account for openings and the model under discussion considers in-plane deformability of the panel and stress block. G Doudak said the two rocking behaviours are dependent on λ and asked what about the hold-down connection stiffness versus the lintel stiffness. De Santis agreed that this is a parameter that has an influence.

D Casagrande and D Santis discussed how to find the lever arm and how to account for other failure modes based on capacity-based design concept.

A Frangi commented that one tries to avoid compression perpendicular to grain stresses in tall buildings with continuous walls and how to account for this as well as for connected walls. J De Santis said that wall on concrete foundation cases would work for continuous walls. In connected walls, the stiffness of the connection is considered more.

W Seim received confirmation that the panel and lintel were assumed strong enough and did not check for their failures.

T Demschner asked about testing for validation. De Santis said testing with openings was not done. T Demschner commented cutting of the openings would be an issue in practice.

A Polastri commented that stiffness of the hold-down is an important parameter.

P Dietsch questioned the stress block assumptions. De Santis said that his FEM model confirmed them.

S Schwendner and De Santis discussed the impact of the vertical load.

Capacity-based design of CLT shear walls with hyperelastic hold downs

Thomas Tannert, School of Engineering, University of Northern British Columbia, Prince George, Canada, thomas.tannert@unbc.ca

Oyawoye Abubakar Ajibola, School of Engineering, University of Northern British Columbia, Prince George, Canada, oyawoye@unbc.ca

Marjan Popovski, Building Systems, FPInnovations, Vancouver, Canada, marjan.popovski@fpinnovations.ca

Keywords: Cross-laminated timber, Seismic load-resisting system, Canadian design provisions, Experimental investigation

1 Introduction

1.1 Cross-laminated timber shear walls

Mass timber products offer better fire protection, homogeneity, dimensional stability, and load resistance than traditional lumber products [Harte, 2017]. As such, significant efforts have been made lately to expand their use in North America. Mass timber products, as part of encapsulated mass timber construction were incorporated into the National Building Code of Canada [NBCC, 2020] for buildings up to 12 stories and in some construction types the International Building Code [IBC, 2021] for buildings up to 18 stories. Cross-laminated timber (CLT), consisting of sawn lumber elements glued together in alternating directions [Brandner et al., 2016], with its high in-plane strength and stiffness in both principal axes, is increasingly being used for lateral force-resisting systems such as shear walls [Tannert et al., 2018; Izzi et al., 2018].

CLT shear walls can be used in either platform construction, where each floor acts as a platform for the floor above, or in balloon construction, where walls continue over several floors [Shahnewaz et al., 2021]. In platform-type structures, see Figure 1, the walls transfer the lateral forces to the story underneath or the foundation via shear connections (often angle brackets). Hold-downs (HDs) are required to resist the uplift forces and transfer them through a continuous load path to the foundation.

Most previous research focused on platform-type CLT shear walls, e.g. by Popovski et al. [2010; 2012]. The findings from this research can be summarized as that: i) shear wall strength, stiffness, ductility, and energy dissipation are governed by its connections; ii) rocking kinematic motion is preferred to dissipate the energy; and iii) the CLT wall panel deformation is most often negligible under in-plane lateral loading. Specifically with regard to moderately ductile platform type CLT structures, it has been shown that the non-linear deformations and energy dissipation occur exclusively in the following connections: a) wall-to-foundation or wall-to-floor panels below (connection 5 in Figure 1); b) vertical joints between the wall panels (connection 4 in Figure 1); and c) discrete HDs, when designed for energy dissipation.

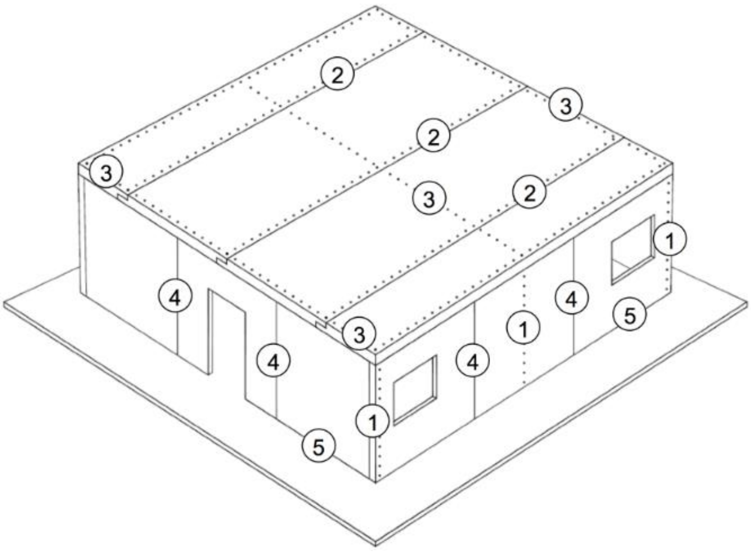

Figure 1: Connections in typical platform-type CLT construction (schematic courtesy of CWC)

1.2 Canadian Design Provisions for CLT shear walls

In Canada, the National Building Code [NBCC 2020] refers to the Canadian Standard for Engineering Design in Wood [CSA O86, 2019] for detailing provisions intended to ensure that rocking is the energy dissipative kinematic mechanism. Seismic design provisions for CLT shear walls in platform-type applications were first introduced in the update No. 1 to the 2014 edition of CSA O86 [2016]. The standard required that CLT structures in seismic zones must be designed using capacity design principles with at least moderately ductile connections for energy dissipation at specified locations, while all other connections must be non-dissipative with sufficient overstrength. Non-linear deformations were permitted in discontinuous HDs (discrete HDs in each storey), while if continuous steel rods are used along the height of the building as HD, they have to remain linear elastic. The yielding hierarchy should consist of the vertical joints between the wall panels (connection 4 in Figure 1) yielding first or at the same time with the connections connecting the walls to the foundation or the floor panels underneath working in uplift (connection 5 in Figure 1). Continuous steel rods are required to remain elastic at all times but still allow the assumed rigid body motion (rotation, sliding, or both) to occur.

Discrete HDs were allowed to be energy dissipative connections and they could be connected to the HDs on the floor above or below using a steel rod. This provision aligned with most of published literature on HD design and also with the proposed Eurocode 8, which regards HDs as dissipative connections [Follesa et al., 2018]. Since experimental tests on CLT shearwalls with brackets with small diameter fasteners, such as nails or wood screws [e.g. Popovski et al., 2010], showed that they contribute to resistance in the vertical (uplift) direction as well, the angle brackets were allowed to resist both shear and uplift forces, and consideration of the shear-uplift interaction of load carrying capacity of the brackets was required using a circular domain in the CSA O86 [2016] provisions.

The design provisions for CLT shear walls were significantly modified in the current CSA O86 [2019]. Changes resulted from the acceptance of CLT as a seismic force resisting system in the 2020 NBCC with ductility-related seismic force modification factor R_d=2.0 and overstrength-based factor of R_O=1.5. Sliding of the shear connections was taken out as a possible kinematic mode, due to concerns that such a mode may result in a portion of the building sliding at certain levels during the seismic response. This also excluded the need for shear-uplift interaction when assessing the resistance of shear connections.

Some of the important changes in the 2019 CSA O86 related to the connections include: i) The factored resistance of discrete HDs shall be at least 20% greater than the forces developed in them when the connections between CLT segments reach their nominal resistance; ii) Continuous steel rods used as HDs to be anchored at each floor level and designed to remain elastic while allowing for the expected uplift due to overturning of the shearwalls; and iii) Energy dissipative connection shall be designed to ensure that all principle inelastic deformations and all principle energy dissipation occurs in: a) connections between vertical joints of adjacent shearwall segments; and b) shear connections of shearwalls to foundations or floors underneath, in uplift only. While no definitions are provided for ‘principle inelastic deformations and principle energy dissipation’, HDs have to be interpreted as capacity-protected non-dissipative connections which shall remain elastic. These changes basically eliminated HDs from being considered for yielding and energy dissipation in uplift. This was done to satisfy concerns of the NBCC Standing Committee on Earthquake Design that a yielding HD may not provide satisfactory uplift load transfer along the height of the building during the seismic response.

1.3 Contemporary and hyperelastic hold downs

Conventional light-frame wood connections include HDs and angle brackets fastened to CLT panels with dowel-type fasteners [Shen et al., 2013; Gavric et al., 2015; Popovski et al. 2016]. Such connections are often not suitable for tall mass-timber buildings in high seismic areas for their capacity limitations, and their failure modes which include local damage to the CLT. To overcome these limitations, several low-damage HDs have been investigated, such as post-tensioned connections [Pei et al., 2019], friction-based connections [Hashemi et al., 2020], glued-in steel plates [Zhang et al., 2018], and internal-perforated steel plates [Dege and Tannert, 2022]. For an overview on contemporary HD solutions for mass timber shear walls, please see Tannert and Loss [2022].

To comply with the changed Canadian design provisions [CSA O86, 2019], there was a need to develop HDs with high load-carrying and deformation capacities while remaining elastic. A material with such properties is a hyperelastic rubber. The components of the HD include the elastomeric bearing layers, steel plates, and a steel rod with nuts, as illustrated in Figure 2. The structural performance of internal-bearing hyperelastic HDs for CLT shear walls, studied by Asgari et al. [2021], showed that the rubber pad's effective compressive mechanical properties are a function of its shape factor, *SF*, and –to a small extent– the loading speed. Ductile HD failure can be achieved as long as the steel rod is the weakest link in the setup; however, all other members must be capacity protected to avoid brittle failure.

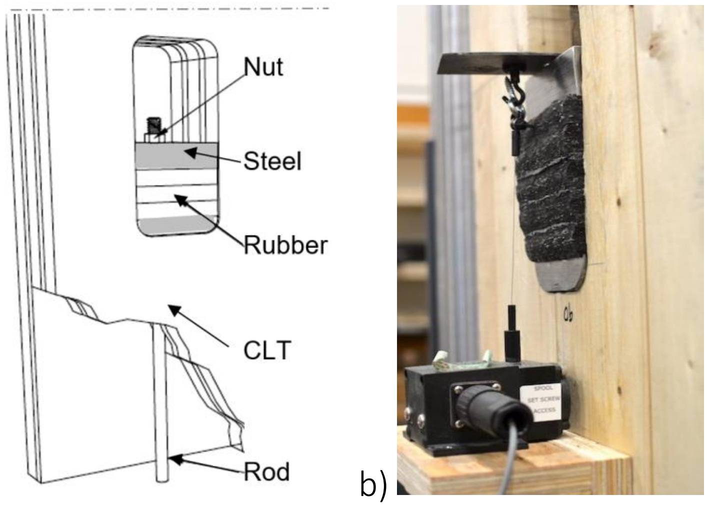

a) b)

Figure 2: Hyperelastic hold-down: a) schematic of main components, b) photo

1.4 Objectives

The objective of the research presented herein was to develop a HD with elastomeric bearings that is able to provide the required uplift for CLT shear walls, so that the CLT panels are able to develop the needed rocking behaviour, without strength and stiffness degradation. To achieve this objective, experimental investigations were conducted at the University of Northern British Columbia Wood Innovation Research Laboratory to provide the required input data for a capacity-based design procedure for CLT shear walls with hyperelastic HDs. First, the yield strength of the steel rods was verified, and the brittle resistance of CLT panels with openings placed at different edge and end distances was determined. Then, the stiffness and strength of surface-mounted screwed spline joints, and the performance of the hyperelastic HDs with different sizes of rubber pads were investigated at the component level. Finally, full-scale CLT shear walls with hyperelastic HDs were tested under reversed cyclic loading. Based on the results of the investigations presented herein, a capacity-design procedure for the hyper-elastic hold-downs was proposed.

2 Experimental investigations

2.1 Materials

The rubber pads were Masticord™, a composite consisting of an elastomer with random-oriented synthetic fibres, with a compressive strength of 55.2 MPa and initial crack strain of 40%. Rubber pads 90 x 140 mm and 140 x 140 mm with different thickness, specifically 1-5 layers of 25.4 mm, were produced. An example of such pad is shown in Figure 3a. The steel rods were ASTM A193 grade B7 with a diameter of 19.1 mm. Their mean yield and ultimate load-carrying capacities, determined on six samples, were 167 kN and 190 kN, respectively, with the coefficients of variation (CoV) smaller than 3%.

The CLT panels were 5-ply 139 mm thick (35+17+35+17+35), strength grade V2 according to CSA O86 [2019]. The average moisture content and apparent density of the CLT were 10.6% and 486 kg/m^3, respectively. It was shown [Asgari et al., 2022], that the block tear-out resistance of CLT panels with a single large-diameter connector (an example of such failed specimen is shown in Figure 3c), can be conservatively determined considering the lesser of the resistance between the rolling shear failure plane along the glue-lines between layers, Equation (1), and the tension parallel to the grain failure plane in the layers parallel to the load, Equation (2):

$$R_{w,I} = f_s \cdot 2 \cdot n_s \cdot a_c \cdot a_1 \qquad (1)$$

$$R_{w,II} = f_t \cdot 2 \cdot a_c \cdot t_t \qquad (2)$$

where f_s is the rolling shear strength, n_s is the number of shear planes between CLT layers, a_c is the edge distance, a_1 is the loaded end distance, f_t is the rolling shear strength, and t_t is the total thickness of all CLT layers parallel to the load.

The custom-made bearing-plates for the HD assembly and shear keys for the full-scale tests were of CSA-G420.21 grade 44W/300W. Finally, the splines for the panel-to-panel shear connection were made of 25.4 mm thick D-fir plywood; these were attached with ø8×100 mm partially threaded self-tapping screws, see Figure 3d. Their strength and stiffness as a function of the number of screws was determined on 12 samples.

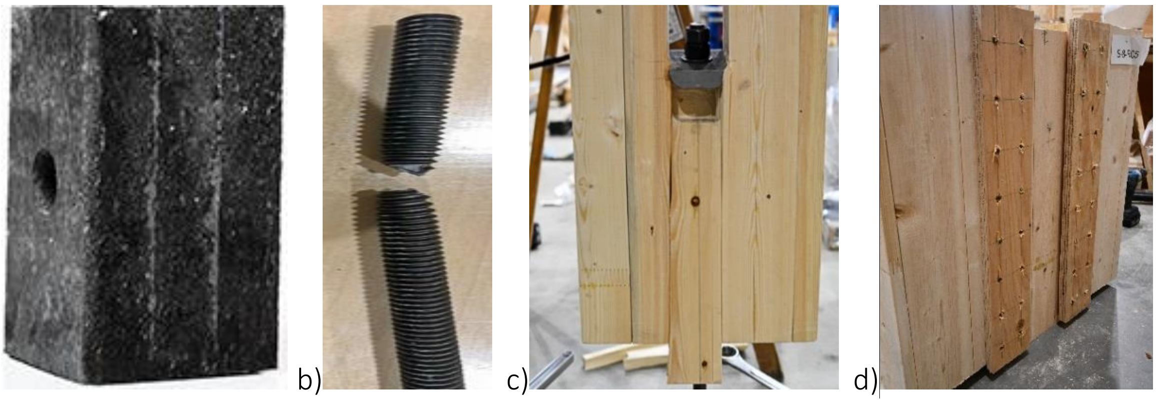

a) b) c) d)

Figure 3: Materials used for testing: a) elastomeric rubber pads; b) steel rod failure in tension; c) failure of a CLT panel with a single large fastener; d) tested spline joint

2.2 Component-level HD tests

Component-level tests were conducted to study the impact of three parameters on the HD performance: 1) the rubber pad width (90 mm and 140 mm); 2) the rubber pad thickness (1-5 layers of each 25.4 mm); and 3) the loading rate (10 mm/min; 50 mm/min, and 250 mm/min). The legend in Figure 4a directly relates to these parameters. The pads were restricted from bulging in the direction of the wall by the sides from the CLT opening. The rubber pad was inserted into a rectangular opening in the CLT panel with rounded corners to reduce stress concentrations. A 25.4 mm hole was drilled through the centre of each panel, linking the panel end with the opening to allow installation of the steel rod, see Figure 2. Tension load was applied to the steel rods using a universal testing machine at up to a target load of 120kN, chosen to ensure that the steel rod remained elastic throughout the test. All tests were repeated three times. The relative uplift of the rubber pads was recorded on both sides of the assembly by using two Linear Variable Differential Transformers (LVDTs). The curves in Figure 4a represent the average measurements of the two LVDT of the HD assemblies with the 90 mm wide rubber pads.

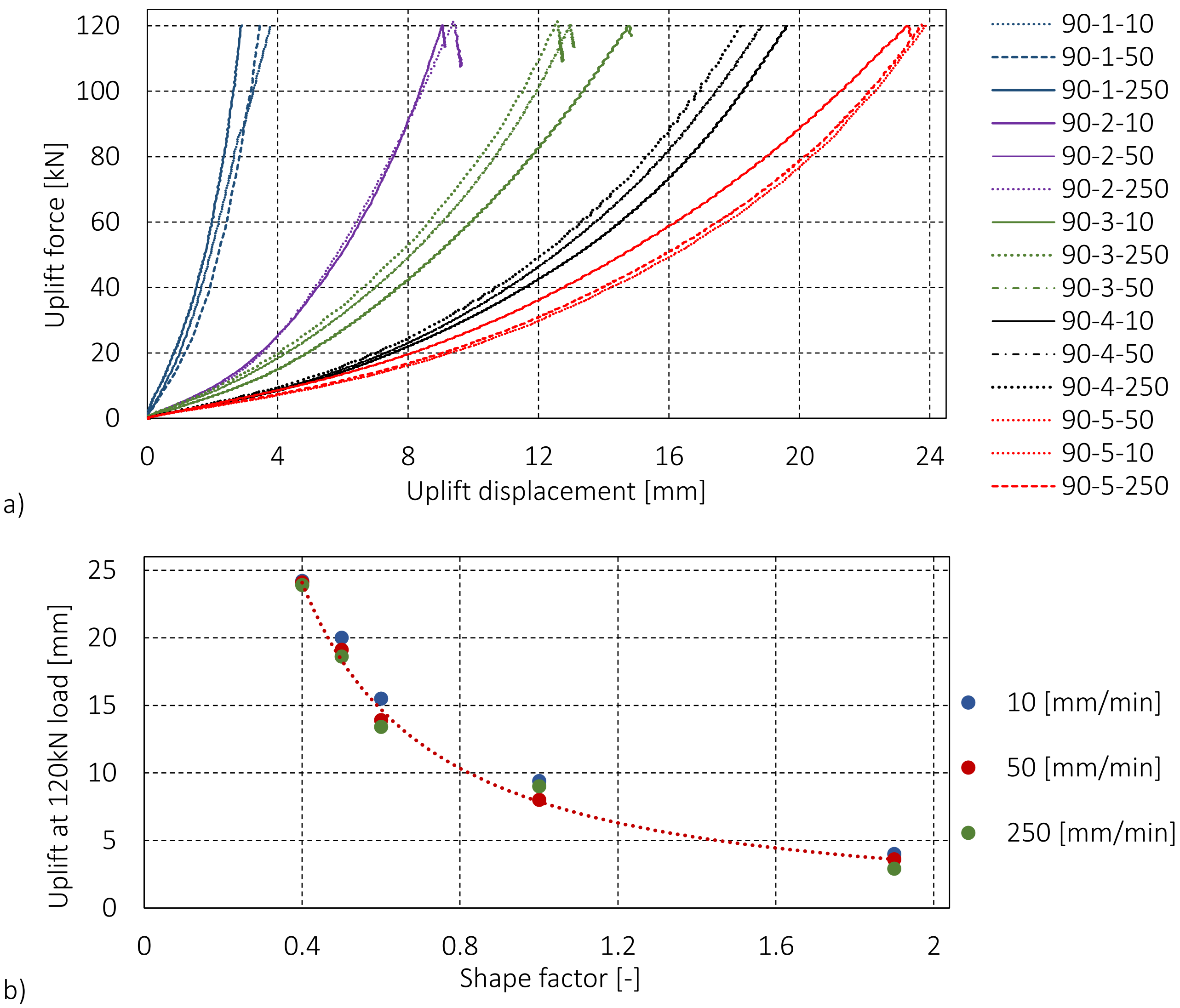

Figure 4: Component-level results of HD assemblies with 90 mm wide rubber pads: a) Load-uplift deformation; b) uplift deformation at 120 kN target load as function of shape factor and rate of loading

The load-displacement behaviour of the HD assemblies under quasi-static monotonic loading was non-linear hyperelastic with increasing stiffness at increasing deformations. The displacements curves followed a similar trend and were a function of the rubber thickness and the rubber loaded area. These parameters define the shape factor, *SF*, which, accounting for the hole at the centre of the rubber and the two constrained sides, can be computed using equation (3):

$$SF = [d_R \cdot w_R - \pi \cdot \varphi^2/4] / 2 \cdot w_R \cdot t_R \quad (3)$$

where, d_R, w_R, and t_R, are the rubber pad depth, width, and thickness, respectively, and φ is the diameter of the centric hole.

As illustrated in Figure 4b, HD assemblies with smaller *SF* reached the largest displacements, while the impact of the rate of loading was minimal.

2.3 Full-scale shear wall tests

The component level tests were used to design a full-scale coupled CLT shear wall with hyperelastic HDs. Herein, an interstorey drift target for seismic design was set to reach at least 3.5%, exceeding the 2.5% limit according to NBCC [2020]. In the tests, 3.0 m tall and 1.0 m wide CLT panels for an aspect ratio of 3:1 were used. For a lateral target displacement of 105 mm; considering a panel width of 1 m, and accounting for some CLT compression, the uplift at the panel corner is approx. 32 mm, and the target elastic uplift displacement at the HD location is approx. 25 mm.

The desired kinematic behavior of CLT shear walls was coupled-wall rocking, as shown in Figure 5a, assured by the capacity-protected shear key connectors, presented in Figure 5b, that prevented wall sliding without adding uplift resistance at target displacements. The shear keys, that resisted the in-plane shear force, were mounted at the midpoint of each CLT panel, and used elliptical holes to decouple the shear from the uplift resistance. The vertical panel-to-panel connection was designed to yield, while the CLT panels and the shear key were capacity-protected.

a) 

b) 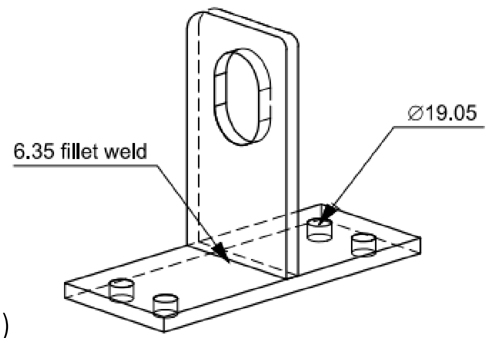

Figure 5: Full-scale shear wall tests: a) couples wall rocking kinematics; b) shear key details

The lateral load was applied at the top of the left panel using a 250 kN actuator; a constant vertical load of 10 kN/m was applied, representing a moderately loaded wall. The monotonic tests were conducted at 25 mm/min until the wall resistance dropped to below 80% of the applied maximum force F_{max}. The reversed cyclic tests followed the CUREE loading protocol [ASTM E2126, 2019]. The horizontal, vertical, and relative panel displacements were recorded with a total of 8 LVDTs and string potentiometers.

Full-scale shear wall tests were conducted varying the following parameters: i) two rubber pad widths (90 mm and 140 mm); ii) three rubber pad thicknesses (3, 4 and 5 layers of 25.4 mm); and iii) stiffness of the vertical panel to panel joint (15 and 21 screws per shear plane for walls with 90 mm wide rubber pads; 12 and 24 screws per shear plane for the walls with 140 mm wide rubber pads). Herein, only the total lateral displacement and panel uplift of selected shear walls with 90 mm rubber pads is presented in Figures 6 and 7, respectively, with the labels corresponding to the three varied parameters.

The panels went through coupled-panel kinematic, exhibiting a clear centre of rotation at the toe of each panel, as shown in Figure 5a. The load-displacement behaviours, illustrated in the plots of Figures 6 and 7, were a function of the spline stiffness and the rubber pad thickness. Thicker rubber pads (5 layers vs. 3 layers) exhibited lower stiffness and therefore provided larger displacement capacity. A higher number of screws (21 vs. 15) proportionally increased the shear wall strength but had no impact on stiffness.

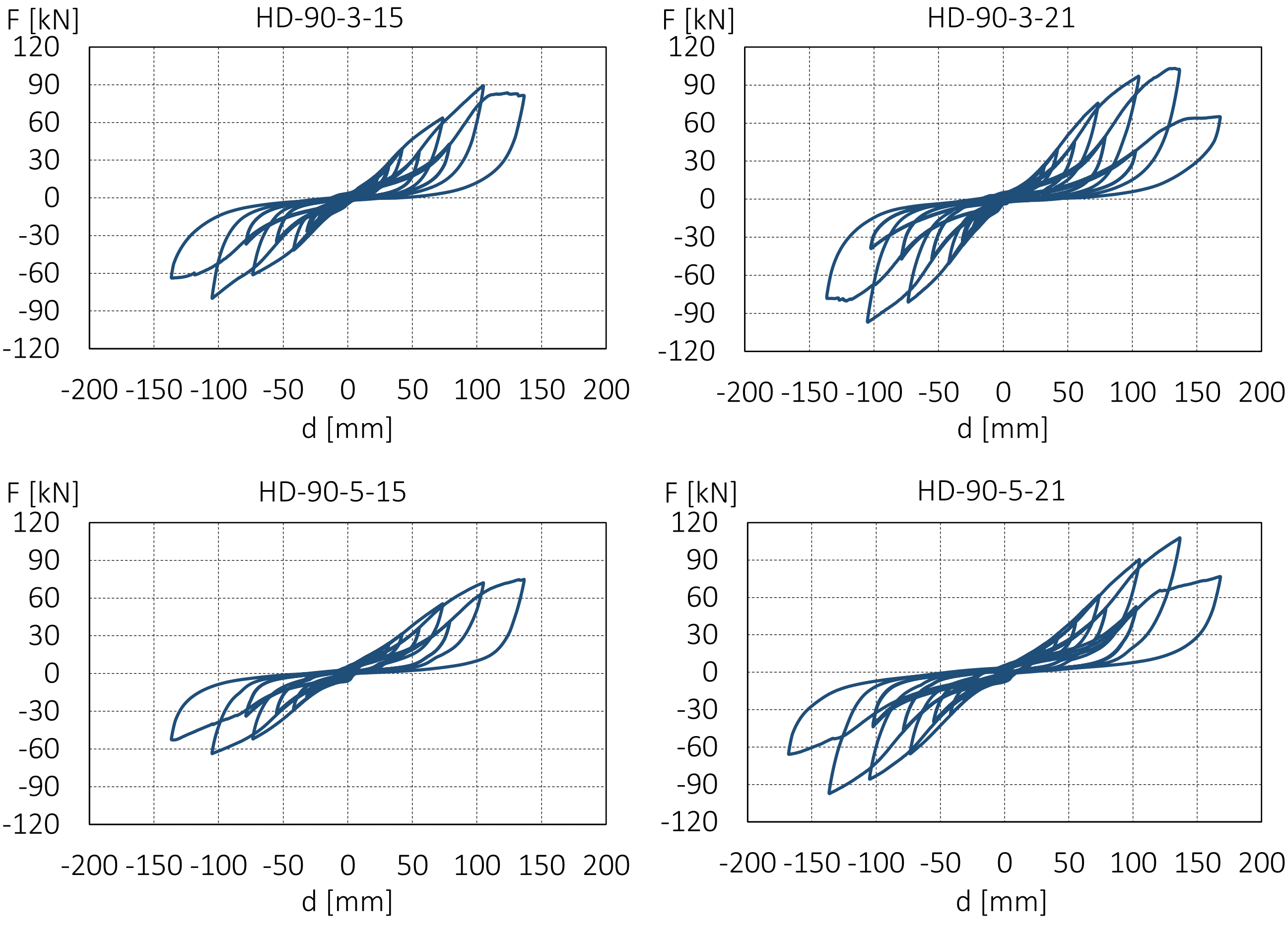

Figure 6: Typical reversed cyclic load-displacement curves of CLT shear walls with hyper-elastic HDs

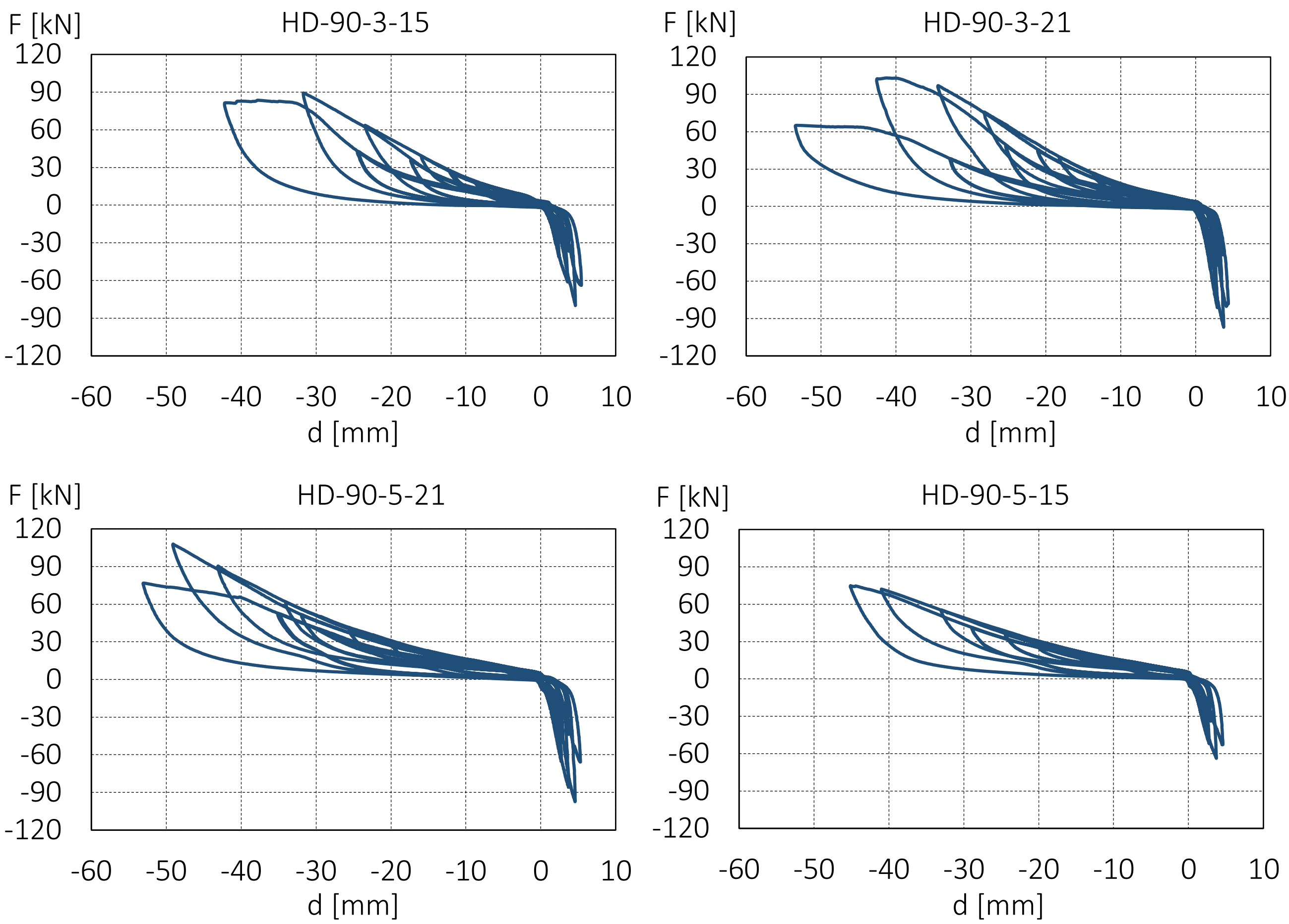

Figure 7: Typical reversed cyclic load-HD uplift curves of CLT shear walls with hyper-elastic HDs

Failure was characterized first by yielding of the screws in the panel-to-panel shear connection, and then subsequent yielding of the steel rods in the HDs, as shown in Figure 8a and 8b. The CLT panels remained damage-free and were re-used for multiple tests without any visual degradation, providing a resilient shear wall solution where after an earthquake only the steel rods and surface-splines must be replaced. The photo in Figure 8c shows a panel after seven tests; this was facilitated by re-tightening the steel rods and off-setting the screw-pattern in the splines.

a) b) c)

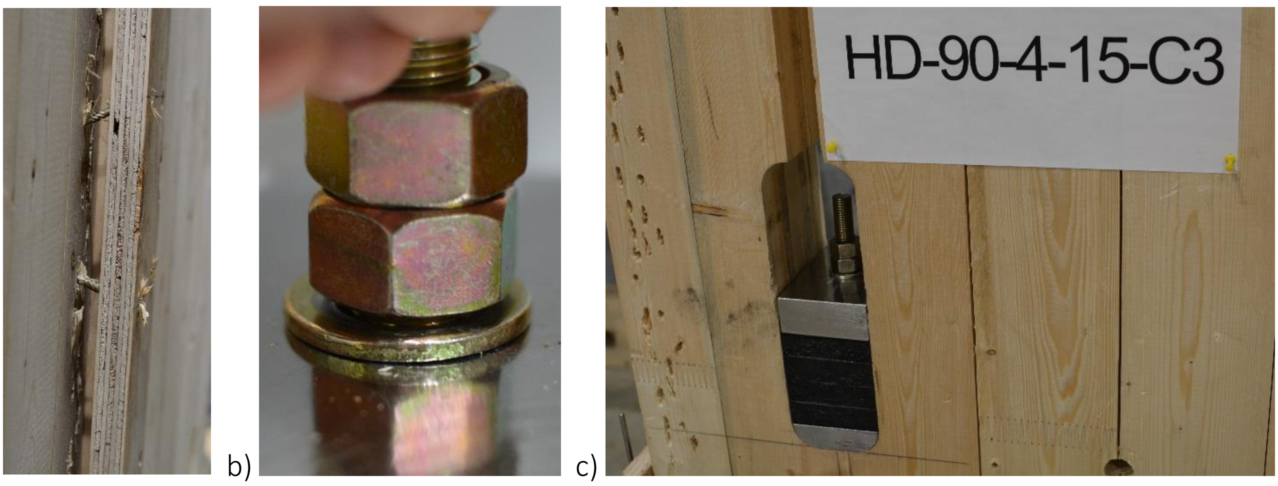

Figure 8: a) failure in spline; b) elongated steel rod; c) damage-free CLT panel after multiple tests

2.4 Capacity-based design procedure

The primary objective of the research presented herein was to develop a capacity-based design procedure for CLT shear walls with hyperelastic HDs. Secondary objectives consisted of the mechanical characterisation of the hyperelastic material as a function of its shape factor, and the determination of minimum edge and end distances for the HD to avoid brittle failure in the CLT.

Herein, two levels of capacity-protection are suggested, see Figure 9. The first level avoids failure of the CLT and prevents the rubber pad from exceeding its ultimate strain capacity of 40%. This can be achieved by ensuring sufficient margin between the peak load of the steel rod F_{peak}, the failure load of the CLT panel $F_{U,CLT}$ and the rubber pad $F_{U,rubber}$. The second level of protection applies an overstrength factor of 1.3 to ensure that the hold-down remain elastic throughout the experiment.

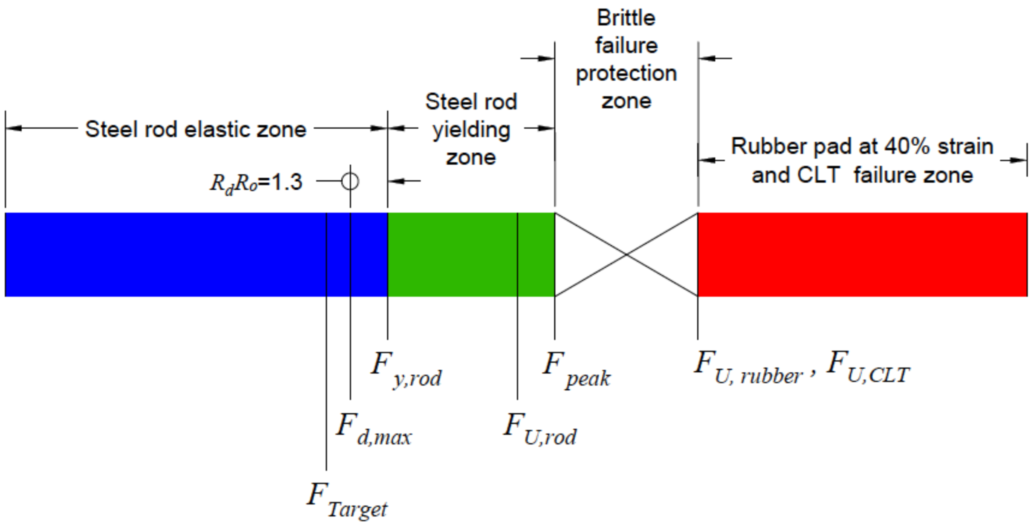

Figure 9: Capacity-based design principle for couples CLT shear walls with hyper-elastic HDs

3 Conclusions

The component level hold-down tests and full-scale tests of shear walls with hold-downs demonstrated that: i) the HDs can remain elastic under rocking kinematics provided that the elastic limit of the steel rod is not exceeded; ii) increasing the rubber pad thickness reduces the HD stiffness; iii) increasing the rubber pad width increases the HD stiffness; iv) failure of the rod is the subsequent desired ductile mode; v) sufficient CLT width can prevent undesired brittle CLT failure before steel yielding; and vi) the shear wall strength and stiffness for selected target displacements is a function of rubber shape factor and the panel-to-panel shear connection properties.

The proposed hyperelastic HD assembly provides design engineers with a low-damage and resilient alternative to contemporary HD solutions to meet the current Canadian design provisions for platform-type CLT shearwalls that require HDs to remain elastic. Further research will investigate the performance of the hyperelastic HD assembly in multi-storey platform construction.

Acknowledgements

The research was funded by the Government of British Columbia through a BC Innovate Ignite grant, a Forest Innovation Investment Wood First grant, and a BC Leadership Chair. The support by the UNBC lab technicians James Andal, Michael Billups and Ryan Stern is greatly appreciated. Materials were provided by Structurlam Mass Timber Corporation (CLT) and JVI Inc. (elastomeric bearing pads).

References

Asgari H, Tannert T, Ebadi MM, Loss C, Popovski P (2021) Hyperelastic hold-down solution for CLT shear walls. Const. Build. Mat. 289: 123173

Asgari H, Tannert T, Loss C (2022) Block tear-out resistance of CLT panels with single large-diameter connectors. Eur. J. Wood Prod. 80: 805–816

ASTM E2126 (2019) Standard test methods for cyclic (reversed) load test for shear resistance of vertical elements of the lateral force resisting systems for buildings, American Society for Testing and Materials (ASTM), West Conshohocken, PA.

Brandner R, Flatscher G, et al. (2016) Cross laminated timber (CLT): overview and development. Eur. J. Wood Prod. 74: 331-335.

CSA O86 (2016) Canadian Standard Engineering Design in Wood, Update No.1 2016. Canadian Standards Association, Mississauga, Canada.

CSA O86 (2019) Canadian Standard Engineering Design in Wood, Canadian Standards Association, Mississauga, Canada.

Dires S, Tannert T (2022) CLT shear walls with internal perforated steel plates as shear connector and hold-down. Construction and Building Materials 346: 128389

Follesa M, Fragiacomo M, et al. (2018) The new provisions for the seismic design of timber buildings in Europe. Engineering Structures, 168: 736-747.

Gavric I, Fragiacomo M, Ceccotti A (2015) Cyclic behaviour of typical metal connectors for cross-laminated (CLT) structures. Materials and Structures, 48: 1841–1857.

Harte A (2017) Mass timber–the emergence of a modern construction material, J. of Struct. Integrity Maint. 2: 121-132.

Hashemi A, Bagheri H, et al. (2020) Enhanced seismic performance of timber structures using resilient connections: full-scale testing and design procedure, J. Struct. Eng. 146: 04020180.

International Code Council (ICC), International Building Code, International Code Council Inc., Falls Church, VA, 2021.

Izzi M, Polastri A, Fragiacomo M (2018) Investigating the hysteretic behaviour of cross-laminated timber wall systems due to connections. Journal of Structural Engineering, 144(4).

NBCC - National Building Code of Canada, National Research Council Canada, Ottawa, Canada, 2020.

Pei S, van de Lindt JW, et al. (2019) Experimental seismic response of a resilient 2-story mass-timber building with post-tensioned rocking walls, J. Struct. Eng. 145: 04019120.

Popovski M, Gavric I (2016) Performance of a 2-story CLT house subjected to lateral loads, J. Struct. Eng. 142, E4015006.

Popovski M, Karacabeyli E (2012) Seismic Behaviour of Cross-Laminated Timber Structures. In proc. 12th World Conference on Timber Engineering.

Popovski M, Schneider J, Schweinsteiger M (2010) Lateral Load Resistance of Cross-Laminated Wood Panels. In proc. of 11th World Conference on Timber Engineering.

Shahnewaz M, Dickof C, Tannert T (2021) Seismic Behavior of Balloon Frame CLT Shear Walls with Different Ledgers. J. Struct. Eng. 147: 04021137.

Shen YL, Schneider S J, et al. (2013) Hysteresis behavior of bracket connection in cross-laminated timber shear wall, Const. Build Mat. 48: 980-991.

Tannert T, Follesa M, et al. (2018) Seismic design of CLT buildings. Wood Fiber Science, 50: 3–26.

Tannert T, Loss C (2022) Contemporary and Novel Hold-Down Solutions for Mass Timber Shear Walls. Buildings 12: 202.

Zhang X, Popovski M, Tannert T (2018) High-capacity hold-down for mass-timber buildings, Const. Building Mater. 164: 688-703.

DISCUSSION

The paper was presented by T Tannert

F Lam asked about the strength degradation characteristics under repeated loading in relation to low damage claims. T Tannert said the strength degradation occurred primarily in the spline connection and yielding of the steel which could be improved by capacity-based design of these components.

P Dietsch said optimization of the spline connection is needed with more clear determination of their resistance. T Tannert agreed and said the use of plywood spline is easy for installation.

U Kuhlmann said the system is based on a sequence of failure and steel yielding is an over stress. T Tannert said yielding in the spline defines the capacity of the shear wall. Yielding of the steel rod would not be catastrophic. U Kuhlmann asked if aging tests of the rubber were done. T Tannert said the choice was bridge bearing rubber which should be quite safe.

H Blass asked where designers would get information on the spline capacity. T Tannert said the Canadian code requires information on mean and 95 percentile values of yielding of the connection. This however is not readily available to the designers and would need to be tested in house.

M Fragiacomo was surprised that Canadian structural design of LCT shear walls requires elastic performance of the hold-downs. T Tannert said leading companies come up with innovative solutions. The standardization committee based their decision on concrete wall design philosophy.

G Doudak asked how the spline joints contribute to energy dissipation when hold-downs do not dissipate energy.

T Tannert discussed the analogy that angle brackets can contribute in energy dissipation only in uplift and not in sliding, so shear keys with oval shaped slot are typically used now.

G Doudak said the original work on CLT shearwalls requires energy dissipation of the angle brackets and asked whether this system can meet the Rd Ro target. T Tannert said he does not know and will work on this.

W Seim asked if there was any time history analysis with strain rate consideration and asked about overall building performance. T Tannert said no strain rate consideration was done and the whole building performance is under consideration.

A Polastri questioned whether one can have this large uplift with this hold-down. T Tannert said inter-story drift of 5% was intended as limitation of the hold-down system. He acknowledged the floor will be lifted.

Influence of temperature resistance of bond lines on charring of glulam beams

Alar Just, Tallinn University of Technology, RISE Research institutes of Sweden

Simon Aicher, MPA University of Stuttgart

Jane Liise Nurk, Tallinn University of Technology

Maximillian Henning, MPA University of Stuttgart

Keywords: glulam, bond line integrity in fire, fire design, European Charring Model

1 Introduction

Adhesives state the essential prerequisite for the manufacture of large timber construction elements from rigidly bonded solid wood boards of growth and processing bound limited dimensions. In the first two decades after the invention of glulam up to the 1930s, adhesives based on natural organic substances like blood and proteins were used. Such adhesives can have high dry strength but are weak when water or temperature is applied. These adhesives were then replaced by synthetic ones, firstly in the early 1930s by (phenol)-resorcinol-formaldehyde (RF / PRF) adhesives and then by urea-formaldehyde (UF) adhesives. Numerous tests have shown that the boil water resistant duroplastic RF/PRF adhesives are very stable at high temperatures up to/beyond charring of wood (Dorn and Egner, 1967; Klippel 2014). Contrary hereto the UF adhesives later classified in Europe as type II adhesives have significantly reduced water resistance (e.g. Raknes (1997) and are less temperature stable and fire resistant although the latter was not communicated sufficiently. The RF-, PRF- and UF- adhesives were exclusively used up until the 1980s, when the presently existing timber standards for "cold" and fire design were being developed. From the 1980s onwards adhesives with various chemical compositions have been added to the market. Firstly the duroplastic melamine-urea-formaldehyde and pure melamine formaldehyde (MUF / MF) adhesives followed in the mid-90s by the moisture hardening one-component polyurethane (1C-PUR) adhesives, then followed by the emulsion-polymer isocyanate (EPI) adhesives. In order to speed up curing times, being of utmost high economic importance significant amounts of polyvinyl acetate (PVAc) has been added to the hardeners of MUF adhesives with drawbacks on temperature stability. Each of the developed adhesives has its advantages and disadvantages regarding strength, water and/or temperature resistance, application robustness and price.

According to EN 1995-1-2:2004, chapter 3.5, the behaviour of bond line in fire may not be considered explicitly if the bond line is made of phenol-formaldehyde and aminoplastic, Type I adhesives according to EN 301. Regarding the general principle that adhesives shall produce joints of such strength that the integrity of the bond is maintained in the assigned fire resistance period, a footnote hints at the point that some adhesives show softening considerably below the charring temperature of wood.

Contrary to the present fire design specifications the new Eurocode for fire design of timber structures (prEN 1995-1-2:2021) will contain different design scenarios and parameters depending on the behaviour of bond lines at elevated temperatures. Differences are made in charring rates of laminated wood products after charring has passed the bond line. Depending on the ability of the bond line to prevent the fall-off of the charred layer, the linear or step model for charring is applied. The latter model takes into account that the insulating and protecting char layer is missing, therefore enforcing an increased charring rate up to a newly developed char coal depth of 25 mm. The basic difference between the linear and the stepped design model is shown in Figure 1. A basic dilemma of the new approach to the fire resistance of bonded structural elements however is, that at present no commonly agreed testing and classification method for heat and fire resistance of structural wood adhesives exists in Europe. Contrary in North America standardized test methods and assessment procedures exist to address the stated problem.

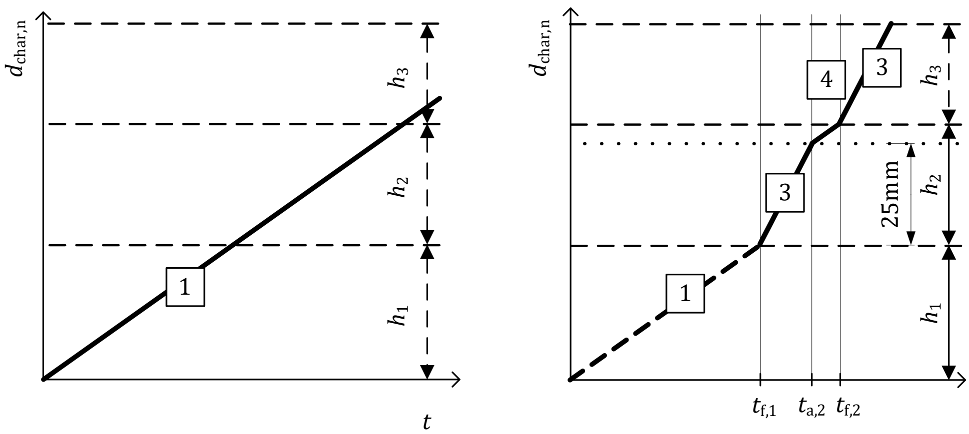

Figure 1. Linear (left) and step-model (right) for charring. Dashed lines represent the bondlines.

In order to close the mentioned knowledge gap, hereinafter reported research work has been performed jointly within the frame essentially in an ERA-Net Forest Value project FIRENWOOD by research partners RISE Sweden / Norway, Tallinn University of Technology, Materials Testing Institute of University Stuttgart and Technical University of Munich. The here presented research work and findings focus on testing and analysis of charring scenarios of glulam beams built up from boards with well-known properties (densities, MOE) and bond lines made of variety of different adhesives approved for structural applications.

2 Test beams

2.1 Adhesives and timber

Within the FIRENWOOD project 11 different adhesives consisting of four generically different adhesive families (PRF, MUF, PUR, EPI) were selected. All employed adhesives are presently positively tested with regard to their relevant performance standards and are acknowledged for structural bonding of glulam (GLT) at normal temperatures according to EN 14080. In the FIRENWOOD project these adhesives are tested in engineered wood applications at different small, meso and macro scales. Investigations on the adhesive dependent fire behaviour of glulam is part of the project, however funding related with a reduced number of adhesives. In order to comprise all adhesives in the GLT related fire investigations a complementary research project has been granted by the German Association of Glulam Manufactures (Studiengemeinschaft Holzleimbau, hereinafter called GA-GLT) with a special focus on polycondensation adhesives. Consequently, this paper reports on the combined FIRENWOOD and GA-GLT investigations and results.

The wood material was spruce (*Picea abies*) grown in southwestern Germany. The cross-sectional board dimensions were 250 mm by 40 mm before kiln drying and bonding. The length of the boards was about 5 m. All boards (about 11 m³) were strength graded at company Schwörerhaus to strength class T22. In this context modulus of elasticity (MOE) and density were assigned retrievable to the boards. Based on the density distribution of all boards ranging from 360 to 590 kg/m³ four density groups 1 to 4 with average density values (kg/m³) of 475, 462, 450 and 436 were established. For each group the density scatter was extremely low, denoted by a coefficient of variation (COV) < 1%.

2.2 Glulam beams – build-up and manufacture

All 11 adhesive brands were used to produce the glued-laminated timber (GLT) beams for this study. The cross-sectional widths and depths of the beams were chosen as 230 x 275 mm with regard to a principial achievement of 90 minutes fire resistance. In order to enable a best possible differentiation of the temperature / fire resistance of the different adhesives biased as little as possible from variation in the wood quality between the different beams a high effort was dedicated to achieve GLT build-ups with almost "identic" lamination material.

The build-up of the beams consisting of ten laminations was then performed in such manner that for all 11 GLT beams with a length of 5,5 m and throughout not finger jointed boards the outermost fire exposed lamination 1 was chosen from density group 1. Analogously, the next outer laminations 2 to 4 consisted of density groups 2 to 4 (see Figure 2). The laminations of a specific density group were assigned randomly to each of the manufactured beams. The mid-depth laminations 5 and 6 conformed to strength class T14 as not enough T22 laminations were available; the upper four laminations 7 to 10 were T22 again then taken from the distribution remnants. The described build-up procedure delivered 11 wood-wise very closely matching cross-sectional GLT beam lay-ups. The laminations of each of the beams were then face-bonded with a different adhesive. This was performed at GLT manufacturer Zischka, Böblingen, enabling this procedure by means of different equipment and different adhesive dependent application procedures. The cramping was performed in a hydraulic press with a pressure of 0.8 N/mm². After curing and planning the beams were cut lengthwise to segments of 2000 mm and 3000 mm. The shorter beams were then used for the reported fire tests whereas the longer ones are retained for additional loaded fire resistance tests. Between the adjacent end grain faces of the two beams several cross-sectional slices were taken, serving for delamination and shear tests.

2.3 GLT bond line strength and integrity prior to fire exposure

In order to avoid biased assessments of the bond behaviour obtained in the fire tests sufficient bond strength at ambient climate conditions and bond line integrity vs. water-induced shrinkage/swelling as well as vs. moderate temperate impacts (60°C) had to be assured. To this aim bond line shear strength tests as well as delamination tests were performed according to EN 14080 and related to the respective standard requirements.

In a brief summary it can be stated that the bond line shear tests revealed very high dry shear strengths denoted by an overall average of 9,21 ±1,41 N/mm^2. The delamination tests with method A of EN 14080, Annex C, delivered for the bond lines of the four highest fire exposed laminations 1 to 4 an average value for total delamination 2,9 %. So, the shear strength and delamination results exceeded the minimum requirements of EN 14080 well.

Further specific small scale tests developed within the frame of the FIRENWOOD project were performed and the results compared.

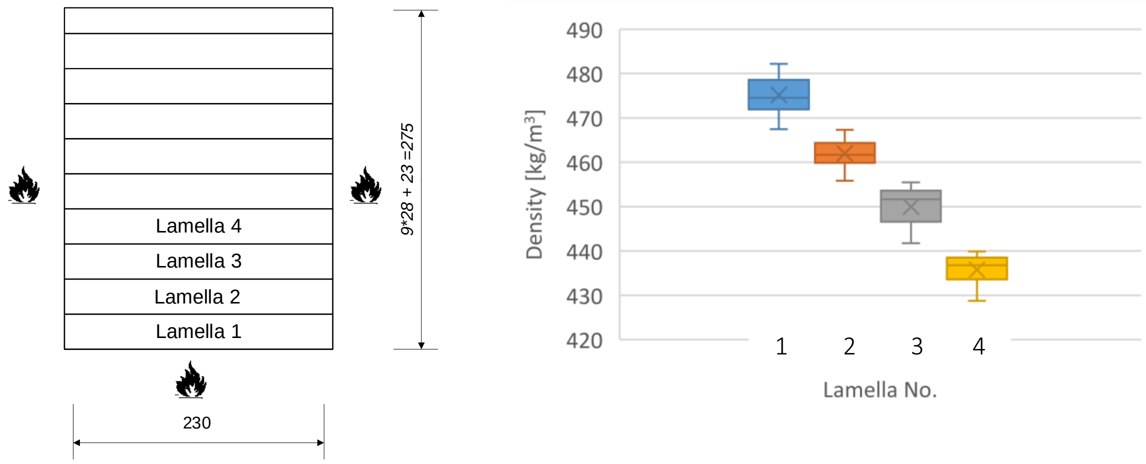

Figure 2. Cross-sectional build-up of manufactured glulam beams (left) and densities of the lamellae (right).

3 Fire tests

The main fire tests were performed in a model scale furnace of RISE Fire Research in Trondheim following the ISO 834 standard fire curve. Beams were exposed from three sides in order to assess the resistance to fire up to 90 minutes. Two beams were tested in each test (see Figure 4 and Figure 5). Mass loss of the beams was measured before and after the test.

Figure 3 shows two examples of temperatures measured in the furnace. The tests with beams with minimum (beam 2) and maximum (beam 4) charring are shown. The temperature curves follow ISO-834 curve very well. Influence of rapid increase of the temperature seen in the first minute is neglectable.

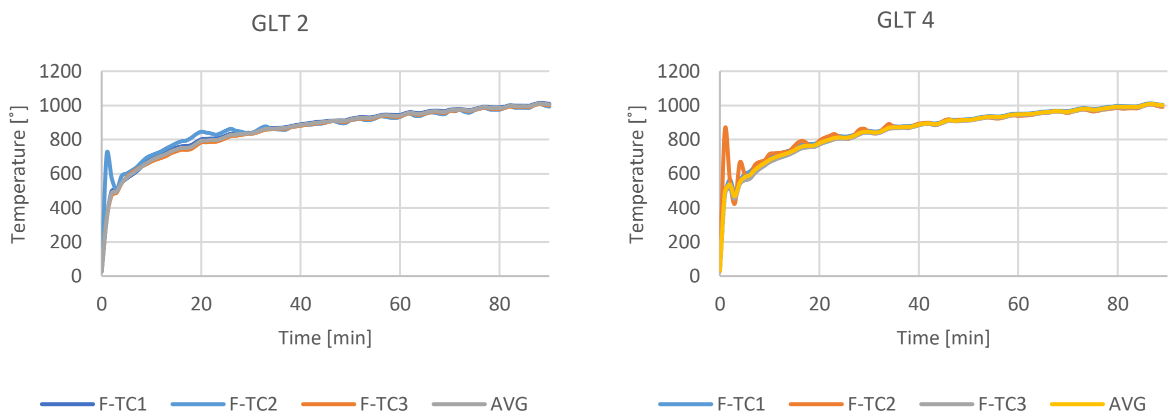

Figure 3. Furnace temperatures for beams 2 and 4.

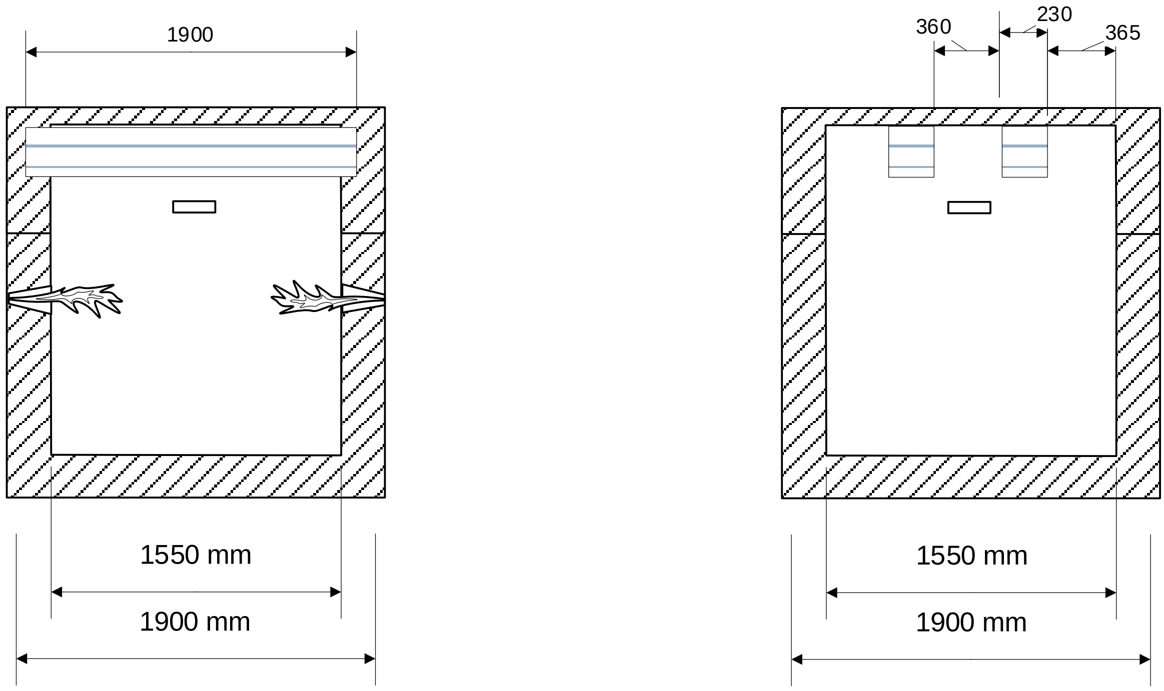

Figure 4. Fire test set-up for glulam beams in model scale furnace.

Figure 5. Fire tests. Beams placed on the furnace (left), beams lifted from the furnace (right).

At exactly 90 minutes the burners were switched off, the beams were removed from the furnace, weighed, and then extinguished. Time from switch off of burners until complete extinguishment did not exceed 2 minutes.

The charring scenario is quantified by measurements of the residual cross-sections of the beams.

4 Fire test results and discussion

The fire tests demonstrated that charring of glulam beams with similar properties of wooden lamellae have resulted with different charring depths for charring perpendicular to bond lines. The charring from the lateral sides, along the bond lines is similar to all the beams.

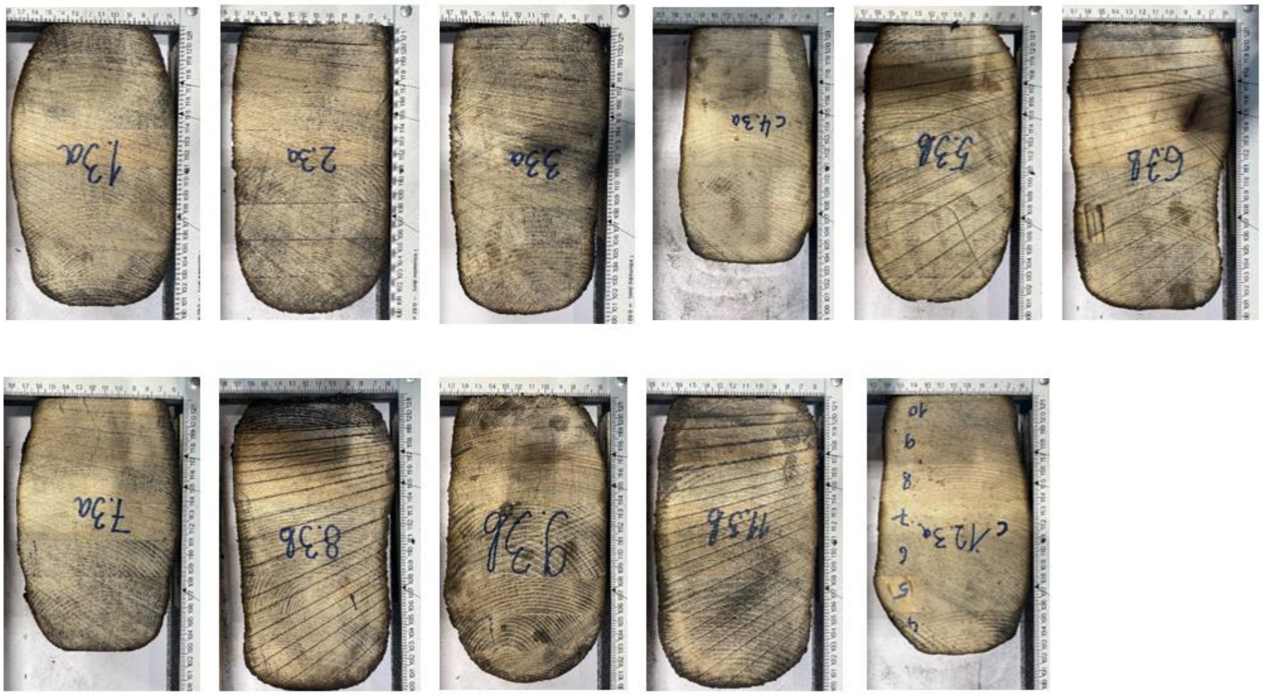

Figure 6. Residual cross-section at mid-span of each beam.

Five cross-sectional slices with thicknesses of 30 mm were cut from each beam at distances of 300 mm. The cross-sections were cleaned from char layer and the residual dimensions were measured.

The mid-span slices of each beam are shown in Figure 6. First number on the marking shows the number of adhesive. Second number shows the number of slice of each beam. Images are shown in similar way as they have been in the furnace. Figure 7 depicts the charring depths for the direction perpendicular to bond lines of the five cross-sections of each beam whereby charring depth is measured vertically at mid-width of the cross-section.

The charring depths on the lateral sides, along the bond lines are presented as average from both sides of the cross-sections, measured at mid thickness of lamination No. 5. This is the first lamella that has not been influenced by charring from the bottom side of the beam. Measurements for all 5 cross-sections of all the beams are shown on Figure 8.

Average cross-section depth and width as well as mass loss measurements are given in Table 3.

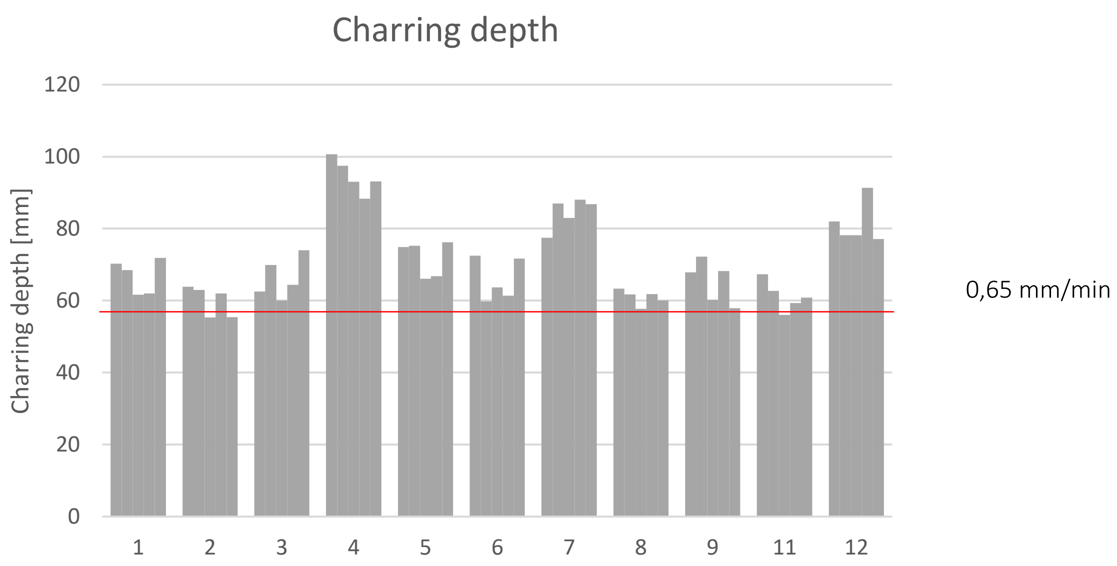

Figure 7. Charring depths on the fire exposed side.

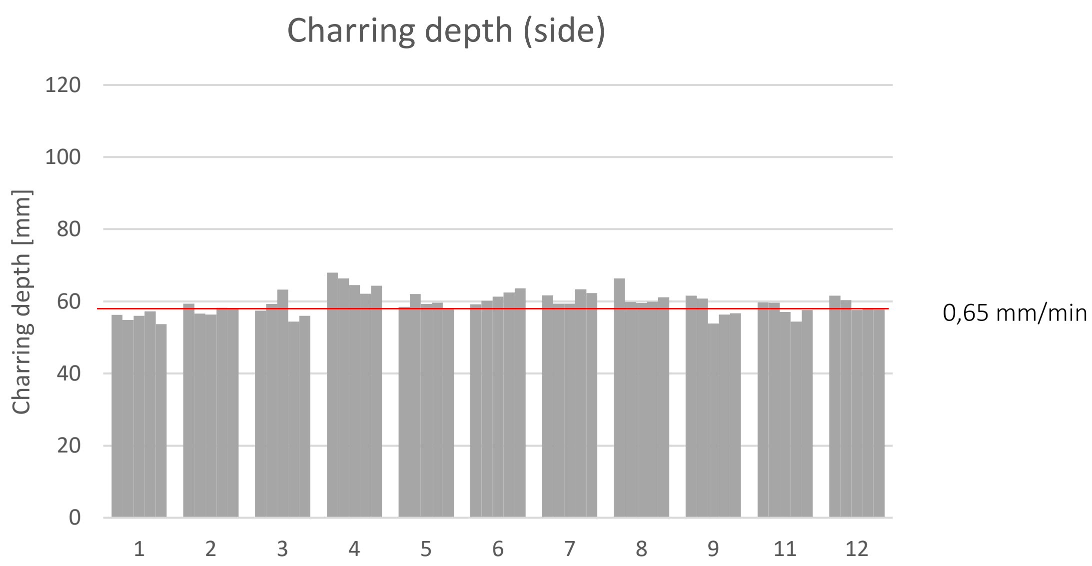

Figure 8. Charring depths on the lateral sides.

Based on the results, partly significant differences in shape and size of the residual cross-sections can be noticed. See Figure 7. Since the wood properties are similar to all beams, it should be concluded that difference in charring is influenced by the bond lines.

Charring of the beams indicates that bond lines with some tested adhesives can cause heat delamination of the lamellae. After the fall-off of charred layer there has been increased charring of the next layer because of missing of protecting char layer.

It can be noticed that the charring is much more uniform for all beams as compared to vertical charring. See Figure 8.

Charring shown on Figure 7 and Figure 8 is compared with the charring rate 0,65 mm/min.

Table 3. Charring depths of residual cross-sections.

	Mass before	Mass after	Residual cross-section depth	Residual width of lamella 5	Residual width of lamella 6
Beam No.	kg	kg	mm	mm	mm
1	57,3	29,3	208,1	118,8	122,1
2	56,7	31,2	215,1	114,6	118,1
3	55,9	30,1	208,8	113,8	116,4
4	53,1	24	180,5	99,9	104
5	56,4	28	203,2	111,1	112,9
6	57,8	30,3	209,2	107,3	105,4
7	56,9	27,8	190,5	104,6	112,2
8	57	30,5	214,1	107,3	107,9
9	56	28,8	209,7	114,3	114
11	55,6	31,5	213,8	114,6	121,6
12	57,8	29	193,6	111,8	114,9

Concluding to the GLT fire tests it can be stated that charring of glulam beams with very similar properties of the wooden laminations resulted in different charring depths for charring perpendicular to the bond lines. The charring from the lateral sides, along the bond lines is however similar for all the beams.

5 Small scale testing

The results from the fire tests are analysed and compared with small scale tests done with the same adhesive systems and similar wood properties at RISE and MPA Stuttgart. In this paper, cone heater test results from RISE are compared with the fire test results.

All 11 adhesives were tested in the cone heater and shear test method (Sterley 2018, Sterley 2022). GLT specimens with dimensions 100x100x60 mm were tested at RISE in Stockholm under cone heater followed by shear capacity test of bond line. Specimen consisted of two layers (20 + 40 mm). The outermost layer was 20 mm thick. The tested bond line surface was then reduced to 50 x 50 mm by cutting a notch on all sides using a thin band saw (see Figure 9).

Two thermocouples were placed parallel to the bond inside the notch, close to the bond line, with ceramic wool insulation protecting from outside. The specimen is protected on all four lateral sides by gypsum plasterboard with 10 mm overlap (Gypsum board, Type F, thickness 15 mm). Test specimens were wrapped by aluminium tape on the sides. This was to prevent charring on the sides. The final exposed surface was 80 x 80 mm (see Figure 9).

The specimen was placed under the cone so that the bottom of the cone is 25 mm above the top of the test specimen. The time started when the shutter was removed from the cone heater (at the start of the heat exposure). The temperature development was observed using two thermocouples measurements. The specimen was heated until average temperature 290°C measured by 2 thermocouples was reached.

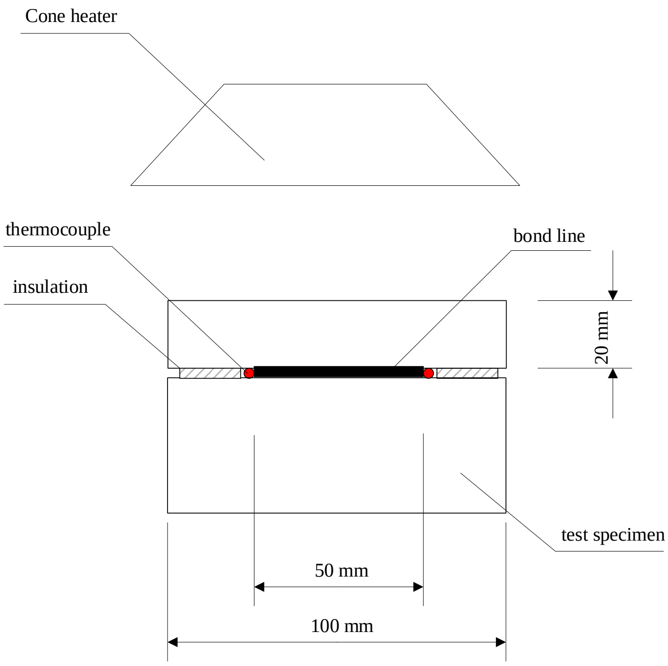

Figure 9. Test setup (left) and test specimen (right).

Once the temperature was reached the specimen was removed from the cone heater. and moved to the shear testing machine (Figure 10). The specimen was loaded in shear along the grain direction until failure. The failure load and failure mode (adhesive or char failure) were recorded. Test results are given in Table 4.

Figure 10. Shear test of the bondline (left) and cross-section of the tested specimen (right).

Table 4. Average test results for each adhesive.

	Test time	Temperature	Shear capacity
Specimen No.	min	ºC	N
1	26,3	294	164
2	28,5	295	337
3	28,7	299	539
4	27,2	291	0
5	26,8	291	94
6	26,1	293	399
7	28,7	292	11
8	23,3	292	343
9	27,6	295	278
11	27,5	292	322
12	30,3	292	93
Solid wood	24,3	296	443

Comparison of small scale test results with the charring results in the furnace tests is shown on Figure 11. The assessment criteria for choosing linear or stepped model is proposed as 225 N in this test method. Compared to the charring tests the method gives conservative results for adhesive No.1. For other adhesives the small scale method gives appropriate results. Conservatively, this relatively simple cone heater and shear method can be used for estimating the effect of bondline integrity when choosing the charring model. For more exact estimation the furnace testing should be performed.

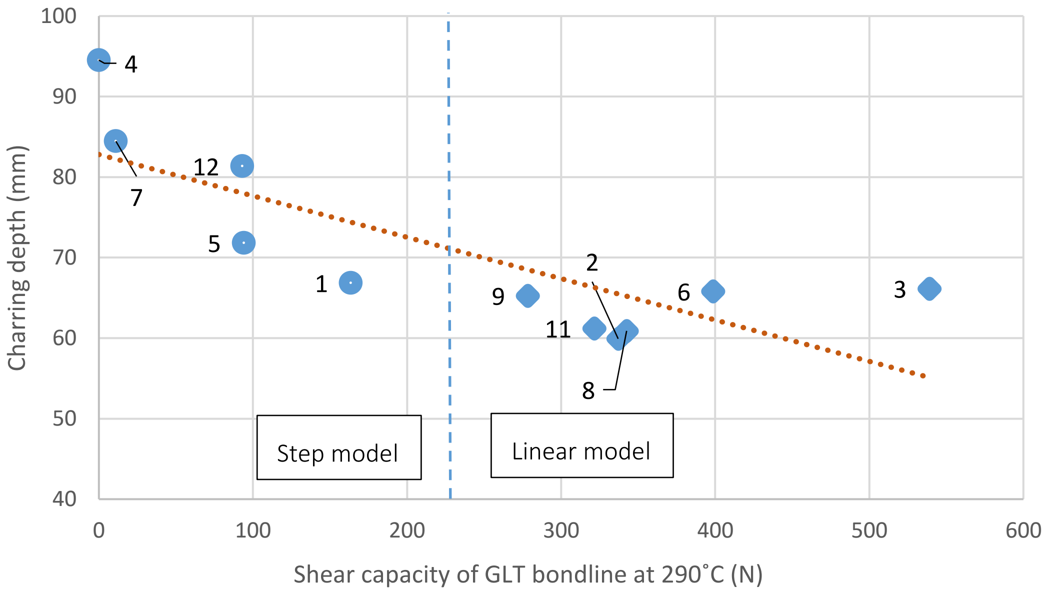

Figure 11. Charring depths compared with shear capacities in cone heater shear method.

6 Outcome

The fire tests of this study showed that glulam beams with well-known wood properties and bond lines made of variety of different adhesives approved for structural applications had different final charring depths in 90 minutes standard fire exposure. That indicates the need for choice between linear or stepped charring models on the fire exposed sides depending on charring direction and bond line integrity.

Project Team of EN 1995-1-2 have proposed that the bond line integrity may be assumed as maintained for phenol-formaldehyde Type I adhesives according to EN 301. For other adhesives there can not be made conclusions according to adhesive family. The bond line integrity should be assessed by testing. There is a comparative charring rate method proposed in prEN 1995-1-2:2021 and small scale methods under development in FIRENWOOD project and new temperature resistance classifications developed within the frame of CEN/TC 193/SC1).

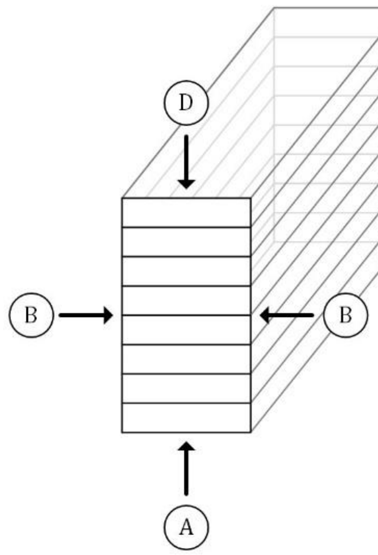

Figure 12. Charring directions for glulam beam (prEN 1995-1-2:2021).

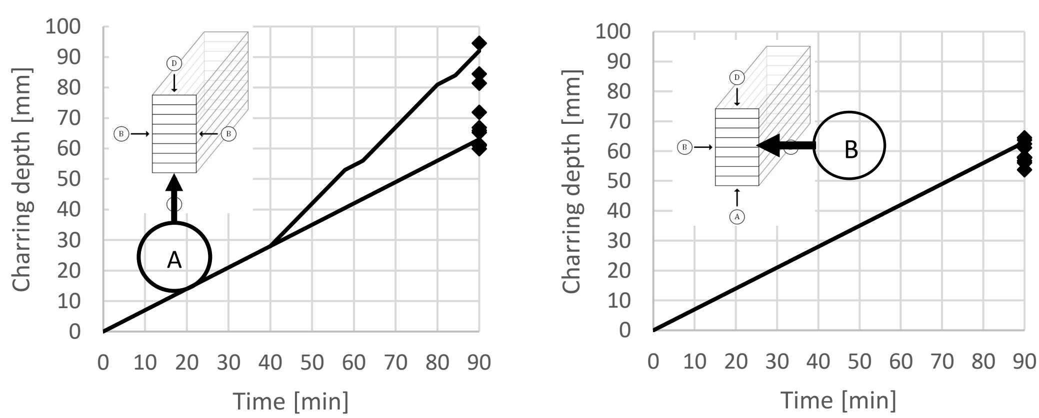

Figure 13. Charring in direction A (left), and direction B (right).

Stepped model for charring shall be applied for charring from direction A (see Figure 13) in the case when bond line integrity is not fulfilled.

For charring direction A, when bondline integrity is maintained, and charring direction B and D in all cases, the linear charring model should be applied. Black dots on Fig 13 represent test results from this research. The lines represent proposed design models for charring (linear and stepped model).

It should also be stated that lamella thickness 28 mm used in glulam beams of this study is thinner than used in practice. The bondline integrity of the glulam beams with 40 mm lamellae have much less influence on final charring depth compared to the beams in this study. For example, for R60 structures, according to design model, there is no influence of bondline integrity to the charring depth of glulam beams when 42 mm lamella thickness is used.

Lamella thickness and bond line integrity of face bond adhesive will be necessary parameters for fire design of glulam beams according to prEN 1995-1-2:2021.

The charring scenarios influenced by bond line integrity in fire can also be roughly predicted by small scale test methods. The work with the small scale methods is ongoing at MPA Stuttgart, Tallinn University of Technology and RISE.

Acknowledgements

The authors acknowledge RISE Fire Research, Zischka, Studiengemeinschaft Holzleimbau e.V, Fachverband der Holzindustrie Österreichs, AkzoNobel Adhesives AB, BASF SE, Dynea AS, Henkel & Cie. AG, Kiilto Oy and FIRENWOOD project in ERA-NET Cofund Action 'ForestValue – Innovating forest-based bioeconomy'.

7 References

EN 1995-1-2, Eurocode 5: Design of timber structures - Part 1-2: General - Structural fire design. 2009. EN 1995-1-2:2004/AC:2006/AC:2009. Brussels: European Committee for Standardization (CEN).

CEN/TC 250/SC 5/WG 4 N 180: SC5.T4 Final Document of prEN 1995-1-2 on fire. 2021. N-document. Brussels: CEN - CENELEC.

Dorn, H., Egner, K. (1967) Flame tests on laminated trusses under bending load. Holz Roh-Werkstoff, Vol 25 (8), pp. 308-320

Frangi, A, Fontana, M, Mischler, A. (2004) Shear behaviour of bond lines in glued laminated timber beams at high temperatures. Wood Science and Technology, vol. 38, pp. 119-126.

Klippel, M. (2014) Fire safety of bonded structural timber elements, PhD thesis of ETH Zürich.

Mäger, K. N., Just, A., Sterley, M. & Olofsson, R. (2021) Influence of adhesives on fire resistance of wooden I-joists. Santiago, Chile, World Conference on Timber Engineering. August 9-12, 2021.

Nurk, J.L (2021) Effect of adhesives on fire resistance of engineered wood structures. Master thesis. Tallinn University of Technology.

Raknes, E. (1997) Durability of structural wood adhesives after 30 years aging. Holz Roh-Werkstoff, Vol 55, pp. 83-90

Sterley, M., Noren, J. (2018) Fire resistant adhesive bonds for load bearing timber structures. Development of a small-scale test method. Smart Housing Småland. SHS report 2018-002.

Sterley, M., Olofsson, R., Månsson, I., Nurk, J.L., Just.A. (2022) Small-scale tests with adhesive bonds with CLT, GLT and finger joints. FIRENWOOD D3.3. RISE, Stockholm.

DISCUSSION

The paper was presented by A Just

S Winter disagreed with the conclusions. 1) EC5 acceptance of the results in full range would need information on the type of glue tested, beam cross section, layup details, and density. 2) He commented about 3 side charring with rate of 0.7mm/min. He commented about the uncertainties in fire tests and discussed the differences in performance of different adhesives. 3) He commented about different charring depths with different methods for the side and edge. He could not see a real need to consider different charring rate for different directions. 4) As lamination thickness is not known a priori for design, he questioned whether one needs to recalculate after lamination thickness is known. S Aicher said that detailed information will be available in a workshop for adhesive suppliers and will be open to public soon. S Aicher said that there is extreme difference in adhesive behaviour for temperature about 250 °C. Classification of adhesives based on fire behaviour will be available. He commented that extreme care was needed in selection of laminae to eliminate laminae effects and make the results more repeatable.

S Winter asked if there was any observation of falling down of laminae in glulam fire tests. A Just said are we sure of the suitability of adhesive of CLT for use in GLT. Falling down of laminae in GLT fire tests was not observed.

P Palma and A Just discussed if fire testing of twin beams in a chamber might have influenced the results.

BJ Yeh asked if any charred layer fell off in poor performing adhesives. A Just said it must have fallen off but was not clearly observable.BJ Yeh and A Just discussed difference between charring directions and whether bondline integrity was maintained or not.

H Blass commented that the data showed difference in performance between different adhesives which could not be ignored; hence, the only solution is to take the worst case. S Aicher said that poor performing adhesive manufacturers are aware of the results and are working to improve their product performance. K Mäger said that the intent of the project was to compare different test methods and confirm the charring rate.

A Frangi was not happy with the results but was prepared to accept them. He commented that in EC5 adhesive class will be proposed to distinguish the differences in performance. A Just agreed that the information will be opened and will need to discuss with manufacturers. S Aicher commented as we have different strength classes for timber, we are proposing similar philosophy for adhesives in fire. S Winter stated that it would be important to find a solution with which you don’t point on producers.

The effective width of cross-laminated timber rib panels in fire

Miriam Kleinhenz, Institute of Structural Engineering, ETH Zurich

Andrea Frangi, Institute of Structural Engineering, ETH Zurich

Alar Just, Tallinn University of Technology

Keywords: Massive timber rib panel, cross-laminated timber, effective width, ISO-fire exposure, advanced design method, simplified design method

1 Introduction

The composite structure of cross-laminated timber rib panels consists of cross-laminated timber (CLT) plates connected as flanges to glued-laminated timber (glulam) ribs. Full composite action is provided by a rigid connection between the composite components by means of screw-press gluing (Figure 1). For ribbed cross-sections, the assumption that the cross-section remains plane is incorrect. The simple beam theory according to Euler-Bernoulli is not applicable because the strains in the flange vary pending on the distance from the rib due to the in-plane shear flexibility of the flange, leading to a non-uniform distribution of the longitudinal strains along the flange width. For simplified structural analysis, the effective width defines an equivalent cross-section that provides the same maximum bending stress and effective bending stiffness as the actual cross-section (Chwalla 1936; Timoshenko 1940). Current simplified design methods for timber structures do not contain a determination method of the effective width for timber composite structures, much less for massive timber rib panels (*EN 1995-1-1* 2004; *EN 1995-1-2* 2004). Simplified equations are proposed as the basis for the final document of CLT design for a revised version of Eurocode to determine the effective width at normal temperature for ribbed plates built up from cross-laminated timber plates (*CEN/TC 250/SC 5 N 892* 2018). Based on Bogensperger (2013), the analyses were limited to one CLT plate as top flange. In the case of uniformly distributed loads, Equation 1 determines the effective width at normal temperature b_{ef}

$$b_{ef} = b_{rib} + \sum b_{ef,i} \\ = b_{rib} + b_{f,i} \cdot (0.5 - 0.35 \cdot \left(\frac{b_{f,i}}{l}\right)^{0.9} \cdot \left(\frac{(EA)x}{(GA)xy}\right)^{0.45}) \quad (1)$$

where $b_{ef,i}$ is the effective width at each side of the rib width b_{rib}, $b_{f,i}$ = (b - b_{rib}) is the clear rib distance, l is the span, and $(EA)_x/(GA)_{xy}$ is the ratio per meter width between the in-plane stiffness of the longitudinal CLT layers and the shear stiffness in plane of the gross CLT cross-section. The geometry is explained in Figure 1.

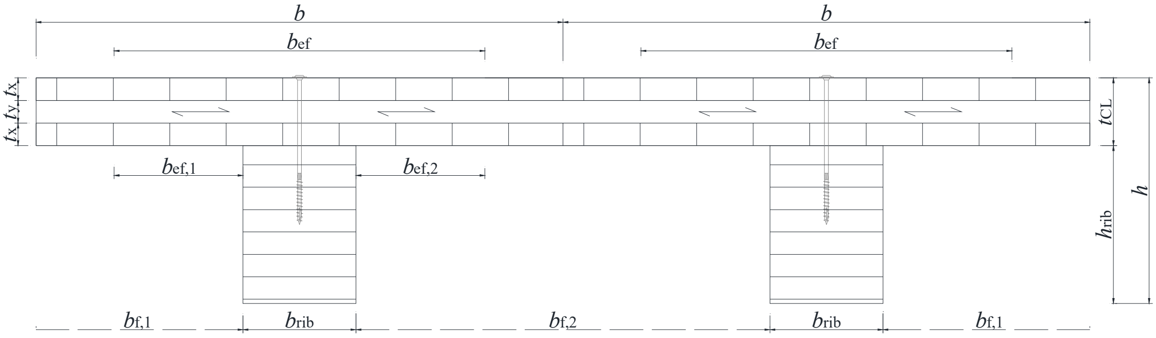

Figure 1. Geometry of the cross-section of cross-laminated timber rib panels.

In a research project, the fire resistance of cross-laminated timber rib panels (CLT rib panels) was studied with experimental and numerical analyses. Two different cross-section types were studied (T-section, box-section). The experimental results of a series of full-scale fire tests showed more than 90 and 120 min of fire resistance and confirmed the assumption that the effect of the composite action was maintained under standard fire (Kleinhenz et al. 2021c; b).

This paper focuses on the numerical simulations of the structural behaviour of CLT rib panels under standard fire to investigate the effective width in fire $b_{ef,fi}$. First, the results of the thermo-mechanical simulations of one tested cross-section are validated against the experimental results. Based on the finite element (FE) model, the results of the most severe extreme cases of a parametric study are presented. Proposals are derived as simplified design rules for the effective width in fire $b_{ef,fi}$. Then, the bending resistance based on the simplified design method is compared with the bending resistance based on an advanced design method and with the experimental results. Finally, simplified design rules for the effective width in fire $b_{ef,fi}$ are proposed for the Eurocode 5 revision (*CEN/TC 250/SC 5/WG 4 N 193* 2021).

2 Experimental investigations

Full-scale fire resistance tests on CLT rib panel cross-sections were performed as presented in Kleinhenz et al. (2021b). Of each cross-section type, one has been designed as initially protected cross-section, as presented in Figure 2 (A, B, C, and D). The fire resistance tests were performed according to European test standards (*EN 1363-1* 2012; *EN 1365-2* 2014). The horizontal furnace had a length l of 5.20 m and a width of

3.00 m. The specimens were simply supported and had three ribs with a CLT width per rib *b* of 0.933 m. In the test setup, a constant mechanical load was applied uniformly via evenly distributed loading points, whereby the moment in the middle of the span corresponded to the target bending moment of the design. The deflection at midspan was measured at each rib. The furnace was controlled with plate thermometers to follow the ISO standard time-temperature curve (*ISO 834-1* 1999). Thermocouples of type K-w-e-0.5/2.2/in-pa were inlaid between the CLT layers according to the recommendations by Fahrni et al. (2018).

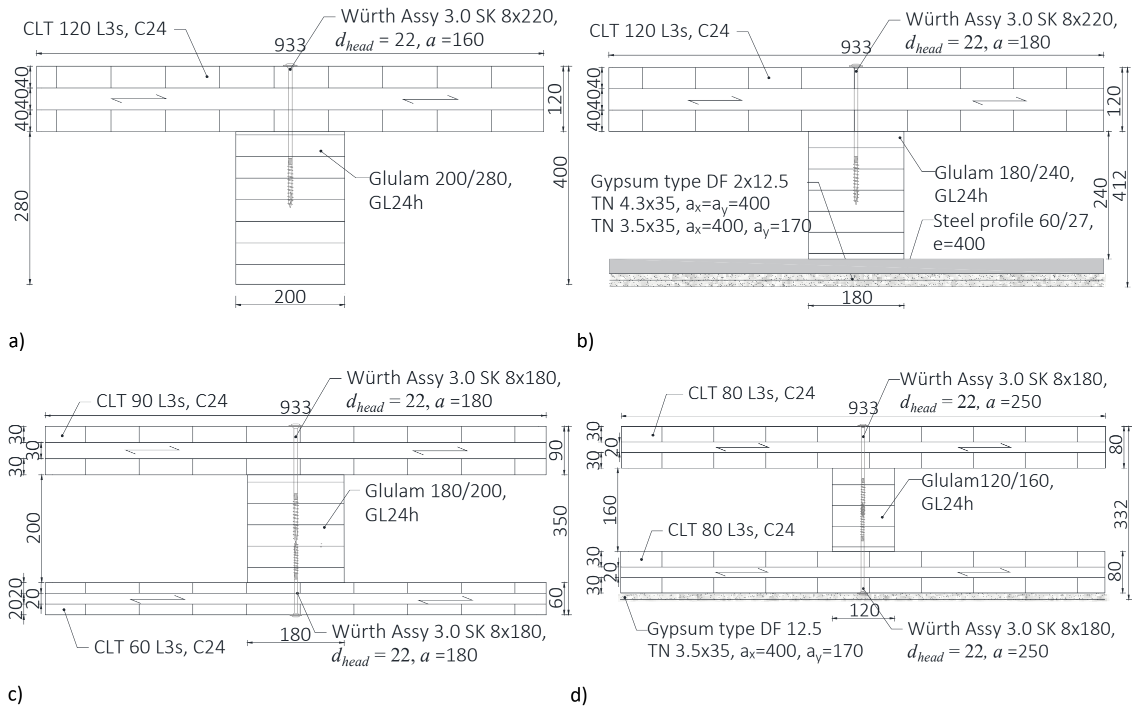

Figure 2. Cross-sections of the experimental program, in [mm]: a) T-section (A); b) T-section initially protected (B); c) Box-section (C); d) Box-section initially protected (D).

3 Numerical investigations

3.1 Modelling assumptions

The following assumptions were derived from the experimental investigations:

- The composite action is maintained under standard fire exposure.
- The influence of the screws and thus the screws themselves are neglected in the thermal simulation. Their loadbearing behaviour is neglected in the thermo-mechanical simulation.
- The thermal simulation takes into account the fall-off of charred CLT layers but not the fall-off of charred glulam layers.
- For comparison with the experimental results, the charred depth is tracked along the 300°C-isotherm according to EN1995-1-2 (2004).

3.2 Finite element models

The numerical investigations comprised uncoupled thermal and thermo-mechanical simulations using 3D FE models. The modelling framework was developed using the Python programming language (Python Software Foundation 2018) and Abaqus Unified FEA software suite for finite element analysis (Dassault Systemes 2019). The cross-section of a T-section was sketched and extruded to one deformable part. A geometric symmetry simplification was considered in the form of a vertical symmetry plane in the middle of the cross-section in longitudinal direction and a vertical symmetry plane at midspan. The support was defined as roller support. The generated part was partitioned into flange and rib. The flange was partitioned into the CLT layers, the material orientations of which were defined by local coordinate systems. The contact interactions between flange and rib, and the CLT layers were considered as rigid.

The thermal simulations based on FE heat transfer models were conducted based on the temperature-dependent thermal properties for wood according to the current Eurocode 5-1-2 (*EN 1995-1-2* 2004) and the new set of thermal properties presented in Kleinhenz et al. (2021a). The new set is introduced after fall-off of charred CLT layers to take into account the post-fall-off behaviour of wood. Fall-offs were defined as time steps of the thermal simulations when the average temperature between the CLT layers along a path at midspan exceeded 300°C. In a further simulation step, the FE model without the fallen-off layer was generated and the simulation was continued from the fall-off time starting from a predefined temperature field imported from the previous simulation. The end surfaces at the support, the vertical end of the CLT plate at field centre, and the symmetry planes were defined as adiabatic surfaces. Convective and radiative thermal interactions were defined for the rest of the outer timber surfaces. The top edge was exposed to a constant temperature of 20°C. The thermal interactions of the surfaces at the bottom edges followed a previously defined amplitude of the standard time-temperature curve starting from a predefined temperature field of 20°C. An element size of 10x10 mm^2 was chosen for the cross-section. The element size was halved in height in the CLT layers; i.e. 10x5 mm^2. The element size in longitudinal direction corresponded to the length of the FE model based on the omitted heat transfer in longitudinal direction. A heat transfer and 8-node linear brick element (DC3D8) was used. The interval between the time steps was kept at 5 seconds. At the end, the numerical results of the FE models were sequenced together.

The thermo-mechanical simulations imported the temperature fields of certain time steps. The mechanical load was applied uniformly over the surface. The flexible-in-shear multi-layered FE model resulted in a non-uniform, temperature-dependent strain distribution along the CLT width. Mass-loss due to pyrolysis was taken into account by defining the density of the materials as temperature-dependent. The density at normal temperature (20°C) was 465 kg/m^3 for CLT and 420 kg/m^3 for glulam. Material properties are discussed as linear-elastic and temperature-dependent orthotropic. The material properties at normal temperature (20°C) were taken for CLT and glulam from Table 1. The shear modulus in-plane of the gross CLT cross-section G_{xy} and the rolling shear modulus of CLT G_r were determined according to Equation 2 and 3

$$G_{xy} = min\left(\frac{650}{1 + 2.6 \cdot \left(\frac{t_l}{b_l}\right)^{1.2}}; 450\right) \tag{2}$$

$$G_r = min\left(30 + 17.5 \cdot \left(\frac{b_l}{t_l}\right); 100\right) \tag{3}$$

where t_l is the thickness of the lamination, and b_l is either the width of the lamination, the distance between the edge and a groove or the spacing between grooves within the lamination (Brandner et al. 2016; Ehrhart et al. 2015). The latter was taken as average distance between grooves of the edge-bonded laminations, declared as 150 mm by Stora Enso.

*Table 1. Material properties for CLT (*CEN/TC 250/SC 5 N 892 *2018) and glulam (*EN 14080 *2013).*

Material	E_x	E_y	E_z	G_{xy}	G_{xz}	G_r	v_{xy} [2)]	v_{xz} [2)]	v_{yz} [2)]
	[N/mm²]	[N/mm²]	[N/mm²]	[N/mm²]	[N/mm²]	[N/mm²]	[-]	[-]	[-]
CLT24	12500 [1)]	450	450	Eq. 2	650	Eq. 3	0.395	0.395	0.41
GL24h	11500	300	300	650	650	65	0.395	0.395	0.41

[1)] Value given by Stora Enso.
[2)] Values based on Bodig and Jayne (1993)

The temperature-dependent reduction in material properties was modelled by the bilinear simplification according to the current Eurocode 5-1-2 (*EN 1995-1-2* 2004). Following the approach by Chen et al. (2020), the temperature-dependent reduction factors for the engineering constants were implemented as summarized in Table 2 (Hodel 2021). At 100°C, the moduli of elasticity and the shear moduli were multiplied by the average value of the reduction factors for the modulus of elasticity parallel to the grain in compression and in tension according to the current Eurocode 5-1-2 (*EN 1995-1-2* 2004). The Poisson's ratios were kept unchanged. The meshing size was set as 20 mm. In the generated mesh, the stress/displacement element type C3D8I was used. The 20-node quadratic brick element C3D20R was used for the longitudinal CLT layers.

Table 2. Temperature-dependent reduction factors for the moduli of elasticity E, the shear moduli G, and the Poisson's ratios v according to Chen et al. (2020)

Temperature	$k_{\theta,E}$	$k_{\theta,G}$	$k_{\theta,v}$
[°C]	[-]	[-]	[-]
20	1.00	1.00	1.00
100	0.425	0.425	1.00
300	0.01	0.01	1.00

3.3 Effective width in fire

The longitudinal stress distribution within the CLT plate was extracted and the effective width was calculated per specified time step in accordance with Ahn et al. (2004). Figure 3 illustrates the initial effective width, when all fibres exhibit ambient temperature.

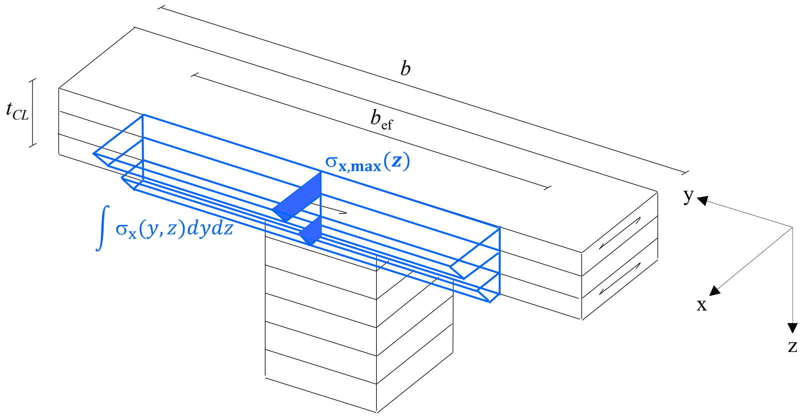

Figure 3. Determination of the effective width at normal temperature.

The numerical effective width in fire $b_{ef,fi,sim}$ was determined according to Equation 4

$$b_{ef,fi,sim} = \frac{\int \sigma_{x,fi}(y,z)dydz}{\sigma_{x,max,fi}(z)} = \frac{F_{x,tot,fi}}{F_{x,max.fi}} \tag{4}$$

where $\int \sigma_{x,fi}(y,z)dydz$ is the integral of all temperature-dependent longitudinal bending stresses along the thickness and along the width of the residual cross-section of the CLT plate (short: total force of the CLT plate in fire $F_{x,tot,fi}$), and $\sigma_{x,max,fi}(z)$ is the maximum temperature-dependent longitudinal bending stress distribution along the thickness of the residual cross-section of the CLT plate at rib centre of the FE model (short: trapezoidal force at rib centre in fire $F_{x,max,fi}$).

The temperature-dependent longitudinal bending stresses were taken along the CLT width and along the thickness of the longitudinal CLT layers at 5 mm intervals. The bending stresses of the transversal CLT layers were neglected. The temperature-related reduction of the stiffness of the elements based on Table 2 led to a reduction close to zero for temperatures at 300°C. As soon as the mean temperature of elements in the longitudinal CLT layers exhibited 300°C, they were not part of the residual cross-section and did not contribute to the longitudinal bending stresses. The approach was taken to consider only elements above the 300°C isotherm in the CLT plate. As a simplified approach, the position of the 300°C isotherm, thus the charred depth in CLT layer *i* on the fire-exposed side $d_{char,layer,i,sim}$ was estimated according to Equation 5

$$d_{char,layer,i,sim} = \beta_{layer,i,sim} \cdot \left(t - t_{300°C,layer,i-1,sim}\right) \tag{5}$$

with

$$\beta_{layer,i,sim} = \frac{d_{layer,i,sim}}{t_{300°C,layer,i,sim} - t_{300°C,layer,i-1,sim}} \tag{6}$$

where $\beta_{layer,i,sim}$ is the charring rate of CLT layer *i* in mm/min, *t* is the specified time step for the import of the temperature field from the thermal simulation, $d_{layer,i,sim}$ is the thickness of layer *i* of the FE model, $t_{300°C,layer,i,sim}$ is the fall-off time of layer *i*, and $t_{300°C,layer,i-1,sim}$ is the fall-off time of the previous layer.

3.4 Validation

The FE models were validated against the experimental results of cross-section A representing the initially unprotected T-section (Figure 2). The uniformly distributed load was taken from the fire resistance test (Kleinhenz et al. 2021b). Figure 4 presents the numerical results of the FE models of cross-section A. The experimental results are included for the charred depth in the CLT layers, the deflection, and the deflection rate. The results show very good agreement. The performance criteria for failure of the load-bearing capacity as limit values for the amount of the deflection and the deflection rate according to prEN1363-1 (2018) were not reached.

3.5 Results

Figure 4c1 presents the total force of the CLT plate in fire $F_{x,tot,fi}$ and the trapezoidal force at rib centre in fire $F_{x,max,fi}$, based on the simplified approach and based on a precise approach (determination of the 300°C isotherm obtained from the thermal simulations). For the simplified approach, the specific times steps were defined as 0 min, 30 min, $t_{300°C,layer,i}$, and 90 min. For the precise approach, an interval of 15 min was chosen. The two approaches differ only marginally.

Figure 4c2 shows the ratios of effective width in fire to CLT width $b_{ef,fi,sim}/b$. Differences between simplified and precise approach are maximum 4% in absolute terms. The initial ratio of effective width in fire to CLT width $b_{ef,fi,sim}/b$ (t=0 min) is 84%, which represents the ratio of effective width at normal temperature to CLT width $b_{ef,sim}/b$. The curve shows a temperature-dependent decrease with an increased exposure time. First, the effective width in fire $b_{ef,fi,sim}/b$ remains unchanged, since the total force of the CLT plate in fire $F_{x,tot,fi}$ and the trapezoidal force in fire $F_{x,max,fi}$ show comparable increase in the rate of change. After the fall-off of the charred CLT layer at 63 min, the trapezoidal force in fire $F_{x,max,fi}$ shows a 4-fold higher increase in the rate of change than the total force of the CLT plate in fire $F_{x,tot,fi}$, which leads to a reduction of the effective width in fire $b_{ef,fi,sim}$. The stresses are accumulated in the part of the remaining CLT plate at the rib centre. The ratio of effective width in fire to CLT width $b_{ef,fi,sim}/b$ decreases to 69%. The ratio of effective width at normal temperature to CLT width b_{ef}/b according to Equation 1 results in 64%, included in Figure 4c2. The ratio of effective width in fire to CLT width $b_{ef,fi,sim}/b$ remains above this value. Until test termination of

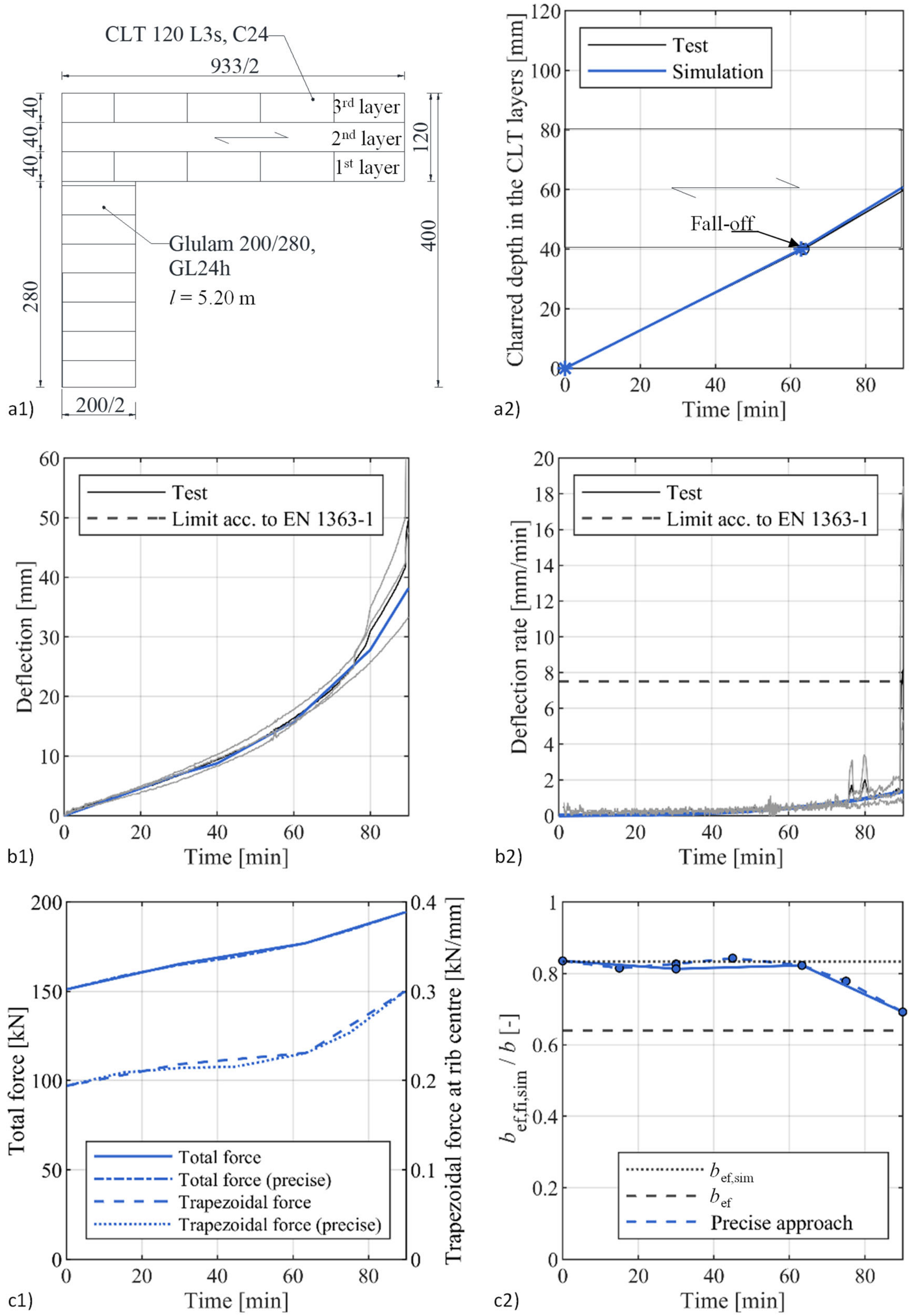

Figure 4. Numerical results of cross-section A including the experimental results (until test termination): a1) Cross-section; a2) Charred depth in CLT layers; b1)+b2) Deflection and deflection rate compared to the performance criteria according to prEN1363-1 (2018); c1) Total force and trapezoidal force at rib centre in fire; c2) Effective width in fire compared to the effective width at normal temperature according to Equation 1.

the fire resistance test, thus a fire resistance of 90 min, the effective width at normal temperature b_{ef} according to Equation 1 gives an approximation of the effective width in fire $b_{ef,fi,sim}$ on the safe side.

4 Parametric study

A parametric study was performed to investigate the effective width in fire obtained from the simulation $b_{ef,fi,sim}$. The investigation was limited to cross-sections of a T-section (see Figure 2), as for the effective width at normal temperature b_{ef} according to Equation 1. The experimental and numerical investigations conclude that an underestimation of the effective width leads to a more severe underestimation of the structural behaviour for box-sections than for T-sections (Kleinhenz 2022; Kleinhenz et al. 2021b). It is assumed that limits of the effective width in fire obtained from the simulation $b_{ef,fi,sim}$ for T-sections should also apply to box-sections.

The following parameter range of the parametric study was chosen in accordance with the parameter range expected in practice for ribbed plates built up from cross laminated timber plates and ribs (*CEN/TC 250/SC 5 N 892* 2018):

- $0.02 \leq b_{f,i}/l \leq 0.25$, for the ratio of clear rib distance to span
- $0.18 \leq \sum t_x/t_{CL} \leq 0.80$, for the ratio of total thickness of the longitudinal CLT layers to height of the CLT plate
- $14 \leq l/h \leq 22$, for the ratio of span to overall height.

System set-ups and CLT lay-ups are based on the European Technical Assessment ETA 20/0893 (2020) and the final document of CLT design (*CEN/TC 250/SC 5 N 892* 2018). The thickness of the CLT layers and the number of layers have an influence on the fire behaviour of the CLT plate and the fall-off times of the charred CLT layers. In Kleinhenz (2022), the investigations include three groups of extreme cases: thick layers of 40 mm, thin layers of 20 mm (5-layered CLT plate), and thin layers of 20 mm (3-layered CLT plate). Thick CLT layers delay the charring progress and stabilise the effective width in fire $b_{ef,fi,sim}$. As for cross-section A, the effective width at normal temperature b_{ef} according to Equation 1 gives an approximation of the effective width in fire $b_{ef,fi,sim}$ on the safe side: $b_{ef,fi,sim} \geq b_{ef}$.

In this paper, the results are shown for the most severe group: thin layers of 20 mm (3-layered CLT plate). Thinner layers lead to an increased charring behaviour and a faster reduction of the effective width in fire $b_{ef,fi,sim}$. Figure 5 presents the results. Different ratios of clear rib distance to span $b_{f,i}/l$ are covered to account for different floor stiffness values. The minimum cross-section with the highest floor stiffness $b_{f,i}/l = 0.06$ is represented by extreme case 1b. The maximum cross-section with the lowest floor stiffness $b_{f,i}/l = 0.25$ is represented by extreme case 3b. The duration of the simulations was less than 60 min. The total force in fire $F_{x,tot,fi}$ and the trapezoidal force in fire $F_{x,max,fi}$ show a temperature-dependent increase with an increased exposure time. The values are higher for extreme cases of decreased stiffness, since the CLT width of the system and thus the applied load per rib are higher. The effective width in fire $b_{ef,fi,sim}$ was determined up to the time step at which the penultimate CLT layer fell off, which means that one CLT layer was still in place.

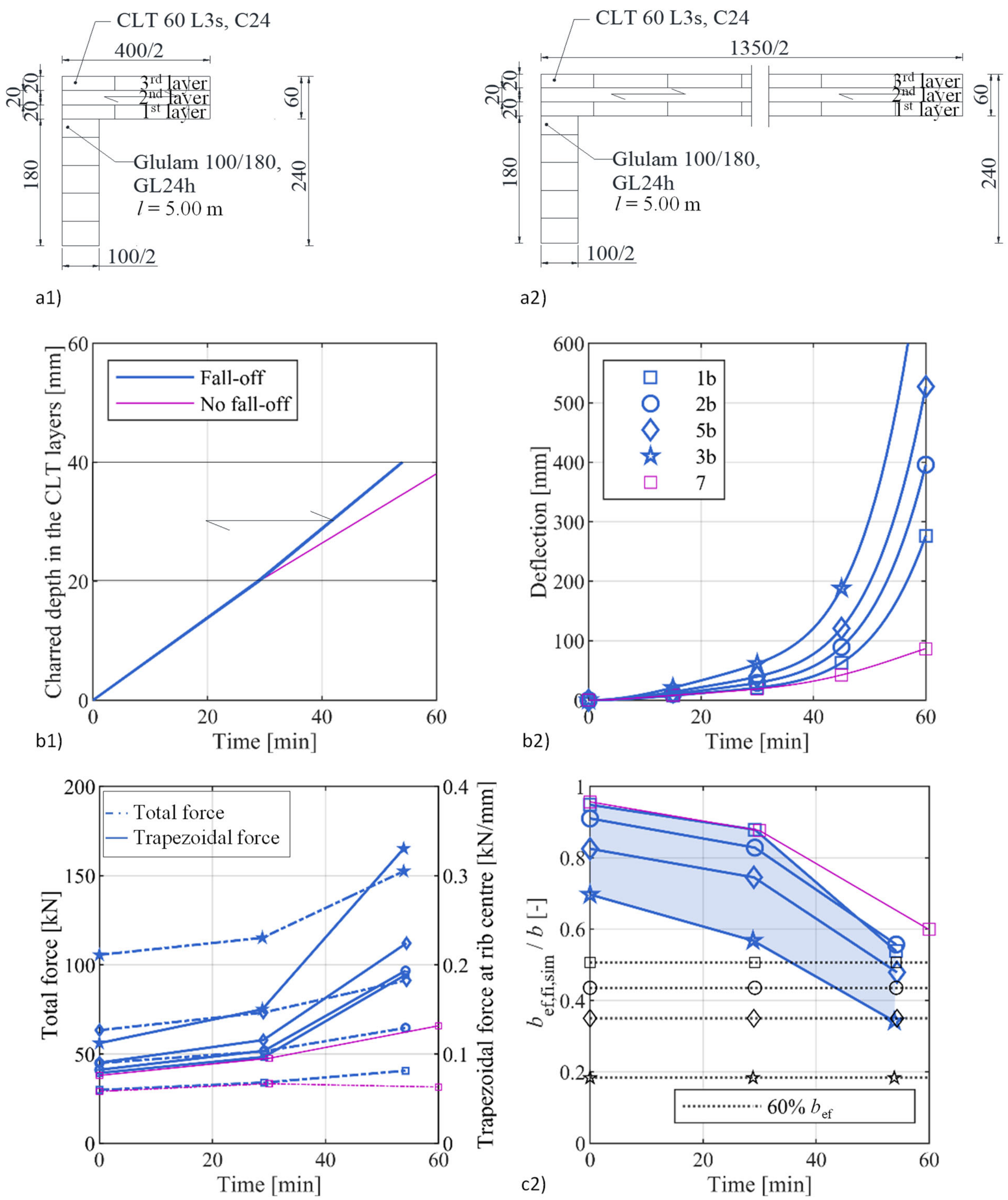

Figure 5. Numerical results over time of the extreme cases 'thin layers, 3-layered': a1)-a2) Minimum / Maximum cross-section; b1) Charred depth in CLT layers; b2) Deflection; c1) Total force and trapezoidal force at rib centre in fire; c2) Ratio of effective width in fire to CLT width related to a limit value based on Equation 1.

The initial ratios of effective width to CLT width $b_{ef,sim}/b$ result between 96% and 70%. The effective widths in fire $b_{ef,fi,sim}$ show a temperature-dependent reduction with an increased exposure time. After the fall-off of the first charred CLT layer, the trapezoidal force in fire $F_{x,max,fi}$ shows an up to 3-times higher increase in the rate of change than the total force in fire $F_{x,tot,fi}$, which leads to a higher reduction of the effective width in fire $b_{ef,fi,sim}$. Until the fall-off of the second charred CLT layer, the ratios of effective width in fire to CLT width $b_{ef,fi,sim}/b$ decrease to values between 56% and 34%. The influence of the shear lag effect of the ribbed floor system increases. The stresses are accumulated in the part of the remaining CLT plate at the rib centre, while parts far from the rib experience higher shear deformations. A sharp increase of the effective width's reduction is observed when effectively only one longitudinal CLT layer remains. The extreme case 7 is identical to extreme case 1b with the exception that fall-off of charred CLT layers was not taken into account. The effective width in fire $b_{ef,fi,sim}$ is only up to 10% higher in absolute terms for extreme case 7. For all extreme cases, the ratios of effective widths at normal temperature b_{ef} according to Equation 1 were undercut by the ratios of the effective widths in fire $b_{ef,fi,sim}$. A limit value was determined as 60% of the effective widths at normal temperature according to Equation 1: $b_{ef,fi,sim} \geq 0.60\, b_{ef}$. The values per extreme case are included in Figure 5c2.

5 Bending resistance in fire

A simplified design method for modelling CLT rib panels in fire is developed in Kleinhenz (2022) in accordance with the revised version of Eurocode 5 (*CEN/TC 250/SC 5/WG 4 N 193* 2021). The effective cross-section method is applied to determine the part of the cross-section which strength and stiffness properties are assumed to be unaffected for a certain fire resistance time (effective cross-section). In the case of initially protected cross-sections, encapsulated phases (no charring) and protected charring phases (decreased charring rate) are defined by the estimated start times of charring t_{ch} and the estimated fall-off times of gypsum plasterboards t_f.

For the effective cross-section, the calculation method of rigidly bonded components (Bernoulli-beam) is applied. The bending stiffness of the transversal CLT layers is taken as zero. The neutral axis in fire is located in the centre of gravity in fire of the effective cross-section $z_{s,fi}$, determined according to Equation 7

$$z_{s,fi} = \frac{\sum(E_i \cdot A_{i,ef} \cdot a_{i,fi})}{\sum(E_i \cdot A_{i,ef})} \tag{7}$$

where E_i is the mean value of the individual component's modulus of elasticity, $A_{i,ef}$ is its cross-section area of the effective cross-section in fire, and $a_{i,fi}$ is the distance to its centroid from a selected origin in fire.

The effective bending stiffness in fire $(EI)_{ef,fi}$ is computed according to Equation 8

$$(EI)_{ef,fi} = \sum\left(\frac{E_i \cdot b_{i,ef} \cdot h_{i,ef}^3}{12} + E_i \cdot b_{i,ef} \cdot h_{i,ef} \cdot z_{i,fi}^2\right) \tag{8}$$

where E_i is the mean value of the individual component's modulus of elasticity, $b_{i,ef}$ is its width of the effective cross-section in fire, $h_{i,ef}$ is its height of the effective cross-section in fire, and $z_{i,fi}$ is the distance of its centroid to the global centre of gravity in fire $z_{s,fi}$.

The resistance moment in fire $M_{R,fi}$ is determined according to Equation 9

$$M_{R,fi} = \frac{f_{t,mean} \cdot (EI)_{ef,fi}}{E_i \cdot z_{bot,fi}} \tag{9}$$

where $f_{t,mean}$ is the mean tensile strength of the glulam rib (taken as 26.2 N/mm^2) or the bottom CLT plate (taken as 27.1 N/mm^2), $(EI)_{ef,fi}$ is the effective bending stiffness of the effective cross-section in fire, E_i is the mean value of the modulus of elasticity of the glulam rib or the bottom CLT plate, and $z_{bot,fi}$ is the z-coordinate at the bottom edge of the glulam rib or at the bottom edge of the bottom CLT plate of the effective cross-section in fire.

The effective width in fire $b_{ef,fi}$ defines the width of the longitudinal CLT layers of the effective cross-section in fire $b_{i,ef}$ and is involved in both the determination of the global centre of gravity in fire $z_{s,fi}$, and the effective bending stiffness of the composite cross-section in fire $(EI)_{ef,fi}$. A determination method of an effective width in fire is not included in Eurocode 5 (*CEN/TC 250/SC 5/WG 4 N 193* 2021; *EN 1995-1-2* 2004). As Eurocode 5 approach is defined, where the effective width in fire $b_{ef,fi}$ is limited to the rib width of the effective cross-section in fire $b_{rib,ef}$. In addition, two further approaches are proposed for improvement of the effective width in fire $b_{ef,fi}$, based on the conclusions of the parametric study. The effective width in fire $b_{ef,fi}$ is taken as

- Eurocode 5: $b_{ef,fi} = \ b_{rib,ef}$
- Proposal 1: $b_{ef,fi} = \begin{cases} b_{ef} & , if \ \ t_x \geq 40\,mm \\ 0.60 \cdot b_{ef}, & if \ \ t_x < 40\,mm \end{cases}$
- Proposal 2: $b_{ef,fi} = \ 0.60 \cdot b_{ef}$

where b_{ef} is the effective width at normal temperature according to Equation 1, and t_x is the thickness of the longitudinal CLT layer. The design rules apply for both the effective width in fire at midspan and the effective width in fire at the support. For the box-sections of this paper, the effective width in fire $b_{ef,fi}$ is calculated separately for the top and the bottom CLT plates.

Figure 6 presents the bending resistance in fire of the simplified design method per tested cross-section (A, B, C, and D), of which one of each cross-section type was initially protected (B, and D). The results depend on the approach for the determination of the effective width in fire $b_{ef,fi}$ (Eurocode 5, proposal 1, and proposal 2). Experimental results were taken based on the target bending moments of the fire resistance tests (Kleinhenz et al. 2021b). Furthermore, numerical results for three cases of the effective width (60%, 80%, and 100% of the CLT width) are included as the results of an advanced design method. The minimum case "60% of the CLT width" represents the average effective width at normal temperature b_{ef} according to Equation 1 of the tested cross-sections. In Kleinhenz (2022), the numerical results are calculated by a thermo-mechanical model based on thermo-mechanical simulations using a linear 2D FE beam model in SAFIR® (Franssen and Gernay 2017). The failure times of the fire resistance tests were used as criterion for the fall-off time of gypsum plasterboards in the advanced design method.

The bending resistance in fire is defined as a fraction of the resistance moment in fire of a specific exposure time and the initial resistance moment at time step t = 0 min of the cross-section with 100% CLT width of the advanced design method, or in short $M_{R,fi}(t)/M_{R,fi,100}(t=0)$. The results are shown until experimental failure time or simulation stop. The bending resistance is higher for a cross-section with a larger effective width in fire $b_{ef,fi}$. Cross-sections A and B with a thickness of the CLT layers of 40 mm show different analytical results for proposal 1 or proposal 2. The results of proposal 1 agree well with the numerical results using 60% of the CLT width as effective width in fire. Proposal 2 leads to values that are on average 10% lower than for proposal 1. Both proposals give good estimates of the fire resistance times. Eurocode 5 leads to values that are on average 30% lower than for proposal 1. The thicknesses of the CLT layers of cross-sections C and D are thinner than 40 mm. Thus, the analytical results for proposal 1 and proposal 2 are identical. Proposal 2 leads to values that are on average 50% lower than for the numerical results using 60% of the CLT width as effective width in fire. Eurocode 5 leads to values that are on average 70% lower. The gap decreases with increased exposure time. After the fall-off of the bottom CLT plate, the box-section changes to a T-section, which is less dependent on the effective width. The differences in bending resistance between the different effective widths are larger for box-sections than for T-sections.

6 Conclusion

This paper investigates the effective width in fire $b_{ef,fi}$ obtained from the thermo-mechanical simulations and compares the results to the effective width at normal temperature b_{ef} according to Equation 1. The investigation was limited to a parameter range expected in practice and cross-sections of a T-section. Based on the conclusions of the parametric study, two proposals are considered as improvements for the effective width in fire $b_{ef,fi}$. Proposal 1 and proposal 2 lead to clear improvements compared to the Eurocode 5 approach. The differences between proposal 1 and proposal 2 are minor. The authors propose to introduce into the Eurocode 5-1-2 revision the following determination of the effective width in fire for ribbed plates built up from cross-laminated timber plates: $b_{ef,fi} = 0.60 \cdot b_{ef}$.

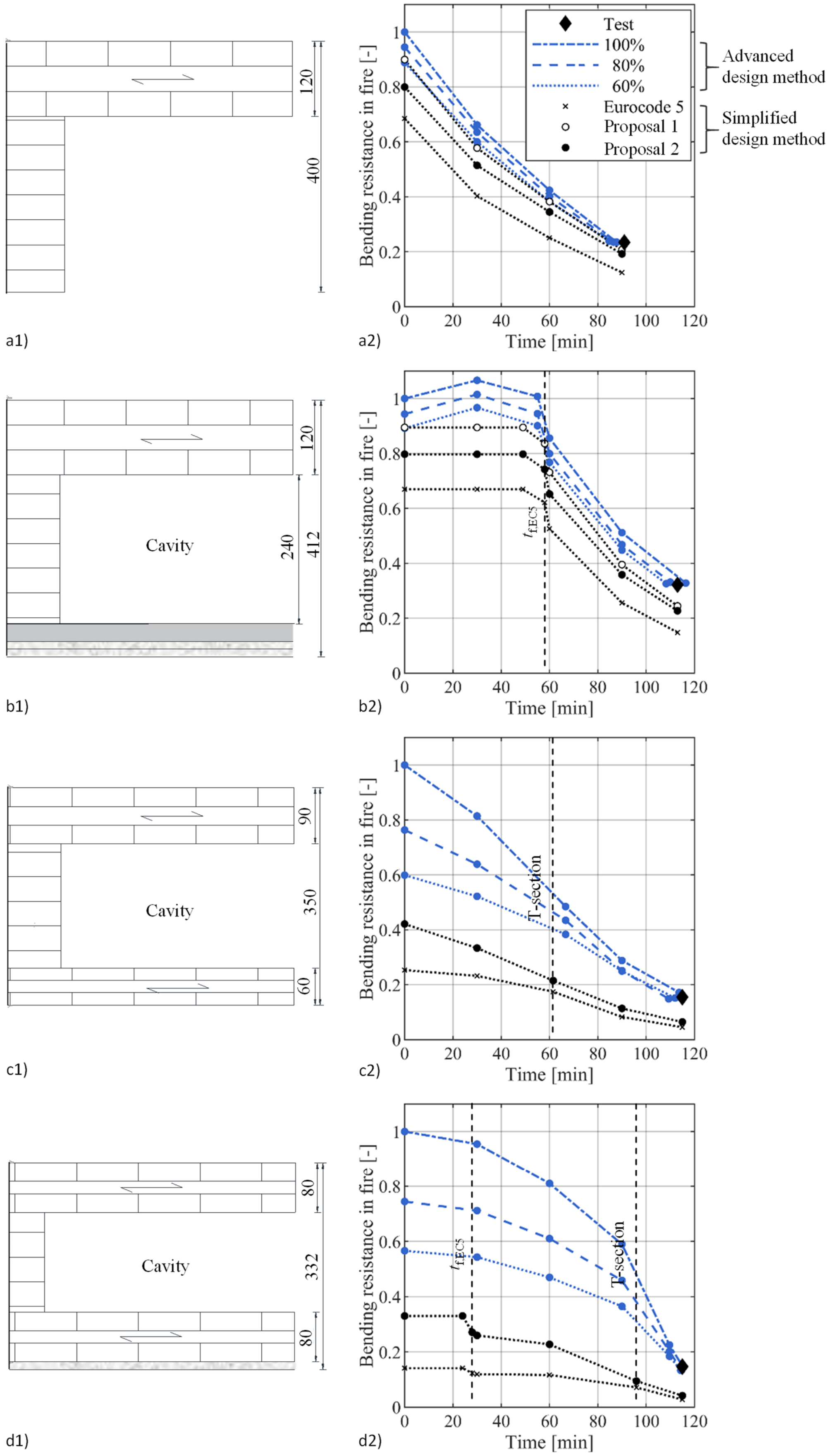

Figure 6. Bending resistance per cross-section (until failure time) in comparison to the numerical results for the three cases of the effective width (until simulation stop) and the experimental results (at failure time): a) A; b) B; c) C; d) D.

For box-sections, the high influence of the effective width leads to higher differences and a clear underestimation of the fire resistance. An optimization should be targeted in combination with an optimization of the effective width at normal temperature b_{ef}.

7 Acknowledgement

The authors gratefully acknowledge the financial support from Stora Enso Wood Products GmbH in Ybbs, Austria, with special thanks to Niko Kumer, Thomas Demschner, and Julien Lapere. The process of Python scripting has been brought forward thanks to the work of the master thesis of Pascal Hodel. The authors gratefully acknowledge the contributions of Pedro Palma (Empa, Dübendorf), and Katrin Nele Mäger (Tallinn University of Technology).

8 References

Ahn, I.-S., M. Chiewanichakorn, S. S. Chen, and A. J. Aref. 2004. "Effective flange width provisions for composite steel bridges." *Engineering Structures*, 26 (12): 1843–1851. https://doi.org/10.1016/j.engstruct.2004.07.009.

Bodig, J., and B. A. Jayne. 1993. *Mechanics of wood and wood composites*. Malabar, Fla.: Krieger Pub.

Bogensperger, T. 2013. *Darstellung und praxistaugliche Aufbereitung für die Ermittlung mitwirkender Plattenbreiten von BSP-Elementen, Research Report focus_sts 2.2.3_1*. Graz, Austria.

Brandner, R., G. Flatscher, A. Ringhofer, G. Schickhofer, and A. Thiel. 2016. "Cross laminated timber (CLT): overview and development." *Eur. J. Wood Prod.*, 74 (3): 331–351. https://doi.org/10.1007/s00107-015-0999-5.

CEN/TC 250/SC 5 N 892: M515 SC5.T1 Phase 1 Final deliverables - SC5.T1 Final Document of prEN 1995-1-1 on CLT. 2018. N-document. Brussels: CEN - CENELEC.

CEN/TC 250/SC 5/WG 4 N 193: Consolidated draft prEN 1995-1-2 for informal enquiry. 2021. N-document. Brussels: CEN - CENELEC.

Chen, Z., C. Ni, C. Dagenais, and S. Kuan. 2020. "A Temperature-Dependent Plastic-Damage Constitutive Model Used for Numerical Simulation of Wood-Based Materials and Connections." *J. Struct. Eng.*, 146 (3): 04019225. https://doi.org/10.1061/(ASCE)ST.1943-541X.0002524.

Chwalla, E. 1936. "Die Formeln zur Berechnung der voll mittragenden Breite dünner Gurt- und Rippenplatten." *Bautechnik*, 10: 73–78.

Dassault Systemes. 2019. "Abaqus FEA."

Ehrhart, T., R. Brandner, G. Schickhofer, and A. Frangi. 2015. "Rolling Shear Properties of some European Timber Species with Focus on Cross Laminated Timber (CLT):

Test Configuration and Parameter Study." *International Network on Timber Engineering Research (INTER) – Proceedings of the 2nd Meeting*. Šibenik, Croatia: ETH Zurich.

EN 1363-1:2012, Fire resistance tests - Part 1: General requirements. 2012. EN 1363-1:2012. Brussels: European Committee for Standardization (CEN).

EN 1365-2:2014, Fire resistance tests for loadbearing elements - Part 2: Floors and roofs. 2014. EN 1365-2:2014. Brussels: European Committee for Standardization (CEN).

EN 1995-1-1, Eurocode 5: Design of timber structures - Part 1-1: General - Common rules and rules for buildings. 2004. EN 1995-1-1:2004/AC:2006/A1:2008/A2:2014. Brussels: European Committee for Standardization (CEN).

EN 1995-1-2, Eurocode 5: Design of timber structures - Part 1-2: General - Structural fire design. 2004. EN 1995-1-2:2004/AC:2006/AC:2009. Brussels: European Committee for Standardization (CEN).

EN 14080:2013, Timber structures - Glued laminated timber and glued solid timber - Requirements. 2013. EN 14080:2013. Brussels: European Committee for Standardization (CEN).

ETA 20/0893: Stora Enso CLT Rib Panels - Prefabricated wood-based loadbearing stressed skin panels. 2020. ETA 20/0893 of 2020/12/01. Nordhavn: ETA-Danmark A/S.

Fahrni, R., J. Schmid, M. Klippel, and A. Frangi. 2018. "Correct temperature measurements in fire exposed wood." *World Conference on Timber Engineering (WCTE) - 10th World Conference on Timber Engineering*. Seoul, South Korea.

Franssen, J.-M., and T. Gernay. 2017. "Modeling structures in fire with SAFIR: theoretical background and capabilities." *Fire Engineering*, 8 (3): 300–323. https://doi.org/10.1108/JSFE-07-2016-0010.

Hodel, P. 2021. "CLT Rib Panels - Simulation der Tragfähigkeit im Brandfall." Master thesis. Zürich: ETH.

ISO 834-1:1999, Fire-resistance tests - Elements of building construction - Part 1: General requirements. 1999. ISO 834-1:1999. International Organization for Standardization (ISO).

Kleinhenz, M. 2022. "Cross-laminated timber rib panels in fire." Doctoral thesis. Zürich: ETH.

Kleinhenz, M., A. Just, and A. Frangi. 2021a. "Temperature-dependent thermal properties for cross-laminated timber exposed to standard fire." *International Network on Timber Engineering Research (INTER) – Proceedings of the 6th Meeting*. Online.

Kleinhenz, M., A. Just, and A. Frangi. 2021b. "Experimental analysis of cross-laminated timber rib panels at normal temperature and in fire." *Engineering Structures*, 246: 113091. https://doi.org/10.1016/j.engstruct.2021.113091.

Kleinhenz, M., M. Sterley, A. Just, and A. Frangi. 2021c. “The composite action of cross-laminated timber rib panels at elevated temperatures.” *AOSFST 2021 – 12th Asia-Oceania Symposium on Fire Science and Technology*. Brisbane, Australia: The University of Queensland.

prEN 1363-1:2018, Fire resistance tests - Part 1: General requirements. 2018. prEN 1363-1:2018. Brussels: European Committee for Standardization (CEN).

Python Software Foundation. 2018. “Python (version 3.7).”

Timoshenko, S. P. 1940. *Strength of materials - Part II Advanced Theory and Problems*. New York - Toronto - London: D. Van Nostrand Company, inc.

DISCUSSION

The paper was presented by M Kleinhenz

H Blass commented about shear deformation. Rigid connection for the GLT and rolling shear deformation in the CLT.

M Kleinhenz replied that the gamma method or advanced gamma method was considered. In long members shear was not a problem. Consideration of the cross layer showed real stress distribution for comparison with the simplified stress distribution.

M Fragiacomo commented that the width of the rib reduced a lot which would affect the glueline between the CLT and GLT. M Kleinhenz responded that the model would overestimate the temperature of the glueline as the falling off of charred material was assumed to occur instantaneously which is conservative.

Fire design methods for timber frame assemblies – an improved model for the Separating Function Method

Michael Rauch, Technical University of Munich

Norman Werther, Technical University of Munich

Alar Just, Tallinn University of Technology

Stefan Winter, Technical University of Munich

Keywords: Fire protection, fire resistance, separating function, timber elements, gypsum boards, wood-based panels, charring rate

1 Introduction

In consequence of the revision of the Eurocodes, verification methods based on calculation models of the fire resistance of timber elements are becoming increasingly important. At the same time, the aspiration of resource-efficient construction methods leads to the application of renewable materials - which are usually combustible - in multi-storey timber buildings. For timber elements, such as cross laminated timber (CLT) or timber frame assemblies (TFA), the possibilities to calculate the fire resistance according to EN 1995-1-2 (2004) are strictly limited. Manufacturer-neutral design methods lead to greater flexibility compared to producer specific approval documents. While the structural engineer already applies calculation-based verification methods for the load-bearing capacity of timber elements, calculation models for the separating function are often unknown or not used in practice. This paper describes a holistic and expandable calculation model for the Separating Function Method (SFM) which is applicable until 120 min fire resistance and further extensions for the practical use of the existing model in prEN 1995-1-2.

2 Motivation

During a comprehensive analysis of existing calculation methods for the SFM in COST-Action FP 1404 (Just et al., 2018), the EN 1995-1-2 (2004), the method by Schleifer (2009) and the improvements by Mäger and Just (2018) were compared to each other, to identify gaps and improvement potentials. The aim of the evaluation was to extend the calculation method for the SFM for a scope of application up to 120 min fire resistance. Within this analysis, the different methods and the influence of different construction layers (materials) were investigated. In this paper an extended model for the SFM and improvements for the performance of wood-based panels and of gypsum boards are described.

3 Concept of the calculation Model

3.1 Existing concept of the calculation model for the SFM

In prEN 1995-1-2 (2021) the SFM, based on Schleifer (2009) with the extensions by Mäger and Just (2018), is proposed as future method to evaluate timber frame and solid timber elements under standard fire exposure with respect to compartmentation. Here the fire resistance is the sum of the protection times of the individual layer of an assembly, considering a maximum temperature criterion of 270° C (temperature increase ΔT = 250 K) for all layers except of the last layer and the contribution of the insulation capacity (temperature increase ΔT = 140 K) of the last layer (see Figure 1).

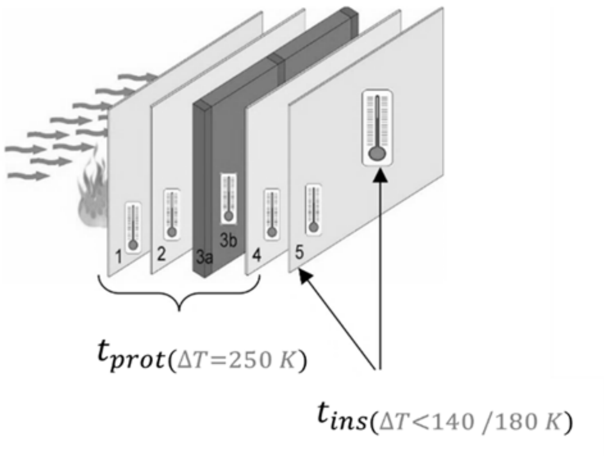

Figure 1. Shematical description of the separating function method (SFM) according to Schleifer (2009).

The fire resistance (criterium I) of the whole assembly can be calculated as follows:

$$t_{ins} = \sum_{i=1}^{i=n-1} t_{prot,i} + t_{ins,n} \tag{1}$$

$$t_{prot,i} = (t_{prot,0,i} \cdot k_{pos,exp,i} \cdot k_{pos,unexp,i} + \Delta t_i) \cdot k_{j,i} \tag{2}$$

$$t_{ins,n} = (t_{ins,0,n} \cdot k_{pos,exp,n} + \Delta t_n) \cdot k_{j,n} \tag{3}$$

where:

$t_{prot,i}$ is the protection time of the considered layer *i*, in min;

$t_{ins,n}$ is the insulation time of the last layer *n*, in min;

$t_{prot,0,i}$	is the basic protection time of the considered layer *i*, in min;
$k_{pos,exp,i}$	is the position coefficient that takes into account the influence of layers preceding the layer considered;
$k_{pos,unexp,i}$	is the position coefficient that takes into account the influence of layers backing the layer considered;
$k_{j,i}$	is the joint coefficient for layer *i*;
Δt_i	is the correction time for considered layer *i*, in min.

Equations for different building materials and layers, considering the position within the assembly and the joint design, allow the calculation of the protection and insulation time of different assemblies. For the fire exposed layer, the benefit of fire protection systems, which still protects the backing layers after reaching the 270° C criterion can be considered. This method is based on the k_2-factor according to prEN 1995-1-2 (2021) and the publication of Mäger and Just (2018).

3.2 New concept for the protection time of protected layers

During the research project F-REI 90 (Rauch, et al. 2022) a series of fire tests with long fire exposure was conducted and used for the development of an improved model (Rauch, 2022) for the SFM. The concept of the new approach allows to consider the benefit of the fire protection system for all layers in the construction, depending on the failure times of the protecting layers. This method combines the advantages of the calculation method based on Schleifer (2009) – all protection layers are considered implicitly by specific equations - and of Mäger and Just (2018), where the failure and the protective effect of the fire exposed layer (fire-protection system) is considered explicitly by the k_2-factor. The explicit consideration of the failure (t_f) of protecting layers leads to more realistic results of the calculation model.

The new concept is based on the protection times (t_{prot}), the failure times (t_f) and the k_2-factor (k_2) for each layer. The method is flexible to include new materials or improvements for the equations of individual layers and fully compatible to the calculation model of prEN 1995-1-2 (2021).

Figure 2 corresponds to the current model of prEN 1995-1-2 (2021), based on the approach of Mäger and Just (2018). The basic protection time of layer two can be increased by the k_2-factor which includes the preheating and the protective effect of the layer on the fire exposed side (STEP 1). In the improved model (Rauch, 2022) the preheating can be considered explicitly by the $k_{pos,exp}$ value. Thus, an ideal basic protection time was calculated which could be combined with the existing factors for the preheating ($k_{pos,exp}$) and for the influence of the backing material ($k_{pos,unexp}$).

STEP 1 (prEN 1995-1-2)	STEP 2 (improved model)

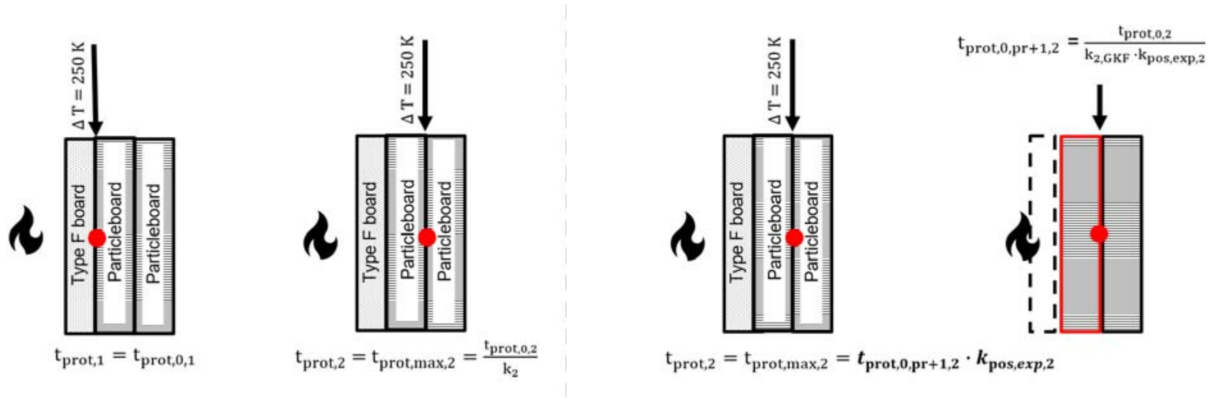

$t_{prot,i}$	is the protection time of the considered layer *i*, in min;
$t_{prot,0,pr+1,2}$	is the maximum basic protection time of the protected layer 2 (ideal basic protection time) in min;
$t_{prot,max,2}$	is the maximum protection time of the second layer (fully protected layer) in min;
$k_{pos,exp,2}$	is the position coefficient of layer 2 that takes into account the influence of layers preceding the layer considered;

Figure 2. A new concept for the SFM – example of protected particle boards in combination with a gypsum plasterboard (Type F) fire protection system.

This improved method allows to calculate a **basic protection time** for each layer, depending on if it is fully protected or directly exposed to the fire. Both protection times are defined by reaching a temperature increase of 250 K behind the layer and can be combined with the position coefficients to calculate the **protection time**.

Thus, the protection time of the construction layer can vary between a fully protected layer (Figure 3 – period C and Equation 5) or the protection time of the layer without a protective layer (Figure 3 – period A – Equation 4).

$$t_{prot,i} = t_{prot,0,i} \cdot k_{pos,exp} \cdot k_{pos,unexp} \tag{4}$$

$$t_{prot,pr+1,i} = t_{prot,0,pr+1,i} \cdot k_{pos,exp,pr+1,i} \cdot k_{pos,unexp} \tag{5}$$

$$t_{prot,0,pr+1,i} = \frac{t_{prot,0,i}}{k_2 \cdot k_{pos,exp,pr+1,i}} = \begin{cases} t_{prot,max,2} + 0{,}6 \cdot t_{prot,i-1} & \text{with } \sum t_{prot,i-1} \leq \frac{t_{prot,0,pr+1,i}}{2} \\ \sqrt[3]{\frac{t_{prot,max,2}{}^2}{0{,}25}} \cdot t_{prot,i-1} & \sum t_{prot,i-1} > \frac{t_{prot,0,pr+1,i}}{2} \end{cases} \tag{6}$$

$$k_{pos,exp,pr+1,i} = \begin{cases} 1 - 0{,}6 \cdot \dfrac{\sum t_{prot,i-1}}{t_{prot,0,pr+1,i}} & with \quad \sum t_{prot,i-1} \leq \dfrac{t_{prot,0,pr+1,i}}{2} \\ 0{,}5 \cdot \sqrt{\dfrac{t_{prot,0,pr+1,i}}{\sum t_{prot,i-1}}} & \quad\quad\;\; \sum t_{prot,i-1} > \dfrac{t_{prot,0,pr+1,i}}{2} \end{cases} \tag{7}$$

where:

$t_{prot,0,i}$	is the basic protection time of the considered layer *i*, in min;
$t_{prot,i}$	is the protection time of the considered layer *i*, in min;
$t_{prot,0,pr+1,i}$	is the maximum basic protection time of a protected layer (ideal basic protection time) in min;
$t_{prot,pr+1,i}$	is the maximum protection time of a protected layer (ideal basic protection time) in min;
$k_{pos,exp,i}$	is the position coefficient that takes into account the influence of layers preceding the layer considered;
$k_{pos,unexp,i}$	is the position coefficient that takes into account the influence of layers backing the layer considered;

If the preceding layer fails (falls-off) before the maximum temperature increase of 250 K is reached, the protection time of the layer can be calculated by linear interpolation (Figure 3 – period B). The benefit of the protection time between the protected and unprotected layer can be calculated by adding the ΔT value (Figure 3).

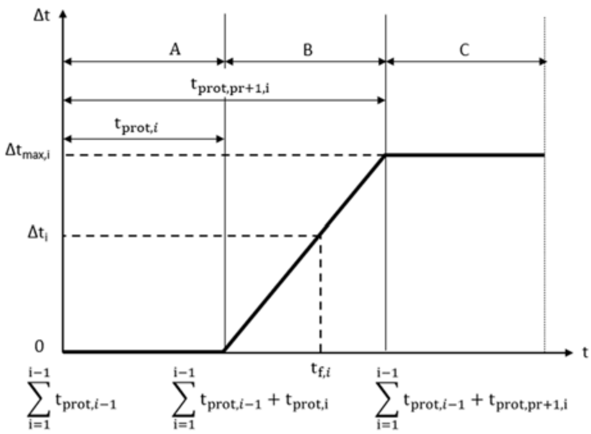

Figure 3. The benefit of protected layers *ΔT* by linear interpolation (B) between non protected layers (A) and fully protected layers (C).

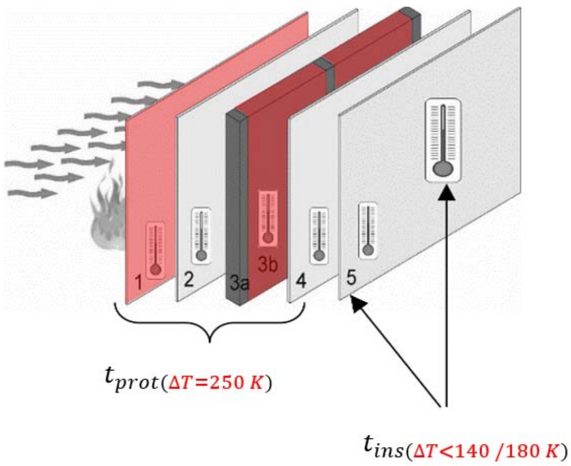

Figure 4. Example for different protection layers in an assembly:
Protection Layer 1: Type F on the fire exposed side.
Protection Layer 3: Stone wool cavity insulation.

In the new method the effect of the protection of layers after reaching 250 K at its unexposed side (e.g. gypsum plasterboard Type F, gypsum fibreboard, stone wool,…) until the failure (e.g. fall-off, melting,…) can be considered for all layers of the construction. Additionally, the new method allows to combine the protection time of unprotected and protected layers with the position coefficient of the exposed and unexposed side (EQ 5). The ΔT value can be calculated and added to the equation but is not necessary anymore. The calculated protection time includes the preheating (considered by $k_{pos,exp}$) and the protective effect, which is included in $t_{prot,pr+1}$.This method additionally gives the opportunity to calculate multi-layer fire protection systems of different layers of gypsum boards.

3.3 Validation

For fire protection systems on the exposed side, the results correspond to the model of prEN 1995-1-2 (2021). For constructions with more than one protection system or with protective layers inside of the construction (e.g. stone wool insulation layers, which stay in the cavity) the new model helps to get more economic results which are still conservative (Table 1).

Table 1. Validation – Tests with stone wool cavity insulation used as fire protection system.

Construction		$t_{ins,test}$	$t_{ins,Schleifer}$	$t_{ins,Mäger}$	$t_{ins,this\ Model}$
Test 1	(Rauch 2022)	> 116 min	85 min	82 min	124 min
Test 2	(Scheidel et.al. 2021)	> 120 min	52 min	52 min	93 min
Test 3	(König et.al. 1997)	103 min	71 min	73 min	83 min

4 Extension and harmonization of design equations

4.1 Basics

The model according to prEN 1995-1-2 (2021) for the SFM is based on the component additive method according to Schleifer (2009). The model of this approach (cf. chapter 3) extends this calculation model and is compatible to the existing calculation methods of prEN 1995-1-2. The input parameter and the equations for protection times (t_{prot}), insulation times (t_{ins}) and failure times (t_f) can be implemented in both models. During the investigation of the calculation method, additional studies for specific layers / materials were conducted.

For wood-based boards the calculation of the start time of charring ($t_{ch,300°C}$) according EN 1995-1-2 (2004) and the protection times ($t_{prot,270°C}$) according to Schleifer

(2009) lead to significant different results although the temperature criteria are comparable. However, previous investigations by the authors indicates that both models can be harmonized (cf. section 4.2)

For gypsum plasterboards Type F an evaluation of full-scale fire tests according to a database held by TalTech and TUM (which is confidential in terms of producers) show lower values for the start of charring (t_{ch}) compared to the protection time of prEN 1995-1-2 (2021), which are based on the investigations of Schleifer (2009). Thus, new design equations for the start of charring (t_{ch}) were conducted (cf. section 4.3).

4.2 Wood-based panels – a harmonized model based on charring rates

The basic design charring rates of wood-based panels according to EN 1995-1-2 (2004) are indicated in Table 2. The charring is based on the 300° C isotherm.

Table 2. Basic design charring rates of wood-based panels according to EN 1995-1-2(2004).

	β_0 [mm/min]	Initial density [kg/m³]	Initial thickness [mm]
Solid wood panel	0,9	450	20
Plywood	1,0	450	20
Wood-based-panels except plywood	0,9	450	20

For panels with a thickness $h_p \leq 20$ mm the charring rate must be increased by the factor k_h. The variation in densities ρ_k can be taken into account by multiplying the charring rate by the factor k_ρ. These modification factors are given in EN 1995-1-2 (2004) and correspond to prEN 1995-1-2 (2021) with:

$$k_h = \begin{cases} 1{,}0 \; for \; h_p \geq 20mm \\ \sqrt{\dfrac{20}{h_p}} \end{cases} \tag{8}$$

$$k_\rho = \sqrt{\frac{450}{\rho_k}} \tag{9}$$

According to Schleifer protection times are defined by the 250 K temperature increase (typically 270° C) of wood-based panels, backed by another wood-based panel. Because of the high gradient of the temperature rise behind a wood-based panel between 270° C (t_{prot}) and 300° C (t_{ch}) the times until reaching theses temperature criteria are almost equal. The results of the simulation with the material properties according to Rauch (2022) and the test results show good accordance and the steep curve gradient could be confirmed (Figure 5).

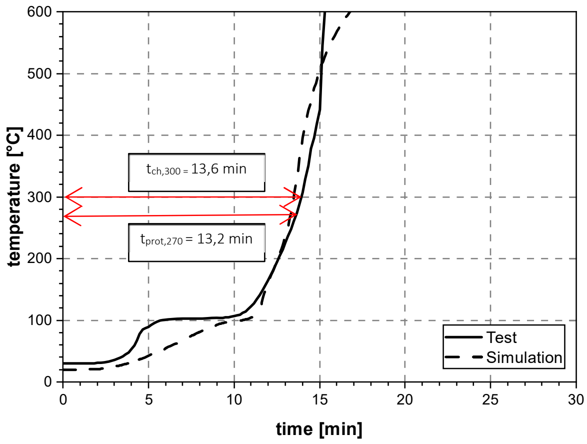

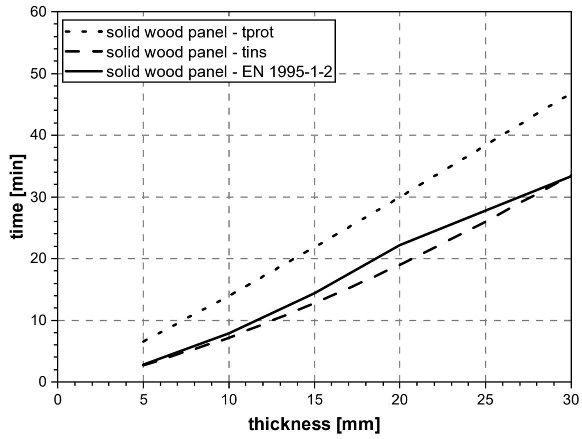

Figure 5. Temperature increase behind a 15 mm medium density fibre board in the test and in the simulation model.

Figure 6. Charring according EN 1995-1-2 (2004), protection times (t_{prot}) and insulation times (t_{ins}) according to Schleifer (2009) for a solid wood panel.

The charring model according EN 1995-1-2 (2004) (solid line in Figure 6) differs from the basic protection times for the panels (dotted line) and shows a good match with the insulation time (dashed line). Based on a literature study (Wörle, 2019; Werther, 2016; Norén & Östman, 1996) it becomes clear, that the published charring rates are based on different measurements. In some tests the charring of a panel was measured by the residual cross-section, other authors measured the temperature increase on the unexposed side. Compared to the protection times of Schleifer (2009) the lower values of EN 1995-1-2 (2004) are the results of the measurement (charring through) on the unexposed side, which correspond nearly with the insulation times according to the SFM. The harmonized charring rates according to Table 3 were calculated by the protection times taking into account the influence of the backing materials. The results confirm the influence of the backing material to the protection times and on the charring rate (average value over the board thickness). With the introduction of the SFM the backing materials can be considered and thus, both models can be homogenized. As a result reduced charring rates were derived.

Table 3. Homogenized charring rates of wood-based panels.

	β_0 [mm/min]	Initial density [kg/m³]	Initial thickness [mm]
Solid wood panel	0,65	450	20
Particle board	0,72	450	20
OSB and fibre boards	0,9	450	20

For solid wood panels (backed by another solid wood panel) the value of 0,65 mm/min confirms the charring rate used for the first layer of CLT-elements according to prEN 1995-1-2(2021). Thus, in future the same charring rates can be used within the calculation of the charring depth and the calculation of protection times for wood-based panels. The influence of the backing material can be considered by the position coefficients in the SFM.

$$t_{prot,0} = \frac{h_p}{\beta_0 \cdot k_\rho \cdot k_h} \qquad (10)$$

where:

$t_{prot,0}$	is the basic protection time of the considered layer *i*, in min;
h_p	thickness of the board
β_0	basic design charring rate
k_ρ	density factor according EN 1995-1-2 (2004)
k_h	thickness factor according EN 1995-1-2 (2004)

Instead of the existing exponential equation given by Schleifer (2009) to describe the insulation times (t_{ins}) for wood-based panels or solid wood as last layer, the temperature profile within the cross section can be used to determine the minimum distance between the 300° C isotherm and reaching 160° C (140 K temperature increase) on the unexposed side. Here, the thickness of the boards shows an influence on the temperature gradient, thus, the minimum residual thickness (d_{res}) is dependent of the board thickness, as shown in Figure 7.

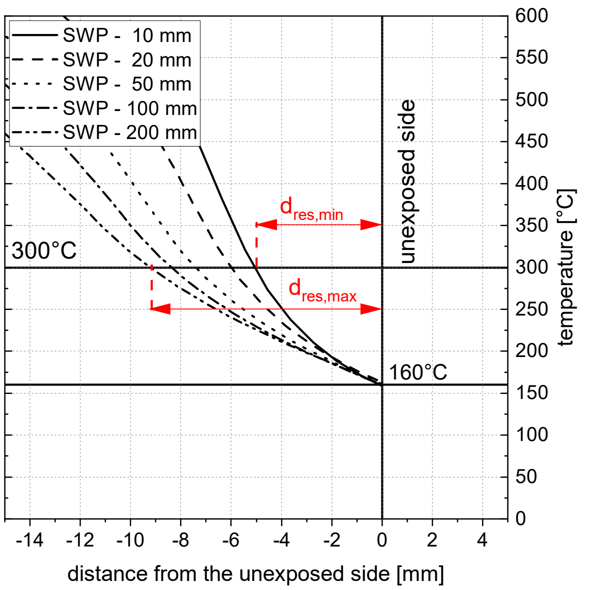

Figure 7. Temperature profile for different board thicknesses beween the 300° C isotherme and the 160° C isotherme on the unexposed side of a solid wood panel (SWP).

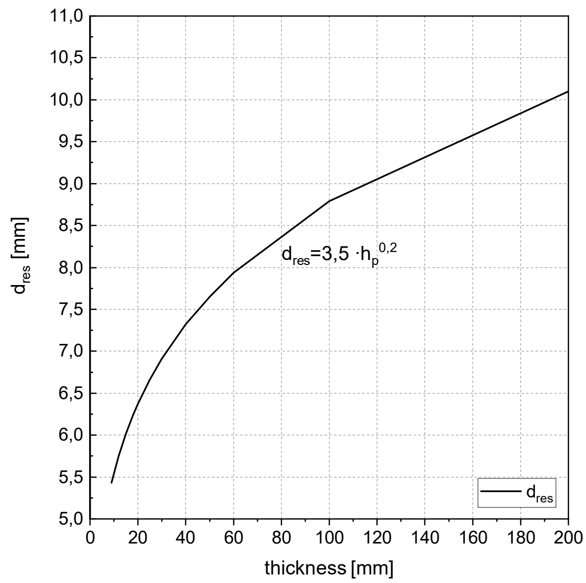

Figure 8. Equation for the residual crossection depending on the board thickness (h_p).

The comparison of the homogenized model shows good correlation with the existing model of Schleifer (2009) (VS) and the numerical simulations (Figure 9 & Figure 10). For particle boards with thicknesses ≥ 30 mm, the new model is more conservative.

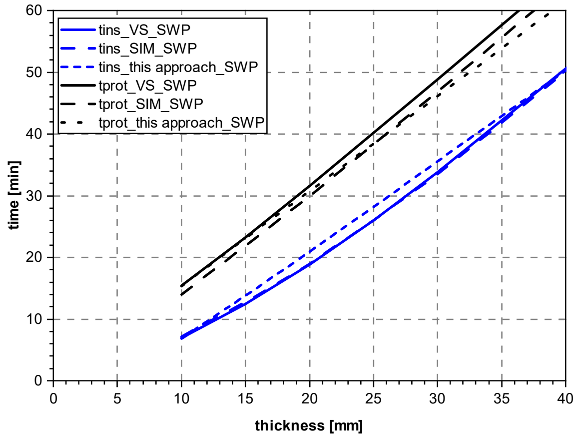

Figure 9. Comparison of the calculation model and the simulation model for solid-wood panels (SWP).

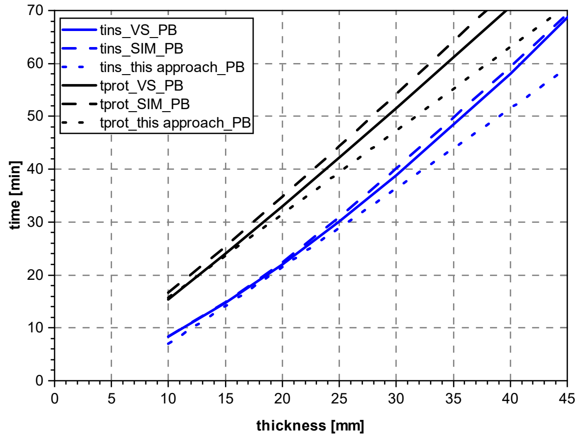

Figure 10. Comparison of the calculation model and the simulation model for particle boards (PB).

4.3 Gypsum plasterboards – Proposal for new protection times

An evaluation of different full-scale fire tests during the research project F-REI 90 (Rauch et.al., 2022) shows a difference between the protection times according to the SFM (Schleifer, 2009 & prEN 1995-1-2,2021) and the test results. Thus, the collected data from the database of TalTech and TUM were further evaluated and compared to the simulation model (Figure 11).

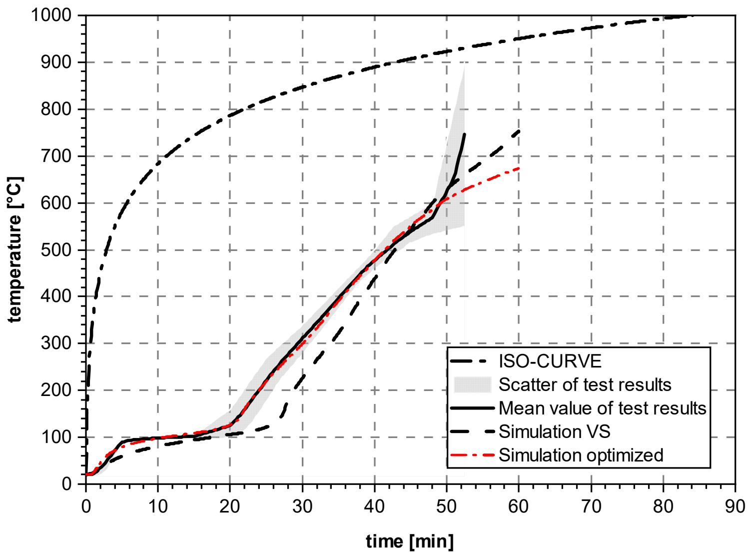

Figure 11. Simulation model based on the material properties according to Schleifer (2009) (VS) and optimized material properties according to Rauch (2022) (Simulation optimized) in comparision to the scatter of test results of gypsum plasterboards Type F backed by massive timer elements or wood-based panels.

According to Figure 11 the existing material model according to Schleifer (2009) was optimized in Rauch (2022) and new material parameters for the simulation were proposed. The optimized simulation model show good correlation to the mean value of the test results (black line) and was used to determine new design equations for the basic protection time of gypsum plasterboards Type F ($t_{prot,0,TypeF}$).

The improved equation was determined by a linear regression of the simulation results for different board thicknesses. The 300° C criteria was used as temperature criteriaon for the char layer according to EN 1995-1-2 and EN 13381-7 and was also used for this approach. The result of the calculation was a linear equation of the protection time for gypsum plasterboards (Type F) which show good accordance to the simulation and the test results (Figure 12).

$$t_{prot,0} = t_{ch} = 2{,}79 \cdot h_p - 13{,}9 \approx 2{,}8 \cdot h_p - 14 \tag{11}$$

where

t_{prot}	[min]	protection time
t_{ch}	[mm]	start time of charring
h_p	[mm]	thickness of the gypsum plasterboard Type F

The result (EQ 11) confirms the existing equation according in EN 1995-1-2 (2004), based on the investigations of König & Walleij (1999).

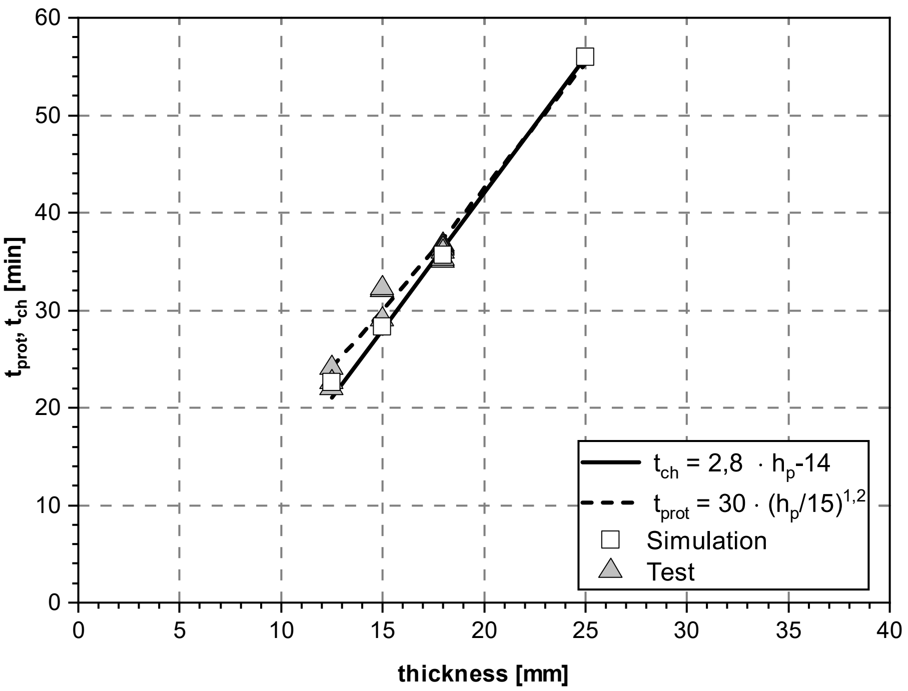

Figure 12. Comparison of the calculation model for t_{ch}, new approach and equation for start of charring according to EN 1995-1-2 (2004), the equation for the protection time according to prEN 1995-1-2 (2021) and the results of the simulation and the test results.

5 Outcome

Based on the model for the SFM according to Schleifer (2009) and the improved Model according to Mäger & Just (2018) an extended calculation model considering the advantages of both models was developed. In this model the failure times of each layer (like the fall-off of biobased insulations layers) or the positive influence of insulation layers - which stays in place for the whole fire resistance (e.g. stone wool) – can be considered. This model is compatible to the existing model according to prEN 1995-1-2 and allows to include existing results for individual layers.

For wood-based panels the protection times according to the SFM, based on Schleifer (2009), were homogenized with the charring model. The new charring rate is based on values of wood-based panels, backed by another wood-based panel. Void cavities and insulation materials reduce the protection time and thus could be considered by an increasing charring rate.

- Solid-wood-panel: 0,65 mm/min (450 kg/m³)
- Particle board: 0,72 mm/min (450 kg/m³)
- OSB- /wood-fibre board: 0,9 mm/min (450 kg/m³)

Homogenized charring rates for wood-based panels can be used to calculate the protection times (t_{prot}) for the SFM and to calculate the start of charring (t_{ch}) as well as the contribution for the insulation time in the SFM.

Based on a series of fire tests and a finite element simulation (Rauch, 2022), protection times for gypsum boards were carried out which confirm the existing equation of EN 1995-1-2(2004)

$$t_{\mathrm{prot,0}} = \mathrm{t}_{ch} = 2{,}80 \cdot h_p - 14 \tag{12}$$

where

$t_{prot,0}$	[min]	basic protection time
t_{ch}	[mm]	start time of charring
h_p	[mm]	thickness of the gypsum plasterboard Type F

The results of this approach can be implemented in the SFM of the future Eurocode prEN 1995-1-2. Thus, the optimized equations improve the fire resistance regarding compartmentation and the start of charring as crucial influencing factor of the load bearing capacity for timber frame assemblies and solid timber structures.

6 Outlook

Further experimental and numerical investigations can be implemented in the calculation model and help to extend the field of application. Additionally, producer specific values can be used to optimize the calculation method for specific products. In the improved method the fall-off can be considered for each layer in the construction as an explicit parameter. Thus, materials with smaller failure times or materials with failure times, which exceed the protection time, can be added to the model.

It becomes apparent that the failure times and the protection factor k_2 are increasingly important in the calculation model and additional investigations are necessary to improve these factors in future.

7 Acknowledgment

The authors acknowledge the support of the German research program Zukunft Bau within the research project F-REI 90 (Rauch et.al. 2022). The project was only possible by the support of the industry for the material of the test specimens and the additional results of fire tests.

8 References

Eurocode 5 (2004) Design of timber structures – Part 1-2: Structural fire design. CEN (EN 1995-1-2).

CEN/TC 250/SC 5/WG 4 N 180: SC5.T4 Final Document of prEN 1995-1-2 on fire. 2021. N-document. Brussels: CEN - CENELEC.

Just, A., Schmid, J., (eds)(2018), Guidance Document for implementation of materials and products in fire design methods of timber frame assemblies, COST Action FP 1404, Zürich, Switzerland.

König, J. & Walleij, L. (1999). One-dimensional Charring of Timber Exposed to Standard and Parametric Fires in Initially Unprotected and Postprotection Situations. Rapport (Trätek, Rapport I 9908029). Institutet för Träteknisk Forskning. Stockholm.

König, J., Norén, K., Olesen, F. & Hansen, F. (1997). Timber frame assemblies exposed to standard and parametric fires: Part 1: Fire tests. Institutet för Träteknisk Forskning, Stockholm

Mäger, K. N., Just, A. & Frangi, A. (2018). Improvements to the Component Additive Method. SiF 2018– The 10th International Conference on Structures in Fire. Ulster University, Belfast, UK.

Norén, J. & Östman, B. (1986). Contribution To Fire Resistance from Building Panels. Fire Safety Science, 1, S. 325–335.

Rauch, M., Werther, N., Suttner, E., Winter S. (2022): F-REI 90: Ein analytisches Berechnungsverfahren für Holzrahmen- und Holzmassivbauteile bis zu einer Feuerwiderstandsdauer von 90 Minuten. BBSR-Online-Publikation

Rauch, M. (2022), Beurteilung der raumabschließenden Funktion brandbeanspruchter Holzbauteile mittels einer „Component Additive Method". Dissertation. Technical University Munich, Munich.

Scheidel, S., Dienst, S., Götz, T., Kornadt, O. (2021) Brandschutztechnisches Verhalten von raumabschließenden Holzrahmenkonstruktionen. Bauphysik. https://doi.org/10.1002/bapi.202100016

Schleifer, V. (2009) Zum Verhalten von raumabschliessenden mehrschichtigen Holzbauteilen im Brandfall, PhD Thesis ETH No. 18156, ETH Zurich.

Werther, N. (2016). Einflussgrößen auf das Abbrandverhalten von Holzbauteilen und deren Berücksichtigung in empirischen und numerischen Beurteilungsverfahren. Dissertation. Technische Universität München. München.

Wörle, V. (2019). Ganzheitliche Betrachtung der Abbrandrate von Holz und Holzwerkstoffen: Einflüsse, Rahmenbedingungen der Brandbeanspruchung und Vorgehen bei der Ermittlung. Masterarbeit. Technische Universität München. München.

DISCUSSION

The paper was presented by M Rauch

K Mäger received confirmation that a calibration method can be found in PhD thesis. They also agreed that the current method is more conservative when the number of protection layer increases. M Rauch said for long fires, the problem was the quasi-mechanical behaviour. M Rauch added that different input values were used and the stone wool would stay in place.

A Frangi and M Rauch discussed the long fire performance and the choice of temperature criterion. The criterion of 270 °C was used for wood-based boards. For other materials different values should be considered. A Frangi referred to the chosen power equation and questioned whether there is a need for such precision given the variability. M Rauch agreed but this was based on test results.

The fire protection of timber members using gypsum boards

Alar Just, Tallinn University of Technology

Michael Rauch, Technical University of Munich

James Walker, Milner Associates

Norman Werther, Technical University of Munich

Keywords: fire design, timber, gypsum plasterboards, gypsum fibreboards, failure time

1 Introduction

The effect of fire protective linings, to improve the fire resistance of timber elements, is taken into account by determining the start time of charring (t_{ch}) behind the lining and the failure time ($t_{f,}$) of the lining. According to the European Charring Model, these times distinguish between different linear charring phases of the protected timber member. There is no charring in Phase 0. Charring in Phase 2 is relatively slow while the protection remains in place. After failure of the protection, charring in Phase 3 is fast. Following the formation of a consolidated char layer, Phase 4 charring slows again (see Figure 1). Phase 1 charring is for initially unprotected timber and is not relevant here. The start time of charring t_{ch} is mainly defined by the material properties of the lining and the backing material. The failure time of the protection t_f is dependent on the lining material, the fastening system, the backing material and also the orientation. The protection provided by linings is shortest when backed by insulation materials and longer when backed by massive timber or void cavities.

Gypsum boards are widely used materials to protect timber structures against fire. The start times of charring in the new prEN 1995-1-2 are based on the new Separating Function Method (SFM) as verified by tests. The difference between the start time of charring behind gypsum plasterboard covering timber frame assemblies (TFAs) and massive timber members is taken into account by using different position coefficients for the gypsum board ($k_{pos,unexp}$).

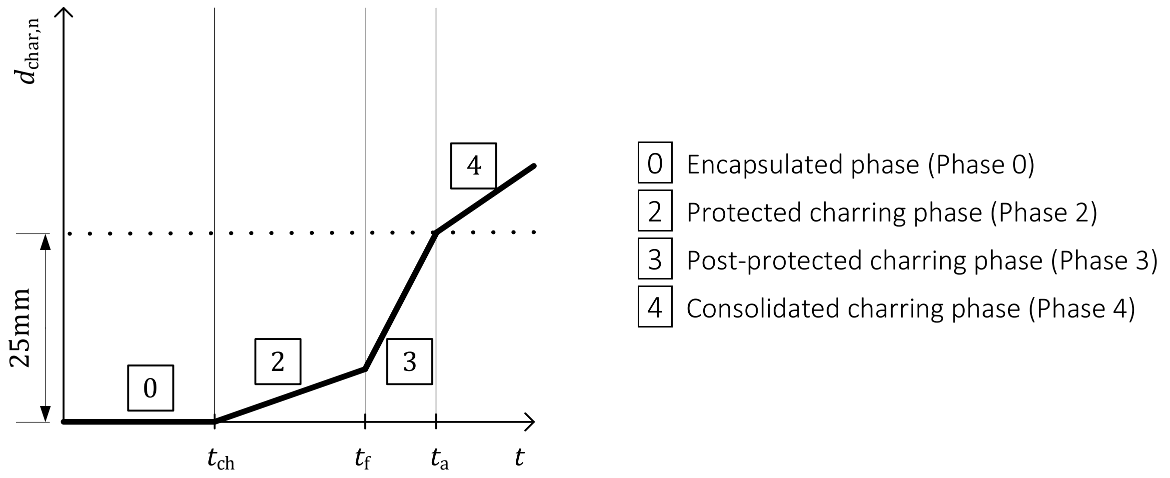

Figure 1. European Charring Model for initially protected timber member.

The start time of charring (protection time) and the failure times will be influenced by the following factors (Figure 2.):

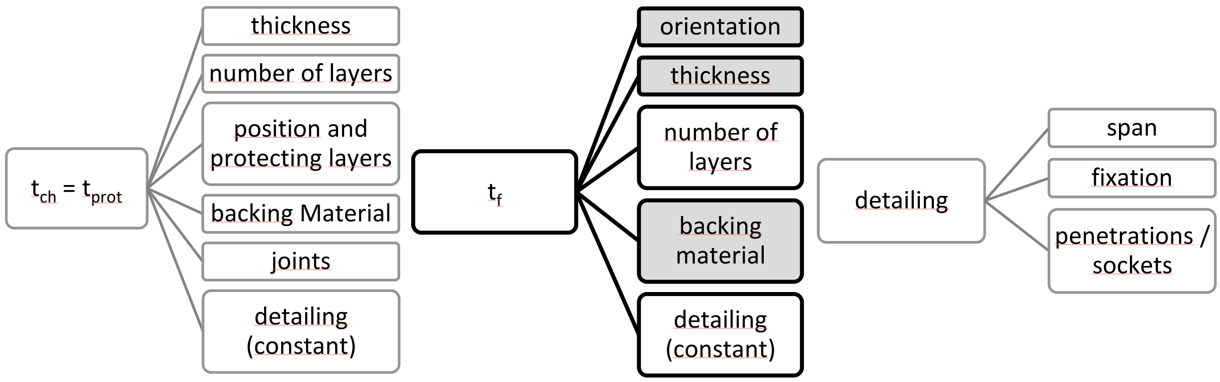

Figure 2. Influencing factors for the start time of charring (t_{ch}) and the failure times (t_f) of gypsum boards. The grey filled parameters for t_f were varied during the experimental investigation.

The time at which the temperatures behind the protection reaches 300 °C as well as the failure time of the protection are necessary for the calculation model of prEN 1995-1-2. Both, observations and temperature measurements were evaluated to get values for t_f and t_{ch}. The failure times of gypsum plasterboards are evaluated for TFAs. It is known that the failure times of gypsum plasterboards on TFAs are longer when backed by void cavities compared with TFAs with cavity insulation. From testing, it is also clear that the failure times of gypsum plasterboards on massive timber members are considerably longer compared to TFAs with insulation.

This paper focuses on the analysis and determination of failure times for gypsum plasterboards Type A, Type DF (GtDF) and gypsum fibreboards (GF) on massive timber structures and void cavities.

2 Failure times based on full scale test results

Failure of gypsum board in the assembly depends on different parameters. Failure can happen due to not sufficient spacing and anchorage length of fasteners, spacing of studs, type of the board, thickness of the board, orientation of the assembly (wall or floor) and also backing material.

Modelling of the behaviour of gypsum boards including the crack behaviour is too complicated. In prEN 1995-1-2:2022 generic values for failure times of gypsum plasterboards are proposed. These generic values are based on statistical analysis of a database consisting of 450 full-scale fire test results and are valid under certain detailing rules only. The database itself is confidential in terms of producers and is held by TUM and TalTech.

In 2016, CEN TC250 SC5 WG4 (the working group responsible for updating the fire part of Eurocode 5) decided to use 5%-fractile values for the failure times from the database. Kraudok (2020) made a statistical analysis for gypsum plasterboards Type A and Type F in wall and floor applications and derived 5%, 20% and 50% fractile values of the failure times along with design equations (Table 1). Eskla (2021), Kiholane (2021) and Õismets (2021) made a sensitivity analysis to evaluate the effect of failure times on the fire resistance of TFAs, linear glulam members and plane CLT members.

Table 1. Failure times of gypsum plasterboards, Type F on timber frame assemblies (Kraudok 2020).

Design case TFA with gypsum plasterboard	Failure time (t_f)		
	5% fractile value	20% fractile	50%-fractile
	min	min	min
Walls			
Type F, 1 layer	$3.6h_p-14$	$4.6h_p-25$	$4.5h_p-12$
Type F, 2 layers	$3.4h_p-27$	$4.4h_p-50$	$2.0h_p+31$
Floors			
Type F, 1 layer	$1.3h_p+7.5$	$1.3h_p+8.6$	$0.2h_p+32$
Type F, 2 layers	$0.4h_p+39$	$1.5h_p+15$	$4.0h_p-44$
h_p – total thickness of layer(s) in mm			

Figure 3 and *Figure 4* show the fire resistance of timber frame wall assemblies using 5%, 20% and 50% fractiles of the failure times for one layer of gypsum plasterboard, Type F. For assemblies with PL1 (e.g. stone wool) cavity insulation, there is almost no difference in the calculated fire resistance. According to the calculation model of prEN 1995-1-2, a later failure leads to faster charring of the timber studs. For assemblies with PL2 (e.g. glass wool) cavity insulation, there is some difference using the 5% fractile value and 20% fractile value. However, the difference is not considered significant. The behaviour of PL2 insulation, after failure of the protection, is considered by the recession of the insulation with a rate of 30 mm/min.

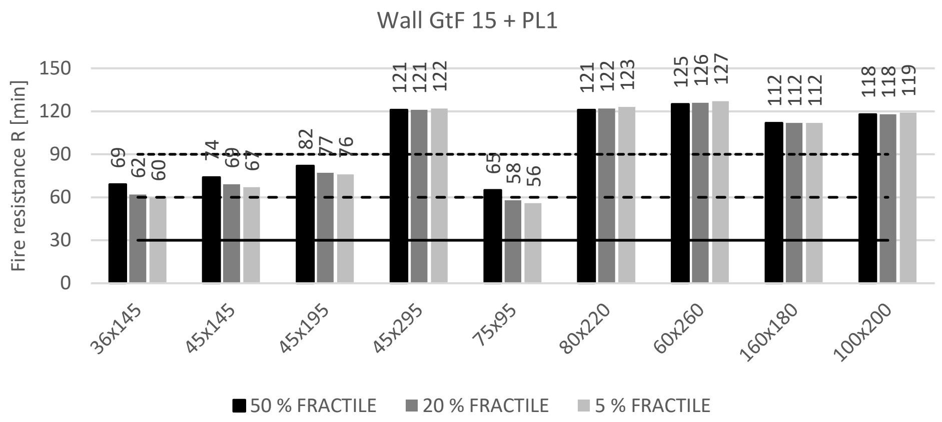

Figure 3. Fire resistance (R) of timber frame walls with PL1 insulation (stone wool) and different stud cross-sections using different fractile values of failure times of gypsum boards GtF 15 mm (Eskla 2021).

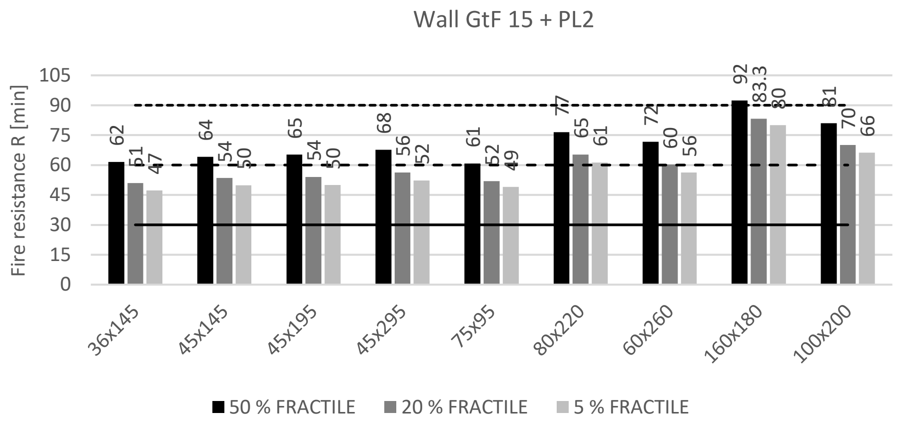

Figure 4. Fire resistance (R) of timber frame walls with PL2 insulation (glass wool) and different stud cross-sections using different fractile values of failure times of gypsum boards GtF 15 mm (Eskla 2021).

The analysis of the influence of different fractile values for the fall-off times of the gypsum plasterboards to the overall fire resistance of the assembly showed that 20% fractile values are appropriate to be used to calculate fire resistance.

3 Protection on massive timber

In the project CLT protect, existing experimental data for failure times were evaluated and extended by a series of comparative (according to EN 1363) fire tests of walls and ceilings. These reference values were extended by small-scale fire tests to investigate different thicknesses and orientations. The results confirm the expectation, that failure times of gypsum boards fixed to CLT- elements or to wood-based boards exceed the failure times of gypsum boards backed by insulation materials, typically used for TFAs.

The project was divided into five different working packages to evaluate the failure times of the gypsum linings according to Figure 7.

- Collection and analysis of fire test data with gypsum boards,
- Performing comparative fire tests using Type DF and GF,
- Thermal simulations with effective thermal properties for further investigations,
- Evaluation of the collected data and test results to determine failure times and
- Proposal of optimized failure times on massive timber elements.

To evaluate the failure times of existing fire tests, the results included in the previously mentioned database were assessed according to the failure times of gypsum board on CLT elements or wood-based boards.

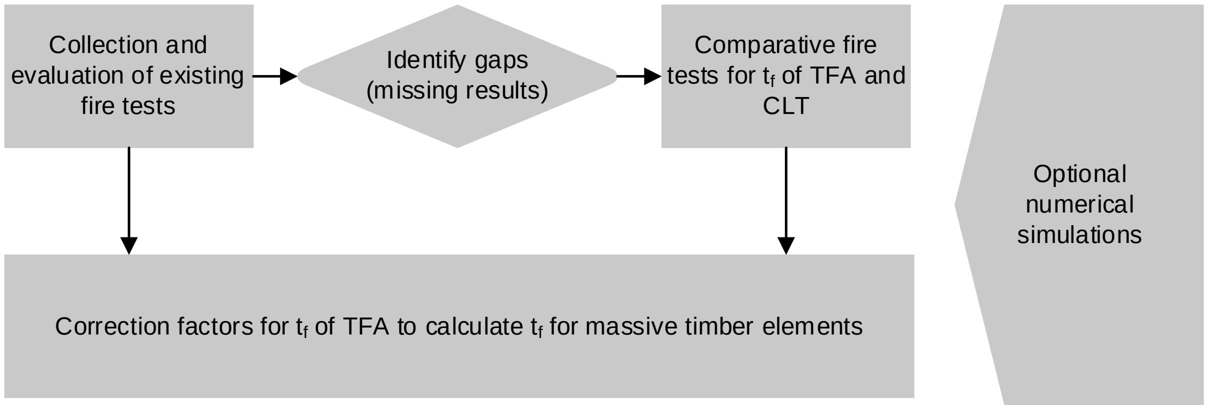

Figure 5. Working packages of the project CLT- Protect

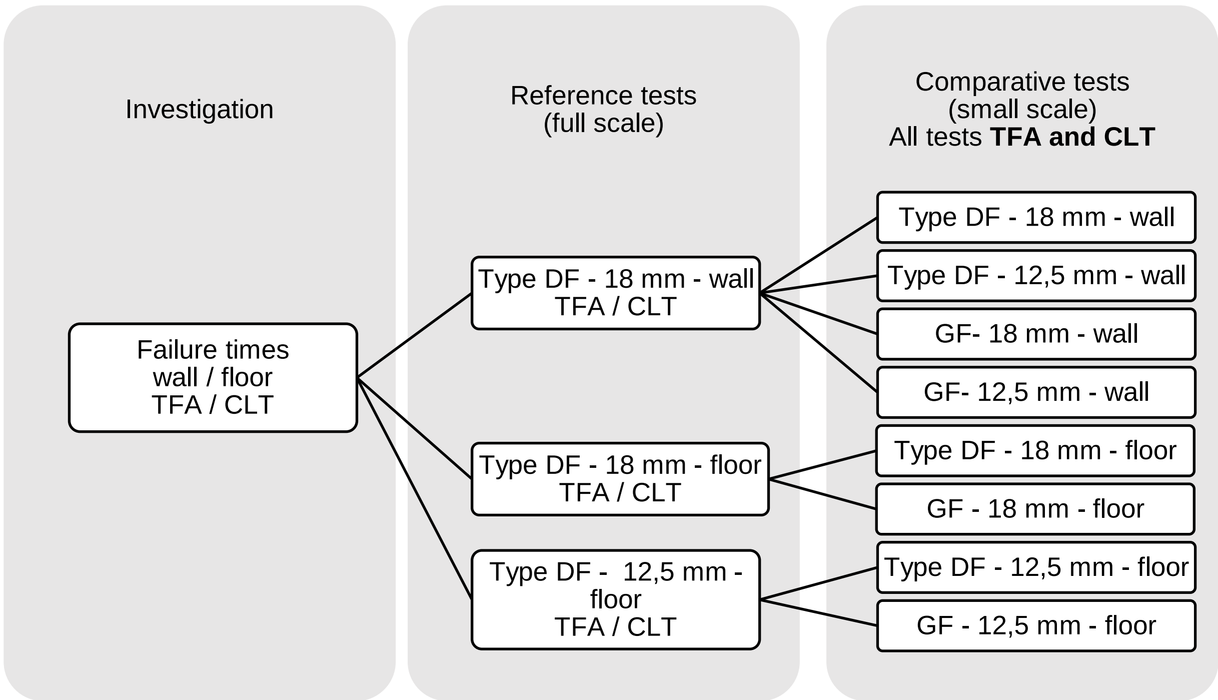

Figure 6. Test concept.

For a direct comparison of the fire rated claddings fixed on TFA and CLT, the test specimens (wall / ceiling) were split into two panels. Thus, an almost equal fire exposure could be adopted. The full-scale wall specimens (marked with W-...-FS in Table 2) had dimensions of 3 x 3 m and consisted of two different parts. See Figure 7. One part was a TFA element and the other one was a cross laminated timber element (CLT). The cross-section of the frame in the TFA element was w/h = 80/120 mm. The cross-section thickness of the CLT-element was h = 120 mm. The full-scale floor specimens (marked with F-..._FS in Table 2) had dimensions 3 x 4 m and consisted also of two different parts – TFA and CLT. See Figure 8. The cross-section of the frame in the TFA element was w/h = 80/200 mm. The cross-section thickness of the CLT-element was h = 230 mm. The CLT-element was divided into two panels, which were connected by a joint with an external spline w/h = 110/30 mm. The specimens were covered with gypsum boards, Type DF (thickness 12,5 mm or 18 mm, density 804 kg/m³) on the exposed side. The board on the exposed side was fastened with staples (according to ETA-18/0163) with a fixation distance of 80 mm. One complete board (1250 mm x 2000 mm) was mounted on the CLT and one on the TFA. The span of the boards between the fixation was varied (board one: 500 mm | board two: 625 mm). For the variation of the span, the GtDF boards were fixed on battens underneath the main loadbearing construction. The compartments of the TFA elements were filled with 160 mm stone wool insulation (density ≈ 33 kg/m³), between the battens with 40 mm stone wool insulation (density ≈ 40 kg/m³).

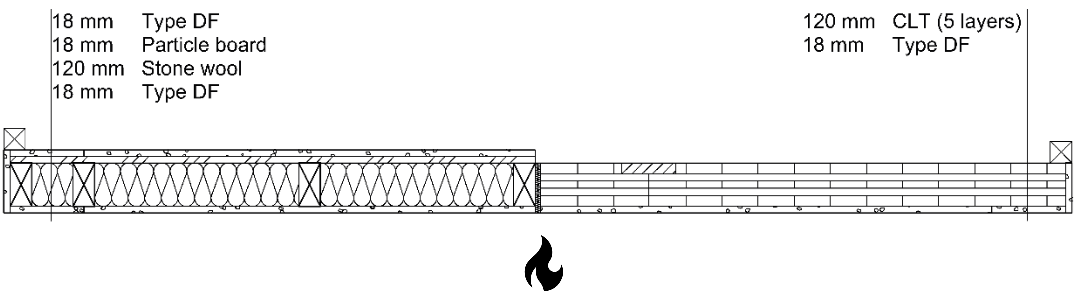

Figure 7. Section of the full-scale wall specimen.

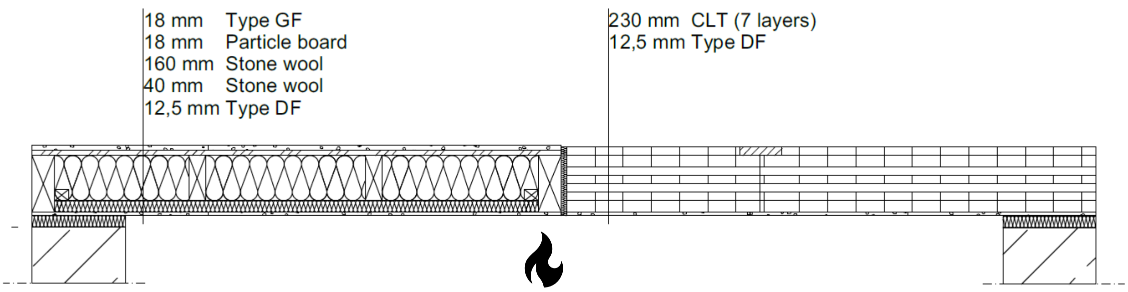

Figure 8. Section of the full-scale floor specimen.

Figure 10 shows temperature measurements in a comparative ceiling test.

Small-scale fire tests with 12,5 mm and 18 mm boards were conducted in the F-REI 90 project (Rauch et al 2022). The span and the fixation in the test specimens with a total dimension of approx. 1,2 x 1,2 m of the wall and the ceiling was identical to the full-scale tests. The observations and the temperature measurements of the F-REI 90 project can be used for investigation of the failure behaviour.

Figure 9. Comparative fire test of timber frame assembly and massive timber protected by gypsum plasterboard, Type DF. Left- wall test. Right – ceiling test.

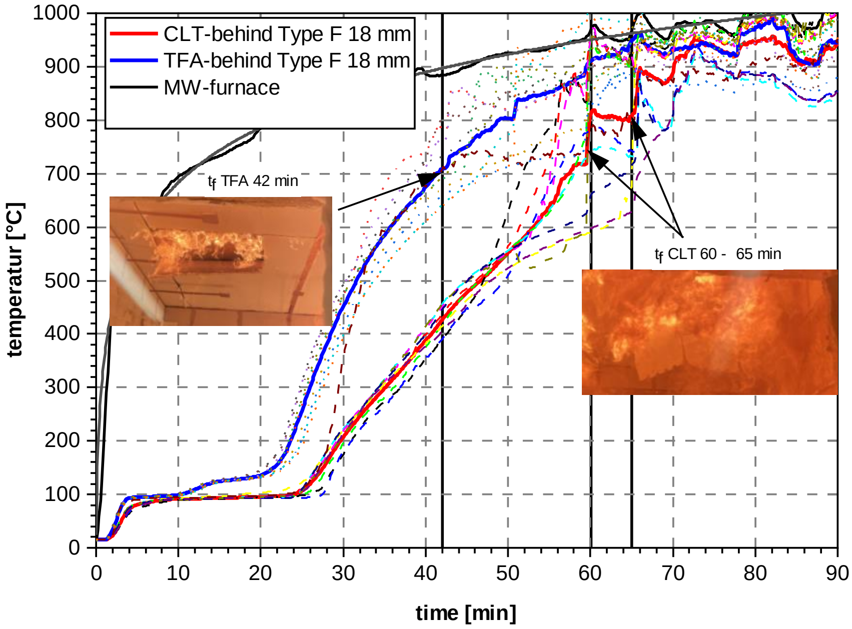

Figure 10. Comparative temperature measurements from a ceiling test of timber frame assembly and massive timber protected by gypsum plasterboard, Type DF, thickness 18 mm.

Additional small-scale fire tests with 12,5 mm and 18 mm gypsum fibreboards (GF) extend the results of the Type DF boards. For comparison reasons, the dimensions and the fixations were adapted to the existing tests.

The evaluation of the t_f-values were in accordance with the rules in EN 13381-7. The failure time was reached, if a piece of the board ≥ 0,25 m^2 detached from the assembly or the difference between the temperature behind the gypsum board and the furnace temperature was less than 50 K. The dimension of 0,25 m^2 was estimated by observation.

Additional small-scale tests were conducted to compare the results of different thicknesses and the behaviour of Gypsum fibreboards (GF).

Table 2. Test results – failure times t_f and start time of charring t_{ch} of GtDF and GF boards.

Test No.	Name	Start of charring t_{ch}	Failure time t_f	Failure temperature
		min	min	ºC
1	W-CLT-GtDF-18mm-1m	33,1	85,1	917
2	W-CLT-GtDF-18mm-FS	32	83	811
3	W-CLT-GtDF-12,5mm-1m	19,8	61,4	893
4	W-CLT-GF-18mm-1m	42,9	90	781
5	W-CLT-GF-12,5mm-1m	26,7	38	560
6	W-TFA-GtDF-18mm-1m	27,7	77	894
7	W-TFA-GtDF-18mm-1m	28,7	n.o.	-
8	W-TFA-GtDF-18mm-FS	25,8	84	784
9	W-TFA-GtDF-12,5mm-1m	16,4	56	918
10	W-TFA-GF-18mm-1m	36,2	69	882
11	W-TFA-GF-12,5mm-1m	20,1	33	810
12	F-CLT-GtDF-18mm-1m	36,2	84	766
13	F-CLT-GtDF-18mm-FS	35,4	57	837
14	F-CLT-GtDF-12,5mm-1m	23,3	56,5	684
15	F-CLT-GtDF-12,5mm-FS	22,3	37	574
16	F-CLT-GF-18mm-1m	43,4	54	610
17	F-CLT-GF-12,5mm-1m	27,3	29	403
18	F-TFA-GtDF-18mm-1m	26,1	46	667
19	F-TFA-GtDF-18mm-FS	26	42	635
20	F-TFA-GtDF-12,5mm-1m	15	16	528
21	F-TFA-GtDF-12,5mm-FS	16,3	40,1	827
22	F-TFA-GF-18mm-1m	34,1	44	694
23	F-TFA-GF-12,5mm-1m	17,3	21	633

The failure of the 12,5 mm Type DF-board on the ceiling of TFA (F-TFA-GtDF-12,5mm-1m) was very early (Figure 13) compared to all the other results in the literature and compared to values in prEN 1995-1-2. The reason was a problem of the fixation during the production. This caused an earlier failure of the 12,5 mm thick board. The fixation of the 12,5 mm GtDF board with a horizontal orientation (ceiling) according to DIN 18181 demands a maximum fixation distance of 500 mm. In the test a distance of 625 mm was used. Compared to the full scale test the increased fixation distance had less influence and the early failure could be explained by the production failure. So far, this result will not be considered for the evaluation of the failure times.

Figure 11 to Figure 14 show a comparison of the test results compared the equations of prEN 1995-1-2.

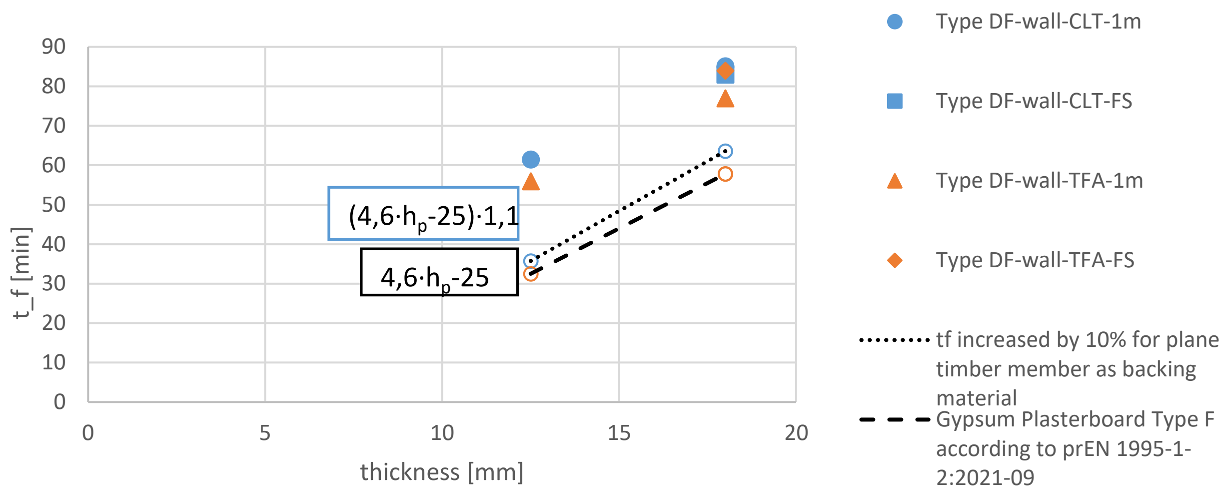

Figure 11. Failure time of gypsum boards Type DF on CLT and TFA walls. Results of the Full-scale (FS) tests and the 1-m- tests.

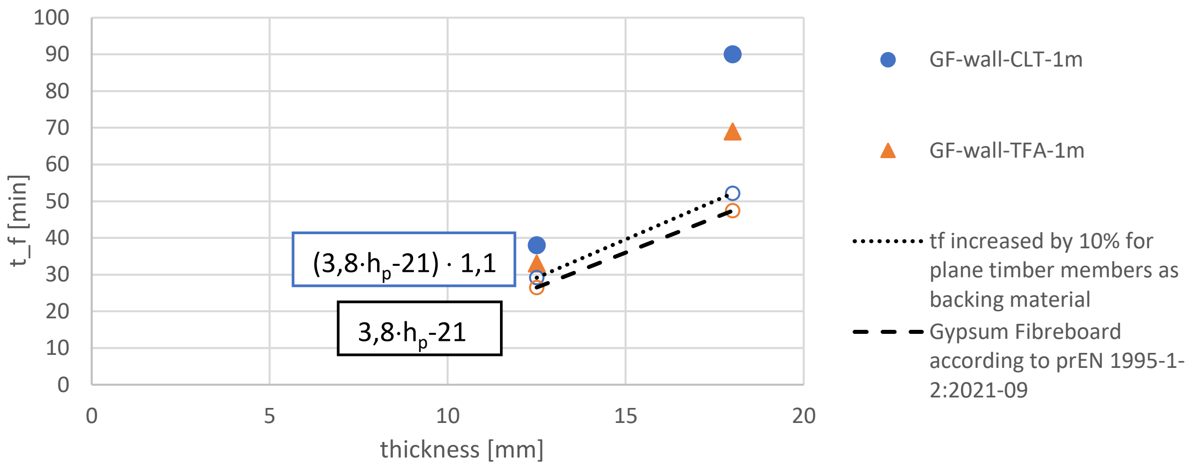

Figure 12. Failure time of gypsum fibreboards (GF) on CLT and TFA wall elements.

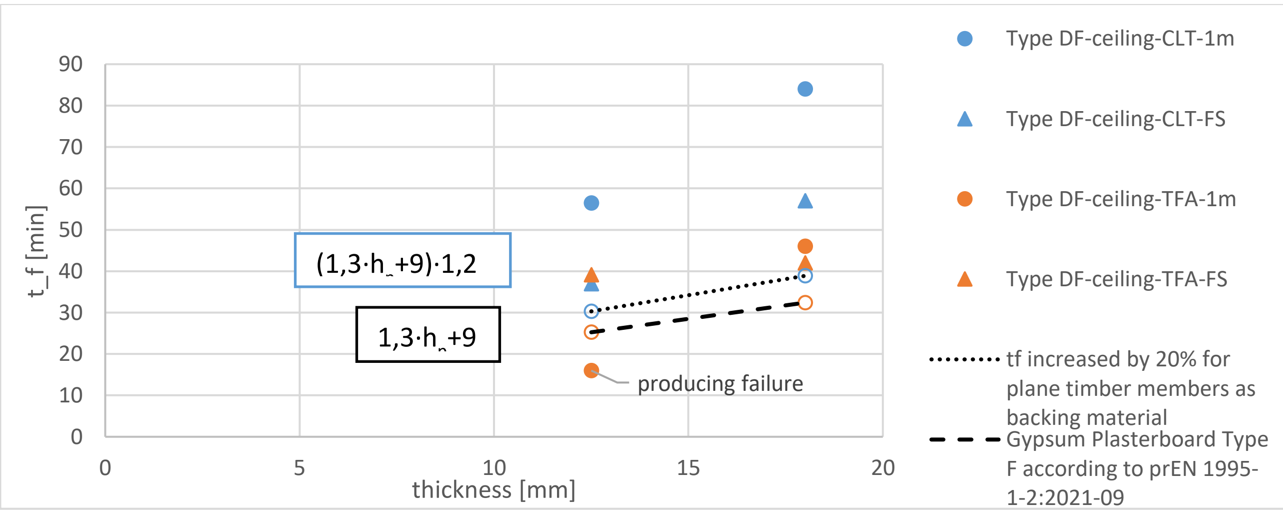

Figure 13. Failure time of gypsum boards Type DF on CLT and TFA ceilings. Results of the Full-scale (FS) tests and the 1-m- tests.

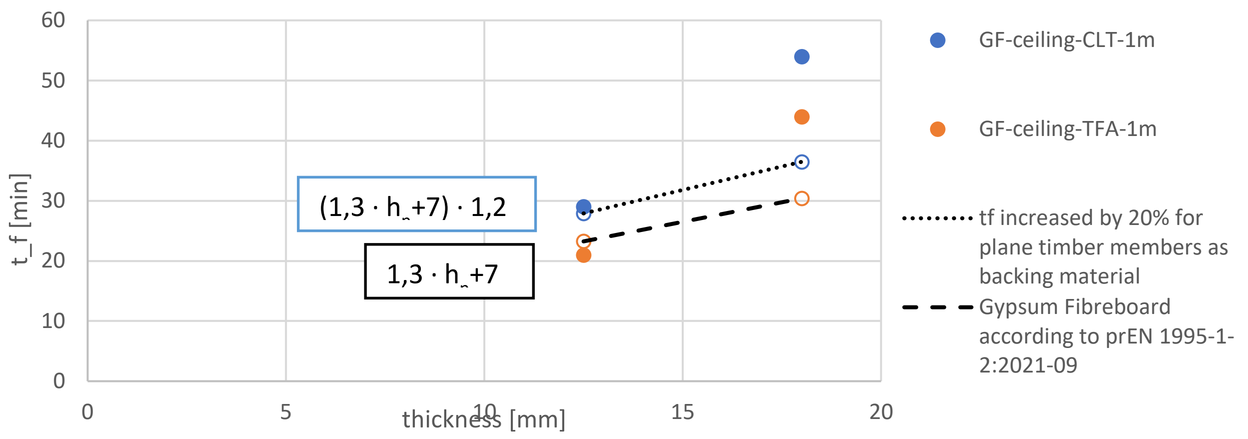

Figure 14. Failure time of gypsum fibreboards (GF) on CLT and TFA ceilings.

In addition to the experimental analyses thermal simulations were conducted. The numerical approach for the evaluation of gypsum board failure times is based on a temperature criterion. An investigation of the material properties as input values for the finite element simulation and their influence was conducted by Rauch (2022). To evaluate the failure times, temperatures between 400 °C and 900 °C must be investigated behind the gypsum boards. Therefore, the existing effective material properties (depending on the board thickness and the backing material) are less precise and must be calibrated by further test results. A calibration method for these properties is included in Rauch (2022).

Regarding the test results, it can be concluded that for floors the benefit seems to be more than 10 % and even more than 20 % compared to the mean values of the thermocouples. Based on these results the following benefits for the fall off times of gypsum boards on CLT- Elements or wood-based panels compared to TFA (backed by insulation materials) are proposed:

- Walls: value for TFA + 10 % for Type F and GF boards
- Ceilings: value for TFA + 20 % for Type F and GF boards

4 Protection on assemblies with void cavities

As part of the Structural Timber Association's (STA) fire safety in use research, a campaign of EN 1365-1 fire testing on timber frame wall assemblies was undertaken with different materials in the cavity. Further fire test data for floors tested to EN 1365-2 were supplied by the UK Engineered Wood Products Committee (EWPC). In some tests, the wall and floor cavities were left as voids while in other tests the cavities were filled with glass wool (GW) or PIR insulation. In addition to the thermocouples prescribed by the test standards, additional thermocouples were positioned behind the plasterboard protection to allow the measurement of the start time of charring (t_{ch}) and the progression of heat through the assembly. The additional thermocouples in the wall tests were positioned at various locations throughout the assembly. See Figure 15.

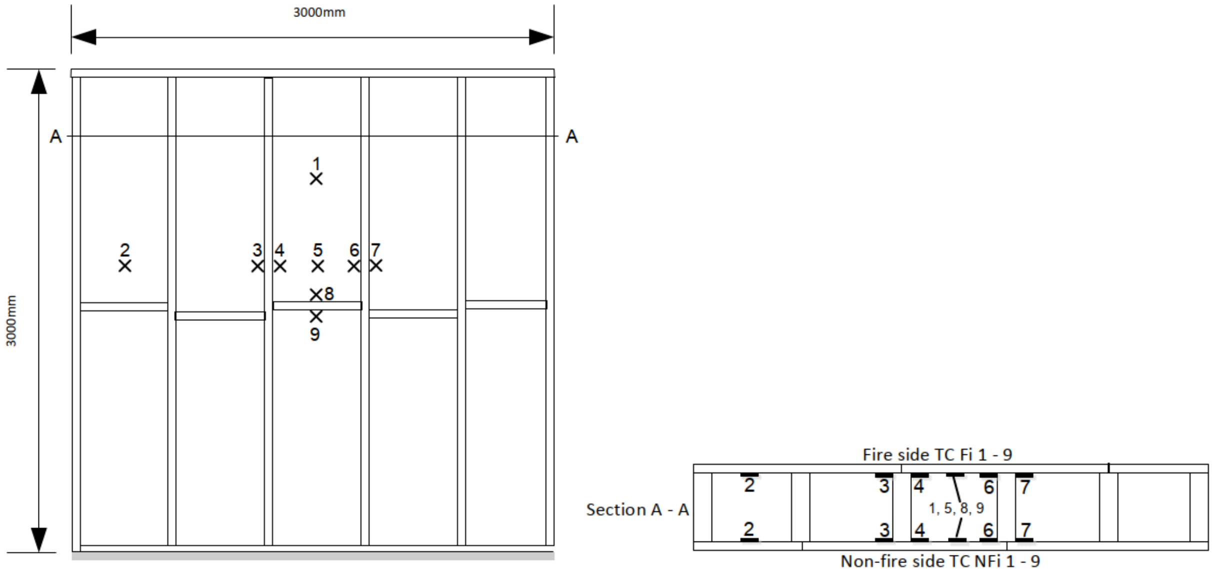

Figure 15. Additional thermocouples installed in the wall assemblies.

The walls were constructed using 1 or 2 layers of 15 mm Type A plasterboard fixed to 38mm wide C16 timber studs using Ø3.5mm drywall screws at 300 mm centres. The floors were constructed using 1 layer of 15 mm Type A plasterboard directly fixed to the 45 mm wide bottom flange of an I-joists using Ø3.5 mm drywall screws at 230 mm centres. The wall studs and floor joists were positioned at 600 mm centres. All joints were taped and filled with a gypsum filling and finishing compound. Similar tests were carried out with void cavities, glass wool filled cavities and, for walls only, PIR insulation filled cavities with a 20 mm air gap between the PIR and plasterboard.

A summary of the test results is given in Table 3, including: the start time of charring, time at 400°C, plasterboard failure time and the average temperature behind the fire protection system at a time 10% above the intended fire test duration (33 minutes for 30-minute tests and 66 minutes for 60-minute tests).

Table 3. Test results for wall and floor assemblies: t_{ch}, t_f and temperature behind the plasterboard

Test No.	Name	Start Char t_{ch}	Time at 400°C $t_{400°C}$	Failure time t_f	Temp after 33/66 mins
		min	min	min	°C
1	W-Void 1x15mm*	22,0	26,0	No failure	482
2	W-GW 1x15mm	21,1	22,2	39,0	735
3	W-PIR 1x15mm	21,5	23,1	32,0	861
4	W-Void 2x15mm*	64,8	80,0	No failure	311
5	W-GW 2x15mm	58,8	61,4	69,0	646
6	W-PIR 2x15mm	55,3	58,7	66,0	814
7	F-Void 1x15mm*	26,5	35,0	No failure	384
8	F-GW 1x15mm	28,2	29,3	32,0	842

For wall and floor assemblies with void cavities the start time of charring is generally later than for similar assemblies filled with glass wool or PIR insulation. In all cases, the fire protection for assemblies containing void cavities did not fail according to the criteria in EN 13381-7. However, for assemblies with insulated cavities, the failure of the protection system is always attributed to the temperature behind the fire protection system increasing to within 50°C of the furnace temperature. At the end of the test, the temperatures behind the fire protection system are significantly less for assemblies with void cavities than for assemblies with insulated cavities. Taking a simplified conservative assessment of the plasterboard failure time as the time taken to reach 400°C behind the plasterboard (Schleifer 2009), void cavities take at least 12% longer to reach 400°C than the equivalent insulated cavity.
The temperature profiles behind the plasterboard protection for wall and floor assemblies with void cavities and insulated cavities are presented in Figure 16 and Figure 17.

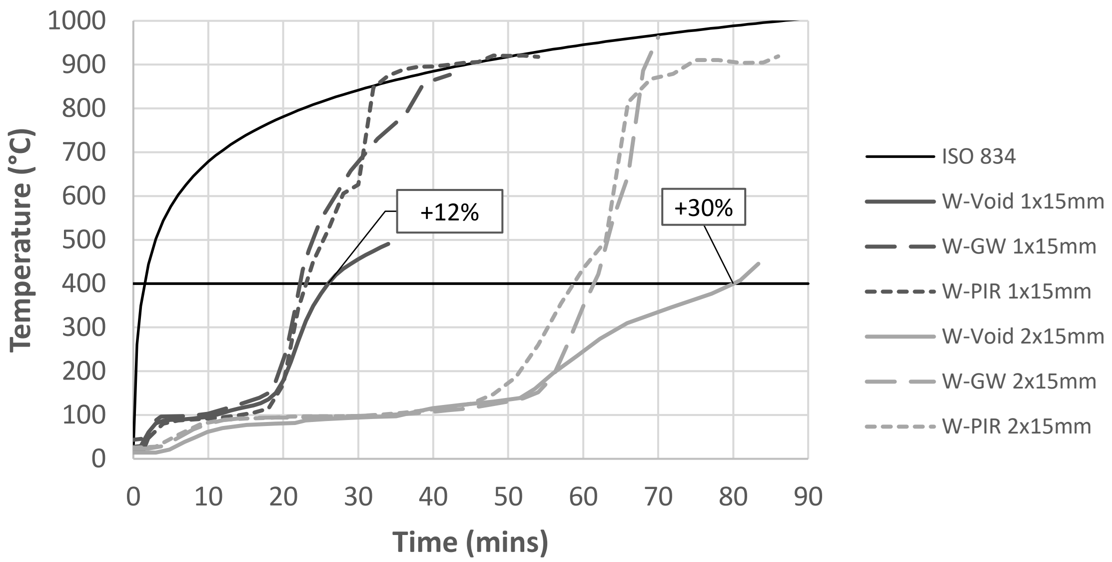

Figure 16.Temperature profile behind plasterboard for walls with insulated and void cavities with 1 and 2 layers of 15mm Type A plasterboard

It is worth noting that two layers of 15 mm Type A plasterboard offers more than double the protection of a single layer of Type A plasterboard and that 15 mm Type A plasterboard performed better on the floor assembly than on the wall assembly.

Based on the analysis of the temperature profiles, the following can be concluded. The temperature readings behind the plasterboard protection for all tests follow a similar trend irrespective of the configuration. However, the behaviour of assemblies with void cavities deviates from the behaviour of assemblies with insulated cavities during the latter stages of the test.

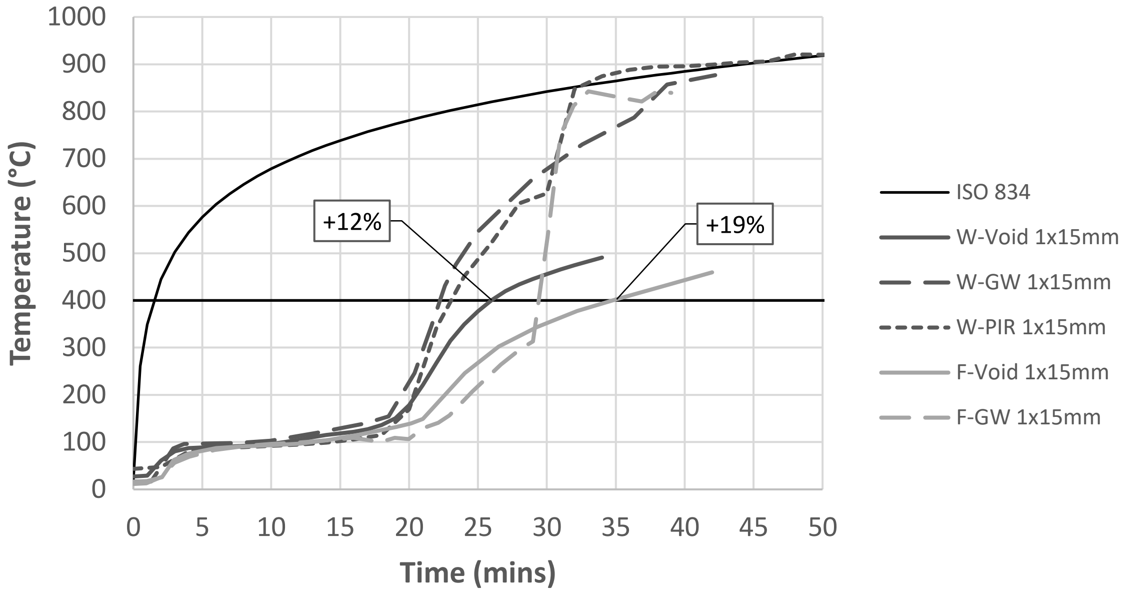

Figure 17. Temperature profile behind plasterboard for walls (W) and floors (F) with insulated and void cavities with 1 layer of 15mm Type A plasterboard

In the first few minutes of the test, the temperature behind the plasterboard increases rapidly until the gypsum reaches approximately 100°C, between 3-5 minutes after commencement of the test, at which point the temperature starts to plateau as moisture held within the plasterboard absorbs energy as it changes phase. Soon after, at approximately 130°C, the gypsum undergoes a chemical change which absorbs significant amounts of heat (*Fire safety in timber buildings 2010)* from the furnace and causes an ongoing plateau of the temperature profile behind the plasterboard. Once the chemical change of the gypsum is complete, the temperature behind the plasterboard starts to increase rapidly; it is at this point that the behaviour of void cavities departs from the behaviour of insulated cavities. The rapid temperature rise begins after approximately 20 minutes for wall and floor assemblies with 1 layer of 15 mm Type A plasterboard and approximately 50 minutes for wall assemblies with 2 layers of 15 mm Type A plasterboard.

The temperature increase for void cavities and insulated cavities is approximately 40°C/minute and 80°C/minute respectively. The temperature within the insulated cavities increase rapidly until the furnace temperature is reached (one of the definitions of failure according to EN 13381-7), whereas for void cavities, the temperature does not exceed 500°C before structural failure occurs (R). This difference in temperature rise is attributed to the ability of an air-filled void cavity to dissipate heat away from the plasterboard face by convection. Given that failure of the plasterboard is largely driven by the temperature at which the gypsum undergoes a second chemical change which occurs between 600°C and 700°C which causes ablation of the plasterboard, the rate of temperature increase after the first plateau significantly influences the failure of the plasterboard

In addition to the comparative floor tests for void and insulated cavities, the EWPC supplied over 50 test reports of full scale fire tests to EN 1365-2 for floors with void cavities with different thicknesses of plasterboard. Since many of the fire tests were carried out with only the thermocouples as required by the test, it was not possible to compare temperature profiles behind the plasterboard protection. EN 13381-7 provides a means to determine the failure time of the plasterboard by observing the loss of plasterboard during the test, but not all test reports consistently report the loss of plasterboard. One consistent feature of all EN 1365-2 tests are the locations of the five thermocouples on the unexposed face, used primarily to measure the mean temperature rise, but also to detect the maximum temperature rise individually. A common trend in the 30-minute floor fire tests is that there is a noticeable gradient change in the mean temperature recorded on the unexposed floor deck that approximately corresponds with a significant loss of plasterboard when recorded in the observations within the test report.

From a heat transfer perspective, it follows that while the plasterboard is in place the heat from the furnace must transfer through the plasterboard, void and deck before registering an increase in temperature in the thermocouples. However, once the plasterboard fails, the heat from the furnace only needs to transfer through the deck to register an increase in temperature in the thermocouples. The time at which there is a distinct change in the temperature-time gradients recorded in the mean temperature on the unexposed surface of the test specimen is therefore considered to be the plasterboard failure time. Given the large data set, the statistical distribution of plasterboard failure time could be determined, allowing statistical analysis to determine the mean and 5% fractile plasterboard failure times.

The plasterboard failure times for joisted floor systems with void cavities and with a single layer of 12,5 mm Type A and 15 mm Type A are shown in Figure 18.

A summary of the statistical plasterboard failure time derived from testing is compared with the prEN 1995-1-2 calculation in Table 4.

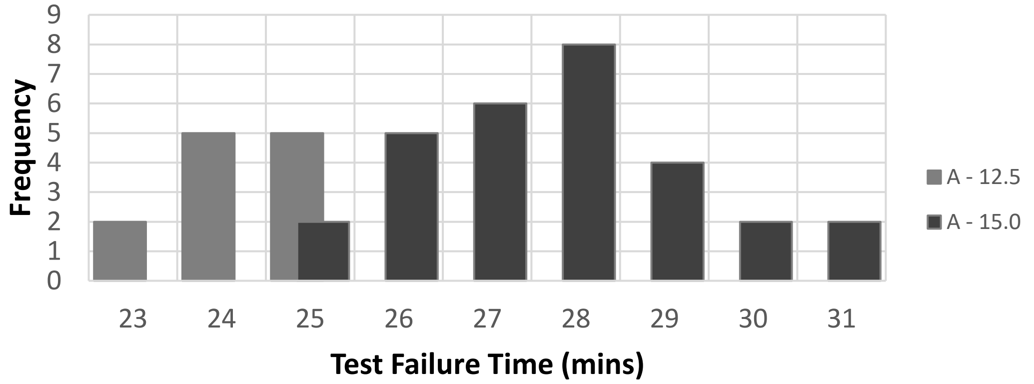

Figure 18. Cumulative distribution of plasterboard failure times for floors with void cavities.

Table 4. Comparison of plasterboard failure time for floor assemblies with void cavities

Plasterboard Protection System	Test (mean) t_f	Test (5^{th} fractile) t_f	prEN 1995-1-2 t_f	Difference Test/calc
	min	min	min	%
1x12.5mm Type A	24,3	22,0	17,5	126%
1x15.0mm Type A	27,7	25,2	22,5	112%

In conclusion, an analysis of the temperature profiles behind the plasterboard protection on full-scale wall and floor fire tests shows that a void cavity typically takes between 12% and 30% longer than an insulated cavity to reach 400°C on the cavity face of the plasterboard. A statistical analysis of fire tests on floor assemblies with void cavities shows that the 5% fracttile plasterboard failure time is at least 12% longer than the currently proposed calculation procedure in prEN 1995-1-2 for plasterboard.

- The plasterboard failure time t_f can be increased by 10% for wall and floor assemblies backed by void cavities.

5 Outcome

The main outcome of this research is the proposal for failure times (t_f)of gypsum plasterboards differentiated according to backing materials or void. These failure times are necessary input parameters for the SFM and the European charring model in the prEN 1995-1-2.

Acknowledgements

The authors acknowledge CEI-Bois, the “Fachverband der Holzindustrie Österreichs” and Svenskt Trä (the Swedish wood industry) for financing the project CLT Protect. The project was only possible by the support of the industry for the material of the test specimens and the additional fire tests for gypsum fibreboards. Further acknowledgements go to the Structural Timber Association and the Engineered Wood Products Committee for providing fire test data for timber frame wall and floor assemblies to evaluate the effect of void cavities.

6 References

CEN/TC 250/SC 5/WG 4 N 180: SC5.T4 Final Document of prEN 1995-1-2 on fire. 2021. N-document. Brussels: CEN - CENELEC.

Just, A, Schmid, J and König, J (2010). Gypsum Plasterboards Used as Fire Protection - Analysis of a database,” SP Report: 2010:29, Stockholm, Sweden.

Fire safety in timber buildings (2010) Technical Guideline for Europe. SP Technical research Institute of Sweden, Wood Technology. SP Report 2010:19. Stockholm, Sweden.

Eurocode 5 (2004) Design of timber structures – Part 1-2: Structural fire design. CEN (EN 1995-1-2).

Kraudok, K. (2015) Protective effect of gypsum plasterboards for the fire design of timber structures. Master thesis. TUT. Tallinn, Estonia

Mäger, K. N.; Just, A.; Schmid, J.; Werther, N.; Klippel, M.; Brandon, D.; Frangi, A. (2018). Procedure for implementing new materials to the component additive method. Fire Safety Journal.10.1016/j.firesaf.2017.09.006

Kraudok, K., Just, A. Evaluation of fall-off times for gypsum plasterboards. COST FP1404 WG2 TG4 meeting in Athens. 18.-19.9.2017.

Kraudok, K., Just, A. (2021) Analysis of the database of full-scale fire tests with gypsum boards, TalTech Report SE-21-01., Tallinn.

Just, A., Mäger, K.N., Kraudok, K. CLT protected by gypsum boards. Design models. COST FP1404 WG2 TG1 meeting in Vienna. 4.-5.7.2018.

Kiholane, K (2021), Sensitivity analysis of the design methods of linear glulam timber members proposed for new generation of Eurocode 5-1-2. Master thesis of Tallinn University of Technology.

Eskla, K (2021) Sensitivity analysis of the design methods of timber frame assemblies proposed for new generation of Eurocode 5-1-2. Master thesis of Tallinn University of Technology.

Õismets, M, (2021) Sensitivity analysis of the design methods of plane timber members made of cross-laminated timbe proposed for new generation of Eurocode 5-1-2. Master thesis of Tallinn University of Technology.

Rauch, M., Werther, N., Suttner, E., Winter, S (2022) F-REI 90: Ein analytisches Berechnungsverfahren für Holzrahmen- und Holzmassiv-bauteile bis zu einer Feuerwiderstandsdauer von 90 Minuten. BBSR-Online-Publikation

Rauch, Michael (2022): Beurteilung der raumabschließenden Funktion brandbeanspruchter Holzbauteile mittels einer „Component Additive Method". Dissertation. Technical University Munich, Munich.

Schleifer, V (2009) Zum Verhalten von raumabschliessenden mehrschichtigen Holzbauteilen im Brandfall, PhD Thesis ETH No. 18156, ETH Zurich.

DISCUSSION

The paper was presented by A Just

P Dietsch and A Just confirmed the findings that TFA with void has a later failure time and TFA filled with mineral wool is the worst. A Just said in cases of CLT with gypsum, wood can absorb the heat while mineral wool does not. P Dietsch and A Just discussed how this might affect failure time of CLT.

S Winter said in terms of failure times spacing of members and fasteners has an influence on the failure of gypsum boards. M Rauch said fastener spacing was not considered. A Just added that the worst case was considered and agreed that this aspect could be examined further.

A Frangi and A Just discussed the observed increases were based on the 20th percentile. The choice of 20th percentile was based on the intent to have the 1st barrier as safe as possible. One can consider the mean value and this issue warrants further investigation and discussions.

S Winter stated that for insulated void cavity, there should be no airgaps between insulation and wood assembly.

Beams with notches or slits – Extensions of the Gustafsson approach

Erik Serrano, Division of Structural Mechanics, Lund University, Sweden

Robert Jockwer, Division of Structural Engineering, Chalmers University of Technology, Gothenburg, Sweden

Henrik Danielsson, Division of Structural Mechanics, Lund University, Sweden

Keywords: notched beams, fracture mechanics, crack propagation, shear capacity, moment capacity

1 Introduction

1.1 Background

In the current version of Eurocode 5 (EC5), [1], design of beams notched at the support is based on the so-called Gustafsson approach [2]. In later work (see e.g. [3]–[7]) further background, overview and discussions on this and other methods are given. Also, the influence of various geometry and material parameters on the performance of beams with notches and holes, and on the predictive capabilities of the methods are given. In other standards and handbooks, see e.g. [8], [9] and [10], alternative approaches can be found.

The case of an end-notched beam without taper, shown in Figure 1 below, defines the basic geometry parameters as given in EC5 (for non-tapered notches).

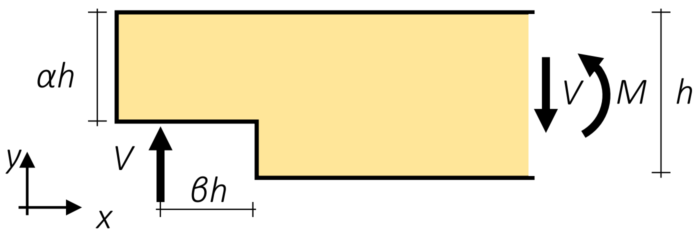

Figure 1. Definition of basic geometry parameters for end-notched beam.

As originally presented by Gustafsson, and as included in EC5, the design formulae are, of course, derived based on a number of simplifying assumptions, some of which are related to the loading conditions of the notched beam. As an example, in [2] it was assumed that any load on the beam between the support force and the re-entrant corner of the notch could be neglected. Consequently, the bending moment in the beam at the re-entrant corner, M, is assumed to be equal to the shear force, V, times the distance to the line of action of the support reaction force, x, see Figure 2. In reality other situations often occur, involving *e.g.* a notch away from the support and including distributed loading and/or including normal force, see Figure 2. In such cases the relation between bending moment and shear force at the notch is obviously different. Another situation where this is relevant is in cantilevered beam parts, see Figure 2. Also, the Gustafsson approach is limited to beams with rectangular cross-section. Finally, the EC5 approach states that the effect of the stress concentrations at a notch on the opposite side of the support need not to be taken into account, a statement that has been questioned.

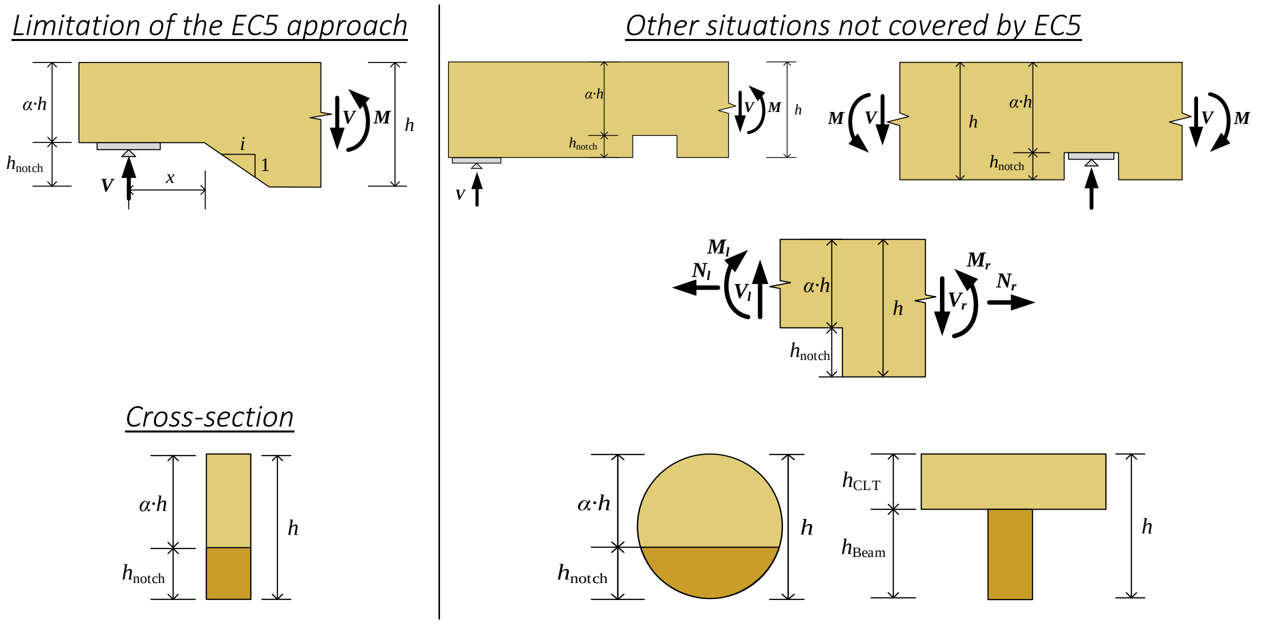

Figure 2. Limitation of the EC5 approach and examples of other situations not covered by EC5.

1.2 Aim

With the above examples in mind, it is indeed clear that it is not always straightforward to apply the current design formulae of EC5. The aim of the present paper is to discuss the basic assumptions of the Gustafsson approach, its possibilities and limitations, relative current and future versions of EC5.

2 Methods

2.1 Linear Elastic Fracture Mechanics (LEFM) and the compliance method

All analyses presented herein are performed within the framework of linear elastic fracture mechanics. This in turns means assuming linear elastic behaviour of the material and assuming load bearing capacity of components being governed only by geometry, boundary conditions, material stiffness and fracture energy.

The framework of LEFM is in general accurate in situations where the fracture process zone of the material is small in relation to other dimensions of the structure (including the size of the crack).

The load bearing capacity is determined by considering the energy balance during crack propagation. Herein, only quasi-static conditions are considered, and thus, during crack propagation, the incremental work of external forces, ∂W_{ext}, should balance the elastic strain energy increment, ∂W_e and the fracture energy needed for an incremental extension of the crack surface, giving:

$$\partial W_{ext} = \partial W_e + G_C \partial A \tag{1}$$

where G_c is the critical energy release rate (N/m) during crack propagation, and ∂A is the increase of crack surface.

In an FE-context, assuming constant external loads during crack propagation, and assuming linear elastic behaviour, Eq. (1) can be written:

$$\alpha_{load}{}^2 \mathbf{P}_0^T (\mathbf{a}_2^0 - \mathbf{a}_1^0) = \frac{1}{2} \alpha_{load}^2 \mathbf{P}_0^T (\mathbf{a}_2^0 - \mathbf{a}_1^0) + G_c \Delta A \tag{2}$$

with α_{load} being a load factor, $\mathbf{P}_0$ representing a reference (unit) loading, and vectors $\mathbf{a}_1^0$ and $\mathbf{a}_2^0$ representing the displacement fields of the structure for crack lengths a_1 and a_2, respectively. From Eq. (2) and assuming 2D-conditions, we then obtain:

$$\alpha_{load} = \sqrt{\frac{G_c \, \Delta A}{\frac{1}{2} \mathbf{P}_0^T (\mathbf{a}_2^0 - \mathbf{a}_1^0)}} = \sqrt{\frac{G_c \, b \, \Delta a}{\Delta W_e}} \tag{3}$$

with b being the out-of-plane width of the crack surface, Δa being the extension of crack length and ΔW_e being the change of elastic strain energy.

2.2 Choice of critical energy release rate

In calculating the load at which crack propagation occurs, cf. Eq. (3), the critical energy release rate, G_c, is needed. Since G_c is dependent on, among other things, the mode of loading, a relevant choice of G_c needs to be done. In the work leading to the current EC5 approach, an assumption on the safe side was done, assuming G_c to be equal to its Mode 1 value (for tension perpendicular to the grain). This approach is used also here for the analytical models.

For models based on 2D solid elements, cracking is assumed to take place by propagation along the grain and for mixed mode situations the Wu criterion [11] is used:

$$\frac{K_I}{K_{IC}} + \left(\frac{K_{II}}{K_{IIC}}\right)^{2.0} = \begin{bmatrix} K_I = \sqrt{E_I G_I} \\ K_{II} = \sqrt{E_{II} G_{II}} \end{bmatrix} \Rightarrow \sqrt{\frac{G_I}{G_{IC}}} + \frac{G_{II}}{G_{IIC}} = 1.0 \tag{4}$$

where index *C* indicates the respective critical quantity at pure mode of loading, and where the parameters E_I and E_{II} are defined in terms of the elastic constants according to:

$$\frac{1}{E_I}=\frac{1}{E_x}\sqrt{\frac{E_x}{2E_y}}\sqrt{\sqrt{\frac{E_x}{E_y}}+\frac{E_x}{2G_{xy}}-\upsilon_{yx}\frac{E_x}{E_y}};\quad \frac{1}{E_{II}}=\frac{1}{E_x}\sqrt{\frac{1}{2}}\sqrt{\sqrt{\frac{E_x}{E_y}}+\frac{E_x}{2G_{xy}}-\upsilon_{yx}\frac{E_x}{E_y}} \quad (5)$$

The critical energy release rate at mixed mode situations, $G_c=G_I+G_{II}$, is calculated from the ratio $k=K_{II}/K_I$. Close to the crack tip this ratio equals $k=\overline{\tau}/\overline{\sigma}$ with $\overline{\tau}$ being the shear stress along grain and $\overline{\sigma}$ the tensile stress perpendicular to grain. This ratio can be estimated by the stress values at the crack tip, or as an average value along a characteristic material length x_0 ahead of the crack tip, see [12, 13]:

$$x_0=\frac{2}{\pi}\frac{E_I G_{IC}}{f_t^2}\frac{E_x}{E_y}\left(\frac{G_{IIC}}{G_{IC}}\right)^2\frac{2}{4k^4}\left(\sqrt{1+4k^2\sqrt{\frac{E_y}{E_x}\frac{G_{IC}}{G_{IIC}}}}-1\right)^2\left(1+\frac{k^2}{(f_v/f_t)^2}\right) \quad (6)$$

2.3 FE-Models based on 2D elements

In order to allow detailed analyses, including the influence of boundary conditions and the influence of mixed-mode behaviour, models based on plane stress solid elements have been employed.

One part of the work presented includes the investigation on support conditions. Two different modelling approaches for end-notched beams have been used, *a)* assuming a stiff plate at the lower side of the beam acting as a hinged support and *b)* beam-alike boundary conditions, by introducing the support force at the free end of the beam, which in turn is modelled as a stiff cross-section, cf. Figure 3. In any case, the distance of *βh* is defined as the distance from the re-entrant corner to the support force.

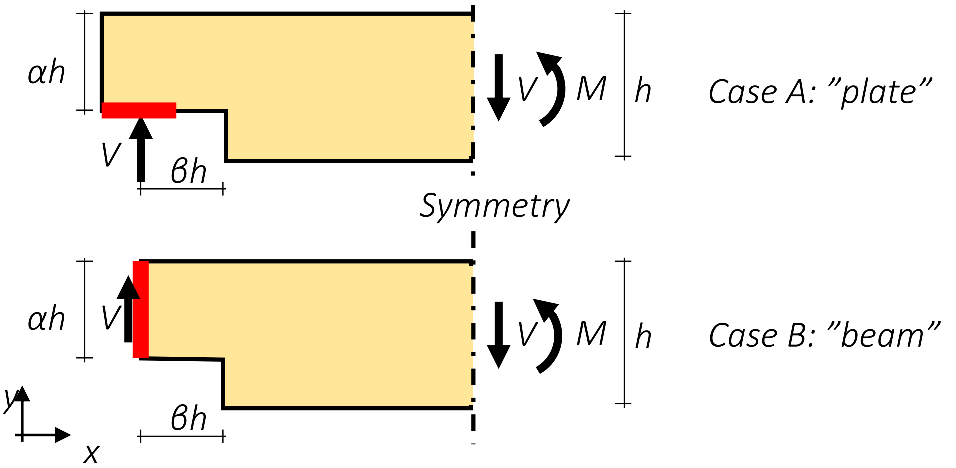

Figure 3. Support conditions. Top: Support plate. Bottom: Beam boundary conditions.

3 Common assumptions and cases analysed

3.1 Material stiffness parameters and EC5-approach

Material stiffness parameters used in the present study are according to Table 1. These parameters represent a typical glulam material. Over the years, the material and product standards have changed, making it difficult to do consistent comparisons between previous research results and code proposals and applying different analysis methods. In addition, some analysis methods make use of additional material parameters apart from those given in codes and standards. As a compromise, a typical value of longitudinal modulus of elasticity was set to 12 000 MPa, which is also in line with the values used when calibrating the EC5 formulae. Based on the values used in previous research, [12], transverse modulus of elasticity (MOE) was set to 400 MPa. To be consistent with the current design approach in EC5 for notched beams, the longitudinal shear modulus, G_{xy}, was set to the same fraction as that assumed in EC5, *i.e.* $G_{xy}=E_x/15.625$

Table 1. Material stiffness parameters.

Symbol	Quantity	Value	Unit	Remark
E_x	MOE along grain	12 000	MPa	-
E_y	MOE across grain	400	MPa	$E_x/30$ from [12]
G_{xy}	Longitudinal shear modulus	768	MPa	$E_x/15.625$ according to EC5

The design approach of EC5 is based on a theoretical expression from [2], where shear force capacity, V_f , is found to be:

$$\frac{3}{2}\frac{V_f}{b\alpha h}=1.5\frac{\sqrt{\dfrac{G_{IC}G_{xy}}{0.6}}}{\sqrt{h}\left(\sqrt{\alpha-\alpha^2}+\beta\sqrt{10(G_{xy}/E_x)}\sqrt{1/\alpha-\alpha^2}\right)}, \tag{7}$$

where geometry parameters are defined in Figure 1. With the assumption of

$$E_x/G_{xy}=15.625 \quad\Rightarrow\quad \sqrt{10G_{xy}/E_x}=0.8 \tag{8}$$

the result is

$$1.5\sqrt{\frac{G_{IC}G_{xy}}{0.6}}/f_v=k_n[\mathrm{mm}^{1/2}]=\begin{cases}4.5 \text{ for LVL}\\ 5.0 \text{ for solid timber}\\ 6.5 \text{ for glulam}\end{cases} \tag{9}$$

With the above, the final expressions are:

$$\tau_d=\frac{1.5V_f}{b\alpha h}\le k_v f_{v,d} \tag{10}$$

with k_v given by

$$k_v = \min\begin{cases} 1 \\ k_n / \left(\sqrt{h}\left(\sqrt{\alpha - \alpha^2} + 0.8\beta\sqrt{1/\alpha - \alpha^2} \right) \right) \end{cases}, \tag{11}$$

where k_n was defined in Eq. (9) and the factor 0.8 in Eq. (8).

Adopting Eqs. (9)–(11) and expressing the results in terms of the reduction factor k_v as a function of α, β and beam depth, h, gives the curves depicted in Figure 4. By backwards calculating from Eq. (9), the equivalent energy release rate corresponding to k_n=6.5 is $G_{IC,\ 6.5}$=179.7 N/m, assuming the shear strength to be f_v=3.5 MPa, a characteristic strength value typically used at the time of introducing the design approach for notched beams in EC5.

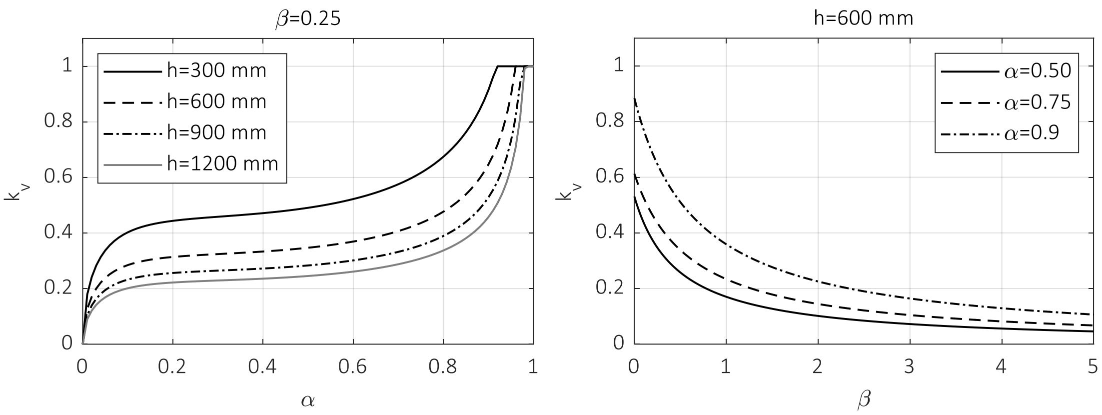

Figure 4. Strength reduction factor k_v for end-notched beams according to EC5.

For the 2D FE-analyses performed in this study, additional material parameters were needed. Apart from Poisson's ratio, also critical energy release rates for mode I and mode II, and material strength values in tension perpendicular to grain and in longitudinal shear were needed. The strength values are needed to estimate the size of the characteristic material length, x_0. The values employed are given in Table 2 and are estimated to be representative for small clear wood volumes (≈1 cm^3), a scale of relevance for the stress concentrations found around the re-entrant corner of a notch.

Table 2. Additional material parameters needed for 2D FE-analyses. Strength values represent mean values for small volumes of clear wood.

ν_{xy}	Poisson's ratio	0.3	-	
G_{IC}	Critical energy release rate, mode I	179.7	N/m	From Eq.(9)
G_{IC}	Critical energy release rate, mode II	629.0	N/m	3.5G_{IC} [12]
f_t	Tensile strength perp. grain	3	MPa	[12]
f_v	Longitudinal shear strength	9	MPa	[12]

Based on the material properties in Table 2, the characteristic material length x_0 would be varying from ca 11 mm at pure mode I (G_{IC}=179.7 N/m) to ca 23 mm at pure mode II (G_{IIC}=629.0 N/m). In the present study, the mixed mode ratio was estimated by the stress ratio at the crack tip. In preliminary analyses, also calculating the mixed mode ratio based on the average along x_0 was tested. The difference was found small, and thus only the crack tip ratio is used, for simplicity.

3.2 Case 1: Beams notched at end support

The situation of an end-notched beam is analysed in order to establish necessary mesh refinement and for verification of the EC5 design formulae.

3.3 Case 2: Beams notched at inner support

The modelling is based on assuming an inner support (mid-support) and this support representing also a symmetry section, *cf.* Figure 5.

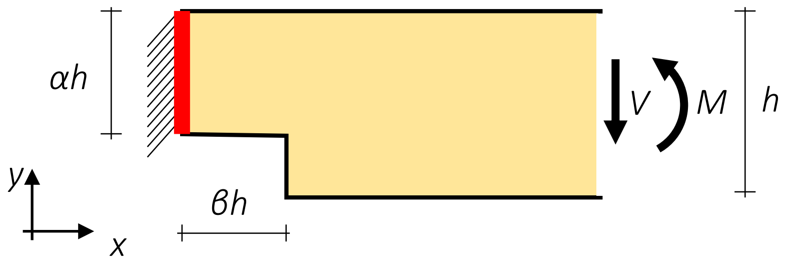

Figure 5. Beam notched at mid support modelled with a fixed end.

3.4 Case 3: General notches and slits far from support

The last case considered is a beam with a notch/slit cut at a distance from the support. The case is described in Figure 6. This situation has been analysed by investigating the geometrical parameters defining the notch, and the ratio *M/V*, the bending moment to shear, at the *centre of the notch*.

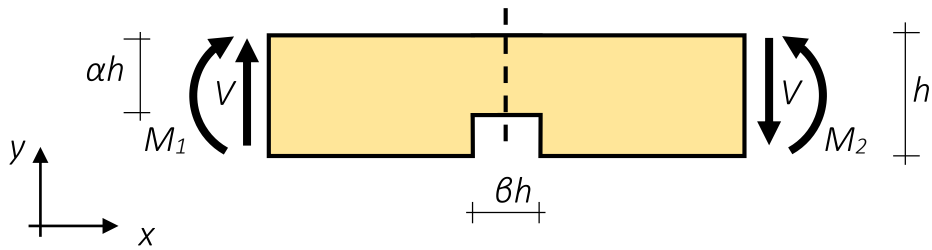

Figure 6. Beam notched away from support. Evaluation of forces refers to mid-section (dashed line).

In the original work of Gustafsson, the energy release rate, *G*, for such a general case of a notched or slit beam is given by:

$$G = \frac{P^2}{b^2\alpha^2 h}\left(\sqrt{\frac{0.6\left(\alpha-\alpha^2\right)}{G_{xy}}} + \frac{x}{h}\sqrt{\frac{6\left(\frac{1}{\alpha}-\alpha^2\right)}{E_x}}\right)^2 \tag{12}$$

where the first term in the parenthesis represents the contribution from the shear action, and the second term represents the contribution from bending action, due to the bending moment from the force, P, at the distance x. The energy release rate due to pure shear force action ($V=P$) is:

$$G=\frac{V^2}{b^2\alpha^2 h}\frac{0.6\left(\alpha-\alpha^2\right)}{G_{xy}} \tag{13}$$

Consequently, the resulting shear strength of a rectangular cross-section can be determined as follows:

$$\tau=\frac{1.5V}{b\alpha h}\leq\frac{1.5\sqrt{\frac{G_c G_{xy}}{0.6}}}{\sqrt{h}\left(\sqrt{\alpha\left(1-\alpha\right)}\right)} \tag{14}$$

The energy release rate due to pure moment action ($M = P\cdot x$) is:

$$G=\frac{M^2}{b^2\alpha^2 h^3}\frac{6\left(\frac{1}{\alpha}-\alpha^2\right)}{E_0} \tag{15}$$

Thus, the resulting bending strength of a rectangular cross-section can be determined as follows:

$$\sigma_M=\frac{M}{\frac{b\left(\alpha h\right)^2}{6}}\leq\frac{\sqrt{6G_c E_0}}{\sqrt{h}\sqrt{\left(\alpha-\alpha^4\right)}} \tag{16}$$

The combination of Eq. (14) and (16) for a notch at an arbitrary position was proposed by Gustafsson as follows:

$$\tau\frac{\sqrt{h}\left(\sqrt{\alpha\left(1-\alpha\right)}\right)}{1.5\sqrt{\frac{G_c G_{xy}}{0.6}}}+\sigma_M\frac{\sqrt{h}\sqrt{\left(\alpha-\alpha^4\right)}}{\sqrt{6G_c E_0}}\leq 1 \tag{17}$$

With

$$\sigma_M=\frac{6M}{b\left(\alpha h\right)^2}\ \text{and}\ \tau=\frac{1.5V}{b\alpha h} \tag{18}$$

This approach yields the same results as the approach for end-notched beams of the Canadian Standard CSA O.86, where the effect of the reduced stiffness at the transition between reduced and full cross-section as proposed by Gustafsson, [2], was neglected, [14]. Eq. (17) is similar to the approaches in the Australian standard AS 1720.1 and in the "Wood Handbook" of the Forest Products Laboratory, [10].

The above approach is used herein in comparison to the 2D FE-analyses of notched/slit beam sections, by applying various ratios M/V, and by investigating various notch geometries.

4 Results

From the results of the FE models and in comparison with the analytical approach in EC5, the following aspects are evaluated:

1. General validation of the FE-models against the EC5 approach
2. Impact of the support conditions on the notch capacity
3. Impact of the notch length on the notch capacity
4. Impact of the notch position on the crack propagation load
5. Impact of the moment/shear force interaction on the notch capacity

The analyses have been performed for $300 < h < 1200$ (mm), $0.5 < \alpha < 0.9$, and $0.25 < \beta < 2.0$ for all cases. Support plate lengths were *h*/6, and in all analyses the beam width was assumed to be 100 mm.

4.1 General validation of the FE-models against the EC5 approach

4.1.1 Consistent boundary conditions and convergence study

As regards the 2D-FE approach, boundary condition Cases A and B (*cf*. Figure 3) were analysed and a convergence study was performed for Case B. Using element sizes ranging from 2.5 to 10 mm, the conclusion is that for the present study an element size of 10 mm is sufficient and still gives reasonable calculation times. Figure 7 presents the estimated critical load as function of crack propagation for element sizes 2.5–10 mm. The mesh used for the case of 10 mm element size is shown in Figure 8 and results are given in Table 3.

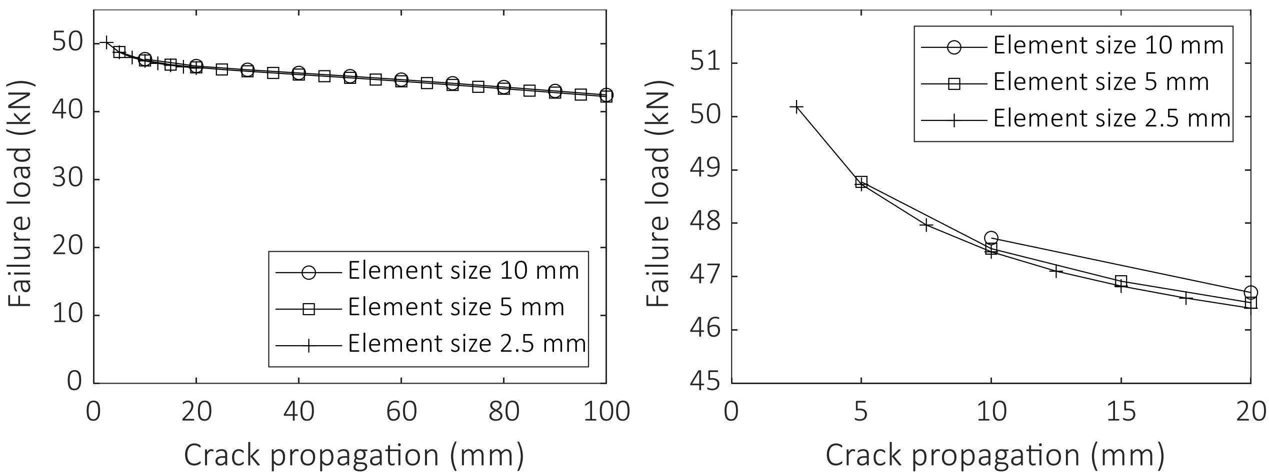

Figure 7. Convergence study of crack propagation analyses for base case (beam boundary conditions). Left: crack propagation 0–100 mm. Right: Partial zoom.

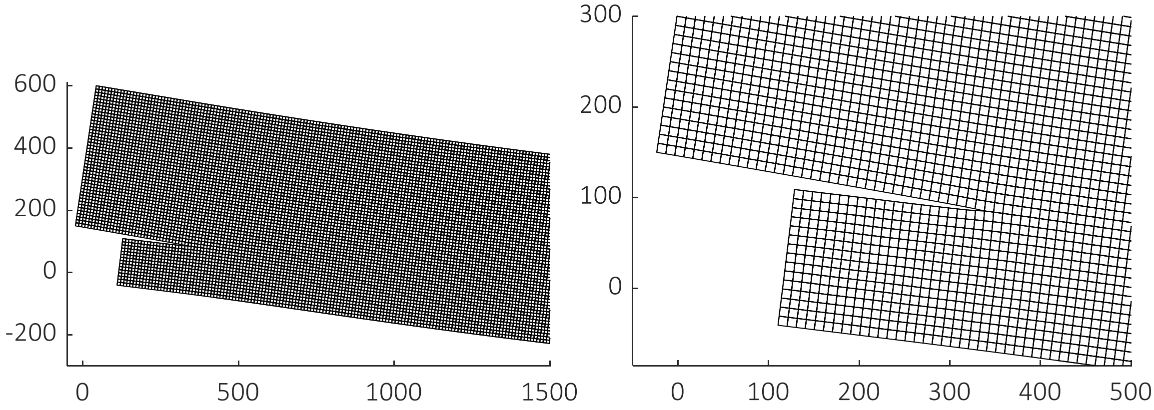

Figure 8. Example of FE-mesh used, here with 10 mm element size and 200 mm long crack. Left: Half of the model is shown (total length is 5h, in this case 3000 mm). Right: Partial zoom.

Table 3. Results for base example including influence of element size. h=600 mm, α=0.75, β=0.25. Critical load for 2D-FE models is based on crack length=20 mm and Case B boundary conditions. Note that the effective critical energy release rate is obtained as a result for 2D-FE analyses.

Approach	Critical load (kN)	Remarks
EC5	45.8	Eq.(9)–Eq.(11), k_n=6.5 ($G_C=G_{IC}$=179.7 N/m as input)
2D-FE	46.7	Element size 10 mm, G_C=203.3 N/m as result
2D-FE	46.5	Element size 5 mm, G_C=202.2 N/m as result
2D-FE	46.4	Element size 2.5 mm, G_C=201.9 N/m as result

The 2D-FE models in general give consistent and very similar results compared to the EC5-approach, if boundary conditions consistent with the assumptions of beam theory are applied, *i.e.* Case B of Figure 3. Thus, the predicted critical load levels and influence of material parameters and geometry parameters are very similar. As an example of this, results from the analyses of Case 1, are given in Table 4.

Table 4. Base example with results showing influence of element size and boundary conditions. h=600 mm, α=0.75, β=0.25. Critical load for 2D-FE models is based on crack length=20 mm.

Approach	Critical load (kN)	Remarks
EC5	45.8	Eq.(7)–Eq.(9), k_n=6.5 ($G_C=G_{IC}$=179.7 N/m)
2D-FE	46.7	Element size 10 mm, <u>*beam boundary conditions*</u>
2D-FE	46.5	Element size 5 mm, <u>*beam boundary conditions*</u>
2D-FE	46.4	Element size 2.5 mm, <u>*beam boundary conditions*</u>
2D-FE	31.1	Element size 5 mm, <u>*support plate*</u>
2D-FE	30.8	Element size 10 mm, <u>*support plate*</u>

The Eurocode 5 approach considers pure Timoshenko beams and disregards local effects from *e.g.* supports or load-introduction. The notch capacities using the EC5 approach and the FE-analyses of the end-notched beams with beam support conditions show similar levels, see Fig. 9. It can be observed, however, that the FE-models yield higher notch capacities for small notch heights (α>0,75).

Jockwer [4] referred this to the dominant effect of Mode 2 fracture for these smaller notches. This could only partly be confirmed by the present FE-analyses, which indeed show that the total energy release rate is more influenced by Mode 2 for large values of α, but this effect accounts for only around 5-10% of the increase in relation to assuming Mode 1 failure.

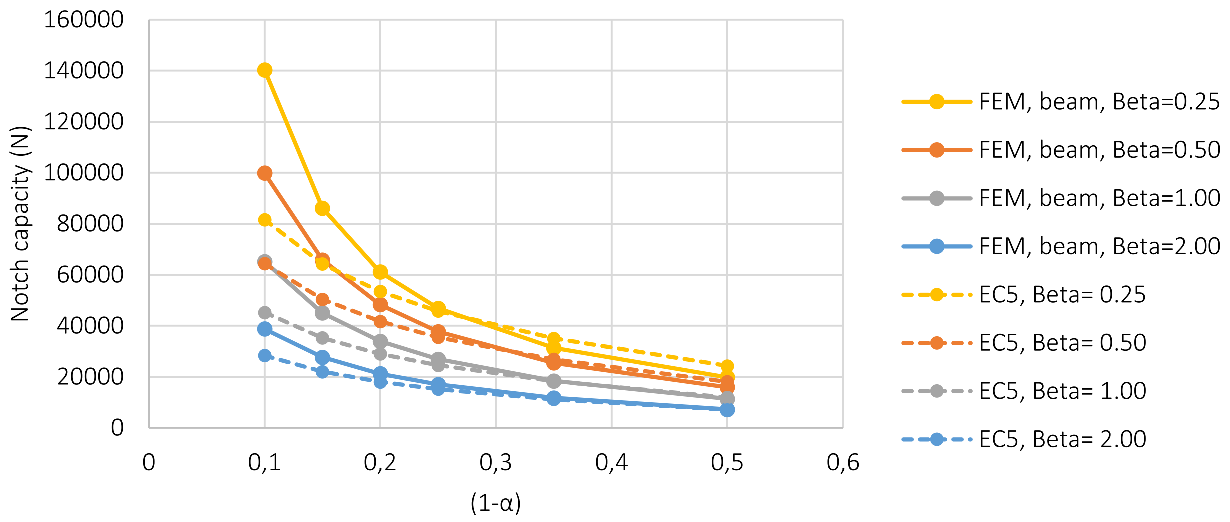

Figure 9. Notch capacities in dependency of notch ratio α according to EC5 and FE-model with beam support boundary conditions for a beam height h=600mm.

4.2 Impact of the support conditions on the notch capacity

The notch capacity for the two different boundary conditions with plate and beam supports (*cf.* Figure 3) are shown in Figure 10. It can be observed that for short notch lengths (β<1), the model with beam support conditions yields considerably higher notch capacities, especially for small notch heights. In contrast, for large notch length (β>1), both support conditions give similar notch capacities. Further, it can be observed that for plate support conditions with the smallest notch length with β=0.25 the notch capacity is even smaller than for the respective longer notch with β=0.5. This is in contradiction to the observations from the model with beam support conditions and the behaviour of the EC5 approach.

An explanation for this behaviour can be found in the interaction of the local stress concentration in compression perpendicular to the grain around the support plate and the stress concentration in tension perpendicular to the grain at the notch corner. Since the load is introduced at the lower edge of the beam, in the case of small values of β, the full height of the reduced part of the beam is not contributing to the force transfer. This phenomenon loses impact for longer notch length, for β=2 no difference between the two support conditions can be observed.

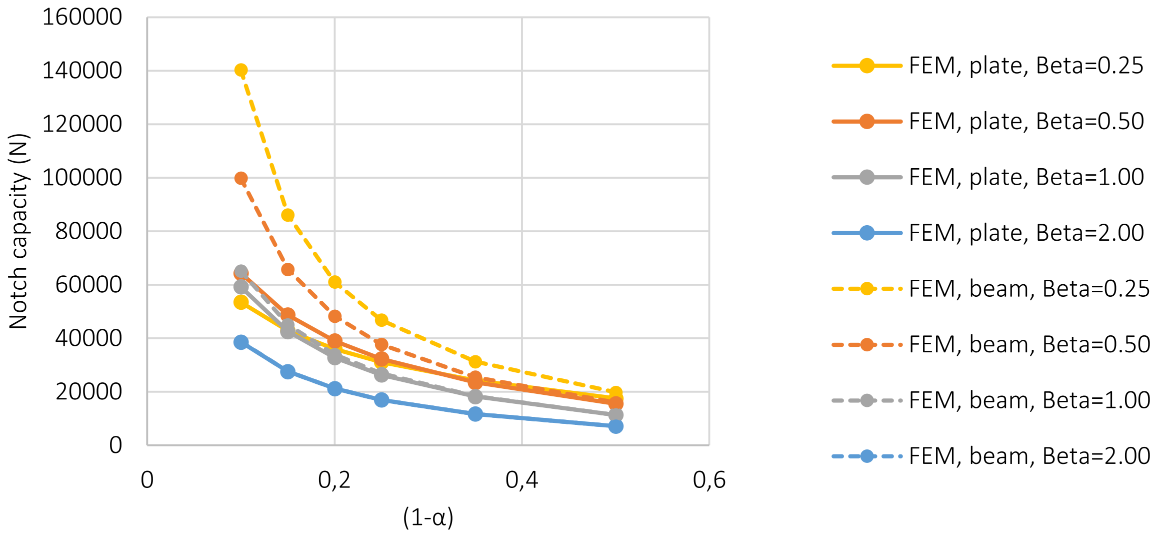

Figure 10. Notch capacities vs. reduced height (1-α) according to FE-model with plate and beam support boundary conditions for a beam height h=600mm. Note that for β=2, the curves coincide.

4.3 Impact of the notch length on the notch capacity

The comparison of the FE models with the EC5 approach shows that especially for the plate support conditions EC5 is more conservative for longer notch lengths (see Figure 11).

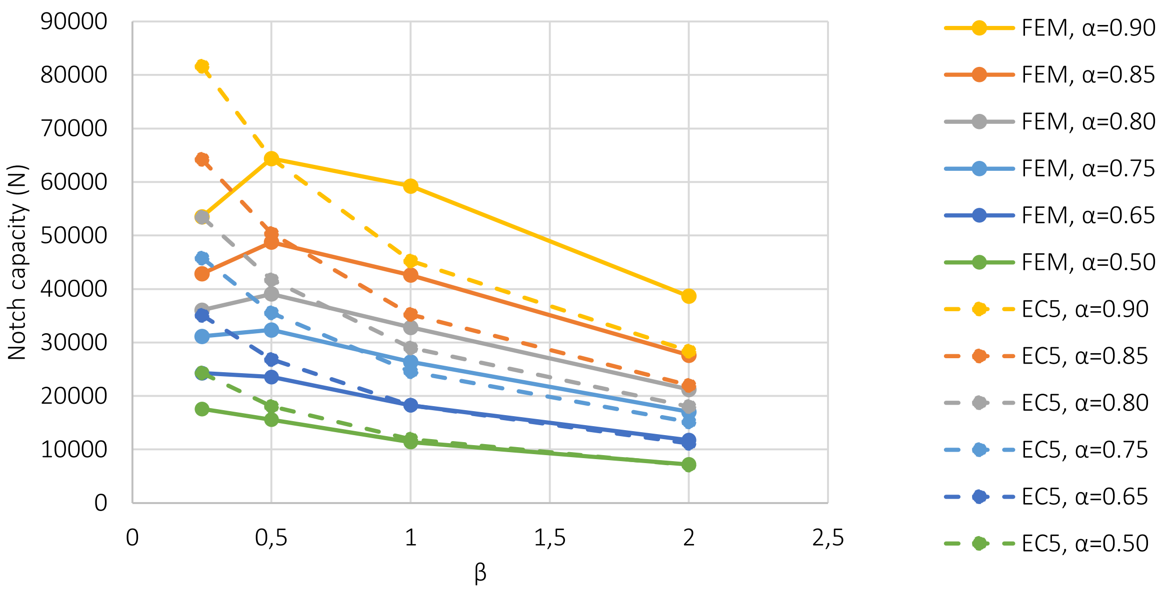

Figure 11. Notch capacities in dependency of notch ratio α according to EC5 approach and FE-model with plate support boundary conditions for a beam height h=300mm.

4.4 Impact of the moment/shear force ratio at support on the notch capacity

At a mid-support of a continuous beam both moment and shear force are acting. Typically, in timber beams ratios *M/V=1h – 4h* can be observed. In the present study, a ratio *M/V=2.5h* was assumed at support. Due to this constant ratio, it can be observed that long notches, β>1 do not influence the capacity of the beam at the support, since the predicted capacity due to crack propagation is way beyond the bending capacity of the reduced cross-section, see Figure 12. Another way of presenting these results is given in Figure 13, showing the relative shear capacity at support (*i.e.* a k_v-factor), assuming the shear strength to be 2.5 MPa and the bending strength to be 28 MPa. Here it is also seen that for small depths (h=300), the failure mode predicted is bending failure (all curves in the top left diagram of Figure 13 coincide and are straight lines).

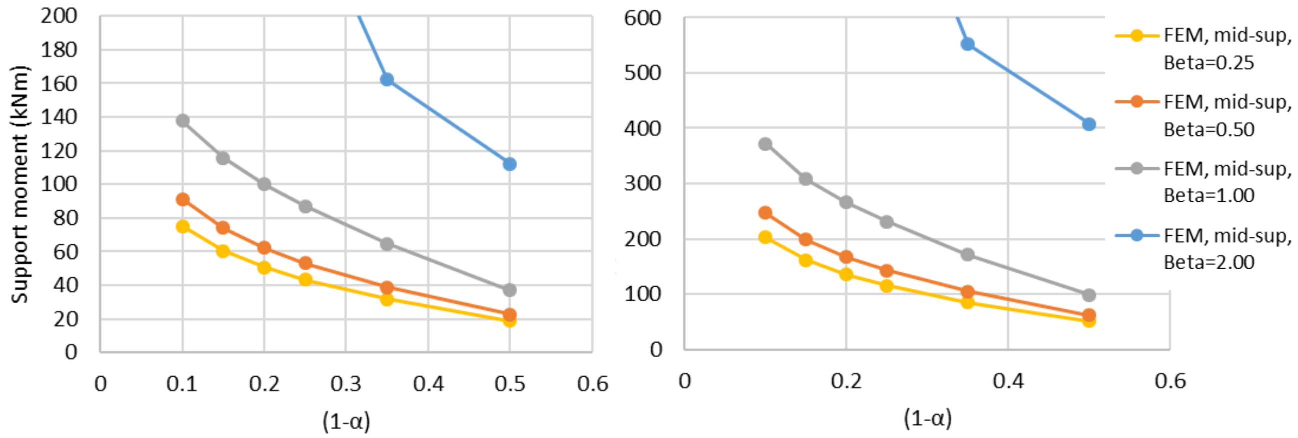

Figure 12. Notch capacities at the mid support in dependency of notch ratio α according FE-model with beam support boundary conditions. M/V=2.5h. Left: h=600 mm, Right: h=1200 mm.

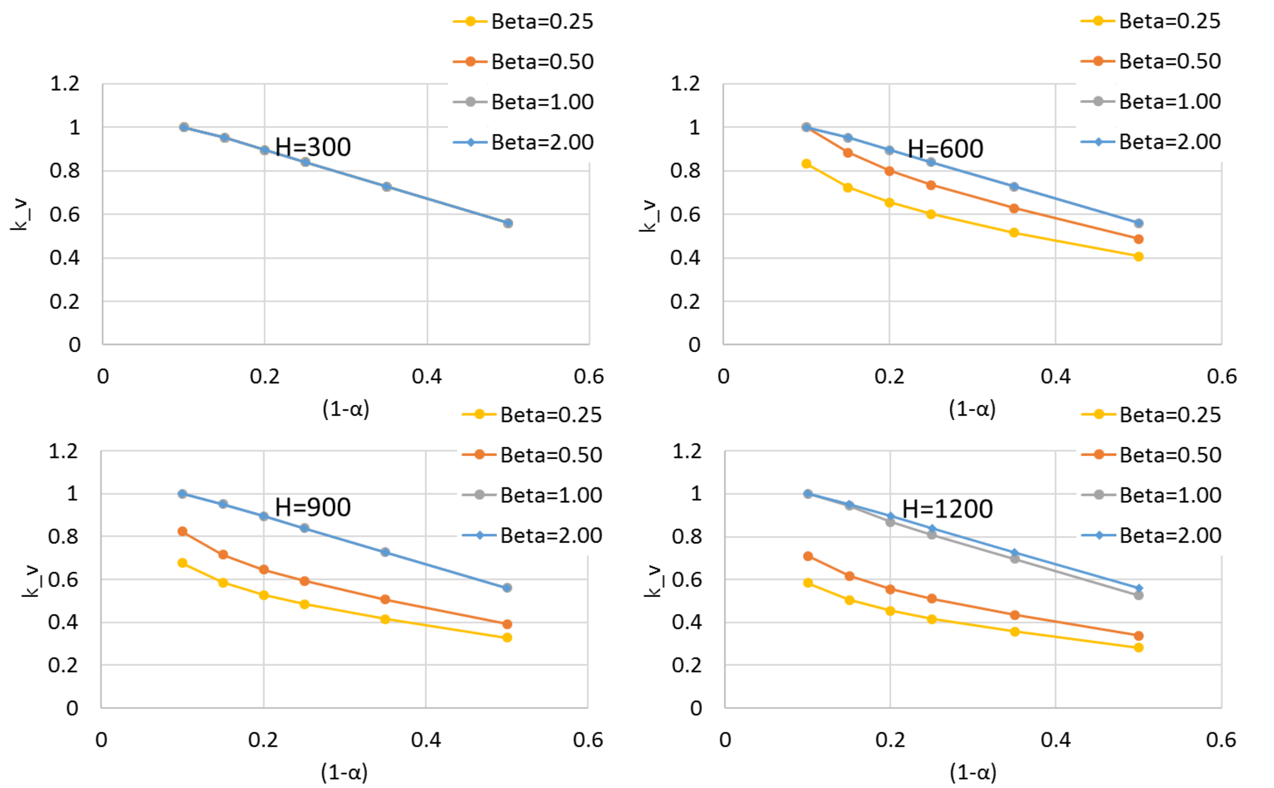

Figure 13. Relative notch capacities (k_v) at the mid support in dependency of notch ratio α. FE-model with beam support boundary conditions. M/V=2.5h. The shear strength and bending strength are set to 2.5 and 28 MPa, respectively.

4.5 General notches and slits far from support – Moment/shear force interaction

Using 2D FE-models similar to the one depicted in Figure 14, analyses of the behaviour of notches far from support were performed.

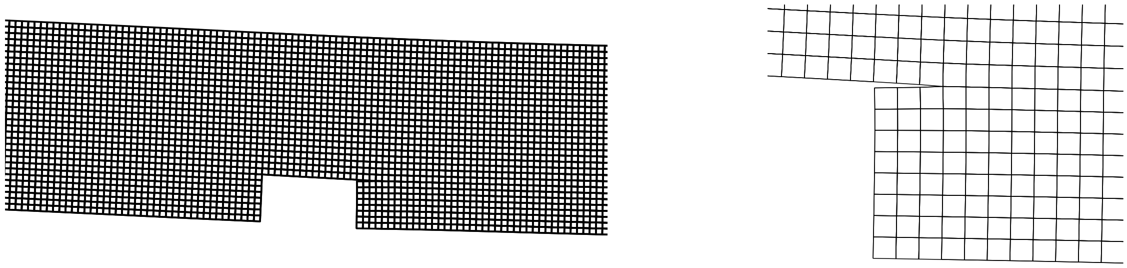

Figure 14. FE-model for analysis of beam notched far from support (left) and partial zoom (right). Here a coarser mesh than used in the analyses is shown for clarity. h=600, α =0.75, β =0.5

The main results are shown in Figure 15, depicting the linear interaction that is obtained from analyses of different combinations of moment and shear force, at the centre of the notch.

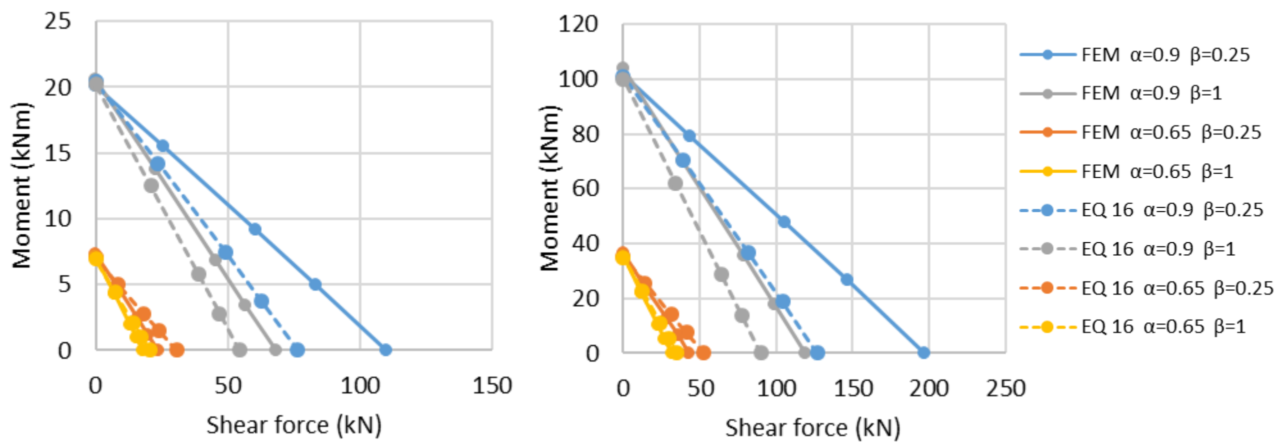

Figure 15. Results from analyses of beam with notch away from support (cf. Figure 14) Moment and shear force refer to the section in the centre of the notch; h=300 (left) h=900 (right).

5 Discussion, conclusions and outlook

5.1 Consequences for design

From the results described above the following conclusions and recommendations for design can be drawn:

The performed FE analysis on end-notched beams shows agreement with the analytical design model in Eurocode 5. This agreement is particularly good for longer notch lengths (large *β*) and large notch heights (small *α*). For smaller notch heights, the Eurocode 5 approach shows more conservative results than the comparable FE models with beam support conditions.

The support conditions have a clear effect on the notch capacity. End-notched beams with plate supports in compression perpendicular to the grain show lower notch capacities than beams with shear support along the beam end. The local and concentrated introduction of forces perpendicular to the grain in close vicinity of the notch corner reduces the notch capacity. However, currently this effect is not considered in the Eurocode 5 design approach. Based on the performed analysis a minimum notch length of β=1 could be considered in design in order to compensate for the stress interaction for plate supports. It is expected that compression perpendicular to the grain reinforcement by screws or glued-in rods and joist hangers with e.g. screws are more beneficial than pure plate support.

At mid supports in continuous beams long notches are less relevant for the beam capacity compared to the beam's shear and moment resistance at the central support. This can be related to the reduction of effective moment at the notch corner with increasing notch length. The negative moment at the mid support causes crack closure mechanisms and, consequently, causes shearing fracture (mode 2) of the notch.

At notches along the span of the beam, the FE models show a linear interaction of the effects from moment and shear force on the notch capacity. A combined analytical model, that is based on the Gustafsson approach, shows good agreement with the trends from the FEM model, but is partly more conservative for small notch heights. Such a model could be used to estimate the capacity of notches in dependency of the applied shear force and moment action at the notch corner.

5.2 Future work

Further research and more detailed analysis are needed, in particular as regards:

- the effect from the local force introduction from the supports of end-notched beams
- the discrepancy between FEM and analytical approach for small notch heights is in need of further investigation, and,
- if possible, a unified design approach of the cases studied herein, should be sought for.

6 References

[1] EN 1995-1-1. Eurocode 5, Design of timber structures: Part 1-1, General – Common rules and rules for buildings. 2004.

[2] P.J. Gustafsson: A study of strength of notched beams. CIB-W18/21-10-1, Parksville, Canada, 1988.

[3] H. Petersson. On design criteria for tension perpendicular to grain, CIB-W18/25-6-4, Åhus, Sweden, 1992.

[4] R. Jockwer, R. Steiger, A. Frangi, J. Köhler. Impact of material properties on the fracture mechanics design approach for notched beams in Eurocode 5, CIB-W18/44-6-1, Alghero, Italy, 2011.

[5] R. Jockwer, A. Frangi, E. Serrano & R. Steiger. Enhanced design approach for reinforced notched beams, CIB-W18/46-6-1, Vancouver, Canada, 2013.

[6] H. Danielsson, P.J. Gustafsson. A beam theory fracture mechanics approach for strength analysis of beams with a hole, INTER/48-19-1, Šibenik, Croatia, 2015.

[7] J. Kunecký, G. Hochreiner. Notches in wood at arbitrary beam location – numerical modelling and challenges. CompWood, Växjö, Sweden, 2019.

[8] Standards Australia International, AS 1720.1-1997: Australian Standard TM - Timber Structures – Part 1: Design methods, Standards Australia International Ltd, Sydney, Australia, 1997.

[9] CSA, O86.1-94: Engineering Design in Wood (Limit States Design), Canadian Standards Association, Etobicoke, Ontario, Canada, 1994.

[10] Forest Products Laboratory: Wood handbook: Wood as an engineering material. General Technical Report FPL-GTR-190. USDA, Forest Service, Forest Products Laboratory, Madison, WI, 2010.

[11] E. M. Wu, Application of fracture mechanics to anisotropic plates. ASME Journal of Applied Mechanics, Series E, 34-4, pp. 967-974, 1967.

[12] P.J. Gustafsson. Mean stress and initial crack approaches. In: S. Aicher, P. J. Gustafsson (Ed.), P Haller & H. Petersson. Fracture Mechanics Models for Strength Analysis of Timber Beams with a Hole or a Notch - A Report of RILEM TC-133. Report TVSM-7134, Division of Structural Mechanics, Lund University, Sweden, 2002.

[13] E. Serrano, P. J. Gustafsson. Fracture mechanics in timber engineering – Strength analyses of components and joints. Materials and Structures 40:87–96, 2006.

[14] I. Smith, G. Springer. Consideration of Gustafsson's proposed Eurocode 5 failure criterion for notched timber beams. Canadian Journal of Civil Engineering, 20(6): 1030–1036, 1993.

DISCUSSION

The paper was presented by E Serrano

P Dietsch asked if the authors were aware of test data that can be used to benchmark their numerical results. E Serrano said original database was available but do not have data on small β.

H Blass questioned the choice of 20 mm crack length defined as failure for critical load. Would the conclusion be different if different crack length was used. E Serrano explained that the influence is not that important as 10 to 30 mm would be a reasonable choice based on fracture mechanics. FEM versus analytical solutions would yield slight difference.

G Hochreiner and E Serrano discussed the issue of lone versus multiple internal forces and assumption of stress distribution based on the original work of Gustafsson.

S Aicher asked why not consider the more realistic situation of the notch having a curvature which would change the energy release. E Serrano said this was a choice and said that the micro angle length should be practically considered. P. Dietsch commented the hole and notch conditions need to be differentiated in terms of potential to add curvature in practice.

R Brander asked why used f_v=3.5 rather than 2.5 in the analysis. E Serrano said that the curve would be shifted slightly.

Contribution to the testing, evaluation and design of cross laminated timber (CLT) in respect to rolling shear

David Glasner[*)1)], Andreas Ringhofer[1)], Reinhard Brandner[1)], Gerhard Schickhofer[1)2)]

[*)] corresponding author; david.glasner@tugraz.at

[1)] Institute of Timber Engineering and Wood Technology, Graz University of Technology

[2)] holz.bau forschungs gmbh, Graz, Austria

Keywords: rolling shear strength; cross laminated timber; CLT; four-point bending test; inclined compression shear test

1 Introduction

Rolling shear is often associated with cross laminated timber (CLT) as a product inherent property coming from the crosswise arrangement of adjacent layers. Besides that, rolling shear is also of relevance for a number of structural details also in conjunction with other structural timber products; see e.g. Ehrhart & Brandner (2018b). Rolling shear is, however, rarely a decisive factor in ULS, although there are some cases where it might become a limiting factor; e.g. i) CLT slabs with low span to depth ratios, ii) notched CLT slabs and iii) CLT beams with openings.

Regarding the determination of rolling shear properties by testing, there are partly contradicting regulations, e.g. EAD 130005-00-0304 (2015) vs. EN 16351 (2021), as well as some different proposals in the literature, e.g. Ehrhart & Brandner (2018b). With focus on CLT, as the EN 16351 (2021) is not harmonised yet, new / adapted CLT products still require a European Technical Assessment (ETA) in Europe. The requirements for an ETA are regulated in the aforementioned EAD which comprises also the test setup for determination of rolling shear properties, see Chapter 2. Long-time experience in testing CLT in the frame of ETA processes at the Lignum Test Centre (LTC) clearly demonstrates that the current procedures acc. to EAD often do not lead to satisfactory nor clear results; partly no rolling shear failures are obtained because of early bending failures, partly a direct stress transfer from loading to support areas leads to interacting stresses in compression perp. to grain and rolling shear, partly – especially for CLT with multiple cross layers n_{CL} – rolling shear cracks occur already prior to the ultimate failure, see Figure 1. The rolling shear cracks are visible by temporary load drops followed by further load increase (up to roughly 20 %) and final bending or mixed failure modes. In such cases, the actual rolling shear failure is hard to pinpoint and thus a reliable and objective definition of rolling shear failure and strength is lacking.

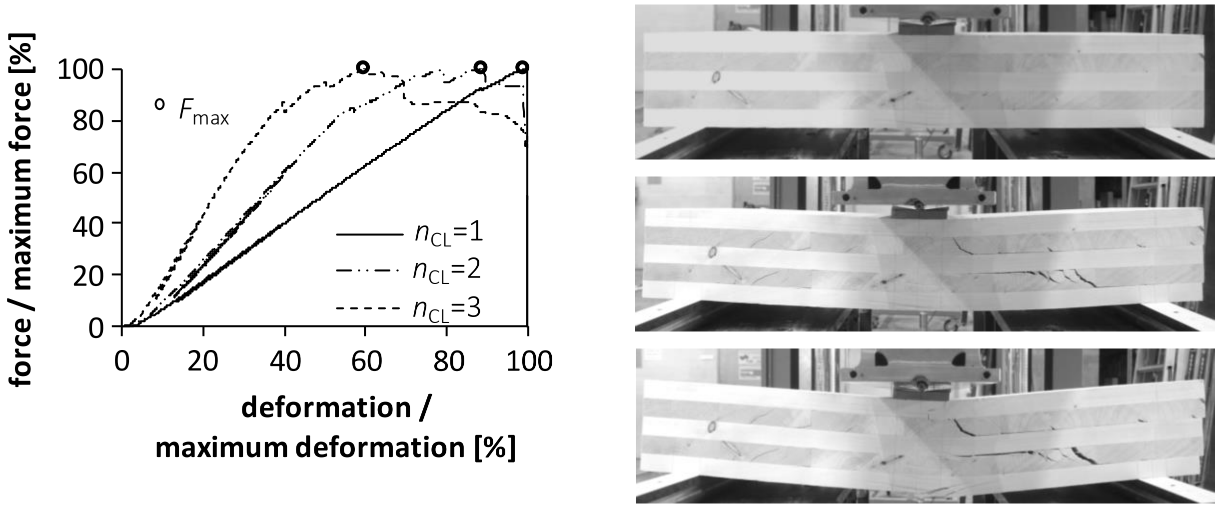

Figure 1 Typical load-displacement curves of 4-point bending test setups tested in the scope of an ETA programme (left); rolling shear crack formation of a 3 point-bending test (right): untested specimen (top), rolling shear crack formation (middle) and crack development and ultimate failure in bending (bottom)

Additionally, the definition of rolling shear stresses is also ambiguous in literature. Although the local anisotropic behaviour of timber is best described by treating stress state and material properties in a cylindrical coordinate system in longitudinal (L), radial (R) and tangential (T) direction (Figure 2), from an engineering perspective it is more suitable to define rolling shear stresses as the shear stress in a global cartesian XYZ-coordinate system, as rolling shear stresses change along the annual ring orientation which is in general unknown to the engineer. As τ_{YZ} in general is a combination of stresses transformed from the local RT- into the global YZ-coordinate system, the corresponding rolling shear strength f_r represents a system property instead of a material property. Within this paper, rolling shear τ_r will be treated in the latter definition, meaning shear in the global YZ coordinate system of the boards.

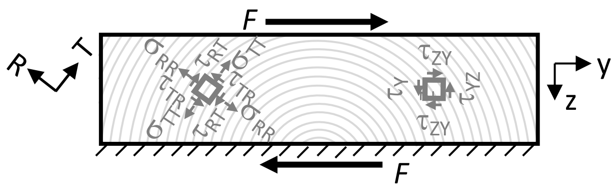

Figure 2 Rolling shear stresses τ_{RT} in the local RT-coordinate system and τ_{YZ} in the global YZ-coordinate system

This contribution aims to provide a better understanding regarding the influence of test and assessment methods on the rolling shear properties of CLT and finally recommends a methodology, which enables the determination of reliable and robust strength properties. Furthermore, a design approach that is consistent with the provided recommendations is presented.

2 State of the art

As outlined in Chapter 1, both in literature and in standardization various test setups exist to determine the rolling shear strength f_r of CLT. Concentrating on the holistic test methods (Ehrhart & Brandner (2018b)), they can be divided into two subgroups: i) out-of-plane bending tests and ii) shearing tests. The most commonly used out-of-plane bending test is the four-point bending (4p-B) test setup, which, depending on the considered standard, varies regarding its geometric parameters according to Figure 3 (left). A special form of the 4p-B test is the three-point bending (3p-B) test where the distance between load introductions a_2 is reduced to the width w_s of the load introduction (Figure 3 middle). An example for the shearing test setups is the inclined compression shear (IS) test, see Figure 3 (right).

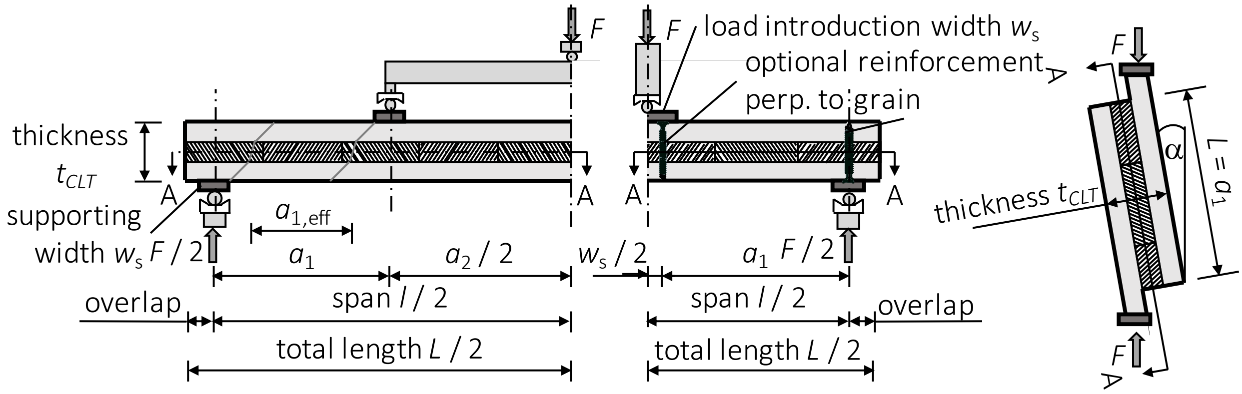

Figure 3 Basic test setup of a 4p-B test (left) a 3p-B test (middle) and an IS test (right) exemplarily for a three-layered CLT element with the relevant geometric parameters

The test setup to be followed for the obtainment of an ETA is regulated by the EAD and in accordance with EN 408 (2012). Following these regulations, CLT elements shall have constant dimensions in width w = 800 mm, span l = 3,000 mm and distance between load bearing and supports a_1 = 450 mm. The evaluation shall be done using either the Shear Analogy Method (SAM) according to Kreuzinger (1999) or the modified γ-method. Conversely, the product standard of CLT, the EN 16351 (2021) provides a 4p-B test configuration with variable dimensions depending on the thickness t_{CLT} with $a_1 = 3\ t_{CLT}$ and $l = 12\ t_{CLT}$ and a width of $w = 4\ w_b$ (but not less than 600 mm, with w_b as the width of the laminations). In contrast to EAD, the Timoshenko beam theory shall be used for the calculation of stresses. To this date, it is unknown whether those two setups yield comparable results and – assuming that results may not be comparable – whether different strengths result from the difference in the test method itself or the varying stress calculation.

Despite representing a stress state similar to the exposure in practice, a major downside of this test method – in particular according to EAD – is the regular occurrence of bending failures at the ultimate load instead of rolling shear. This behaviour was observed in approximately 30 % of more than 300 rolling shear tests, which were carried out at the LTC within the last years by following the guidelines in EAD. In fact, in most of these cases a partial rolling shear failure occurred prior reaching the ultimate force, see Figure 1.

EN 16351 (2021) also offers a rolling shear test configuration adapted from the configuration in EN 789 (2005) where the shear force is applied on the end grain (parallel to the fibre direction) of the outer layers instead of steel plates. The width w shall be a minimum of 100 mm and the length l of the specimens has to be chosen dependent on t_{CLT} so that the diagonal is inclined at α = 14° to the vertical force direction. Aicher et al. (2016) noted that in reference to the IS test in EN 408 (2012) that α should rather refer to the inclination of the resultant force than the specimen diagonal.

Ehrhart & Brandner (2018a) conducted IS tests on single boards of different European soft- and hardwood species. For Norway spruce no influence of the density on f_r was found. Instead, in frame of their parameter study they identified the board aspect ratio w_b / t_b as the main influencing factor on f_r in form of a significant decrease of f_r for aspect ratios below 4. Their recommended equation $f_{r,k} = 0.2 + 0.3\ w_b / t_b$ with a minimum value of 0.8 N/mm² for the CLT strength class CL 24 was included in a former working draft of Eurocode 5 (prEN 1995-1-1 (13 April 2018)) but not in the current draft prEN 1995-1-1 (27 October 2021) where $f_{r,k}$ was set to a constant value of 0.7 N/mm² due to reasons unknown to the authors of this paper. In the meantime, the influence of w_b / t_b was confirmed several times by other IS tests on single boards, e.g. Li et al. (2019) or Nero et al. (2022). In contrast, IS tests of CLT manufactured with spruce-pine-fir (SPF) lumber with a board aspect ratio of w_b / $t_b \approx 2.3$ by Wang et al. (2018) indicate that the board aspect ratio is less relevant if the boards are arranged with contacting narrow faces as no difference in mean strength was found between specimens with and without narrow-face-bonding ($f_{r,mean}$ = 1.50 N/mm² resp. 1.52 N/mm²) but a 25 % decrease for the specimens with 6 mm gaps. A similar behaviour was observed by Gardner et al. (2020) using a three-point bending (3p-B) test setup with $a_1 \approx 3\ t_{CLT}$ for the SPF specimens and $w_b / t_b \approx 5.1$ reporting $f_{r,mean}$ = 1.53 N/mm² for the specimens without gaps and a reduction of $f_{r,mean}$ up to 45 % if the gap width roughly equalled w_b.

O'Ceallaigh et al. (2018) used the 4p-B test setup according EN 16351 (2021) on CLT panels of Irish Sitka spruce with a constant w_b / $t_b \approx 3.8$ and no gaps or relief grooves for all layups. They found that $f_{r,mean}$ decreased from 2.22 N/mm² to 1.30 N/mm² when the thickness t_{CLT} increased from 20-<u>20</u>-20 mm to 40-<u>40</u>-40 mm (transversal layers are underlined) indicating a size effect. An additional 5-layered series with 20-<u>20</u>-20-<u>20</u>-20 mm led to $f_{r,mean}$ = 1.40 N/mm². Due to the minimal resulting $f_{r,k}$ =0.90 N/mm² for the 3s-120 layup, the regulation in the current draft of EC 5 seems rather conservative.

Mestek et al. (2011) observed an increasing $f_{r,mean}$ of up to 20 % when interacting with compressive stresses perp. to grain. In relation to the test setup acc. to EAD this indicates that the rolling shear strength could be overestimated especially for elements with a high t_{CLT} due to the increased ratio of compressive stresses vs. rolling shear stresses as a result of the lower a_1 / t_{CLT}.

To sum Chapters 1 and 2 up, the main influencing parameters regarding the rolling shear strength of CLT have been identified to be i) definition of rolling shear failure and strength, ii) calculation and evaluation methods, iii) test configuration, iv) interaction of rolling shear and stresses perp. to grain, and v) size effects. In the following, a proper definition regarding i) will be proposed in Chapter 3 while Chapter 4 deals with ii) and iii) in particular the different stress distributions of the test configurations. A test program was conducted to address iii) – v) in an isolated manner in combination with a database of 4p-B tests in the scope of ETA obtainment processes. Material and Methods and Results are discussed in Chapters 5 and 6, respectively.

3 Proposed definition of rolling shear failure and strength of CLT

During testing, rolling shear cracks reduce the rolling shear stiffness of the transverse layers which leads to a reduction in effective bending stiffness of the total beam. This, in consequence, results in lower rolling shear stresses in the cross layers and higher normal stresses in the longitudinal layers which at that point or after further load increase lead to a bending failure of the CLT. As a conclusion, the rolling shear strength f_r often is evaluated at a bending failure rather than an actual rolling shear failure.

At the LTC it is common practice to evaluate f_r from the force associated with the first clear rolling shear cracks, F_{crack}, instead automatically from the maximum force F_{max}. This is based on the experience from testing acc. to the EAD and the observation that clear rolling shear cracks may occur clearly below the ultimate force. F_{crack} is determined by identifying drops in force vs. time diagrams in combination with notes in testing protocols. This identification may, however, miss objectivity, i.e. uncertainty coming from individual interpretations cannot be fully prevented. With the aim of a more objective determination of the rolling shear strength, a definition is proposed in analogy to the compressive strength perpendicular to the grain acc. EN 408 (2012). Therein, $f_{c,90}$ is defined as the intersection of the stress-strain curve and a line with the slope of the modulus of elasticity between 10 and 40 % of $f_{c,90}$ with an offset of 1 % strain. Transferred to rolling shear this would demand a continuous recording of the shear deformation. However, these measurements are not deemed suitable as i) the arrangement of a shear field measurement is rather complex, ii) common measurement devices, e.g. displacement transducers, are very likely to be damaged during cracking / fracturing, and iii) as CLT consists of multiple orthogonal layers which are either stressed in longitudinal or rolling shear in frame of a rigid composite it is challenging to measure reliably the rolling shear deformation.

Thus, it is proposed to define f_r at the point of the maximum rolling shear stress that occurred until the effective system stiffness of the CLT plate, determined as secant stiffness within the apparent linear-elastic range, is reduced by 10 %. The methodology is illustrated in Figure 4 and consists of the following steps:

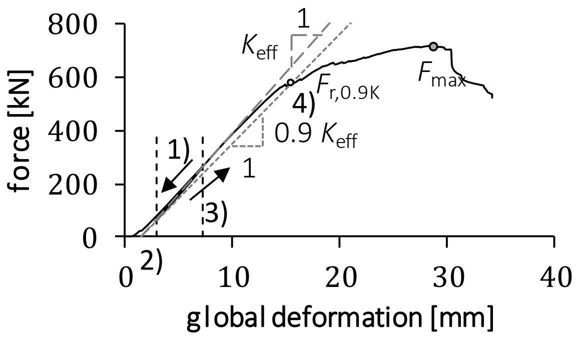

Figure 4 force vs. global deformation and basic methodology for the proposed determination of f_r

1) determination of the effective system stiffness K_{eff} by linear regression of force vs. global deformation between 10 and 40 % of F_{max};
2) calculation of the intersection between the regression function at $F = 0$;
3) generation of a new linear function with a slope of 0.9 K_{eff} through the intersection point from 2);
4) determination of the intersection between the new linear function from 3) with the force-deformation curve. $F_{r,0.9K}$ then is the maximum force occurring up until the intersection at 4) and used to calculate f_r.

4 Comparison of calculation methods

Rolling shear strength values, based on the stresses determined by the three simple beam theories, Shear Analogy Method (SAM), the modified γ-method and the Timoshenko beam theory, are compared with each other and benchmarked with the outcomes from a 2D finite element (FE) shell model. The test database for this comparison was provided by the LTC and includes 15 series from different producers, varying CLT layups and geometric properties; see Table 1. All related tests were executed by a 4p-B test configuration. All test series were manufactured with softwood boards of strength class C24 acc. to EN 338 (2016), hence the corresponding stiffness parameters were assumed for the calculation. In addition, a rolling shear modulus of $G_{r,mean}$ = 100 N/mm² acc. to Ehrhart & Brandner (2018a) was assumed. As a simplification, the Poisson ratios were set to zero as no significant influence was observed in an exemplary parameter variation on one test series. The Young's modulus perp. to the grain was also set to zero for the simple beam theories.

The 2D-FE shell model was assembled with quadrilateral elements with a constant mesh size of 5 mm assuming linear elastic orthotropy. The supports were modelled via beam elements with no axial stiffness and the load introduction in the centre of the beam similarly. A unit point load was applied in the centre of the load introduction beam. All beams had a rectangular cross section, a constant height of 20 mm and a width equal to that of the CLT plate. All FE models were assembled using the axis of symmetry at midspan. Regarding the SAM, a constant spacing between the hinged couplings of the beams of 50 mm was chosen as a compromise between resolution of results and numerical stability.

Table 1 Test series and geometric parameters (see Figure 3) of the 4p-B tests conducted at the LTC

Test series No. [-]	*layup* [mm]	t_{CLT} [mm]	a_1 [mm]	a_2 [mm]	*overlap* [mm]	l [mm]	w_s [mm]
01	40-40-40-40-40-40-40	280	500	2,000	100	3,000	100
02	40-40-20-20-20-40-40	220	500	2,000	100	3,000	100
03	40-20-40-20-40	160	350	2,200	150	2,900	50
04	40-20-40	100	400	2,200	100	3,000	50
05	30-40-30	100	350	2,300	100	3,000	50
06	40-30-40-30-40	180	400	2,200	100	3,000	100
07	30-40-30-40-30-40-30	240	400	2,200	100	3,000	100
08	40-20-40	100	400	2,200	200	3,000	45
09	40-30-40-30-40	180	500	2,000	200	3,000	80
10	40-40-40-40-40-40-40	280	550	1,900	200	3,000	100
11	30-30-30	90	400	2,200	100	3,000	50
12	40-20-40-20-40	160	500	2,000	100	3,000	80
13	40-40-40	120	450	2,100	100	3,000	50
14	40-40-40-40-40	200	500	2,000	100	3,000	80
15	40-40-40-40-40	200	400	1,800	300	2,600	100

In case of a constant shear force along the shear field, the modified γ-method and Timoshenko beam theory would also give a constant shear stress distribution. This is, however, not the case for SAM which gives non-constant shear stresses. This outcome is similar to that from FE analysis, which is used as benchmark because of its most realistic shear stress distribution. Thus, the maximum rolling shear stress $\tau_{r,max}$ along the shear field was evaluated as well as the mean rolling shear stress $\tau_{r,i,mean,a1}$, which is defined as the rolling shear flow along the span in reference to a_1 in transverse layer i, see Eq. (1). For CLT elements with an odd number of transversal layers, only the middle cross layer was evaluated. In the case of an even number of transversal layers, the mean of both cross layers closest to the centre layer was taken. Furthermore, stresses were only evaluated at mid-height of the respective transverse layer (along sections A-A acc. to Figure 3).

$$\tau_{r,i,mean,a_1} = \frac{1}{a_1} \int_{L/2} \tau_{r,i} \mathrm{d}x \qquad (1)$$

The results of the different calculation methods are shown in Figure 5 by referring each to the results of the maximum stress calculated by FE analysis as reference. It can be clearly shown that the differences between the analysed methods are overall

negligible. The extreme values all correspond to test series 2 and 10 which contain double outer layers. Although all simple beam theories overestimate the maximum rolling shear stresses compared to $\tau_{r,FEM,max}$, testing evaluation should follow the same calculation methods that are also most commonly used in design practice meaning

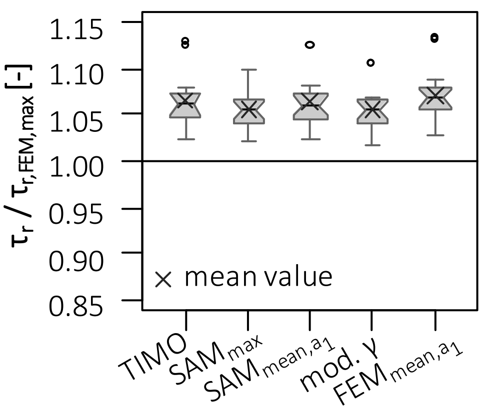

Figure 5 Comparison of the rolling shear stresses gained from the different calculation methods in reference to the maximum stresses of the FE analysis

one of the simple beam theories. For the remainder of this contribution however, $\tau_{r,FEM,mean,a1}$ will be used to calculate stresses in order to be able to carry out a continuous stress interaction of rolling shear stresses and stresses perp. to the grain, see Section 5.1.

To address the difference in strengths in dependence of the configurations, the shear flow of a three-layered element with a layup 40-<u>40</u>-40 mm was analysed using FE models of a 4p-B test configuration acc. to EN 16351 (2021) with $a_2 = 6\ t_{CLT} = 720$ mm, a 3p-B test configuration with $a_2 = w_s = t_{CLT} / 2 = 60$ mm and an IS test with $\alpha = 10$ ° for the same $a_1 = 3\ t_{CLT}$. The overlap was 60 mm for the out-of-plane bending tests.

Figure 6 then shows the shear flows of the different test configurations in reference to $\tau_{r,i,mean,a1}$ acc. Eq. (1). The shear flows are normalized meaning that the areas under the respective curves are of the same size. The ratios of the maximum stresses are given in Table 2. Thereby, it can be seen that the IS test leads to the highest maximum rolling shear stresses compared to the bending test configurations due to the fact that part of the shear flow distributes into the additional material in the overlap and the area between the load introductions.

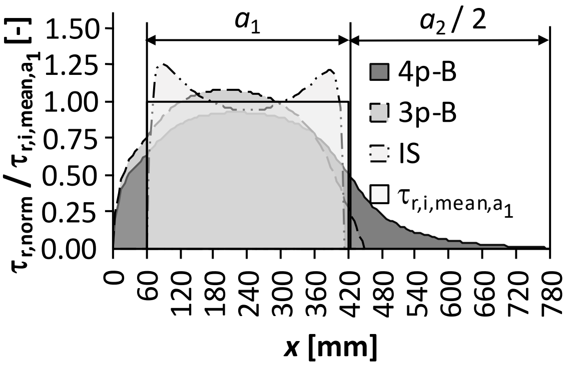

Figure 6 normalized shear flow of the different test configurations

max $\tau_{r,norm,m}$ / max $\tau_{r,norm,n}$	*m*	*4p-B*	*3p-B*	*IS*	*$\tau_{r,i,mean,a1}$*
n					
4p-B		1.00	1.16	1.35	1.08
3p-B		0.86	1.00	1.17	0.93
IS		0.74	0.86	1.00	0.80
$\tau_{r,i,mean,a1}$		0.93	1.08	1.25	1.00

Table 2 ratio of maximum rolling shear stresses for the normalized rolling shear flow

5 Material and Methods

In order to analyse the parameters discussed in Chapter 2 (e.g. test configuration and their geometric properties) in an isolated manner, a test program consisting of in total 13 test series by means of eleven 3p-B test series and two IS test series as shown in Figure 1 was conducted. In order to reduce the material use, 3p-B was chosen in favour of 4p-B. With regard to the CLT specimens, two layups with three layers (L1: 40-<u>20</u>-40 mm; L2: 40-<u>40</u>-40 mm) and one with five layers (L3: 40-<u>40</u>-40-<u>40</u>-40 mm) were tested.

The transversal layers of L1 and all layers of L3 consisted of boards with a w_b = 200 mm (w_b / t_b = 10 resp. 5), the transversal boards of L2 had a w_b = 160 mm (w_b / t_b = 4). All elements were manufactured with softwood of nominal strength class C24 acc. to EN 338 (2016) without narrow-face bonding, visible gaps or relief grooves. All relevant geometric parameters are given in Table 3. Although each layup was produced within a single master panel, during sampling it was ensured that specimens of the same test series contained different cross layers. Nonetheless, the variability between different production batches or manufacturers cannot be represented.

Table 3 Geometric and execution parameters of the additional test program

	Test series [-]	*layup* [mm]	t_{CLT} [mm]	w [mm]	a_1 [mm]	*reinforced perp. to grain* [-]	*overlap* [mm]	w_s [mm]
3p-Bending	PS-100-300-360-V	40-20-40	100	300	360	yes	60	60
	PS-200-300-450-V	40-40-40-40-40	200	300	450	yes	100	60
	PS-120-300-360	40-40-40	120	300	360	no	60	60
	PS-120-800-360	40-40-40	120	800	360	no	60	60
	PS-120-500-200	40-40-40	120	500	200	no	60	60
	PS-120-500-360	40-40-40	120	500	360	no	60	60
	PS-120-500-450	40-40-40	120	800	450	no	60	60
	PS-100-500-360-V	40-20-40	100	500	360	yes	60	60
	PS-120-500-360-V	40-40-40	120	500	360	yes	60	60
	PS-120-500-450-V	40-40-40	120	500	450	yes	60	60
	PS-200-500-450-V	40-40-40-40-40	200	500	450	yes	100	60
Inclined Shear	Test series [-]	layup [mm]	t_{CLT} [mm]	w [mm]	a_1 [mm]	α [°]	- [-]	- [-]
	IS-100-500-360	40-20-40	100	500	360	10	-	-
	IS-120-500-360	40-40-40	120	500	360	10	-	-

To reduce the influence of compression perp. to the grain stresses on rolling shear, in some test series fully-threaded, self-tapping timber screws with a nominal diameter of d_{nom} = 10.0 mm and spacing s = 75 mm were applied as reinforcements at the load introduction and supports.

For stress evaluation, each setup was represented also via FE models which used the methodology presented in Chapter 4. Screws in the reinforced series were modelled as beams with an axial stiffness equal to the effective steel cross section while all other stiffness components were set to zero.

In addition to the mentioned test program, a database of 295 4p-B test results with the geometric properties acc. to Table 1 was considered. The 15 test series of five different manufacturers had transverse layers that were either narrow-face-bonded or consisted of boards with a board ratio of w_b / t_b > 3.6. All specimens were manufactured using softwood boards acc. to EN 338 (2016) and without visible gaps or relief grooves. The rolling shear strengths were corrected to a reference moisture content of u_{ref} = 12 % assuming 3 % strength reduction per percent increase in u as proposed in Brandner et al. (2012) for longitudinal shear.

5.1 Interaction of rolling shear stresses and stresses perpendicular to the grain

The ellipsoidal failure criteria acc. to Steiger & Gehri (2011) and Hoffman (1967), adapted to rolling shear by Akter & Bader (2020), as well as the bilinear model acc. to Mestek et al. (2011) were applied to account for the effect of stresses perp. to the grain on the rolling shear resistance.

These three failure criteria were transformed to yield f_r, see Eqs. (2)–(4). In the case of Hoffmann's criterion, it was assumed that $\sigma_{RR} = \sigma_{90}$, $\sigma_{TT} = 0$ and $\tau_{RT} = \tau_r$. In the scope of these interactions mean strengths were assumed to $f_{c,90}$ = 3.50 N/mm² acc. to Brandner (2018) and $f_{t,90}$ = 1.50 N/mm² acc. to Brandner & Jantscher (2022).

$$f_{r,SIA265} = \sqrt{\frac{\tau_r^{\,2}\left[1-\left(\dfrac{f_{c,90}}{f_{c,90}+f_{t,90}}\right)^2\right]}{1-\dfrac{(f_{c,90}+\sigma_{90})^2}{(f_{c,90}+f_{t,90})^2}}} \quad (2)$$

$$f_{r,Hoffmann} = \sqrt{\frac{\tau_r^2}{1-\dfrac{\sigma_{90}}{f_{t,90}f_{c,90}}\left(f_{c,90}+\sigma_{90}-f_{t,90}\right)}} \quad (3)$$

$$f_{r,Mestek} = \frac{\tau_r}{\min\begin{cases}1+0.35\,\sigma_{c,90}\\ 1.20\end{cases}} \quad (4)$$

For evaluation of the corrected rolling shear stress distributions $\tau_{r,corr,i}(x)$ these failure criteria were continuously applied on the stress distributions $\tau_{r,i}(x)$ and the corresponding $\sigma_{90}(x)$ along section A-A located at the centreline of the cross layer(s); see Figure 7 (left), exemplarily for a 3p-B test. Finally, the strength $f_{r,i}$ corrected for the transverse stress influence was determined acc. to Eq. (1) using $\tau_{r,corr,i}(x)$ instead of $\tau_{r,i}(x)$.

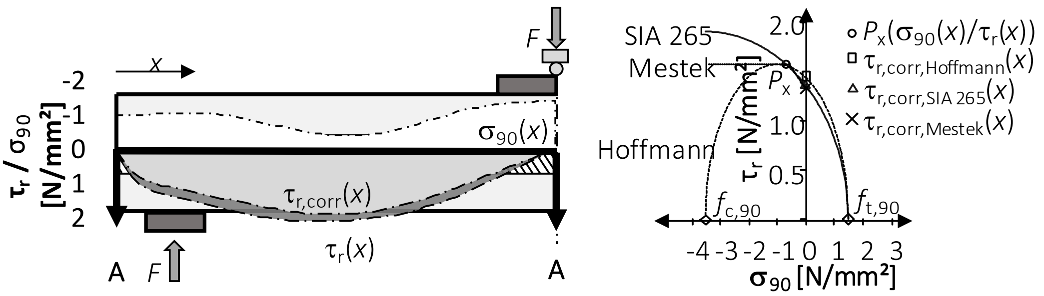

Figure 7 Methodology to account for the interaction of rolling shear stresses and stresses perp. to the grain exemplarily for a three-layer CLT element; left: stress distributions along section A-A; right: stress interaction functions

6 Results and Discussion

Table 4 contains the main results from the experimental campaign while the main statistics of the EAD test series is given in Table 5. With regard to the assumptions in Section 5.1, it is shown that $f_{r,12,Mestek}$ and $f_{r,12,SIA}$ lead to comparable results. Hoffmann's criterion, however, results in higher strengths as it assumes a lower influence of compressive stresses perp to the grain on $f_{r,12}$ without stress interaction. Regardless, it was chosen to use $f_{r,12,SIA}$ acc. Eq. (2) for the further discussion as the interaction is already anchored in standardisation.

Table 4 Summary of the main statistics from the additional test series

		3-point Bending											*Inclined Shear*	
Test series		PS-100-300-360-V	PS-200-300-450-V	PS-120-300-360	PS-120-800-360	PS-120-500-200	PS-120-500-360	PS-120-500-450	PS-100-500-360-V	PS-120-500-360-V	PS-120-500-450-V	PS-200-500-450-V	IS-100-500-360	IS-120-500-360
No. of specimens		6	6	6	6	6[1]	6	6	6	6	6	6	15	12
u [%]	**mean**	**10.9**	**10.9**	**11.0**	**10.9**	**11.0**	**10.9**	**10.3**	**10.9**	**11.0**	**10.6**	**11.2**	**11.3**	**11.5**
	CoV [%]	2.52	1.98	5.42	1.71	4.75	3.41	2.62	5.13	3.74	2.52	2.18	1.64	2.93
ρ_{12} [kg/m³]	**mean**	**478**	**434**	**433**	**445**	**459**	**438**	**446**	**478**	**452**	**446**	**454**	**460**	**432**
	median	478	432	432	447	461	432	446	482	456	452	457	460	433
	CoV [%]	3.60	2.98	1.63	2.83	1.14	3.20	1.42	4.01	2.46	5.12	2.67	1.58	3.39
$f_{r,12}$ [N/mm²]	**mean**	**1.53**	**1.02**	**1.21**	**1.09**	**1.72**	**1.22**	**0.96**	**1.64**	**1.18**	**0.99**	**1.09**	**1.43**	**1.00**
	CoV [%]	8.98	10.3	9.61	11.9	4.37	12.1	12.7	4.96	10.1	8.60	11.8	16.1	15.4
	$LN_{0.05}$	1.32	0.85	1.03	0.89	1.60	0.99	0.77	1.51	1.00	0.86	0.89	1.08	0.75
	$char_{EN14358}$	1.24	0.79	0.97	0.82	1.52	0.91	0.71	1.46	0.94	0.81	0.82	1.02	0.70
$f_{r,12,SIA}$ [N/mm²]	**mean**	**1.50**	**1.00**	**1.16**	**1.04**	**1.51**	**1.17**	**0.93**	**1.60**	**1.16**	**0.98**	**1.07**	**1.37**	**0.98**
	CoV [%]	8.81	10.1	9.22	11.5	3.92	11.7	12.4	4.86	9.90	8.49	11.6	15.7	15.3
	$LN_{0.05}$	1.29	0.83	0.99	0.86	1.41	0.96	0.75	1.48	0.99	0.85	0.87	10.4	0.74
	$char_{EN14358}$	1.22	0.78	0.93	0.80	1.33	0.88	0.69	1.42	0.92	0.80	0.80	0.98	0.69
$f_{r,12,Hoffmann}$ [N/mm²]	**mean**	**1.51**	**1.00**	**1.18**	**1.06**	**1.60**	**1.19**	**0.94**	**1.61**	**1.16**	**0.98**	**1.08**	**1.41**	**0.99**
	CoV [%]	8.88	10.2	9.42	11.7	4.23	11.9	12.5	4.90	10.0	8.53	11.6	16.6	15.6
	$LN_{0.05}$	1.30	0.84	1.01	0.87	1.49	0.97	0.76	1.49	0.99	0.85	0.88	1.05	0.74
	$char_{EN14358}$	1.22	0.78	0.95	0.81	1.42	0.89	0.70	1.43	0.93	0.80	0.81	0.99	0.70
$f_{r,12,Mestek}$ [N/mm²]	**mean**	**1.49**	**0.99**	**1.13**	**1.02**	**1.47**	**1.14**	**0.92**	**1.59**	**1.15**	**0.97**	**1.06**	**1.36**	**0.95**
	CoV [%]	8.75	10.0	9.13	11.3	4.12	11.6	12.2	4.82	9.82	8.45	11.5	15.7	15.1
	$LN_{0.05}$	1.29	0.83	0.98	0.85	1.37	0.94	0.75	1.47	0.98	0.85	0.87	1.03	0.72
	$char_{EN14358}$	1.21	0.77	0.92	0.79	1.30	0.87	0.69	1.41	0.92	0.80	0.80	0.97	0.67

[1] a data malfunction occurred for one specimen, thus it was excluded from further data processing

Table 5 Summary of the main statistics from the EAD test series

Test series		*01*	*02*	*03*	*04*	*05*	*06*	*07*	*08*	*09*	*10*	*11*	*12*	*13*	*14*	*15*
No. of specimens		20	20	16	19	20	19	20	17	20	19	21	20	21	21	19
u [%]	**mean**	**13.2**	**13.4**	**12.8**	**13.4**	**11.4**	**11.0**	**11.1**	**12.3**	**13.3**	**12.9**	**9.94**	**11.9**	**7.87**	**8.68**	**13.1**
	CoV [%]	1.78	3.43	3.06	2.47	2.46	2.27	2.01	5.22	2.44	3.64	12.2[1]	3.22	9.34	3.28	5.23
ρ_{12} [kg/m³]	**mean**	**445**	**442**	**437**	**444**	**446**	**445**	**446**	**444**	**446**	**444**	**472**	**465**	**457**	**461**	**456**
	median	446	442	435	443	446	442	448	443	448	444	464	471	458	460	459
	CoV [%]	1.31	1.06	2.34	1.88	1.77	1.22	1.68	2.53	1.85	1.59	3.64	3.79	1.72	1.10	1.67
$f_{r,12}$ [N/mm²]	**mean**	**1.76**	**2.42**	**2.36**	**1.92**	**1.58**	**2.00**	**1.92**	**1.89**	**1.53**	**1.62**	**1.52**	**1.88**	**1.22**	**1.12**	**1.49**
	CoV [%]	4.53	5.45	5.39	11.0	8.84	3.18	5.09	5.89	6.12	3.66	7.04	5.69	8.66	4.31	6.54
	$LN_{0.05}$	1.63	2.21	2.16	1.58	1.36	1.90	1.77	1.71	1.38	1.52	1.35	1.71	1.06	1.04	1.34
	$char_{EN14358}$	1.59	2.17	2.11	1.53	1.33	1.81	1.74	1.68	1.36	1.47	1.32	1.68	1.03	1.09	1.31
$f_{r,12,SIA}$ [N/mm²]	**mean**	**1.61**	**2.24**	**2.17**	**1.85**	**1.52**	**1.85**	**1.75**	**1.82**	**1.46**	**1.50**	**1.48**	**1.79**	**1.19**	**1.07**	**1.40**
	CoV [%]	4.22	5.08	5.08	10.7	8.55	2.99	4.71	5.71	5.89	3.43	6.87	5.46	8.44	4.16	6.20
	$LN_{0.05}$	1.50	2.05	1.99	1.53	1.31	1.76	1.61	1.66	1.32	1.42	1.31	1.63	1.03	1.00	1.26
	$char_{EN14358}$	1.46	2.02	1.95	1.48	1.28	1.67	1.59	1.63	1.30	1.36	1.29	1.61	1.01	0.97	1.23
$f_{r,12,Hoffmann}$ [N/mm²]	**mean**	**1.67**	**2.33**	**2.27**	**1.88**	**1.54**	**1.92**	**1.82**	**1.85**	**1.49**	**1.55**	**1.49**	**1.83**	**1.20**	**1.09**	**1.44**
	CoV [%]	4.40	5.32	5.35	10.8	8.69	3.13	4.95	5.80	6.03	3.55	6.94	5.61	8.53	4.24	6.40
	$LN_{0.05}$	1.55	2.13	2.07	1.55	1.33	1.82	1.68	1.68	1.35	1.46	1.33	1.67	1.04	1.02	1.29
	$char_{EN14358}$	1.52	2.09	2.03	1.50	1.30	1.74	1.65	1.65	1.32	1.40	1.30	1.64	1.01	0.99	1.26
$f_{r,12,Mestek}$ [N/mm²]	**mean**	**1.58**	**2.17**	**2.14**	**1.82**	**1.49**	**1.83**	**1.71**	**1.79**	**1.44**	**1.47**	**1.46**	**1.77**	**1.17**	**1.06**	**1.38**
	CoV [%]	4.30	5.16	5.10	10.6	8.42	3.03	4.84	5.64	5.92	3.43	6.78	5.50	8.33	4.19	6.25
	$LN_{0.05}$	1.47	1.99	1.97	1.51	1.30	1.74	1.57	1.63	1.31	1.39	1.30	1.61	1.02	0.99	1.24
	$char_{EN14358}$	1.43	1.96	1.93	1.46	1.26	1.65	1.55	1.61	1.28	1.33	1.27	1.59	1.00	0.96	1.21

[1] the high CoV is a result of two batches that were delivered and tested separately

6.1 Discussion of influencing parameters on f_r

6.1.1 Reinforcement against compression perpendicular to the grain

Between PS-120-500-360 and PS-120-500-360-V and between PS-120-500-450 and PS-120-500-450-V no difference was observed in $f_{r,12,SIA,mean}$. However, looking at the difference between $f_{r,12}$ with and without stress interaction it can be seen that the influence of compressive stresses in general is relatively small for those test series so it is possible that reinforcement may still reduce the influence of compressive stresses perp. to the grain in higher stressed areas (e.g. lower a_1 / t_{CLT}).

6.1.2 Specimen width w

Regarding the influence of the width, series PS-100-300-360-V and PS-100-500-360-V; PS-120-300-360, PS-120-500-360 and PS-120-800-360; and PS-200-300-450-V and PS-200-500-450-V were compared using unpaired two-sample t-tests on $\ln(f_{r,12})$ with a resulting minimum p-value of 0.101. Assuming a significance threshold of $\alpha = 0.05$ it can be concluded that in the range of w = 300 – 800 mm no statistically significant influence of specimen width is given.

6.1.3 Test configuration

During the comparison of the test configurations a reduction of $f_{r,mean}$ by 15-20 % and a higher CoV for the results gained by the IS configuration versus the ones by 3p-B was observed for PS-100-500-360-V vs. IS-100-500-360 and PS-120-500-360(-V) vs. IS-120-500-360. The difference in $f_{r,mean}$ is in fact of similar magnitude as the calculated difference of the maximum normalized stresses reported in Chapter 4 indicating that the shear stress transferred into the additional material in the overlap and midspan area is the reason for the deviation.

6.1.4 Shear length a_1 and thickness of the cross layer t_{CL}

The influence of the shear length a_1 is portrayed in

Figure 8 (left) including test series PS-120-500-200, PS-120-500-360 and PS-120-500-450. Thereby, a significant decrease in f_r with increasing a_1 can be observed. There might be two main reasons for the given behaviour: i) the size effect and ii) the increased appearance of compressive stresses perp. to grain for a lower a_1 / t_{CLT} and their positive influence on f_r as outlined in Chapter 2. The rolling shear strength values in these diagrams are, however, already corrected from any influences of transverse stresses. Thus, it is deemed more likely that the diagrams depict a (rather pronounced) volume effect in dependence of a_1.

Figure 8 (right) compares the series IS-100-500-360 vs. IS-120-500-360 and PS-100-500-360-V vs. PS-120-500-360-V. Similar to a_1, a significant decrease with increasing t_{CL} is observed. Power regression analyses reveal a power coefficient of approximately –0.50 for both test setups which is in a comparable range than the coefficient of the power regression for a_1.

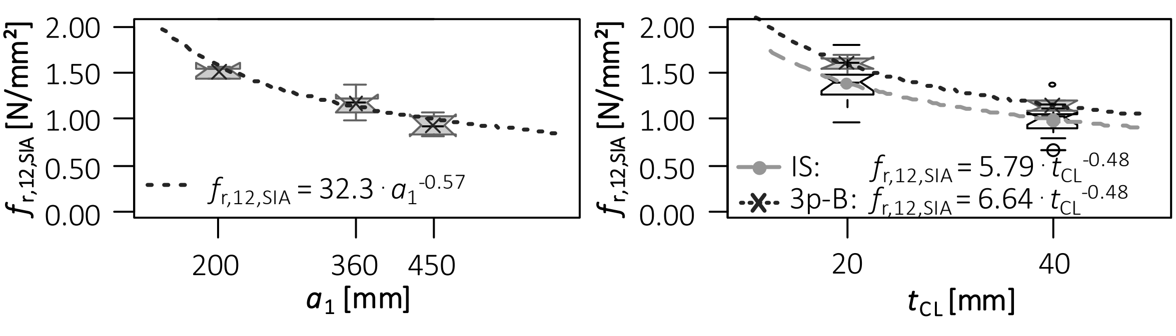

Figure 8 Comparison of f_r vs. a_1 (left) and f_r vs. t_{CL} (right)

Additionally, the decrease of f_r with increasing t_{CL} and a_1 with a power coefficient of approximately –0.5 is confirmed also from the database series as seen in Figure 9. The lower power coefficient for the series with n_{CL} = 3 most likely results from the low difference in $a_1 \cdot t_{CL}$ and limited test data of only two test series in this group. These results are well in line with the findings of O'Ceallaigh et al. (2018) where a power regression of $f_{r,mean}$ dependent on $a_1 \cdot t_{CL}$ would also lead to a power coefficient of approximately –0.50 for the three-layered series mentioned in Chapter 2.

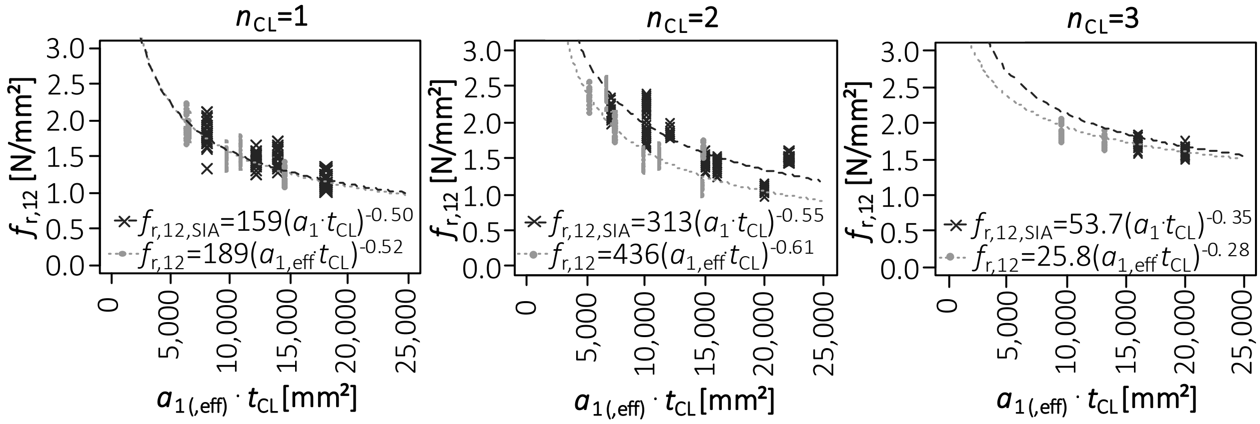

Figure 9 Power regression of data according to the number of cross layers n_{CL}: $f_{r,12,SIA}$ vs. a_1 . t_{CL} and $f_{r,12}$ vs. $a_{1,eff} \cdot t_{CL}$

Besides considering the stress interaction of σ_{90} and τ_r together with the failure criteria in Section 5.1 in frame of FE analyses, a simpler, more practical approach based on the shear stress evaluation acc. to the Timoshenko beam theory was carried out. By adaptation of the referencing volume it is possible to take the stress interaction indirectly into account. In doing so, a_1 is reduced to $a_{1,eff}$ acc. to Eq. (5) and depicted in Figure 3, a length in a sense free of interacting compression perp. to the grain stresses. This approach is derived from the proposal of Brandner (2018) for $k_{c,90}$ of CLT which assumes a load dispersion angle of 45° and 15°, respectively, in longitudinal and transversal direction.

$$a_{1,\text{eff}} = a_1 - \sqrt{w_s \left(w_s + \sum t_{LL} \tan 45 + \sum t_{CL} \tan 15\right)} \tag{5}$$

From Figure 9 it can be concluded that the regression models based on test data directly (via SIA failure criteria) and indirectly (via the simplified approach) adjusted about the influence of transversal stresses are rather close to each other and even match in case of n_{CL} = 1.

6.1.5 Layup

The influence of layup was analysed by the comparison of PS-120-500-450-V and PS-200-500-450-V. Statistically no significant influence was found (t-test; p = 0.137). The comparison of test series in Figure 9, however, indicates a lamination effect meaning a tendency to an increasing f_r with increasing n_{CL}. It is suspected that due to the ongoing conversion of the quasi-rigid connection of longitudinal layers to a – as a theoretical end state – loose connection allows for a certain stress redistribution. However, a lamination effect could not be observed by O'Ceallaigh et al. (2018) as $f_{r,mean}$ also decreased for multiple cross layers as outlined in Chapter 2. It is possible that the lamination effect observed within the scope of this contribution is enabled by the increased compressive stresses of the EAD setup for higher specimens of CLT with multiple cross layers as they may close developing cracks and still allow for load transfer due to friction and dilation effects.

7 Modelling the rolling shear strength

7.1 Basic rolling shear strength model to predict test data

The results of $f_{r,12,SIA}$ of the EAD data base were used to derive a model for the rolling shear strength. As a conclusion of Chapter 6, the main parameters influencing the rolling shear strength in a 4p-B test were identified as i) a_1, ii) t_{CL} and iii) n_{CL}. These parameters were assembled to Eq. (6) serving as a basis for a regression model.

$$f_r = \frac{f_{r,0}\,(c_0 + c_1\, n_{CL})}{\sqrt{1+\dfrac{a_1\, t_{CL}}{A_0}}} \tag{6}$$

Table 6 Coefficients of the model for the mean values and empirical 5%-quantiles

	$f_{r,0}$ [N/mm²]	c_0 [-]	c_1 [-]
$f_{r,mean}$	5.74	0.85	0.15
$f_{r,0.05,emp}$	5.05	0.80	0.20

The reference area A_0 was chosen as 900 mm², the reference strength $f_{r,0}$ was calibrated on the test data with n_{CL} = 1 and assuming no lamination effect (setting the term in brackets to 1.0). Lastly, the empirical constants c_0 and c_1 depicting the lamination effect were derived by linear regression analysis with the total data set. Application of Eq. (6) on the mean rolling shear strengths $f_{r,mean}$ and the empirical 5 % - quantiles $f_{r,0.05,emp}$ of each test series resulted in the coefficients given in Table 6. The increased lamination effect for $f_{r,0.05,emp}$ compared to $f_{r,mean}$ is a result of the lower CoV for $n_{CL} > 1$, see Figure 10 (left). In Figure 10 the model validation plot (middle) and residual plot (right) of the models are illustrated as well. The model overall gives a good prediction of the test data with slight deviations on the upper and lower end.

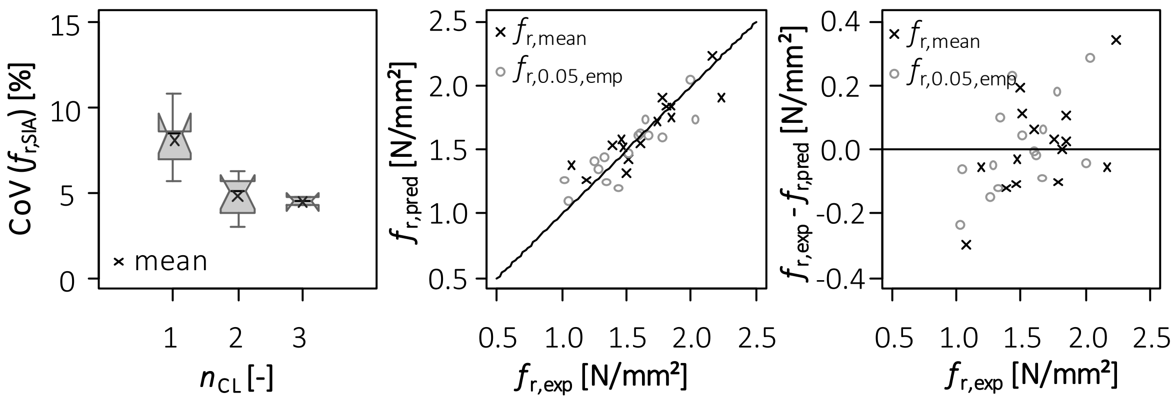

Figure 10 Coefficient of Variation vs. number of cross layers n_{CL} (left); model validation plot (middle) and residual plot (right) for the models $f_{r,mean}$ and $f_{r,0.05,emp}$

7.2 Standardized rolling shear strength model

Aiming that the standardized rolling shear model is consistent with the specifications for 4p-B tests given in EN 16351 (2021), it was decided to set a_1 = 3 t_{CLT}. Given that

$f_{r,0,mean}$ = 5.74 N/mm², the characteristic reference strength was calculated for lognormal distributed data acc. to Fink et al. (2018) assuming CoV ($f_{r,12}$) = 11 % to $f_{r,0,k}$ = 4.78 N/mm². Based on these assumptions, $f_{r,k}$ is given as:

$$f_{r,k} = \frac{4.78\,(0.80 + 0.20\,n_{CL})}{\sqrt{1 + \frac{a_1\,t_{CL}}{900}}} = \frac{4.78\,(0.80 + 0.20\,n_{CL})}{\sqrt{1 + \frac{3\,t_{CLT}\,t_{CL}}{900}}} = \frac{4.78\,(0.80 + 0.20\,n_{CL})}{\sqrt{1 + \frac{t_{CLT}\,t_{CL}}{300}}} \tag{7}$$

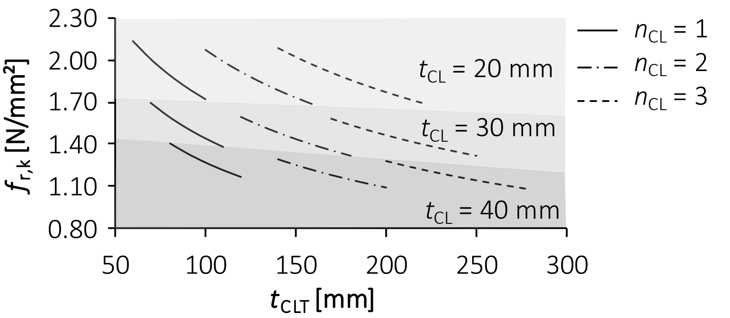

Figure 11 Evaluation of the characteristic rolling shear strength model

Eq. (7) was then evaluated for common layups; see Figure 11. It is observed that the relevant layups form groups with similar $f_{r,k}$ in dependency of t_{CL}. This results from the lamination effect partly counteracting the effect of the increasing a_1 resp. t_{CLT}.

8 Summary, proposals and outlook

It is recommended to use 4p-B tests acc. to EN 16351 (2021) with $a_1 = 3\,t_{CLT}$ and $a_2 = 6\,t_{CLT}$ in order to determine the rolling shear strength of CLT plates, see Figure 3 (left). The specimen width, however, may be reduced to max {2 w_b; 300} mm. 4p-B is favoured instead of 3p-B as the resulting shear distribution better resembles the stress state in building practice. Still, the observed difference between 3p-B and 4p-B tests miss validation but it might be of interest to derive configuration factors for the conversion of test results based on different test setups with the method outlined in Chapter 4.

Due to the aspects outlined in Section 1 rolling shear failure is often hard to identify in 4p-B tests. The definition at first failure, i.e. first formation of rolling shear cracks, might be too subjective. For a more objective approach it is suggested to evaluate f_r based on the stiffness criterion in Section 3. However, the evaluation with this method should be complemented by thorough visual assessment during testing to secure that rolling shear cracks are responsible for the stiffness reduction.

In respect to the test data evaluation it could be shown that Timoshenko beam theory, modified γ-method, Shear Analogy Method and FE analysis using shell models and the mean rolling shear stress according to Eq. (1) lead to equivalent rolling shear stresses for such tests. However, due to the simple calculation procedure it is recommended to use Timoshenko beam theory.

The proposed basic strength model was derived based on data, which was corrected regarding the impact of normal stresses perp. to the grain. During testing however, those stresses will be present regardless. As a result, a higher apparent rolling shear resistance is expected during testing, again arising the necessity to correct the test data. This can be done directly during test data evaluation with the method outlined in Section 5.1. However, when rolling shear strengths are evaluated with one of the beam theories, the indirect method by adapting the referencing volume as outlined in Section 6.1.4 has to be used. As $a_{1,\text{eff}}$ acc. to Eq. (5) differs from the reference shear length of a_1 = 3 t_{CLT}, a correction has to be made acc. to Eq. (8) for the test data to be consistent with the model's assumptions:

$$f_{\text{r},3t_{\text{CLT}}} = f_{\text{r},a_{1,\text{eff}}} \sqrt{\frac{900 + a_{1,\text{eff}} t_{\text{CL}}}{900 + 3 t_{\text{CLT}} t_{\text{CL}}}} \tag{8}$$

For the 'ease-of-use', the determination of $f_{\text{r,k}}$ as product property of CL 24 without gaps and relief grooves as basis for the design is proposed acc. to Eq. (9):

$$f_{\text{r,k}} = 1.10 + 0.03\left(40 - t_{\text{CL}}\right) \ \text{N/mm}^2 \quad \text{with } t_{\text{CL}} \text{ in mm} \tag{9}$$

The rolling shear strength model needs further validation with respect to the apparent lamination effect. Thus, tests in accordance with the proposed test setup on 5- and 7-layered CLT should be conducted. Furthermore, for different layup ratios t_{CL} / t_{LL} a potential influence could be considered. In addition, the effect of low board aspect ratios w_{b} / t_{b}, gaps and relief grooves could be added to the model, i.e. by introducing corresponding reduction factors.

9 Acknowledgement

The presented research was generated in the scope of the research project "Rollschub BSP" and funded by holz.bau forschungs gmbh. Their support is gratefully acknowledged. The permission of the five CLT manufacturers to publish the anonymized test data is also greatly appreciated.

10 References

Aicher, S; Hirsch, M; Christian, Z (2016): Hybrid cross-laminated timber plates with beech wood cross-layers. *Construction and Building Materials* 124:1007–1018.

Akter, S T.; Bader, T K. (2020): Experimental assessment of failure criteria for the interaction of normal stress perpendicular to the grain with rolling shear stress in Norway spruce clear wood. *Holz als Roh- und Werkstoff* 78 (6):1105–1123.

Brandner, R (2018): Cross laminated timber (CLT) in compression perpendicular to plane: Testing, properties, design and recommendations for harmonizing design provisions for structural timber products. *Engineering Structures* 171:944–960.

Brandner, R; Gatternig, W; Schickhofer, G (2012): Determination of Shear Strength of Structural and Glued Laminated Timber.CIB - W18/45-12-2.

Brandner, R; Jantscher, L (2022): Out-of-Plane Tensile Properties of Cross Laminated Timber (CLT). *Buildings* 12 (2):135.

EAD 130005-00-0304 (2015) Solid Wood Slab Element to be used as a Structural Element in Buildings. EOTA.

Ehrhart, T; Brandner, R (2018a): Rolling shear: Test configurations and properties of some European soft- and hardwood species. *Engineering Structures* 172:554–572.

Ehrhart, T; Brandner, R (2018b): Test Configurations for Determining Rolling Shear Properties with Focus on Cross Laminated Timber: A Critical Review. COST Action FP1402/ WG 2.

EN 16351 (2021) Timber structures - Cross laminated timber - Requirements. CEN.

EN 338 (2016) Structural timber - Strength classes. CEN.

EN 408 (2012) Structural timber - Structural timber and glued laminated timber - Determination of some physical and mechanical properties. CEN.

EN 789 (2005) Timber structures - Test methods - Determination of mechanical properties of wood based panels. CEN.

Fink, G; Kohler, J; Brandner, R (2018): Application of European design principles to cross laminated timber. *Engineering Structures* 171:934–943.

Gardner, C; Davids, W G.; Lopez-Anido, R; Herzog, B; Edgar, R; Nagy, E et al. (2020): The effect of edge gaps on shear strength and rolling shear modulus of cross laminated timber panels. *Construction and Building Materials* 259:119710.

Hoffman, O (1967): The Brittle Strength of Orthotropic Materials. *Journal of Composite Materials* 1 (2):200–206.

Kreuzinger, H (1999): Platten, Scheiben und Schalen. Ein Berechnungsmodell für gängige Statikprogramme (in German). *Bauen mit Holz* (1):34–39.

Li, M; Dong, W; Lim, H (2019): Influence of Lamination Aspect Ratios and Test Methods on Rolling Shear Strength Evaluation of Cross-Laminated Timber. *J. Mater. Civ. Eng.* 31 (12):4019310.

Mestek, P; Kreuzinger, H; Winter, S (2011): Design Concept for CLT-Reinforced with Selftapping Screws.CIB - W18/44-7-6.

Nero, R; Christopher, P; Ngo, T (2022): Investigation of rolling shear properties of cross-laminated timber (CLT) and comparison of experimental approaches. *Construction and Building Materials* 316:125897.

O'Ceallaigh, C; Sikora, K; Harte, A (2018): The Influence of Panel Lay-Up on the Characteristic Bending and Rolling Shear Strength of CLT. *Buildings* 8 (9):114.

prEN 1995-1-1 (27.10.2021) Consolidated draft of prEN 1995-1-1. CEN/TC 250/SC 5 N 1488.

prEN 1995-1-1 (13.04.2018) SC5.T1 working draft of design of cross laminated timber in a revised Eurocode 5-1-1. CEN/TC 250/SC 5 T1.

Steiger, R; Gehri, E (2011): Interaction of Shear Stresses and Stresses Perpendicular to the Grain.CIB - W18/44-6-2.

Wang, Z; Zhou, J; Dong, W; Yao, Y; Gong, M (2018): Influence of technical characteristics on the rolling shear properties of cross laminated timber by modified planar shear tests. *Maderas, Cienc. tecnol.* (3):469–478.

DISCUSSION

The paper was presented by D Glasner

H Blass commented that the overlap/overhang at the support will have an influence and questioned about its consideration in the data. D Glasner agreed in general.

H Blass asked about the meaning of FE modeling as rolling shear strength depends on annual ring orientation. D Glasner said that the approach considered system properties where influence of annual ring orientation would be masked. H Blass said thah smeared shear stress can be considered here.

H Blass did not understand the need for the criterion of f_r. He asked why not just use max load. In cases where bending failures occurred rolling strength estimated based on max load would still be conservative. D Glasner responded that rolling shear cracks would typically occur before bending failure hence rolling shear mode governed. H Blass disagreed as max load should be considered. D Glasner said final failure would always be single bending failure but rolling shear failure occurred first. H Blass stated max load is needed for design. A Ringhofer commented that experimental conditions were different from real conditions. H Blass said one should test under realistic conditions as the recommended approach is too conservative.

T Tannert said as the proposed empirical equation only depended on lamination thickness would a_1 be important. D Glasner said a_1 should be dependent on CLT and this has always been considered. Also volume dependency is noted.

T Tannert asked would there be dependency on species and edge gluing conditions. D Glasner said both non edge glued and edge glued material were considered. Past research indicated that with larger board aspect ratio edge gluing influence can be neglected. Only softwood species was considered.

S Aicher said that one has to treat rolling shear strength as an intrinsic property for design. He preferred 4 point bending tests with realistic conditions. One should examine this problem with a more scientific approach including anisotropic behaviour. Gaps between boards also have a large influence. D Glasner responded that gaps could be included as reduction factor.

H Danielsson received confirmation that rolling shear stiffness was not considered.

P Dietsch disagreed with the notion of replacing observations in experiments by interpretation of load-deformation curves.

S Aicher added that a method for intrinsic properties should show failure relative to the target test properties. A Ringhofer disagreed because ETA for CLT would always lead to bending failures.

Proposed design methodologies for timber assemblies subjected to blast loading

Ghasan Doudak, Professor, University of Ottawa, Canada

Christian Viau, Assistant Professor, Carleton University, Canada

Daniel Lacroix, Assistant Professor, University of Waterloo, Canada

Keywords: design, blast, strain-rate, timber, light-frame, glulam, CLT, connections

1 Introduction and background

The effects of blast explosions, characterized by a sudden release of energy generating pressurized shock fronts, have shown the potential to cause severe damage to infrastructure. The recent use of wood as a construction material for mid- and high-rise structures has increased dramatically in Europe and North America, bringing along a heightened risk of these novel structures to be subjected to accidental or intentional blast explosions. As wood has relatively low density and tends to exhibit brittle behaviour (e.g., in flexure), it typically does not have the inherent blast-resistant properties found in other construction materials, such as reinforced concrete and structural steel. Contemporary design codes and standards, such as the Eurocode 1 (2006), aim to guide designers in quantifying and minimizing the risk of progressive collapse as a consequence of accidental loading. One of the main design philosophies currently presented in the Eurocode 1 (2006) is that of key element design. This methodology considers various possible, albeit rare load scenarios, to which critical load-bearing elements may be exposed (Ellingwood, et al., 2007). Key element design is typically the method of last resort, utilized when alternative load path design does not generate a safe overall design of the structure (Cormie, et al., 2009). These elements are expected to be designed using a static-equivalent pressure of 34 kPa applied on either side of the element; a prescriptive requirement that has been derived based on the expected peak loads generated during the event of Ronan Point (ISE, 2010). This approach has been criticized for being simplistic and not appropriate for most design scenarios. Of note, the 34 kPa is to be applied onto the widths of the element with no guidance for the load-collecting aspect of cladding, which may further increase the element's demand (Arup, 2011). Most notably, no guidance on element design and dynamic analysis is provided, particularly in terms of high strain-rate effects, charge determination, and modelling methodologies.

To address the design of structural elements and assemblies against the effects of blast explosions, blast design provisions have been enacted in various countries (e.g. Unified Facilities Criteria Program, 2008; Unified Facilities Criteria Program, 2009; ASCE, 2011; CSA, 2012) with the objective to reduce occupancy injuries and fatalities as well as limit the risk of progressive collapse. The provisions for wood element design found in the current editions of American and Canadian blast standards (i.e., ASCE/SEI 59-11 and CSA S850) were based on a single testing program on light-frame wood structures (Marchand, 2002). The study focused on the overall behaviour of the structures and was limited to qualitative experimental results. Since no in-situ properties of the structural members were measured during testing, published data was used to obtain the strength and stiffness of the specimens in order to conduct a damage assessment and develop design provisions and response limits for wood structures (Oswald, 2005).

Recent research effort has been undertaken at the University of Ottawa's Shock Tube Test Facility with the aim to provide quantification of the performance of timber components. The results from these studies have generated over one hundred full-scale experimental test results and helped develop design methodologies for blast-loaded timber elements and assemblies. The current paper aims to summarize the lessons learnt from a decade's worth of experimental and analytical research on blast-loaded timber members.

2 Blast design of timber elements

Investigations into material behaviour under high strain-rate necessitates comprehensive experimental research programs, which is typically accomplished through live explosion or shock tube testing. While the former replicates the complete effects of a blast event, such as the shock wave, fireball, fragmentation, debris throw, etc., challenges arise with regard to the collection of reliable data. The benefit of laboratory experimentation over live arena testing is the richness of information generated, including pressure-, displacement-, reaction, and strain-time histories. Details on the University of Ottawa Shock Tube and typical testing setups can be found in Lacroix (2013) for light-frame members and in Viau (2020) for glued-laminated timber (glulam) and cross-laminated timber (CLT) members.

2.1 Current Canadian blast code design approach

Static design of wood components is typically considered overly conservative for the purpose of blast design due to the rarity of the event and the cost limitations associated with keeping elements elastic. For the design and analysis of individual structural elements, the Canadian blast design standard (CSA S850) defines the dynamic strength, S_D, as provided in Equation 1:

$$S_D = SIF\ DIF\ S_S \qquad (1)$$

where *SIF* is the strength increase factor, *DIF* is the dynamic increase factor, and S_S is the specified static strength. A material reduction factor equal to unity is assumed due to rarity of the event.

The *SIF* transforms specified design resistance to mean capacity and takes values of 1.2 for glulam and engineered wood products to 1.9 for visually graded lumber, accounting for the material variability. The *DIF* takes into account high strain-rate effects, a phenomenon whereby an apparent increase in strength and/or initial stiffness is observed in viscoelastic materials. These values are typically obtained by relating the dynamic resistance, where failure is obtained within milliseconds to those obtained from static tests, where failure is typically achieved in 1 to 10 minutes.

The current version of the CSA S850 assigns a *DIF* value of 1.4 to all wood element types (CSA, 2012). It should be noted that this value has been corroborated for solid sawn lumber products by several research studies, but is found not to be applicable to other types of engineered wood products, such as glulam and CLT, as will be discussed in subsequent sections.

The rest of this section describes proposed design approaches for light-frame wood stud walls, glulam members and CLT panels, based on results from recent research programs.

2.2 Light-frame wood stud walls (LFW)

LFW consist of repetitive load-bearing members at constant spacing, sheathed with wood panels that are fastened to the studs using mechanical fasteners, such as nails and screws. This type of construction creates a redundant system capable of withstanding the loss of load-bearing studs without collapse of the assembly (Rosowsky, et al., 2005). As mentioned previously, a *DIF* of 1.4 has been established based on dynamic and static testing (e.g. Lacroix and Doudak, 2015b). The results from this study are summarized in Figure 1.

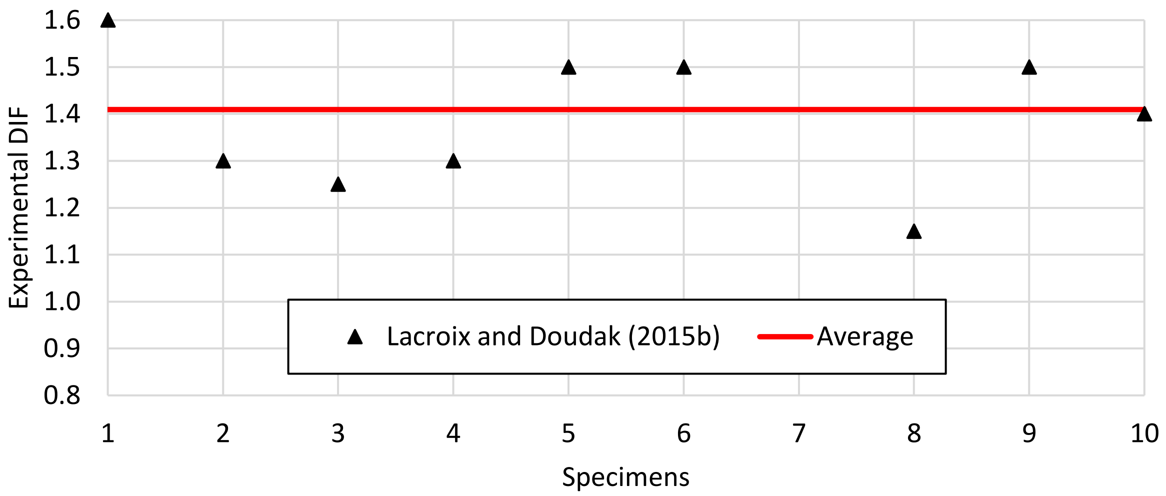

Figure 1. DIF for LFW based on static and dynamic shock tube test results

Although an increase in the dynamic stiffness of studs was reported (Jacques, et al., 2014; Lacroix and Doudak, 2015b), the increase could not be substantiated using statistical analyses. Therefore, no increase is stiffness is generally adopted when resistance curves are used in dynamic analysis.

The current Canadian blast design standard specifies that factors of unity should be assumed for the load sharing factor or system strength factor and load duration factor (CSA, 2019), when determining the dynamic LFW strength. Omitting these factors has been found to be very conservative (Lacroix and Doudak, 2015a). This will be discussed and further verified in the subsequent section on modelling methodologies for LFW.

2.3 Glued-laminated timber (glulam) members

Four experimental programs, investigating the behaviour of seventy-one glulam beams of four different cross-sections, were undertaken (Lacroix and Doudak, 2018; Viau and Doudak, 2021a; b; Wight, et al., 2022). As shown in Figure 2, an average *DIF* of 1.1 on the flexural strength of glulam beams was determined to be statistically significant. This average *DIF* is noticeably lower than that provided in CSA S850 (2012) of 1.4, and as such it can be concluded that current provisions applicable to glulam members are not sufficiently safe.

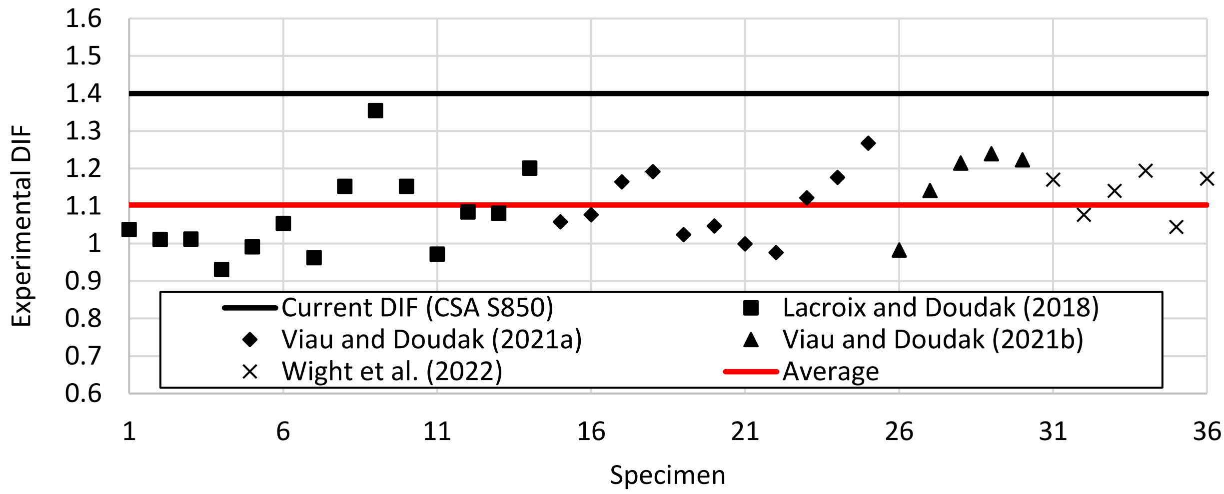

Figure 2. DIF for glulam members based on static and dynamic test results

2.4 CLT members

Three experimental programs, investigating the out-of-plane behaviour of twenty-five cross-laminated-timber (CLT) under static and simulated blast loading, have been conducted (Poulin, et al., 2018; Viau and Doudak, 2019; Doudak, et al., 2022). Static and dynamic reactions were measured to obtain both the modulus of elasticity (*MOE*) and the modulus of rupture (*MOR*). The failure modes from the tests were also documented and related to the material model. As shown in Figure 3, an average *DIF* of 1.27 for the flexural strength of the tested CLT panels was reported. Similar to glulam, this average *DIF* is lower than that provided in CSA S850 (2012) of 1.4, potentially leading to unsafe designs. It is proposed that a *DIF* of 1.2 on the resistance be conservatively utilized for the purpose of calculating the peak resistance of a CLT member.

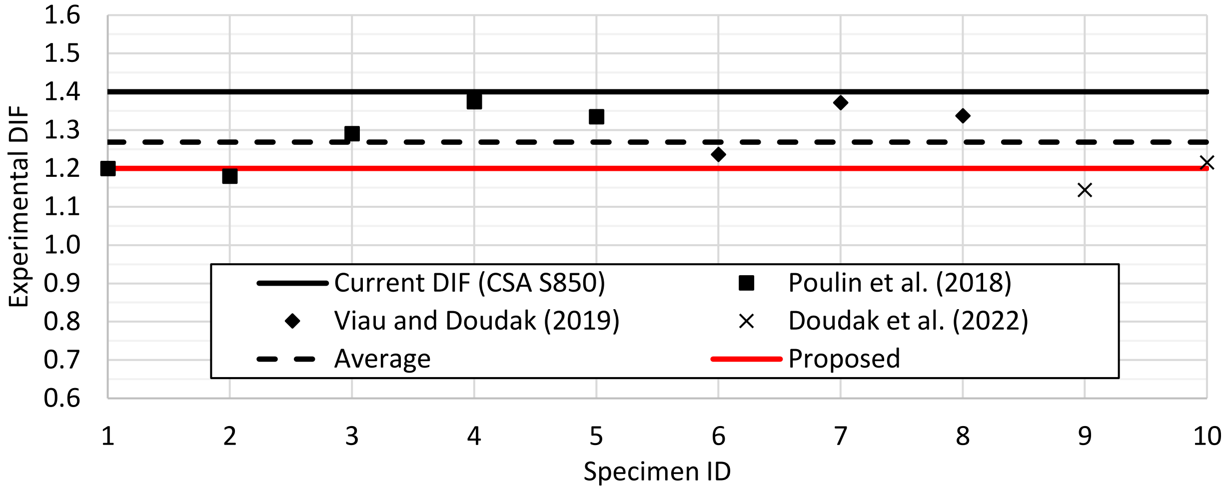

Figure 3. DIF for CLT members based on static and dynamic test results

3 Material-predictive models

Blast loading on structures involves a loading duration that is much smaller than that of earthquakes and wind loading, and therefore the structural response under such short loading can differ quite significantly. Given the shorter time duration associated with blast loading, the inertial forces and kinetic energies cannot be neglected in the analysis. Due to the uncertainties associated with blast loads, simplified modelling techniques such as equivalent single-degree-of-freedom (SDOF) analysis, are often used where applicable over more complex analysis methods. SDOF modelling can be used provided that the dynamic response and failure mode of the structural system being analysed can be accurately represented as a lumped-mass system, and when a single deformation mode controls the dynamic response of the structural system (PDC, 2008). An equivalent system is developed by selecting a point on the real system where maximum deflection occurs (e.g., mid-span) and the mass and stiffness of the system along with the applied forces are lumped at that point. In order to transform the mass, stiffness, and applied loads of the real system to that of an equivalent system, it is necessary to use transformation factors that are determined based on an assumed static deflected shape. The equation of motion, Equation 2, corresponds to an idealized equivalent undamped SDOF system:

$$K_{LM} m\ddot{u}(t)+R(u)=F(t) \qquad (2)$$

where K_{LM} is the load-mass transformation factor, m is the total mass of the system, $R(u)$ is the resistance function of the element, $F(t)$ is the time-varying forcing function, and $\ddot{u}(t)$ is the acceleration of the system. Damping is intentional omitted from Equation 2 as it has little effect on the peak response of the system (Biggs, 1964). Derivations and values of K_{LM} for different loading types and support conditions are available in the literature. Resistance functions, $R(u)$, which describes the resistance as a function of displacement of the structural element being modelled, are required to perform the SDOF analysis and obtain accurate results. For simply supported elements, the peak resistance, R_e, and initial stiffness, K, can be determined using Equations 3 and 4, respectively:

$$R_e = \alpha M_D / L \tag{3}$$

$$K = \beta EI / L^3 \tag{4}$$

where M_D is the dynamic bending strength, E is the elastic modulus, I is the second moment of area, α is the resistance constant (equal to 8 for uniformly distributed load and 6 for four-point bending), and β is the stiffness constant (equal to 76.8 for uniformly distributed load and 56.4 for four-point bending). The elastic displacement, u_e, and maximum displacement, u_{max}, can be found using Equations 5 and 6, respectively:

$$u_e = R_e / K \tag{5}$$

$$u_{max} = \mu_{max}\, u_e \tag{6}$$

where μ_{max} is the maximum ductility ratio of the element being designed.

Ductility ratios (μ) are used in both Canadian and American blast codes to describe prescribed damage levels using a quantifiable metric, known as a response limit. The CSA S850 currently sets a value of μ_{max} equal to 4 for all wood elements (CSA, 2012). This metric allows for the prediction of expected damage level, and level of protection, of a particular element against a specific blast threat. The damage levels and associated response limits as per CSA S850 are summarized in Table 1. Responses greater than μ_{max} correlate to "blowout failure" signifying that the objective of preventing progressive collapse and ensuring life-safety may not be met.

Table 1. Response limits for wood per CSA S850 (2012)

Response Limit, μ	Damage Level
1	Superficial damage
2	Moderate damage
3	Heavy damage
4	Hazardous failure

A generalized resistance curve for a wood beam element is presented in Figure 4 based on Equations 3-6. A resistance equal to R_e is assumed to be maintained upon the elastic displacement being reached. As can be observed in Figure 4, the current blast code assumes that timber elements are assumed capable of having sustained post-peak resistance well into the plastic phase. While it is well-known that timber elements do not possess such post-peak behaviour, this assumed behaviour had led to reasonable predictions of the performance of light-frame stud wall systems. This is partly due to the erroneous and very conservative assumptions associated with system and load duration factors. Furthermore, expanding this concept to other elements, such as glulam and CLT, is not appropriate, as will be discussed in a later section.

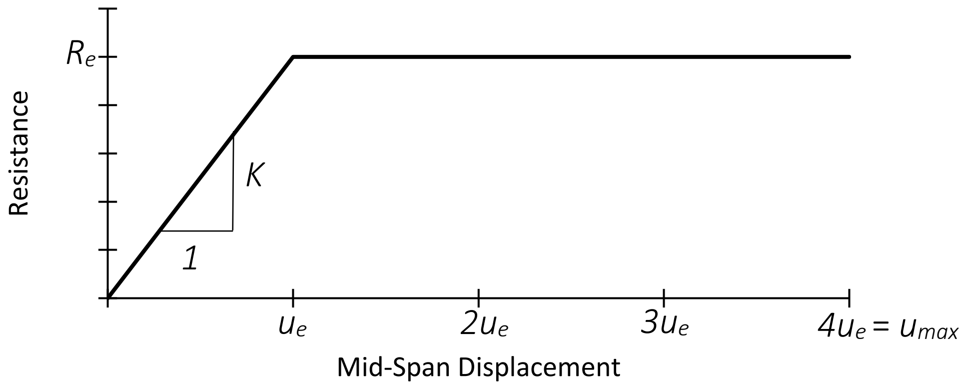

Figure 4. Generalized resistance curve for wood elements according to CSA S850 (2012)

3.1 Resistance curves and response limits for various structural systems

Stud walls are redundant structural systems with ability to share the applied load as well as redistribute the load after the failure of individual components, particularly if debris is limited or contained. As such, the failure of a single stud within a wall does not usually result in a complete wall failure nor does it lead to progressive collapse of the building. A detailed assessment of the behaviour of 33 full-scale light-frame wood stud walls subjected to a total of 48 dynamic tests under simulated blast loading was presented by Viau et al. (2016). A μ_{max} of 2 was determined to be representative of the ultimate state of failure (i.e., blowout failure) for light-frame wood stud walls, rather than the ductility value of 4 currently provided in the Canadian blast design standard (CSA 2012). The study noted that during the documentation of observed damage in the experimental phase, it was deemed very difficult to differentiate between moderate and heavy damage (see Table 1). For practical reasons, a merging of these two damage regions was proposed for the purpose of assessing wood stud walls. Based on the observed damage levels obtained from the experimental study, only four damage regions were proposed, separated by three response limits, corresponding to ductility ratios of 1, 1.5, and 2, respectively.

Based on full-scale static and dynamic tests results, it has been reported that glulam beams under both static and dynamic loading showed no significant post-peak resistance (Lacroix and Doudak, 2018; Viau and Doudak, 2021a; b; Oliveira, et al., 2022; Wight, et al., 2022). This is in conflict with the current approach taken by the Canadian blast code (Figure 4). As such, it is suggested that glulam beams be idealized as linear-elastic with no post-peak resistance (i.e., μ_{max} = 1).

CLT panels of various thicknesses have been observed to have some level of post-peak resistance under both static and dynamic loading (Poulin, et al., 2018; Viau and Doudak, 2019; Doudak, et al., 2022). Based on experimentally obtained resistance curves from Poulin, et al. (2018), Viau, et al. (2018) proposed a generalized approach for constructing the resistance curve for flexure failure. The flexural behaviour can be described as initially linear elastic, after which the loss of the outer longitudinal laminates would cause a sudden drop in resistance. For the 3-ply specimens, this post-peak behaviour was modelled as a sudden drop in resistance (Poulin, et al., 2018).

For the 5-ply specimens, the loss of the outermost laminates means that the specimen would now behave as a 3-ply specimen. The post-peak residual deflections were consistent with μ_{max} = 2.5, based on the experimental findings. Due to the possibility of rolling shear failure in CLT panels, due to the presence of the transverse laminates, the peak resistance obtained in Equation 3 should be verified against the rolling shear strength of the panel and the minimum should be chosen as the representative peak resistance (Doudak, et al., 2022).

The proposed resistance curve and associated response limits for stud walls, glulam, and CLT members are presented in Figure 5. The following section will evaluate the appropriateness of using these proposed curves.

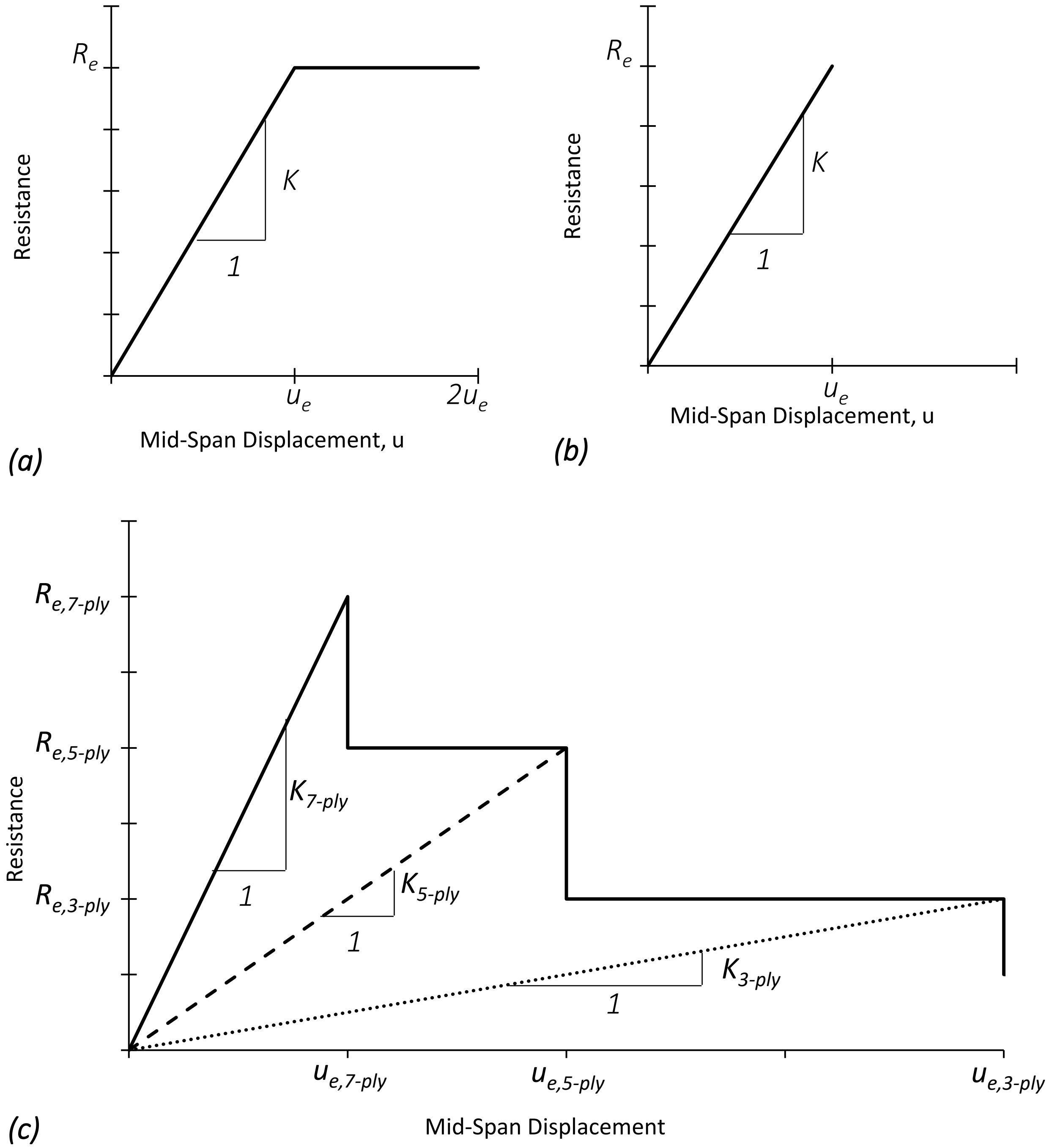

Figure 5. Proposed resistance curves for: (a) stud walls; (b) glulam members; (c) CLT Panels

3.2 Validation of single-degree-of-freedom modelling methodology

Prior to the validation of the proposed design methods, a verification of the modelling approach, including the proposed resistance curves presented in Figure 5, was undertaken. A total of 91 experimental test results from the aforementioned studies on light-frame stud walls, glulam beams, and CLT panels were used for the verification of the modelling approach. For each specimen, SDOF modelling was conducted using the experimentally obtained pressure–time histories, average experimental resistance curves, and member masses as inputs. As shown in Figure 6, an average predicted-to-experimental displacement ratio of 0.99 was obtained, underlining the appropriateness of the proposed SDOF methodology and resistance curves in predicting the behaviour of various timber members and assemblies.

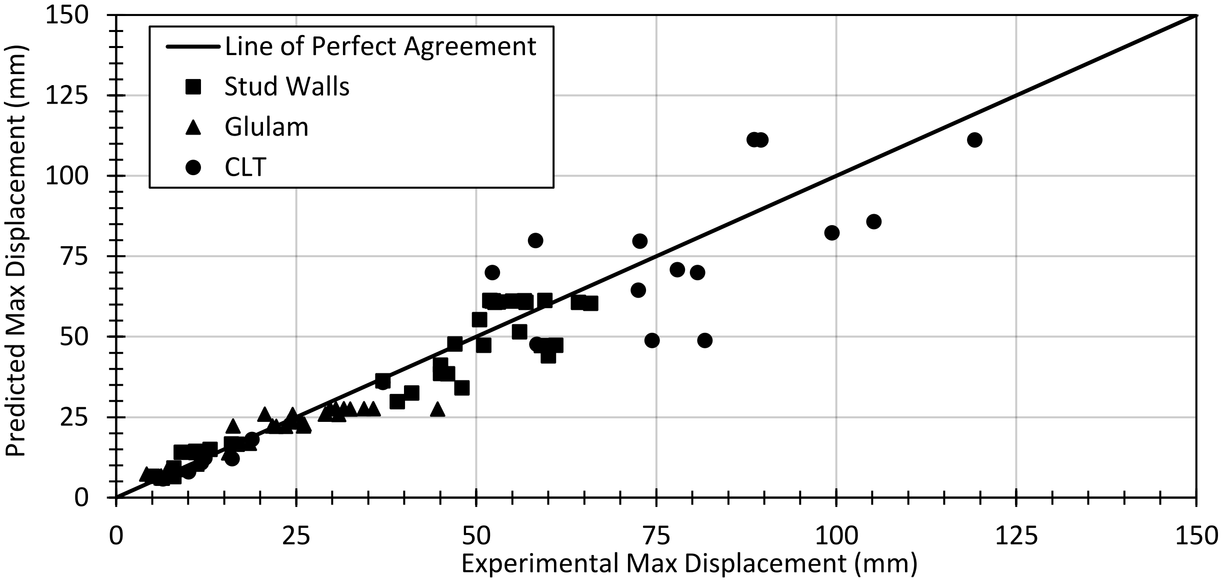

Figure 6. Summary of SDOF modelling methodology validation

3.3 Comparing the proposed design approaches with current blast standard

The full-scale experimental test data presented in Figure 6 were used to evaluate the proposed design methodologies outlined in this paper, as well as conduct a comparison with the current design standard provisions, CSA S850 (CSA, 2012).

The applicability of the proposed design methods is conducted using the material properties obtained from the Canadian wood design standard, CSA O86 (2019), in tandem with the strength modification factors and material predictive models presented in this paper. The peak resistance was used as a metric to quantify the accuracy of the proposed design method in cases where load-cells were utilized and thus experimental resistance curves were available. Where no load-cells were utilized (e.g., light-frame wood stud walls), the metric used to quantify the method accuracy was maximum midspan deflection. Summaries of the results are presented in Figure 7.

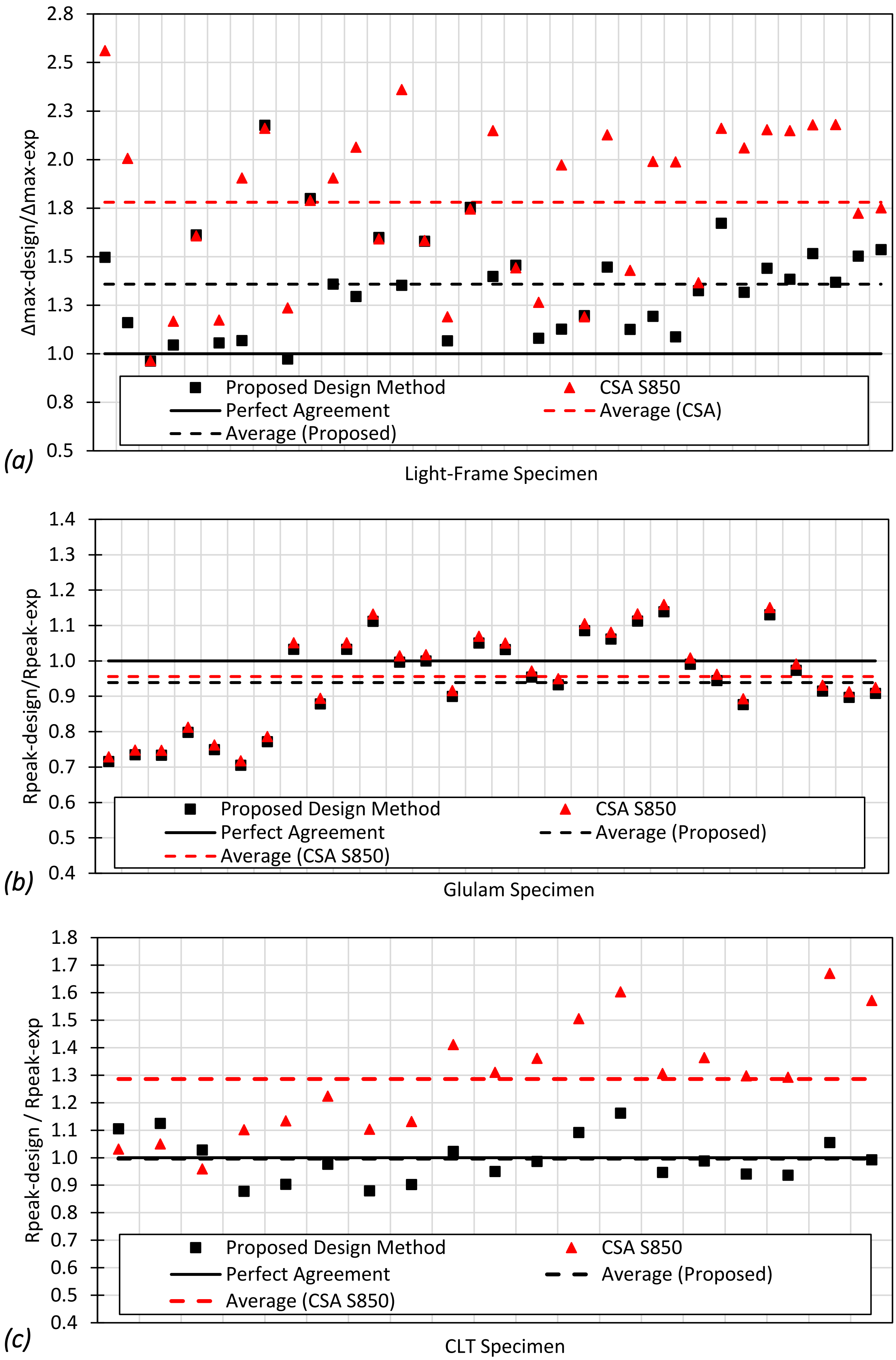

Figure 7. Comparison between proposed and current design methodologies

Overall, it can be seen from Figure 7 that the proposed design methodologies outlined in this paper tend to predict the performance of various wood assemblies subjected to blast loads with better accuracy than that obtained by following current blast design provisions. When comparing the maximum displacement for light-frame wood stud walls (Figure 7(a)), it can be observed that the displacement predictions following the proposed design method tended to be more closely aligned with those observed from the experimental testing. Although overpredicting the maximum displacements is conservative, these overpredictions are the direct result of the value of μ_{max} being equal to 4 in the blast design standard. While the proposed design method for light-frame wood stud walls may predict lower displacements, the damage levels are stricter and based on lower ductility ratios and are, therefore, more accurate than the provisions currently found in the blast standard. Regarding the dynamic glulam specimens, shown in Figure 7(b), the proximity in the results between the proposed design method and that of the current design standard is coincidental. It is noted that the product of the proposed *DIF* and load duration factor is approximately equal to the *DIF* of 1.4 found in the current code provisions. It should be stated that this does not justify the use of 1.4 for *DIF* while requiring that no load duration factor increase is used concurrently. It can be noted that both methods underpredict the peak resistance of the first seven datapoints. This can be attributed to the fact that these specimens were part of an experimental program (Lacroix and Doudak, 2018) with noticeably higher *SIF* (equal to 1.6) compared to the *SIF* (with a value of 1.2), provided in the CSA S850 standard (2012) and as proposed in this paper. It is also important to note that while both the proposed method and that given in CSA S850 (2012) seem to provide very similar predictions of the peak resistance, noticeable discrepancies can be seen when comparing the predicted displacement-time histories, as shown in Figure 8. The current design method from CSA S850 is shown to overpredict maximum displacement by a significant margin, whereas the proposed design method appears to predict the displacement more closely. This is due to the μ_{max} of 4 utilized in the CSA S850 (2012) (Figure 4), whereas the proposed methodology utilizes a μ_{max} of unity (Figure 5(b)).

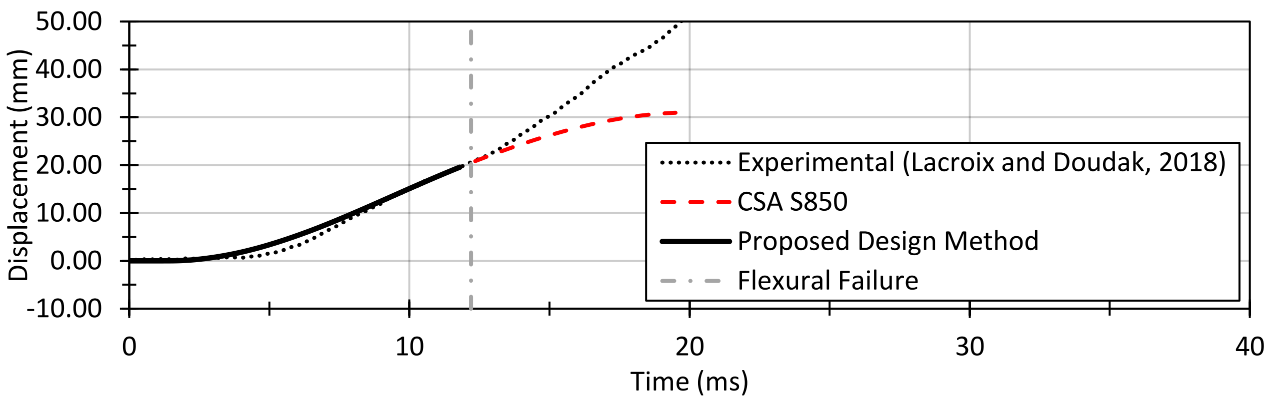

Figure 8. Predicted displacement-time histories of proposed and current design methods for glulam

Finally, the comparison between proposed and code design provisions for the CLT panels differs significantly, as shown in Figure 7(c), where the code design provisions tend to overpredict the dynamic peak resistance of the CLT panels. The discrepancies are primarily caused by the value for the *DIF* in the current blast design standard (CSA 2012).

4 Blast design of timber connections

Current provisions for timber assemblies address the design of connections in a cursory manner, where an overstrength factor is applied to ensure that failure of the connection is prevented (CSA, 2012). The objective of this design approach is to enforce the requirement that failure is reached within the load-bearing element prior to any damage in the connections. While this approach is appropriate for assemblies consisting of structural elements with inherent inelastic dissipating capabilities, such as reinforced concrete and structural steel, wood elements in flexure tend to fail in a brittle manner. Connections designed and detailed in order to contribute to the energy dissipation of the assembly through considerations for hierarchy of yielding and failure between the various components in the assembly have been shown to improve the overall performance of various timber assemblies by allowing for greater blast energies to be subjected prior to permanent damage in the wood element (Viau and Doudak, 2016; 2019; 2021a; b). Lack of consideration for connection contribution has been found to potentially lead to premature connection failure or to a design that is too conservative. Adopting a design philosophy that allows for some inelastic dissipation in connections could lead to enhanced energy dissipation. The applicability of this concept could also be extended to other loading scenarios where energy dissipation is essential. One such scenario in which this concept is heavily utilized is that of seismic design. During cyclic loading scenarios, the connections are often designed with the intent of acting as energy-dissipative fuses through yielding of steel components and fasteners, as well as ductile crushing of the wood fibres. While the nature of seismic loading is quite different than that of blast, the concept can easily be applied to increase the resiliency of wooden assemblies subjected to potential blast threats.

A capacity-based design methodology for the design of energy-dissipative connections has been outlined in Viau and Doudak (2021b), whereby ensuring that the strength of the wood element is at minimum greater than the yield strength of the connection was shown to ensure that yielding occurs in the connection prior to failure in the wood element, with an acceptable probability of wood failure that can be chosen by designer. A similar methodology has been proposed on the ultimate capacity of the connection to ensure that failure of the load-bearing element occurs prior to the ultimate failure of the connection.

While full-scale experimental testing has been conducted on light-frame stud walls (Viau and Doudak, 2016; Lacroix, et al., 2021), glulam beams and columns (Viau and

Doudak, 2021a; b), and CLT assemblies (Côté and Doudak, 2019; Viau and Doudak, 2019; 2021b) pertaining to connection design for blast, additional work is required prior to the development of proposed design methodologies for connections.

5 Conclusions

A comprehensive research program has been established in the past eleven years at the University of Ottawa's Shock Tube Test Facility for the purpose of developing a robust framework for blast design requirements and to address the scarcity in information related to this topic. The program consisted of both experimental and analytical investigations of various typical components and assemblies, including light-frame wood stud walls, glulam members, CLT panels, as well as connections in isolation and as part of timber assemblies. The outcome from these studies have generated close to a hundred full-scale experimental test results and were shown to provide representative and acceptable predictions of load-displacement relationships, peak resistances, and anticipated responses to far-field blast loads. These proposed design methods provide the necessary framework for the development of blast design provisions for timber structures, suitable for design standards such as CSA S850 (2012), ASCE/SEI 59-11 (2011), and disproportionate collapse prevention, such as Eurocode 1 (2006).

6 References

Arup (2011). "Review of international research on structural robustness and disproportionate collapse." Department for Communities and Local Government, London, UK.

ASCE (2011). "Blast Protection of Buildings." *ASCE/SEI 59-11*, American Society of Civil Engineers, Reston, VA.

Biggs, J. M. (1964). *Introduction to Structural Dynamics*, McGraw-Hill, New York, NY.

Cormie, D., Mays, G., and Smith, P. (2009). *Blast Effects on Buildings*, Thomas Telford Ltd, Reston, VA.

Côté, D., and Doudak, G. (2019). "Experimental investigation of cross-laminated timber panels with realistic boundary conditions subjected to simulated blast loads." *Engineering Structures*, 187, 444-456.

CSA (2012). "Design and assessment of buildings subjected to blast loads." *CSA S850*, CSA Group, Mississauga, ON.

CSA (2019). "Engineering design in wood." *CSA O86*, CSA Group, Mississauga, ON.

Doudak, G., Viau, C., and Lacroix, D. N. (2022). "Proposed Design Methods for Timber Members Subjected to Blast Loads." *Journal of Performance of Constructed Facilities*, 36(3), 04022020.

Ellingwood, B., Smilowitz, R., Dusenberry, D., Duthinh, D., Lew, H., and Carino, N. (2007). "Best Practices for Reducing the Potential for Progressive Collapse in Buildings." NIST Interagency/Internal Report (NISTIR), National Institute of Standards and Technology, Gaithersburg, MD.

Eurocode 1 (2006). "Eurocode 1 - Actions on structures - Part 1-7: General actions - Accidental actions." *EN 1991-1-7*, CEN.
ISE (2010). *Practical guide to structural robustness and disproportionate collapse in buildings*, Institution of Structural Engineers, London, UK.
Jacques, E., Lloyd, A., Braimah, A., Saatcioglu, M., Doudak, G., and Abdelalim, O. (2014). "Influence of high strain-rates on the dynamic flexural material properties of spruce–pine–fir wood studs." *Canadian Journal of Civil Engineering*, 41(1), 56-64.
Lacroix, D. (2013). "Behaviour of light-frame wood stud walls subjected to blast loading." MASc Thesis, University of Ottawa, Ottawa, ON.
Lacroix, D., and Doudak, G. (2015a). "Experimental and Analytical Evaluation of the Flexural Capacity of Light-Frame Wood Stud Walls Under Blast Loading - An Assessment of the Canadian Blast Design Standard Provisions." *11th International Conference on Shock & Impact Loads on Structures*, C-I Premier Conference Organisation, Ottawa, ON, 213-221.
Lacroix, D., Viau, C., Battelli, E., and Doudak, G. (2021). "Enhancing the performance of light-frame wood studs using glass fibre-reinforced polymers." *Engineering Structures*, 245, 112973.
Lacroix, D. N., and Doudak, G. (2015b). "Investigation of Dynamic Increase Factors in Light-Frame Wood Stud Walls Subjected to Out-of-Plane Blast Loading." *Journal of Structural Engineering*, 141(6), 04014159.
Lacroix, D. N., and Doudak, G. (2018). "Determining the Dynamic Increase Factor for Glued-Laminated Timber Beams." *Journal of Structural Engineering*, 144(9), 04018160.
Marchand, K. A. (2002). "BAIT, BASS & RODS Testing Results." Applied Research Associates, Prepared for the USAF Force Protection Battlelab.
Oliveira, D., Viau, C., and Doudak, G. (2022). "Behaviour of Heavy Timber Members Subjected to Sequential Shocktube-Simulated Blast Loads." *CSCE 2022 Annual Conference*, Canadian Society for Civil Engineering, Whistler, BC.
Oswald, C. J. (2005). "Component Explosive Damage Assessment Workbook (CEDAW) Methodology Manual V1.0.", Prepared for the Protective Design Center, US Army Corps of Engineers, San Antonio, TX. BakerRisk Project No. 02-0752-001.
PDC (2008). "Single Degree of Freedom Structural Response Limits for Antiterrorism Design." *Technical Report 06-08*, U.S. Army Corps of Engineers, Protective Design Center (PDC), Omaha, NE.
Poulin, M., Viau, C., Lacroix, D. N., and Doudak, G. (2018). "Experimental and Analytical Investigation of Cross-Laminated Timber Panels Subjected to Out-of-Plane Blast Loads." *Journal of Structural Engineering*, 144(2), 04017197.
Rosowsky, D. V., Yu, G., and Bulleit, W. M. (2005). "Reliability of Light-Frame Wall Systems Subject to Combined Axial and Transverse Loads." *Journal of Structural Engineering*, 131(9), 1444-1455.

Unified Facilities Criteria Program (2008). "Structures to resist the effects of accidental explosions (UFC 03-340-02).", United States of America Department of Defense, Washington, D.C.

Unified Facilities Criteria Program (2009). "Design of Buildings to Resist Progressive Collapse (UFC 04-023-03).", United States of America Department of Defense, Washington, D.C.

Viau, C. (2020). "Investigation and Optimization of Connections in Timber Assemblies Subjected to Blast Loading."PhD Dissertation, University of Ottawa, Ottawa, ON.

Viau, C., and Doudak, G. (2016). "Investigating the behaviour of typical and designed wall-to-floor connections in light-frame wood stud wall structures subjected to blast loading." *Canadian Journal of Civil Engineering*, 43(6), 562-572.

Viau, C., and Doudak, G. (2019). "Behaviour and modelling of cross-laminated timber panels with boundary connections subjected to blast loads." *Engineering Structures*, 197, 109404.

Viau, C., and Doudak, G. (2021a). "Behavior and Modeling of Glulam Beams with Bolted Connections Subjected to Shock Tube-Simulated Blast Loads." *Journal of Structural Engineering*, 147(1), 04020305.

Viau, C., and Doudak, G. (2021b). "Energy-Absorbing Connection for Heavy-Timber Assemblies Subjected to Blast Loads–Concept Development and Application." *Journal of Structural Engineering*, 147(4), 04021027.

Viau, C., Lacroix, D., and Doudak, G. "Design Considerations for Cross-Laminated Timber Panels Subjected to Simulated Blast Loads." *Proc., CSCE 2018 Annual Conference*.

Wight, N., Viau, C., and Heffernan, P. J. (2022). "Behaviour and Resistance of Glued-Laminated Timber Subjected to Impact Loading." *CSCE 2022 Annual Conference*, Canadian Society for Civil Engineering, Whistler, BC.

DISCUSSION

The paper was presented by G Doudak

F Lam received clarification that that trial-and-error loading procedures did not cause damage accumulations in the specimens and readings from dynamic load cells were able to estimate the strength of the specimen adequately.

T Tannert asked if the DIF factors were established with matched specimens. G Doudak said that matched specimens were considered at the start of the program. T Tannert said only far field conditions were considered and asked about the near field consideration. G Doudak said far field represented explosion occurring 20 to 100 m away. Near field consideration would be too complicated.

R Jockwer asked if this information can be applicable to other loadings. G Doudak said earthquake conditions may be applicable although cyclic loading should be considered. Also collapse from fire loading may be applicable. R Jockwer asked if conclusions on ductility would be applicable to these cases. G Doudak ductility consideration in this study would be out of plane only whereas seismic conditions could be both out of plane and in plane. F Lam disagreed that this information can be applicable to seismic cases. Along with the points already stated, damping considerations are important in seismic situation and this would not be considered appropriately here.

H Blass asked about the DIF for connections. G Doudak said that only one DIF for the system should be used although he disagreed with the approach as failure mode is important. H Blass said that the research is based on stud wall tests and asked how to consider system behaviour of different components. G Doudak said that different components were also tested but stud failures dictated the DIF.

U Kuhlmann received confirmation that the design was based on average strength and not the 5th percentile.

P Palma asked about the importance of considering the load reversal. G Doudak said that in design you only need to consider positive pressure but have to detail for negative pressure.

EN 1995-1-1 for CEN Formal Enquiry – The evolution of the design of timber structures

Martin Schenk, Technical University of Munich

Stefan Winter, Technical University of Munich

Keywords: Eurocode 5, standardisation, timber, design, general rules, rules for buildings

1 Introduction

This paper provides an over and insight view to the CEN Formal Enquiry draft of the European design standard EN 1995-1-1 entitled *Eurocode 5: Design of timber structures - Part 1-1: General rules - General rules and rules for buildings* [1].

With the CEN Formal Enquiry of EN 1995-1-1 in September 2023, the development of technical content for the document will be completed. This marks the end of a process, which started in 2012 with the mandate M/515 issued by the European Commission and the corresponding response of the Technical Committee CEN/TC 250 of the European Organisation for Standardisation CEN-CENELEC, see [2,3]. The aim of this process was and is to adopt the first generation of European design standards [4] to (i) the current state of the art, to (ii) implement those standards further within the harmonized European building market and to (iii) enhance the ease of use of the documents, see [5,6].

2 General

The second generation of Eurocode 5 (EC5) is structured as following:

- EN 1995-1-1: General rules – General rules and rules for buildings

The first document (part 1-1), main document of the timber design standards, contains general design rules for timber structures together with specific design rules for buildings and civil engineering timber works, see [1].

- **EN 1995-1-2: General rules – Structural Fire design**

Part 1-2 deals with the design of those timber structures which require a loadbearing and/or a separating function in the accidental situation of fire exposure. The document supplements normal temperature design given in part 1-1, see [7].

- **EN 1995-1-3: General rules – Rules for timber-concrete composite structures**

This document will be based on current CEN/TS 19103, see Table 1. After a probation time in practice, the Technical Specification (TS; see [8]) is intended to be further developed to form the third document of part 1. It will contain design rules for timber-concrete composite structures including requirements for materials, design parameters, connections and design under both quasi-constant and variable environmental conditions. Additionally, design methods accounting for e.g. temperature and timber moisture changes will be provided in Annexes.

- **EN 1995-2: Timber bridges**

The second part of Eurocode 5 contains general rules for the design of bridge structures that are made of timber or other wood-based materials in possible combination with concrete, steel or further materials, see [9].

- **EN 1995-3: Execution rules**

The third part of Eurocode 5 provides minimum requirements for fabrication, assembly and erection of timber structures designed in accordance with EN 1995 to ensure that what is built meets the requirements for mechanical resistance, serviceability, durability and fire performance, see [10].

In order to evaluate the consensus among relevant stakeholders (industry, economic actors, public authorities and civil society), CEN standards pass various formal stages [11]. Key milestones in the process of European standardisation are (a) CEN Formal Enquiry and (b) CEN Formal Vote, see [12] and Table 1. At both levels, CEN National Members are consulted. Whilst the Formal Vote acts solely for the acceptance or rejection of a standard, the technical content is assessed in the preceding Formal Enquiry. This implies that the main technical content must be finalised and included in a document at that stage. For further information on the organisation of standardisation and official procedures, see [6,13].

A stable edition of the new generation of EN 1995-1-1 is available after the final delivery of technical contents for the Formal Enquiry draft by 24 June 2022. This brand new EN 1995-1-1 for Formal Enquiry is presented below.

3 EN 1995-1-1 for CEN Formal Enquiry

3.1 Overview

Table 2 provides an overview on the structures of EN 1995-1-1 of the first [4] and second [1] generation. To harmonise the general structure of all Eurocodes, CEN/TC 250 provided a guideline in [5]. The new structure includes two new clauses – '2. Normative References' and '3. Terms, definitions and symbols' – for the whole

*Table 1. Overview on the timeline of Eurocode 5.**

	Formal Enquiry	Formal Vote	Date of availability
EN 1995-1-1	01.09.2023 – 21.12.2023	01.04.2025 – 26.05.2025	01.08.2025
EN 1995-1-2	01.09.2023 – 21.12.2023	01.04.2025 – 26.05.2025	01.08.2025
EN 1995-1-3#	under discussion	under discussion	under discussion
EN 1995-2	01.09.2023 – 21.12.2023	01.04.2025 – 26.05.2025	01.08.2025
EN 1995-3	01.09.2023 – 21.12.2023	01.04.2025 – 26.05.2025	01.08.2025

* Status: July 2022; # The document will succeed CEN/TS 19103 [8].

second generation of European Structural design standards. Additionally some headlines will be slightly adjusted, see e.g. former clause 3 of [4] and new clause 5 of [1] in Table 2.

The structure of the main part of Eurocode 5 will be extended, to include the important topic ‘fatigue’, which was historically anchored in the design of timber bridges, see new clause 10. The clause will allow the design of members under fatigue loading (e.g. machine vibrations). Furthermore the revised clause 11 on ‘connections’ will represent additional prefabrication-friendly provisions for connections free of metallic fasteners. Whereas in the former version of EN 1995-1-1, the design of bracing structures was dealt with under ‘9. Components and assemblies’, composite cross-section verification and requirements for bracing structures will be separated in future. Finally, cross-section verification of composite built-ups are mainly to be carried out according to clause 12. Stiffening structures resisting diaphragm actions, be they timber frame structures or solid timber elements, are regulated in clause 13 [1,4].

While it was easy to agree on rules that are to be added due to e.g. new developments and research findings, it seems much more difficult to agree on rules which could actually be dropped due to lack of relevance and application in practice That being said, at a first glance it seems that the provisions on ‘Structural detailing and control’ will be removed from Eurocode 5. In fact, they were reviewed and serve, mainly and where relevant, as basis for the Eurocode 5 part 3 'Execution rules’ [10].

The ‘bibliography’ as a list of non-normative references is detached from the set of Annexes in [4] (see Table 3) and added as a final register in [1] (see Table 2).

3.2 Key changes and new content

In the following, significant changes and new contents of the CEN Formal Enquiry draft compared to the current EN 1995-1-1 are presented [1,4]. The contents are presented with reservations. The document still has to be technically approved by CEN/TC 250/SC 5 before Formal Enquiry. References to background documents and respective scientific publications are added were adequate.

- **Basis of design** [14]: Clause 4 of the new Eurocode 5 draft will contain ‘general rules’, ‘principles of limit state design’ and ‘basic variables’. The environmental ef-

Table 2. Overview on the structures of generation 1 and 2 of Eurocode 5 part 1-1.

EN 1995-1-1:2010 [4]		prEN 1995-1-1:2023 [1]*	
General	1.	1.	Scope
		2.	Normative references
		3.	Terms, definitions and symbols
Basis of design	2.	4.	Basis of design
Material properties	3.	5.	Materials
Durability	4.	6.	Durability
Basis of structural analysis	5.	7.	Structural analysis
Ultimate limit states	6.	8.	Ultimate limit states
Serviceability limit states	7.	9.	Serviceability limit states
		10.	Fatigue
Connections with metal fasteners	8.	11.	Connections
Components and assemblies	9.	12.	Mechanically and glued webbed or flanged beams
		13.	Planar elements resisting diaphragm action
		14.	Foundations with timber piles
#Structural detailing and control	10.		
Annexes			Annexes
			Bibliography

* Status: July 2022; # The content has been reviewed and serves mainly as basis for new prEN 1995-3 [10].

fects described in the latter will be extensively refined. As one of such effects, categories of moisture differences within timber cross-sections will be described and determined. This will enable a distinction between global and local moisture effects. A new service class 4 for fully saturated wood, applied e.g. for the design of 'foundation with timber piles' is introduced. Whether the definition of stiffness values for structural modelling will stay in clause 4 or will be shifted to clause 7 'structural analysis' is still under discussion. Partial factors for materials will be presented according to new introduced material groups, see below [15]. Additionally, partial factors for e.g. metal fasteners in connections will be provided.

Materials: In hardly any other area has the development of construction products been as dynamic and comprehensive in recent decades as in timber construction. The rules of the second generation of Eurocode 5 will now take into account the most important of those newly developed construction products, e.g. cross laminated timber [16]. In order to maintain clarity for the user in view of the large number of different building products, materials with similar structural behaviour will be grouped together, see Figure 1. Additionally, an informative Annex (see Table 3, Annex L) for the translation of the denomination of individual material properties will be provided. In parallel to the refined definition of moisture contents, material swelling and shrinkage values for design will be given. All material related modification factors (e.g. for the consideration of volume effects) [24,25] will be provided in clause 5. Key change compared to generation 1 is the introduction of a normative Annex (see Table 3, Annex M) in which the Eurocode determines material parameters that shall be declared for the application of Eurocode design.

- **Durability**: To ensure durability over service life, the respective chapter in former version was mainly referring to an appropriate material selection. Now the clause will include further recommendations on e.g. constructive conceptions to avoid deterioration by wood-destroying fungi and insects. Additionally, resistance to corrosion will be aligned by exposure categories with [26]. This allows considering different environmental atmospheres, such as chemically treated wood.

- **Structural analysis**: Clause 7 has been controversially discussed during the drafting process. In addition to principles for structural modelling, imperfections [27] and simplified assumptions for bracing forces, the analysis of effect of actions according to 2nd order theory with Dischinger's method will be given in the clause (Status: July 2022). Thus – with the simplified estimation called Dischinger's method and the simplified methods with strength reduction factors accounting for stability problems (k_c and k_m) in clause 8 – two alternative methods for stability problems are represented in parallel in the code [28].

- **Ultimate limit states** (ULS): The verification of ultimate limit states will be based on failure of cross-sections of members (clause 8), of composite members (clause 12), failure of connections (clause 11) and failure of planar elements resisting diaphragm actions (clause 13). Clause 8 will be extensively revised to cover today's major timber products as previously presented.

The former verification of compressive actions perpendicular to grain has been accounting for ultimate limit states but not respective deformations. However, the latter in particular have a significant influence on the design of multi-storey timber buildings. With generation 2, engineers and clients will now be able to verify compressive effects of actions perpendicular to grain according to three performance classes with different permissible deformation limits [29].

The definition of the strength value to be used in the shear verifications will also be revised to harmonize differing values in the Member States [30].

Additional regulations for members with special geometries will be enhanced.

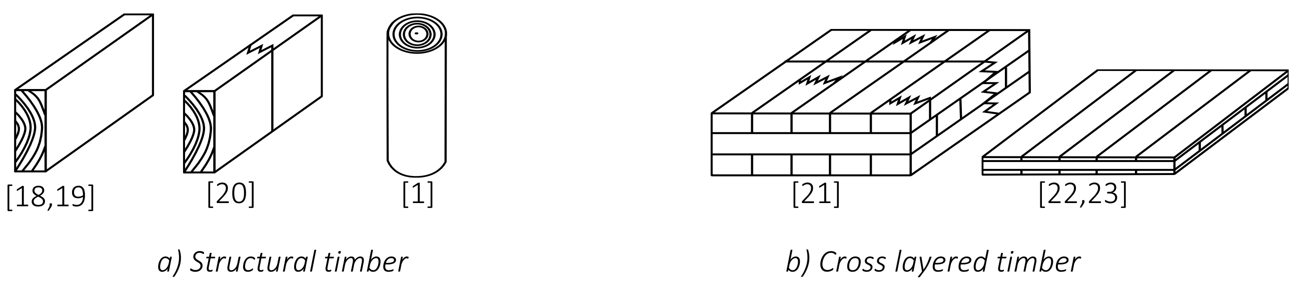

Figure 1. Examples for materials grouped according similar structural behaviour (Status: July 2022; Figure drafted according to [17]).

Among others, rules for holes in beams with circular and rectangular cross-sections are provided [31-33].

An important key development in Eurocode 5 of the second generation is the consistent incorporation of verifications with reinforcing measures for cross-section design. In timber construction, detailing easily can lead to problems. However, planners have so far lacked standardised regulations on e.g. reinforcement in case of actions perpendicular to grain [34]. In generation 2, this is now resolved by adding the reinforcement chapters directly after the respective general cross-section verification [35- 37].

- **Serviceability limit states** (SLS): The verification of serviceability limit states is based on criteria concerning deformations and vibrations aiming at durability, functionality and appearance of the structure as well as at limiting possible discomfort for the user. Whereas in the former version of EC5, the slip modulus for connections was defined in the clause on SLS, this information will be given in future in clause 11 for connections.

In the former draft of the Eurocode, the determination of the respective load combination within the deformation calculation of structures was left open. Now the engineer will receive explicit combinations for checking the serviceability criterion. There, creep is taken into account and also the influences from composite materials.

As previously shown at cross-section verifications, an urgently needed deformation criterion for compressive actions perpendicular to the grain will be added to the new document.

The vibration verification of residential floors remains based on the natural frequency, acceleration and velocity criteria. To the frequency criterion, simplified methods will be added to take into account effects of continuous beams, two-dimensional mass and stiffness and of flexible supports. The subjective perception of vibrations was integrated into the verifications via a so-called response factor. In future, planners and builders will be able to choose between six performance classes and thus design according to the expected use. [38-40]

Connections [41]: Like clause 8 and the material section, the chapter on connections will be revised to cover most important product developments. The scope of application will be expanded from dowel-type fasteners [42] (nails [43], staples [44], dowels, bolts and screws) and shear connectors (split-ring, shear plate, toothed-plate, punched metal plate fasteners) to include bonded-in rods [45], brittle failure [46-54] (see Table 3, Annex A of [4]) and carpentry connections [55]. Another product that has been discussed and will be integrated so far are so-called expanded-tube fasteners.

The new substructure divides connection design clearly to e.g. the axial resistance, lateral resistance and interaction of both, the slip moduli [56], rules for end grain and perpendicular to grain application and the possible requirements in the case that fasteners are used as reinforcement. Regulations for tolerances in execution are integrated in prEN 1995-3 [10,57,58].

- **Mechanically and glued webbed or flanged beams**: The contents of the former chapter components and assemblies, if not moved because relevant for bracing (see clause 7) and diaphragm actions (see clause 13), will be slightly revised [59].

- **Planar elements resisting diaphragm action:** The new draft of the Eurocode will take into account that the racking resistance of buildings depends not only of the racking resistance of walls [60], but always relates to the whole structural system (i.e. also to floors and roofs). As already known from the standard for concrete structures, basic principles for the load distribution in the ground plan of timber buildings will be given.

Load bearing capacity and deformations of timber frame structures with and without openings in single-story structures will be calculable. The same applies to the load-bearing capacity of solid timber elements, e.g. made of cross-laminated timber.

Deformation calculation of structures embedded in a global overall structure with different stiffness properties are currently under discussion and will be added to the document as informative Annex Y for monolithic planar elements resisting diaphragm actions [61] (see Table 3).

- **Foundations with timber piles** [62,63]: The new document will cover the design of foundations with timber piles, i.e. requirements for durability, guidance for cross-section verifications and for stability. Assistance for the determination of product properties, which are not yet covered by a harmonized European product specification, will probably be given in an informative Annex, see Table 3.

3.3 The pursuit of 'ease of use'

One of the most discussed issues in the Eurocode standardisation process is what exact content belongs in a design standard.

CEN/TC 250 formulated the enhanced 'ease of use' as one of the most important principles for the work as a code writer. This includes (1) improved structure and clarity, (2) clear interlinkage of provisions, (3) harmonization of nationally determined parameters, (4) reduction of alternative application rules, (5) deletion of rules with low relevance for practice as well as (6) explanation of the mechanical background of formulas.

'Practitioners' are defined as primary target audience. Practitioners are to be understood as competent civil, structural and geotechnical engineers. Typically, they are experienced qualified professionals able to work autonomously in relevant fields, see [5].

However, it is precisely the implementation of (5) and (6) that often leads to wide-ranging discussions about what content must be in included in a design standard. Two general positions typically emerge from these discussions:

(I) The standard serves as a guideline for the designer. It should be as detailed as possible, i.e. by providing specific examples, covering all of the available products or provide detailed calibration options for each calculation method.

(II) The standard must provide principles and boundary conditions needed for design. Detailing is only needed where safety relevant, i.e. specific examples run the risk of being mistakenly generalized, the standard should cover the main 80% of applied products on site, calculation methods should only be provided where they help the designer in at least 80% of the application cases, otherwise competent engineers may decide for a method independently.

How controversially this is discussed can clearly be observed on the currently quite long list of Annexes of Eurocode 5, see Table 3.

Only normative Annexes have the same legally binding character as the main document. The National Standards Institutes may decide on the applicability of informative Annexes in their respective National Annex [5].

The Annexes of generation 2 will provide extended design rules for robustness (Annex A) [64], cross laminated timber (Annex F), connections with intermediate layers (Annex K) and laminated deck plates (Annex P). Fasteners (punched metal plate fasteners in Annex I and three-dimensional connectors in Annex J), which are not the focus of engineers today, will be moved to normative Annexes. Built-up columns (Annex E) represent a very special application case. Also, the design rules for foundations with timber piles (Annex R) and expanded tube fasteners (Annex O) are of higher importance mainly for a specific group of member states and therefore not in the main document. The verification of planar elements resisting diaphragm actions under extended boundary conditions will be given in Annex U.

Additional calculation methods for the determination of stiffness of composite structures (Annex B), buckling lengths and bracing loads (Annex C) and internal forces (Annex D) will be part of the document [65]. An extended calculation method for the vibrational behaviour of floors will be added in Annex G. Annex H will provide more in-depth information on the calculation of compressive load-bearing capacity of screws taking into account stability phenomena. Information on numerical analysis for uni-directional timber elements will be given in Annex Q. The deformation calculation of planar elements resisting diaphragm actions (Annex Y) has been described above.

With Annex M, Eurocode 5 will provide an interface between the product and the design standards by declaring required material input parameters for design. The transposition of different product properties will be provided by the preceding Annex L. Test methods for product properties or simplified declarations via classes, which are not covered by a European Product Specification so far, will be given in Annex N and Annex S. It is common knowledge that test methods or product classes have no place in a European design standard. But in order to prevent the standstill in the European product standards family from spreading to the design standards, this work-around might be chosen. Informative annexes allow for swift correction or withdrawal in the case of a change of status for construction products standards.

In the end, consensus building is a journey [5]. Considering that the main document for Formal Enquiry will have about 290 pages plus approximately 180 pages of Annexes, a lively discussion about necessary contents is still required. Both positions, (I) and (II) will need to find a common ground.

4 Conclusions and outlook

The importance and scope of the work of all experts involved must not be forgotten, even if many discussions seem to be repeatedly lengthy. Eurocode 5, as part of the Structural Eurocode family, has a decisive influence on the European building market. Through more than 3 million enterprises, the European construction sector provides 18 million jobs and is responsible for 9 % of the European gross domestic product (GDP), see [66].

Looking at the first generation of Eurocodes, it can be stated that these standards existed for a good 20 years. The insight into the new EN 1995-1-1 for CEN Formal Enquiry is therefore a look into the future of an entire generation of civil engineers. And therefore, it is also now the time to take a close look to the draft and examine the final technical content of Eurocode 5.

Acknowledgements

Many thanks to every person who is actively supporting the process of evaluation of the Eurocodes in the committees, preparation of research & development reports, background documents, financial support, review of work stages, etc. Special thanks to Swedish Standards Institute (SIS), the secretary of SC 5 Annika Stenmark and her colleagues, working with great professionalism.

Figure 2. The second generation of Structural Eurocodes (©European commission).

Table 1. Overview on the Annexes of generation 1 and 2 of Eurocode 5 part 1-1.

EN 1995-1-1:2010 [4]	prEN 1995-1-1:2023 [1]*
	Annex A (*informative*) Additional guidance for increasing the robustness of timber structures
(informative) Annex A Block shear and plug shear failure at multiple dowel-type steel-to-timber connections	
(informative) Annex B Mechanically jointed beams	*Annex B* (*informative*) Mechanically jointed beams
	Annex C (informative) Stability and bracing of members and structural systems
	Annex D (normative) Buckling of beam columns – non-linear method
	Annex E (informative) Built-up columns
	Annex F (normative) Additional design provisions for cross laminated timber (CLT)
	Annex G (informative) A general method for vibration analysis of floors
	Annex H (informative) Characteristic load-carrying capacity of screws or rods in axial compression
	Annex I (normative) Connections with punched metal plate fasteners
	Annex J (normative) Design of three-dimensional connectors
	Annex K (normative) Connections with interlayers
	Annex L (informative) Denomination of strengths, stiffnesses, densities, forces, moments and stresses
	Annex M (normative) Material and product properties for design
	Annex N (informative) Classes and determination of material properties
	Annex O (informative) Connections with expanded tube fasteners
	Annex P (normative) Laminated timber decks
	Annex Q (normative) Numerical analysis for uni-directional timber ele-

	ments *Annex R (normative)* Foundations with timber piles *Annex S (informative)* Requirements on logs and pile extensions used as foundation piles *Annex T (informative)* Lateral displacement of multi-storey monolithic shear walls and single-storey segmented shear walls *Annex U (normative)* Framed walls with combined anchorage
(informative) Annex D #Bibliography	

* Status: July 2022; # The Bibliography of [1] will be provided as individual index, see Table 2 and [5].

5 References

[1] CEN/TC 250/SC 5 (ed.) (unpublished): prEN 1995-1-1 for Formal Enquiry - Eurocode 5: Design of timber structures - Part 1-1: General rules - General rules and rules for buildings. Comité Européen de Normalisation (CEN), Brussels, Belgium.

[2] European Commission (ed.) (2012): M/515 EN – Mandate for amending existing Eurocodes and extending the scope of structural Eurocodes. Enterprise and industry directorate-general, Brussels, Belgium.

[3] CEN/TC 250 (ed.) (2022): N993 Response to Mandate M/515 – Towards a second generation of EN Eurocodes. Comité Européen de Normalisation (CEN), Brussels, Belgium.

[4] CEN-CENELEC (ed.) (2010): EN 1995 1-1: Eurocode 5. Design of timber structures – Part 1-1: General – Common rules and rules for buildings. Comité Européen de Normalisation (CEN), Brussels, Belgium.

[5] CEN/TC 250 (ed.) (2021): N1250 Policy guidelines and procedures for CEN/TC 250 Structural Eurocodes. Comité Européen de Normalisation (CEN), Brussels, Belgium.

[6] Kleinhenz M., Winter S., Dietsch P. (2016): Eurocode 5 - a halftime summary of the revision process. World Conference on Timber Engineering (WCTE).

[7] CEN/TC 250/SC 5 (ed.) (unpublished): prEN 1995-1-2 for Formal Enquiry - Eurocode 5: Design of timber structures - Part 1-2: General rules – Structural fire design. Comité Européen de Normalisation (CEN), Brussels, Belgium.

[8] CEN-CENELEC (ed.) (2021): CEN/TS 19013: Eurocode 5: Design of Timber Structures – Structural design of timber-concrete composite structures – Common rules and rules for buildings. Comité Européen de Normalisation (CEN), Brussels, Belgium.

[9] CEN/TC 250/SC 5 (ed.) (unpublished): prEN 1995-3 for Formal Enquiry - Eurocode 5: Design of timber structures - Part 2: Timber bridges. Comité Européen de Normalisation (CEN), Brussels, Belgium.

[10] CEN/TC 250/SC 5 (ed.) (unpublished): prEN 1995-3 for Formal Enquiry - Eurocode 5: Design of timber structures - Part 3: Execution rules. Comité Européen de Normalisation (CEN), Brussels, Belgium.

[11] CEN-CENELEC (ed.) (2022): Enquiry/Formal Vote - Practice of voting. https://boss.cen.eu/reference-material/guidancedoc/pages/fvuapvoting, Status: 26 Feb 2022, Comité Européen de Normalisation (CEN), Brussels, Belgium.

[12] CEN-CENELEC (ed.) (2020): Internal Regulations Part 2 - Common rules for standardization work. Comité Européen de Normalisation (CEN), Brussels, Belgium.

[13] Schenk M., Winter S. (2021): Second generation of Eurocode 5 – Publication schedule and interface between design and product standards. World Conference on Timber Engineering (WCTE).

[14] CEN/TC 250/SC 5 (ed.) (2020): N1245 SC5.T3 Final BGD prEN EN 1995-1-1, subtask 8 Basis of design. Comité Européen de Normalisation (CEN), Brussels, Belgium.

[15] Jockwer R., Fink G., Köhler J. (2020): Review of the reliability of timber structures in 2020s. International Network on Timber Engineering Research (INTER).

[16] CEN/TC 250/SC 5 (ed.) (2019): N1094 SC5.T1 FIN Background doc EN 1995-1-1 on CLT. Comité Européen de Normalisation (CEN), Brussels, Belgium.

[17] CEN-CENELEC (ed.) (2013): EN 14080: Timber structures – Glued laminated timber and glued solid timber – Requirements. Comité Européen de Normalisation (CEN), Brussels, Belgium.

[18] CEN-CENELEC (ed.) (2019): EN 14081-1: Timber structures – Strength graded structural timber with rectangular cross section – Part 1: General requirements. Comité Européen de Normalisation (CEN), Brussels, Belgium.

[19] CEN-CENELEC (ed.) (2013): EN 1912: Structural timber – Strength classes – Assignment of visual grades and species. Comité Européen de Normalisation (CEN), Brussels, Belgium.

[20] CEN-CENELEC (ed.) (2014): EN 15497: Structural finger jointed solid timber – Performance requirements and minimum production requirements. Comité Européen de Normalisation (CEN), Brussels, Belgium.

[21] EOTA (ed.) (2015): EAD 130005-00-0304: Solid wood slab element to be used as structural element in buildings. European Organisation for Technical Assessment (EOTA), Brussels, Belgium.

[22] CEN-CENELEC (ed.) (2015): EN 13986: Wood-based panels for use in construction – Characteristics, evaluation of conformity and marking. Comité Européen de Normalisation (CEN), Brussels, Belgium.

[23] CEN-CENELEC (ed.) (2011): EN 13353: Solid wood panels (SWP) – Requirements. Comité Européen de Normalisation (CEN), Brussels, Belgium.

[24] Frese M., Blaß H. J. (2016): Reliability of Large Glulam Members - Part 1: Data for the Assessment of Partial Safety Factors for the Bending Strength. International Network on Timber Engineering Research (INTER).

[25] Frese M., Egner S., Blaß H. J. (2017): Reliability of large glulam members Part 2: Data for the assessment of partial safety factors for the tensile strength. International Network on Timber Engineering Research (INTER).

[26] CEN-CENELEC (ed.) (2012): EN ISO 9223: Corrosion of metals and alloys – Corrosivity of atmospheres – Classification, determination and estimation (ISO 9223:2012). Comité Européen de Normalisation (CEN), Brussels, Belgium.

[27] Kuhlmann U., Töpler J. (2021): Imperfections of slender glulam beams. International Network on Timber Engineering Research (INTER).

[28] CEN/TC 250/SC 5 (ed.) (2020): N1226 SC5.T3 Final BGD prEN EN 1995-1-1 subtask 3-1 Stability and bracing. Comité Européen de Normalisation (CEN), Brussels, Belgium.

[29] CEN/TC 250/SC 5 (ed.) (2020): N1230 SC5.T3 Final BGD prEN EN 1995-1-1 subtask 3-2 Compression perp. Comité Européen de Normalisation (CEN), Brussels, Belgium.

[30] CEN/TC 250/SC 5 (ed.) (2022): N1561 SC5_WG3_SG3 - Shear verification. Comité Européen de Normalisation (CEN), Brussels, Belgium.

[31] Tapia Camú C., Aicher S. (2017): Improved Design Equations for the Resultant Tensile Forces in Glulam Beams with Holes. International Network on Timber Engineering Research (INTER).

[32] Danzer M., Dietsch P., Winter S. (2018): Round Holes in Glulam Beams Arranged Eccentrically or in Groups. International Network on Timber Engineering Research (INTER).

[33] CEN/TC 250/SC 5 (ed.) (2020): N1233 SC5.T3 Final BGD prEN EN 1995-1-1 subtask 4 Holes in beams. Comité Européen de Normalisation (CEN), Brussels, Belgium.

[34] Dietsch P., Rodemeier S., Blaß H.J. (2019): Transmission of Perpendicular to Grain Forces Using Self-tapping Screws. International Network on Timber Engineering Research (INTER).

[35] Dietsch P. (2016): Reinforcement of Timber Structures - a new section for Eurocode 5. World Conference on Timber Engineering (WCTE).

[36] CEN/TC 250/SC 5 (ed.) (2019): N1095 SC5.T1 FIN Background doc EN 1995-1-1 on Reinforcement. Comité Européen de Normalisation (CEN), Brussels, Belgium.

[37] Danzer M., Dietsch P., Winter S. (2020): Shrinkage behaviour of reinforced glulam members. International Network on Timber Engineering Research (INTER).

[38] Abeysekera I., Hamm P., Toratti T., Lawrence A. (2018): Development of a Floor Vibration Design Method for Eurocode 5. International Network on Timber Engineering Research (INTER).

[39] CEN/TC 250/SC 5 (ed.) (2020): N1242 SC5.T3 Final BGD prEN EN 1995-1-1, subtask 7 Vibrations. Comité Européen de Normalisation (CEN), Brussels, Belgium.

[40] Hamm P., Marcroft J., Toratti T. (2020): Vibrations of floors – Comparison of measured data and suggested design, International Network on Timber Engineering Research (INTER).

[41] CEN/TC 250/SC 5 (ed.) (2021): N1481 SC5.T5 Final BGD Connections, General. Comité Européen de Normalisation (CEN), Brussels, Belgium.

[42] CEN/TC 250/SC 5 (ed.) (2021): N1482 SC5.T5 Final BGD Connections, Staples. Comité Européen de Normalisation (CEN), Brussels, Belgium.

[43] CEN/TC 250/SC 5 (ed.) (2021): N1483 SC5.T5 Final BGD Connections, Bonded-in rods. Comité Européen de Normalisation (CEN), Brussels, Belgium.

[44] Blass H. J., Sandhaas C., Meyer N. (2017): Steel-to-Timber Connections: Failure of Laterally Loaded Dowel-Type Fasteners. International Network on Timber Engineering Research (INTER).

[45] Sandhaas C., Görlacher R. (2017): Nailed joints: Investigation on Parameters for Johansen Model. International Network on Timber Engineering Research (INTER).

[46] Yurrita M., Cabrero J. M. (2017): The Embedment Strength as a System Property. International Network on Timber Engineering Research (INTER).

[47] Yurrita M., Cabrero J. M. (2018): Multiple Shear Plane Timber Connections with Slotted-in Steel Plates and Dowel-type Fasteners: A Study of the Brittle Failure Mode in the Parallel-to-grain Direction. International Network on Timber Engineering Research (INTER).

[48] Yurrita M., Cabrero J. M. (2018): Performance of the Different Models for Brittle Failure in the Parallel-to-Grain Direction for Connections with Dowel-Type Fasteners. International Network on Timber Engineering Research (INTER).

[49] Yurrita M., Cabrero J. M. (2019): Effective Thickness of the Wood Member in a Timber-to-steel Connection with Large Diameter under Brittle Failure. International Network on Timber Engineering Research (INTER).

[50] Blass H. J., Flaig M., Meyer N. (2019): Row Shear and Block Shear Failure of Connections with Axially Loaded Screws. International Network on Timber Engineering Research (INTER).

[51] Yurrita M., Cabrero J. M. (2019): New Analytical Model for Brittle Failure in the Parallel-to-grain Direction of Timber Connections with Large Diameter Fasteners. International Network on Timber Engineering Research (INTER).

[52] Yurrita M., Cabrero J. M. (2020): Brittle failure mode of timber connections with one row of fasteners loaded parallel-to-grain: a new model for splitting failure. International Network on Timber Engineering Research (INTER).

[53] Yurrita M., Cabrero J. M. (2020): Experimental analysis of brittle failure in timber-to-steel connections with small diameter fasteners loaded parallel-to-grain. International Network on Timber Engineering Research (INTER).

[54] Yurrita M., Cabrero J. M. (2021): New analytic model for plug shear of timber connections with small diameter dowel-type fasteners in the parallel-to-grain direction. International Network on Timber Engineering Research (INTER).

[55] CEN/TC 250/SC 5 (ed.) (2021): N1484 SC5.T5 Final BGD Connections, Carpentry. Comité Européen de Normalisation (CEN), Brussels, Belgium.

[56] Jockwer R., Jorrisen A. (2018): Load-Deformation Behaviour and Stiffness of Lateral Connections with Multiple Dowel Type Fasteners. International Network on Timber Engineering Research (INTER).

[57] Toratti T. (2015): An Execution Standard Initiative for Timber Construction. International Network on Timber Engineering Research (INTER).

[58] Frese M., Jordan M. (2018): Deviations Between Planned and Actual Position of Wood Screws - Consequences for their Spacing. International Network on Timber Engineering Research (INTER).

[59] Aicher S., Stritzke C. (2017): Glued Thin-webbed Beams - Amendments to EC 5 for Safe ULS Design. International Network on Timber Engineering Research (INTER).

[60] CEN/TC 250/SC 5 (ed.) (2021): N1239 SC5.T3 Final BGD prEN EN 1995-1-1, subtask 6 Racking resistance of walls. Comité Européen de Normalisation (CEN), Brussels, Belgium.

[61] Casagrande D., Doudak G., Masroor M., 2021): A proposal for capacity-based design of multi-storey CLT buildings. International Network on Timber Engineering Research (INTER).

[62] CEN/TC 250/SC 5 (ed.) (2021): N1236 SC5.T3 Final BGD prEN EN 1995-1-1, subtask 5 Foundation piles. Comité Européen de Normalisation (CEN), Brussels, Belgium.

[63] Ravenshorst G., van Dalen J., Steiger R., van de Kuilen, J.-W. (2021): Connection of timber foundation piles to concrete extension piles. International Network on Timber Engineering Research (INTER).

[64] Palma P., Steiger R., Jockwer R. (2019): Addressing Robustness in the 2nd-Generation EN 1995-1-1 Eurocode 5. International Network on Timber Engineering Research (INTER).

[65] Abeysekera I., Feltham I., Lawrence A. (2021): Buckling of slender timber beam-columns under combined loading, including creep. International Network on Timber Engineering Research (INTER).

[66] CEN-CENELEC (ed.) (2020): CEN and CENELEC Position Paper on the implementation and future of the Construction Product Regulation, Comité Européen de Normalisation (CEN), Brussels, Belgium.

DISCUSSION

The paper was presented by M Schenk

R Jockwer asked what will happen to new knowledge and content as the draft is already being finalized. M Schenk said other CEN documents or amendment documents may be suitable. National Annex and European Technical Approvals are also available; National level for design is also available. S Winter stated that there will not be any amendments within a 2 year period and totally new knowledge is beyond the "state of the art".

G Doudak asked about the logic behind putting some information in the Annex. M Schenk said that normative alternatives are to be avoided and the information in the Annex should be supplemental with provisions of expanded or extended methods.

T Tannert asked what would happen if a single country vote NO to the approval process in 2025. M Schenk said the vote is based on majority and it is also a weighted vote.

U Kuhlmann stated that if the approved version has some mistakes, then possibility of early amendments should be available.

G Hochreiner and M Schenk discussed the target user group of the Eurocode as well-trained engineers with 3 years of experience.

P Dietsch commented about the number of added pages being very large and stated that the suitability of items in the Annex which are only relevant for few countries should be reviewed. A National Annex might be more appropriate. M Schenk agreed in principle. However, he stated the number of pages may not be important as we have electronic version. He agreed that it is more important to consider what do we need in the code.

S Aicher questioned why an informative annex is needed for expanded tube fasteners as a national annex may sufficeS Winter stated that this issue was considered in the past as some countries may need this type of information and some may not. S Aicher also stated that it is questionable to place a proprietary system in a code even more if the used products have no harmonized standards or ETAs.

M Fragiacomo stated that Annex M is important for seismic design. EC 8 specifically asked for this information.

4 INTER Notes, Bad Aibling 2022

Compression resistance of large diameter threaded rods inserted perpendicular to grain

Robert Jockwer, Division of Structural Engineering, Chalmers University of Technology, Gothenburg, Sweden

Keywords: Screws, threaded rods, buckling, reinforcement

1 Introduction

Fully threaded screws are frequently used to reinforce timber in compression perpendicular to the grain, e.g. at beam supports or load introduction points.

Studies and tests on compression perpendicular to the grain reinforcement by fully threaded screws were carried out by Bejtka (2005) and a design approach is proposed (Bejtka, Blaß, 2006). Different failure modes are distinguished such as pushing-in and buckling of the screw as well as compression failure in the surrounding timber. Bejtka validated the design models with tests on groups of two to six screws with outer thread diameter d = 6.5 – 10 mm and screwed-in length between 180–400 mm. The design approach was suggested by various technical approvals and is incorporated into the 2022 version of the Eurocode 5 draft. The design approach is valid for screws of diameter d = 6 – 12 mm.

In this note, tests results on screwed-in threaded rods with outer thread diameter d = 20 mm are presented in order to show the validity of the design approach also for screw diameters larger 10 mm.

2 Methods

Two different test campaigns were carried out at ETH Zurich and EMPA Dübendorf in 2014 and 2015, respectively. All tests were carried out on SFS WB-T 20 mm threaded rods with wood thread along the screw-in length and metric thread along the load introduction.

- Tests on single threaded rods with different screw-in length of l = 520 mm, 670 mm, and 920 mm. The average timber density was ρ = 460 kg/m^3 with a moisture content of approx. 10%.
- Tests on groups of 2, 4, and 6 threaded rods with constant screw-in length of 800 mm. The steel plate for load introduction was flush with the timber causing a

joint reaction of rod and timber. The spacing and distances between the rods was a_1 = 80 mm, a_2 = 60 mm, and a_{4c} = 50 mm.

The load application was in all tests through thick steel plates supported on long nuts on the metric thread of the rods. A clamped support of the rods could be achieved. The load was measured through the applied hydraulic pressure. The deformation was measured through LVDT at different positions at the loading plate and the timber.

The tests showed a ductile failure behaviour with an over-proportional increase in deformation when reaching ultimate load. The tests on single rods showed a local maximum before contact between timber and loading plate. The compression resistance of the groups of rods was calculated by reducing the load with the compression resistance of the timber under the loading plate with $f_{c,90,mean}$ = 5 N/mm^2.

3 Results and discussion

The test results are shown on Figure 1.1 for the series on single rods (left) and groups of rods (right).

In the series of tests on single threaded rods, resistances of approx. 150-175 kN per threaded rod were achieved. After reaching these load levels, larger indentations occurred in the timber and a further increase in resistance was possible in the further course of loading when the loading plate was in full contact with the timber. The rods with screw-in length *l* = 520 mm failed in pushing-in. The opened specimens showed a clear buckling of the threaded rods when the screw-in length was *l* ≥ 670 mm.

In the tests on groups of threaded rods, resistances in the range of 140-180 kN per threaded rod were achieved. There is no clear trend in the decrease of the resistances with increasing number of threaded rods. The groups of rods reached approx. 84-96% of the resistance of a single rod. There is a decrease in the scatter of the values of the resistances with increasing number of rods.

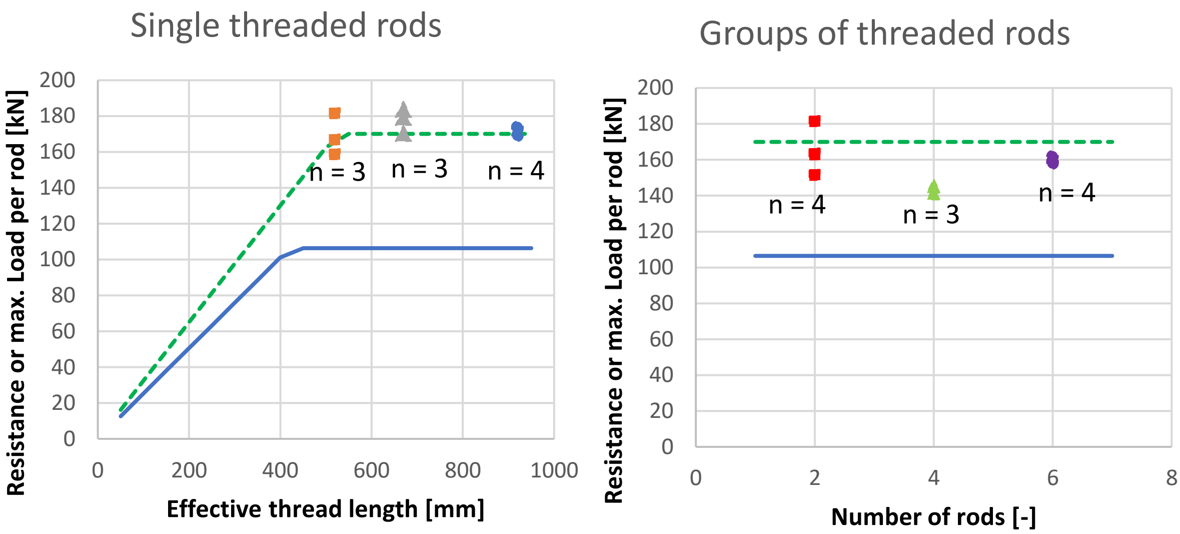

Figure 1.1. Test results and comparison with characteristic curves from the design model as well as mean fit.

In Figure 1.1 it can be seen that the test values are considerably higher than the characteristic curve of the design model, that were derived using the following parameters for GL28h and the WB-T 20 rods (Z-9.1-777): $\boldsymbol{\rho_k}$ = 425 kg/m^3, f_{uk} = 800 N/mm^2, and $f_{ax,k} = 70 \cdot 10^{-6}\, \rho_k^2$. Curves of mean values can be fitted to the test data based on the actual timber density of the specimens. For the fit a fully clamped support condition is assumed for the critical load and the following parameters are chosen: and $d_{ef} = 1.1 \cdot d_{core}$, f_u = 950 N/mm^2, $f_{ax,mean} = 90 \cdot 10^{-6}\, \rho_{mean}^2$.

4 Conclusions

The following conclusions can be drawn:

- The tests on single and groups of multiple threaded rods confirm the design models in the EC5 draft for screw buckling also for large diameters of d = 20 mm. The characteristic values from design models calculated with declared values are considerably lower and conservative compared to the test results.
- The trend is that the bi-linear load-deformation behaviour becomes more pronounced as the number of threaded rods increases, i.e. when the load-bearing resistance is reached, a clear flow plateau is formed and the variability tends to decrease. It appears that with a larger number of threaded rods, a certain degree of load redistribution between the threaded rods is possible.
- There is no pronounced trend in the decrease of the effective bearing resistance due to a group effect with increasing number of threaded rods. In the tests the groups of rods reached approx. 90% of the resistance of a single rod.

5 Acknowledgement

It is thanked Roth Burgdorf AG, Switzerland for the production and sponsoring of the test specimens. The tests were carried out at Empa Dübendorf and ETH Zurich, Switzerland. The support for planning and execution of the tests by Peter Gfeller, Andrea Frangi, Robert Widmann, and René Steiger is gratefully acknowledged. It is thanked T. Ackermann for his contributions in the frame of his master thesis.

6 References

Bejtka I. (2005), Verstärkung von Bauteilen aus Holz mit Vollgewindeschrauben. PhD Thesis, Fakultät für Bauingenieur-, Geo- und Umweltwissenschaften, Universtität Karlsruhe, Karlsruhe, Germany.

Bejtka I., Blaß H. J. (2006), Self-tapping screws as reinforcement in beam supports. In: Proc. of CIB-W18 Meeting 39, Florence, Italy, Paper No. CIB-W18/39-7-2.

Z-9.1-777 (2010), Gewindestangen mit Holzgewinde als Holzverbindungsmittel, Allgemeine bauaufsichtliche Zulassung, Deutsches Institut für Bautechnik.

5 Peer review of papers for the INTER Proceedings

Experts involved:

The reviews are undertaken by long standing members of the INTER group which is a community of experts in the field of timber engineering.

Procedure of peer review

- Submission of manuscripts: all members of the INTER group attending the meeting receive the manuscripts of the papers at least four weeks before the meeting. Everyone is invited to read and review the manuscripts especially in their respective fields of competence and interest.

- Presentation of the paper during the meeting by the author

- Comments and recommendations of the experts, discussion of the paper

- Comments, discussion and recommendations of the experts are documented in the minutes of the meeting and are printed on the front page of each paper.

- Final acceptance of the paper for the proceedings with

    - no changes
    - minor changes
    - major changes
    - or reject

- Revised papers are to be sent to the editor of the proceedings and the chairman of the INTER group

- Editor and chairman check, whether the requested changes have been carried out.

6 Meetings and list of all CIB W18 and INTER Papers

CIB Meetings:

1 Princes Risborough, England; March 1973
2 Copenhagen, Denmark; October 1973
3 Delft, Netherlands; June 1974
4 Paris, France; February 1975
5 Karlsruhe, Federal Republic of Germany; October 1975
6 Aalborg, Denmark; June 1976
7 Stockholm, Sweden; February/March 1977
8 Brussels, Belgium; October 1977
9 Perth, Scotland; June 1978
10 Vancouver, Canada; August 1978
11 Vienna, Austria; March 1979
12 Bordeaux, France; October 1979
13 Otaniemi, Finland; June 1980
14 Warsaw, Poland; May 1981
15 Karlsruhe, Federal Republic of Germany; June 1982
16 Lillehammer, Norway; May/June 1983
17 Rapperswil, Switzerland; May 1984
18 Beit Oren, Israel; June 1985
19 Florence, Italy; September 1986
20 Dublin, Ireland; September 1987
21 Parksville, Canada; September 1988
22 Berlin, German Democratic Republic; September 1989
23 Lisbon, Portugal; September 1990
24 Oxford, United Kingdom; September 1991
25 Åhus, Sweden; August 1992
26 Athens, USA; August 1993
27 Sydney, Australia; July 1994
28 Copenhagen, Denmark; April 1995
29 Bordeaux, France; August 1996
30 Vancouver, Canada; August 1997
31 Savonlinna, Finland; August 1998
32 Graz, Austria; August 1999

33 Delft, The Netherlands; August 2000
34 Venice, Italy; August 2001
35 Kyoto, Japan; September 2002
36 Colorado, USA; August 2003
37 Edinburgh, Scotland; August 2004
38 Karlsruhe, Germany; August 2005
39 Florence, Italy; August 2006
40 Bled, Slovenia; August 2007
41 St. Andrews, Canada; August 2008
42 Dübendorf, Switzerland; August 2009
43 Nelson, New Zealand; August 2010
44 Alghero, Italy; August 2011
45 Växjö, Sweden; August 2012
46 Vancouver, Canada; August 2013

INTER Meetings:

47 Bath, United Kingdom; August 2014
48 Šibenik, Croatia; August 2015
49 Graz, Austria; August 2016
50 Kyoto, Japan; August 2017
51 Tallinn, Estonia; August 2018
52 Tacoma WA, USA; August 2019
53 Online Meeting; August 2020
54 Online Meeting; August 2021
55 Bad Aibling, Germany 2022

The titles of the CIB W 18 and INTER papers (starting from 2014) are included in the complete list of CIB/INTER papers: http://holz.vaka.kit.edu/392.php